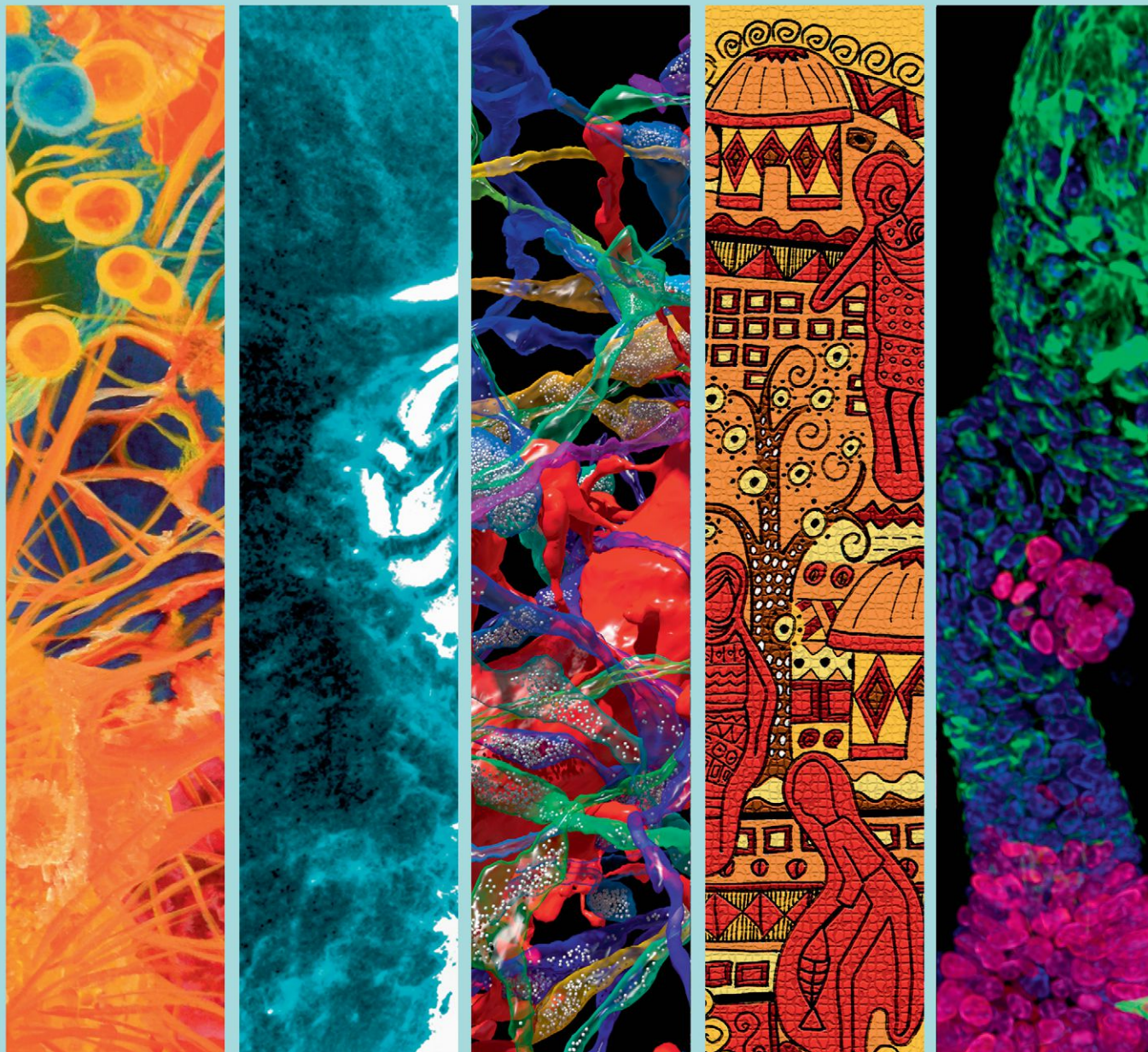


Cell

Best of 2015



Featuring Collections of SnapShots and Timelines

A MAJOR LEAP FORWARD IN PHENOTYPING

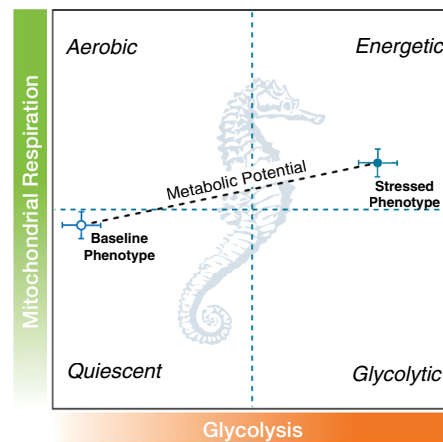
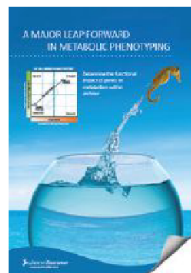
Determine the functional impact of genes on metabolism in an hour



XFp Cell Energy Phenotype Test Kit

Using as few as 15,000 live cells and an XFp Analyzer, the XF Cell Energy Phenotype Test identifies your cells' metabolic phenotype as well as their metabolic potential - the utilization of mitochondrial respiration and glycolysis.

Request a [FREE](#) poster and energy phenotype analysis of your cells at www.seahorsebio.com/pheno



Focused on antibodies for 40 years.
Not on advertising.



Bethyl Laboratories, Inc. has been dedicated to supporting scientific discovery through its qualified antibody products and custom antibody services since its founding in 1972.

Every antibody that Bethyl sells has been manufactured to exacting standards at its sole location in Montgomery, Texas, and has been validated in-house by Bethyl's team of scientists. Antibodies are tested across a range of applications including western blot, immunoprecipitation, immunohistochemistry, immunocytochemistry, ChIP, proximity ligation assay and ELISA.

Currently, Bethyl's portfolio consists of over 7,150 catalog products; offering close to 5,700 primary antibodies targeting over 2,700 proteins and 1,450 secondary antibodies raised against immunoglobulins from over 25 species. Trial sizes are available for over 4,000 antibodies targeting more than 2,350 protein targets. They are conveniently priced at \$50 and serve as an opportunity to discover for yourself why our antibodies are really good.

For really good antibodies, visit bethyl.com/trialsize

Terms & Conditions: \$50 pricing for US customers only; international customers please contact your distributor for details. Trial sizes (catalog # ending in "-T") are not available for all antibodies and existing promotions or discounts do not apply.

© 2015 Bethyl Laboratories, Inc. All rights reserved.



SAY GOOD-BYE TO THE DARKROOM



**Introducing the ZOE™ Fluorescent Cell Imager.
No darkroom, no training, no overwhelming user interface.**

Combining brightfield capabilities with multichannel fluorescence, this cell imager is both affordable and easy to use — your perfect solution for routine cell culture and imaging applications.

Learn more at [bio-rad.com/info/newzoe](https://www.bio-rad.com/info/newzoe)

BIO-RAD

We make human cells.

We can't state it more simply: We manufacture human cells from induced pluripotent stem cells. Our highly pure iCell® and MyCell® products are consistent and reproducible from lot-to-lot, enabling you to focus on the biology . . . and what drives your research.

True Human Biology. Why use an animal or immortalized cell model as a proxy when a true human model, consistent across lots, is available? If you have a phenotype of interest, we can make iPSCs and terminal cells from your donors.

Highly Characterized. Highly Predictive. Our cells have the appropriate gene and protein expression and the relevant physiological response of the target cell type, with numerous peer-reviewed publications detailing their characterization and predictivity of human response.

MORE Cells. CDI provides more cells than other providers: 96-well capacity per vial. GUARANTEED.

**Any cell type.
Any genotype.
Any quantity.**



**CELLular
Dynamics
international**
a FUJIFILM company

You make:

safer medicines
discoveries
therapies
breakthroughs



Check out the iCell community of scientists who discuss the difference iCell products have made in their research:

www.cellulardynamics.com/community

Foreword



Welcome to the 4th annual *Best of Cell* compendia, which highlights a great year at *Cell*.



We have selected the papers presented here based on a number of criteria. We began by looking at the most highly read papers based on article downloads and html usage. Within this list, we sought papers that best represent the scope and breadth of *Cell*. We've included papers that we were exceptionally excited about when they first came in, papers that we found ourselves talking about in the hallways of the office and at the proverbial water cooler, and papers that the reviewers were extremely enthusiastic about. Additionally, we've considered the altmetric rankings of all papers published in 2015 to give perspective and depth to our collection.



Looking at the papers with the greatest numbers of downloads gives a sense of which papers caught the eye of a large swath of the scientific community. Of course, this measure is heavily slanted towards articles published in the beginning of the year, so we took efforts to control for that.

In addition to Reviews and Articles, we've also included a selection of SnapShots that we hope will pique your interest and help your research. New for 2015 is the Timeline short format, and we've included the first two of those as well.

Cell was conceived of as and continues to be a journal representing the broad interests of the biology community. Over the years, the boundaries of this community have expanded to welcome chemists, physicists, clinicians, and a host of other researchers in the spirit of collaboration and cross-pollination of ideas. *Cell's* scope has grown with the community, and you'll see that reflected in this collection.

Clearly, any list like this must also omit many important and valuable papers, but hopefully this collection gives you a flavor of some of the standout moments of the year. Additionally, we are limited by page space and encourage you to visit www.cell.com/cell to see some of the exciting science we are privileged to publish, including our new Stories format, Selects, and other highlight pieces such as our new Bench to Bedside articles. Beyond what we can print on these pages, we continue to offer compelling podcasts, video abstracts, and Cell PaperFlicks to widen the ways in which we present exciting science to our readers.

Of course, all of this great science would not be featured in *Cell* if it were not for the support of the scientists who submit their best work for consideration, provide expertise as advisors and peer reviewers, serve on our editorial board, and read the journal and share our enthusiasm for exciting biology. *Cell* is first and foremost a journal of, by, and for scientists. Thank you all for your contributions.

We hope that you will enjoy reading this special collection, and we welcome your feedback on how we are doing at the journal (you can also access this collection online at www.cell.com/bestof, where you can see freely available digital editions of other Cell Press *Best of...* collections). Please feel free to leave a comment at Cell.com on a paper that has caught your interest, drop us a line at celleditor@cell.com, or email one of the editors directly. We are always happy to hear from you.

We hope that you have had a fruitful 2015, and we look forward to working with you in 2016 and beyond.

Finally, we are grateful for the generosity of our sponsors, who helped to make this reprint collection possible.

Emilie, Elena, Karen, Robert, Lara, Steve, Sri, Jiaying, Mirna, Joao, Marta, and Cindy



MojoSort™

Magnetic Cell Separation System

The MojoSort™ Magnetic Cell Separation System is designed for the separation of target populations using positive or negative selection. MojoSort™ nanoparticles deliver excellent purity and yield at an unmatched, affordable price. Magnetically sorted cells can be used for multiple downstream applications.

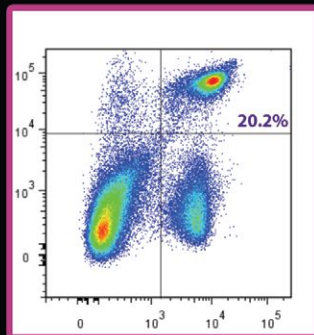


MojoSort™ advantages:

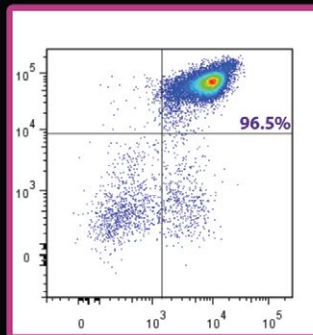
- Small and large test size formats to meet research needs
- Robust performance
- Preserved cell functionality after sorting
- Excellent price

Add some Mojo to your experiment and explore the possibilities!

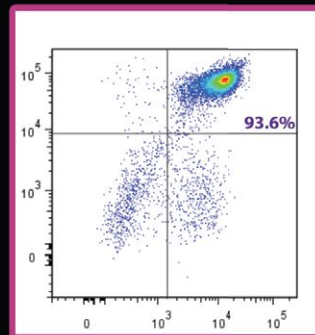
Before Isolation



After MojoSort™ Isolation



After Competitor Isolation



CD3 APC

A suspension of single cells from pooled C57BL/6 mouse spleen and lymph nodes was prepared to isolate CD4⁺ T cells using the MojoSort™ Mouse CD4 T Cell Isolation Kit. Cells were stained with PE anti-mouse CD4 (clone RM4-4), APC anti-mouse CD3ε (145-2C11), and 7-AAD. Grateful Dead cells were excluded from the analysis.

To learn more, visit: biolegend.com/mojosort



BioLegend is ISO 9001:2008 and ISO 13485:2003 Certified

Toll-Free Tel: (US & Canada): 1.877.BIOLEGEND (246.5343)

Tel: 858.768.5800

biolegend.com

08-0052-23

World-Class Quality | Superior Customer Support | Outstanding Value

Cell

Best of 2015

SnapShots

Renal Cell Carcinoma	<i>Samra Turajlic, James Larkin, and Charles Swanton</i>
Spliceosome Dynamics I	<i>Markus C. Wahl and Reinhard Lührmann</i>
T Cell Exhaustion	<i>Kristen E. Pauken and E. John Wherry</i>
Olfactory Classical Conditioning of <i>Drosophila</i>	<i>Ronald L. Davis</i>
CRISPR-RNA-Guided Adaptive Immune Systems	<i>Joshua Carter and Blake Wiedenheft</i>
Origins of DNA Replication	<i>Rachel L. Creager, Yulong Li, and David M. MacAlpine</i>
Growing Organoids from Stem Cells	<i>Toshiro Sato and Hans Clevers</i>
Sensing and Signaling by Cilia	<i>Kurt Zimmerman and Bradley K. Yoder</i>
Insulin/IGF1 Signaling	<i>David K.G. Ma, Christian Stolte, James R. Krycer, David E. James, and Seán I. O'Donoghue</i>
Intrinsic Structural Disorder	<i>Mainak Guharoy, Kris Pauwels, and Peter Tompa</i>
Genetics of Parkinson's Disease	<i>José Brás, Rita Guerreiro, and John Hardy</i>
Motile Cilia	<i>Feng Zhou and Sudipto Roy</i>
Interactions between B Cells and T Cells	<i>Stuart G. Tangye, Robert Brink, Christopher C. Goodnow, and Tri Giang Phan</i>
Astrocytes in Health and Disease	<i>Shane Liddelow and Ben Barres</i>
Sensing and Signaling by Cilia	<i>Kurt Zimmerman and Bradley K. Yoder</i>

Timelines

Checkpoint Blockade	<i>Joao Monteiro</i>
Sending Out an SOS	<i>Brian Plosky</i>

(continued)

Minireviews and Reviews

An Adenine Code for DNA: A Second Life for N6-Methyladenine

Holger Heyn and Manel Esteller

The Hunger Genes: Pathways to Obesity

Agatha A. van der Klaauw and I. Sadaf Farooqi

The Role of Chromosome Domains in Shaping the Functional Genome

Tom Sexton and Giacomo Cavalli

Immune Checkpoint Targeting in Cancer Therapy: Toward Combination Strategies with Curative Potential

Padmanee Sharma and James P. Allison

Articles and Resources

SOX17 Is a Critical Specifier of Human Primordial Germ Cell Fate

Naoko Irie, Leehee Weinberger, Walfred W.C. Tang, Toshihiro Kobayashi, Sergey Viukov, Yair S. Manor, Sabine Dietmann, Jacob H. Hanna, and M. Azim Surani

Early Divergent Strains of *Yersinia pestis* in Eurasia 5,000 Years Ago

Mark M. Yore, Ismail Syed, Pedro M. Moraes-Vieira, Teja Zhang, Mark A. Herman, Edwin A. Homan, Rajesh T. Patel, Jennifer Lee, Shili Chen, Odile D. Peroni, Abha S. Dhaneshwar, Ann Hammarstedt, Ulf Smith, Timothy E. McGraw, Alan Saghatelian, and Barbara B. Kahn

Epigenetic Priming of Memory Updating during Reconsolidation to Attenuate Remote Fear Memories

Simon Rasmussen, Morten Erik Allentoft, Kasper Nielsen, Ludovic Orlando, Martin Sikora, Karl-Göran Sjögren, Anders Gorm Pedersen, Mikkel Schubert, Alex Van Dam, Christian Moliin Outzen Kapel, Henrik Bjørn Nielsen, Søren Brunak, Pavel Avetisyan, Andrey Epimakhov, Mikhail Viktorovich Khalyapin, Artak Gnuni, Aivar Kriiska, Irena Lasak, Mait Metspalu, Vyacheslav Moiseyev, Andrei Gromov, Dalia Pokutta, Lehti Saag, Liivi Varul, Levon Yepiskoposyan, Thomas Sicheritz-Pontén, Robert A. Foley, Marta Mirazón Lahr, Rasmus Nielsen, Kristian Kristiansen, and Eske Willerslev

Personalized Nutrition by Prediction of Glycemic Responses

David Zeevi, Tal Korem, Niv Zmora, David Israeli, Daphna Rothschild, Adina Weinberger, Orly Ben-Yacov, Dar Lador, Tali Avnit-Sagi, Maya Lotan-Pompan, Jotham Suez, Jemal Ali Mahdi, Elad Matot, Gal Malka, Noa Kosower, Michal Rein, Gili Zilberman-Schapira, Lenka Dohnalová, Meirav Pevsner-Fischer, Rony Bikovsky, Zamir Halpern, Eran Elinav, and Eran Segal

Variation in the Human Immune System Is Largely Driven by Non-Heritable Influences

Petter Brodin, Vladimir Jojic, Tianxiang Gao, Sanchita Bhattacharya, Cesar J. Lopez Angel, David Furman, Shai Shen-Orr, Cornelia L. Dekker, Gary E. Swan, Atul J. Butte, Holden T. Maecker, and Mark M. Davis

(continued)

Saturated Reconstruction of a Volume of Neocortex

Narayanan Kasthuri, Kenneth Jeffrey Hayworth, Daniel Raimund Berger, Richard Lee Schalek, José Angel Conchello, Seymour Knowles-Barley, Dongil Lee, Amelio Vázquez-Reina, Verena Kaynig, Thouis Raymond Jones, Mike Roberts, Josh Lyskowski Morgan, Juan Carlos Tapia, H. Sebastian Seung, William Gray Roncal, Joshua Tzvi Vogelstein, Randal Burns, Daniel Lewis Sussman, Carey Eldin Priebe, Hanspeter Pfister, and Jeff William Lichtman

Genome-wide CRISPR Screen in a Mouse Model of Tumor Growth and Metastasis

Sidi Chen, Neville E. Sanjana, Kaijie Zheng, Ophir Shalem, Kyungheon Lee, Xi Shi, David A. Scott, Jun Song, Jen Q. Pan, Ralph Weissleder, Hakho Lee, Feng Zhang, and Phillip A. Sharp

A 3D Map of the Human Genome at Kilobase Resolution Reveals Principles of Chromatin Looping

Suhas S.P. Rao, Miriam H. Huntley, Neva C. Durand, Elena K. Stamenova, Ivan D. Bochkov, James T. Robinson, Adrian L. Sanborn, Ido Machol, Arina D. Omer, Eric S. Lander, and Erez Lieberman Aiden

***COLD1* Confers Chilling Tolerance in Rice**

Yun Ma, Xiaoyan Dai, Yunyuan Xu, Wei Luo, Xiaoming Zheng, Dali Zeng, Yajun Pan, Xiaoli Lin, Huanhuan Liu, Dajian Zhang, Jun Xiao, Xiaoyu Guo, Shujuan Xu, Yuda Niu, Jingbo Jin, Hui Zhang, Xun Xu, Legong Li, Wen Wang, Qian Qian, Song Ge, and Kang Chong

Prospective Derivation of a Living Organoid Biobank of Colorectal Cancer Patients

Marc van de Wetering, Hayley E. Francies, Joshua M. Francis, Gergana Bounova, Francesco Iorio, Apollo Pronk, Winan van Houdt, Joost van Gorp, Amaro Taylor-Weiner, Lennart Kester, Anne McLaren-Douglas, Joyce Blokker, Sridevi Jaksani, Sina Bartfeld, Richard Volckman, Peter van Sluis, Vivian S.W. Li, Sara Seepo, Chandra Sekhar Pedamallu, Kristian Cibulskis, Scott L. Carter, Aaron McKenna, Michael S. Lawrence, Lee Lichtenstein, Chip Stewart, Jan Koster, Rogier Versteeg, Alexander van Oudenaarden, Julio Saez-Rodriguez, Robert G.J. Vries, Gad Getz, Lodewyk Wessels, Michael R. Stratton, Ultan McDermott, Matthew Meyerson, Mathew J. Garnett, and Hans Clevers

Selective Elimination of Mitochondrial Mutations in the Germline by Genome Editing

Pradeep Reddy, Alejandro Ocampo, Keiichiro Suzuki, Jinping Luo, Sandra R. Bacman, Sion L. Williams, Atsushi Sugawara, Daiji Okamura, Yuji Tsunekawa, Jun Wu, David Lam, Xiong Xiong, Nuria Montserrat, Concepcion Rodriguez Esteban, Guang-Hui Liu, Ignacio Sancho-Martinez, Dolores Manau, Salva Civico, Francesc Cardellach, Maria del Mar O'Callaghan, Jaime Campistol, Huimin Zhao, Josep M. Campistol, Carlos T. Moraes, and Juan Carlos Izpisua Belmonte

(continued)

TALK TO HENRIK

PrecisA Monoclonals are precise, accurate and targeted. The stringent production process and characterization procedure ensures premium performance in approved applications, with defined specificity, multiplexing opportunities, secured continuity and stable supply.

If you're in need of an antibody to target a protein we don't list in our online catalog you might be interested in our antibody co-development program. Learn more today at atlasantibodies.com/talktohenrik



Henrik is our R&D Manager

MADE IN SWEDEN

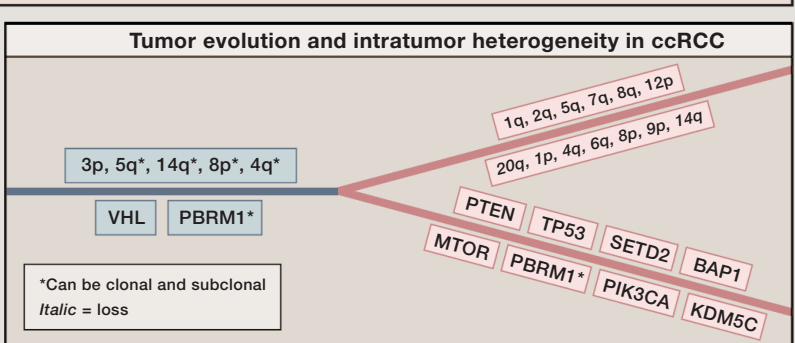
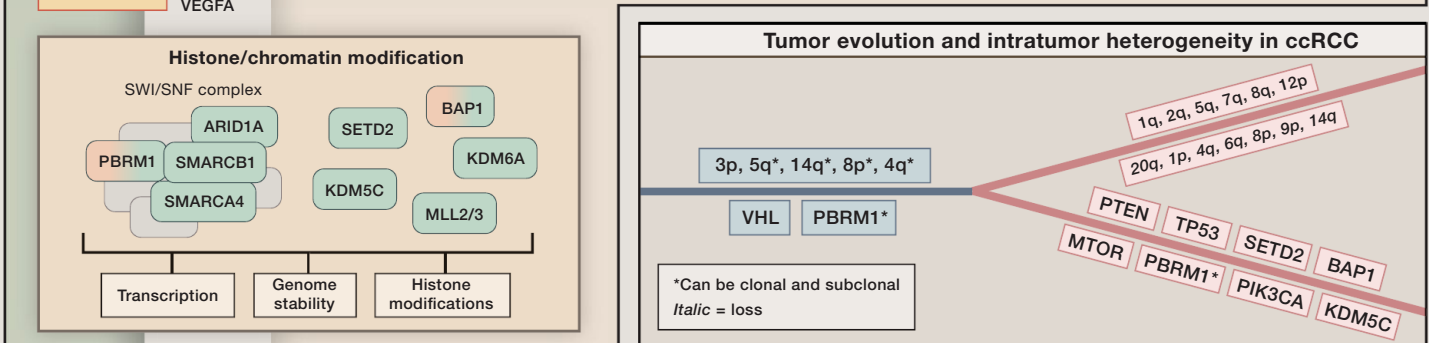
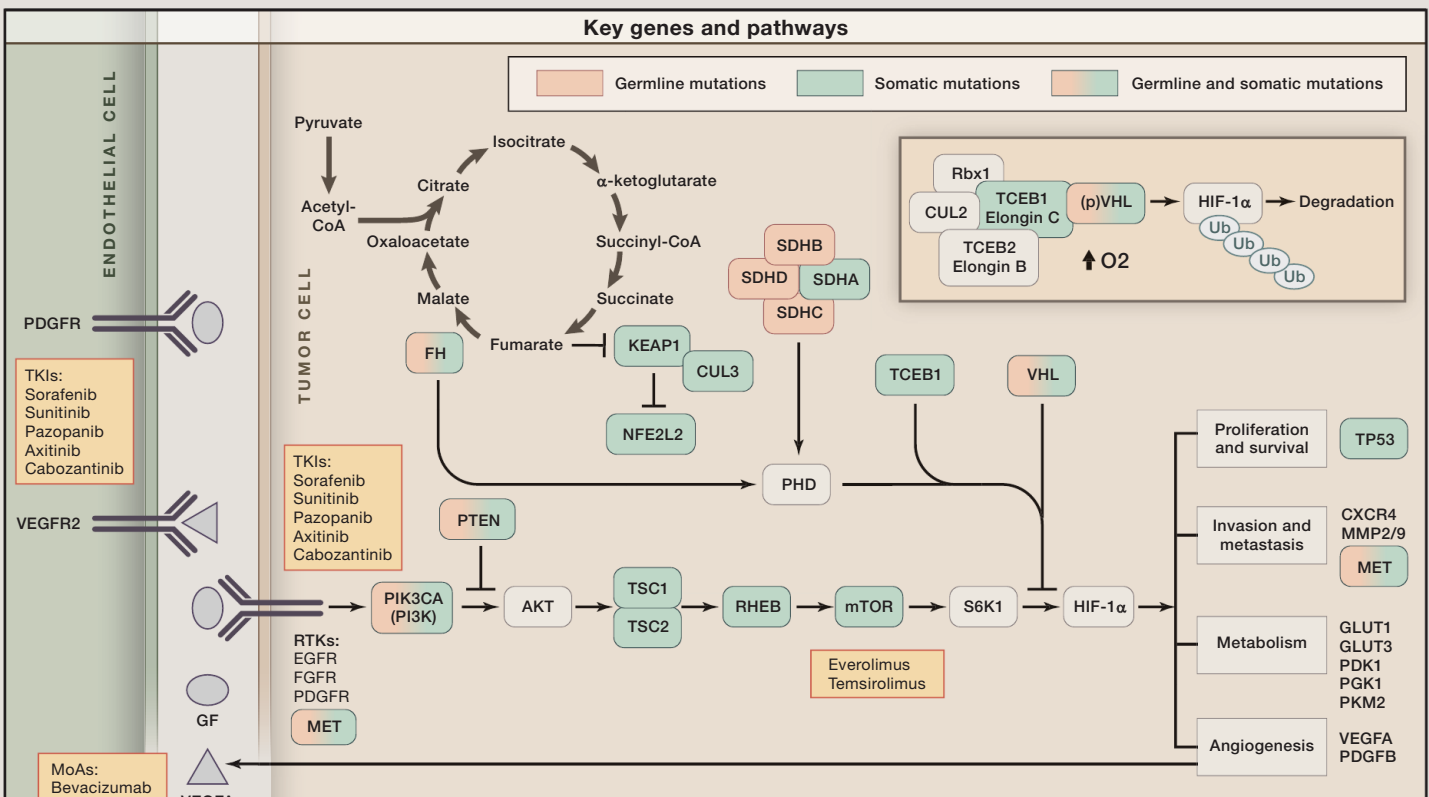
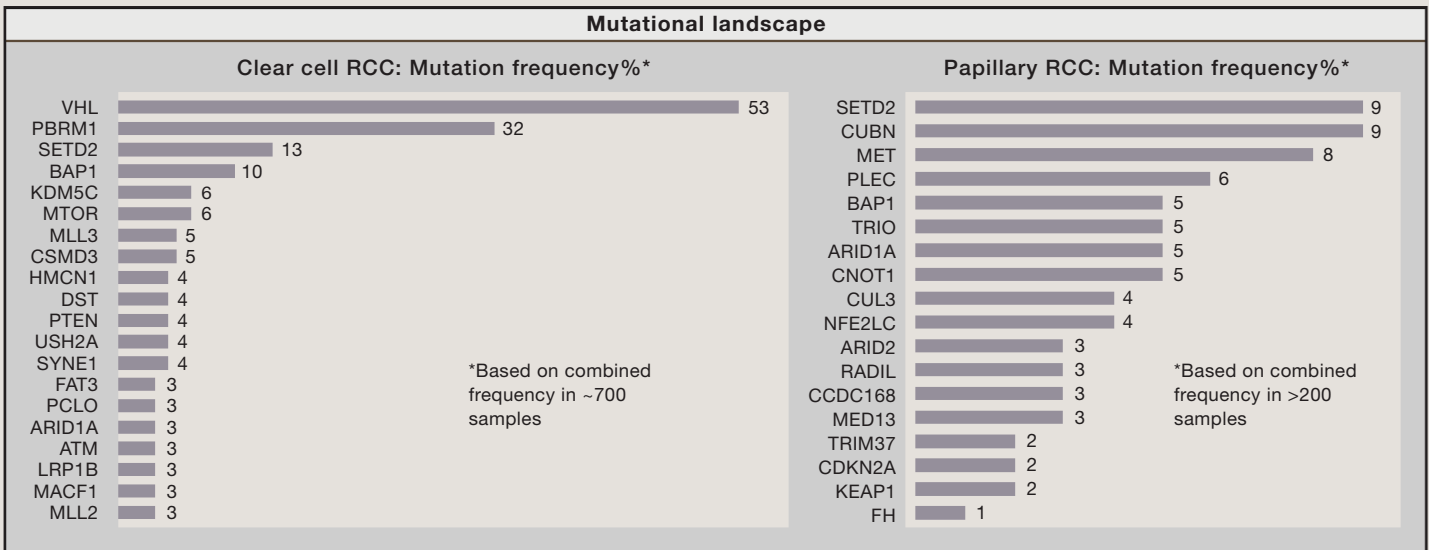
 **ATLAS ANTIBODIES**
Totally human

SnapShot: Renal Cell Carcinoma

Samra Turajlic,^{1,2} James Larkin,² and Charles Swanton¹

¹The Francis Crick Institute, 44 Lincoln's Inn Fields, London WC2A 3LY, UK

²Renal Unit, The Royal Marsden Hospital, London SW3 6JJ, UK



IN VIVO IMAGING PROBES

Figure 1

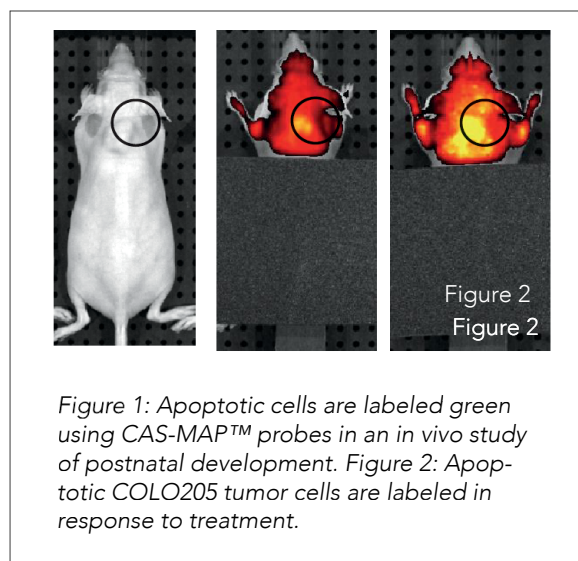
Detect apoptosis & caspase activity in cancer, embryonic development & ischemic conditions.

In vivo imaging probes bring greater insight to your preclinical research. CAS-MAP™ imaging probes allow you to distinguish between apoptotic and healthy cells *in vivo*.

In vivo imaging probes are injected IV. The probes are cell-permeant and bind to active caspases while unbound probe is removed via the circulatory system. Visualize using live animal imaging or harvest tissue for *ex vivo* analysis by microscopy or FACS.

Translate from cell to animal using *in vivo* imaging probes.

Download application note:
vergentbio.com/invivo
844.803.0346

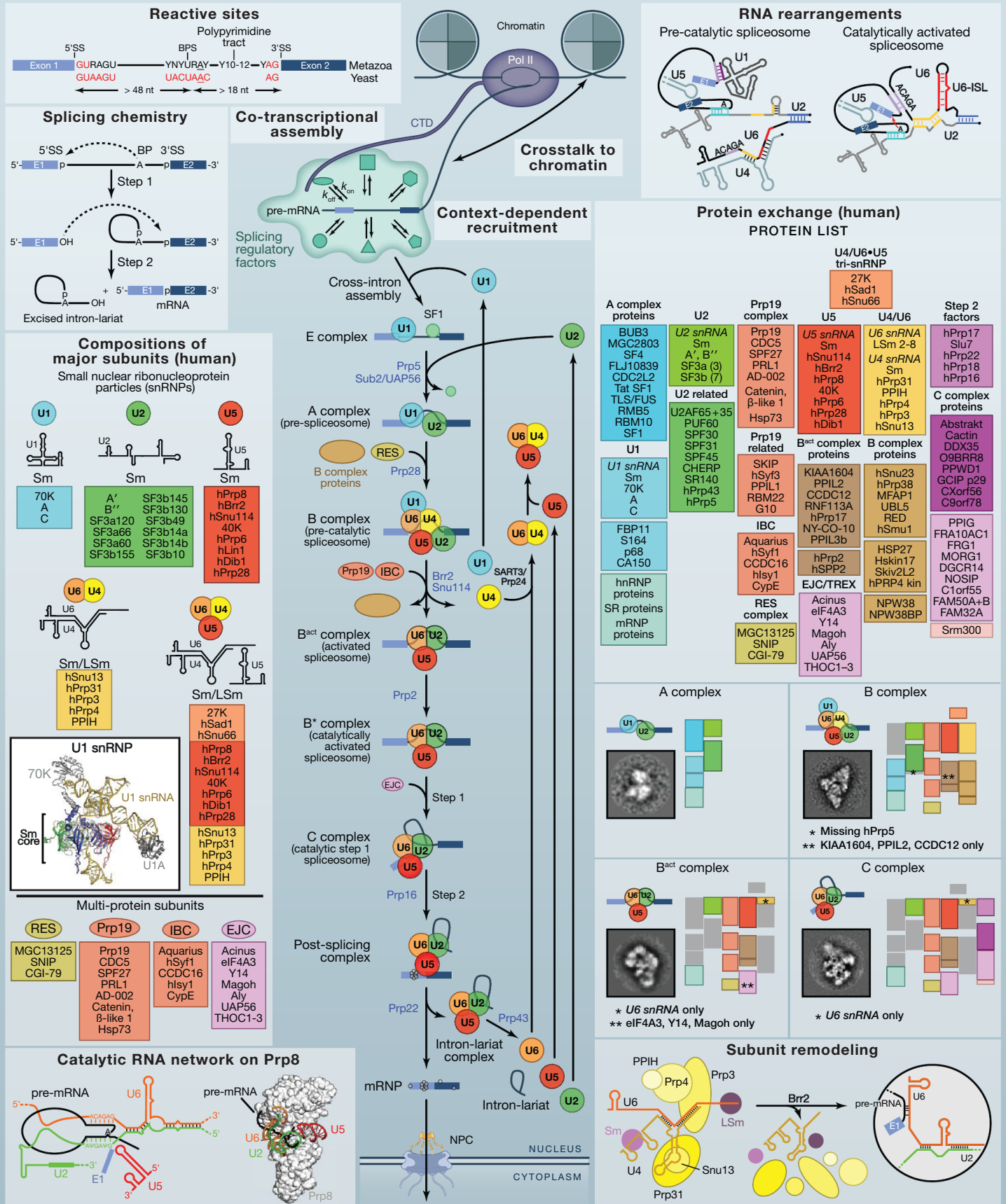


SnapShot: Spliceosome Dynamics I

Markus C. Wahl¹ and Reinhard Lührmann²

¹Laboratory of Structural Biochemistry, Freie Universität Berlin, Takustraße 6, 14195 Berlin, Germany

²Department of Cellular Biochemistry, Max Planck Institute for Biophysical Chemistry, Am Fassberg 11, 37077 Göttingen, Germany





Are you still injecting?

Focus on your research instead, and let ALZET® Osmotic Pumps do the dosing for you.

ALZET pumps are a superior alternative to repetitive injections and other dosing methods that require frequent animal handling. These fully implantable pumps provide continuous and precise administration, for up to 6 weeks with a single pump, to unrestrained lab animals as small as mice. ALZET pumps are economical and easy to use by research personnel. Connection to a catheter enables direct delivery to vessels, cerebral ventricles, and other target sites. Learn more at alzet.com.

Now available: iPRECIO Pumps

- Programmable
- Refillable
- Implantable
- Small size for mice and rats

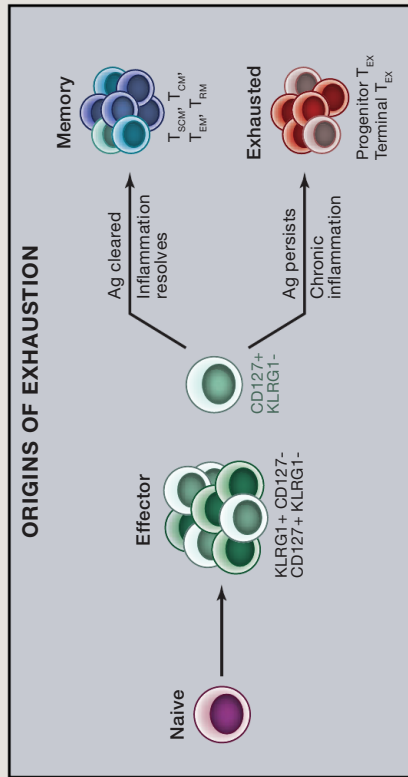
Learn more at www.alzet.com/iprecio



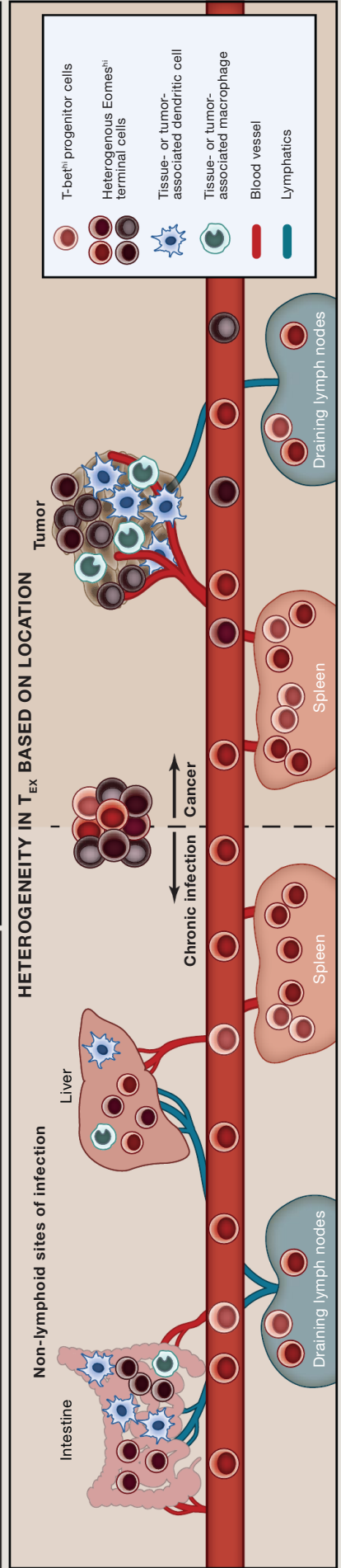
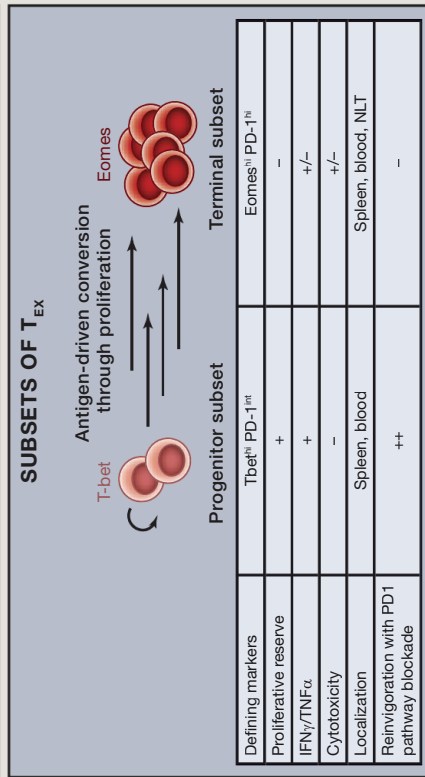
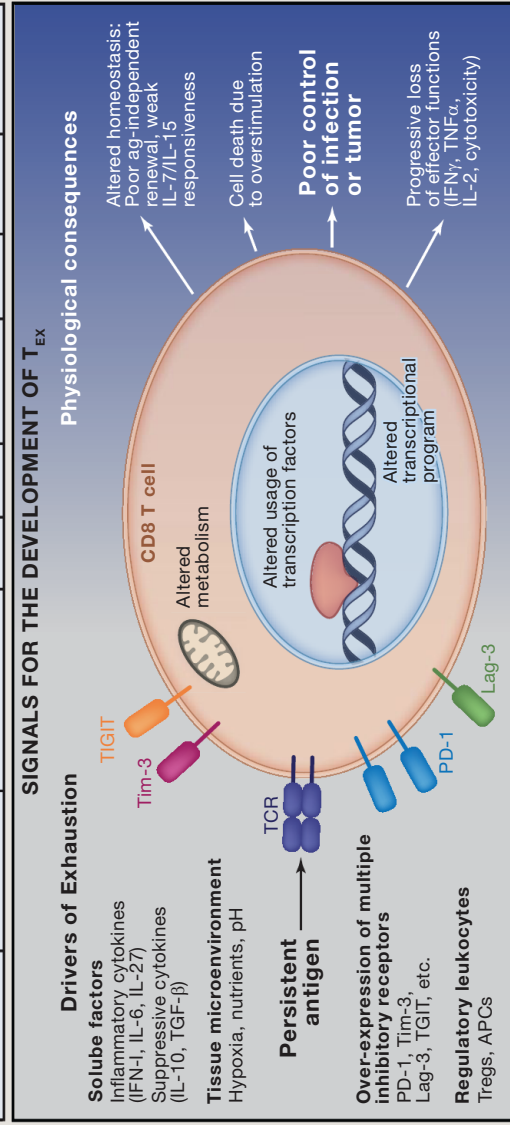
SnapShot: T Cell Exhaustion

Kristen E. Pauken and E. John Wherry

Department of Microbiology and Institute for Immunology, University of Pennsylvania, Philadelphia, PA 19104, USA



Property	Naive	Effector	Memory				Exhausted
	Quiescent cells circulating through lymphoid tissues and blood	Generated following priming in the presence of antigen, costimulation, and inflammation	Common following acute infection and vaccination				Common during chronic infections and cancer due to persistent stimulation
Subsets		KLRG1 ⁺ , CD127 ⁻	T _{SCM}	T _{EM}	T _{RM}	Progenitor	Terminal Progeny
Markers	CD44 ^{low} , CD62L ⁺	CD44 ^{high} , CD62L ⁻ , Granzyme B, Perforin	CD85, Sca1	CD62L ⁻	CD69 ⁺ , CD103 ⁺	T-bet ^{hi} , PD-1 ^{int}	Eomes ^{hi} , PD-1 ^{hi}
Proliferative capacity	+++	+/-	+++	++	-	+/-	-
Effector capacity	-	+++	+++	+++	+++	+++	+/-
Location	LN, spleen, blood	Spleen, blood, peripheral tissues	LN, spleen, blood	Spleen, blood, non-lymphoid tissues	Non-lymphoid tissues	Spleen, blood	Spleen, blood, non-lymphoid tissues



ThawSTAR™

biocision®

Automated Cell Thawing System

the solution:

the problem:



Solve the water bath problem.

- Standardized cell thawing
- High recovery, viability and reproducibility
- Ideal for use in the hood

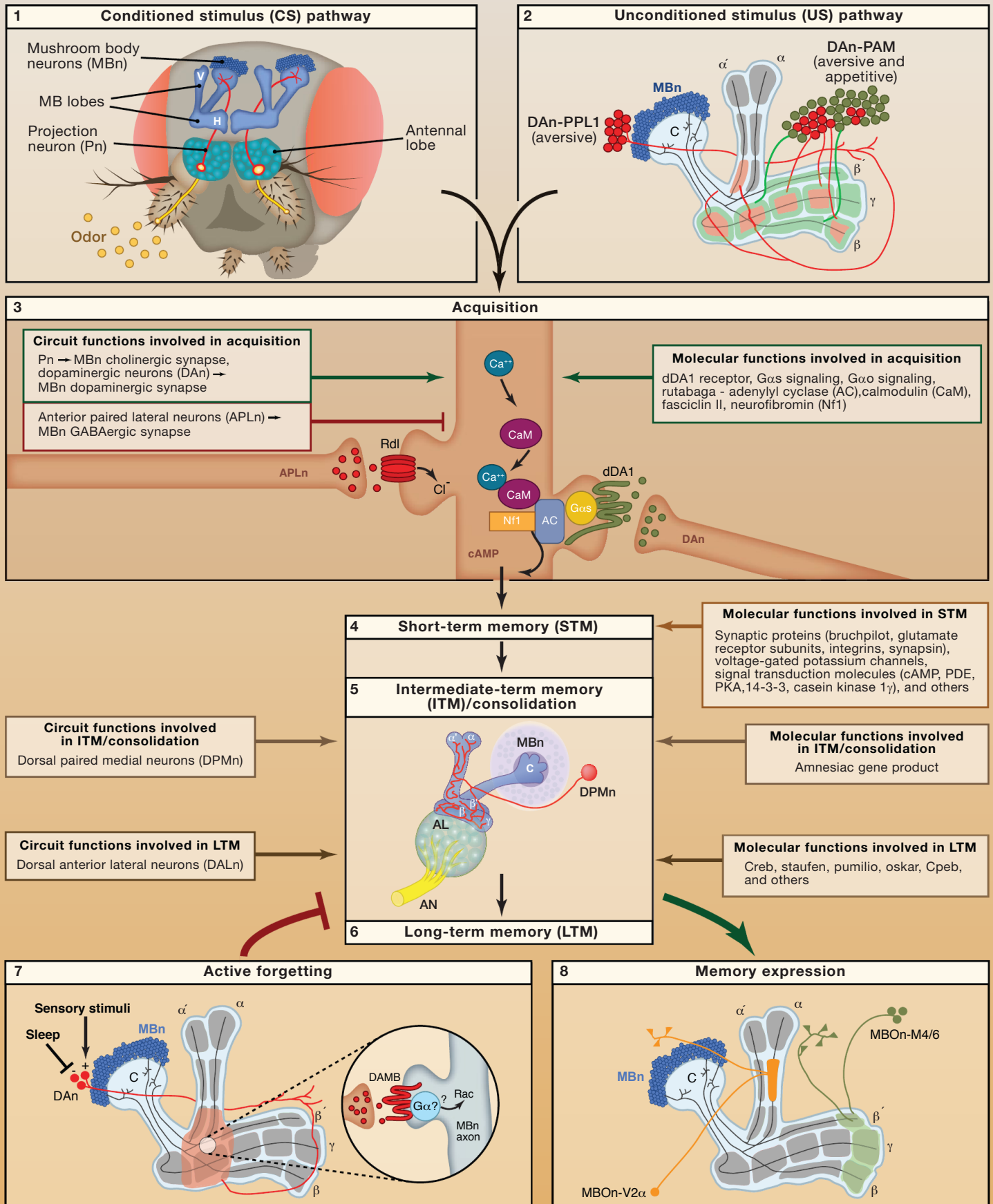


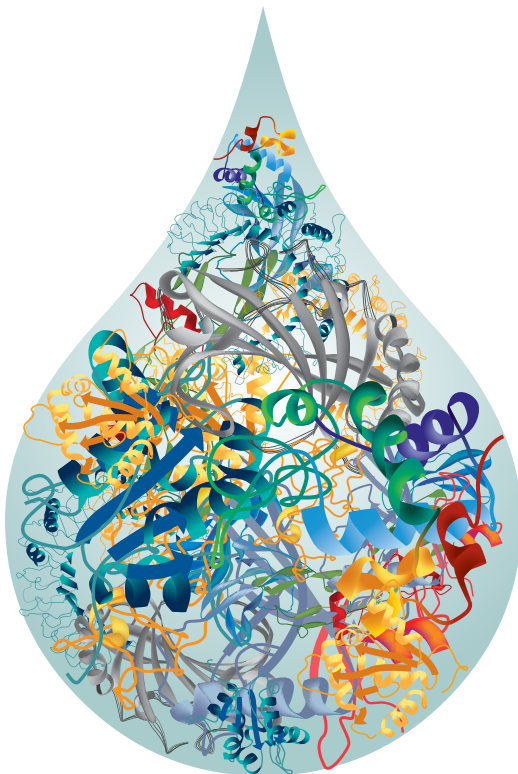
Visit: www.biocision.com/thawstar/cell

SnapShot: Olfactory Classical Conditioning of *Drosophila*

Ronald L. Davis

Department of Neuroscience, The Scripps Research Institute Florida, Jupiter, FL 33458, USA





What's in Your Sample? Find Your Answers!

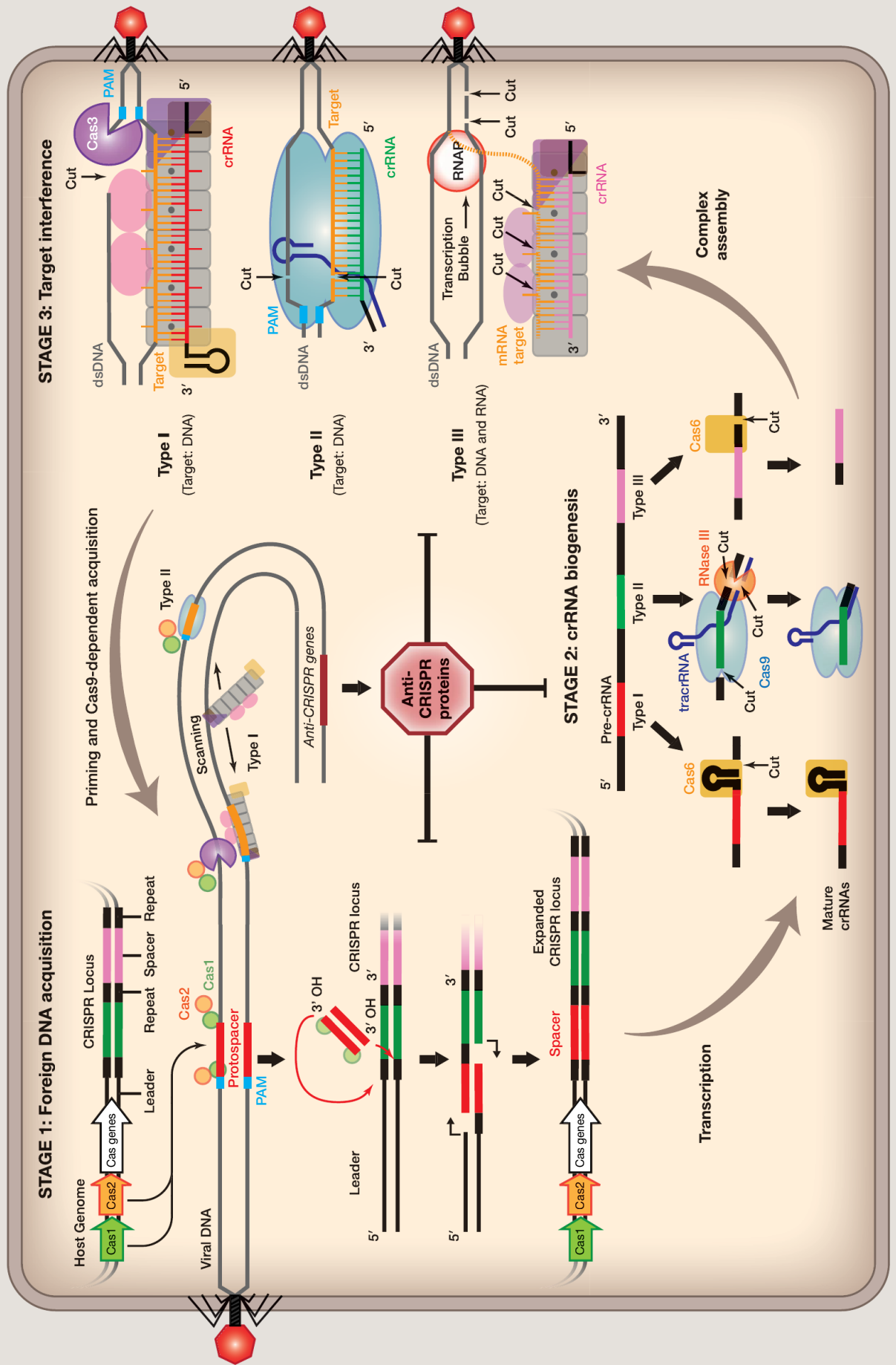


[rnsystems.com/
Immunoassays](https://rnsystems.com/Immunoassays)

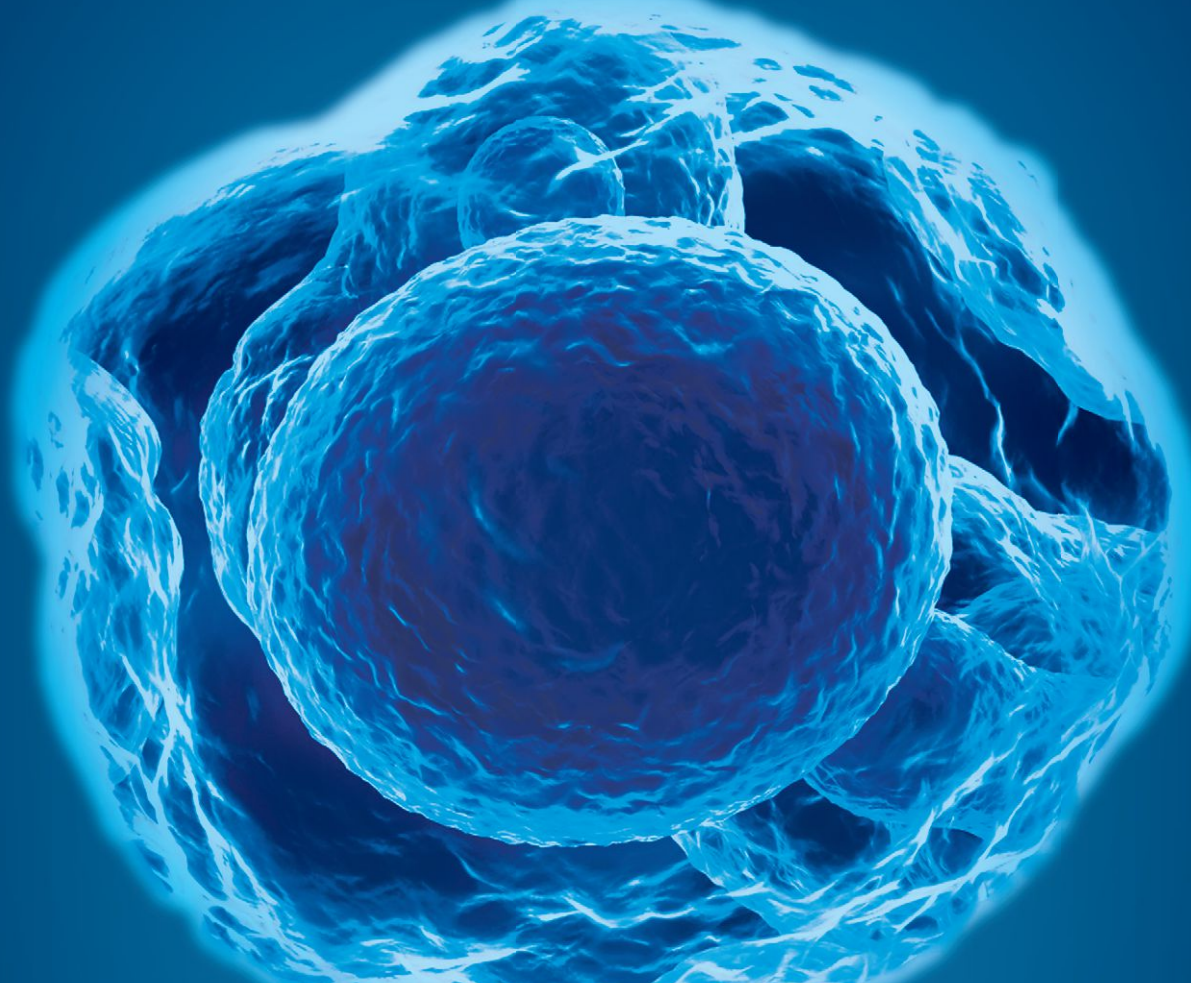
Snapshot: CRISPR-RNA-Guided Adaptive Immune Systems

Joshua Carter and Blake Wiedenheft
 Montana State University, Department of Microbiology and Immunology, Bozeman, MT 59717, USA

Cell



**SIMPLE. EFFECTIVE.
AFFORDABLE.**



CELL-BASED ASSAYS

VIABILITY

TOXICITY

PROLIFERATION

OXYGEN CONSUMPTION

REPORTER

METABOLISM

PROTEIN SYNTHESIS

PHAGOCYTOSIS & AUTOPHAGY

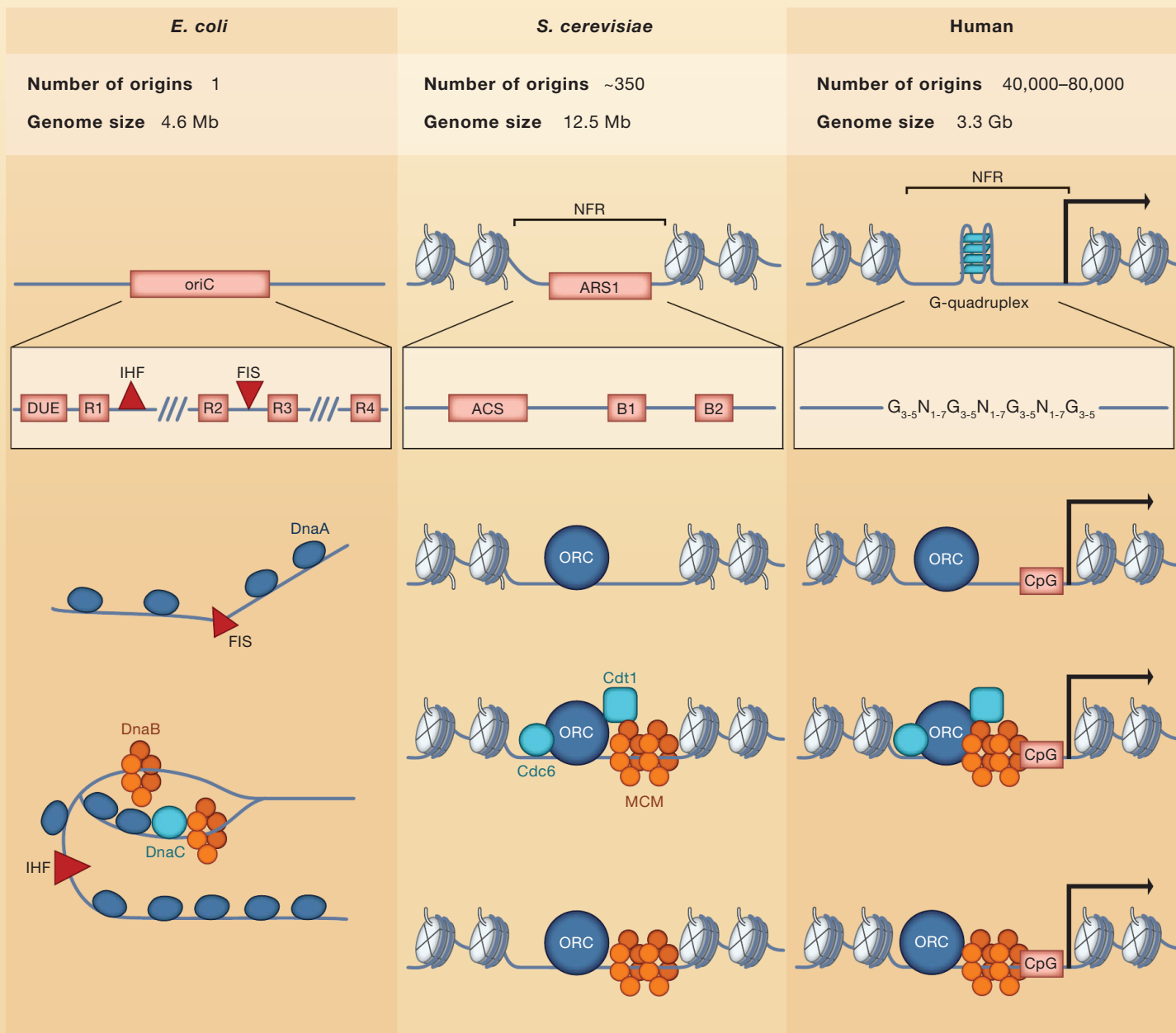


**BIOCHEMICALS • ASSAY KITS • ANTIBODIES
PROTEINS • RESEARCH SERVICES**

Visit www.caymanchem.com for more information

SnapShot: Origins of DNA Replication

Rachel L. Creager, Yulong Li, and David M. MacAlpine
 Department of Pharmacology and Cancer Biology, Duke University Medical Center,
 Durham, NC 27710, USA

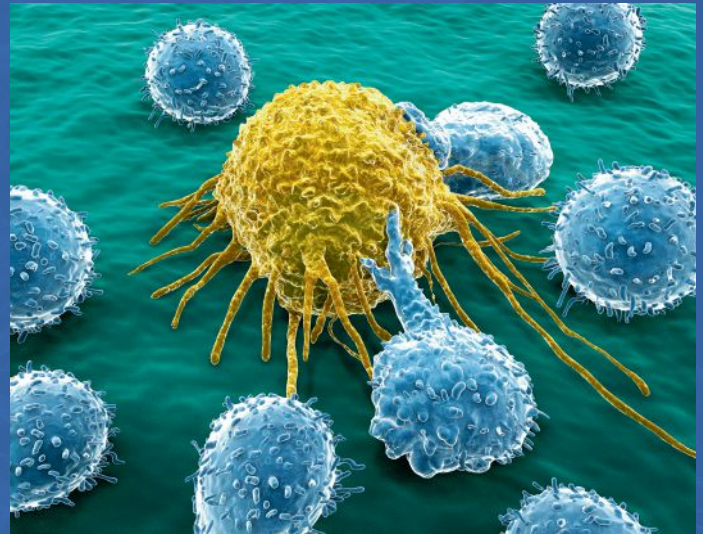


Histone PTM	Enzyme	Function	Organism
H4K20me1	PR-Set7	Promotes pre-RC assembly	Human, mouse
H4K20me2	Suv4-20h1/2	ORC recruitment via ORC1 BAH domain	Metazoa
H3K4me2	COMPASS complex	Origin activation	Yeast
H3K27me	ATXR5, ATRX6	Represses re-replication of heterochromatic origins	Arabidopsis
H3K36me	Set2	Regulates Cdc45 association with origins	Yeast
H3K79me2	DOT1L	Enriched at origins, loss of DOT1L leads to re-replication	Human
H3K4me3 demethylation	KDM5C/JARID1C	Promotes early-origin activation	Human
H4Ac	Hbo1	Promotes pre-RC assembly	Human, xenopus, fly
Bulk H3 and H4 acetylation	Multiple HATs	Regulates developmentally programmed origin of the β -globin locus	Human
H4K5Ac/H4K12Ac	Hat1p/Hat2p	Hat1/Hat2 interact with and enhance the function of ORC	Yeast
H4K16Ac	MOF	Promotes male-specific early-origin activation on the X chromosome	Fly
H3,H4 deacetylation	Rpd3	Delays late-origin activation, developmental transition in origin specificity	Yeast, fly
H3,H4 deacetylation	Sir2p	Inhibits pre-RC assembly at a subset of origins	Yeast
H4K5Ac deacetylation	Sum1/Rfm1/Hst1	Enhances efficiency of replication initiation at a subset of origins	Yeast
H2B Ub	Bre1	Enriched at origins, impacts fork elongation	Yeast

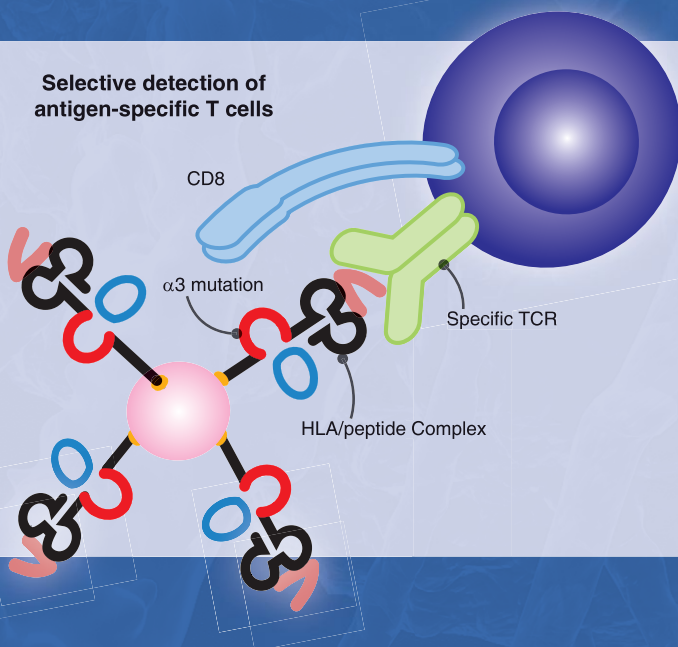
MHC Class I & II Tetramers • MHC Monomers • CD1d Tetramers

MBL has been providing tetramer reagents for over a decade and has recently extended its portfolio through the acquisition of the Beckman Coulter iTag™ MHC Tetramer product line. MBL International is your source for quality reagents for detection of antigen-specific T cells and NKT cells.

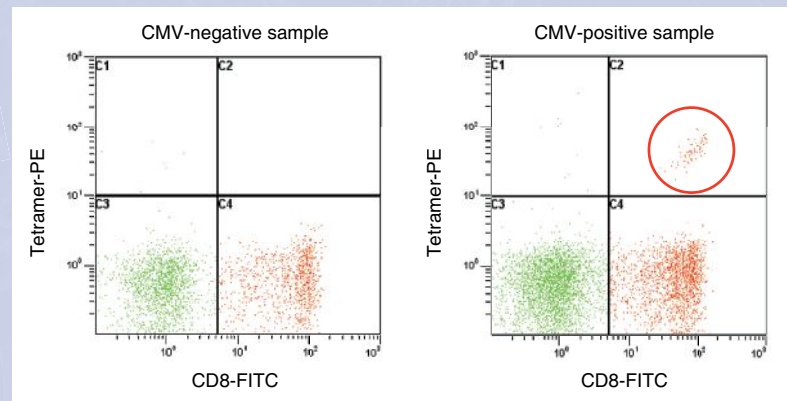
- Increased specificity of proprietary $\alpha 3$ mutation
- Wide selection of alleles: Human, Mouse, Rhesus Macaque, Chicken
- Identification of Ag-specific CD8⁺ and CD4⁺ T cells
- Assay flexibility using biotinylated MHC monomers
- Detection of NKT cells using CD1d tetramers



Selective detection of antigen-specific T cells



HLA-A*02:01 CMV pp65 Tetramer



Contact MBL International today to learn more about our products and how we can help you discover ways to make your science more efficient and effective.

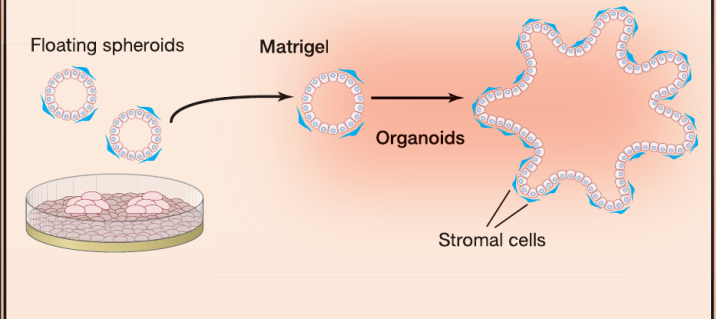
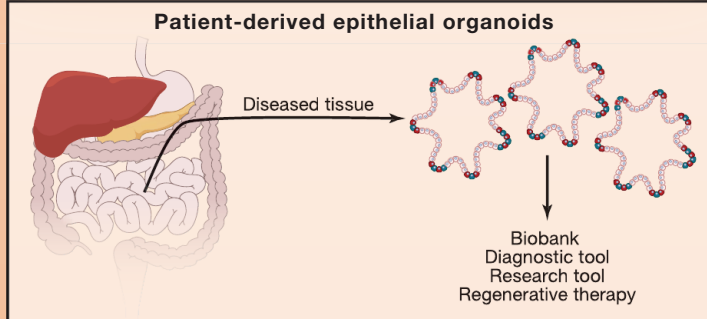
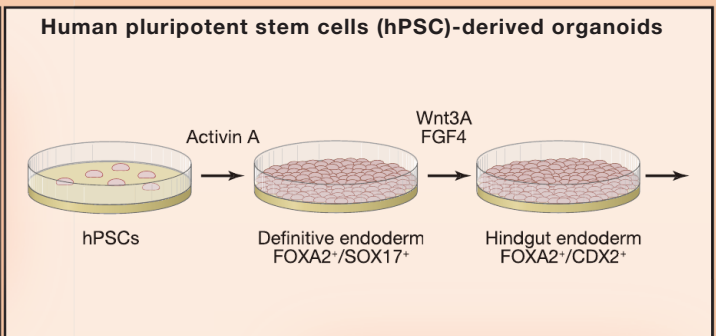
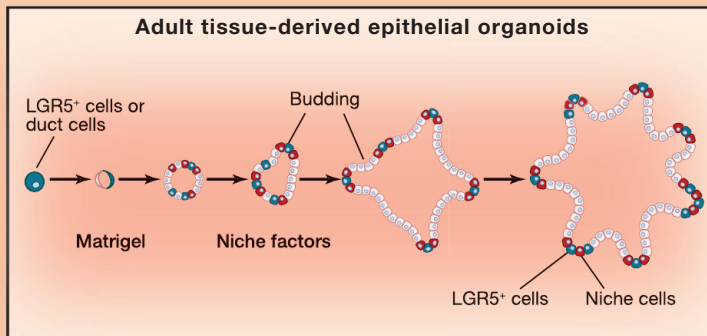
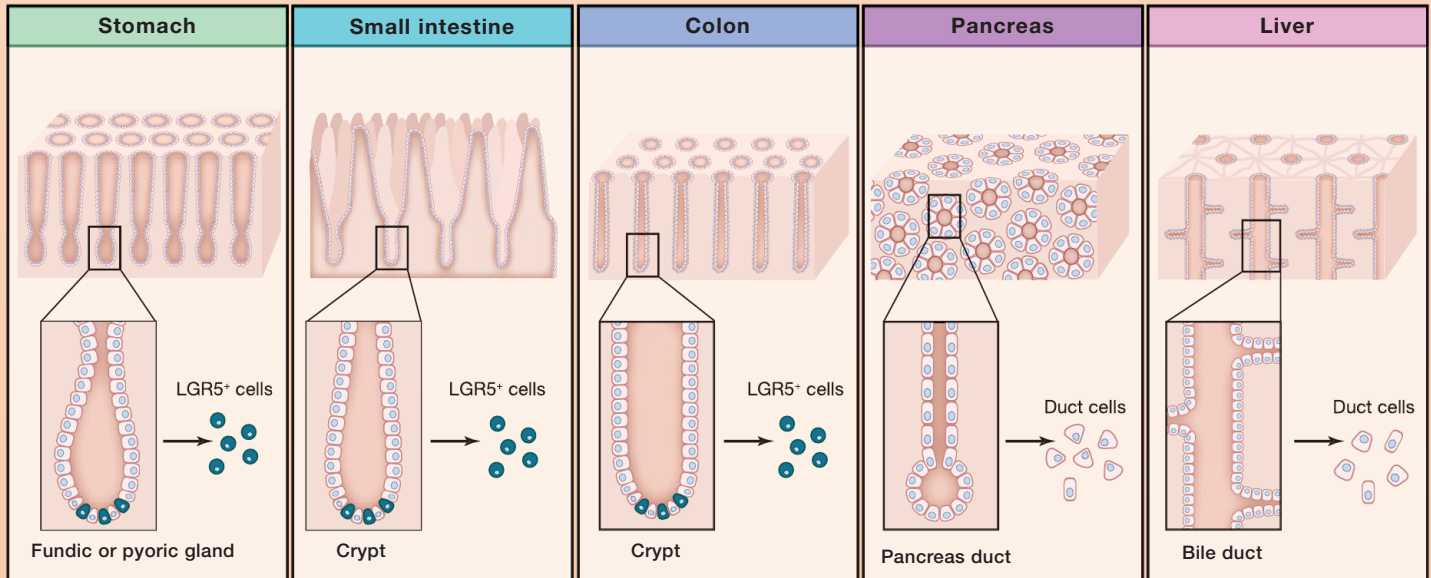
mblintl.com • 800-200-5459 • 781-939-6963

SnapShot: Growing Organoids from Stem Cells

Toshiro Sato¹ and Hans Clevers²

¹Department of Gastroenterology, Keio University School of Medicine, 160-8582 Tokyo, Japan

²Hubrecht Institute, KNAW and University Medical Centre Utrecht, Uppsalalaan 8, 3584CT Utrecht, the Netherlands

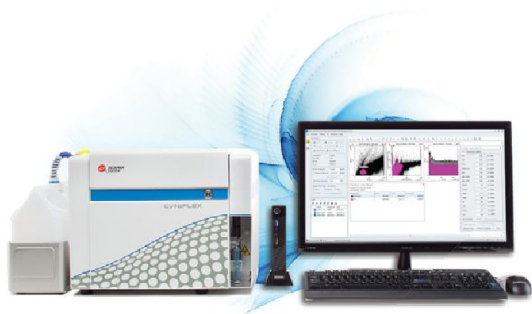


Type of tissue	Source	Stem cell culture condition (niche factors)	Differentiation culture condition
Stomach	Adult mouse	EGF, Noggin, R-spondin, Wnt-3A, FGF10	EGF, R-spondin
	Adult human	EGF, Noggin, R-spondin, Wnt-3A, FGF10	EGF, R-spondin
	hPSC	EGF	EGF
Small intestine	Adult mouse	EGF, Noggin, R-spondin	EGF, Noggin, R-spondin
	Adult human	EGF, Noggin, R-spondin, Wnt-3A TGF-b inhibitor, p38 inhibitor	EGF, Noggin, R-spondin, TGF-b inhibitor
	hPSC	EGF	EGF
Colon	Adult mouse	EGF, Noggin, R-spondin, Wnt-3A	EGF, Noggin, R-spondin
	Adult human	EGF, Noggin, R-Spondin, Wnt-3A, TGF-b inhibitor, p38 inhibitor	EGF, Noggin, R-spondin, TGF-b inhibitor
Pancreas	Adult mouse	EGF, Noggin, R-spondin, Wnt-3A, FGF10, Nicotinamide	EGF, Noggin, R-spondin, Wnt-3A
	Adult human	EGF, Noggin, R-spondin, Wnt-3A, FGF10, TGF-b inhibition, Nicotinamide	Not reported
Liver	Adult mouse	EGF, Noggin, R-spondin, Wnt-3A, FGF10, HGF, Nicotinamide	EGF, Noggin, FGF10, TGF-b inhibition, Notch inhibition
	Adult human	EGF, Noggin, R-spondin, Wnt-3A, FGF10, HGF, Nicotinamide, TGF-b inhibitor, Forskolin	EGF, Noggin, FGF10, TGF-b inhibition, Notch inhibition, BMP7

EXQUISITE SENSITIVITY.



HARNESS THE POWER OF ADVANCED SENSITIVITY AND RESOLUTION.



The CytoFLEX Flow Cytometer has the dynamic range to see dim and bright populations in the same sample. And with 15 parameters, including 13 channels for fluorescent detection, heterogeneous populations can be defined with exquisite clarity.

Learn more at goo.gl/Ew8KYw

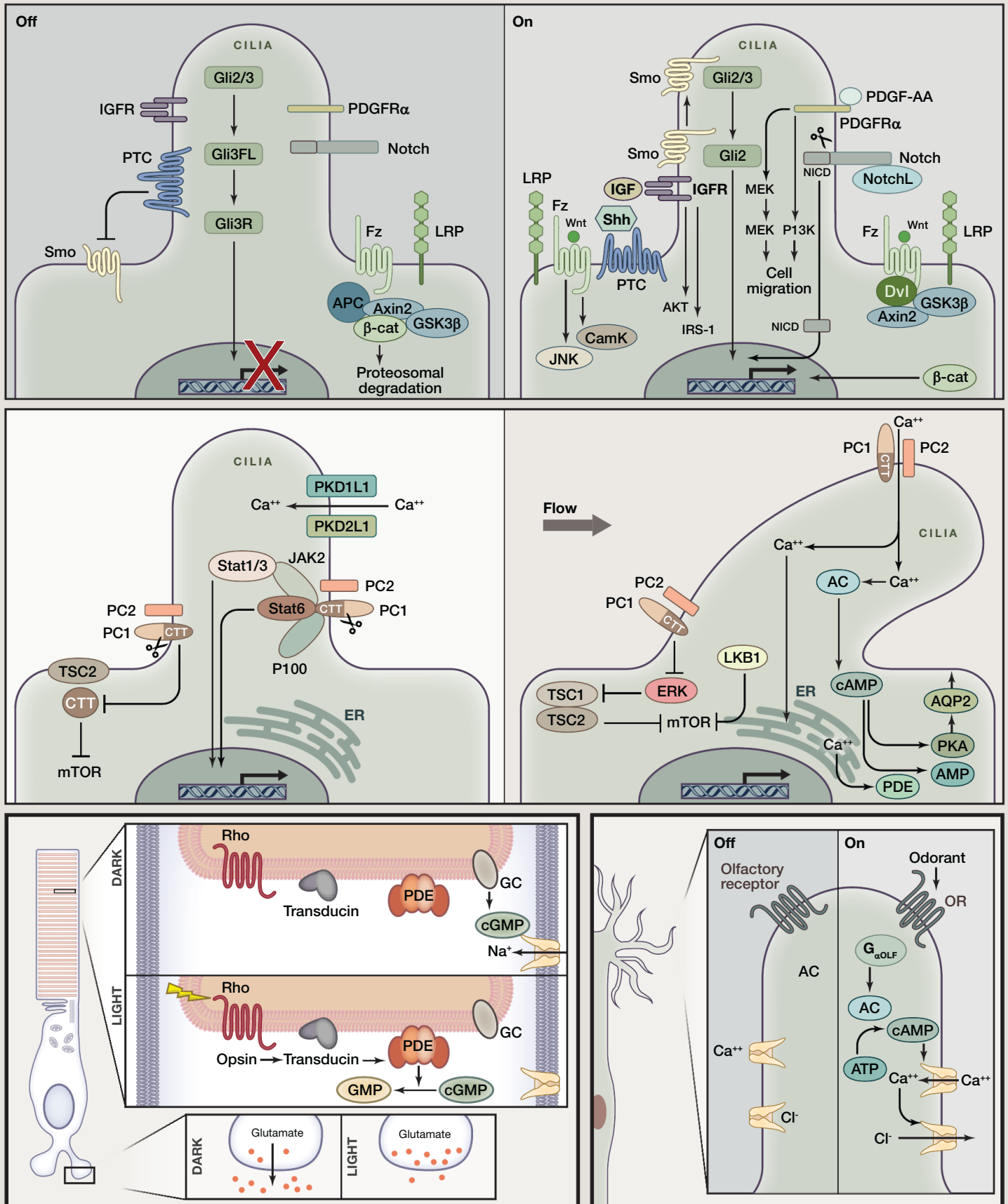
© 2015 Beckman Coulter Life Sciences. All rights reserved. CytoFLEX is for research use only. Class 1 Laser Product. Not for use in diagnostic purposes. CytoFLEX and CytExpert are trademarks of Xitogen Technologies (Suzhou), Inc., a Beckman Coulter company. Beckman Coulter, the stylized logo and fast track to success are trademarks of Beckman Coulter, Inc. Beckman Coulter and the stylized logo are registered in the USPTO. All other trademarks are the property of their respective owners.

 **BECKMAN
COULTER**
Life Sciences

SnapShot: Sensing and Signaling by Cilia

Kurt Zimmerman and Bradley K. Yoder

Department of Cell, Developmental, and Integrative Biology, University of Alabama at Birmingham, Birmingham, AL 35294, USA

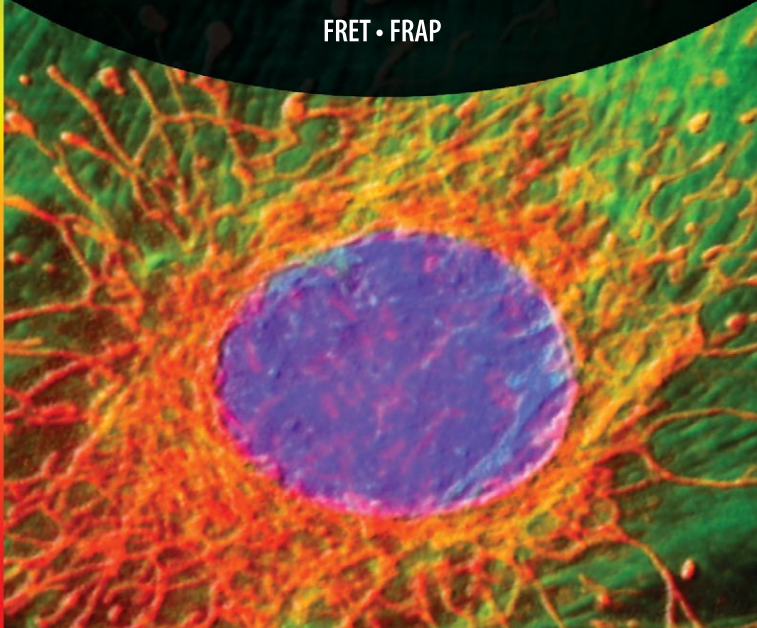


**ADVANCED FLUORESCENCE
IMAGING SYSTEMS**

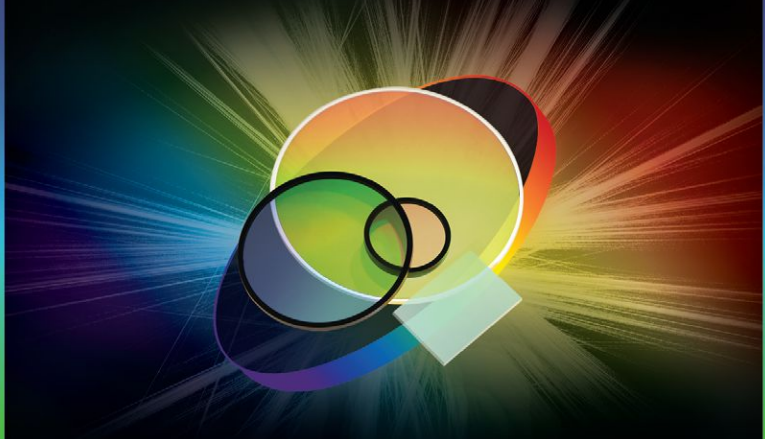


Imaging products from 89 North, Cairn Research
and CrestOptics create light re-engineered.

Confocal Imaging • Super-Resolution Imaging
High-Speed Ratiometric Imaging • Optogenetics • Photoactivation
Photoconversion • Simultaneous Multichannel Imaging
FRET • FRAP

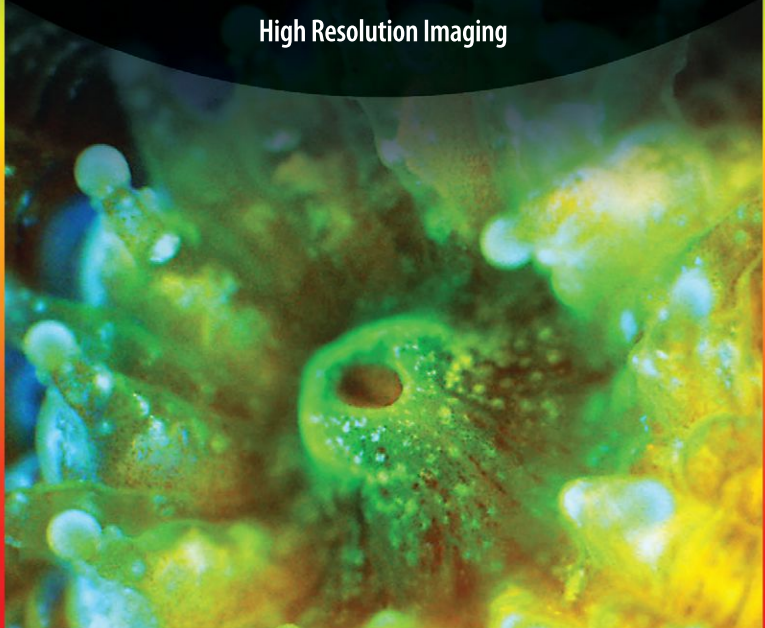


**DURABLE HIGH TRANSMISSION
SPUTTERED FILTERS FROM UV TO NIR**



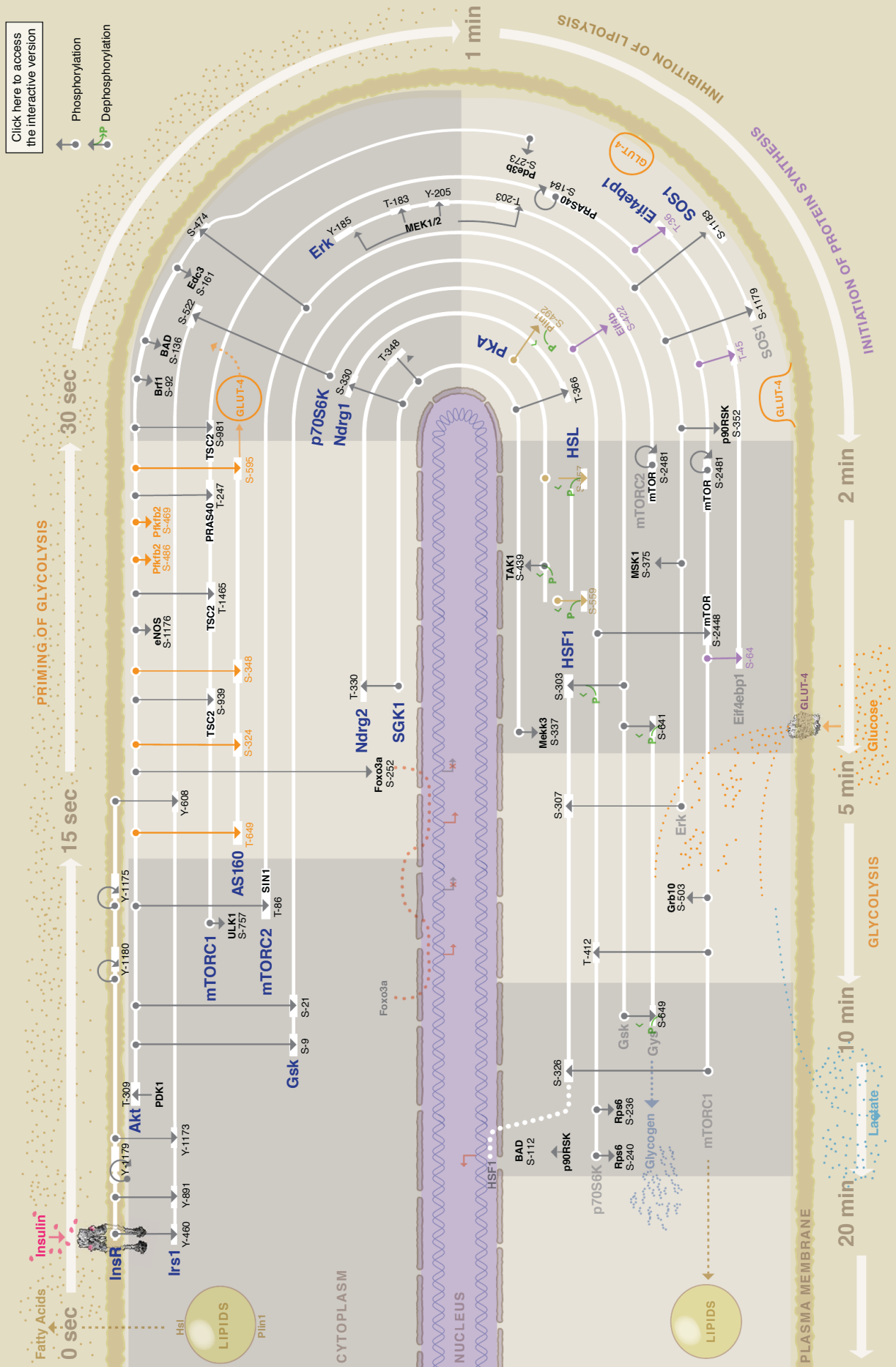
From super-resolution to Raman spectroscopy,
Chroma filters give you more options.

Flow Cytometry • Machine Vision
Point-of-Care • Laser Applications
Raman • Fluorescence • Astronomy
High Resolution Imaging



ENHANCED SnapShot: Insulin/IGF1 Signaling

David K.G. Ma,^{1,2} Christian Stolte,³ James R. Krycer,⁴ David E. James,^{4,5} and Seán I. O'Donoghue^{1,3}
¹Garvan Institute of Medical Research, Darlinghurst NSW 2010, Australia, ²School of Computer Science and Engineering, UNSW Sydney, NSW 2052, Australia, ³CSIRO, North Ryde NSW 1670, Australia, ⁴Charles Perkins Centre, School of Molecular Bioscience, The University of Sydney, NSW 2006, Australia, ⁵Sydney Medical School, The University of Sydney, NSW 2006, Australia



Dharmacon™

RNAi, Gene Expression, and Gene Editing



Specific, functional, and scalable

CRISPR-Cas9 gene editing

Simplify CRISPR-Cas9 gene editing with Dharmacon **predesigned CRISPR guide RNA reagents**. Selected by the **proprietary Dharmacon CRISPR RNA algorithm**, **these genome-wide products** are designed with unparalleled specificity checking, plus selection criteria trained and validated on functional knockout data. Now you can easily order specific, functional, predesigned CRISPR guide RNAs – without any time-consuming design steps or tedious cloning – for editing one gene or thousands.

Optimized tools for confident CRISPR-Cas9 genome engineering

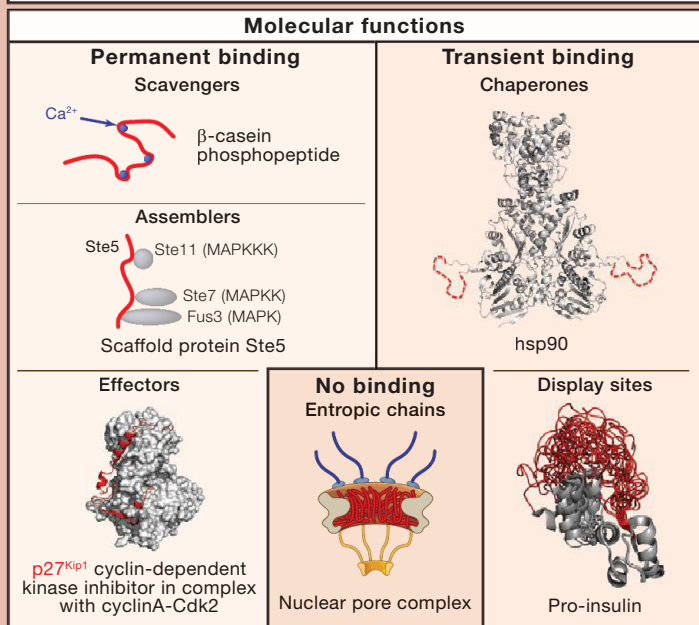
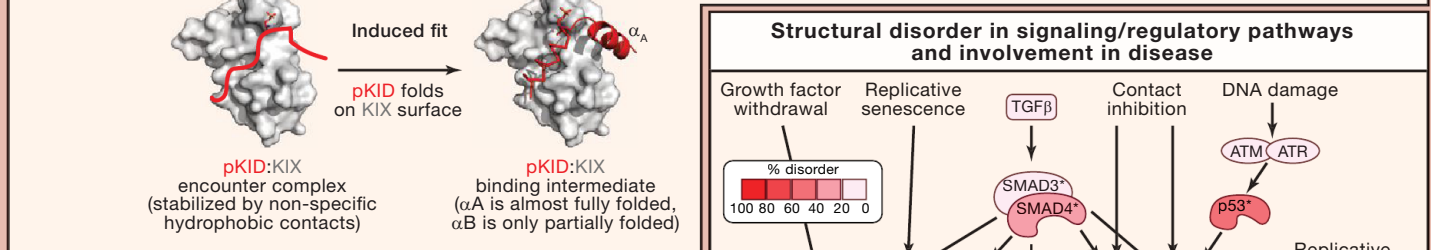
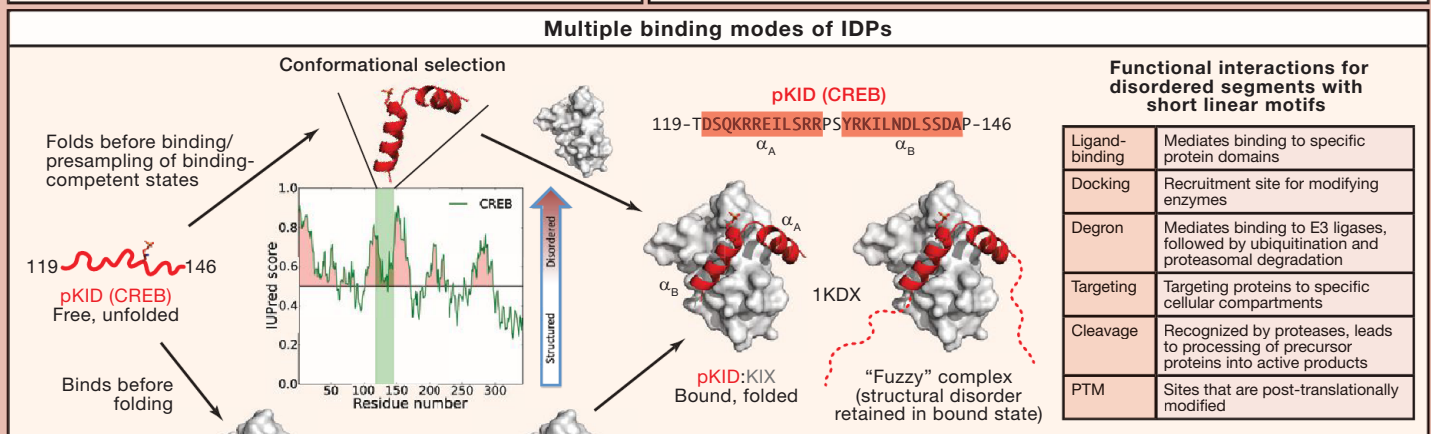
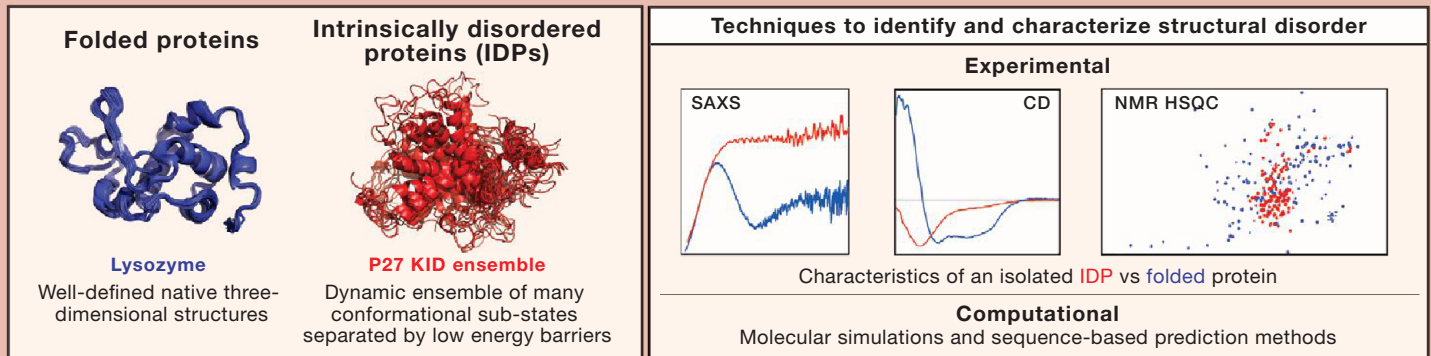
gelifesciences.com/dharmacon

SnapShot: Intrinsic Structural Disorder

Mainak Guharoy,^{1,2} Kris Pauwels,^{1,2} and Peter Tompa^{1,2,3}

¹VIB Structural Biology Research Center (SBRC), Vlaams Instituut voor Biotechnologie, 1050 Brussel, Belgium,

²Structural Biology Brussels (SBB), Vrije Universiteit Brussel, 1050 Brussel, Belgium, ³Institute of Enzymology, Research Centre for Natural Sciences of the Hungarian Academy of Sciences, 1117 Budapest, Hungary



Protein functions	Associated IDPs	Disease
Transcription functions	p53, c-Myc	Cancer
Chromatin-organizing proteins	High mobility group proteins	Breast, colon, gastric, and gastrointestinal cancer
Signaling adaptors and scaffolds	BRCA-1, titin, MAP2, axin	Cancer, cardiomyopathy
Cytoskeletal proteins	Tau protein, MAP2	Alzheimer's disease, tauopathies
Cell-cycle regulation	p21, p27Kip1, inhibitor-2	Breast and prostate cancer, Alzheimer's disease

The BMG LABTECH All Stars

Innovative, high-performance microplate readers for all assay needs



CLARIOstar®

The most sensitive monochromator-based microplate reader. Equipped with revolutionary LVF monochromators™, it is the perfect reader for flexible assay development.

PHERAstar® FSX

The new gold standard for High Throughput Screening. The PHERAstar FSX is the new reference multi-mode plate reader, combining highest sensitivity with the fastest read times.

Omega series

Upgradeable single to multi-mode filter-based microplate readers. The Omega series offers a combination of flexibility and performance for any life science application.

SPECTROstar® Nano

Microplate reader with ultra-fast detection of UV/Vis absorbance. Spectra from 220 - 1000 nm are detected in less than one second per sample in microplates and cuvettes.

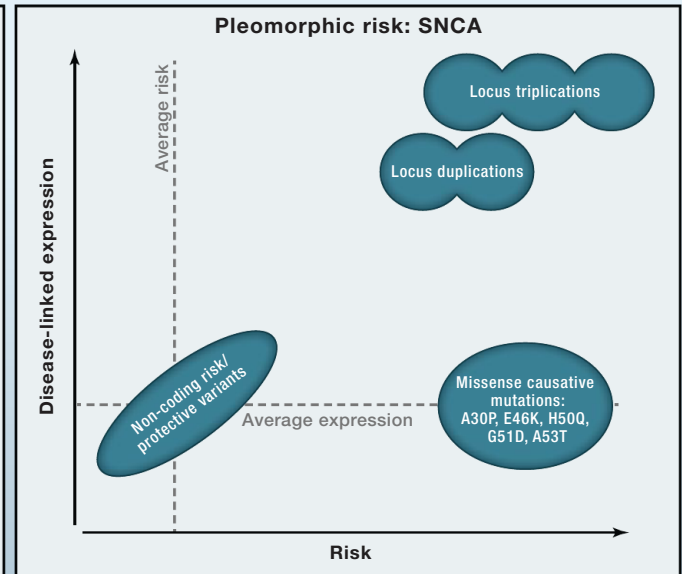
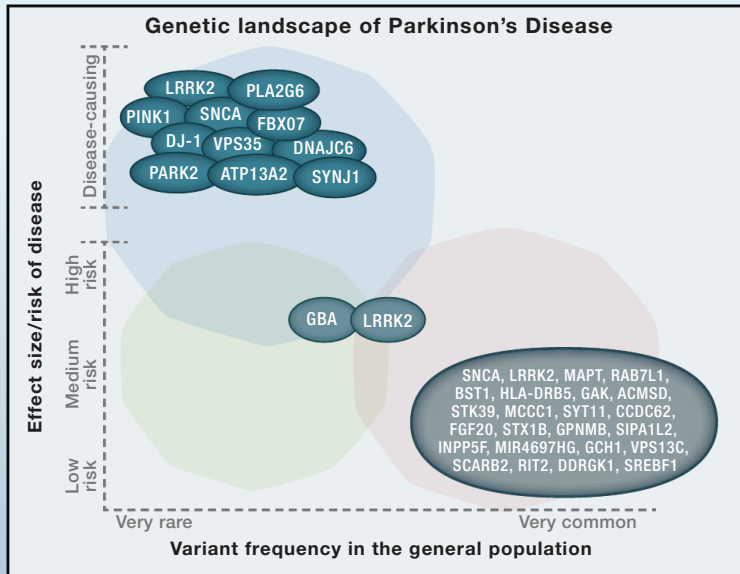
Find all our microplate readers on www.bmglabtech.com


BMG LABTECH
The Microplate Reader Company

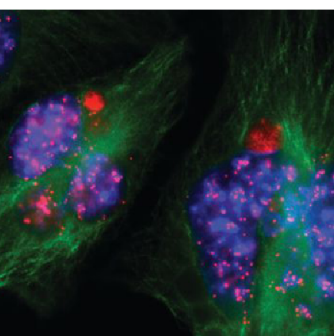
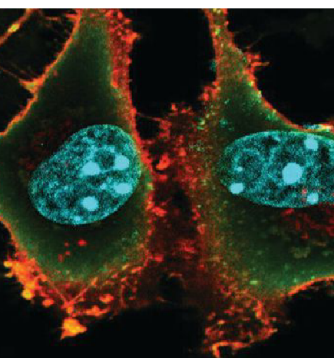
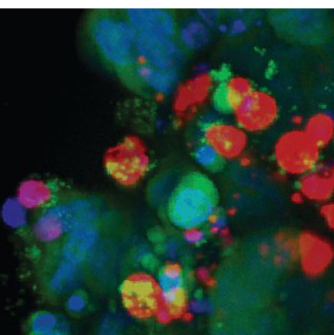
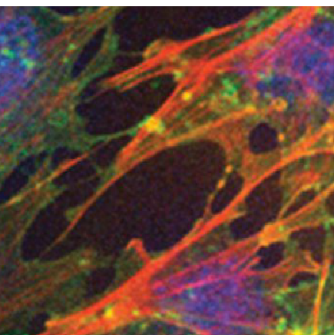
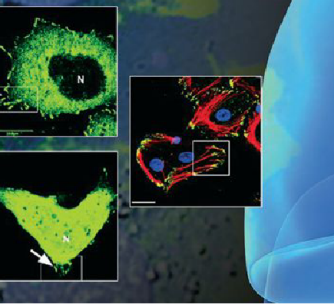
SnapShot: Genetics of Parkinson's Disease

José Brás, Rita Guerreiro, and John Hardy

Department of Molecular Neuroscience, Institute of Neurology, University College London, Queen Square, London WC1N 1PJ, UK



Gene official symbol	Gene name	Location	Possible pathways / pathological biological processes
MENDELIAN GENES			
SNCA	Synuclein, alpha	4q21	Synaptic function; mitochondrial function; autophagy/lysosomal degradation
PARK2	Parkin RBR E3 ubiquitin protein ligase	6q25.2-q27	Mitochondrial function/mitophagy; ubiquitination; synaptic function
PINK1	PTEN -induced putative kinase 1	1p36	Mitochondrial function/mitophagy
PARK7/DJ-1	Parkinson protein 7	1p36.23	Inflammation/immune system; mitochondrial function
LRRK2	Leucine-rich repeat kinase 2	12q12	Synaptic function; inflammation/immune system; autophagy/lysosomal degradation
PLA2G6	Phospholipase A2, group VI	22q13.1	Mitochondrial function
FBX07	F-box protein 7	22q12.3	Ubiquitination; mitochondrial function/mitophagy
VPS35	Vacuolar protein sorting 35 homolog (<i>S. cerevisiae</i>)	16q12	Autophagy/lysosomal degradation; endocytosis
ATP13A2	ATPase type 13A2	1p36	Mitochondrial function; autophagy/lysosomal degradation
DNAJC6	DnaJ (Hsp40) homolog, subfamily C, member 6	1p31.3	Synaptic function; endocytosis
SYNJ1	Synaptojanin 1	21q22.2	Synaptic function; endocytosis
RISK GENES			
GBA	Glucosidase, beta, acid	1q21	Inflammation/immune system; autophagy/lysosomal degradation; metabolic pathways
RISK LOCI			
MAPT	Microtubule-associated protein tau	17q21.1	Microtubule stabilization and axonal transport
RAB7L1	RAB7, member RAS oncogene family-like 1	1q32	Autophagy/lysosomal degradation
BST1	Bone marrow stromal cell antigen 1	4p15	Immune system
HLA-DRB5	Major histocompatibility complex, class II, DR beta 5	6p21.3	Inflammation/immune system
GAKI	Cyclin-G-associated kinase	4p16	Autophagy/lysosomal degradation; synaptic function; endocytosis
ACMSD	Aminocarboxymuconate semialdehyde decarboxylase	2q21.3	Tryptophan metabolism; metal ion binding; metabolic pathways
STK39	Serine threonine kinase 39	2q24.3	Inflammation/immune system; protein kinase binding; cellular stress response
SYT11	Synaptotagmin XI	1q21.2	Synaptic function; transporter activity; metal ion binding; substrate for PARK2
FGF20	Fibroblast growth factor 20	8p22	Growth factor activity; FGF receptor binding
STX1B	Syntaxin 1B	16p11.2	Synaptic function; SNAP receptor activity; protein domain-specific binding
GNPMB	Glycoprotein (transmembrane) nmb	7p15	Integrin binding; heparin binding; cancer pathways
SIP1L2	Signal-induced proliferation-associated 1 like 2	1q42.2	GTPase activator activity
INPP5F	Inositol polyphosphate-5-phosphatase F	10q26.11	Phosphoric ester hydrolase activity
MIR4697HG	MIR4697 host gene (non-protein coding)	11q25	
GCH1	GTP cyclohydrolase 1	14q22.1-q22.2	GTP binding; calcium ion binding; BH4 metab; metabolic pathways
VPS13C	Vacuolar protein sorting 13 homolog C (<i>S. cerevisiae</i>)	15q22.2	Endocytosis
DDRGK1	DDRGK domain containing 1	20p13	Protein binding
MCCC1	Methylcrotonoyl-CoA carboxylase 1 (alpha)	3q27	Biotin carboxylase activity; methylcrotonoyl-CoA carboxylase activity; metabolic pathways
SCARB2	Scavenger receptor class B, member 2	4q21.1	Autophagy/lysosomal degradation; receptor activity (lysosomal receptor for GBA targeting); enzyme binding
CCDC62	Coiled-coil domain containing 62	12q24.31	Nuclear receptor coactivator; cancer pathways
RIT2	Ras-like without CAAX 2	18q12.3	Synaptic function; calmodulin binding; GTP binding
SREBF1	Sterol regulatory element binding transcription factor 1	17p11.2	Chromatin binding; cholesterol and steroid metabolic processes



2016 SCIENTIFIC CONFERENCES

Presenting the most significant research on cancer etiology, prevention, diagnosis, and treatment

Fourth AACR-IASLC International Joint Conference: Lung Cancer Translational Science From the Bench to the Clinic

*Conference Chairpersons: Karen L. Kelly and
Alice T. Shaw*

*Co-Chairpersons: Stephen B. Baylin, Jeffrey A.
Engelman, Roy S. Herbst, and Pierre P. Massion*
January 4-7, 2016 • San Diego, CA

The Function of Tumor Microenvironment in Cancer Progression

*Conference Co-Chairpersons: Raghu Kalluri, Robert A.
Weinberg, Douglas Hanahan, and Morag Park*
January 7-10, 2016 • San Diego, CA

Patient-Derived Cancer Models: Present and Future Applications from Basic Science to the Clinic

*Conference Co-Chairpersons: Manuel Hidalgo,
Hans Clevers, S. Gail Eckhardt, and Joan Seoane*
February 11-14, 2016 • New Orleans, LA

10th AACR-JCA Joint Conference on Breakthroughs in Cancer Research: From Biology to Therapeutics

Co-Chairpersons: Frank McCormick and Tetsuo Noda
February 16-20, 2016 • Maui, HI

AACR Precision Medicine Series: Cancer Cell Cycle-Tumor Progression and Therapeutic Response

Conference Chairperson: Julien Sage
*Co-Chairpersons: Karen E. Knudsen and
J. Alan Diehl*
February 28-March 2, 2016 • Orlando, FL

AACR Annual Meeting 2016

Program Committee Chairperson: Scott A. Armstrong
April 16-20, 2016 • New Orleans, LA

Pancreatic Cancer

*Conference Co-Chairpersons: Manuel Hidalgo,
Christine Iacobuzio-Donahue, and
Robert H. Vonderheide*
May 12-15, 2016 • Orlando, FL

AACR Precision Medicine Series: Targeting the Vulnerabilities of Cancer

*Conference Co-Chairpersons: Stephen W. Fesik,
Jeffrey E. Settleman, and Paul Workman*
May 16-19, 2016 • Miami, FL

Engineering and Physical Sciences in Oncology

*Conference Co-Chairpersons: Rakesh Jain,
Robert Langer, and Joan Brugge*
June 25-28, 2016 • Boston, MA

Translational Control of Cancer: A New Frontier in Cancer Biology and Therapy

*Conference Co-Chairpersons: Jennifer A. Doudna,
Frank McCormick, Davide Ruggero, and
Nahum Sonenberg*
October 27-30, 2016 • San Francisco, CA

DNA Repair: Tumor Development and Therapeutic Response

*Conference Co-Chairpersons: Robert G. Bristow,
Theodore S. Lawrence, and Maria Jasin*
November 2-5, 2016 • Montreal, Quebec, Canada

EORTC-NCI-AACR Molecular Targets and Cancer Therapeutics Symposium

November 29-December 2, 2016 • Munich, Germany

Learn more and register at
www.AACR.org/Calendar

AACR American Association
for Cancer Research
FINDING CURES TOGETHER™

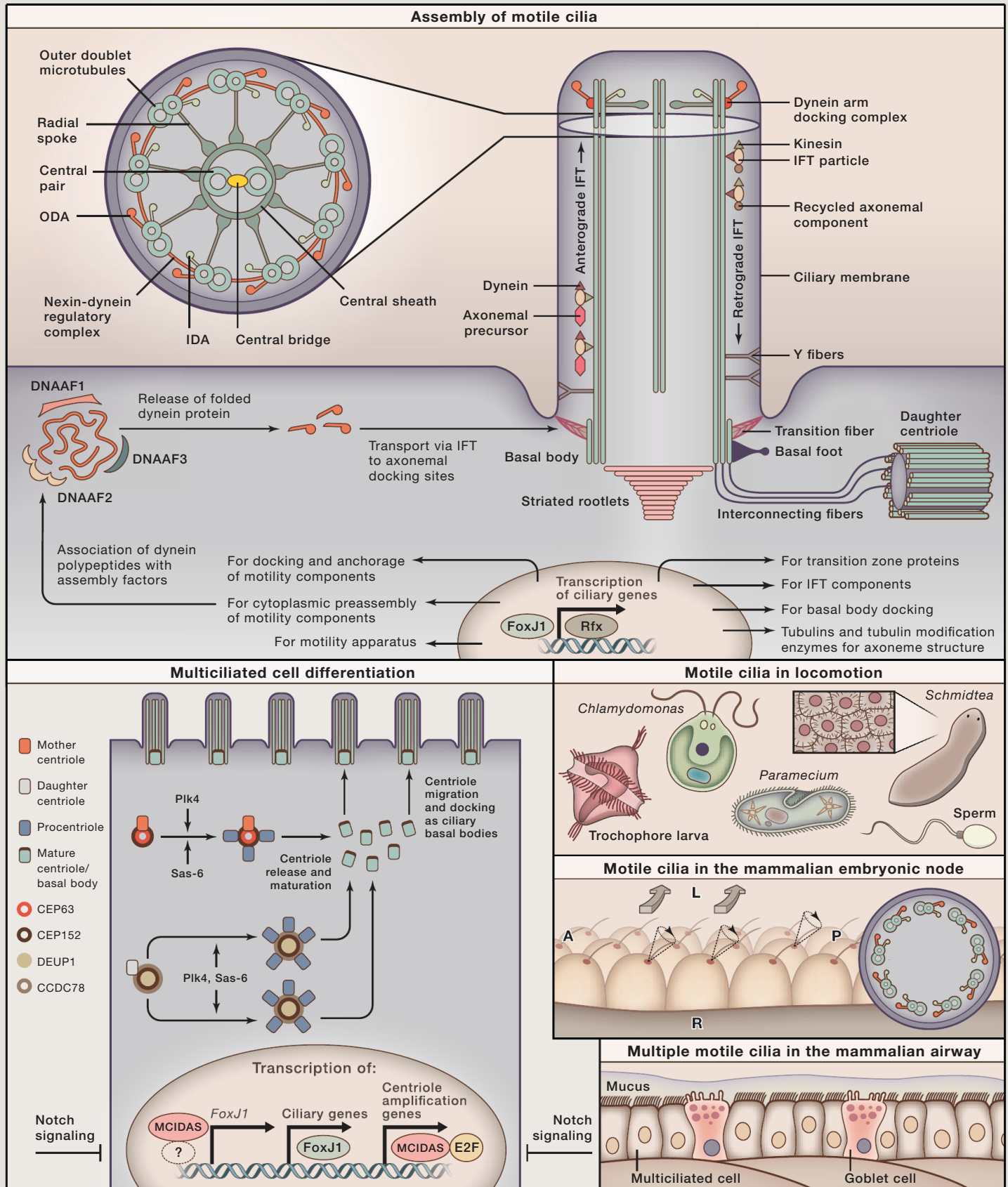
SnapShot: Motile Cilia

Feng Zhou¹ and Sudipto Roy^{1,2,3}

¹Institute of Molecular and Cell Biology, Proteos, Singapore 138673, Singapore

²Department of Biological Sciences, National University of Singapore, Singapore 117543, Singapore

³Department of Pediatrics, National University of Singapore, Singapore 119228, Singapore



HUMANIZED NSG™ MICE

SOPHISTICATED. INNOVATIVE. VERSATILE.

JAX humanized NSG™ is the platform of choice for studying immuno-oncology, viral host-pathogen interactions, or the development of novel drug therapies.

**START YOUR
STUDY TODAY!**

Expect delivery of your order
within 7-10 business days.



1-800-422-6423 (US, Canada & Puerto Rico)
1-207-288-5845 (from any location)

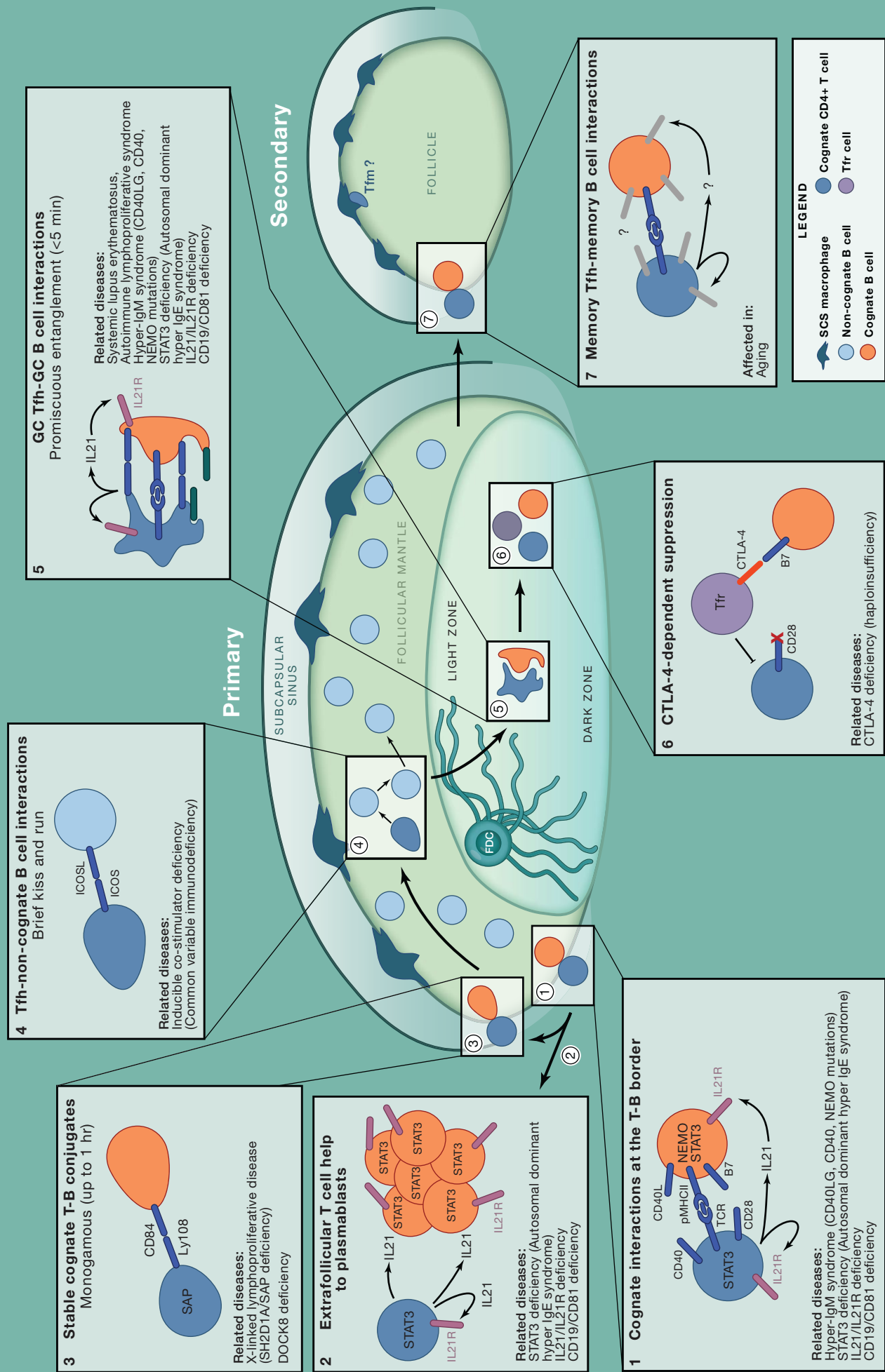
jax.org/humanized-mice



Snapshot: Interactions between B Cells and T Cells

Stuart G. Tangye,^{1,2} Robert Brink,^{1,2} Christopher C. Goodnow,^{1,2} and Tri Giang Phan^{1,2}

¹Immunology Division, Garvan Institute of Medical Research, Darlinghurst NSW 2010, Australia; ²St Vincent's Clinical School, 2010 UNSW, Australia



The 2016 Keystone Symposia Meeting Series

Systems Immunology: From Molecular Networks to Human Biology (A1)

Jan 10–14, 2016 | Big Sky, Montana | USA

Cytokine JAK-STAT Signaling in Immunity & Disease (A2)

Jan 10–14, 2016 | Steamboat Springs, Colorado | USA

Molecular & Cellular Basis of Growth & Regeneration (A3)

Jan 10–14, 2016 | Breckenridge, Colorado | USA

Nuclear Receptors: Full Throttle (J1)

joint with **Metabolism, Transcription & Disease (J2)**

Jan 10–14, 2016 | Snowbird, Utah | USA

Biology of Down Syndrome: Impacts Across the Biomedical Spectrum (A4)

Jan 24–27, 2016 | Santa Fe, New Mexico | USA

Traumatic Brain Injury: Clinical, Pathological & Translational Mechanisms (J3)

joint with **Axons: From Cell Biology to Pathology (J4)**

Jan 24–27, 2016 | Santa Fe, New Mexico | USA

Drug Discovery for Parasitic Diseases (A5)

Jan 24–28, 2016 | Tahoe City, California | USA

Small RNA Silencing: Little Guides, Big Biology (A6)

Jan 24–28, 2016 | Keystone, Colorado | USA

Purinergic Signaling (J5) *joint with* Cancer Immunotherapy: Immunity & Immunosuppression Meet Targeted Therapies (J6)

Jan 24–28, 2016 | Vancouver, British Columbia | Canada

Neurological Disorders of Intracellular Trafficking (A7)

Jan 31–Feb 4, 2016 | Keystone, Colorado | USA

Cell Biology & Immunology of Persistent Infection (A8)

Jan 31–Feb 4, 2016 | Banff, Alberta | Canada

The Cancer Genome (Q1) *joint with* Genomics & Personalized Medicine (Q2)

Feb 7–11, 2016 | Banff, Alberta | Canada

Fibrosis: From Basic Mechanisms to Targeted Therapies (Q3)

joint with **Stromal Cells in Immunity (Q4)**

Feb 7–11, 2016 | Keystone, Colorado | USA

Plant Epigenetics: From Genotype to Phenotype (B1)

Feb 15–19, 2016 | Taos, New Mexico | USA

Obesity & Adipose Tissue Biology (B2)

Feb 15–19, 2016 | Banff, Alberta | Canada

Noncoding RNAs in Health & Disease (Q5)

joint with **Enhancer Malfunction in Cancer (Q6)**

Feb 21–24, 2016 | Santa Fe, New Mexico | USA

G Protein-Coupled Receptors: Structure, Signaling & Drug Discovery (B3)

Feb 21–25, 2016 | Keystone, Colorado | USA

New Frontiers in Understanding Tumor Metabolism (Q7)

joint with **Immunometabolism in Immune Function & Inflammatory Disease (Q8)**

Feb 21–25, 2016 | Banff, Alberta | Canada

T Follicular Helper Cells & Germinal Centers (B4)

Feb 26–Mar 1, 2016 | Monterey, California | USA

Immunity in Skin Development, Homeostasis & Disease (B5)

Feb 28–Mar 2, 2016 | Tahoe City, California | USA

Tuberculosis Co-Morbidities & Immunopathogenesis (B6)

Feb 28–Mar 3, 2016 | Keystone, Colorado | USA

Stem Cells & Cancer (C1)

Mar 6–10, 2016 | Breckenridge, Colorado | USA

Cancer Vaccines: Targeting Cancer Genes for Immunotherapy (X1)

joint with **Antibodies as Drugs (X2)**

Mar 6–10, 2016 | Whistler, British Columbia | Canada

Ubiquitin Signaling (X3) *joint with* NF- κ B & MAP Kinase Signaling in Inflammation (X4)

Mar 13–17, 2016 | Whistler, British Columbia | Canada

Islet Biology: From Cell Birth to Death (X5)

joint with **Stem Cells & Regeneration in the Digestive Organs (X6)**

Mar 13–17, 2016 | Keystone, Colorado | USA

Chromatin & Epigenetics (C2)

Mar 20–24, 2016 | Whistler, British Columbia | Canada

HIV Persistence: Pathogenesis & Eradication (X7) *joint with* HIV Vaccines (X8)

Mar 20–24, 2016 | Olympic Valley, California | USA

Cancer Pathophysiology: Integrating the Host & Tumor Environments (C3)

Mar 28–Apr 1, 2016 | Breckenridge, Colorado | USA

Modern Phenotypic Drug Discovery: Defining the Path Forward (D1)

Apr 2–6, 2016 | Big Sky, Montana | USA

Mitochondrial Dynamics (D2)

Apr 3–7, 2016 | Steamboat Springs, Colorado | USA

Heart Failure: Genetics, Genomics & Epigenetics (Z1)

joint with **Cardiac Development, Regeneration & Repair (Z2)**

Apr 3–7, 2016 | Snowbird, Utah | USA

Myeloid Cells (D3)

Apr 10–14, 2016 | Killarney, County Kerry | Ireland

New Therapeutics for Diabetes & Obesity (G1)

Apr 17–20, 2016 | La Jolla, California | USA

Gut Microbiota, Metabolic Disorders & Beyond (D4)

Apr 17–21, 2016 | Newport, Rhode Island | USA

Epigenetic & Metabolic Regulation of Aging & Aging-Related Diseases (E1)

May 1–5, 2016 | Santa Fe, New Mexico | USA

Positive-Strand RNA Viruses (N1)

May 1–5, 2016 | Austin, Texas | USA

Nucleic Acid Sensing Pathways: Innate Immunity, Immunobiology & Therapeutics (E2)

May 8–12, 2016 | Dresden | Germany

State of the Brain (R1)

May 22–26, 2016 | Alpbach | Austria

New Approaches to Vaccines for Human & Veterinary Tropical Diseases (M1)

May 22–26, 2016 | Cape Town | South Africa

B Cells at the Intersection of Innate & Adaptive Immunity (E3)

May 29–Jun 2, 2016 | Stockholm | Sweden

Understanding the Function of Human Genome Variation (K1)

May 31–Jun 4, 2016 | Uppsala | Sweden

Autophagy: Molecular & Physiological Mechanisms (V1)

Jun 5–9, 2016 | Whistler, British Columbia | Canada

Common Mechanisms of Neurodegeneration (Z3)

joint with **Microglia in the Brain (Z4)**

Jun 12–16, 2016 | Keystone, Colorado | USA

Exosomes/Microvesicles: Novel Mechanisms of Cell-Cell Communication (E4)

Jun 19–22, 2016 | Keystone, Colorado | USA

Translational Vaccinology for Global Health (S1)

Oct 26–30, 2016 | London | United Kingdom

Phytobiomes: From Microbes to Plant Ecosystems (S2)

Nov 8–12, 2016 | Guarujá, São Paulo | Brazil

Hemorrhagic Fever Viruses (S3)

Dec 4–8, 2016 | Santa Fe, New Mexico | USA

Cellular Stress Responses and Infectious Agents (S3)

Dec 4–8, 2016 | Santa Fe, New Mexico | USA



KEYSTONE SYMPOSIA™
on Molecular and Cellular Biology
Accelerating Life Science Discovery

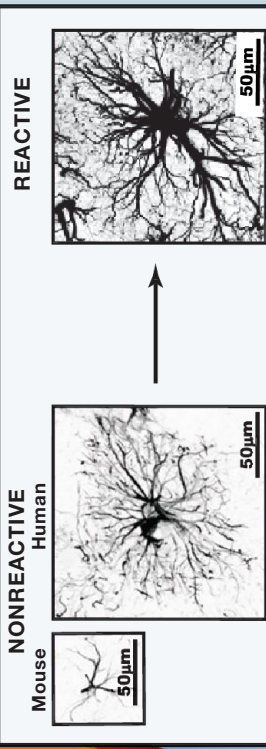
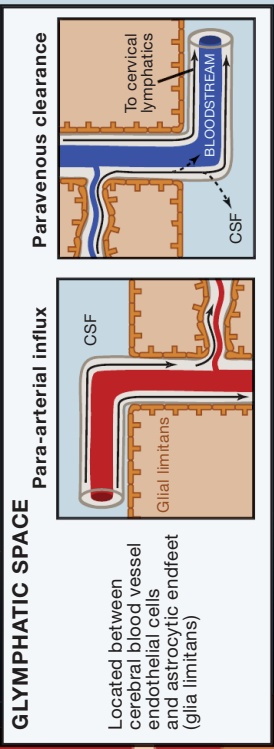
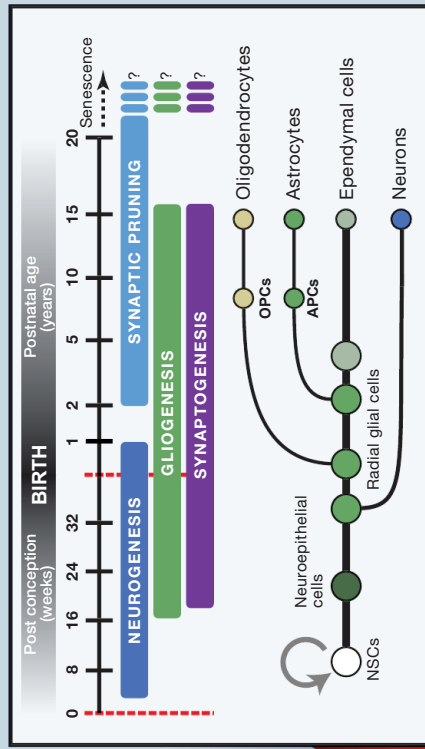
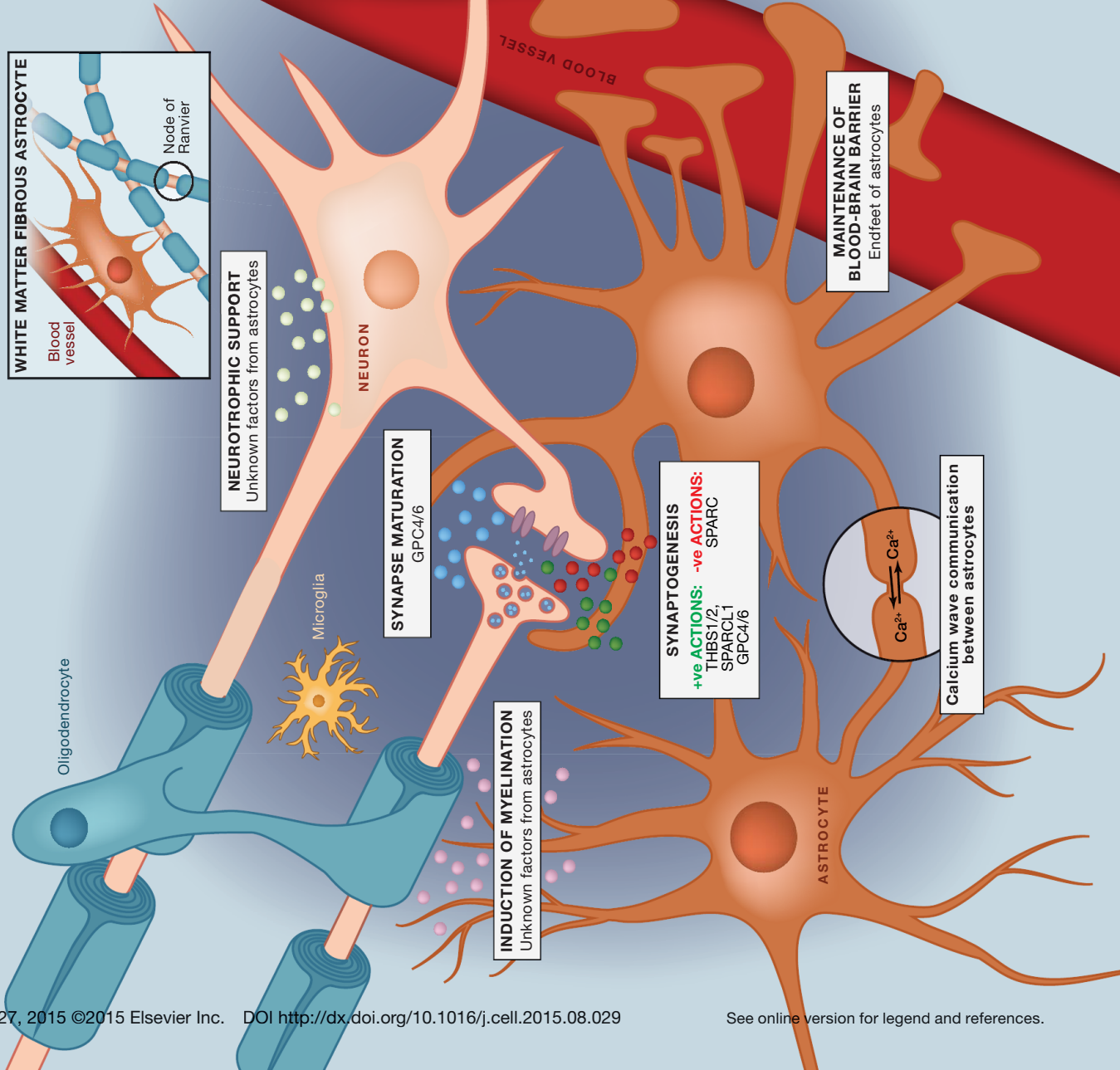
www.keystonesymposia.org/meetings | 1.800.253.0685 | 1.970.262.1230

SnapShot: Astrocytes in Health and Disease

Shane Liddelow^{1,2} and Ben Barres¹

¹Department of Neurobiology, Stanford University, Stanford, CA 94305, USA

²Department of Pharmacology and Therapeutics, The University of Melbourne, Melbourne, Victoria 3010, Australia



Multiple mediators from injury and disease, eg., A1 (neuroinflammation), A2 (ischemia)

ASTROCYTE REACTIVITY (REACTIVE ASTROGLIOSIS)	
Cell proliferation	Scar-forming reactive astrocytes
Cell migration	Yes
Tiling domains intact?	No
Resolution of reactivity?	Yes
Interactions with other CNS cells	Potentially (with removal of noxious stimuli)
	Neural cells (neurons and oligodendrocytes)
	No (permanent)
	No (non-neural cells (inflammatory and fibrotic cells))

BAKER

Environments For Science™

From the moment when
the pieces fell into place,
and you saw the big picture,

through late nights reviewing literature,
designing procedures,
testing hypotheses —

nothing fell through the cracks,
because too much was at stake.

The work you did then
advanced your field,
and your career.

We are proud to have been there,
protecting your work, and you,
with the very best in air containment,
contamination control, and
controlled environment technology.

Now, as your work gives rise
to new discoveries —

**We can't wait to see
what you do next.**



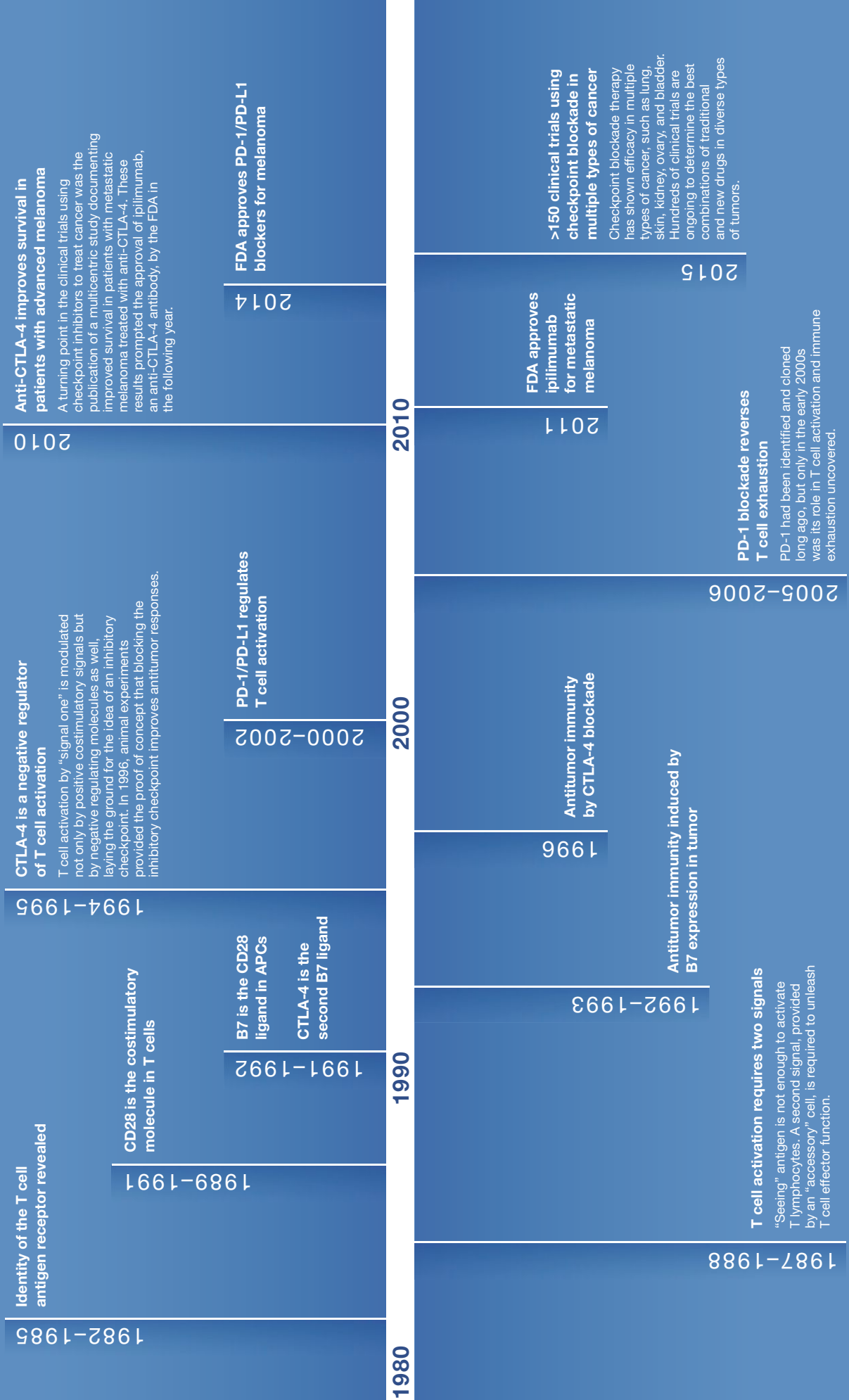
bakerco.com

Biological Safety Cabinets • Clean Benches • Fume Hoods • CO₂ Incubators • Hypoxia & Anaerobic Workstations

Timeline: Checkpoint Blockade

Joao Monteiro, Editor
Cell

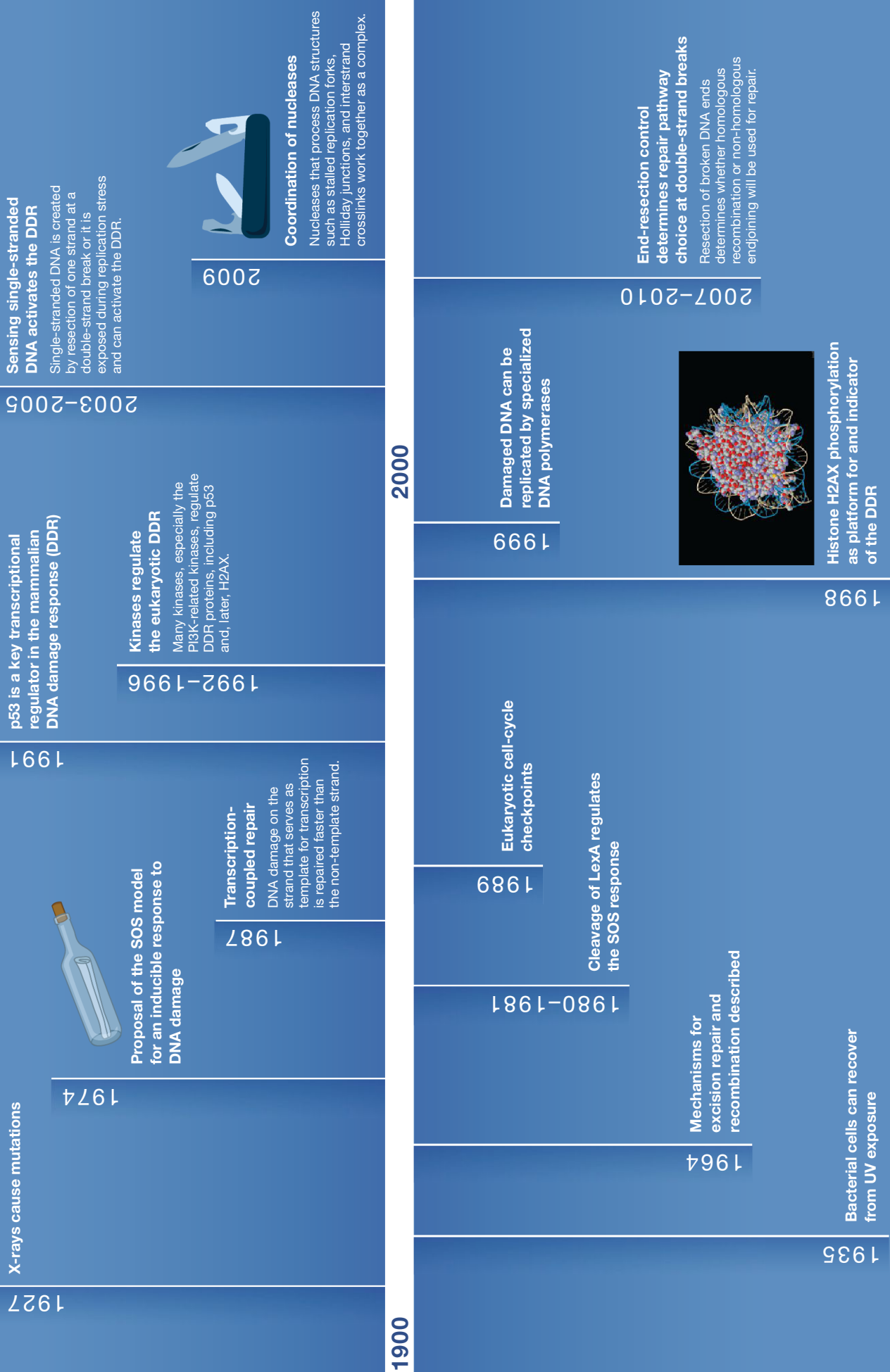
Cell



Timeline: Sending Out an SOS

Brian Plosky, Deputy Editor
Molecular Cell

Cell



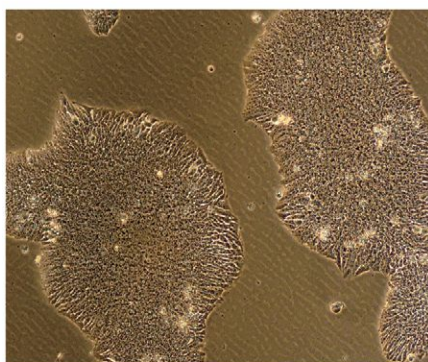
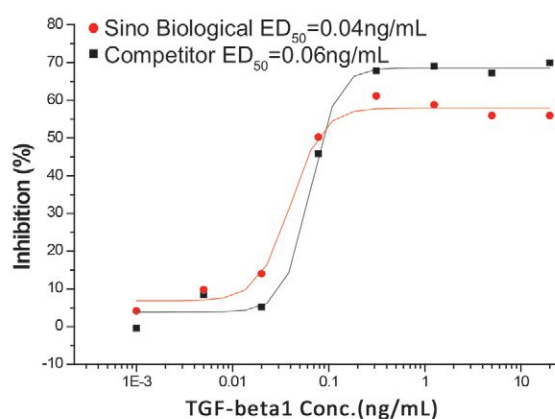
Cytokines & Growth Factors in Cell Culture

>> Produced in house

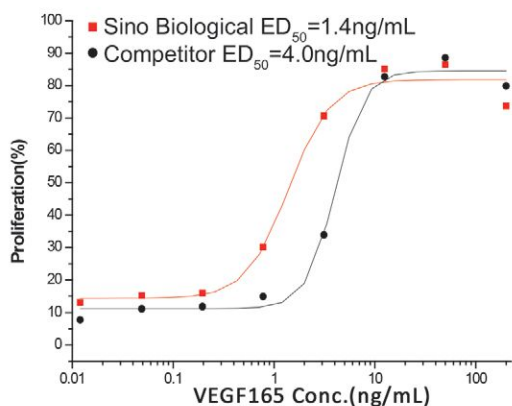
>> Bulks in stock

>> Multiple species

>> Save up to 60%



hESC cultured with TGF-β1+bFGF



Measured in a cell proliferation assay using HUVEC



Sino Biological Inc.

Biological Solution Specialist

www.sinobiological.com

An Adenine Code for DNA: A Second Life for N6-Methyladenine

Holger Heyn¹ and Manel Esteller^{1,2,3,*}

¹Cancer Epigenetics and Biology Program (PEBC), Bellvitge Biomedical Research Institute (IDIBELL), 08908 L'Hospitalet de Llobregat, Barcelona, Catalonia, Spain

²Department of Physiological Sciences II, School of Medicine, University of Barcelona, 08036 Barcelona, Catalonia, Spain

³Institució Catalana de Recerca i Estudis Avançats (ICREA), 08010 Barcelona, Catalonia, Spain

*Correspondence: mesteller@idibell.cat

<http://dx.doi.org/10.1016/j.cell.2015.04.021>

DNA N6-methyladenine (6mA) protects against restriction enzymes in bacteria. However, isolated reports have suggested additional activities and its presence in other organisms, such as unicellular eukaryotes. New data now find that 6mA may have a gene regulatory function in green alga, worm, and fly, suggesting m6A as a potential “epigenetic” mark.

The Origins of Adenine Methylation

Genetic constraints hamper the response of cells to the changing environment and represent a hurdle to adaptations that characterize living organisms. Thus, dynamic modifications that expand the genetic code beyond A, G, C, and T are necessary. Among the most studied, 5-methylcytosine (5mC) exerts a predominant role due to its important activities in mammals to establish the epigenetic setting and its relevance in human disorders, particularly cancer (Heyn and Esteller, 2012). 5mC has been named the fifth base of DNA, and only lately has a second modification in DNA, 5-hydroxymethylcytosine (5hmC), emerged as a contender for human cells (Kohli and Zhang, 2013). Other derivatives, such as 5-formylcytosine and 5-carboxylcytosine, are so far considered transitory byproducts of oxidative demethylation (Kohli and Zhang, 2013). However, this can be an anthropocentric view. N4-methylcytosine (4mC) is very common in bacteria but absent in mammals. There is an even more intriguing DNA modification: N6-methyladenine (6mA) (Figure 1A).

6mA represents a dominant modification in bacteria, while 5mC is absent in many prokaryotic genomes (Fang et al., 2012). In bacteria, 6mA was initially reported to be part of restriction-modification (R-M) systems—bacterial defense mechanisms against phages and plasmids that are able to distinguish between host and invader DNA (Arber and Dussoix, 1962). Specifically, the presence of 6mA in the host prevents the digestion of its genome by DNA methylation-sensitive restriction enzymes. In contrast, foreign unmethylated DNA lacks the protection and is readily degraded when entering the cells. R-M system-positive strains are equipped with DNA methyl-transferase and endonuclease counterparts with common sequence recognition motifs.

However, the fact that other methyl-transferases lack a restriction enzyme counterpart and that m6A is important for viability in specific bacterial strains suggests a defense-independent function. Specifically, adenine methylation is established as a bacterial epigenetic mark. Exemplary, solitary adenine methylases, such as Dam in *E. coli*, are involved in DNA replication, wherein sister-strand synthesis can only be

initiated in the presence of methylated adenine at replication origin (Wion and Casadesús, 2006). Dam-mediated methylation also regulates replication initiator factors.

6mA guides the discrimination between original and newly synthesized DNA strand after replication. As de novo adenine methylation is delayed during the cell cycle, the newly synthesized strand is recognized by repair enzymes and the Dam motif enables endonuclease processing with subsequent repair processes (Wion and Casadesús, 2006). Adenine methylation has further functional implication in the cell cycle, repression of transposable elements, and gene regulatory processes (Fang et al., 2012). 6mA also reduces the stability of base pairings, hence favoring transcriptional initiation by lowering the energy to open DNA duplexes. Dam activity can be hindered by binding of competing proteins, resulting in the formation of non-methylated sites. Strikingly, the protection from methylation is an inherited state that, however, can be modified by environmental conditions (Wion and Casadesús, 2006). Thus, adenine methylation displays similar characteristics in prokaryotes as cytosine methylation does in eukaryotes, further underscoring its importance throughout generations.

Adenine Methylation: An Evolutionary Conserved Mechanism

Although some studies hypothesized the presence of 6mA in eukaryotic genomes decades ago, its implication in epigenetics in eukaryotes remains elusive (Ratel et al., 2006). Compared to the highly abundant 5mC in the eukaryotic kingdom, levels of 6mA were suggested to be minimal and thus only detectable by highly sensitive technologies. Nevertheless, several studies reported the presence of 6mA in eukaryotic genomes, particularly in ciliates, chlorophyte algae, and dinoflagellates (Achwal et al., 1983; Gomers-Ampf and Borst, 1995; Ratel et al., 2006). In certain cases, 6mA exists in substantial amounts, with 0.5%–10% of adenines being methylated.

Sequence analysis predicted the presence of adenine methyl-transferases and demethylases in several eukaryotic organisms (Iyer et al., 2011) (Figure 1A). The presence of methyl-transferase

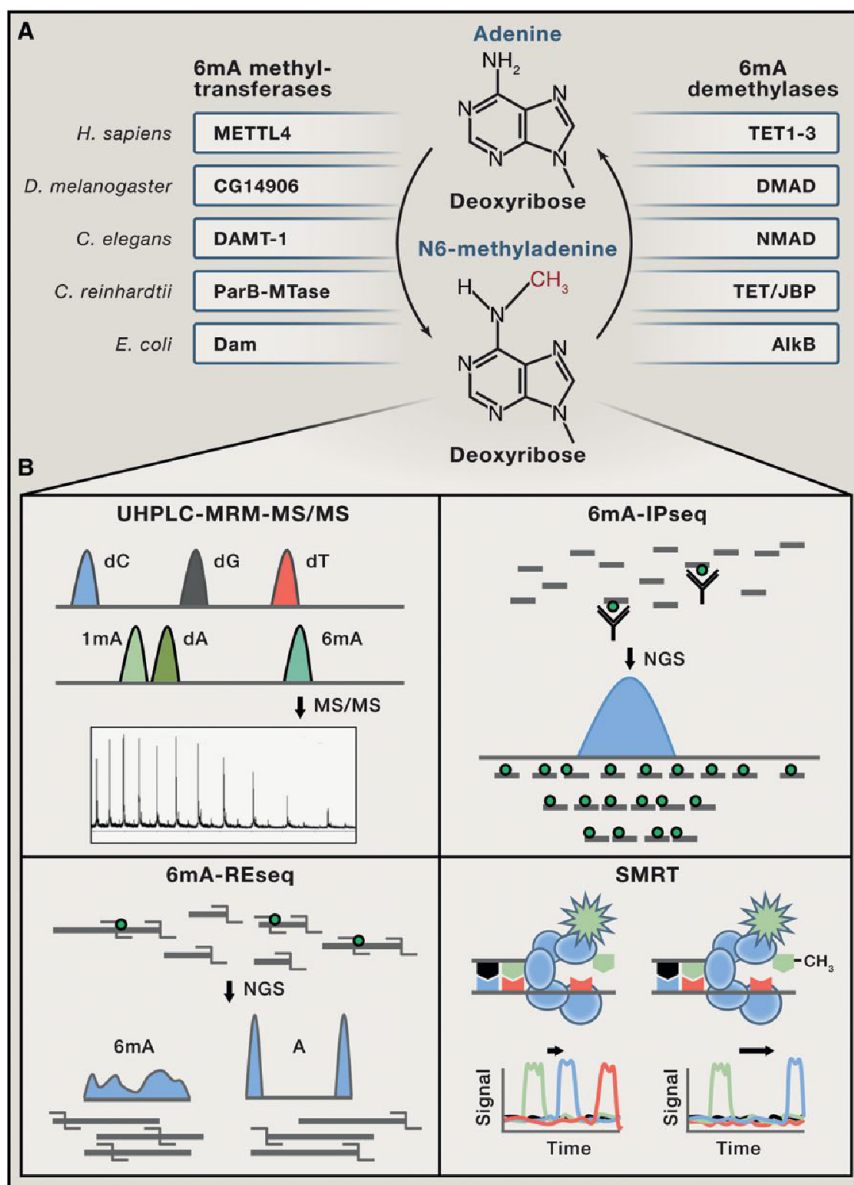


Figure 1. Processing and Detection of N6-Methyladenine

(A) Adenine bases of DNA are modified by N6-methyladenine (6mA) methyl-transferases and 6mA demethylases. The modifying enzymes are conserved in all super-kingdoms of life, with putative activity also in *Homo sapiens* (TET1–3 proteins have so far proven activities as 5mC oxidases).

(B) Methyladenine is detectable by chromatography-based technologies, such as the ultra-high performance liquid chromatography-triple quadrupole mass spectrometry coupled with multiple-reaction monitoring (UHPLC-MRM-MS/MS) method or sequencing approaches. For the specific quantification of methyladenine, next-generation sequencing (NGS)-based strategies are coupled with immunoprecipitation of 6mA (6mA-IPseq) or restriction enzyme guidance (6mA-REseq). Direct quantification at base-pair resolution is enabled by third-generation sequencing methods, such as the single-molecule real-time (SMRT) technology, wherein variant enzyme kinetics identify modified DNA bases.

had yet to be identified (Hattman et al., 1978). Using sequencing-based mapping strategies, Fu et al. produce the first genome-wide reference map for methyladenine in *C. reinhardtii* (Fu et al., 2015). Moreover, the authors provide evidence for an epigenetic function in transcriptional regulation. After confirming abundant 6mA levels by highly sensitive liquid-chromatography and mass-spectrometry methodologies (Figure 1B), they show that 6mA levels are stable and inherited during multiple replication phases. Immunoprecipitation-based sequencing strategies (Figure 1B) identify sequence motifs susceptible to undergo adenine methylation, which are different from the prokaryotic consensus sequences. Subsequently, restriction enzyme-guided resequencing produces a 6mA reference methylome of *C. reinhardtii* at base-pair

orthologs within transposable elements led to the hypothesis of a *cis*-acting control mechanism to secure host genome integrity. Consistently, such a mechanism was identified in *E. coli*, suggesting a conserved function of 6mA as safeguard of the genome (Roberts et al., 1985).

Now, three studies in this issue of *Cell* report the presence of 6mA in three different eukaryotic genomes—*Chlamydomonas reinhardtii*, *Caenorhabditis elegans*, and *Drosophila melanogaster*—with putative epigenetic function (Zhang et al., 2015; Greer et al., 2015; Fu et al., 2015). The authors present evidence for spatiotemporal-regulated 6mA modifications during development. Moreover, 6mA is associated to gene regulatory events.

The green alga *C. reinhardtii* has long been reported to harbor substantial levels of 6mA, but its spatial distribution and function

had yet to be identified (Hattman et al., 1978). Intriguingly, although the methyl-transferase consensus sequence is equally distributed in the genome, 6mA is highly enriched at gene promoters but depleted at the transcription start sites. Consistently, 6mA profiles reveal periodic patterns of 130–140 bp distances and hence a potential association to nucleosome positioning at promoter regions. The presence of 6mA at gene promoters is positively correlated with increased transcriptional activity.

While adenine methylation has been previously described in *C. reinhardtii*, its presence in 6mA *C. elegans* has not been reported despite the presence of putatively active methyl-transferases in the worm genome. Greer et al. now report 6mA to be present in *C. elegans* and functionally involved in epigenetic transgenerational inheritance (Greer et al., 2015). In *C. elegans*, mutants lacking histone demethylase *spr-5*, responsible for

dimethylation of the histone H3 at lysine 4, represent a paradigm of inheritance. Although no phenotype is detectable in early generations, the mutant worms become progressively infertile in later generations, accompanied by increasing histone H3 methylation levels. Surprisingly, Greer et al. now describe that *spr-5* mutants reveal elevated levels of 6mA, accumulating during generations. 6mA in *C. elegans* is shown to be added by the newly identified DNA N6-adenine methyl-transferase 1 (DAMT-1) and dynamically removed by the N6-methyladenine demethylase 1 (NMAD-1). Strikingly, mutations in NMAD-1 lead to accelerated accumulation of 6mA and, moreover, speed up the sterility phenotype in *nmad-1* and *spr-5* double-knockout worms.

Overall, 6mA in *C. elegans* is rather low in wild-type animals (0.025%) but is increased 10-fold in *spr-5* mutant animals. It is noteworthy that, unlike in flies (see below), adenine methylation in *C. elegans* is ubiquitously present in all cell types. Technically, 6mA is determined by different technologies, ranging from global to base-pair resolution profiles using single-molecule real-time (SMRT) sequencing (Figure 1B). Particularly, the latter approach leads to the identification of specific sequence motifs, suggesting a locally regulated deposition of 6mA. However, its functional role remains elusive. Future functional genomics approaches, including a systematic integration of transcriptional profiles, are needed.

The absence of conclusive evidence for cytosine or adenine methylation in *D. melanogaster* has led to the hypothesis that gene regulation takes place without DNA modifications. However, as 6mA is present in eukaryotes at very low levels, Zhang et al. speculate that an impaired function of the putative DNA demethylase DMAD (DNA 6mA demethylase) leads to detectable 6mA in *D. melanogaster* (Zhang et al., 2015). Indeed, using highly sensitive methods (Figure 1B), the authors identify adenine methylation, predominantly in very early developmental stages of the fly embryos (0.07%), but also in somatic cell types. The late-embryo extracts also exhibit elevated demethylating activity compared with early stages.

Demethylation dynamics could be associated with the TET-like protein DMAD, which is dynamically regulated during development. Moreover, DMAD modifies 6mA levels *in vitro* and *in vivo*, and altered demethylase activity leads to increased embryo lethality. 6mA is also detectable in somatic tissue, particularly in ovary and brain cells. Here, 6mA is restricted to certain cell types, being highly abundant in germline cells while losing intensities during germ cell differentiation. In line with these results, DMAD levels increase during egg differentiation, and DMAD mutants present elevated 6mA levels in their ovaries, accompanied by a higher number of undifferentiated cells. Furthermore, high levels of DMAD in brain suggest an antagonistic function in methyl-transferase activities and a dominant suppression of 6mA levels in neurons. 6mA is determined to be enriched in transposon gene bodies, with a putative function in transcriptional activation during early embryonic stages and in undifferentiated cell types.

From the current 6mA knowledge, *C. elegans* and *D. melanogaster* do not present methylcytosine in their genomes. Although the existence of 5mC in *Drosophila* was under controversial discussion for years, recent studies using whole-genome bisulfite sequencing mostly excluded the presence of

5mC in *D. melanogaster* DNA sequence (Raddatz et al., 2013). Hence, the studies by Greer et al. and Zhang et al. suggest 6mA as the unique DNA methylation modification and potentially functional epigenetic mark in *C. elegans* and *D. melanogaster*, respectively. Although the global levels of 6mA are rather low, its local enrichment and sequence specificity point to regulated processing throughout development and differentiation. Future studies need to further establish its role as epigenetic mark and its function in gene regulation.

However, 6mA and 5mC have been described to co-exist in the *C. reinhardtii* genome. Consistently, methyl-transferases and demethylases are conserved in the green alga (Iyer et al., 2011) (Figure 1A). Now, base-pair resolution landscapes of both DNA modifications in *C. reinhardtii* reveal a likely complementary function of 6mA and 5mC, indicated by their spatial separation in the genome (Fu et al., 2015). While 5mC is enriched at the gene bodies of lowly expressed transcripts, 6mA accumulates at the promoter region of highly active genes. It is remarkable that 5mC in *Chlamydomonas* exists at lower levels than observed in higher eukaryotes and is not restricted to CpG motifs (Feng et al., 2010). Taken together, the evidence suggests 6mA to represent an active epigenetic mark in *C. reinhardtii*, while 5mC is likely to be involved in processes downstream of transcriptional initiation.

Intriguingly, although cytosine methylation represents by far the dominant DNA modification in *Homo sapiens*, the machinery to modify adenine nucleotides is conserved during evolution. In this regard, the methyl-transferase-like 4 (METTL4) is similar to DAMT-1 in *C. elegans* (Greer et al., 2015) (Figure 1A). Moreover, active demethylases of the TET family proteins, such as DMAD in *D. melanogaster*, exhibit specificity for methyl adenines and thus might also be implicated in 6mA dynamics in higher eukaryotes (Iyer et al., 2011). In this regard, early studies also reported 6mA in human tissue, specifically placenta (Achwal et al., 1983). However, the presence and function of the adenine code in mammals need to be confirmed by applying novel ultrasensitive detection technologies (Figure 1B). These technologies will play a key role in improving our understanding on the complexity of DNA modifications in the biology of eukaryotic life and will be discussed below.

The detection of 6mA in human placenta encourages speculations of a specialized function of adenine methylation in specific cell types. Taking into account the mutagenic nature of 5mC, continuously dividing cell types, such as adult stem cells, might have conserved an epigenetic mechanism that better supports the integrity of the DNA template. 6mA presents a potential alternative to 5mC to avoid the accumulation of *de novo* mutations in the immortal DNA strand. In line, 6mA is determined to be highly abundant in early stages of development and undifferentiated reproductive tissue in *D. melanogaster*, supporting the hypothesis of an epigenetic mark with restricted function in pluripotent cell types (Zhang et al., 2015).

Sensitive Detection of Adenine Methylation of DNA

Many of the questions that we have now for 6mA remained open not so long ago for 5mC and 5hmC. For these two cases, the development of bisulfite sequencing and other genome-scale analyses has provided many of the requested answers. Though

the same user-friendly powerful technologies does not exist for 6mA, there are already promising tools to entangle the presence and role of this enigmatic modification in eukaryotes (Figure 1B). Let's briefly summarize them.

Ultra-High Performance Liquid Chromatography-Triple Quadrupole Mass Spectrometry

This approach allows the sensitive detection of nucleotide modifications, such as 5mC and 6mA, at very low abundance (Ito et al., 2011). Briefly, the digested DNA is separated by reverse-phase ultra-high performance liquid chromatography (UHPLC) coupled with mass spectrometry detection using tandem mass spectrometers (MS/MS). Following detection of specific nucleotide modifications, quantification is achieved using a standard curve that is simultaneously analyzed in the sample of interest. It is important to discard any potential contamination from Mycoplasma or bacterial DNA.

6mA-Immunoprecipitation Sequencing

Immunoprecipitation coupled with next-generation sequencing was previously established for 5mC detection in mammalian genomes (Weber et al., 2005). 6mA-immunoprecipitation sequencing (6mA-IPseq) utilizes a specific antibody for methyladenine to enrich modified fragments from the sequencing library. Following the alignment of sequencing reads to the reference genome, 6mA-modified regions present enriched mapping frequencies. 6mA-IPseq allows charting the spatial distribution of the epigenetic mark. Subsequent sequence enrichment analysis can also point to consensus recognition motifs for the adenine methyl-transferases.

Restriction Enzyme-Based 6mA Sequencing

Restriction enzyme-based 6mA sequencing (6mA-REseq) relies on the determination of consensus target sequences of adenine methylation, followed by the identification of restriction enzymes with respective recognition sites and sensitivity for the DNA modification (Fu et al., 2015). Technically, genomic DNA is fragmented with a 6mA-sensitive enzyme, followed by random shearing of the template. It results in an enrichment of unmethylated (digested) sequence motifs at the ends of the sequencing reads. Conversely, methylated adenine prevents digestion and is enriched in inner fractions of the reads. Consequently, 6mA levels are readily inferred from the relative position of the restriction enzyme consensus sequence.

Single-Molecule Real-Time Sequencing

Initial genome-wide methyladenine maps at base-pair resolution were obtained in *E. coli* genomes using single-molecule real-time (SMRT) sequencing (Clark et al., 2012; Fang et al., 2012; Murray et al., 2012). SMRT, a third-generation sequencing technique, is based on the processing of fluorescence-labeled nucleotides by DNA polymerases. The fluorescence label is not incorporated in the de novo synthesized strand but is cleaved away during the process. Meanwhile, the label emits light that is captured in the nanophotonic visualization chamber. High-fidelity polymerases are capable of synthesizing long continuous strands at a high speed, allowing a fast sequencing process and high read lengths. Importantly, the incorporation of a modified nucleotide, such as 6mA, presents different kinetics compared with unmodified adenine, allowing the direct inference of the modification status of each base.

Conclusions

m6A is a covalent modification of DNA that exerts an essential role in bacteria, where it is associated with genome protection via R-M systems. Furthermore, formation of m6A plays roles in bacterial DNA replication, mismatch repair, and gene transcription. Its presence in the genomes of several eukaryotes reinforces the notion that m6A is widespread and suggests its still unknown activities. The accompanying articles in this issue of *Cell* describe a transcriptional regulatory role for m6A in *Chlamydomonas*, and its detection, although at low levels, in *D. melanogaster* and *C. elegans* indicates an expanded function for 6mA. The development of improved technologies to unambiguously quantify and characterize 6mA in different biological contexts will be a necessary step in this exciting journey.

REFERENCES

- Achwal, C.W., Iyer, C.A., and Chandra, H.S. (1983). *FEBS Lett.* 158, 353–358.
- Arber, W., and Dussoix, D. (1962). *J. Mol. Biol.* 5, 18–36.
- Clark, T.A., Murray, I.A., Morgan, R.D., Kislyuk, A.O., Spittle, K.E., Boitano, M., Fomenkov, A., Roberts, R.J., and Korlach, J. (2012). *Nucleic Acids Res.* 40, e29.
- Fang, G., Munera, D., Friedman, D.I., Mandlik, A., Chao, M.C., Banerjee, O., Feng, Z., Losic, B., Mahajan, M.C., Jabado, O.J., et al. (2012). *Nat. Biotechnol.* 30, 1232–1239.
- Feng, S., Cokus, S.J., Zhang, X., Chen, P.-Y., Bostick, M., Goll, M.G., Hetzel, J., Jain, J., Strauss, S.H., Halpern, M.E., et al. (2010). *Proc. Natl. Acad. Sci. USA* 107, 8689–8694.
- Fu, Y., Luo, G.-Z., Chen, K., Deng, X., Yu, M., Han, D., Hao, Z., Liu, J., Lu, X., Dore, L.C., et al. (2015). *Cell* 161, this issue, 879–892.
- Gommers-Ampt, J.H., and Borst, P. (1995). *FASEB J. Off.* 9, 1034–1042.
- Greer, E.L., Blanco, M.A., Gu, L., Sendinc, E., Liu, J., Aristizabal-Corrales, D., Hsu, C.-H., Aravind, L., He, C., and Shi, Y. (2015). *Cell* 161, this issue, 868–878.
- Hattman, S., Kenny, C., Berger, L., and Pratt, K. (1978). *J. Bacteriol.* 135, 1156–1157.
- Heyn, H., and Esteller, M. (2012). *Nat. Rev. Genet.* 13, 679–692.
- Ito, S., Shen, L., Dai, Q., Wu, S.C., Collins, L.B., Swenberg, J.A., He, C., and Zhang, Y. (2011). *Science* 333, 1300–1303.
- Iyer, L.M., Abhiman, S., and Aravind, L. (2011). *Prog. Mol. Biol. Transl. Sci.* 101, 25–104.
- Kohli, R.M., and Zhang, Y. (2013). *Nature* 502, 472–479.
- Murray, I.A., Clark, T.A., Morgan, R.D., Boitano, M., Anton, B.P., Luong, K., Fomenkov, A., Turner, S.W., Korlach, J., and Roberts, R.J. (2012). *Nucleic Acids Res.* 40, 11450–11462.
- Raddatz, G., Guzzardo, P.M., Olova, N., Fantappiè, M.R., Rampp, M., Schaefer, M., Reik, W., Hannon, G.J., and Lyko, F. (2013). *Proc. Natl. Acad. Sci. USA* 110, 8627–8631.
- Ratel, D., Ravanat, J.-L., Berger, F., and Wion, D. (2006). *BioEssays* 28, 309–315.
- Roberts, D., Hoopes, B.C., McClure, W.R., and Kleckner, N. (1985). *Cell* 43, 117–130.
- Weber, M., Davies, J.J., Wittig, D., Oakeley, E.J., Haase, M., Lam, W.L., and Schübeler, D. (2005). *Nat. Genet.* 37, 853–862.
- Wion, D., and Casadesús, J. (2006). *Nat. Rev. Microbiol.* 4, 183–192.
- Zhang, G., Huang, H., Liu, D., Cheng, Y., Liu, X., Zhang, W., Yin, R., Zhang, D., Zhang, P., Liu, J., et al. (2015). *Cell* 161, this issue, 893–906.

slas
2016

5th annual
INTERNATIONAL
CONFERENCE & EXHIBITION

JANUARY
23-27

SAN DIEGO CONVENTION CENTER
SAN DIEGO :: CALIFORNIA

INFORMATION.
INNOVATION.
INSPIRATION.



VISIT SLAS2016.ORG
FOR FULL PROGRAM
INFORMATION.

SAN DIEGO
CONVENTION CENTER

JANUARY
23-27, 2016



 **slas**
Come Transform Research

SLAS2016.ORG

The Hunger Genes: Pathways to Obesity

Agatha A. van der Klaauw¹ and I. Sadaf Farooqi^{1,*}

¹University of Cambridge Metabolic Research Laboratories and NIHR Cambridge Biomedical Research Centre, Wellcome Trust-MRC Institute of Metabolic Science, Addenbrooke's Hospital, Cambridge CB2 0QQ, UK

*Correspondence: isf20@cam.ac.uk

<http://dx.doi.org/10.1016/j.cell.2015.03.008>

The global rise in the prevalence of obesity and associated co-morbidities such as type 2 diabetes, cardiovascular disease, and cancer represents a major public health concern. The biological response to increased consumption of palatable foods or a reduction in energy expenditure is highly variable between individuals. A more detailed mechanistic understanding of the molecular, physiological, and behavioral pathways involved in the development of obesity in susceptible individuals is critical for identifying effective mechanism-based preventative and therapeutic interventions.

Introduction

Obesity is defined as an increase in fat mass that is sufficient to adversely affect health (Sperrin et al., 2014; Whitlock et al., 2009). While the absolute quantification of fat mass is usually only performed in the research setting, body mass index (BMI; weight in kg/height in meters²) is a useful surrogate marker. Using the World Health Organization (WHO) definition of a BMI more than 30 kg/m² to define obesity, 30% of Americans and 10%–20% of Europeans are classified as obese, with the prevalence rising in many developing countries (<http://www.who.int>). As body mass index increases, so does the relative risk of type 2 diabetes, hypertension, and cardiovascular disease (Berrington de Gonzalez et al., 2010). Furthermore, an increase in the prevalence of childhood obesity (11%–17% in Europe and the US) has driven an increase in medical problems such as type 2 diabetes mellitus in adolescents (Fagot-Campagna, 2000). At a societal level, obesity is associated with disability, mortality, and substantial health costs. At an individual level, severe obesity is often associated with a multitude of clinical problems, including sleep disturbance and respiratory difficulties, joint and mobility issues, as well as considerable social stigma, which can affect quality of life as well as educational attainment and job opportunities (Puhl and Brownell, 2001).

In this Review, we provide a perspective on the contribution of environmental, genetic, and other factors to the development of obesity. We discuss how these factors impact the molecular and physiological mechanisms that regulate energy intake and energy expenditure in humans and highlight ongoing strategies to dissect the complex neural circuits and pathways that modulate energy homeostasis and their potential to be targeted by preventative and therapeutic interventions.

Obesity as a Disorder of Energy Homeostasis

Humans, like other mammals, are able to regulate their body weight over long periods of time despite day-to-day variation in the number of calories consumed and in levels of energy expenditure, irrespective of the level of adiposity. Fundamentally, factors that influence changes in body weight must ultimately disrupt the balance between energy intake and expenditure over time, the utilization of substrates (fat, protein, carbo-

hydrate), and/or nutrient partitioning (storage of excess calories). Physiological studies in healthy normal weight individuals have shown that total energy expenditure decreases by an average of 10% with acute caloric restriction and increases with caloric excess (Ravussin et al., 2014). However, in humans, the homeostatic regulation of energy balance is easily overwhelmed by external stimuli. For example, in a study in which people were given free access to food, the average daily intake exceeded 150% of energy requirements. In such experimental settings, and potentially in the free-living environment, some individuals seem more readily able to resist weight change with overeating, possibly due to inter-individual variation in the energy costs of weight gain (Ravussin et al., 2014).

Environmental Factors Drive the Rise in Obesity Prevalence

The increasing prevalence of obesity worldwide (an approximate doubling in the last 30 years), the inverse relationship between obesity and socioeconomic class, and the secular trend toward increasing obesity in developing countries associated with urbanization provide clear evidence of the environmental influences on weight gain (Ogden et al., 2014; Popkin, 2006). The adoption of relatively sedentary lifestyles due to reduced physical activity at work and in leisure time coupled with an abundance of easily available, energy-rich, highly palatable foods represents a nutrition transition that, according to the World Health Organization, is now one of the greatest risk factors for ill health worldwide (<http://www.hsph.harvard.edu>) (Figure 1). Interestingly, some recent analyses of trends in obesity prevalence have suggested a decline or stabilization of obesity prevalence, especially in children in the US and some European countries, findings that are consistent with dynamic models using prevalence data and birth and death rates (Ogden et al., 2014; Thomas et al., 2014). However, many countries have either increasing (China) or decreasing (European countries) birth rates, so the potential global impact of these estimations is not readily predictable. Recent studies show that second-generation migrants to the US from all ethnic groups are heavier than their parents who migrated but that people from some ethnic groups are more likely to gain weight than others upon

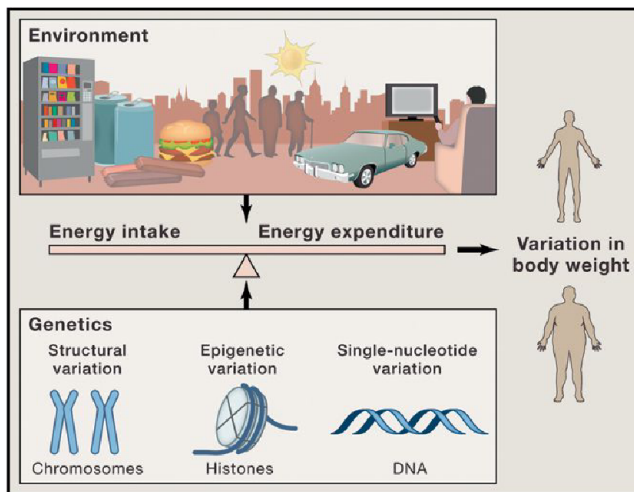


Figure 1. Contribution of Genes and Environmental Factors to Weight Gain

Human adiposity is influenced by complex interactions between genetic and environmental influences. The current environment potentially facilitates the development of obesity. Abundance of highly processed food has a major impact on energy intake, whereas numerous other environmental factors, such as television watching, leisure activities, and transport, negatively affect energy expenditure. In any environment, there is a variation in body fat and BMI in large part influenced by genetic variation disrupting energy homeostasis by either decreasing energy expenditure or increasing energy intake.

transitioning to a more obesogenic environment (Singh and Lin, 2013), suggesting that, in addition to strong environmental drivers, genetic factors play a role in influencing obesity susceptibility.

Individual Susceptibility to Weight Gain Is Highly Variable—Role of Genetic Factors

In any environment, whether energy rich or energy lacking, there is considerable individual variation in body weight and fat mass, suggesting that human adiposity is influenced by complex interactions between genetic, developmental, behavioral, and environmental influences. Evidence for genetic contributions to body weight comes from family, twin, and adoption studies, which cumulatively demonstrate that the heritability (fraction of the total phenotypic variance of a quantitative trait attributable to genes in a specified environment) of BMI is between 0.71 and 0.86 (Silventoinen et al., 2008). Heritability estimates can change over time and can differ between populations. Recent studies in a UK sample of 5,092 twin pairs aged 8–11 years growing up during a time of dramatic rises in obesity confirmed substantial heritability for BMI and waist circumference (77% for both), while there was a very modest shared-environment effect, and the remaining environmental variance was unshared (Wardle et al., 2008b). Interestingly, similar heritability estimates have been found when studying monozygotic and dizygotic twins who were reared together and apart (Allison et al., 1996) and in adoption studies in which adopted children were discovered to have body sizes that were more similar to those of their biological parents than their adopted parents (Sørensen et al., 1989).

The high heritability of phenotypes related to obesity supports the contribution of genetic factors but does not indicate the number of genes or how those genes interact with environmental factors. The “thrifty gene hypothesis” suggests that we harbor genetic variants that favor efficient food collection and fat deposition to survive periods of famine and that, in the face of the easy availability of food, these genes/variants are disadvantageous. However, an alternative hypothesis is that obesity is selected against by the risk of predation. This hypothesis suggests that random mutations and genetic drift, rather than directed selection, have influenced changes in the population distribution of fat mass that may be more readily reconcilable with the findings that, even in Western societies, most people are not obese (Speakman, 2007).

Evidence for the interaction of inherited factors with changes in energy intake and expenditure was provided by landmark experimental overfeeding studies by Bouchard and colleagues, who showed that weight gain induced by overfeeding mono- and dizygous twin pairs under direct supervision was highly correlated within twin pairs but varied widely among pairs of twins (Bouchard et al., 1990). Similarly, the response to negative energy balance via an exercise regime was also heritable (Bouchard et al., 1996). Notably, the inter-twin correlations were greater for weight loss than for weight gain, suggesting tighter biological control of the response to negative energy balance.

Hypothalamic Circuits Regulating Energy Homeostasis

Ultimately, signals from cumulative genetic and environmental influences that reflect changing energy status have to be detected and integrated by brain circuits that can, through their projections, regulate energy balance. In the early 1900s, clinical reports of patients with tumors involving hypothalamo-pituitary structures associated with food-seeking behavior and obesity suggested that the hypothalamus may be involved in the regulation of body weight. Chemical and electrolytic lesioning experiments in animals in the 1930s and 1940s established the key role of the hypothalamus in the regulation of energy homeostasis. The degree of weight gain/weight loss seen in these experiments was, in part, determined by the size and precise location of the lesions, which suggested that there were specific hypothalamic circuits that promote or suppress feeding behavior (Anand and Brobeck, 1951; Hetherington and Ranson, 1940).

The hypothalamus is essentially a hub for key circuits that integrate sensory inputs; compare those inputs to basic “set points,” or parameters for body temperature, electrolyte balance, sleep-wake cycle, circadian rhythms, and energy homeostasis; and then initiate a set of responses by activating autonomic, endocrine, and behavioral outputs that aim to maintain these set points (homeostasis). The hypothalamus regulates autonomic nervous system activation via neurons that directly innervate parasympathetic and sympathetic preganglionic neurons, as well as neurons in the brainstem that control autonomic reflexes. Individual pre-autonomic neurons project to multiple levels of the spinal cord, where they selectively innervate end organs such as the heart, kidney, and adipose tissue. Autonomic innervation of the pancreas contributes to the regulation of insulin and glucagon secretion.

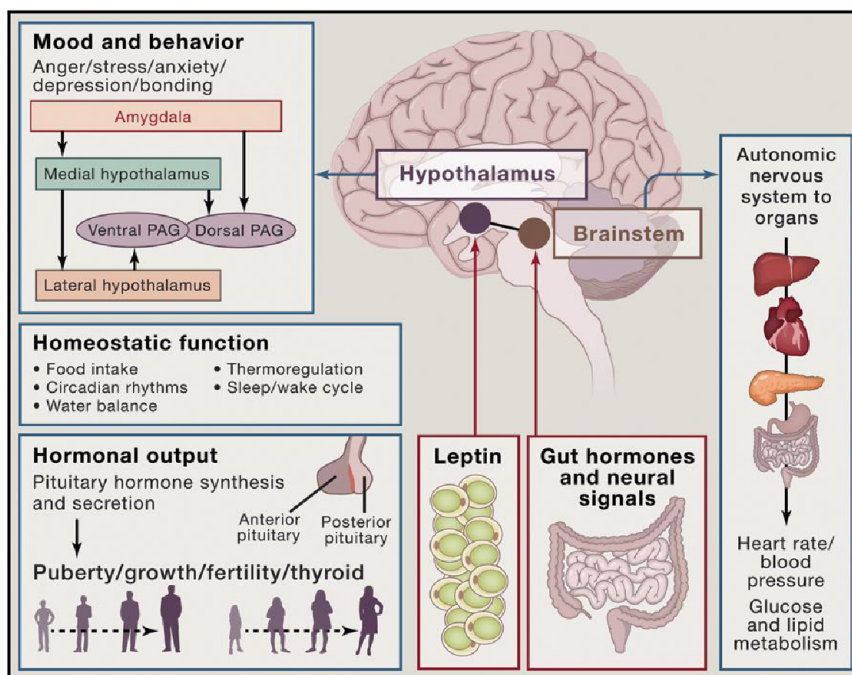


Figure 2. Leptin: A Master Regulator of Human Energy Homeostasis

The adipocyte-derived hormone leptin signals nutritional depletion and initiates a series of changes in energy intake, energy expenditure, autonomic nervous system tone, and neuroendocrine function in order to maintain energy homeostasis. The hypothalamus primarily coordinates many of these processes and also regulates circadian rhythms, temperature, and sleep. Through neuronal connections to the amygdala and periaqueductal gray (PAG) the hypothalamus also modulates a range of behaviors and moods such as stress, anger, anxiety, and aggression. Via its connections to the brainstem—direct and indirect via the cortex—neurons in the hypothalamus modulate autonomic nervous system tone which, in turn, influences many metabolic processes in peripheral tissues, such as the liver, pancreas, heart, and gut. Beyond energy homeostasis, leptin also has important effects on immune function and puberty.

fall in leptin levels (Chan et al., 2003), which then triggers a series of changes in energy intake, energy expenditure, and neuroendocrine function in order to maintain energy homeostasis.

Molecular Characterization of the Circuits Involved in Energy Homeostasis

While the location of the neural circuits regulating energy homeostasis was apparent from the early 1930s, a critical advance came as a result of parabiosis experiments in inbred strains of mice with severe obesity (*ob/ob* and *db/db*), which suggested the existence of a circulating factor that regulated weight (Coleman, 1973; Coleman and Hummel, 1969). The identification of this hormone, leptin, through positional cloning of the *ob* gene that was mutated in severely obese *ob/ob* mice (Zhang et al., 1994) paved the way for the identification and characterization of the neural circuits regulating energy homeostasis. Normalization of the phenotype of severely obese leptin-deficient *ob/ob* mice (characterized by increased food intake, reduced energy expenditure, hypogonadism, low thyroid hormone levels, elevated levels of corticosterone, and low blood pressure), by central leptin administration proved that leptin is a key regulator of energy homeostasis (Campfield et al., 1995; Halaas et al., 1995; Pelleymounter et al., 1995).

Leptin—A Master Regulator of Human Energy Homeostasis

Early human studies showing that leptin mRNA concentrations in adipose tissue and serum leptin concentrations correlated positively and very closely with the amount of fat mass (Considine et al., 1996; Maffei et al., 1995) led to the notion that leptin's primary role was to signal increasing energy stores. However, it rapidly became clear that most people are relatively resistant to rising endogenous or exogenously administered leptin (Heymsfield et al., 1999). Instead, leptin's physiological role in humans, as in mice (Ahima et al., 1996), appears to be to signal nutritional depletion, such that fasting or weight loss results in a

Evidence supporting leptin's role in human physiology emerged from the identification and characterization of severely obese people with homozygous loss-of-function mutations that reduce the production, secretion, or biological activity of leptin (Montague et al., 1997; Strobel et al., 1998; Wabitsch et al., 2015) or disrupt signaling through the leptin receptor (Clément et al., 1998; Farooqi et al., 2007b). While these disorders are rare, being found in 1%–5% of patients with severe obesity, their characterization has demonstrated that leptin regulates energy balance, neuroendocrine pathways, and the autonomic nervous system (Figure 2). These genetic findings have been supported and extended by elegant studies by many investigators in normal weight in the context of fasting or the weight-reduced state (Rosenbaum et al., 2002, 2005; Welt et al., 2004) and in patients with lipodystrophic syndromes characterized by relative leptin deficiency due to a loss of adipose tissue mass (Oral et al., 2002).

Impaired leptin signaling in humans is characterized by an intense drive to eat (hyperphagia), reduced sympathetic tone, mild hypothyroidism, hypogonadism, and impaired T-cell-mediated immunity, features that are reversed with the administration of recombinant human leptin in people with mutations in the leptin gene (Farooqi et al., 1999, 2002; Licinio et al., 2004; Ozata et al., 1999). Leptin also appears to be a major driver of the increase in blood pressure seen with weight gain, as blood pressure is low in obese mice and humans with disrupted leptin signaling (in contrast to diet-induced obesity in rodents/more common forms of obesity in humans) (Simonds et al., 2014).

Leptin mediates its effects by binding to the long form of the leptin receptor expressed on hypothalamic neuronal populations in the arcuate nucleus of the hypothalamus and other brain regions (Münzberg and Myers, 2005). While homozygous mutations that disrupt the expression, binding activity, and signaling

of the LEPR have been reported (Clément et al., 1998; Farooqi et al., 2007b), mutations that disrupt the downstream signaling cascade have not as yet been clearly associated with obesity. One possible exception is the adaptor molecule, Src homology 2 (SH2) B adaptor protein 1 (SH2B1), which is a key endogenous positive regulator of leptin sensitivity (Maures et al., 2007). However, *SH2B1* mutations have not been shown to disrupt leptin sensitivity, and SH2B1 modulates signaling by a variety of receptor tyrosine kinases, which may explain the additional phenotypes, including severe insulin resistance and behavioral abnormalities, reported in mutation carriers (Doche et al., 2012).

Leptin as a Therapeutic Agent

Recombinant human leptin (metreleptin) is highly effective in patients with no circulating or bioinactive leptin and in those with low endogenous levels with exercise-induced amenorrhea and lipodystrophy. Recombinant leptin has been administered successfully to patients with congenital leptin deficiency for more than 15 years on a named patient basis and was recently approved by the Food and Drug Administration (FDA) for the treatment of generalized lipodystrophy. In contrast, metreleptin has minimal efficacy for more common forms of obesity, which may represent a leptin-tolerant or leptin-resistant state (Heymsfield et al., 1999). In a recent clinical trial, leptin administered in combination with another weight loss agent, pramlintide, a synthetic analog of the pancreatic peptide amylin, had beneficial effects on weight loss, although the precise mechanisms underlying these effects are not entirely clear (Smith et al., 2007). A number of intervention studies have shown that some of the counter-regulatory responses to caloric restriction can be modified by leptin administration, including changes in skeletal muscle and autonomic and neuroendocrine adaptation (Rosenbaum et al., 2002, 2005). This form of intervention could be a useful adjunct in weight-loss maintenance, an area that merits further exploration.

Melanocortin Peptides and Their Receptors

Leptin stimulates primary neurons in the arcuate nucleus of the hypothalamus, which express pro-opiomelanocortin (POMC), which is posttranslationally processed to yield the melanocortin peptides (alpha, beta, and gamma MSH), which are agonists at melanocortin 3 and 4 receptors (Mc3r and Mc4r) expressed on second-order neurons. Leptin signaling modulates energy balance through a combination of melanocortin-dependent/independent pathways. These hypothalamic pathways interact with other brain centers to coordinate energy intake and energy expenditure (Morton et al., 2014).

Several lines of evidence support the critical role of melanocortin signaling in human energy balance. Homozygous null mutations in *POMC* result in severe obesity (Krude et al., 1998), while heterozygous loss-of-function mutations in α - and β -melanocyte-stimulating hormone (α - and β -MSH) significantly increase obesity risk (Biebermann et al., 2006; Lee et al., 2006). Targeted genetic disruption of *Mc4r* in mice leads to increased food intake, increased lean mass, and linear growth (Huszar et al., 1997), phenotypes that overlap entirely with those seen in humans with loss-of-function mutations in *MC4R* (Farooqi et al., 2003). Heterozygous *MC4R* mutations are found in 2%–

5% of people with childhood-onset obesity, making this the commonest gene in which highly penetrant variants contribute to obesity (Farooqi et al., 2000; Vaisse et al., 2000). Most disease-causing *MC4R* mutations disrupt the expression and trafficking of MC4R to the cell surface (Lubrano-Bertheliet et al., 2006; Xiang et al., 2006). In cells, pharmacological chaperones can increase cell surface expression and signaling of mutant GPCRs, which represents a potentially rational therapeutic approach for this condition (René et al., 2010).

As complete loss-of-function *MC4R* mutations are associated with a more severe form of obesity than partial loss-of-function mutations (Farooqi et al., 2003), modulation of melanocortinergic tone has been the focus of drug development strategies for some time. However, despite promising pre-clinical studies, the first generation of MC4R agonists were small molecules that failed primarily due to safety issues (Van der Ploeg et al., 2002), particularly increases in blood pressure. Loss-of-function *MC4R* mutations are associated with a reduced prevalence of hypertension, low systolic blood pressure, lower urinary noradrenaline excretion, and reduced peripheral nerve sympathetic nervous system activation, revealing that MC4R-expressing neurons represent a key circuit linking changes in weight with changes in blood pressure (Greenfield et al., 2009; Sayk et al., 2010). More recently, a potent melanocortin receptor agonist, RM-493, has been administered as part of a Phase 1B proof-of-concept clinical trial in obese patients, including one cohort of patients with heterozygous loss-of-function mutations in *MC4R*, in whom there was promising weight loss after 4 weeks. If this compound moves forward, this may be one of the first examples of a personalized medicine approach for treating obesity in people with a genetically characterized subtype of obesity.

Processing and Trafficking of Melanocortin Peptides and Receptors

Melanocortin peptides are processed by enzymes including prohormone convertase 1 (PCSK1), which is involved in the cleavage of the precursor peptide POMC into ACTH, which is then further cleaved to generate α -MSH by carboxypeptidase E (Pritchard et al., 2002). Impaired *POMC* processing may contribute to the obesity seen in people with homozygous/compound heterozygous mutations in *PCSK1* who also have glucocorticoid deficiency, hypogonadotropic hypogonadism, and postprandial hypoglycaemia (as a result of impaired processing of proinsulin to insulin) (Jackson et al., 1997; O'Rahilly et al., 1995). Impaired processing of gut-derived peptides may contribute to the neonatal enteropathy seen in *PCSK1* deficiency (Jackson et al., 2003; Martín et al., 2013). Intriguingly, common variants that affect the enzymatic activity of *PCSK1* have been associated with obesity in multiple European, Asian, and Mexican populations, providing a clear example where both common and rare variants in the same gene can influence a spectrum of variation in body weight (Benzinou et al., 2008; Choquet et al., 2013; Rouskas et al., 2012).

Several human obesity disorders (e.g., Alström syndrome and Bardet-Biedl syndrome) disrupt genes involved in ciliary function (Ansley et al., 2003). The role of neuronal cilia in protein trafficking—in particular, of GPCRs involved in energy homeostasis as well as in leptin signaling (Ainsworth, 2007)—is beginning to

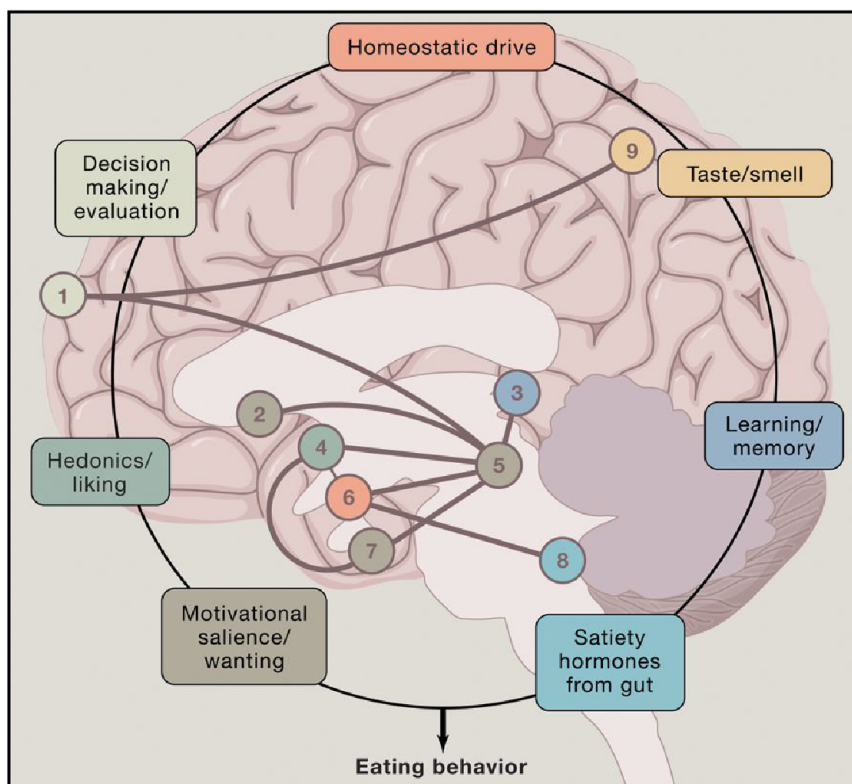


Figure 3. Neural Circuits Involved in Eating Behavior

Neural control of essential behaviors like eating requires the integration of multiple neural signals from different nodes in the brain. Dopaminergic circuits in regions such as the striatum (2), ventral tegmental area (5), and amygdala (7) encode motivational salience and wanting. Opioidergic circuits in regions such as the nucleus accumbens and the ventral pallidum (4) encode hedonic liking. These brain areas and others are integrated with the hypothalamus, cortical areas, and brainstem areas in the regulation of appetite and food intake. Brain regions: (1) prefrontal cortex, (2) dorsal striatum, (3) hippocampus, (4) nucleus accumbens/ventral pallidum, (5) ventral tegmental area, (6) hypothalamus, (7) amygdala, (8) nucleus of solitary tract, (9) gustatory/somatosensory cortex.

brain regions that contribute to the modulation of eating behavior (Betley et al., 2013; Wu et al., 2009) (Figure 3).

Several lines of evidence suggest that brain-derived neurotrophic factor (BDNF), a nerve growth factor that signals via the tyrosine kinase receptor tropomyosin-related kinase B (TrkB), is important not only in energy balance, but also in anxiety and aggression. Haplo-insufficient mice and mice in which BDNF has

been deleted postnatally are obese with hyperphagia and hyperactivity (Lyons et al., 1999; Xu et al., 2003); this unusual combination of phenotypes is also seen in individuals with genetic disruption of BDNF and TrkB (Gray et al., 2006; Yeo et al., 2004). While a Trkb agonist results in weight loss in mice (Tsao et al., 2008), central administration had no effect on food intake in primates (Perreault et al., 2013). Its potential utility in the treatment of a number of neurodegenerative diseases is still being explored (Yang et al., 2014).

Sim1 is a transcription factor involved in the development of the paraventricular and supraoptic nuclei of the hypothalamus and additionally may mediate signaling downstream of Mc4r (Michaud et al., 1998). *Sim1* haplo-insufficiency in mice and deletions, balanced translocations, and loss-of-function mutations in humans cause severe obesity (Bonfond et al., 2013; Holder et al., 2000; Ramachandrapa et al., 2013). Oxytocin mRNA levels are reduced in mouse models of *Sim1* deficiency, and oxytocin administration reduces food intake in *Sim1*-haploinsufficient animals (Kublaoui et al., 2008). Impaired oxytocinergic signaling has also been implicated in the hyperphagia and obesity seen in Prader-Willi Syndrome (PWS) (Swaab et al., 1995), caused by lack of expression of a cluster of maternally imprinted snoRNAs on chromosome 15 (Sahoo et al., 2008). People with PWS and with *SIM1* mutations exhibit a spectrum of behavioral abnormalities that overlap with autism-like features and could be related to reduced oxytocinergic signaling (Ramachandrapa et al., 2013), although this has not been tested.

Development and Maintenance of Neural Circuits Involved in Eating Behavior

Functional dissection of the neuronal circuits involved in the regulation of energy balance has until recently been limited to dissecting relatively simple linear relationships between neuronal populations that, in reality, are likely to be overlapping and interconnected. Peripheral signals such as leptin can modulate the development and maintenance of these neural circuits (Bouret et al., 2004) and their ability to adapt signaling by altering synaptic inputs (Pinto et al., 2004). While our current understanding of the dynamic and integrated nature of these neuronal networks is still at an early stage, optogenetic tools and other methodologies that permit the manipulation of gene expression in specific populations of neurons are paving the way for major advances in our understanding of the neural circuits connecting

emerge. Furthermore, conditional postnatal knockout of proteins involved in intraflagellar transport in neurons and specifically when targeted to *pomc* neurons in mice results in hyperphagia and obesity (Davenport et al., 2007).

Additionally, there is currently a great deal of interest in identifying chaperones and accessory proteins that might modulate melanocortin signaling and melanocortin-dependent pathways. *Mrap2*, an accessory protein that interacts with *Mc4r* (and potentially other GPCRs) (Sebag et al., 2013) leads to obesity when disrupted in mice (Asai et al., 2013). Rare variants in *MRAP2* have been associated with severe obesity in humans, although the detailed molecular mechanisms underlying this association are not known (Asai et al., 2013).

Central administration of oxytocin in rodents is anorexigenic, and rodents that lack oxytocin or the oxytocin receptor become

obese (Olson et al., 1991). The exact sites of action of locally released oxytocin are unknown but likely involve areas with high oxytocin receptor expression, such as the VMH and amygdala. α -MSH, through its effects on MC4R, induces dendritic release of oxytocin, and this locally released oxytocin may be involved in the regulation of appetite (Sabatier et al., 2003). Modulation of central oxytocin signaling therefore forms another potential target in the treatment of obesity (Morton et al., 2014).

Neural Circuits Involved in Eating Behavior

The most consistent phenotype associated with genetic disruption of leptin-melanocortin signaling in humans is hyperphagia, an increased drive to eat (O’Rahilly and Farooqi, 2008). Additionally, detailed characterization of eating behavior in large numbers of twins suggests that eating behavior phenotypes such as satiety responsiveness, eating in the absence of hunger, reinforcing value of food, and the capacity to voluntarily inhibit eating are potentially heritable components of eating behavior (Carnell et al., 2008). This is not surprising, as one of the primary functions of the brain during periods of negative energy balance is to reprioritize behavioral outputs to obtain and consume food, thereby replenishing depleted energy stores. Ensuring sufficient energy stores is critical for survival of the species and, based on our understanding in other mammalian species, multiple processes that defend against starvation and fasting are hardwired.

In addition to this homeostatic regulation of eating behavior, which is driven by energy demands, hedonic food intake (i.e., beyond the need for energy repletion) in response to the rewarding properties of food (Kenny, 2011) is an important contributor to overeating. The palatability of a particular food source is assumed to be related to the flavor and taste of that food; high-fat diets are generally considered more palatable than low-fat diets and are preferentially overconsumed. Neural circuits involving the amygdala, the striatonigral pathway, orbito- and prefrontal cortex, and hippocampus have been implicated in transposing motivational aspects of stimuli into motor responses, as well as in hedonic evaluation of the stimulus and associative learning about the hedonic properties of food (Figure 3). Food reward has been considered to be encoded by distinct neural substrates, opioidergic brain pathways mediating liking (pleasure/palatability), whereas the wanting of food (incentive motivation) appears to be mediated by dopaminergic circuits (Berridge, 1996; Pecina et al., 2003). The overarching role of these responses is to shift attention and effort toward obtaining food reward.

Hormonal regulators of energy homeostasis can also act on brain reward circuits, most notably on the mesoaccumbens dopamine system, to increase or decrease the incentive value of food depending on energy requirements. This suggests that obtaining the pleasurable effects of food is a powerful motivating force that can override homeostatic satiety signals, and in agreement with this, meals that consist of palatable food are generally consumed with greater frequency and in greater portion size than those consisting of less palatable food. As a single meal of increased portion size can trigger increased food intake over several days, such hedonic overeating is likely to be an important contributor to weight gain and the development of obesity.

Human Brain Imaging Studies—Insights into Food Reward

Neural processes such as food reward can be challenging to measure in humans. Imaging studies using functional MRI (fMRI) permit the measurement of blood-oxygen-level dependent (BOLD) signals that reflect neural activity in specific regions involved in the response to food cues (Selvarajah et al., 2014). Pictures of food activate dopaminergic regions such as ventral striatum, and these effects are modulated by homeostatic state (Ziauddeen et al., 2012). In leptin-deficient humans, images of food (compared to non-food images) are associated with a marked increase in neuronal activation in the ventral striatum (Farooqi et al., 2007a). This response was normalized by 7 days of leptin treatment before significant weight loss had occurred, consistent with the view that activation in the ventral striatum does not directly encode the “liking” but, rather, the motivational salience, or “wanting,” of food. Studies in obese volunteers in an energy-restricted, partially leptin-deficient state are consistent with the view that these responses are part of the physiological response to energy restriction (Rosenbaum et al., 2008) and are in keeping with findings in experimental studies in rodents (Fulton et al., 2006; Hommel et al., 2006).

Compared to obese controls, obese people with *MC4R* mutations have a preserved pattern of activation of the reward system to visual food cues, suggesting involvement of MC4R in the dopaminergic reward circuitry in humans (van der Klaauw et al., 2014). These findings are supported by evidence in rodents, which suggests that melanocortin signaling modulates food reward. Of note, fMRI studies in Prader-Willi Syndrome have also shown higher neural activity to food cues in reward areas compared to matched obese controls such as accumbens, amygdala, and ventromedial prefrontal cortex (Hinton et al., 2006).

The μ -opioid receptor system that subserves the neural substrates of “liking of food” is a key mediator in the hedonic valuation process of food intake. In addition, μ -opioid receptors were found to mediate the autoinhibition of β -endorphin on hypothalamic *pomc* neurons (Cowley et al., 2003). Antagonism of μ -opioid receptors thus likely results in alterations of hedonic valuation of food as well as potentially attenuates downregulation of *pomc* neuronal activity. Indeed, in humans, the μ -opioid receptor antagonist naloxone reduces the hedonic responses to, and consumption of, palatable foods. In clinical trials, the μ -opioid receptor antagonist GSK1521498 reduces the hedonic response to and motivation for high-fat foods (Ziauddeen et al., 2013). Recently, the combination of naltrexone, an opioid receptor antagonist with high affinity for the μ -opioid receptor, and bupropion, an atypical antidepressant that inhibits reuptake of dopamine and norepinephrine and increases activity of POMC neurons (Contrave) was approved for treatment of obesity by the FDA.

Taste and Food Preference

The orosensory properties of foods are perceived through a combination of taste, texture, and olfaction. The heritability of taste is well established in twin and family studies, with heritability estimates of 30%–50% for pleasantness, consumption, and cravings for sweet foods (Keskkitalo et al., 2008). The central

sensing mechanisms for nutrients and quality of food have only recently become the subject of studies. Fat provides twice as many calories per gram as protein or carbohydrate. It is well established that palatable food that is rich in fat and refined sugars promotes larger meal sizes, less postprandial satiety, and greater caloric intake than diets that are high in carbohydrates but low in fat (Salbe et al., 2004). Traditionally, there have been contrasting perspectives on the mechanisms underlying food palatability. The homeostatic view of palatability suggests that palatability reflects the underlying biological need for nutrients, while the hedonic view of palatability suggests that certain foods engage reward processing and are therefore palatable. Studies in rodents have suggested that specific neural pathways, for example, involving the melanocortin-4 receptor (*Mcr4r*), play a role in the preference for dietary fat and against dietary sucrose (Panaro and Cone, 2013). To date, very few studies have addressed the preference for specific nutrients in humans, although twin studies have found heritability estimates of 53%–62% for the intake of/preference for foods that are high fat/sucrose. There is considerable research being performed within the food industry focusing on the development of foods that offer some of the sensory properties of fat (fat mimetics) but do not have a high fat content. The potential to modify foods for health benefits is an area of considerable development; such work will need to take into consideration an understanding of the fundamental biology that underpins aspects of eating behavior.

Gut-Derived Satiety Signals

Peptides such as ghrelin, peptide YY (PYY), and glucagon-like peptide 1 (GLP-1) are secreted from gut entero-endocrine cells in response to meal ingestion and the presence of nutrients in the intestinal lumen (Batterham et al., 2002; Turton et al., 1996). Pioneering human infusion studies have demonstrated that a number of gut peptides modulate food intake when administered acutely in humans (Tan and Bloom, 2013), suggesting that modulating satiety signals could be a useful therapeutic strategy in obesity (Finan et al., 2015). The synthetic GLP-1 receptor agonist liraglutide has recently been approved for the treatment of obesity alone by the FDA. Several other gut peptide analogs, as well as gut hormone receptor agonists, are currently being studied in clinical trials (Tan and Bloom, 2013).

Satiation, the sensation of fullness that results in meal termination and satiety, the persistence of fullness that determines the timing to the next meal, are heritable traits that influence weight gain (Carnell et al., 2008). Although common obesity seems to be associated with low circulating PYY levels (Batterham et al., 2006), rare genetic variants in PYY or its receptors have not been associated with obesity. Fasting ghrelin levels have been found to be increased in children (Haqq et al., 2003) and adults with PWS (Cummings et al., 2002), potentially contributing to the hyperphagia and impaired satiety associated with this syndrome, although the potential mechanisms involved are not known.

Additionally, there is a growing literature on changes in the composition of the gut microbiome in response to acute/short-term changes in the diet, chronic states such as obesity and bariatric surgery (Turnbaugh et al., 2006), and the impact of specific organisms on nutrient absorption and on metabolic parameters in mice and humans (Cox et al., 2014).

Targeting Energy Expenditure

A number of large family-based population studies, most notably the Quebec family study, have addressed the contribution of genetic versus environmental factors to energy expenditure, including physical activity (Pérusse et al., 1989). For example, the heritability of exercise participation is entirely accounted for by common familial environment, while for physical activity level, the heritability is ~20%. As such, promotion of increased levels of physical activity is a useful strategy for weight loss and, in particular, for weight maintenance.

In contrast, basal metabolic rate (BMR) and respiratory quotient (ratio of carbohydrate versus fat oxidation; a marker of substrate utilization) are highly heritable (47% and 36%, respectively) (Bouchard and Tremblay, 1990). Very few genes have been shown to modulate BMR in humans, although the reduced basal metabolic rate reported in obese people harboring loss-of-function mutations in the cellular scaffolding protein *KSR2* (kinase suppressor of Ras2) suggests that genetic variation in energy expenditure phenotypes may contribute to weight gain in some individuals (Pearce et al., 2013). In this study, almost all of the *KSR2* variants identified in obese individuals impaired glucose oxidation and fatty acid oxidation in cells, suggesting a defect in substrate utilization, which was rescued by the addition of metformin. Further work will be needed to see whether these observations can be replicated in experimental clinical studies and to investigate the cellular mechanisms underlying these effects which, in part, may be mediated by the interaction of *KSR2* with the cellular fuel sensor, AMP-kinase (Brommage et al., 2008; Costanzo-Garvey et al., 2009).

The development of compounds that might increase energy expenditure is being explored as a possible therapeutic strategy. One potential route is to activate brown adipose tissue, thereby generating heat through uncoupling protein 1 (UCP1) (Lowell and Spiegelman, 2000). UCP1-positive cells in white adipose tissue depots in rodents (often called beige/brite cells) can be stimulated to dissipate energy by thermogenesis and pharmacological stimulation of these processes, potentially through circulating myokines that drive brown-fat-like development (Wu et al., 1999), has attracted the interest of a number of pharmaceutical companies. Although UCP1-positive cells that show similarity to murine beige adipocytes have been found in human fat depots (Wu et al., 1999), the translation of these findings in rodents to therapies that can be administered safely in humans presents some challenges. For example, what influences the exact amount of brown fat and/or beige fat available in adult humans, and can this be increased? To what extent do sex steroids (or other gender-specific factors) influence the activity/quantity of brown/beige fat, as women seem to have more than men (Cypess et al., 2009)? How much extra energy would be expended through the stimulation/overstimulation of such processes, and would this be clinically relevant? Would an increase in energy expenditure lead to a compensatory increase in food intake, and how might such an effect be managed?

Building an Integrated View of the Pathways that Regulate Energy Homeostasis

Given the complexity of neurobiological processes underlying body weight homeostasis, it is likely that future drugs will need

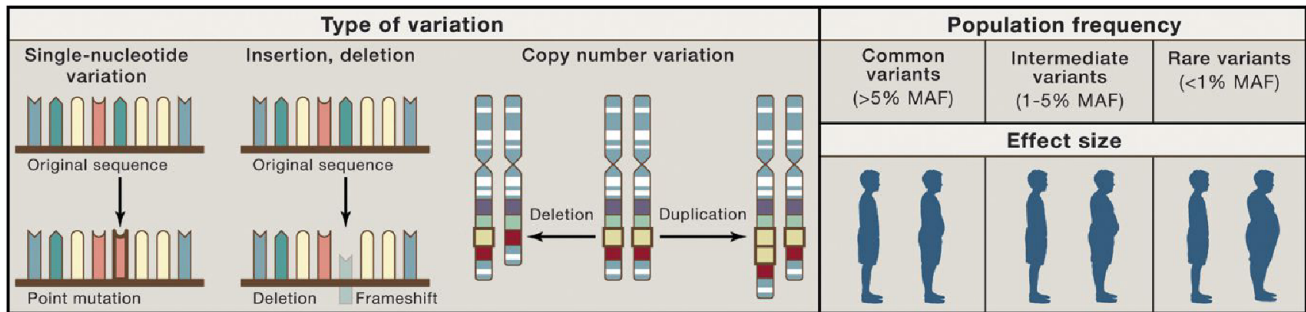


Figure 4. Types of Genetic Variation Contributing to Body Weight Regulation

Genetic effects on body weight are mediated by different types of variants, their frequency in the population, and the effect of the variant on the phenotype. Variants include single-nucleotide variations in which only one nucleotide is changed, copy number variations in which a stretch of DNA is repeated or deleted (often containing many genes), or small insertions and deletions of a few base pairs. Common variants are found at a minor allele frequency (MAF) of more than 5% in a population, whereas intermediate (1%–5%) and rare variants (< 1%) are found at lower frequencies. Generally, the effect size of common obesity-associated variants on body weight is modest. Several rare variants have been associated with severe obesity.

to be directed at highly specific targets and may consist of combinations of compounds that target different mechanisms, as illustrated by recent studies demonstrating the efficacy of dual melanocortin-4 receptor and GLP-1 receptor agonism (Clemmensen et al., 2015). The central and peripheral regulation of food intake, energy expenditure, physical activity, fat absorption, and oxidation are all being explored as potential mechanisms that can be targeted in rodent studies. In parallel, genetic approaches into human eating behavior and obesity may inform the focus of experimental approaches in rodents and might generate new potential drug targets in which the potential relevance to humans may be established at an earlier stage than has previously been the case.

Common Genetic Variants and Genome-wide Association Studies

Genetic influences are likely to operate across the weight spectrum but may be more penetrant when studying childhood-onset obesity and at both extremes of the BMI distribution—thinness and severe obesity. Genetic variance depends on the nature and amount of mutational variance in a population, the segregation and frequency of the alleles that influence a trait in a particular population, the effect sizes of the variants (which may be additive or non-additive), the mode of gene action, and the degree of genetic control of phenotypic variance of the trait in question (Figure 4).

Genome-wide association studies (GWAS) seek to identify the common variants (minor allele frequency [MAF] of more than 5%) that contribute to the heritability of common diseases. High-throughput arrays have facilitated the genotyping of thousands of common variants (directly or by imputation) in large population-based cohorts on whom BMI data is available. The first GWAS-derived loci to be reported were intronic variants in *FTO* (fat mass and obesity associated) and a variant ~200 kb downstream of *MC4R* (Dina et al., 2007; Frayling et al., 2007; Loos et al., 2008). To date, more than 80 genetic loci associated with BMI and body fat distribution (often measured by waist-to-hip ratio) have been identified by GWAS approaches, and many of these have been replicated in different populations and ethnicities (Locke et al., 2015). GWAS in childhood-onset obesity and

in severely obese children and adults have shown that there is some overlap between the common variants that contribute to early-onset and adult-onset weight gain, but also that both of these approaches can identify novel variants (Bradfield et al., 2012; Wheeler et al., 2013). Cumulatively, the common variants identified in GWAS are characterized by modest effect sizes (per allele odds ratios between 1.1 and 1.5), and the proportion of variability of BMI explained by GWAS-identified loci to date remains relatively modest (< 5%). Nevertheless, variants that explain a small proportion of phenotypic variance may provide substantial biological or therapeutic insights, although the road to establishing causal variants and their functional relevance is often a challenging one.

GWAS-associated loci are often identified by the name of the nearest gene; this may or may not be the gene in which variation contributes to variation in BMI. Some of the GWAS loci encompass genes previously appreciated to play a role in energy homeostasis (e.g., *LEPR*, *SH2B1*, *MC4R*, *BDNF*), and in some cases, specific variants have been associated with changes in expression based on eQTL data (Wheeler et al., 2013). Other loci contain genes that seem to be plausible biological candidates or can suggest genes for which there was no previous evidence (Locke et al., 2015). Many of the signals identified to date map to non-coding regions of the genome that may potentially be involved in gene regulation.

The strongest association signal for BMI has consistently been found with variants in the first intron of *FTO*, which have been associated with increased BMI and eating behavior in a number of studies (Cecil et al., 2008; Wardle et al., 2008a). Deletion or overexpression of *fto* and other genes in this region (*IRX3*, *RPGRIP1L*) in rodents (Church et al., 2010; Fischer et al., 2009; Gerken et al., 2007; Stratigopoulos et al., 2008) (Smemo et al., 2014) can impact energy homeostasis. Despite these obvious challenges, these studies have demonstrated progress toward identifying new biology based on GWAS (Tung et al., 2014).

Is there yet more common variation to find? Newly developed statistical methods that assess the contribution of common genetic variation across the genome (Zhu et al., 2015) support the growing consensus that there is a long tail of common

variation. As such, meta-analyses of even larger population-based data sets are currently underway. The available evidence suggests that BMI is highly polygenic (high number of contributing genes) (Gusev et al., 2014). One of the challenges of such studies is how to capture the full spectrum of genetic variation (Figure 4), including complex multi-allelic CNVs, which show lower linkage disequilibrium with surrounding SNPs and are consequently less detectable by conventional SNP-based genome-wide association studies. For example, in a large family-based association study of Swedish families ascertained through the identification of siblings who were discordant for obesity, integrating data from CNV analysis with transcriptomic data from adipose tissue revealed an association with copies of *AMY1* with obesity (Falchi et al., 2014).

Finding New Rare Highly Penetrant Variants

Rare variants, which outnumber common variants in the human genome, may explain a proportion of the heritability of obesity and may be more readily identified at the extremes of the phenotypic distribution. The earliest studies were performed in children with clinically identifiable syndromes often associated with developmental delay or dysmorphic features as well as obesity. Rare CNVs that often disrupt a number of genes have recently been implicated in highly penetrant forms of obesity (Bochukova et al., 2010; Walters et al., 2010). Candidate gene studies based on the molecules known to cause severe obesity in experimental animals have shown that these genes also contribute to childhood-onset human obesity, often in the absence of developmental delay. The functional and physiological characterization of these mutations and of the mutation carriers has illustrated a high degree of convergence of the mechanisms that regulate energy balance across mammalian species.

Exome sequencing of cohorts with severe childhood-onset and adult-onset obesity, as well as those at the extremes of the BMI distribution in population-based cohorts, is well underway and may lead to the identification of new genes whose functions will need to be explored in cells, model organisms, and humans. Whole-genome sequencing provides the “most complete” view of genomic variation but poses challenges in terms of proving causality, but these are beginning to be addressed. Recent studies have now shown that human inducible pluripotent stem cell (iPSC)-derived neurons may facilitate a mechanistic understanding of how specific genes disrupt cellular and neuronal mechanisms that may be involved in the pathogenesis of obesity (Wang et al., 2015).

Therapeutics Opportunities in Obesity

Lifestyle modification remains the first step in weight management. While intervention programs that focus on supporting people to change their diet and/or levels of physical activity can be effective in inducing weight loss in the short to medium term in some people, they lose efficacy in the long term. As such, in addition to the focus on prevention of obesity, treatment of obese patients, preferably at a stage before complications have emerged, is an important priority (Gray et al., 2012). However, current therapeutic options in obesity are very limited; the only currently approved anti-obesity drug for long-term use in

the US and Europe is Orlistat, which reduces intestinal lipid absorption by inhibiting pancreatic lipase and often has limiting adverse effects that preclude its long term use.

Previously available anti-obesity drugs targeted cannabinoid signaling (rimonabant), noradrenergic (phentermine) and serotonergic signaling (fenfluramine, dexfenfluramine), and reuptake (sibutramine). These compounds were moderately effective but, as with many centrally acting agents, at the expense of many off-target effects, reflecting lack of specificity of the neural targets. Lorcaserin, a selective 5HT_{2c}R agonist with limited activity at the other serotonin receptors, has been approved for use in the US (Smith et al., 2010), although concerns about potential cardiac valvulopathy and cancer risk have prevented European approval of the drug to date. The combination of the anticonvulsant topiramate and phentermine, which increases central noradrenaline levels (Qsymia), is also approved in some countries.

Finally, development of personalized medicine by selecting the optimal pharmacological intervention for particular people through genetics or other molecular/cellular analyses is an exciting and evolving area. Synthetic-biology-inspired therapeutic systems that integrate sensor and effector devices into cells have been developed to monitor disease-relevant metabolites, process on/off level control, and coordinate adjusted therapeutic responses. These systems have the potential to restore metabolite homeostasis in a seamless, automatic, and self-sufficient manner, which is particularly attractive for future gene- and cell-based therapies. As an example, a closed-loop synthetic intracellular lipid-sensing receptor (LSR)-pramlintide circuit represents a potential prototype for such a cell-based therapy. The LSR sensor captures a wide range of lipids within their physiologic concentration range, becomes dose-dependently activated by peak fatty acid levels, and is turned off at physiological concentrations (Rössger et al., 2013). Such emerging methodologies offer fresh perspectives for drug delivery and potentially personalized medicine in the future.

ACKNOWLEDGMENTS

We would like to thank the many colleagues, collaborators, and referring Physicians with whom we have worked over the years. We thank the Wellcome Trust, MRC, ERC, NIHR Cambridge Biomedical Research Centre, and Bernard Wolfe endowment for their support for this work. Importantly, we would like to thank the patients and their families for their contributions. Further information can be found at <http://www.goos.org.uk>.

REFERENCES

- Ahima, R.S., Prabakaran, D., Mantzoros, C., Qu, D., Lowell, B., Maratos-Flier, E., and Flier, J.S. (1996). Role of leptin in the neuroendocrine response to fasting. *Nature* 382, 250–252.
- Ainsworth, C. (2007). Cilia: tails of the unexpected. *Nature* 448, 638–641.
- Allison, D.B., Kaprio, J., Korkeila, M., Koskenvuo, M., Neale, M.C., and Hanyakawa, K. (1996). The heritability of body mass index among an international sample of monozygotic twins reared apart. *Int. J. Obes. Relat. Metab. Disord.* 20, 501–506.
- Anand, B.K., and Brobeck, J.R. (1951). Hypothalamic control of food intake in rats and cats. *Yale J. Biol. Med.* 24, 123–140.
- Ansley, S.J., Badano, J.L., Blacque, O.E., Hill, J., Hoskins, B.E., Leitch, C.C., Kim, J.C., Ross, A.J., Eichers, E.R., Teslovich, T.M., et al. (2003). Basal body

- dysfunction is a likely cause of pleiotropic Bardet-Biedl syndrome. *Nature* **425**, 628–633.
- Asai, M., Ramachandrapa, S., Joachim, M., Shen, Y., Zhang, R., Nuthalapati, N., Ramanathan, V., Strohlic, D.E., Ferket, P., Linhart, K., et al. (2013). Loss of function of the melanocortin 2 receptor accessory protein 2 is associated with mammalian obesity. *Science* **341**, 275–278.
- Batterham, R.L., Cowley, M.A., Small, C.J., Herzog, H., Cohen, M.A., Dakin, C.L., Wren, A.M., Brynes, A.E., Low, M.J., Ghatei, M.A., et al. (2002). Gut hormone PYY(3-36) physiologically inhibits food intake. *Nature* **418**, 650–654.
- Batterham, R.L., Heffron, H., Kapoor, S., Chivers, J.E., Chandarana, K., Herzog, H., Le Roux, C.W., Thomas, E.L., Bell, J.D., and Withers, D.J. (2006). Critical role for peptide YY in protein-mediated satiation and body-weight regulation. *Cell Metab.* **4**, 223–233.
- Benzinou, M., Creemers, J.W., Choquet, H., Lobben, S., Dina, C., Durand, E., Guerardel, A., Boutin, P., Jouret, B., Heude, B., et al. (2008). Common nonsynonymous variants in PCSK1 confer risk of obesity. *Nat. Genet.* **40**, 943–945.
- Berridge, K.C. (1996). Food reward: brain substrates of wanting and liking. *Neurosci. Biobehav. Rev.* **20**, 1–25.
- Berrington de Gonzalez, A., Hartge, P., Cerhan, J.R., Flint, A.J., Hannan, L., MacInnis, R.J., Moore, S.C., Tobias, G.S., Anton-Culver, H., Freeman, L.B., et al. (2010). Body-mass index and mortality among 1.46 million white adults. *N. Engl. J. Med.* **363**, 2211–2219.
- Betley, J.N., Cao, Z.F., Ritola, K.D., and Sternson, S.M. (2013). Parallel, redundant circuit organization for homeostatic control of feeding behavior. *Cell* **155**, 1337–1350.
- Biebermann, H., Castañeda, T.R., van Landeghem, F., von Deimling, A., Escher, F., Brabant, G., Hebebrand, J., Hinney, A., Tschöp, M.H., Grüters, A., and Krude, H. (2006). A role for beta-melanocyte-stimulating hormone in human body-weight regulation. *Cell Metab.* **3**, 141–146.
- Bochukova, E.G., Huang, N., Keogh, J., Henning, E., Purmann, C., Blaszczyk, K., Saeed, S., Hamilton-Shield, J., Clayton-Smith, J., O'Rahilly, S., et al. (2010). Large, rare chromosomal deletions associated with severe early-onset obesity. *Nature* **463**, 666–670.
- Bonnefond, A., Raimondo, A., Stutzmann, F., Ghossaini, M., Ramachandrapa, S., Bersten, D.C., Durand, E., Vatin, V., Balkau, B., Lantieri, O., et al. (2013). Loss-of-function mutations in SIM1 contribute to obesity and Prader-Willi-like features. *J. Clin. Invest.* **123**, 3037–3041.
- Bouchard, C., and Tremblay, A. (1990). Genetic effects in human energy expenditure components. *Int. J. Obes.* **14**, 49–55.
- Bouchard, C., Tremblay, A., Després, J.P., Nadeau, A., Lupien, P.J., Thériault, G., Dussault, J., Moorjani, S., Pinaut, S., and Fournier, G. (1990). The response to long-term overfeeding in identical twins. *N. Engl. J. Med.* **322**, 1477–1482.
- Bouchard, C., Tremblay, A., Després, J.P., Nadeau, A., Lupien, P.J., Moorjani, S., Thériault, G., and Kim, S.Y. (1996). Overfeeding in identical twins: 5-year postoverfeeding results. *Metabolism* **45**, 1042–1050.
- Bouret, S.G., Draper, S.J., and Simerly, R.B. (2004). Trophic action of leptin on hypothalamic neurons that regulate feeding. *Science* **304**, 108–110.
- Bradfield, J.P., Taal, H.R., Timpson, N.J., Scherag, A., Lecoeur, C., Warrington, N.M., Hypponen, E., Holst, C., Valcarcel, B., Thiering, E., et al.; Early Growth Genetics Consortium (2012). A genome-wide association meta-analysis identifies new childhood obesity loci. *Nat. Genet.* **44**, 526–531.
- Brommage, R., Desai, U., Revelli, J.P., Donoviel, D.B., Fontenot, G.K., Dacosta, C.M., Smith, D.D., Kirkpatrick, L.L., Coker, K.J., Donoviel, M.S., et al. (2008). High-throughput screening of mouse knockout lines identifies true lean and obese phenotypes. *Obesity (Silver Spring)* **16**, 2362–2367.
- Campfield, L.A., Smith, F.J., Guisez, Y., Devos, R., and Burn, P. (1995). Recombinant mouse OB protein: evidence for a peripheral signal linking adiposity and central neural networks. *Science* **269**, 546–549.
- Carnell, S., Haworth, C.M., Plomin, R., and Wardle, J. (2008). Genetic influence on appetite in children. *Int. J. Obes.* **32**, 1468–1473.
- Cecil, J.E., Tavendale, R., Watt, P., Hetherington, M.M., and Palmer, C.N. (2008). An obesity-associated FTO gene variant and increased energy intake in children. *N. Engl. J. Med.* **359**, 2558–2566.
- Chan, J.L., Heist, K., DePaoli, A.M., Veldhuis, J.D., and Mantzoros, C.S. (2003). The role of falling leptin levels in the neuroendocrine and metabolic adaptation to short-term starvation in healthy men. *J. Clin. Invest.* **111**, 1409–1421.
- Choquet, H., Kasberger, J., Hamidovic, A., and Jorgenson, E. (2013). Contribution of common PCSK1 genetic variants to obesity in 8,359 subjects from multi-ethnic American population. *PLoS ONE* **8**, e57857.
- Church, C., Moir, L., McMurray, F., Girard, C., Banks, G.T., Teboul, L., Wells, S., Brüning, J.C., Nolan, P.M., Ashcroft, F.M., and Cox, R.D. (2010). Overexpression of Fto leads to increased food intake and results in obesity. *Nat. Genet.* **42**, 1086–1092.
- Clément, K., Vaisse, C., Lahlou, N., Cabrol, S., Pelloux, V., Cassuto, D., Gurmelen, M., Dina, C., Chambaz, J., Lacorte, J.M., et al. (1998). A mutation in the human leptin receptor gene causes obesity and pituitary dysfunction. *Nature* **392**, 398–401.
- Clemmensen, C., Finan, B., Fischer, K., Tom, R.Z., Legutko, B., Seherer, L., Heine, D., Grassl, N., Meyer, C.W., Henderson, B., et al. (2015). Dual melanocortin-4 receptor and GLP-1 receptor agonism amplifies metabolic benefits in diet-induced obese mice. *EMBO Mol. Med.* **7**, 288–298.
- Coleman, D.L. (1973). Effects of parabiosis of obese with diabetes and normal mice. *Diabetologia* **9**, 294–298.
- Coleman, D.L., and Hummel, K.P. (1969). Effects of parabiosis of normal with genetically diabetic mice. *Am. J. Physiol.* **217**, 1298–1304.
- Considine, R.V., Sinha, M.K., Heiman, M.L., Kriauciunas, A., Stephens, T.W., Nyce, M.R., Ohannesian, J.P., Marco, C.C., McKee, L.J., Bauer, T.L., et al. (1996). Serum immunoreactive-leptin concentrations in normal-weight and obese humans. *N. Engl. J. Med.* **334**, 292–295.
- Costanzo-Garvey, D.L., Pfluger, P.T., Dougherty, M.K., Stock, J.L., Boehm, M., Chaika, O., Fernandez, M.R., Fisher, K., Kortum, R.L., Hong, E.G., et al. (2009). KSR2 is an essential regulator of AMP kinase, energy expenditure, and insulin sensitivity. *Cell Metab.* **10**, 366–378.
- Cowley, M.A., Cone, R., Enriori, P., Louiselle, I., Williams, S.M., and Evans, A.E. (2003). Electrophysiological actions of peripheral hormones on melanocortin neurons. *Ann. N Y Acad. Sci.* **994**, 175–186.
- Cox, A.J., West, N.P., and Cripps, A.W. (2014). Obesity, inflammation, and the gut microbiota. *Lancet Diabetes Endocrinol.* **3**, 207–215.
- Cummings, D.E., Clement, K., Purnell, J.Q., Vaisse, C., Foster, K.E., Frayo, R.S., Schwartz, M.W., Basdevant, A., and Weigle, D.S. (2002). Elevated plasma ghrelin levels in Prader Willi syndrome. *Nat. Med.* **8**, 643–644.
- Cypess, A.M., Lehman, S., Williams, G., Tal, I., Rodman, D., Goldfine, A.B., Kuo, F.C., Palmer, E.L., Tseng, Y.H., Doria, A., et al. (2009). Identification and importance of brown adipose tissue in adult humans. *N. Engl. J. Med.* **360**, 1509–1517.
- Davenport, J.R., Watts, A.J., Roper, V.C., Croyle, M.J., van Groen, T., Wyss, J.M., Nagy, T.R., Kesterson, R.A., and Yoder, B.K. (2007). Disruption of intracellular transport in adult mice leads to obesity and slow-onset cystic kidney disease. *Curr. Biol.* **17**, 1586–1594.
- Dina, C., Meyre, D., Gallina, S., Durand, E., Körner, A., Jacobson, P., Carlsson, L.M., Kiess, W., Vatin, V., Lecoeur, C., et al. (2007). Variation in FTO contributes to childhood obesity and severe adult obesity. *Nat. Genet.* **39**, 724–726.
- Doche, M.E., Bochukova, E.G., Su, H.W., Pearce, L.R., Keogh, J.M., Henning, E., Cline, J.M., Saeed, S., Dale, A., Cheetham, T., et al. (2012). Human SH2B1 mutations are associated with maladaptive behaviors and obesity. *J. Clin. Invest.* **122**, 4732–4736.
- Fagot-Campagna, A. (2000). Emergence of type 2 diabetes mellitus in children: epidemiological evidence. *J. Pediatr. Endocrinol. Metab.* **13**(6), 1395–1402.
- Falchi, M., El-Sayed Moustafa, J.S., Takousis, P., Pesce, F., Bonnefond, A., Andersson-Assarsson, J.C., Sudmant, P.H., Dorajoo, R., Al-Shafai, M.N., Bottolo, L., et al. (2014). Low copy number of the salivary amylase gene predisposes to obesity. *Nat. Genet.* **46**, 492–497.
- Farooqi, I.S., Jebb, S.A., Langmack, G., Lawrence, E., Cheetham, C.H., Prentice, A.M., Hughes, I.A., McCamish, M.A., and O'Rahilly, S. (1999). Effects of recombinant leptin therapy in a child with congenital leptin deficiency. *N. Engl. J. Med.* **341**, 879–884.

- Farooqi, I.S., Yeo, G.S., Keogh, J.M., Aminian, S., Jebb, S.A., Butler, G., Cheetham, T., and O'Rahilly, S. (2000). Dominant and recessive inheritance of morbid obesity associated with melanocortin 4 receptor deficiency. *J. Clin. Invest.* *106*, 271–279.
- Farooqi, I.S., Matarese, G., Lord, G.M., Keogh, J.M., Lawrence, E., Agwu, C., Sanna, V., Jebb, S.A., Perna, F., Fontana, S., et al. (2002). Beneficial effects of leptin on obesity, T cell hyporesponsiveness, and neuroendocrine/metabolic dysfunction of human congenital leptin deficiency. *J. Clin. Invest.* *110*, 1093–1103.
- Farooqi, I.S., Keogh, J.M., Yeo, G.S., Lank, E.J., Cheetham, T., and O'Rahilly, S. (2003). Clinical spectrum of obesity and mutations in the melanocortin 4 receptor gene. *N. Engl. J. Med.* *348*, 1085–1095.
- Farooqi, I.S., Bullmore, E., Keogh, J., Gillard, J., O'Rahilly, S., and Fletcher, P.C. (2007a). Leptin regulates striatal regions and human eating behavior. *Science* *317*, 1355.
- Farooqi, I.S., Wangensteen, T., Collins, S., Kimber, W., Matarese, G., Keogh, J.M., Lank, E., Bottomley, B., Lopez-Fernandez, J., Ferraz-Amaro, I., et al. (2007b). Clinical and molecular genetic spectrum of congenital deficiency of the leptin receptor. *N. Engl. J. Med.* *356*, 237–247.
- Finan, B., Yang, B., Ottaway, N., Smiley, D.L., Ma, T., Clemmensen, C., Chabenne, J., Zhang, L., Habegger, K.M., Fischer, K., et al. (2015). A rationally designed monomeric peptide triagonist corrects obesity and diabetes in rodents. *Nat. Med.* *21*, 27–36.
- Fischer, J., Koch, L., Emmerling, C., Vierkotten, J., Peters, T., Brüning, J.C., and Rüther, U. (2009). Inactivation of the *Fto* gene protects from obesity. *Nature* *458*, 894–898.
- Frayling, T.M., Timpson, N.J., Weedon, M.N., Zeggini, E., Freathy, R.M., Lindgren, C.M., Perry, J.R., Elliott, K.S., Lango, H., Rayner, N.W., et al. (2007). A common variant in the *FTO* gene is associated with body mass index and predisposes to childhood and adult obesity. *Science* *316*, 889–894.
- Fulton, S., Pissios, P., Manchon, R.P., Stiles, L., Frank, L., Pothos, E.N., Maratos-Flier, E., and Flier, J.S. (2006). Leptin regulation of the mesoaccumbens dopamine pathway. *Neuron* *51*, 811–822.
- Gerken, T., Girard, C.A., Tung, Y.C., Webby, C.J., Saudek, V., Hewitson, K.S., Yeo, G.S., McDonough, M.A., Cunliffe, S., McNeill, L.A., et al. (2007). The obesity-associated *FTO* gene encodes a 2-oxoglutarate-dependent nucleic acid demethylase. *Science* *318*, 1469–1472.
- Gray, J., Yeo, G.S., Cox, J.J., Morton, J., Adlam, A.L., Keogh, J.M., Yanovski, J.A., El Gharbawy, A., Han, J.C., Tung, Y.C., et al. (2006). Hyperphagia, severe obesity, impaired cognitive function, and hyperactivity associated with functional loss of one copy of the brain-derived neurotrophic factor (*BDNF*) gene. *Diabetes* *55*, 3366–3371.
- Gray, L.J., Cooper, N., Dunkley, A., Warren, F.C., Ara, R., Abrams, K., Davies, M.J., Khunti, K., and Sutton, A. (2012). A systematic review and mixed treatment comparison of pharmacological interventions for the treatment of obesity. *Obes. Rev.* *13*, 483–498.
- Greenfield, J.R., Miller, J.W., Keogh, J.M., Henning, E., Satterwhite, J.H., Cameron, G.S., Astruc, B., Mayer, J.P., Brage, S., See, T.C., et al. (2009). Modulation of blood pressure by central melanocortinergic pathways. *N. Engl. J. Med.* *360*, 44–52.
- Gusev, A., Lee, S.H., Trynka, G., Finucane, H., Vilhjálmsson, B.J., Xu, H., Zang, C., Ripke, S., Bulik-Sullivan, B., Stahl, E., et al.; Schizophrenia Working Group of the Psychiatric Genomics Consortium; SWE-SCZ Consortium; Schizophrenia Working Group of the Psychiatric Genomics Consortium; SWE-SCZ Consortium (2014). Partitioning heritability of regulatory and cell-type-specific variants across 11 common diseases. *Am. J. Hum. Genet.* *95*, 535–552.
- Halaas, J.L., Gajiwala, K.S., Maffei, M., Cohen, S.L., Chait, B.T., Rabinowitz, D., Lallone, R.L., Burley, S.K., and Friedman, J.M. (1995). Weight-reducing effects of the plasma protein encoded by the obese gene. *Science* *269*, 543–546.
- Haqq, A.M., Farooqi, I.S., O'Rahilly, S., Stadler, D.D., Rosenfeld, R.G., Pratt, K.L., LaFranchi, S.H., and Purnell, J.Q. (2003). Serum ghrelin levels are inversely correlated with body mass index, age, and insulin concentrations in normal children and are markedly increased in Prader-Willi syndrome. *J. Clin. Endocrinol. Metab.* *88*, 174–178.
- Hetherington, A.W., and Ranson, S.W. (1940). Hypothalamic lesions and adiposity in the rat. *Anat. Rec.* *78*, 149–172.
- Heysfield, S.B., Greenberg, A.S., Fujioka, K., Dixon, R.M., Kushner, R., Hunt, T., Lubina, J.A., Patane, J., Self, B., Hunt, P., et al. (1999). Recombinant leptin for weight loss in obese and lean adults: a randomized, controlled, dose-escalation trial. *JAMA* *282*, 1568–1575.
- Hinton, E.C., Holland, A.J., Gellatly, M.S., Soni, S., Patterson, M., Ghatei, M.A., and Owen, A.M. (2006). Neural representations of hunger and satiety in Prader-Willi syndrome. *Int. J. Obes.* *30*, 313–321.
- Holder, J.L., Jr., Butte, N.F., and Zinn, A.R. (2000). Profound obesity associated with a balanced translocation that disrupts the *SIM1* gene. *Hum. Mol. Genet.* *9*, 101–108.
- Hommel, J.D., Trinko, R., Sears, R.M., Georgescu, D., Liu, Z.W., Gao, X.B., Thurmon, J.J., Marinelli, M., and DiLeone, R.J. (2006). Leptin receptor signaling in midbrain dopamine neurons regulates feeding. *Neuron* *51*, 801–810.
- Huszar, D., Lynch, C.A., Fairchild-Huntress, V., Dunmore, J.H., Fang, Q., Berkemeier, L.R., Gu, W., Kesterson, R.A., Boston, B.A., Cone, R.D., et al. (1997). Targeted disruption of the melanocortin-4 receptor results in obesity in mice. *Cell* *88*, 131–141.
- Jackson, R.S., Creemers, J.W., Ohagi, S., Raffin-Sanson, M.L., Sanders, L., Montague, C.T., Hutton, J.C., and O'Rahilly, S. (1997). Obesity and impaired prohormone processing associated with mutations in the human prohormone convertase 1 gene. *Nat. Genet.* *16*, 303–306.
- Jackson, R.S., Creemers, J.W., Farooqi, I.S., Raffin-Sanson, M.L., Varro, A., Dockray, G.J., Holst, J.J., Brubaker, P.L., Corvol, P., Polonsky, K.S., et al. (2003). Small-intestinal dysfunction accompanies the complex endocrinopathy of human proprotein convertase 1 deficiency. *J. Clin. Invest.* *112*, 1550–1560.
- Kenny, P.J. (2011). Reward mechanisms in obesity: new insights and future directions. *Neuron* *69*, 664–679.
- Keskitalo, K., Silventoinen, K., Tuorila, H., Perola, M., Pietiläinen, K.H., Rissanen, A., and Kaprio, J. (2008). Genetic and environmental contributions to food use patterns of young adult twins. *Physiol. Behav.* *93*, 235–242.
- Krude, H., Biebermann, H., Luck, W., Horn, R., Brabant, G., and Grüters, A. (1998). Severe early-onset obesity, adrenal insufficiency and red hair pigmentation caused by *POMC* mutations in humans. *Nat. Genet.* *19*, 155–157.
- Kublaoui, B.M., Gemelli, T., Tolson, K.P., Wang, Y., and Zinn, A.R. (2008). Oxytocin deficiency mediates hyperphagic obesity of *Sim1* haploinsufficient mice. *Mol. Endocrinol.* *22*, 1723–1734.
- Lee, Y.S., Challis, B.G., Thompson, D.A., Yeo, G.S., Keogh, J.M., Madonna, M.E., Wraight, V., Sims, M., Vatin, V., Meyre, D., et al. (2006). A *POMC* variant implicates beta-melanocyte-stimulating hormone in the control of human energy balance. *Cell Metab.* *3*, 135–140.
- Licinio, J., Caglayan, S., Ozata, M., Yildiz, B.O., de Miranda, P.B., O'Kirwan, F., Whitty, R., Liang, L., Cohen, P., Bhasin, S., et al. (2004). Phenotypic effects of leptin replacement on morbid obesity, diabetes mellitus, hypogonadism, and behavior in leptin-deficient adults. *Proc. Natl. Acad. Sci. USA* *101*, 4531–4536.
- Locke, A.E., Kahali, B., Berndt, S.I., Justice, A.E., Pers, T.H., Day, F.R., Powell, C., Vedantam, S., Buchkovich, M.L., Yang, J., et al.; LifeLines Cohort Study; ADIPOGen Consortium; AGEN-BMI Working Group; CARDIOGRAMplusC4D Consortium; CKDGen Consortium; GLGC; ICBP; MAGIC Investigators; MuTHER Consortium; MIGen Consortium; PAGE Consortium; ReproGen Consortium; GENIE Consortium; International Endogene Consortium (2015). Genetic studies of body mass index yield new insights for obesity biology. *Nature* *518*, 197–206.
- Loos, R.J., Lindgren, C.M., Li, S., Wheeler, E., Zhao, J.H., Prokopenko, I., Inouye, M., Freathy, R.M., Attwood, A.P., Beckmann, J.S., et al.; Prostate, Lung, Colorectal, and Ovarian (PLCO) Cancer Screening Trial; KORA; Nurses' Health Study; Diabetes Genetics Initiative; SardiNIA Study; Wellcome Trust Case

- Control Consortium; FUSION (2008). Common variants near MC4R are associated with fat mass, weight and risk of obesity. *Nat. Genet.* **40**, 768–775.
- Lowell, B.B., and Spiegelman, B.M. (2000). Towards a molecular understanding of adaptive thermogenesis. *Nature* **404**, 652–660.
- Lubrano-Berthelier, C., Dubern, B., Lacorte, J.M., Picard, F., Shapiro, A., Zhang, S., Bertrais, S., Hercberg, S., Basdevant, A., Clement, K., and Vaisse, C. (2006). Melanocortin 4 receptor mutations in a large cohort of severely obese adults: prevalence, functional classification, genotype-phenotype relationship, and lack of association with binge eating. *J. Clin. Endocrinol. Metab.* **97**, 1811–1818.
- Lyons, W.E., Mamounas, L.A., Ricaurte, G.A., Coppola, V., Reid, S.W., Bora, S.H., Wihler, C., Koliatsos, V.E., and Tessarollo, L. (1999). Brain-derived neurotrophic factor-deficient mice develop aggressiveness and hyperphagia in conjunction with brain serotonergic abnormalities. *Proc. Natl. Acad. Sci. USA* **96**, 15239–15244.
- Maffei, M., Halaas, J., Ravussin, E., Pratley, R.E., Lee, G.H., Zhang, Y., Fei, H., Kim, S., Lallone, R., Ranganathan, S., et al. (1995). Leptin levels in human and rodent: measurement of plasma leptin and ob RNA in obese and weight-reduced subjects. *Nat. Med.* **1**, 1155–1161.
- Martin, M.G., Lindberg, I., Solorzano-Vargas, R.S., Wang, J., Avitzur, Y., Bandsma, R., Sokollik, C., Lawrence, S., Pickett, L.A., Chen, Z., et al. (2013). Congenital proprotein convertase 1/3 deficiency causes malabsorptive diarrhea and other endocrinopathies in a pediatric cohort. *Gastroenterology* **145**, 138–148.
- Maures, T.J., Kurzer, J.H., and Carter-Su, C. (2007). SH2B1 (SH2-B) and JAK2: a multifunctional adaptor protein and kinase made for each other. *Trends Endocrinol. Metab.* **18**, 38–45.
- Michaud, J.L., Rosenquist, T., May, N.R., and Fan, C.M. (1998). Development of neuroendocrine lineages requires the bHLH-PAS transcription factor SIM1. *Genes Dev.* **12**, 3264–3275.
- Montague, C.T., Farooqi, I.S., Whitehead, J.P., Soos, M.A., Rau, H., Wareham, N.J., Sewter, C.P., Digby, J.E., Mohammed, S.N., Hurst, J.A., et al. (1997). Congenital leptin deficiency is associated with severe early-onset obesity in humans. *Nature* **387**, 903–908.
- Morton, G.J., Meek, T.H., and Schwartz, M.W. (2014). Neurobiology of food intake in health and disease. *Nat. Rev. Neurosci.* **15**, 367–378.
- Münzberg, H., and Myers, M.G., Jr. (2005). Molecular and anatomical determinants of central leptin resistance. *Nat. Neurosci.* **8**, 566–570.
- O’Rahilly, S., and Farooqi, I.S. (2008). Human obesity: a heritable neurobehavioral disorder that is highly sensitive to environmental conditions. *Diabetes* **57**, 2905–2910.
- O’Rahilly, S., Gray, H., Humphreys, P.J., Krook, A., Polonsky, K.S., White, A., Gibson, S., Taylor, K., and Carr, C. (1995). Brief report: impaired processing of prohormones associated with abnormalities of glucose homeostasis and adrenal function. *N. Engl. J. Med.* **333**, 1386–1390.
- Ogden, C.L., Carroll, M.D., Kit, B.K., and Flegal, K.M. (2014). Prevalence of childhood and adult obesity in the United States, 2011–2012. *JAMA* **311**, 806–814.
- Olson, B.R., Drutarosky, M.D., Chow, M.S., Hruby, V.J., Stricker, E.M., and Verbalis, J.G. (1991). Oxytocin and an oxytocin agonist administered centrally decrease food intake in rats. *Peptides* **12**, 113–118.
- Oral, E.A., Simha, V., Ruiz, E., Andewelt, A., Premkumar, A., Snell, P., Wagner, A.J., DePaoli, A.M., Reitman, M.L., Taylor, S.I., et al. (2002). Leptin-replacement therapy for lipodystrophy. *N. Engl. J. Med.* **346**, 570–578.
- Ozata, M., Ozdemir, I.C., and Licinio, J. (1999). Human leptin deficiency caused by a missense mutation: multiple endocrine defects, decreased sympathetic tone, and immune system dysfunction indicate new targets for leptin action, greater central than peripheral resistance to the effects of leptin, and spontaneous correction of leptin-mediated defects. *J. Clin. Endocrinol. Metab.* **84**, 3686–3695.
- Panaro, B.L., and Cone, R.D. (2013). Melanocortin-4 receptor mutations paradoxically reduce preference for palatable foods. *Proc. Natl. Acad. Sci. USA* **110**, 7050–7055.
- Pearce, L.R., Atanassova, N., Banton, M.C., Bottomley, B., van der Klaauw, A.A., Revelli, J.P., Hendricks, A., Keogh, J.M., Henning, E., Doree, D., et al.; UK10K consortium (2013). KSR2 mutations are associated with obesity, insulin resistance, and impaired cellular fuel oxidation. *Cell* **155**, 765–777.
- Pecina, S., Cagniard, B., Berridge, K.C., Aldridge, J.W., and Zhuang, X. (2003). Hyperdopaminergic mutant mice have higher “wanting” but not “liking” for sweet rewards. *J. Neurosci.* **23**, 9395–9402.
- Pelleymounter, M.A., Cullen, M.J., Baker, M.B., Hecht, R., Winters, D., Boone, T., and Collins, F. (1995). Effects of the obese gene product on body weight regulation in ob/ob mice. *Science* **269**, 540–543.
- Perreault, M., Feng, G., Will, S., Gareski, T., Kubasiak, D., Marquette, K., Vugmeyster, Y., Unger, T.J., Jones, J., Qadri, A., et al. (2013). Activation of TrkB with TAM-163 results in opposite effects on body weight in rodents and non-human primates. *PLoS ONE* **8**, e62616.
- Pérusse, L., Tremblay, A., Leblanc, C., and Bouchard, C. (1989). Genetic and environmental influences on level of habitual physical activity and exercise participation. *Am. J. Epidemiol.* **129**, 1012–1022.
- Pinto, S., Roseberry, A.G., Liu, H., Diano, S., Shanabrough, M., Cai, X., Friedman, J.M., and Horvath, T.L. (2004). Rapid rewiring of arcuate nucleus feeding circuits by leptin. *Science* **304**, 110–115.
- Popkin, B.M. (2006). Global nutrition dynamics: the world is shifting rapidly toward a diet linked with noncommunicable diseases. *Am. J. Clin. Nutr.* **84**, 289–298.
- Pritchard, L.E., Turnbull, A.V., and White, A. (2002). Pro-opiomelanocortin processing in the hypothalamus: impact on melanocortin signalling and obesity. *J. Endocrinol.* **172**, 411–421.
- Puhl, R., and Brownell, K.D. (2001). Bias, discrimination, and obesity. *Obes. Res.* **9**, 788–805.
- Ramachandrapa, S., Raimondo, A., Cali, A.M., Keogh, J.M., Henning, E., Saeed, S., Thompson, A., Garg, S., Bochukova, E.G., Brage, S., et al. (2013). Rare variants in single-minded 1 (SIM1) are associated with severe obesity. *J. Clin. Invest.* **123**, 3042–3050.
- Ravussin, Y., Leibel, R.L., and Ferrante, A.W., Jr. (2014). A missing link in body weight homeostasis: the catabolic signal of the overfed state. *Cell Metab.* **20**, 565–572.
- René, P., Le Gouill, C., Pogozeva, I.D., Lee, G., Mosberg, H.I., Farooqi, I.S., Valenzano, K.J., and Bouvier, M. (2010). Pharmacological chaperones restore function to MC4R mutants responsible for severe early-onset obesity. *J. Pharmacol. Exp. Ther.* **335**, 520–532.
- Rosenbaum, M., Murphy, E.M., Heymsfield, S.B., Matthews, D.E., and Leibel, R.L. (2002). Low dose leptin administration reverses effects of sustained weight-reduction on energy expenditure and circulating concentrations of thyroid hormones. *J. Clin. Endocrinol. Metab.* **87**, 2391–2394.
- Rosenbaum, M., Goldsmith, R., Bloomfield, D., Magnano, A., Weimer, L., Heymsfield, S., Gallagher, D., Mayer, L., Murphy, E., and Leibel, R.L. (2005). Low-dose leptin reverses skeletal muscle, autonomic, and neuroendocrine adaptations to maintenance of reduced weight. *J. Clin. Invest.* **115**, 3579–3586.
- Rosenbaum, M., Sy, M., Pavlovich, K., Leibel, R.L., and Hirsch, J. (2008). Leptin reverses weight loss-induced changes in regional neural activity responses to visual food stimuli. *J. Clin. Invest.* **118**, 2583–2591.
- Rössger, K., Charpin-El-Hamri, G., and Fussenegger, M. (2013). A closed-loop synthetic gene circuit for the treatment of diet-induced obesity in mice. *Nat. Commun.* **4**, 2825.
- Rouskas, K., Kouvatzi, A., Paletas, K., Papazoglou, D., Tsapas, A., Lobbens, S., Vatin, V., Durand, E., Labruno, Y., Delplanque, J., et al. (2012). Common variants in FTO, MC4R, TMEM18, PRL, AIF1, and PCSK1 show evidence of association with adult obesity in the Greek population. *Obesity (Silver Spring)* **20**, 389–395.
- Sabatier, N., Caqueneau, C., Dayanithi, G., Bull, P., Douglas, A.J., Guan, X.M., Jiang, M., Van der Ploeg, L., and Leng, G. (2003). Alpha-melanocyte-stimulating hormone stimulates oxytocin release from the dendrites of hypothalamic

- neurons while inhibiting oxytocin release from their terminals in the neurohypophysis. *J. Neurosci.* 23, 10351–10358.
- Sahoo, T., del Gaudio, D., German, J.R., Shinawi, M., Peters, S.U., Person, R.E., Garnica, A., Cheung, S.W., and Beaudet, A.L. (2008). Prader-Willi phenotype caused by paternal deficiency for the HBII-85 C/D box small nucleolar RNA cluster. *Nat. Genet.* 40, 719–721.
- Salbe, A.D., DelParigi, A., Pratley, R.E., Drewnowski, A., and Tataranni, P.A. (2004). Taste preferences and body weight changes in an obesity-prone population. *Am. J. Clin. Nutr.* 79, 372–378.
- Sayk, F., Heutling, D., Dodt, C., Iwen, K.A., Wellhoner, J.P., Scherag, S., Hinney, A., Hebebrand, J., and Lehnert, H. (2010). Sympathetic function in human carriers of melanocortin-4 receptor gene mutations. *J. Clin. Endocrinol. Metab.* 95, 1998–2002.
- Sebag, J.A., Zhang, C., Hinkle, P.M., Bradshaw, A.M., and Cone, R.D. (2013). Developmental control of the melanocortin-4 receptor by MRAP2 proteins in zebrafish. *Science* 341, 278–281.
- Selvarajah, D., Choudhary, P., and Farooqi, I.S. (2014). Wired for obesity? *Diabetes* 63, 4016–4017.
- Silventoinen, K., Magnusson, P.K., Tynelius, P., Kaprio, J., and Rasmussen, F. (2008). Heritability of body size and muscle strength in young adulthood: a study of one million Swedish men. *Genet. Epidemiol.* 32, 341–349.
- Simonds, S.E., Pryor, J.T., Ravussin, E., Greenway, F.L., Dileone, R., Allen, A.M., Bassi, J., Elmquist, J.K., Keogh, J.M., Henning, E., et al. (2014). Leptin mediates the increase in blood pressure associated with obesity. *Cell* 159, 1404–1416.
- Singh, G.K., and Lin, S.C. (2013). Dramatic increases in obesity and overweight prevalence among Asian subgroups in the United States, 1992–2011. *ISRN Prev. Med.* 2013, 898691.
- Smemo, S., Tena, J.J., Kim, K.H., Gamazon, E.R., Sakabe, N.J., Gómez-Marín, C., Aneas, I., Credidio, F.L., Sobreira, D.R., Wasserman, N.F., et al. (2014). Obesity-associated variants within FTO form long-range functional connections with IRX3. *Nature* 507, 371–375.
- Smith, S.R., Blundell, J.E., Burns, C., Ellero, C., Schroeder, B.E., Kesty, N.C., Chen, K.S., Halseth, A.E., Lush, C.W., and Weyer, C. (2007). Pramlintide treatment reduces 24-h caloric intake and meal sizes and improves control of eating in obese subjects: a 6-wk translational research study. *Am. J. Physiol. Endocrinol. Metab.* 293, E620–E627.
- Smith, S.R., Weissman, N.J., Anderson, C.M., Sanchez, M., Chuang, E., Stubbe, S., Bays, H., Shanahan, W.R., and Behavioral, M.; Behavioral Modification and Lorcaserin for Overweight and Obesity Management (BLOOM) Study Group (2010). Multicenter, placebo-controlled trial of lorcaserin for weight management. *N. Engl. J. Med.* 363, 245–256.
- Sørensen, T.I., Price, R.A., Stunkard, A.J., and Schulsinger, F. (1989). Genetics of obesity in adult adoptees and their biological siblings. *BMJ* 298, 87–90.
- Speakman, J.R. (2007). A nonadaptive scenario explaining the genetic predisposition to obesity: the “predation release” hypothesis. *Cell Metab.* 6, 5–12.
- Sperrin, M., Marshall, A.D., Higgins, V., Buchan, I.E., and Renehan, A.G. (2014). Slowing down of adult body mass index trend increases in England: a latent class analysis of cross-sectional surveys (1992–2010). *Int. J. Obes.* 38, 818–824.
- Stratigopoulos, G., Padilla, S.L., LeDuc, C.A., Watson, E., Hattersley, A.T., McCarthy, M.I., Zeltser, L.M., Chung, W.K., and Leibel, R.L. (2008). Regulation of Fto/Ftm gene expression in mice and humans. *Am. J. Physiol. Regul. Integr. Comp. Physiol.* 294, R1185–R1196.
- Strobel, A., Issad, T., Camoin, L., Ozata, M., and Strosberg, A.D. (1998). A leptin missense mutation associated with hypogonadism and morbid obesity. *Nat. Genet.* 18, 213–215.
- Swaab, D.F., Purba, J.S., and Hofman, M.A. (1995). Alterations in the hypothalamic paraventricular nucleus and its oxytocin neurons (putative satiety cells) in Prader-Willi syndrome: a study of five cases. *J. Clin. Endocrinol. Metab.* 80, 573–579.
- Tan, T., and Bloom, S. (2013). Gut hormones as therapeutic agents in treatment of diabetes and obesity. *Curr. Opin. Pharmacol.* 13, 996–1001.
- Thomas, D.M., Weedermann, M., Fuemmeler, B.F., Martin, C.K., Dhurandhar, N.V., Bredlau, C., Heymsfield, S.B., Ravussin, E., and Bouchard, C. (2014). Dynamic model predicting overweight, obesity, and extreme obesity prevalence trends. *Obesity (Silver Spring)* 22, 590–597.
- Tsao, D., Thomsen, H.K., Chou, J., Stratton, J., Hagen, M., Loo, C., Garcia, C., Sloane, D.L., Rosenthal, A., and Lin, J.C. (2008). TrkB agonists ameliorate obesity and associated metabolic conditions in mice. *Endocrinology* 149, 1038–1048.
- Tung, Y.C., Yeo, G.S., O’Rahilly, S., and Coll, A.P. (2014). Obesity and FTO: Changing Focus at a Complex Locus. *Cell Metab.* 20, 710–718.
- Turnbaugh, P.J., Ley, R.E., Mahowald, M.A., Magrini, V., Mardis, E.R., and Gordon, J.I. (2006). An obesity-associated gut microbiome with increased capacity for energy harvest. *Nature* 444, 1027–1031.
- Turton, M.D., O’Shea, D., Gunn, I., Beak, S.A., Edwards, C.M., Meeran, K., Choi, S.J., Taylor, G.M., Heath, M.M., Lambert, P.D., et al. (1996). A role for glucagon-like peptide-1 in the central regulation of feeding. *Nature* 379, 69–72.
- Vaisse, C., Clement, K., Durand, E., Hercberg, S., Guy-Grand, B., and Froguel, P. (2000). Melanocortin-4 receptor mutations are a frequent and heterogeneous cause of morbid obesity. *J. Clin. Invest.* 106, 253–262.
- van der Klaauw, A.A., von dem Hagen, E.A., Keogh, J.M., Henning, E., O’Rahilly, S., Lawrence, A.D., Calder, A.J., and Farooqi, I.S. (2014). Obesity-associated melanocortin-4 receptor mutations are associated with changes in the brain response to food cues. *J. Clin. Endocrinol. Metab.* 99, E2101–E2106.
- Van der Ploeg, L.H., Martin, W.J., Howard, A.D., Nargund, R.P., Austin, C.P., Guan, X., Drisko, J., Cashen, D., Sebhat, I., Patchett, A.A., et al. (2002). A role for the melanocortin 4 receptor in sexual function. *Proc. Natl. Acad. Sci. USA* 99, 11381–11386.
- Wabitsch, M., Funcke, J.B., Lennerz, B., Kuhnle-Krahl, U., Lahr, G., Debatin, K.M., Vatter, P., Gierschik, P., Moepps, B., and Fischer-Posovszky, P. (2015). Biologically inactive leptin and early-onset extreme obesity. *N. Engl. J. Med.* 372, 48–54.
- Walters, R.G., Jacquemont, S., Valsesia, A., de Smith, A.J., Martinet, D., Andersson, J., Falchi, M., Chen, F., Andrieux, J., Lobbens, S., et al. (2010). A new highly penetrant form of obesity due to deletions on chromosome 16p11.2. *Nature* 463, 671–675.
- Wang, L., Meece, K., Williams, D.J., Lo, K.A., Zimmer, M., Heinrich, G., Martin Carli, J., Leduc, C.A., Sun, L., Zeltser, L.M., et al. (2015). Differentiation of hypothalamic-like neurons from human pluripotent stem cells. *J. Clin. Invest.* 125, 796–808.
- Wardle, J., Carnell, S., Haworth, C.M., Farooqi, I.S., O’Rahilly, S., and Plomin, R. (2008a). Obesity associated genetic variation in FTO is associated with diminished satiety. *J. Clin. Endocrinol. Metab.* 93, 3640–3643.
- Wardle, J., Carnell, S., Haworth, C.M., and Plomin, R. (2008b). Evidence for a strong genetic influence on childhood adiposity despite the force of the obesogenic environment. *Am. J. Clin. Nutr.* 87, 398–404.
- Welt, C.K., Chan, J.L., Bullen, J., Murphy, R., Smith, P., DePaoli, A.M., Karalis, A., and Mantzoros, C.S. (2004). Recombinant human leptin in women with hypothalamic amenorrhea. *N. Engl. J. Med.* 351, 987–997.
- Wheeler, E., Huang, N., Bochukova, E.G., Keogh, J.M., Lindsay, S., Garg, S., Henning, E., Blackburn, H., Loos, R.J., Wareham, N.J., et al. (2013). Genome-wide SNP and CNV analysis identifies common and low-frequency variants associated with severe early-onset obesity. *Nat. Genet.* 45, 513–517.
- Whitlock, G., Lewington, S., Sherliker, P., Clarke, R., Emberson, J., Halsey, J., Qizilbash, N., Collins, R., and Peto, R.; Prospective Studies Collaboration (2009). Body-mass index and cause-specific mortality in 900 000 adults: collaborative analyses of 57 prospective studies. *Lancet* 373, 1083–1096.
- Wu, Z., Puigserver, P., Andersson, U., Zhang, C., Adelmant, G., Mootha, V., Troy, A., Cinti, S., Lowell, B., Scarpulla, R.C., and Spiegelman, B.M. (1999). Mechanisms controlling mitochondrial biogenesis and respiration through the thermogenic coactivator PGC-1. *Cell* 98, 115–124.
- Wu, Q., Boyle, M.P., and Palmiter, R.D. (2009). Loss of GABAergic signaling by AgRP neurons to the parabrachial nucleus leads to starvation. *Cell* 137, 1225–1234.

- Xiang, Z., Litherland, S.A., Sorensen, N.B., Proneth, B., Wood, M.S., Shaw, A.M., Millard, W.J., and Haskell-Luevano, C. (2006). Pharmacological characterization of 40 human melanocortin-4 receptor polymorphisms with the endogenous proopiomelanocortin-derived agonists and the agouti-related protein (AGRP) antagonist. *Biochemistry* 45, 7277–7288.
- Xu, B., Goulding, E.H., Zang, K., Cepoi, D., Cone, R.D., Jones, K.R., Tecott, L.H., and Reichardt, L.F. (2003). Brain-derived neurotrophic factor regulates energy balance downstream of melanocortin-4 receptor. *Nat. Neurosci.* 6, 736–742.
- Yang, Y.J., Li, Y.K., Wang, W., Wan, J.G., Yu, B., Wang, M.Z., and Hu, B. (2014). Small-molecule TrkB agonist 7,8-dihydroxyflavone reverses cognitive and synaptic plasticity deficits in a rat model of schizophrenia. *Pharmacol. Biochem. Behav.* 122, 30–36.
- Yeo, G.S., Connie Hung, C.C., Rochford, J., Keogh, J., Gray, J., Sivaramakrishnan, S., O'Rahilly, S., and Farooqi, I.S. (2004). A de novo mutation affecting human TrkB associated with severe obesity and developmental delay. *Nat. Neurosci.* 7, 1187–1189.
- Zhang, Y., Proenca, R., Maffei, M., Barone, M., Leopold, L., and Friedman, J.M. (1994). Positional cloning of the mouse obese gene and its human homologue. *Nature* 372, 425–432.
- Zhu, Z., Bakshi, A., Vinkhuyzen, A.A., Hemani, G., Lee, S.H., Nolte, I.M., van Vliet-Ostaptchouk, J.V., Snieder, H., Esko, T., Milani, L., et al.; The LifeLines Cohort Study (2015). Dominance genetic variation contributes little to the missing heritability for human complex traits. *Am. J. Hum. Genet.* 96, 377–385.
- Ziauddeen, H., Farooqi, I.S., and Fletcher, P.C. (2012). Obesity and the brain: how convincing is the addiction model? *Nat. Rev. Neurosci.* 13, 279–286.
- Ziauddeen, H., Chamberlain, S.R., Nathan, P.J., Koch, A., Maltby, K., Bush, M., Tao, W.X., Napolitano, A., Skeggs, A.L., Brooke, A.C., et al. (2013). Effects of the mu-opioid receptor antagonist GSK1521498 on hedonic and consummatory eating behaviour: a proof of mechanism study in binge-eating obese subjects. *Mol. Psychiatry* 18, 1287–1293.

The Role of Chromosome Domains in Shaping the Functional Genome

Tom Sexton^{1,*} and Giacomo Cavalli^{2,*}

¹Institute of Genetics and Molecular and Cellular Biology (IGBMC), 1 rue Laurent Fries, 67404 Illkirch, France

²Institute of Human Genetics (IGH), 141 rue de la Cardonille, 34396 Montpellier, France

*Correspondence: sexton@igbmc.fr (T.S.), giacomo.cavalli@igh.cnrs.fr (G.C.)

<http://dx.doi.org/10.1016/j.cell.2015.02.040>

The genome must be highly compacted to fit within eukaryotic nuclei but must be accessible to the transcriptional machinery to allow appropriate expression of genes in different cell types and throughout developmental pathways. A growing body of work has shown that the genome, analogously to proteins, forms an ordered, hierarchical structure that closely correlates and may even be causally linked with regulation of functions such as transcription. This review describes our current understanding of how these functional genomic “secondary and tertiary structures” form a blueprint for global nuclear architecture and the potential they hold for understanding and manipulating genomic regulation.

Eukaryotic genomes must be tightly folded and packaged to be contained within cell nuclei. Since initial observations of heterochromatin by Emil Heitz in the 1930s, it has become more and more appreciated that this packaging is highly organized and may be closely linked to transcriptional control. Over the last two decades, many studies have assessed the spatial proximity and nuclear organization of specific genomic loci, using microscopic techniques, such as fluorescent in situ hybridization (FISH), or molecular biology techniques, such as chromosome conformation capture (3C). Collectively, these studies demonstrated a correlation between chromatin topology and underlying gene activity, without resolving whether chromosome folding is a cause or consequence of genomic functions (Cavalli and Misteli, 2013; de Laat and Duboule, 2013).

Topology and activity appear linked at different scales within the nucleus. At the kilobase-to-megabase scale, distal regulatory elements such as enhancers were found to come into direct contact with their target genes via chromatin loops (Palstra et al., 2003). At the megabase scale, genes were observed to significantly co-occupy functional sites within the nucleus, such as foci of Polycomb proteins (Bantignies et al., 2011) or of active RNA polymerase (Schoenfelder et al., 2010), specifically in cells where the genes have the same activity. At the scale of the whole nucleus, chromosomes occupy discrete territories, which are non-randomly organized to place gene-poor chromosomes in the predominantly heterochromatic periphery and gene-rich regions in the euchromatic interior. The transcriptional activity of specific genes has been correlated with their nuclear positioning relative to the periphery, and more specifically the repressive nuclear lamina (Peric-Hupkes et al., 2010), as well as to their position relative to the bulk of the chromosome territory (Chauveil et al., 2006). Intriguing recent work has even decoupled chromatin decondensation from transcriptional activation, showing that opening chromatin without concomitant gene activation is sufficient for relocalization of genes to the nuclear

interior (Therizols et al., 2014). Overall, these case studies support a hierarchical, multi-scale model where expression of a gene may influence or be influenced by its local chromatin interactions, its associations with other potentially coordinately controlled genes and the regulatory environment provided by its nuclear location.

Average conformations of chromatin have been more systematically characterized by coupling 3C to high-throughput sequencing (Hi-C) to derive large catalogs of pairwise chromatin interactions within populations of nuclei (Lieberman-Aiden et al., 2009). Initial, lower-resolution Hi-C studies demonstrated that active chromatin predominantly associates with other active regions, and repressed chromatin associates with other silent regions with little inter-mixing of the two types (Lieberman-Aiden et al., 2009). More recently, high-resolution chromatin interaction maps revealed that metazoan genomes fold into distinct modules called physical domains or topologically associated domains (TADs), whereby genomic interactions are strong within a domain but are sharply depleted on crossing the boundary between two TADs (Dixon et al., 2012; Nora et al., 2012; Sexton et al., 2012). The presence of TADs is less clear for non-animal species. Although Hi-C is unable to give any information on TAD dynamics or cell-to-cell variability, the domains identified correlate well with many markers of chromatin activity, such as histone modifications and replication timing (Dixon et al., 2012; Sexton et al., 2012). TADs can also contain coordinately regulated genes (Le Dily et al., 2014; Nora et al., 2012). The described organization of the genome into functional domains containing different types of chromatin (Ernst et al., 2011; Ho et al., 2014) thus reflects the average folded state of the chromosome.

TADs appear to form the modular basis for higher-order chromosomal structures (Sexton et al., 2012), which in themselves may be built up from key stabilizing interactions between regulatory elements (Giorgetti et al., 2014). Such an arrangement is reminiscent of protein folding, whereby hierarchical stabilization

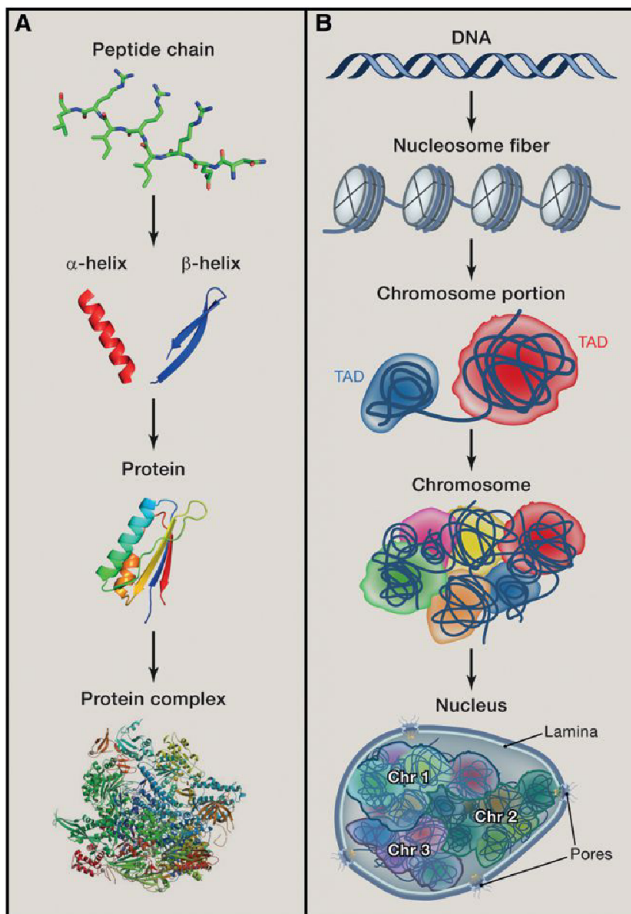


Figure 1. Analogous Hierarchical Organization of Protein and Genome Structure

(A and B) Primary structures comprising the amino acid or nucleotide sequence (packaged into a nucleosomal fiber in eukaryotic chromatin) on a single polymeric chain form locally stabilized interactions to fold into secondary structures, such as polypeptide alpha-helices or beta-sheets, or chromatin TADs. These domains in turn hierarchically co-associate to form a tertiary structure of a protein or chromosome. The co-associations of multiple, separately encoded subunits forms the final quaternary structure of a protein complex or entire genome. Protein structures taken or derived from the RCSB database (PDB 2KVQ, or 4BBR for quaternary structure).

of secondary structures such as alpha-helices leads to the final tertiary structure, whose conformation is crucial to protein function (Figure 1). Genome folding is not as rigidly or thermodynamically defined as protein structure—single-cell experiments reveal a high variability of adopted genomic configurations (Nagano et al., 2013; Noordermeer et al., 2011a). Further, it has not been shown that a specific chromosome structure is essential for genomic functions. However, considering chromosome topology as a principle of folding, and TADs as chromosomal secondary structures, is a useful starting analogy. Here, we discuss the relationship between DNA sequence (primary structure), genomic sub-structures such as TADs (secondary structure), overall chromosome folding (tertiary structure), and genome function, positing that TADs and other localized structures form a blueprint for coordinated genome control.

Chromatin Loops in Gene Regulation

Seminal studies of the beta-globin locus showed that the globin gene promoter more frequently interacted with distal enhancers than intervening sequence, specifically in erythroid tissue where the gene was transcribed (Palstra et al., 2003). Such results were confirmed for other enhancer-promoter combinations (Kieffer-Kwon et al., 2013; Li et al., 2012; Sanyal et al., 2012) and suggest that chromatin looping brings genes and their regulatory elements in close proximity. For simplicity, we will also refer to these phenomena as loops, although in many cases they are more likely to represent a statistical ensemble of transient contacts than true stable structures (Giorgetti et al., 2014). Many enhancer-promoter combinations share binding of common transcription factors, and enhancers are also frequently transcribed, especially when involved in interactions with target genes (Sanyal et al., 2012). Such chromatin loops are thus proposed to set up an “active chromatin hub,” providing a chromatin environment more permissive to transcription than factors bound directly to the promoter alone (Mousavi et al., 2013; Palstra et al., 2003). In support of this model, enhancer-promoter interactions within the human *OCT4* locus, a gene encoding a key pluripotency transcription factor, distinguish induced pluripotent stem cells from non-reprogrammed cells (Zhang et al., 2013). The non-reprogrammed cells had equivalent binding of the inducing factors at the promoter and enhancer but no *OCT4* expression. However, it remains an open question whether chromatin looping is a cause or consequence of transcriptional activation. Recent elegant experiments have engineered chromatin loops within the mouse beta-globin locus by exogenously targeting the dimerization domain of the transcription factor Ldb1, which is naturally present at the enhancers of the globin locus control region (Deng et al., 2012; Deng et al., 2014). These induced chromatin loops could partially rescue adult beta-globin expression in mutants for erythroid transcription factors (Deng et al., 2012) or stimulate fetal globin expression out of its normal developmental context (Deng et al., 2014). Chromatin topology can thus be causally linked to transcriptional regulation. As the globin genes are very highly expressed in erythroid tissues, it will be interesting to see the functional consequences of induced chromatin loops in less transcriptionally permissive genomic and cell-type contexts.

The beta-globin active chromatin hub is progressively formed during hematopoiesis (Palstra et al., 2003) and involves binding sites for erythroid-specific transcription factors (Drissen et al., 2004 for example), so enhancer-promoter contacts were proposed to occur exclusively in cells where the target gene is being transcribed. Although many cell-type-specific chromatin loops have been characterized from more systematic approaches (Heidari et al., 2014; Sanyal et al., 2012), evidence is also emerging that chromatin topology and transcriptional regulation can be temporally uncoupled. A recent analysis of the interaction profiles of a hundred *Drosophila* mesodermal enhancers found that more than 90% of the interactions were detectable before mesoderm specification and were commonly linked to genes with paused RNA polymerase (Ghavi-Helm et al., 2014). This result suggests that chromatin loops may commonly poise a gene for expression but that another signal is required for complete transcriptional firing. In support of this model, induced looping within the beta-globin locus rescued transcription

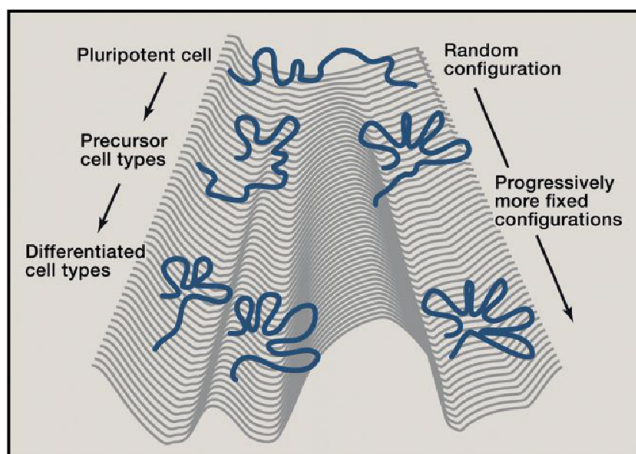


Figure 2. Waddington Landscape of Chromatin Loop Configurations throughout Development

Pluripotent cells able to form any lineage (top) have largely unstructured local chromatin topologies. Progressive lineage restriction throughout development, tracing paths through the landscape from top to bottom, may be accompanied by progressive constraint of the specific chromatin loop topologies as only a limited repertoire of enhancer-promoter contacts are permitted and fixed.

initiation, but not efficient elongation when the essential transcription factor GATA-1 was lacking (Deng et al., 2012). Furthermore, Hi-C analysis of a human fibroblast cell line showed conservation of enhancer-promoter interactions around responsive genes before and after treatment with the cytokine TNF- α (Jin et al., 2013).

These seemingly opposing views of enhancer-promoter chromatin loop dynamics may be reconciled by a Waddington landscape model of chromatin architecture (Figure 2). Non-expressed genes form more promiscuous contacts in pluripotent cells than in differentiated cells (de Wit et al., 2013; Splinter et al., 2011). Repertoires of tissue-specific interactions may then be set up in precursor cells as their differentiation potential is restricted, effectively limiting the sets of genes with a permissive chromatin environment for further induction. Fully differentiated cells may then benefit from their pre-formed active chromatin hubs for rapid transcriptional responses to appropriate signals. Although this model has yet to be formally assessed, chromatin states themselves exhibit a similar progressive developmental restriction (Zhu et al., 2013). Furthermore, there is more tissue-type variation in the chromatin states of enhancers than of promoters (Ernst et al., 2011). Finally, a recent analysis has suggested that enhancer-promoter interactions are variable in different cell types (He et al., 2014). Together, these data suggest that enhancers carry a large regulatory potential, and although the mechanistic details of *when* and *how* they stimulate transcription are not yet clarified, chromatin loops appear a ubiquitous means of relaying enhancer-promoter communication.

Architectural Chromatin Loops—Building up the Secondary Structures

In addition to specific transcription factors, ubiquitous proteins have also been linked to chromatin loops, in particular the insu-

lator protein CTCF (Splinter et al., 2006), the cohesin complex (Hadjur et al., 2009), and the general co-activating Mediator complex (Kagey et al., 2010). Mediator is predominantly found at loops between promoters and enhancers and between promoters, in agreement with its general activation role (Conaway and Conaway, 2011). Consistently, Mediator-linked interactions are more cell-type-specific (Phillips-Cremins et al., 2013). In contrast, CTCF tends not to be present at enhancer-promoter loops. It is more commonly associated with constitutive, longer-range chromatin interactions (Phillips-Cremins et al., 2013; Sanyal et al., 2012), although some cell-type-specific CTCF-mediated interactions have been reported (Hou et al., 2010). CTCF is enriched at TAD borders (Dixon et al., 2012; Hou et al., 2012; Sexton et al., 2012), and CTCF-mediated loops are implicated in maintenance of TAD structure (Giorgetti et al., 2014) and are thus believed to play a more fundamental architectural role in chromosome folding. Various case studies have implicated CTCF-mediated loops in insulator function, preventing communication between distal regulatory elements (Kurukuti et al., 2006 for example). However, many CTCF sites have recently been shown not to be a barrier to enhancer-promoter interactions (Sanyal et al., 2012). The functional consequences of these more developmentally stable chromatin architectures are thus likely to be complex and context-dependent. Similarly, CTCF binding alone cannot account for TAD border function (discussed in more detail in later sections). Cohesins are associated with both cell-type-specific enhancer-based loops and constitutive, CTCF-mediated loops, although both types of loops can also be cohesin-independent (DeMare et al., 2013; Phillips-Cremins et al., 2013). In agreement, cohesin has been shown to interact with CTCF (Rubio et al., 2008) and forms direct complexes with Mediator (Kagey et al., 2010) and certain transcription factors (Wei et al., 2013). The cohesin complex comprises a ring structure that physically maintains sister chromatid attachment after DNA replication (Nasmyth and Haering, 2009). Though yet to be demonstrated, a similar structure could be envisioned to stabilize chromatin loops on cohesin recruitment. Abrogation of cohesin causes perturbation of chromatin loops with subsequent effects on transcriptional control (Hadjur et al., 2009; Seitan et al., 2013; Sofueva et al., 2013; Zuin et al., 2014). Overall, chromatin loops appear important for the possibly inter-linked functions of transcriptional regulation and maintenance of higher-order chromosome folding. A full proteomic appraisal of the factors present at chromatin loops may help us better understand how they are recruited to their specific sites in a developmental context and how and when they are able to effect looping.

Chromosomal Secondary Structures—“Facultative” and “Constitutive” TADs

The three-dimensional organization of many metazoan genomes into discretely folded kilobase-to-megabase sized TADs is particularly striking due to their agreement with many linear (or one-dimensional) measurements of chromatin activity; for example, histone modifications (Dixon et al., 2012; Sexton et al., 2012), coordinated gene expression (Le Dily et al., 2014; Nora et al., 2012), lamina association (Dixon et al., 2012), and DNA replication timing (Dixon et al., 2012; Pope et al., 2014).

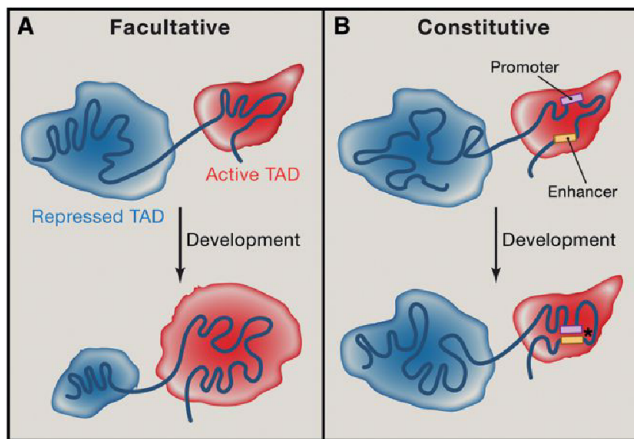


Figure 3. Facultative and Constitutive TAD Models of Regulated Developmental Gene Expression Programs

(A) Active (red) and repressed (blue) chromatin domains form separate facultative TADs which spatially segregate their regulatory environments. During development, some genes are activated and leave the repressive TAD to enter the growing facultative active TAD by a shift in the boundary between TADs. (B) Boundary positions do not change in constitutive TADs. Gene expression changes are effected via altered intra-TAD chromatin interactions; for example by developmental stage-specific presence of enhancer-promoter chromatin loops (asterisk; positions of sequences participating in this loop in both cell types are highlighted in yellow and pink).

TADs thus appear to be chromosomal secondary structures that reflect a tendency to divide the genome into distinct, autonomously regulated regions. This model is supported by the finding that TADs determine the scope of most enhancers' activities (Ghavi-Helm et al., 2014; Shen et al., 2012; Symmons et al., 2014). The mechanisms of TAD establishment and maintenance are largely unknown. In particular, a critical issue to be resolved is whether TADs constitute a structural blueprint that defines chromosome architecture within which gene regulatory changes are overlaid, or are themselves dynamically built by transcriptional silencing or activation machineries. A case in point for TAD organization by transcription arises from studies aimed at understanding the spatial and temporal collinearity of mouse Hox gene expression. These genes are sequentially activated during development, and according to anterior-posterior body position, in order along the chromosomal fiber. The active genes are marked by trimethylation of lysine-4 of histone H3 (H3K4me3) and the silent regions are coated with trimethylation of lysine-27 of histone H3 (H3K27me3). Hox gene activation is accompanied by a transition in the chromatin modification (Soshnikova and Duboule, 2009). Strikingly, the Hox gene loci form distinct topological domains which mirror these chromatin domains precisely, with the active domain expanding and the silent domain shrinking according to collinear gene activation (Noordermeer et al., 2011b). Such a dynamic model of chromosome topology implies that “facultative TADs” spatially confine co-regulated genomic regions but may actually be defined by the underlying transcriptional activity and/or chromatin state (Figure 3A). However, ablation of H3K27me3 in mouse ES cells by knockout of the Polycomb group gene *Eed* had no effect on TAD structures around the X-inactivation locus (Nora et al., 2012). Further, genome-wide comparisons of TADs in disparate

mouse and human cell lines and tissues revealed that most TADs seem invariant with cell type (Dixon et al., 2012). Although many TADs at gene deserts or clusters of ubiquitously expressed housekeeping genes would not necessarily be expected to change in these different cell types, the large number of “constitutive TADs” suggests that many are genuine chromosomal secondary structures. These may thus represent a ground state spatial configuration on which subsequent regulatory features are overlaid (Figure 3B). In support of this view, entire TADs containing coordinately responsive genes to progesterone treatment can be structurally re-modeled while their borders remain unchanged (Le Dily et al., 2014). In between these extreme views of chromosome topology, high-resolution analysis of a handful of TADs during ES cell differentiation identified them to be predominantly stable but noted developmental dynamics of smaller “sub-TADs” within them (Phillips-Cremens et al., 2013). As the resolution of genome-wide chromatin interaction maps improves, so will our appreciation of the interplay between developmentally stable and dynamic chromosomal secondary structures and of the cause-effect relationships between TADs and genome function.

Establishing, Maintaining, and Re-Building Chromosomal Secondary Structures

Despite (or perhaps because of) their many correlations with different epigenomic features, unravelling the causal factors in TAD establishment and maintenance remains a challenge. TAD borders in *Drosophila* are very significantly associated with binding of various insulator proteins (Hou et al., 2012; Sexton et al., 2012); CTCF is the only one of these factors conserved in mammals and is also enriched at constitutive TAD borders (Dixon et al., 2012). However, the full link between insulators and chromosome topology remains unclear—in one genome-wide study around a quarter of TAD borders did not contain CTCF and only 15% of CTCF binding sites were present at TAD boundaries (Dixon et al., 2012). Further, knockdown of CTCF in a human cell line caused an increase in the chromatin interactions spanning TAD borders but did not completely disrupt TAD organization (Zuin et al., 2014). This result is consistent with the persistent demarcation of H3K27me3 domains in *Drosophila* on CTCF knockdown (Van Bortle et al., 2012). In mammals, but not *Drosophila*, cohesin is also significantly found at TAD borders, although again the majority of binding sites are not at borders (Nora et al., 2012; Phillips-Cremens et al., 2013). Furthermore, cohesin abrogation in post-mitotic cells has no (Seitan et al., 2013; Zuin et al., 2014) or weak (Sofueva et al., 2013) effects on TAD border function. Although the effects of persisting levels of functional CTCF or cohesin cannot be ruled out in these studies, collectively it appears that these so-called “architectural proteins” contribute to the functional organization of the genome but that chromosomal secondary structures are largely epistatic to them.

TAD borders are also highly enriched in transcriptionally active genes (Dixon et al., 2012; Hou et al., 2012; Sexton et al., 2012), although the presence of borders at silent domains and the majority of transcribed genes residing inside domains mean that transcription alone cannot account for TAD organization. However, the known effects of RNA polymerase binding and

elongation on local DNA topology (Lavelle, 2014) suggest that gene expression programs and chromatin organization could have a profound effect on higher-order chromosome folding. In active chromatin, not only do enhancers contact promoters, but the promoters of expressed genes also contact each other (Li et al., 2012; Sanyal et al., 2012), and these interactions could favor TAD formation. Furthermore, active yeast genes form loops between their start and end sites to coordinate initiation and termination events, and this phenomenon appears to be conserved for at least some mammalian genes (Grzechnik et al., 2014). Transcription units could conceivably form a type of facultative mini-TAD. In support of this, active topological domains are smaller and more structurally complex than silent domains (Hou et al., 2012; Sexton et al., 2012; Sofueva et al., 2013). TAD borders are also enriched in housekeeping genes (Dixon et al., 2012). Evidence is mounting that housekeeping or widely expressed genes have fundamentally different regulatory sequences and chromatin states than developmentally regulated genes (Rach et al., 2011; Schauer et al., 2013; Zabidi et al., 2014). It will be interesting to see if these features, rather than maintained transcription per se, could contribute to TAD organization.

The tendency of chromatin domains of the same type to establish strong interactions is not limited to active chromatin domains. Polycomb domains are formed by clusters of Polycomb-bound sites that form preferential interactions, both intra-TAD (Lanzuolo et al., 2007; Schuettengruber et al., 2014) and inter-TAD (Bantignies et al., 2011; Sexton et al., 2012). Likewise, HP1-bound heterochromatin is involved in specific interactions (Csink and Henikoff, 1996; Sexton et al., 2012). Recent polymer physics-based modeling showed that the simple assumption of the existence of homotypic interactions between domains formed of these chromatin types is sufficient to generate polymer structures mimicking those shown in Hi-C contact maps (Jost et al., 2014). This result suggests that chromatin components of each type of chromatin domain may contribute to establish TADs. The role of boundary factors such as CTCF could thus be to strengthen the stability of the boundaries between domains of different chromatin types or to sharpen their localization.

One experimental test that has appreciably disrupted topological domain structure was the deletion of a 58-kb region spanning a TAD border within the X-inactivation locus. This perturbation resulted in complete loss of border function and the establishment of a new TAD border approximately 50 kb downstream of the deletion site (Nora et al., 2012). Interestingly, the de novo creation of a TAD boundary near to the deleted one was predicted from physical models and suggests that the chromosomes of many genomes have an intrinsic tendency to fold into topological domains (Giorgetti et al., 2014). Thus, at least some topological domain boundaries have a genetic component. Although it has yet to be demonstrated experimentally, disease phenotype association studies have also suggested that around one tenth of human pathologies caused by genomic deletions could involve perturbed topological domain function (Ibn-Salem et al., 2014). Finer dissection of the *cis*-sequence requirements of TAD borders and testing their function outside of their usual genomic contexts, should be fruitful in explaining

the mechanistic basis of chromosome organization and in enabling chromosome domain engineering.

Global chromosome structure is regulated throughout the cell cycle. Hi-C experiments have further shown that, whereas TAD organization is largely conserved throughout interphase, the domains are lost during mitosis (Naumova et al., 2013). The robust detection of conserved TADs in early G1 cells suggests that they can be efficiently re-built. Characterization of the proteins and chromatin marks that persist on mitotic chromosomes, the so-called “bookmarking” factors, is an area of current intense study, which may yield some clues as to how TADs can be established at each cell cycle (Zaret, 2014). For example, it has been shown in *Drosophila* that the Polycomb group protein PSC persists on only a subset of binding sites during mitosis and that these are predominantly interphase TAD boundaries (Follmer et al., 2012). However, it is unclear how this bookmarking is regulated, if or how it controls TAD organization, or how the many TADs that are not mitotically bound by PSC are regulated. DNA damage and the chromatin remodeling accompanying its repair are also likely to affect the organization of the associated TADs. Although previous results have shown that heterochromatin domains have different induced mobility and/or repair mechanisms in response to double-stranded breaks (Chiolo et al., 2011; Lemaitre et al., 2014), it is still unknown how TADs are maintained or restored in different nuclear environments. Overall, genetic elements, transcription, and the binding of architectural proteins have all been correlated with TAD borders. Future research should tease out whether they are causes or consequences of TAD folding, how these factors interplay in such organization, and their roles in re-building TADs after mitosis.

Chromosomal Secondary Structures in Genome Evolution

TAD organization appears to be a conserved, but not universal phenomenon (Table 1); TADs are readily observed in *Drosophila* (Hou et al., 2012; Sexton et al., 2012) and mammalian (Dixon et al., 2012; Nora et al., 2012) genomes but are less clearly defined in *Arabidopsis* (Feng et al., 2014; Grob et al., 2014), *Plasmodium falciparum* (Ay et al., 2014), and yeasts (Duan et al., 2010; Tanizawa et al., 2010). Although more systematic chromatin interaction maps of different organisms are required to make further conclusions, it is interesting that species with clear TAD genomic organization match those with conservation of the insulator protein CTCF (Heger et al., 2012), further supporting its role as a genomic architectural protein. However, closer analysis of chromatin interaction maps of non-metazoan species reveals some topological domain-like organizations, such as the very large “structural domains” in *Arabidopsis* (Grob et al., 2014), or the tens of kilobase-sized “globules” in *Schizosaccharomyces pombe*, which correlate with the organization of convergent genes and cohesin binding sites (Mizuguchi et al., 2014). More strikingly, the chromosome of the bacterium *Caulobacter crescentus* also adopts TAD-like domains, which are highly sensitive to transcriptional activity and negative supercoiling (Le et al., 2013). Thus, genomic folding into potentially self-organized modules appears to be a common strategy for very diverse types of chromatin, perhaps reflecting an intrinsic ability for chromatin

Table 1. Overview of the Absence or Presence of Chromosome Topological Domains, as Well as Their Observed Sizes, Based on Current Studies

Organism	Evidence for TADs or Similar Domains	Domain Size	Methods Used	References
<i>C. crescentus</i>	Yes	30–420 kb	Hi-C and a sub-genome-wide derivative (5C)	Le et al., 2013
<i>S. cerevisiae</i>	No	NA	A genome-wide 4C derivative	Duan et al., 2010
<i>S. pombe</i>	Yes	50–100 kb	Hi-C	Mizuguchi et al., 2014
<i>P. falciparum</i>	Only around a specific group of genes	10–50 kb	Hi-C	Ay et al., 2014
<i>A. thaliana</i>	Controversial	> 1 Mb in one study; no TADs in another	Hi-C	Feng et al., 2014; Grob et al., 2014
<i>D. melanogaster</i>	Yes	10–980 kb	Hi-C	Sexton et al., 2012
<i>M. musculus</i>	Yes	100 kb–5 Mb	Hi-C, 5C	Dixon et al., 2012; Nora et al., 2012
<i>H. sapiens</i>	Yes	100 kb–5 Mb in one study, 40 kb–3 Mb in another	Hi-C	Dixon et al., 2012; Rao et al., 2014

to be compacted in a way that can be easily opened and recondensed without entangling of chromosome fibers (Lieberman-Aiden et al., 2009). Until very recently, the TAD size of an organism appeared to scale with the average gene or chromosome length (Table 1). However, Hi-C coupled to extremely deep sequencing has identified human domains at a similar scale to that observed in *Drosophila* (Rao et al., 2014). Caution with respect to the resolutions afforded by different studies is thus required when trying to make cross-species comparisons of chromosome folding.

Comparison of mouse and human chromatin interaction maps revealed a high degree of TAD organization conservation around syntenic regions (Dixon et al., 2012). If these domains truly represent autonomously functional units of the genome, then rearrangements of whole TADs may be favored over ones that split TADs apart. Although such selection has not been formally proven, random P element insertions are highly enriched at TAD boundaries (Hou et al., 2012), suggesting that they may be genetic loci particularly susceptible or permissive to rearrangement events. It is also curious that distal human sequences which are syntenic in the mouse genome retain long-range chromatin interactions, tens of millions of years after the synteny break (Véron et al., 2011). This is not an isolated observation as Polycomb-dependent long-range contacts between Hox loci are conserved among fly species that diverged around 40 million years ago (Bantignies et al., 2011). Genome evolution could thus potentially be driven by re-arranging their secondary structures, analogous to the evolution of proteins by shuffling domain-coding exons (Liu and Grigoriev, 2004). Conversely, the spatial organization of TADs may also influence the sequence divergence within them. A recent comparative genomics study in *Drosophilid* species found that the dual transcription factor/Polycomb recruiter protein PHO bound only to consensus motif sequences outside of a Polycomb context but was able to bind far weaker motifs within TADs marked by H3K27me3 (a hallmark of Polycomb-mediated repression) (Schuettengruber et al., 2014). Of note, these Polycomb-linked PHO sites participated in stronger chromatin interactions, consistent with known looped interactions

between Polycomb group response elements (Lanzuolo et al., 2007). Such co-operative interactions within specific TADs were proposed to stabilize PHO binding, allowing a greater tolerance of motif sequence divergence (Schuettengruber et al., 2014). Thus DNA sequence appears to influence chromosome folding, and 3D chromosome structure in turn may influence sequence evolution (Figures 4A and 4B). These data call for more work in order to understand whether this principle may apply to the binding of a wide variety of transcription factors in eukaryotes.

Toward Tertiary Chromosomal Structures

At current sequencing depths, Hi-C experiments are able to give fairly detailed views of TAD organization, but the resolution of longer-range (and interchromosomal) contacts is more limited. Although there is evidence to suggest that TADs hierarchically co-associate to build up larger chromosomal structures (Sexton et al., 2012), the precise nature of such spatial configurations remains mysterious. FISH studies of long-range gene co-associations in mouse erythroid cells or *Drosophila* embryos detected specific long-range interactions in only a few percent of cells, despite their robust detection by 4C (a 3C variant detecting all interactions with a specific bait sequence), suggesting that many chromosomal configurations are present within a population of cells (Bantignies et al., 2011; Noordermeer et al., 2011a; Schoenfelder et al., 2010). Despite this apparent diversity in global chromosome structure, several groups have attempted to model the average conformation (or conformations), which best globally fit the underlying interaction maps (for example Duan et al., 2010; Nagano et al., 2013; Figure 4C), whereas others have used more precise physical models to try and explain either the general features of Hi-C maps (Barbieri et al., 2012; Jost et al., 2014; Lieberman-Aiden et al., 2009) or obtain higher-resolution views of smaller genomic regions (Giorgetti et al., 2014; Le Dily et al., 2014). More and higher-resolution interaction maps will allow the validity of these models to be tested, but already they have been able to provide testable hypotheses as to which genomic regions are the most crucial for structural integrity (Giorgetti et al., 2014).

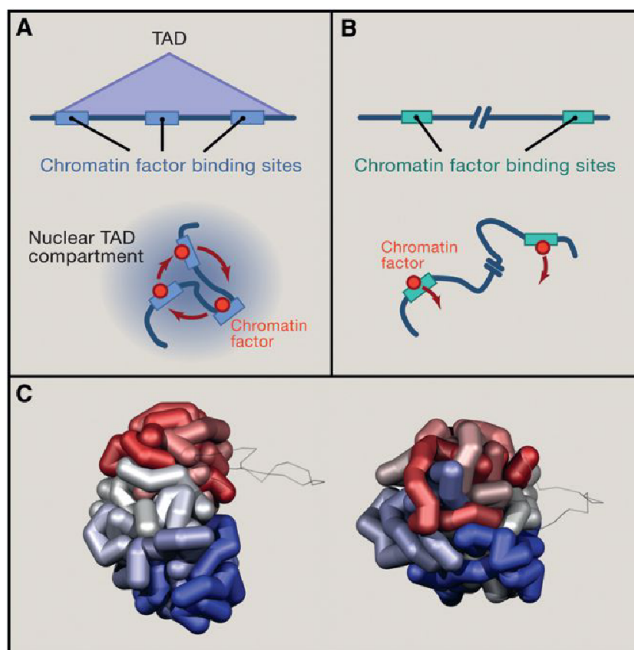


Figure 4. TAD-Dependent Enhancement of Chromatin Factor Targeting and Chromosome Conformation Heterogeneity

(A) Top: A hypothetical TAD that contains three binding sites (in blue) for a chromatin factor is represented. Bottom: Intra-TAD contacts bring the chromatin binding sites in close proximity and form a 3D compartment where the chromatin factor is concentrated via formation of either homodimers or of self-interacting chromatin complexes. This architecture favors the maintenance of factor binding since, once the factor dissociates from a target site, the high relative concentration of other binding sites present in the same TAD favors rebinding.

(B) A genomic region with isolated binding sites for a chromatin factor (green) is shown. In the isolated context, the factor is rapidly lost in the nucleoplasm after dissociation from its target and therefore its replenishment from nucleoplasmic regions with lower relative concentration is less efficient. In this model, proposed by (Schuettengruber et al., 2014), 3D association of factor binding sites via intra-TAD contacts can favor the maintenance of robust chromatin targeting compared to non-TAD isolated factor binding sites.

(C) The tertiary structures of two mouse male T_H1 cell X chromosomes, inferred from two separate single-cell Hi-C experiments, showing that single cells of a population can have diverse chromosome structures (Nagano et al., 2013). The chromosomal position of the fiber is shown as a color scale, going from red (centromeric end) to blue (telomeric end). The gray line represents regions with low constraints due to low mappability in the Hi-C experiment. Image provided by Csilla Varnai and Peter Fraser.

Comparisons of the chromatin interaction maps derived from multiple single-cell Hi-C experiments consistently revealed a high diversity in long-range contact repertoires but found that TADs were surprisingly persistent, suggesting that they are genuinely more stable sub-structures of the chromosome (Nagano et al., 2013; Figure 4C). What is currently unclear is how much of the structural heterogeneity is due to stable alternative genomic configurations and how much can be explained by chromosomal dynamics. Tagging mammalian DNA loci with multiple copies of binding sites for fluorescently labeled *lac* or *tet* repressors has revealed that chromatin is highly mobile but constrained within a restricted subnuclear volume (Lucas et al., 2014; Masui et al., 2011). This constrained diffusion is affected by developmental stage and attachment to nuclear landmarks

such as the periphery or nucleoli. On a larger scale, photobleaching studies of fluorescently labeled histones revealed that arrays of chromatin domains can undergo coordinated long-range movements (Cheutin and Cavalli, 2012). It is interesting to speculate that these domains could correlate with TADs (or groups of adjacent TADs), which have also been proposed to form the physical limit for the observed rapid sub-diffusion of chromatin (Lucas et al., 2014). Therefore, TADs may constitute the physical microenvironment in which neighboring functional elements interact, while occasional movements of strings of adjacent TADs may allow for large-scale rearrangement of chromosome structure and for the formation of new contacts among distant chromatin loci. A fascinating research area is to investigate whether these long-range movements might be specifically induced and regulated.

Moreover, very little is known about the conservation of chromosome structures across cell cycles; initial photobleaching experiments gave conflicting results for global chromosome positioning after mitosis (Gerlich et al., 2003; Walter et al., 2003). However, an elegant recent study suggests that at least some chromosome configurations can be remodeled during cell division. Lamina-associated chromatin was tagged during a short time period, and then its nuclear location(s) were traced through subsequent cell cycles (Kind et al., 2013). Only around one third of the lamina-associated chromatin called from population-average studies contacted the lamina at any given point in a single cell and, more strikingly, these regions were reshuffled during mitosis. Recent advances allow fluorescent DNA tagging without the insertion of large exogenous sequences (Chen et al., 2013; Miyanari et al., 2013; Saad et al., 2014). Their systematic application is likely to shed more light on the dynamics underpinning enhancer-promoter contacts, TAD stability and long-range interactions, and ultimately address whether they can be inherited across interphase and through subsequent cell cycles. Overall, whereas chromosomes are organized arrangements of seemingly stable secondary structures, they may adopt many different “tertiary structures” within a population, with as yet unclear dynamics of how these variants may interchange.

Long-Range Interactions—Non-Opposites Attract

Focused 3C variants and FISH studies have uncovered a plethora of co-associations between genes separated by megabases, or occupying different chromosomes, usually occurring at frequencies that are low but much higher than expected by chance. Such long-range interactions are commonly between genes sharing regulation by a common factor, such as Polycomb-mediated repression (Bantignies et al., 2011; Denholtz et al., 2013), or activation by tissue-specific (Papantonis et al., 2012; Schoenfelder et al., 2010), or pluripotency-linked transcription factors (Apostolou et al., 2013; de Wit et al., 2013; Denholtz et al., 2013; Wei et al., 2013), occurring specifically in cell types where the regulation is mediated. Many groups have proposed the existence of functional spatial gene networks, whereby the clustering of genes at nuclear foci enriched in their regulatory factors facilitates their coordinate expression (Bantignies et al., 2011; Papantonis et al., 2012; Schoenfelder et al., 2010). Support for this model has come from detailed analysis of the acute co-association of three human TNF-alpha

stimulated genes: an induced double-stranded DNA break in one gene completely abolishes its transcription but also severely impairs expression of the other target genes, concomitant with loss of co-association (Fanucchi et al., 2013). Most strikingly, this network is hierarchical, as break formation in the gene *SAMD4A* perturbs expression of both the genes *TNFAIP2* and *SLC6A5*, but *SAMD4A* is unaffected by breaks in either of the other genes. Similarly, a break in *TNFAIP2* perturbs *SLC6A5* expression but not vice versa. These examples of spatial co-regulated gene networks are very evocative; however in general, many combinations of genes sharing modes of regulation are not uncovered as interacting partners in 4C experiments. Furthermore, some gene co-associations linked to embryonic stem cell differentiation and formation of induced pluripotent cells precede the transcriptional changes by several days (Apostolou et al., 2013; Wei et al., 2013). It is also noteworthy that the observed spatial association of co-regulated genes in *S. cerevisiae* (Duan et al., 2010) was completely recapitulated when chromosomal structures were modeled from a few basic physical principles (Tjong et al., 2012). Thus, seemingly regulated spatial gene networks may actually be an indirect effect of chromosome folding mechanics, although the principles behind any potential direct regulation are even less clear than those determining enhancer-promoter communication or TAD organization at this stage.

Over multiple scales of chromosome organization, a recurring theme is the prevalence of homotypic or “like-with-like” interactions, whether this is the dimerization of proteins within chromatin loops (Deng et al., 2012), potential spatial networks of co-regulated genes (Schoenfelder et al., 2010) or a tendency for active and repressed chromatin to segregate (Lieberman-Aiden et al., 2009). Such configurations are the expected outcomes of self-organizing systems: a chance encounter between two loci bound by common regulatory factors increases the factors’ local concentrations, so that when a factor dissociates it is more likely to be re-trapped by the cluster of binding sites within its locale than to diffuse away to another location (Kang et al., 2011; Rajapakse et al., 2009). As association of the majority of DNA-bound factors with their cognate sites is transient (Phair and Misteli, 2000), self-organized spatial clustering of related genetic loci may be important for their efficient regulation. This model is consistent with the maintenance of active chromatin hubs at expressed genes (Palstra et al., 2003), the formation of Polycomb repressive domains (Lanzuolo et al., 2007), and perhaps their evolutionary robustness to motif mutations (Schuettengruber et al., 2014), and heterochromatic clustering (Taddei et al., 2009). As TAD organization mirrors underlying functional chromatin domains so well, we posit that TADs may be similarly self-organized structures that increase the local concentrations of diffusible regulatory factors around their sites of activity (Figures 4A and 4B). TADs may thus not only be an effective manner of preventing aberrant communication between genetic loci, but they may also allow for genes to be more efficiently bound by their effectors for stronger or more rapid transcriptional responses. Furthermore, the surprising finding that large-scale chromosome structures are actually more compact on perturbation of intra-TAD loops also suggests that TADs may be important for global chromosome structure maintenance (Tark-Dame et al., 2014).

Perspectives

Mounting evidence shows that the genome is a dynamic yet highly organized hierarchical structure, built up from progressive stabilization of homotypic, potentially functional contacts between genes and regulatory elements. TADs present some conceptual analogy to secondary structures of proteins. These structures clearly have dynamics and cell-to-cell variability but also show a surprising developmental and evolutionary robustness, suggesting that they may be chromosome building blocks required for appropriate genome function. However, hypotheses about how TADs are organized and their functions are difficult to directly assess for two main reasons. First, up till now they have only been detected by population-average studies in fixed cells; TADs have yet to be visualized in single cells or followed in real time. Clearly, the way in which TADs may impinge on gene expression depends on whether they are genuinely stable structures or more a reflection of a ground state of inherent chromatin dynamics. Second, TADs appear robust to the initial perturbation studies that have been tried (for example, CTCF or cohesin abrogation), so it has been difficult to pinpoint any “causative” factor. Major advances in the future will tackle these two issues with live imaging of chromatin interactions in single cells (and following such interaction dynamics over the cell cycle), proteomic studies of which factors (if any) distinguish interacting loci from non-interacting ones and finer genetic dissection of the elements contributing to TAD borders or key architectural loops.

Returning to the protein folding analogy, genomes appear to be built up from the stabilization of progressively higher-order conformations, from TAD secondary structures to chromosomal tertiary structures, to the organized arrangement of chromosome territories into a final quaternary structure. With few exceptions, the structure of a protein cannot be predicted solely from its amino acid sequence. However, once the structure is resolved, the key residues contributing to the protein’s function can be readily identified and engineered. As our knowledge of TADs and specific chromatin loops increases, we posit that similar structure-informed reverse genetic engineering will allow us to manipulate the genome, with myriad applications. For example, de novo creation of autonomously regulated TADs would reduce any side effects of linked transgenes, and the engineering of switchable chromatin loops may allow for fine manipulation of gene expression. In summary, we are entering an exciting time in the field of nuclear organization. Mechanistic links are beginning to be assigned to what were previously only correlations between chromatin conformations and transcriptional regulation. Combined with the revolution in genome engineering tools such as CRISPR, we are in an unprecedented position to not only model, but also modulate, genome structure.

ACKNOWLEDGMENTS

We thank Cyril Sarrauste de Menthiere and Albert Weixlbaumer for help with the figures, and Csilla Varnai and Peter Fraser for contributing Figure 4C. Research at the G.C. lab is supported by grants from the European Research Council (ERC-2008-AdG No 232947), the CNRS, the European Network of Excellence EpiGeneSys, the Agence Nationale de la Recherche, and the Fondation ARC. Research at the T.S. lab is supported by INSERM, the ATIP-Avenir program, and the Laboratoire d’Excellence INRT.

REFERENCES

- Apostolou, E., Ferrari, F., Walsh, R.M., Bar-Nur, O., Stadtfeld, M., Cheloufi, S., Stuart, H.T., Polo, J.M., Ohsumi, T.K., Borowsky, M.L., et al. (2013). Genome-wide chromatin interactions of the Nanog locus in pluripotency, differentiation, and reprogramming. *Cell Stem Cell* *12*, 699–712.
- Ay, F., Bunnik, E.M., Varoquaux, N., Bol, S.M., Prudhomme, J., Vert, J.P., Noble, W.S., and Le Roch, K.G. (2014). Three-dimensional modeling of the *P. falciparum* genome during the erythrocytic cycle reveals a strong connection between genome architecture and gene expression. *Genome Res.* *24*, 974–988.
- Bantignies, F., Roure, V., Comet, I., Leblanc, B., Schuettengruber, B., Bonnet, J., Tixier, V., Mas, A., and Cavalli, G. (2011). Polycomb-dependent regulatory contacts between distant Hox loci in *Drosophila*. *Cell* *144*, 214–226.
- Barbieri, M., Chotalia, M., Fraser, J., Lavitas, L.M., Dostie, J., Pombo, A., and Nicodemi, M. (2012). Complexity of chromatin folding is captured by the strings and binders switch model. *Proc. Natl. Acad. Sci. USA* *109*, 16173–16178.
- Cavalli, G., and Misteli, T. (2013). Functional implications of genome topology. *Nat. Struct. Mol. Biol.* *20*, 290–299.
- Chaumeil, J., Le Baccon, P., Wutz, A., and Heard, E. (2006). A novel role for Xist RNA in the formation of a repressive nuclear compartment into which genes are recruited when silenced. *Genes Dev.* *20*, 2223–2237.
- Chen, B., Gilbert, L.A., Cimini, B.A., Schnitzbauer, J., Zhang, W., Li, G.W., Park, J., Blackburn, E.H., Weissman, J.S., Qi, L.S., and Huang, B. (2013). Dynamic imaging of genomic loci in living human cells by an optimized CRISPR/Cas system. *Cell* *155*, 1479–1491.
- Cheutin, T., and Cavalli, G. (2012). Progressive polycomb assembly on H3K27me3 compartments generates polycomb bodies with developmentally regulated motion. *PLoS Genet.* *8*, e1002465.
- Chiolo, I., Minoda, A., Colmenares, S.U., Polyzos, A., Costes, S.V., and Karpen, G.H. (2011). Double-strand breaks in heterochromatin move outside of a dynamic HP1a domain to complete recombinational repair. *Cell* *144*, 732–744.
- Conaway, R.C., and Conaway, J.W. (2011). Function and regulation of the Mediator complex. *Curr. Opin. Genet. Dev.* *21*, 225–230.
- Csank, A.K., and Henikoff, S. (1996). Genetic modification of heterochromatic association and nuclear organization in *Drosophila*. *Nature* *381*, 529–531.
- de Laat, W., and Duboule, D. (2013). Topology of mammalian developmental enhancers and their regulatory landscapes. *Nature* *502*, 499–506.
- de Wit, E., Bouwman, B.A., Zhu, Y., Klous, P., Splinter, E., Versteegen, M.J., Krijger, P.H., Festuccia, N., Nora, E.P., Welling, M., et al. (2013). The pluripotent genome in three dimensions is shaped around pluripotency factors. *Nature* *501*, 227–231.
- DeMare, L.E., Leng, J., Cotney, J., Reilly, S.K., Yin, J., Sarro, R., and Noonan, J.P. (2013). The genomic landscape of cohesin-associated chromatin interactions. *Genome Res.* *23*, 1224–1234.
- Deng, W., Lee, J., Wang, H., Miller, J., Reik, A., Gregory, P.D., Dean, A., and Blobel, G.A. (2012). Controlling long-range genomic interactions at a native locus by targeted tethering of a looping factor. *Cell* *149*, 1233–1244.
- Deng, W., Rupon, J.W., Krivega, I., Breda, L., Motta, I., Jahn, K.S., Reik, A., Gregory, P.D., Rivella, S., Dean, A., and Blobel, G.A. (2014). Reactivation of developmentally silenced globin genes by forced chromatin looping. *Cell* *158*, 849–860.
- Denholtz, M., Bonora, G., Chronis, C., Splinter, E., de Laat, W., Ernst, J., Pellegrini, M., and Plath, K. (2013). Long-range chromatin contacts in embryonic stem cells reveal a role for pluripotency factors and polycomb proteins in genome organization. *Cell Stem Cell* *13*, 602–616.
- Dixon, J.R., Selvaraj, S., Yue, F., Kim, A., Li, Y., Shen, Y., Hu, M., Liu, J.S., and Ren, B. (2012). Topological domains in mammalian genomes identified by analysis of chromatin interactions. *Nature* *485*, 376–380.
- Drissen, R., Palstra, R.J., Gillemans, N., Splinter, E., Grosveld, F., Philippen, S., and de Laat, W. (2004). The active spatial organization of the beta-globin locus requires the transcription factor EKLf. *Genes Dev.* *18*, 2485–2490.
- Duan, Z., Andronescu, M., Schutz, K., McIlwain, S., Kim, Y.J., Lee, C., Shendure, J., Fields, S., Blau, C.A., and Noble, W.S. (2010). A three-dimensional model of the yeast genome. *Nature* *465*, 363–367.
- Ernst, J., Kheradpour, P., Mikkelsen, T.S., Shoshani, N., Ward, L.D., Epstein, C.B., Zhang, X., Wang, L., Issner, R., Coyne, M., et al. (2011). Mapping and analysis of chromatin state dynamics in nine human cell types. *Nature* *473*, 43–49.
- Fanucchi, S., Shibayama, Y., Burd, S., Weinberg, M.S., and Mhlanga, M.M. (2013). Chromosomal contact permits transcription between coregulated genes. *Cell* *155*, 606–620.
- Feng, S., Cokus, S.J., Schubert, V., Zhai, J., Pellegrini, M., and Jacobsen, S.E. (2014). Genome-wide Hi-C analyses in wild-type and mutants reveal high-resolution chromatin interactions in *Arabidopsis*. *Mol. Cell* *55*, 694–707.
- Follmer, N.E., Wani, A.H., and Francis, N.J. (2012). A polycomb group protein is retained at specific sites on chromatin in mitosis. *PLoS Genet.* *8*, e1003135.
- Gerlich, D., Beaudouin, J., Kalbfuss, B., Daigle, N., Eils, R., and Ellenberg, J. (2003). Global chromosome positions are transmitted through mitosis in mammalian cells. *Cell* *112*, 751–764.
- Ghavi-Helm, Y., Klein, F.A., Pakozdi, T., Ciglar, L., Noordermeer, D., Huber, W., and Furlong, E.E. (2014). Enhancer loops appear stable during development and are associated with paused polymerase. *Nature* *512*, 96–100.
- Giorgetti, L., Galupa, R., Nora, E.P., Piolot, T., Lam, F., Dekker, J., Tiana, G., and Heard, E. (2014). Predictive polymer modeling reveals coupled fluctuations in chromosome conformation and transcription. *Cell* *157*, 950–963.
- Grob, S., Schmid, M.W., and Grossniklaus, U. (2014). Hi-C analysis in *Arabidopsis* identifies the KNOT, a structure with similarities to the flamenco locus of *Drosophila*. *Mol. Cell* *55*, 678–693.
- Grzechnik, P., Tan-Wong, S.M., and Proudfoot, N.J. (2014). Terminate and make a loop: regulation of transcriptional directionality. *Trends Biochem. Sci.* *39*, 319–327.
- Hadjur, S., Williams, L.M., Ryan, N.K., Cobb, B.S., Sexton, T., Fraser, P., Fisher, A.G., and Merkschlager, M. (2009). Cohesins form chromosomal cis-interactions at the developmentally regulated IFNG locus. *Nature* *460*, 410–413.
- He, B., Chen, C., Teng, L., and Tan, K. (2014). Global view of enhancer-promoter interactome in human cells. *Proc. Natl. Acad. Sci. USA* *111*, E2191–E2199.
- Heger, P., Marin, B., Bartkuhn, M., Schierenberg, E., and Wiehe, T. (2012). The chromatin insulator CTCF and the emergence of metazoan diversity. *Proc. Natl. Acad. Sci. USA* *109*, 17507–17512.
- Heidari, N., Phanstiel, D.H., He, C., Grubert, F., Jahanbani, F., Kasowski, M., Zhang, M.Q., and Snyder, M.P. (2014). Genome-wide map of regulatory interactions in the human genome. *Genome Res.* *24*, 1905–1917.
- Ho, J.W., Jung, Y.L., Liu, T., Alver, B.H., Lee, S., Ikegami, K., Sohn, K.A., Minoda, A., Tolstorukov, M.Y., Appert, A., et al. (2014). Comparative analysis of metazoan chromatin organization. *Nature* *512*, 449–452.
- Hou, C., Dale, R., and Dean, A. (2010). Cell type specificity of chromatin organization mediated by CTCF and cohesin. *Proc. Natl. Acad. Sci. USA* *107*, 3651–3656.
- Hou, C., Li, L., Qin, Z.S., and Corces, V.G. (2012). Gene density, transcription, and insulators contribute to the partition of the *Drosophila* genome into physical domains. *Mol. Cell* *48*, 471–484.
- Ibn-Salem, J., Köhler, S., Love, M.I., Chung, H.R., Huang, N., Hurler, M.E., Haendel, M., Washington, N.L., Smedley, D., Mungall, C.J., et al. (2014). Deletions of chromosomal regulatory boundaries are associated with congenital disease. *Genome Biol.* *15*, 423.
- Jin, F., Li, Y., Dixon, J.R., Selvaraj, S., Ye, Z., Lee, A.Y., Yen, C.A., Schmitt, A.D., Espinoza, C.A., and Ren, B. (2013). A high-resolution map of the three-dimensional chromatin interactome in human cells. *Nature* *503*, 290–294.

- Jost, D., Carrivain, P., Cavalli, G., and Vaillant, C. (2014). Modeling epigenome folding: formation and dynamics of topologically associated chromatin domains. *Nucleic Acids Res.* *42*, 9553–9561.
- Kagey, M.H., Newman, J.J., Bilodeau, S., Zhan, Y., Orlando, D.A., van Berkum, N.L., Ebmeier, C.C., Goossens, J., Rahl, P.B., Levine, S.S., et al. (2010). Mediator and cohesin connect gene expression and chromatin architecture. *Nature* *467*, 430–435.
- Kang, J., Xu, B., Yao, Y., Lin, W., Hennessy, C., Fraser, P., and Feng, J. (2011). A dynamical model reveals gene co-localizations in nucleus. *PLoS Comput. Biol.* *7*, e1002094.
- Kieffer-Kwon, K.R., Tang, Z., Mathe, E., Qian, J., Sung, M.H., Li, G., Resch, W., Baek, S., Pruett, N., Grøntved, L., et al. (2013). Interactome maps of mouse gene regulatory domains reveal basic principles of transcriptional regulation. *Cell* *155*, 1507–1520.
- Kind, J., Pagie, L., Ortobzokoyun, H., Boyle, S., de Vries, S.S., Janssen, H., Amendola, M., Nolen, L.D., Bickmore, W.A., and van Steensel, B. (2013). Single-cell dynamics of genome-nuclear lamina interactions. *Cell* *153*, 178–192.
- Kurukuti, S., Tiwari, V.K., Tavosoidana, G., Pugacheva, E., Murrell, A., Zhao, Z., Lobanenko, V., Reik, W., and Ohlsson, R. (2006). CTCF binding at the H19 imprinting control region mediates maternally inherited higher-order chromatin conformation to restrict enhancer access to Igf2. *Proc. Natl. Acad. Sci. USA* *103*, 10684–10689.
- Lanzuolo, C., Roure, V., Dekker, J., Bantignies, F., and Orlando, V. (2007). Polycomb response elements mediate the formation of chromosome higher-order structures in the bithorax complex. *Nat. Cell Biol.* *9*, 1167–1174.
- Lavelle, C. (2014). Pack, unpack, bend, twist, pull, push: the physical side of gene expression. *Curr. Opin. Genet. Dev.* *25*, 74–84.
- Le, T.B., Imakaev, M.V., Mirny, L.A., and Laub, M.T. (2013). High-resolution mapping of the spatial organization of a bacterial chromosome. *Science* *342*, 731–734.
- Le Dily, F., Baù, D., Pohl, A., Vicent, G.P., Serra, F., Soronellas, D., Castellano, G., Wright, R.H., Ballare, C., Filion, G., et al. (2014). Distinct structural transitions of chromatin topological domains correlate with coordinated hormone-induced gene regulation. *Genes Dev.* *28*, 2151–2162.
- Lemaître, C., Grabarz, A., Tsouroula, K., Andronov, L., Furst, A., Pankotai, T., Heyer, V., Rogier, M., Attwood, K.M., Kessler, P., et al. (2014). Nuclear position dictates DNA repair pathway choice. *Genes Dev.* *28*, 2450–2463.
- Li, G., Ruan, X., Auerbach, R.K., Sandhu, K.S., Zheng, M., Wang, P., Poh, H.M., Goh, Y., Lim, J., Zhang, J., et al. (2012). Extensive promoter-centered chromatin interactions provide a topological basis for transcription regulation. *Cell* *148*, 84–98.
- Lieberman-Aiden, E., van Berkum, N.L., Williams, L., Imakaev, M., Ragoczy, T., Telling, A., Amit, I., Lajoie, B.R., Sabo, P.J., Dorschner, M.O., et al. (2009). Comprehensive mapping of long-range interactions reveals folding principles of the human genome. *Science* *326*, 289–293.
- Liu, M., and Grigoriev, A. (2004). Protein domains correlate strongly with exons in multiple eukaryotic genomes—evidence of exon shuffling? *Trends Genet.* *20*, 399–403.
- Lucas, J.S., Zhang, Y., Dudko, O.K., and Murre, C. (2014). 3D trajectories adopted by coding and regulatory DNA elements: first-passage times for genomic interactions. *Cell* *158*, 339–352.
- Masui, O., Bonnet, I., Le Baccon, P., Brito, I., Pollex, T., Murphy, N., Hupé, P., Barillot, E., Belmont, A.S., and Heard, E. (2011). Live-cell chromosome dynamics and outcome of X chromosome pairing events during ES cell differentiation. *Cell* *145*, 447–458.
- Miyazawa, Y., Ziegler-Birling, C., and Torres-Padilla, M.E. (2013). Live visualization of chromatin dynamics with fluorescent TALEs. *Nat. Struct. Mol. Biol.* *20*, 1321–1324.
- Mizuguchi, T., Fudenberg, G., Mehta, S., Belton, J.M., Taneja, N., Folco, H.D., FitzGerald, P., Dekker, J., Mirny, L., Barrowman, J., and Grewal, S.I. (2014). Cohesin-dependent globules and heterochromatin shape 3D genome architecture in *S. pombe*. *Nature* *516*, 432–435.
- Mousavi, K., Zare, H., Dell'orso, S., Grøntved, L., Gutierrez-Cruz, G., Derfoul, A., Hager, G.L., and Sartorelli, V. (2013). eRNAs promote transcription by establishing chromatin accessibility at defined genomic loci. *Mol. Cell* *51*, 606–617.
- Nagano, T., Lubling, Y., Stevens, T.J., Schoenfelder, S., Yaffe, E., Dean, W., Laue, E.D., Tanay, A., and Fraser, P. (2013). Single-cell Hi-C reveals cell-to-cell variability in chromosome structure. *Nature* *502*, 59–64.
- Nasmyth, K., and Haering, C.H. (2009). Cohesin: its roles and mechanisms. *Annu. Rev. Genet.* *43*, 525–558.
- Naumova, N., Imakaev, M., Fudenberg, G., Zhan, Y., Lajoie, B.R., Mirny, L.A., and Dekker, J. (2013). Organization of the mitotic chromosome. *Science* *342*, 948–953.
- Noordermeer, D., de Wit, E., Klous, P., van de Werken, H., Simonis, M., Lopez-Jones, M., Eussen, B., de Klein, A., Singer, R.H., and de Laat, W. (2011a). Variegated gene expression caused by cell-specific long-range DNA interactions. *Nat. Cell Biol.* *13*, 944–951.
- Noordermeer, D., Leleu, M., Splinter, E., Rougemont, J., De Laat, W., and Duboule, D. (2011b). The dynamic architecture of Hox gene clusters. *Science* *334*, 222–225.
- Nora, E.P., Lajoie, B.R., Schulz, E.G., Giorgetti, L., Okamoto, I., Servant, N., Piolot, T., van Berkum, N.L., Meisig, J., Sedat, J., et al. (2012). Spatial partitioning of the regulatory landscape of the X-inactivation centre. *Nature* *485*, 381–385.
- Palstra, R.J., Tolhuis, B., Splinter, E., Nijmeijer, R., Grosveld, F., and de Laat, W. (2003). The beta-globin nuclear compartment in development and erythroid differentiation. *Nat. Genet.* *35*, 190–194.
- Papantonis, A., Kohro, T., Baboo, S., Larkin, J.D., Deng, B., Short, P., Tsutsumi, S., Taylor, S., Kanki, Y., Kobayashi, M., et al. (2012). TNF α signals through specialized factories where responsive coding and miRNA genes are transcribed. *EMBO J.* *31*, 4404–4414.
- Peric-Hupkes, D., Meuleman, W., Pagie, L., Bruggeman, S.W., Solovei, I., Brugman, W., Gräf, S., Flicek, P., Kerkhoven, R.M., van Lohuizen, M., et al. (2010). Molecular maps of the reorganization of genome-nuclear lamina interactions during differentiation. *Mol. Cell* *38*, 603–613.
- Phair, R.D., and Misteli, T. (2000). High mobility of proteins in the mammalian cell nucleus. *Nature* *404*, 604–609.
- Phillips-Cremins, J.E., Sauria, M.E., Sanyal, A., Gerasimova, T.I., Lajoie, B.R., Bell, J.S., Ong, C.T., Hookway, T.A., Guo, C., Sun, Y., et al. (2013). Architectural protein subclasses shape 3D organization of genomes during lineage commitment. *Cell* *153*, 1281–1295.
- Pope, B.D., Ryba, T., Dileep, V., Yue, F., Wu, W., Denas, O., Vera, D.L., Wang, Y., Hansen, R.S., Canfield, T.K., et al. (2014). Topologically associating domains are stable units of replication-timing regulation. *Nature* *515*, 402–405.
- Rach, E.A., Winter, D.R., Benjamin, A.M., Corcoran, D.L., Ni, T., Zhu, J., and Ohler, U. (2011). Transcription initiation patterns indicate divergent strategies for gene regulation at the chromatin level. *PLoS Genet.* *7*, e1001274.
- Rajapakse, I., Perlman, M.D., Scalzo, D., Kooperberg, C., Groudine, M., and Kosak, S.T. (2009). The emergence of lineage-specific chromosomal topologies from coordinate gene regulation. *Proc. Natl. Acad. Sci. USA* *106*, 6679–6684.
- Rao, S.S., Huntley, M.H., Durand, N.C., Stamenova, E.K., Bochkov, I.D., Robinson, J.T., Sanborn, A.L., Machol, I., Omer, A.D., Lander, E.S., and Aiden, E.L. (2014). A 3D map of the human genome at kilobase resolution reveals principles of chromatin looping. *Cell* *159*, 1665–1680.
- Rubio, E.D., Reiss, D.J., Welch, P.L., Disteche, C.M., Filippova, G.N., Baliga, N.S., Aebbersold, R., Ranish, J.A., and Krumm, A. (2008). CTCF physically links cohesin to chromatin. *Proc. Natl. Acad. Sci. USA* *105*, 8309–8314.
- Saad, H., Gallardo, F., Dalvai, M., Tanguy-le-Gac, N., Lane, D., and Bystrycky, K. (2014). DNA dynamics during early double-strand break processing revealed by non-intrusive imaging of living cells. *PLoS Genet.* *10*, e1004187.
- Sanyal, A., Lajoie, B.R., Jain, G., and Dekker, J. (2012). The long-range interaction landscape of gene promoters. *Nature* *489*, 109–113.

- Schauer, T., Schwalie, P.C., Handley, A., Margulies, C.E., Flicek, P., and Ladurner, A.G. (2013). CAST-ChIP maps cell-type-specific chromatin states in the *Drosophila* central nervous system. *Cell Rep.* **5**, 271–282.
- Schoenfelder, S., Sexton, T., Chakalova, L., Cope, N.F., Horton, A., Andrews, S., Kurukuti, S., Mitchell, J.A., Umlauf, D., Dimitrova, D.S., et al. (2010). Preferential associations between co-regulated genes reveal a transcriptional interactome in erythroid cells. *Nat. Genet.* **42**, 53–61.
- Schuettengruber, B., Oded Elkayam, N., Sexton, T., Entrevan, M., Stern, S., Thomas, A., Yaffe, E., Parrinello, H., Tanay, A., and Cavalli, G. (2014). Cooperativity, specificity, and evolutionary stability of Polycomb targeting in *Drosophila*. *Cell Rep.* **9**, 219–233.
- Seitan, V.C., Faure, A.J., Zhan, Y., McCord, R.P., Lajoie, B.R., Ing-Simmons, E., Lenhard, B., Giorgetti, L., Heard, E., Fisher, A.G., et al. (2013). Cohesin-based chromatin interactions enable regulated gene expression within preexisting architectural compartments. *Genome Res.* **23**, 2066–2077.
- Sexton, T., Yaffe, E., Kenigsberg, E., Bantignies, F., Leblanc, B., Hoichman, M., Parrinello, H., Tanay, A., and Cavalli, G. (2012). Three-dimensional folding and functional organization principles of the *Drosophila* genome. *Cell* **148**, 458–472.
- Shen, Y., Yue, F., McCleary, D.F., Ye, Z., Edsall, L., Kuan, S., Wagner, U., Dixon, J., Lee, L., Lobanenkov, V.V., and Ren, B. (2012). A map of the cis-regulatory sequences in the mouse genome. *Nature* **488**, 116–120.
- Sofueva, S., Yaffe, E., Chan, W.C., Georgopoulou, D., Vietri Rudan, M., Mira-Bontenbal, H., Pollard, S.M., Schroth, G.P., Tanay, A., and Hadjur, S. (2013). Cohesin-mediated interactions organize chromosomal domain architecture. *EMBO J.* **32**, 3119–3129.
- Soshnikova, N., and Duboule, D. (2009). Epigenetic temporal control of mouse *Hox* genes in vivo. *Science* **324**, 1320–1323.
- Splinter, E., Heath, H., Kooren, J., Palstra, R.J., Klous, P., Grosveld, F., Galjart, N., and de Laat, W. (2006). CTCF mediates long-range chromatin looping and local histone modification in the beta-globin locus. *Genes Dev.* **20**, 2349–2354.
- Splinter, E., de Wit, E., Nora, E.P., Klous, P., van de Werken, H.J., Zhu, Y., Kaaij, L.J., van Ijcken, W., Gribnau, J., Heard, E., and de Laat, W. (2011). The inactive X chromosome adopts a unique three-dimensional conformation that is dependent on *Xist* RNA. *Genes Dev.* **25**, 1371–1383.
- Symmons, O., Uslu, V.V., Tsujimura, T., Ruf, S., Nassari, S., Schwarzer, W., Ettwiller, L., and Spitz, F. (2014). Functional and topological characteristics of mammalian regulatory domains. *Genome Res.* **24**, 390–400.
- Taddei, A., Van Houwe, G., Nagai, S., Erb, I., van Nimwegen, E., and Gasser, S.M. (2009). The functional importance of telomere clustering: global changes in gene expression result from SIR factor dispersion. *Genome Res.* **19**, 611–625.
- Tanizawa, H., Iwasaki, O., Tanaka, A., Capizzi, J.R., Wickramasinghe, P., Lee, M., Fu, Z., and Noma, K. (2010). Mapping of long-range associations throughout the fission yeast genome reveals global genome organization linked to transcriptional regulation. *Nucleic Acids Res.* **38**, 8164–8177.
- Tark-Dame, M., Jerabek, H., Manders, E.M., Heermann, D.W., and van Driel, R. (2014). Depletion of the chromatin looping proteins CTCF and cohesin causes chromatin compaction: insight into chromatin folding by polymer modelling. *PLoS Comput. Biol.* **10**, e1003877.
- Therizols, P., Illingworth, R.S., Courilleau, C., Boyle, S., Wood, A.J., and Bickmore, W.A. (2014). Chromatin decondensation is sufficient to alter nuclear organization in embryonic stem cells. *Science* **346**, 1238–1242.
- Tjong, H., Gong, K., Chen, L., and Alber, F. (2012). Physical tethering and volume exclusion determine higher-order genome organization in budding yeast. *Genome Res.* **22**, 1295–1305.
- Van Bortle, K., Ramos, E., Takenaka, N., Yang, J., Wahi, J.E., and Corces, V.G. (2012). *Drosophila* CTCF tandemly aligns with other insulator proteins at the borders of H3K27me3 domains. *Genome Res.* **22**, 2176–2187.
- Véron, A.S., Lemaitre, C., Gautier, C., Lacroix, V., and Sagot, M.F. (2011). Close 3D proximity of evolutionary breakpoints argues for the notion of spatial synteny. *BMC Genomics* **12**, 303.
- Walter, J., Schermelleh, L., Cremer, M., Tashiro, S., and Cremer, T. (2003). Chromosome order in HeLa cells changes during mitosis and early G1, but is stably maintained during subsequent interphase stages. *J. Cell Biol.* **160**, 685–697.
- Wei, Z., Gao, F., Kim, S., Yang, H., Lyu, J., An, W., Wang, K., and Lu, W. (2013). Klf4 organizes long-range chromosomal interactions with the oct4 locus in reprogramming and pluripotency. *Cell Stem Cell* **13**, 36–47.
- Zabidi, M.A., Arnold, C.D., Schernhuber, K., Pagani, M., Rath, M., Frank, O., and Stark, A. (2014). Enhancer—core-promoter specificity separates developmental and housekeeping gene regulation. *Nature* **518**, 556–559.
- Zaret, K.S. (2014). Genome reactivation after the silence in mitosis: recapitulating mechanisms of development? *Dev. Cell* **29**, 132–134.
- Zhang, H., Jiao, W., Sun, L., Fan, J., Chen, M., Wang, H., Xu, X., Shen, A., Li, T., Niu, B., et al. (2013). Intrachromosomal looping is required for activation of endogenous pluripotency genes during reprogramming. *Cell Stem Cell* **13**, 30–35.
- Zhu, J., Adli, M., Zou, J.Y., Verstappen, G., Coyne, M., Zhang, X., Durham, T., Miri, M., Deshpande, V., De Jager, P.L., et al. (2013). Genome-wide chromatin state transitions associated with developmental and environmental cues. *Cell* **152**, 642–654.
- Zuin, J., Dixon, J.R., van der Reijden, M.I., Ye, Z., Kolovos, P., Brouwer, R.W., van de Corput, M.P., van de Werken, H.J., Knoch, T.A., van Ijcken, W.F., et al. (2014). Cohesin and CTCF differentially affect chromatin architecture and gene expression in human cells. *Proc. Natl. Acad. Sci. USA* **111**, 996–1001.

Cell SnapShot archive

SnapShot: Non-Resectable Adenocarcinoma

Rebecca S. Heist and Jeffrey A. Engelman
Massachusetts General Hospital, Boston, MA

Stage	Est. % ^a	General treatment recom
IA	14%	Surgical resection
IB	10%	Surgical resection, can consid
IIA	8%	Surgical resection followed by
IIB	5%	Surgical resection followed by
IIIA	16%	Multimodality treatment: chem
IIIB	8%	Multimodality treatment: chem
IV	41%	Chemotherapy, consider targ

^aEstimated from SEER validation set of proposed 7th edition of TNM staging system in higher to pathologic stage because clinical

Mutation spectrum in Adenocarcinoma

Mutations in TP53 and KRAS are common occurrences in this chart due to high overlap with other mutations.

SnapShot: Chromatin Capture

Ofir Hakim and Tom Misteli
National Cancer Institute, NIH, Bethesda, MD

CROSSLINK

CUTTING

LIGATION

REVERSE CROSSLINKS

DETECTION

COMPUTATIONAL ANALYSIS

Principle	IC	IG
Coverage	Commonly < 1Mb	Commonly < 1Mb
Detection	Local specific PCR	HT-seq/sequencing
Limitations	Low throughput and coverage	Limited coverage
Examples	Determine interaction between a known promoter and enhancer	Determine comprehensively higher order interactions in a defined region

SnapShot: Physiological Signaling

Takashi Kadowaki, Naoto Kubota, Kohjiro Ueki
Department of Diabetes and Metabolic Diseases
Bunkyo-ku, Tokyo 113-8655, Japan

CELL TYPE/ ORGAN

Systemic	IR	Protein
	IRS-1	App tone
	IRS-2	Retz nom
Brain	IR	Obe incr
	IRS-2	Obe type
Liver	IR	Norr incr
	IRS-1	Norr refex
	IRS-2	Norr incr
	IRS-1/IRS-2	Norr incr
Skeletal muscle	IR	Norr incr
	IRS-1	Norr incr
	IRS-2	Norr incr
	IRS-1/IRS-2	Norr incr
Heart	IR	Norr outp
Kidney	IR	Norr incr
β cell	IR	Norr stim
Macrophage	IRS-2	Imps
	IRS-1	Norr incr
	IRS-2	Norr incr
Endothelial cell	IR	Norr incr
	IRS-1	Norr incr
	IRS-2	Norr incr
	IRS-1/IRS-2	Norr incr

SnapShot: Retinoid Signaling

Sandeep Kumar¹ and Gregg Duester²
¹Sanford-Burnham Medical Research Institute, Pines Road, La Jolla, CA 92037, USA
²Genentech, Inc., South San Francisco, CA 940

SnapShot: Caspase

Guy S. Salvesen¹ and Avi Ashkenazi²
¹Sanford-Burnham Medical Research Institute, Pines Road, La Jolla, CA 92037, USA
²Genentech, Inc., South San Francisco, CA 940

Apoptosis Initiator

- Caspase-8
- Caspase-10
- C-FLIP_L
- Caspase-9
- Caspase-2

Apoptosis Effector

- Caspase-3
- Caspase-7
- Caspase-6

Inflammation

- Caspase-1
- Caspase-4
- Caspase-5

Keratinocyte different

- Caspase-14

Recruitment domains

- CARD
- DED
- L

SnapShot: High-Throughput Sequencing App

Hong Han,¹ Razvan Nufiu,¹ Jason Moffat,¹ and 'Barting and Best Department of Medical Res

Genome Sequencing/Resequencing

- Genome-wide polymorphism and mutation mapping
- Genome assembly

Transcriptome Sequencing/RNA-Seq

- Total RNA, total RNA minus rRNA, poly(A)-selected RNA
- Gene expression profiling
- Long noncoding RNA profiling
- Alternative splicing and trans-splicing profiling
- Alternative polyadenylation profiling
- Mapping transcription initiation sites
- Mapping RNA editing sites (coupled with DNA-Seq)
- Targeted RNA-Seq, Direct RNA-Seq, Strand-seq RNA-Seq, Nascent RNA-Seq

Small RNA Sequencing

- e.g., microRNA/Piwi-interacting RNA profiling
- Argonaute (Ago)/PITS-CLIP
- Mapping interactions between microRNAs and mRNAs

Cell introduces the new SnapShot archive, with >200 SnapShots — sorted and categorized — from chromatin remodelers and autophagy to cancer and autism. All SnapShots published from a year ago or more are open access and freely available.

R&D SYSTEMS
a biotechne® brand

CellPress cell.com/snapshots



view the archive

Immune Checkpoint Targeting in Cancer Therapy: Toward Combination Strategies with Curative Potential

Padmanee Sharma^{1,2,*} and James P. Allison^{1,*}

¹Department of Immunology

²Department of Genitourinary Medical Oncology

MD Anderson Cancer Center, Houston, TX 77030, USA

*Correspondence: padsharma@mdanderson.org (P.S.), jallison@mdanderson.org (J.P.A.)

<http://dx.doi.org/10.1016/j.cell.2015.03.030>

Research in two fronts has enabled the development of therapies that provide significant benefit to cancer patients. One area stems from a detailed knowledge of mutations that activate or inactivate signaling pathways that drive cancer development. This work triggered the development of targeted therapies that lead to clinical responses in the majority of patients bearing the targeted mutation, although responses are often of limited duration. In the second front are the advances in molecular immunology that unveiled the complexity of the mechanisms regulating cellular immune responses. These developments led to the successful targeting of immune checkpoints to unleash anti-tumor T cell responses, resulting in durable long-lasting responses but only in a fraction of patients. In this Review, we discuss the evolution of research in these two areas and propose that intercrossing them and increasing funding to guide research of combination of agents represent a path forward for the development of curative therapies for the majority of cancer patients.

Introduction

The scientific community united against a common enemy in 1971 when President Nixon signed a bill initiating the “War on Cancer,” which provided funding for scientific research focused on improving our understanding and treatment of cancer. Without doubt, the intervening years were followed by great advances in the elucidation of the molecular mechanisms that regulate growth and death of normal cells, including a deep understanding of how these pathways progressively go awry during the development of cancer. This understanding led to the era of genomically targeted therapies and “precision medicine” in the treatment of cancer. Genomically targeted therapies can result in remarkable clinical responses. The ability of cancer cells to adapt to these agents by virtue of their genomic instability and other resistance mechanisms eventually leads to disease progression in the majority of patients nonetheless. Unraveling the mechanisms by which cancer cells become resistant to drugs and developing new agents to target the relevant pathways have become logical next steps in this approach for cancer treatment. However, given the genetic and epigenetic instability of cancer cells, it is likely that each new drug or combination of drugs targeting the tumor cells will meet with more complex mechanisms of acquired resistance. Recent findings suggest that T cells, bearing antigen receptors that are generated by random rearrangement of gene segments, followed by selective processes that result in a vast repertoire of T cell clones, provide sufficient diversity and adaptability to match the complexity of tumors. Discoveries regarding regulation of T cell responses have provided key principles regarding immune

checkpoints that are being translated into clinical success, with durable responses and long-term survival greater than 10 years in a subset of patients with metastatic melanoma, as well as yielding promising results in several other tumor types. Now, with the perspective of combining genomically targeted agents and immune checkpoint therapies, we are finally poised to deliver curative therapies to cancer patients. To support this goal and accelerate these efforts, changes in directions of research support and funding may be required.

Precision Medicine: Targeting the Drivers

In the past three decades, enormous strides have been made in elucidating the molecular mechanisms involved in the development of cancer (Hanahan and Weinberg, 2011). It is now clear that the oncogenic process involves somatic mutations that result in activation of genes that are normally involved in regulation of cell division and programmed cell death, as well as inactivation of genes involved in protection against DNA damage or driving apoptosis (Bishop, 1991; Solomon et al., 1991; Weinberg, 1991; Knudson, 2001). These genetic links led to the decision early in the war on cancer to undertake sequencing of cancer genomes to provide a comprehensive view of somatic mutational landscapes in cancer and identify possible therapeutic targets. Infrastructure and funding were provided to coordinate the sequencing efforts. It has become apparent that the level of somatic mutations differs widely between and within different tumor types ranging from very low rates in childhood leukemias to very high rates in tumors associated with carcinogens (Alexandrov et al., 2013).

Mutations can be divided into two broad classes: those whose products “drive” tumorigenesis in a dominant fashion and “passengers” with no obvious role in the tumor causation. The Cancer Genome Atlas (TCGA) projects have enabled identification of many of these mutations (Chen et al., 2014; Cancer Genome Atlas Research Network, 2014). This has allowed for the rational design of drugs that target and selectively interfere with oncogenic signaling pathways. This approach has revolutionized cancer medicine by moving away from the “one size fits all” approach—for instance, traditional chemotherapy, which attacks all dividing cells, including both cancer-differentiating or regenerating normal cells—to a more personalized strategy of treating patients with a specific drug only if their cancer bears particular molecular mutations that are target of that drug.

As an example of genomically targeted therapies, an inhibitor against BRAF was developed when it was discovered that ~40%–60% of cutaneous melanomas carry mutations in BRAF, which induces constitutive activation of the MAPK pathway (Curtin et al., 2005; Davies et al., 2002). In a randomized phase III trial comparing a BRAF inhibitor (vemurafenib) versus dacarbazine, the vemurafenib treatment group had a response rate of ~48% versus 5% in the dacarbazine arm (Chapman et al., 2011). However, the median duration of response was short, only 6.7 months (Sosman et al., 2012). Another oncogenic pathway that has been targeted is the tyrosine kinase chromosomal rearrangement, which results in the fusion oncogene EML4-ALK that is found in ~5% of NSCLC patients (Soda et al., 2007). The EML4 fusion partner mediates ligand-independent oligomerization and/or dimerization of anaplastic lymphoma kinase (ALK), resulting in constitutive kinase activity. Standard chemotherapies in this subgroup of patients have been associated with response rates of up to 10% (Hanna et al., 2004). Crizotinib, a tyrosine kinase inhibitor targeting ALK (Kwak et al., 2010), was shown to elicit a response rate of ~65% with a median duration of response of less than 8 months in a phase III trial (Shaw et al., 2013). Although there was a significant increase in progression-free survival for patients treated with crizotinib, regrettably, there was no overall survival benefit in the interim analysis. Therefore, although the concept of targeting “driver mutations” has great merit and has demonstrated clinical responses, the reality remains that the majority of patients treated with these agents will derive short-term clinical responses with eventual development of resistance mechanisms that lead to disease progression and death.

Mechanisms operative in acquired resistance fall into three main categories: alterations in the targeted gene (as a result of mutation, amplification, or alternative splicing); other changes that do not affect the original target but re-activate the signaling pathway involved (i.e., NRAS and MEK mutations in BRAF mutant melanoma); and changes that activate alternate pathways (such as activation of growth factor receptors). Considerable effort has gone into finding ways to enhance efficacy of genomically targeted therapies. One effort involves multiple agents that target different molecules in the same pathway, such as the combination of a BRAF inhibitor and a MEK-inhibitor (Larkin et al., 2014; Robert et al., 2015a). This approach helps to reduce compensatory feedback loops, as well as to block the development of resistance due to mutations downstream that

pathway. A different strategy consists of blocking parallel pathways to prevent emerging resistance (Martz et al., 2014). Still, the chief challenge of these combinatorial approaches is the multiplicity of resistance mechanisms and the fact that different mechanisms may be in operation in different cells due to intratumor heterogeneity. Given these observations, it is difficult to envision realistic approaches to effectively overcome the myriad of resistance mechanisms that may arise in the course of cancer treatment. The continued evolvability of the tumor cells and their mechanisms of escape from targeted therapies raise the question as to whether combinations of genomically targeted agents will ever be curative.

Advantages of Mobilizing T Cells for Cancer Therapy

As the knowledge of the intricate biology of cancer has progressed, so has the understanding of the fundamental cellular and molecular mechanisms that orchestrate the interplay of the innate and adaptive arms of the immune system. In a simplistic way, the innate system is composed primarily of cytokines, the complement system, and phagocytes such as macrophages, neutrophils, dendritic cells, and natural killer (NK) cells. Cells of the innate immune system have hard-wired receptors to detect products of infectious microorganisms and dying cells. Macrophages and neutrophils provide an early defense against microorganisms, whereas dendritic cells provide a key interface to the adaptive immune system, composed of B and T cells with their somatically generated, clonally expressed repertoire of antigen receptors.

The understanding of the basic principles governing the controlling immunity provided the rationale for the development of powerful strategies to actively engage the immune system for cancer therapy. Strategies to unleash T cells against tumors are particularly compelling, as the activity of these cells presents important features that are advantageous over other cancer therapies. The first is their specificity. T cells express antigen receptors that recognize cell-surface complexes of MHC molecules and peptides sampled from virtually all the proteins in the cell and are not limited to peptide antigens derived from cell-surface molecules. The second feature is memory. Primary T cell responses are generally followed by the production of long-lived memory T cells with accelerated kinetics of secondary response if the antigen recurs. Finally, the T cell response is adaptable and can accommodate not only tumor heterogeneity but also responses to novel antigens expressed by recurring tumors. It has been calculated that the somatic recombination process that generates the antigen receptors of T cells can generate as many as 10^{15} different receptors (Davis and Bjorkman, 1988). Of this theoretical number, each individual human has perhaps 10^9 different receptors. The immense size of the repertoire suggests that the immune system is indeed well equipped to deal with mutability and adaptability of cancer.

Harnessing T Cell Responses to Tumor Antigens

With the advent of genomic and cDNA expression cloning methods and sequencing of peptides eluted from tumor cell MHC molecules, an avalanche of tumor antigens defined by tumor-specific T cells has been identified in both mice and in humans. Most of these are shared between cancer cells of different

individuals and fall into four groups: products of oncogenic viruses (Epstein-Barr virus in certain leukemias and human papilloma virus in cervical and some head and neck cancers); antigens related to tissue-specific differentiation molecules (tyrosinase and related proteins in melanoma and prostate-specific antigen and prostatic acid phosphatase in prostate cancer); molecules normally expressed only during fetal development (carcino-embryonic antigen in colon cancer, α -fetoprotein in liver cancer); and cancer-testes (CT) antigens, which are normally expressed during gametogenesis but are found in many cancer cells as a result of changes in epigenetic regulation (MAGE and NY-ESO-1).

Additionally, somatic mutations also can result in the generation of tumor-specific peptides with the potential to bind major histocompatibility complex (MHC) molecules and therefore be recognized by the immune system as neoantigens (Sjöblom et al., 2006; Segal et al., 2008). The analysis of the epitope landscape of breast and colon carcinoma cells revealed that the products of seven to ten mutant genes in colorectal and breast cancer, respectively, have the potential for binding to HLA-A*0201 alone. Because each heterozygote individual carries as many as 6 different HLA class I genes, this means an average of 42–60 potential neoantigens that can be presented to T cells. In support of these estimates, recent studies have demonstrated that neoantigens generated by somatic mutation are recognized by T cells in both mouse and human cancers (Linnemann et al., 2015; Gros et al., 2014; Tran et al., 2014; Gubin et al., 2014).

At first, as a result of earlier studies identifying shared antigens, the field of cancer immunotherapy became focused on developing therapeutic vaccines to expand T cells against these shared antigens expressed on tumors. Many studies focused on stimulating T cell responses with peptides, proteins, whole-tumor cells including those modified to express cytokines, DNA, recombinant viral-based vaccines, or antigen-pulsed dendritic cells given alone or in combination with various adjuvants or cytokines. Although these trials were conducted with the best available science at the time and provided promising anecdotal evidence that induction of immune responses could elicit clinical benefit, they remained largely negative and generally failed to show objective clinical responses (see Rosenberg et al., 2004 for review). Enthusiasm waned somewhat as the number of failed clinical trials mounted.

Many reasons might have contributed to the failure of these vaccination strategies, including choice of antigen, failure to provide adequate costimulation, or functional inactivation of tumor-reactive T cells (Melerio et al., 2014). A number of T-cell-extrinsic suppressive mechanisms such as TGF β , FoxP3⁺ regulatory T cells (Treg), and tryptophan metabolites (IDO) that can hamper anti-tumor responses have also been identified, and there have been efforts to minimize the suppressive effects of these in pre-clinical and clinical studies.

Unraveling the Complexity of T Cell Activation

Another contributing factor to the failure of earlier cancer vaccine trials was perhaps the lack of understanding and appreciation of the full complexity of cell-intrinsic pathways that regulate T cell activation. By the late 1980s, it was known that simple engage-

ment of peptide/MHC complexes by the antigen receptor is insufficient for activation of T cells and may render them anergic (Jenkins and Schwartz, 1987; Mueller et al., 1989). In order to become fully activated, T cells must encounter antigen in the context of antigen-presenting cells (APCs) such as dendritic cells, which provide costimulatory signals mediated by B7 molecules (B7-1 and B7-2) that will engage their ligand, CD28, in the T cell (Greenwald et al., 2005). Thus, T cells specific for a tumor antigen will not be activated by an initial encounter with tumor cells or may even be rendered anergic because, with the exception of a few lymphomas, tumors do not express costimulatory B7 molecules (Townsend and Allison, 1993). Thus, tumors are essentially invisible to T cells until the T cells are activated as a result of cross-priming by dendritic cells that present tumor antigens acquired from dying tumor cells. Simultaneous recognition of antigen/MHC complexes and costimulatory ligands by T cells initiates a complex set of genetic programs that result in cytokine production, cell-cycle progression, and production of anti-apoptotic factors that result in proliferation and functional differentiation of T cells. Consistent with the importance of both antigen receptor and costimulatory signals in initiating anti-tumor responses, many therapeutic vaccines now incorporate both antigen and dendritic cells or agents that enhance costimulatory signaling.

By the mid-90s, it became clear that T cell priming elicits not only programs leading to induction of T cell responses but also a parallel program that will eventually stop the response. The critical inhibitory program is mediated by CTLA-4, a homolog of CD28 that also binds B7-1 and B7-2, although with much greater avidity than that CD28. Expression of the *ctla-4* gene is initiated upon T cell activation, and it traffics to and accumulates in the immunological synapse, eventually attenuating or preventing CD28 costimulation by competition for B7 binding and negative signaling (Walunas et al., 1994; Krummel and Allison, 1995). The fact that *ctla-4* knockout mice suffer from a rapid and lethal lymphadenopathy (Waterhouse et al., 1995; Tivol et al., 1995; Chambers et al., 1997) speaks for a negative role for CTLA-4 in limiting T cell responses to prevent damage to normal tissues.

Thus, activation of T cells as a result of antigen receptor signaling and CD28 costimulation is followed not only by induction of genetic programs leading to proliferation and functional differentiation but also by induction of an inhibitory program mediated by CTLA-4, which will ultimately stop proliferation. Extrapolating this paradigm to anti-tumor T cell responses, if eradication of the tumor has not been completed by the time that the inhibitory signal of CTLA-4 is triggered, the T cells will be turned off and will be unable to complete the task. Importantly, this also suggests that, after this program is initiated, vaccines used to stimulate antigen receptor signaling may actually serve to strengthen the “off” signal as a result of additional induction of *ctla-4* expression by antigen receptor signaling. In any event, this suggests the importance of shifting strategies for cancer immunotherapy from activating T cells to unleashing them.

Inactivating the Brakes to Increase Anti-tumor Immunity

Consistent with the observations that CD28 and CTLA-4 had opposing effects on T cell responses in vitro, in the late 90s, it

was found that, although blocking antibodies to CD28 impaired anti-tumor responses in mice, blocking antibodies to CTLA-4 enhanced anti-tumor responses in mouse tumor models (Leach et al., 1996). In fact, the treatment of mice with anti-CTLA-4 antibodies as monotherapy results in complete tumor rejection and long-lived immunity. Later on, mechanistic studies revealed that anti-tumor activity was associated with increased ratio of both CD4 and CD8 effector cells to FoxP3⁺ regulatory T cells (Quezada et al., 2006). The success of CTLA-4 blockade in these initial studies raised two compelling points. First, because the target molecule was on the T cell and not the tumor cell, it was feasible to imagine that the same strategy would work on many different histologic tumors, as well as on tumors caused by different genetic lesions. Second, taking into consideration that CTLA-4 inhibited CD28-mediated costimulation by a cell-intrinsic mechanism (Peggs et al., 2009), its blockade could allow for enhanced T cell costimulation, which in turn would increase the efficacy of tumor vaccines, as well as agents that kill tumor cells under conditions that promote inflammatory responses. These possibilities were further supported by the results of a series of studies in different mouse models, including the demonstration that blockade of CTLA-4 was not limited to any particular tumor type but was rather broadly effective. CTLA-4 also was able to synergize with a vaccine consisting of tumor cells engineered to express the cytokine GM-CSF to eradicate tumors (Hurwitz et al., 1998; van Elsas et al., 1999). Finally, CTLA-4 could be combined with local delivery of irradiation, cryoablation, or an oncolytic virus to induce systemic tumor immunity and eradication of distant metastases (Zamarin et al., 2014; Waitz et al., 2012; Tang et al., 2014). These preclinical studies supported the development of clinical anti-CTLA-4 therapy.

Immune Checkpoint Therapy: The Clinical Success

CTLA-4 blockade was translated to the clinic with a fully human antibody to human CTLA-4 (ipilimumab, Medarex, Bristol-Myers Squibb). Tumor regression was observed in phase I/II trials in patients with a variety of tumor types, including melanoma, renal cell carcinoma, prostate cancer, urothelial carcinoma, and ovarian cancer (Yang et al., 2007; Hodi et al., 2008; Carthon et al., 2010; van den Eertwegh et al., 2012). Two phase III clinical trials with ipilimumab were recently completed in prostate cancer, the first in patients with castrate-resistant prostate cancer who had not received prior chemotherapy treatment and the second in a more advanced disease setting, in which patients with castrate-resistant prostate cancer presented disease that had progressed on chemotherapy treatment. The former trial is yet to be reported. The latter trial reports the lack of statistical significance (*p* value of 0.053) to indicate a survival benefit for patients who received ipilimumab treatment. However, subset analyses indicate that patients who have favorable clinical characteristics such as lack of liver metastases do benefit from ipilimumab therapy (Kwon et al., 2014). Two phase III clinical trials with anti-CTLA-4 (ipilimumab) were also conducted in patients with advanced melanoma and demonstrated improved overall survival for patients treated with ipilimumab (Hodi et al., 2010; Robert et al., 2011). Importantly, these trials indicate long-term durable responses with greater than 20% of treated patients

living for more than 4 years, including a recent analysis indicating survival of 10 years or more for a subset of patients (Schadendorf et al., 2015). The FDA approved ipilimumab as treatment for patients with melanoma in 2011.

The clinical success of anti-CTLA-4 opened a new field termed “immune checkpoint therapy” as additional T cell intrinsic pathways were identified and targeted for clinical development (Sharma et al., 2011; Pardoll, 2012). Another T-cell-intrinsic inhibitory pathway identified after CTLA-4 was that mediated by PD-1 (programmed death 1) and its ligand PD-L1. PD-1 was initially cloned in 1992 in a study of molecules involved in negative selection of T cells by programmed cell death in the thymus (Ishida et al., 1992). Its function as an immune checkpoint was not established until 2000 upon identification of its ligands (Freeman et al., 2000). PD-L1 was then shown to protect tumor cells by inducing T cell apoptosis (Dong et al., 2002). Later, preclinical studies in animal models evaluated anti-PD-1 and anti-PD-L1 antibodies as immune checkpoint therapies to treat tumors (Keir et al., 2008).

Much like CTLA-4, PD-1 is expressed only in activated T cells. However, unlike CTLA-4, PD-1 inhibits T cell responses by interfering with T cell receptor signaling as opposed to outcompeting CD28 for binding to B7. PD-1 also has two ligands, PD-L1 and PD-L2. PD-L2 is predominantly expressed on APCs, whereas PD-L1 can be expressed on many cell types, including cells comprising the immune system, epithelial cells, and endothelial cells. Antibodies targeting PD-L1 have shown clinical responses in multiple tumor types, including melanoma, renal cell carcinoma, non-small-cell lung cancer (Brahmer et al., 2012), and bladder cancer (Powles et al., 2014). Similarly, phase I clinical trials with a monoclonal antibody against PD-1 demonstrated clinical responses in multiple tumor types, including melanoma, renal cell carcinoma, non-small-cell carcinoma (Topalian et al., 2012), Hodgkin’s lymphoma (Ansell et al., 2015), and head and neck cancers (Seiwert et al., 2014, *J. Clin. Oncol.*, abstract). Recently, a large phase I clinical trial with an anti-PD-1 antibody known as MK-3475 showed response rates of ~37%–38% in patients with advanced melanoma, including patients who had progressive disease after prior ipilimumab treatment (Hamid et al., 2013), triggering the approval of MK-3475 (pembrolizumab, Merck) by the FDA in September 2014. A phase III clinical trial that treated patients with metastatic melanoma with a different anti-PD-1 antibody (nivolumab, Bristol-Myers Squibb, BMS) also demonstrated improved responses and overall survival benefit as compared to chemotherapy treatment (Robert et al., 2015b). Nivolumab was FDA approved for patients with metastatic melanoma in December 2014. In addition, nivolumab was FDA approved in March 2015 for patients with previously treated advanced or metastatic non-small-cell lung cancer based on a phase III clinical trial, which reported an improvement in overall survival for patients treated with nivolumab as compared to patients treated with docetaxel chemotherapy.

Because CTLA-4 and PD-1 regulate different inhibitory pathways on T cells, combination therapy with antibodies targeting both molecules was tested and found to improve anti-tumor responses in a pre-clinical murine model (Curran et al., 2010). A recently reported phase I clinical trial with anti-CTLA-4 in combination with anti-PD-1 also demonstrated tumor regression

in ~50% of treated patients with advanced melanoma, in most cases with tumor regression of 80% or higher (Wolchok et al., 2013). There are ongoing clinical trials with anti-CTLA-4 (ipilimumab, BMS or tremelimumab, MedImmune/Astrazeneca) plus anti-PD-1 or anti-PD-L1 in other tumor types, with preliminary data indicating promising results (Hammers et al., 2014, *J. Clin. Oncol.*, abstract; Callahan et al., 2014, *J. Clin. Oncol.*, abstract) that highlight this combination as an effective immunotherapy strategy for cancer patients.

As with other cancer therapies, immune checkpoint therapies may lead to side effects and toxicities (see Postow et al., 2015; Gao et al., 2015 for recent reviews). Briefly, these side effects consist of immune-related adverse events that are defined by inflammatory conditions, including dermatitis, colitis, hepatitis, pancreatitis, pneumonitis, and hypophysitis. These side effects can be managed and usually involve administration of immunosuppressive agents such as corticosteroids, which do not appear to interfere with clinical benefit that is derived from the immune checkpoint agents. The profile of side effects that occur with both anti-CTLA-4 and anti-PD-1/PD-L1 antibodies is similar; however, the side effects appear to occur more frequently in the setting of anti-CTLA-4 therapy as compared to anti-PD-1 and anti-PD-L1 therapies. The continued success of immune checkpoint therapies in the clinic will require education of the oncology community regarding recognition and treatment of the side effects elicited by these agents.

Novel Immunologic Targets for Cancer Immunotherapy

Although blockade of the CTLA-4 and PD-1/PD-L1 pathways is furthest along in clinical development, it only represents the tip of the iceberg in the realm of potential targets that can serve to improve anti-tumor responses. Ongoing studies on regulation of immune responses have led to the identification of multiple other immunologic pathways that may be targeted for the development of therapies, either as monotherapy or in combination strategies, for the successful treatment of cancer patients. These include immune checkpoints or inhibitory pathways, as well as co-stimulatory molecules, which act to enhance immune responses. A partial list of new immune checkpoints that are being evaluated in pre-clinical tumor models and/or in the clinic with cancer patients includes LAG-3 (Triebel et al., 1990), TIM-3 (Sakuishi et al., 2010), and VISTA (Wang et al., 2011), whereas co-stimulatory molecules include ICOS (Fan et al., 2014), OX40 (Curti et al., 2013), and 4-1BB (Melero et al., 1997).

Of these emerging immune checkpoints, LAG-3 is the furthest along in clinical development with a fusion protein (IMP321, Immuntep) and an antibody (BMS-986016, BMS) in clinical trials. The fusion protein was tested as monotherapy in patients with renal cell carcinoma, which was well tolerated and led to stabilization of disease in some patients (Brignone et al., 2009). IMP321 was also tested in combination with paclitaxel chemotherapy in patients with metastatic breast cancer, which led to an objective response rate of 50% (Brignone et al., 2010). Based on these promising results, a phase III clinical trial is expected to begin accrual in 2015. Other clinical trials are ongoing with an antibody against LAG-3 (BMS-986016), which is also being tested in combination with anti-PD-1 (nivolumab) (NCT01968109, <http://www.clinicaltrials.gov>). TIM-3 is another

immune checkpoint for which agents are being developed for clinical testing. Pre-clinical studies indicate that TIM-3 is co-expressed with PD-1 on tumor-infiltrating lymphocytes, and combination therapy targeting these two pathways improves anti-tumor immune responses (Sakuishi et al., 2010). Finally, an antibody targeting VISTA was recently shown to improve anti-tumor immune responses in mice (Le Mercier et al., 2014), with clinical development soon to follow. Again, these agents represent only a partial list of the immune checkpoint agents that are currently under development for clinical testing, with expectations that they will be tested in combination strategies based on in-depth analyses of human tumors to provide an understanding of co-expression of these, and other immunologic targets, to guide rational combinations.

Regarding the co-stimulatory molecules, OX40 and 41BB, which are members of the TNF-receptor superfamily, are furthest along in clinical development. A murine anti-OX40 antibody, given as a single dose, was tested in a phase I clinical trial and found to have an acceptable safety profile, as well as evidence of anti-tumor responses in a subset of patients (Curti et al., 2013). Humanized antibodies against OX40 are expected to enter clinical trial in 2015. Anti-41BB (BMS-663513) is a fully humanized monoclonal antibody that has been tested in a phase I/II study in patients with melanoma, renal cell carcinoma, and ovarian cancer, with promising clinical responses, as well as toxicities, especially at higher doses, which led to re-evaluation of the dose and schedule of treatment (Sznol et al., 2008, *J. Clin. Oncol.*, abstract). Currently, there are five clinical trials with anti-41BB (urelumab, BMS-663513) that are recruiting patients with various tumor types (<http://www.clinicaltrials.gov>), including combination with anti-PD-1 (nivolumab), with data expected to be presented from these trials during the next 1 to 2 years. The third co-stimulatory molecule is inducible co-stimulator (ICOS), a member of the CD28/B7 family whose expression increases on T cells upon T cell activation. ICOS⁺ effector T cells (Teff), as opposed to ICOS⁺ regulatory T cells (Treg), increase after patients receive treatment with anti-CTLA-4 (Liakou et al., 2008), correlating with clinical benefit in a small retrospective study (Carthon et al., 2010). ICOS thus may serve as a pharmacodynamic biomarker to indicate that anti-CTLA-4 has “hit its target” enhancing T cell activation (Ng Tang et al., 2013). Also, the association of agonistic targeting of ICOS and blockade of CTLA-4 can lead to improved anti-tumor immune responses and tumor rejection in mice (Fan et al., 2014). Anti-ICOS antibodies are expected to enter into clinical trials in 2015. It is likely that combination therapy to simultaneously engage co-stimulatory pathways and limit inhibitory pathways will be a successful path forward to provide clinical benefit. Importantly, based on the profile of toxicities observed to date, it will be critical to closely monitor these combination strategies for potential adjustments of dosage and management of toxicities that may arise.

Reconciliation: Curative Therapeutic Combinations

The last few decades have witnessed the emergence of two effective but fundamentally different strategies for cancer therapy, each with its own strengths and weaknesses. Genomic-guided identification of mutations that drive cancer has led to

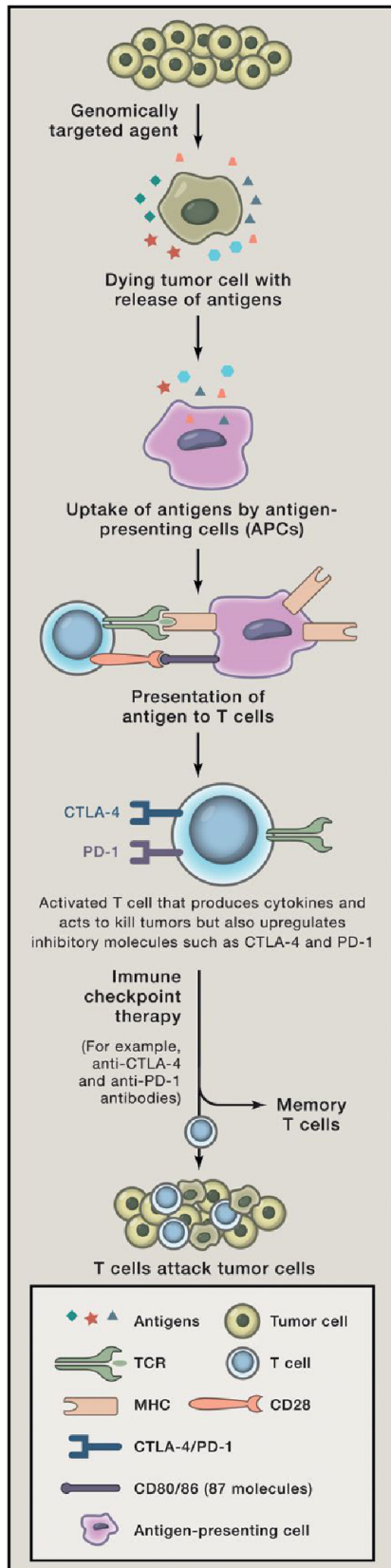


Figure 1. Combination Therapy May Improve Anti-tumor Responses

Depiction of tumor cells dying as a result of genomically targeted therapies with release of tumor antigens; tumor antigens are taken up by APCs and are presented in the context of B7 costimulatory molecules to T cells; T cells recognize antigens on APCs to become activated; activated T cells also up-regulate inhibitory checkpoints such as CTLA-4 and PD-1; immune checkpoint therapy prevents attenuation of T cell responses, thereby allowing T cells to kill tumor cells; and T cells may differentiate into memory T cells that can re-activate in the presence of recurrent tumor.

the development of drugs that result in remarkable responses in the majority of patients whose tumors have the targeted lesion, but the responses are relatively short-lived. As was the case with chemotherapies, it is not unreasonable that combinations of genomically targeted agents will be more powerful against cancer than single agents. It is possible that the use of multiple agents may enhance their effectiveness in terms of increasing overall survival. However, the myriad of mechanisms of acquired resistance and the complexity of the target landscape due to inherent genomic instability may prove extremely difficult to overcome through the sole use of genomically targeted strategies, attaining to achieve cure. In contrast, immune checkpoint therapy is inherently multivalent because targeting a single checkpoint can potentially release T cells with specificity for peptides derived from many different antigens present in a tumor, including differentiation, cancer testis, and even neoantigens generated by mutational events inherent in the genomic instability that drives cancer (Snyder et al., 2014; Linnemann et al., 2015). As a result of the generation of improved anti-tumor T cell responses, immune checkpoint therapy results in durable responses but only in a fraction of patients. As discussed in the previous sections, it is certainly possible to target multiple immune checkpoints with different mechanisms for improved anti-tumor responses in greater numbers of patients. Will patients benefit from combination of these two strategies?

Efforts to combine molecularly targeted agents and immunotherapy have already begun. A phase I clinical trial with agents that inhibit receptor tyrosine kinases, sunitinib, or pazopanib, in combination with anti-PD-1, was recently reported and showed promising overall response rates of 40%–50% in patients with metastatic renal cell carcinoma (RCC) (Amin et al., 2014, *J. Clin. Oncol.*, abstract). These types of combinations will require further follow-up to evaluate for survival and durability of responses. An area that has not yet received enough attention is the immunological impact of genetically targeted agents. Vemurafenib, an FDA-approved BRAF inhibitor used for the treatment of melanoma, has been shown to increase expression of tumor antigens and MHC molecules (Frederick et al., 2013), increasing the sensitivity of the tumor cells to immune attack. Vemurafenib also has potent effects on T cells, enhancing the effects of antigen-mediated activation, perhaps as a result of enhanced activation of the MAP kinase pathway after T cell antigen receptor signaling (Atefi et al., 2014). These data suggest that certain agents may be well suited for combination with immunotherapy. However, a clinical trial testing a BRAF inhibitor (vemurafenib) in combination with anti-CTLA-4 (ipilimumab) was terminated due to hepatotoxicity (Ribas et al., 2013). A second clinical trial with a BRAF inhibitor (dabrafenib) in combination with anti-CTLA-4 (ipilimumab) is currently ongoing, and

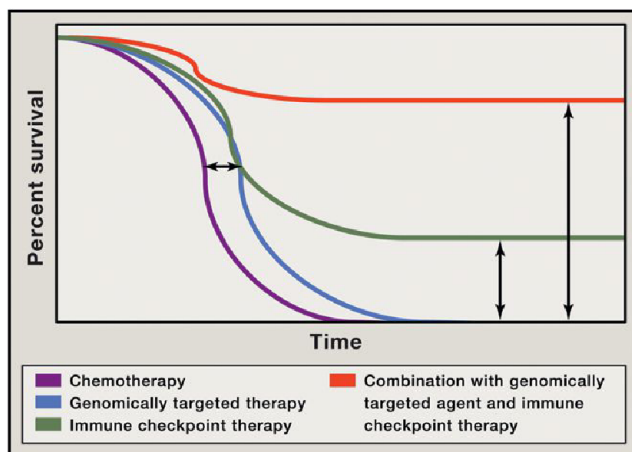


Figure 2. Improved Overall Survival as a Result of Combination Therapy

Depiction of Kaplan-Meier survival curve with genomically targeted agents (blue line) as compared to standard therapies (purple line), indicating an improvement in median overall survival but lack of durable responses; improved median overall survival and durable responses in a fraction of patients treated with immune checkpoint therapy (green line); possibility for improved median overall survival with durable responses for the majority of patients in the setting of combination treatment with genomically targeted agents and immune checkpoint therapy (red line).

preliminary data indicate that this combination appears to be well tolerated (Puzanov et al., 2014, *J. Clin. Oncol.*, abstract), which highlights the need to consider differences in drugs, dose, and/or schedule when evaluating agents for combination strategies. Understanding how different genetically targeted agents affect the responsiveness to immunotherapy may help guide choices of combinations of drugs.

From a mechanistic perspective, it is possible that combination strategies with immune checkpoint therapies and genomically targeted agents will result in induction of immune memory, leading to more durable control of tumor growth than what is achievable with either modality alone. Genomically targeted therapies with high objective response rates actually could serve as “cancer vaccines,” inducing the killing of tumor cells and resulting in the release of tumor antigens and neoantigens, which can then be presented by APCs to tumor-specific T cells (Figure 1). These T cells would become activated but also upregulate inhibitory checkpoints such as CTLA-4 and PD-1, which can be blocked with antibodies to permit enhanced anti-tumor T cell responses, including memory T cell responses, to enable long-term control of disease and possible cure. In addition, the use of targeted agents to directly kill tumor cells, with release of tumor antigens, may focus the activated immune response generated by immunotherapy agents on tumor antigens rather than self-antigens expressed on normal tissues, resulting in fewer adverse events. Furthermore, identification of neoantigens may result in the development of personalized vaccines composed of these neoantigens for novel vaccine strategies plus immune checkpoint agents (Gubin et al., 2014; Tran et al., 2014; Linnemann et al., 2015).

Although it is clear that clinical responses can be elicited with immune checkpoint therapies or genomically targeted agents, it

appears that genomically targeted agents alone tend to improve median survival without providing long-term durable responses (Figure 2, blue line). Targeting immune checkpoints improves median survival but remarkably also provides long-term durable responses, raising the tail of the survival curve (Figure 2, green line). When combined, these therapies are likely to have an additive or even synergistic therapeutic effect that not only would potentially further improve median survival but would also raise the tail of the survival curve, increasing the number of patients that appreciate long-term clinical benefit (Figure 2, red line).

A Future of Curative Cancer Therapies

Federal funding for research has been overwhelmingly directed toward genomically targeted therapies as compared to immune checkpoint therapies. The fundamental research that led to the identification of CTLA-4 as an immune checkpoint, as well as the pre-clinical studies showing the potential of its blockade in cancer therapy, were funded by the National Cancer Institute, but since then, there have been no major initiatives to accelerate progress in this area. Given the durability of the responses that have been obtained with immune checkpoint therapies, it seems reasonable also to allocate enough funds and resources to research focused on immune checkpoint therapies and combination therapy of genomically targeted agents and immunotherapy with promising curative potential. Efforts to determine the impact of genomically targeted therapies on the immune system should also be prioritized, as they will help to identify which agents can enhance anti-tumor T cell responses and guide the choice of combinations from the two classes of agents. At this stage, it does not seem a stretch to say that increasing funding to combination therapies will be key to development of new safe treatments that may prove to be curative for many patients with many types of cancer.

ACKNOWLEDGMENTS

P.S. and J.P.A. are founders and advisors for Jounce Therapeutics. P.S. also serves as a consultant for Bristol-Myers Squibb, Amgen, and Glaxo SmithKline. J.P.A. is an inventor of intellectual property owned by the University of California, Berkeley, and licensed to Bristol-Myers Squibb and has received royalties from Bristol-Myers Squibb. Our research is supported by a PCF Challenge Grant in Immunology (J.P.A. and P.S.), NCI/NIH 1-R01 CA1633793-01 (P.S.), Cancer Prevention Research in Texas grants (J.P.A. and P.S.), and a Stand Up To Cancer–Cancer Research Institute Cancer Immunology Dream Team Translational Cancer Research Grant (P.S. and J.P.A.). Stand Up To Cancer is a program of the Entertainment Industry Foundation administered by the American Association for Cancer Research.

REFERENCES

- Alexandrov, L.B., Nik-Zainal, S., Wedge, D.C., Aparicio, S.A., Behjati, S., Biankin, A.V., Bignell, G.R., Bolli, N., Borg, A., Børresen-Dale, A.L., et al.; Australian Pancreatic Cancer Genome Initiative; ICGC Breast Cancer Consortium; ICGC MML-Seq Consortium; ICGC PedBrain (2013). Signatures of mutational processes in human cancer. *Nature* 500, 415–421.
- Ansell, S.M., Lesokhin, A.M., Borrello, I., Halwani, A., Scott, E.C., Gutierrez, M., Schuster, S.J., Millenson, M.M., Cattray, D., Freeman, G.J., et al. (2015). PD-1 blockade with nivolumab in relapsed or refractory Hodgkin's lymphoma. *N. Engl. J. Med.* 372, 311–319.
- Atefi, M., Avramis, E., Lassen, A., Wong, D.J., Robert, L., Foulad, D., Cerniglia, M., Titz, B., Chodon, T., Graeber, T.G., et al. (2014). Effects of MAPK and PI3K

- pathways on PD-L1 expression in melanoma. *Clin. Cancer Res.* 20, 3446–3457.
- Bishop, J.M. (1991). Molecular themes in oncogenesis. *Cell* 64, 235–248.
- Brahmer, J.R., Tykodi, S.S., Chow, L.Q., Hwu, W.J., Topalian, S.L., Hwu, P., Drake, C.G., Camacho, L.H., Kauh, J., Odunsi, K., et al. (2012). Safety and activity of anti-PD-L1 antibody in patients with advanced cancer. *N. Engl. J. Med.* 366, 2455–2465.
- Brignone, C., Escudier, B., Grygar, C., Marcu, M., and Triebel, F. (2009). A phase I pharmacokinetic and biological correlative study of IMP321, a novel MHC class II agonist, in patients with advanced renal cell carcinoma. *Clin. Cancer Res.* 15, 6225–6231.
- Brignone, C., Gutierrez, M., Mefti, F., Brain, E., Jarcau, R., Cvitkovic, F., Bousetta, N., Medioni, J., Gligorov, J., Grygar, C., et al. (2010). First-line chemioimmunotherapy in metastatic breast carcinoma: combination of paclitaxel and IMP321 (LAG-3lg) enhances immune responses and antitumor activity. *J. Transl. Med.* 8, 71.
- Cancer Genome Atlas Research Network (2014). Comprehensive molecular characterization of gastric adenocarcinoma. *Nature* 513, 202–209.
- Carthon, B.C., Wolchok, J.D., Yuan, J., Kamat, A., Ng Tang, D.S., Sun, J., Ku, G., Troncoco, P., Logothetis, C.J., Allison, J.P., and Sharma, P. (2010). Preoperative CTLA-4 blockade: tolerability and immune monitoring in the setting of a presurgical clinical trial. *Clin. Cancer Res.* 16, 2861–2871.
- Chambers, C.A., Sullivan, T.J., and Allison, J.P. (1997). Lymphoproliferation in CTLA-4-deficient mice is mediated by costimulation-dependent activation of CD4+ T cells. *Immunity* 7, 885–895.
- Chapman, P.B., Hauschild, A., Robert, C., Haanen, J.B., Ascierto, P., Larkin, J., Dummer, R., Garbe, C., Testori, A., Maio, M., et al.; BRIM-3 Study Group (2011). Improved survival with vemurafenib in melanoma with BRAF V600E mutation. *N. Engl. J. Med.* 364, 2507–2516.
- Chen, Y., McGee, J., Chen, X., Doman, T.N., Gong, X., Zhang, Y., Hamm, N., Ma, X., Higgs, R.E., Bhagwat, S.V., et al. (2014). Identification of druggable cancer driver genes amplified across TCGA datasets. *PLoS ONE* 9, e98293.
- Curran, M.A., Montalvo, W., Yagita, H., and Allison, J.P. (2010). PD-1 and CTLA-4 combination blockade expands infiltrating T cells and reduces regulatory T and myeloid cells within B16 melanoma tumors. *Proc. Natl. Acad. Sci. USA* 107, 4275–4280.
- Curti, B.D., Kovacsics-Bankowski, M., Morris, N., Walker, E., Chisholm, L., Floyd, K., Walker, J., Gonzalez, I., Meeuwssen, T., Fox, B.A., et al. (2013). OX40 is a potent immune-stimulating target in late-stage cancer patients. *Cancer Res.* 73, 7189–7198.
- Curtin, J.A., Fridlyand, J., Kageshita, T., Patel, H.N., Busam, K.J., Kutzner, H., Cho, K.H., Aiba, S., Bröcker, E.B., LeBoit, P.E., et al. (2005). Distinct sets of genetic alterations in melanoma. *N. Engl. J. Med.* 353, 2135–2147.
- Davies, H., Bignell, G.R., Cox, C., Stephens, P., Edkins, S., Clegg, S., Teague, J., Woffendin, H., Garnett, M.J., Bottomley, W., et al. (2002). Mutations of the BRAF gene in human cancer. *Nature* 417, 949–954.
- Davis, M.M., and Bjorkman, P.J. (1988). T-cell antigen receptor genes and T-cell recognition. *Nature* 334, 395–402.
- Dong, H., Strome, S.E., Salomao, D.R., Tamura, H., Hirano, F., Flies, D.B., Roche, P.C., Lu, J., Zhu, G., Tamada, K., et al. (2002). Tumor-associated B7-H1 promotes T-cell apoptosis: a potential mechanism of immune evasion. *Nat. Med.* 8, 793–800.
- Fan, X., Quezada, S.A., Sepulveda, M.A., Sharma, P., and Allison, J.P. (2014). Engagement of the ICOS pathway markedly enhances efficacy of CTLA-4 blockade in cancer immunotherapy. *J. Exp. Med.* 211, 715–725.
- Frederick, D.T., Piris, A., Cogdill, A.P., Cooper, Z.A., Lezcano, C., Ferrone, C.R., Mitra, D., Boni, A., Newton, L.P., Liu, C., et al. (2013). BRAF inhibition is associated with enhanced melanoma antigen expression and a more favorable tumor microenvironment in patients with metastatic melanoma. *Clin. Cancer Res.* 19, 1225–1231.
- Freeman, G.J., Long, A.J., Iwai, Y., Bourque, K., Chernova, T., Nishimura, H., Fitz, L.J., Malenkovich, N., Okazaki, T., Byrne, M.C., et al. (2000). Engagement of the PD-1 immunoinhibitory receptor by a novel B7 family member leads to negative regulation of lymphocyte activation. *J. Exp. Med.* 192, 1027–1034.
- Gao, J., He, Q., Subudhi, S., Aparicio, A., Zurita-Saavedra, A., Lee, D.H., Jimenez, C., Suarez-Almazor, M., and Sharma, P. (2015). Review of immune-related adverse events in prostate cancer patients treated with ipilimumab: MD Anderson experience. *Oncogene*.
- Greenwald, R.J., Freeman, G.J., and Sharpe, A.H. (2005). The B7 family revisited. *Annu. Rev. Immunol.* 23, 515–548.
- Gros, A., Robbins, P.F., Yao, X., Li, Y.F., Turcotte, S., Tran, E., Wunderlich, J.R., Mixon, A., Farid, S., Dudley, M.E., et al. (2014). PD-1 identifies the patient-specific CD8+ tumor-reactive repertoire infiltrating human tumors. *J. Clin. Invest.* 124, 2246–2259.
- Gubin, M.M., Zhang, X., Schuster, H., Caron, E., Ward, J.P., Noguchi, T., Ivanova, Y., Hundal, J., Arthur, C.D., Krebber, W.J., et al. (2014). Checkpoint blockade cancer immunotherapy targets tumour-specific mutant antigens. *Nature* 515, 577–581.
- Hamid, O., Robert, C., Daud, A., Hodi, F.S., Hwu, W.J., Kefford, R., Wolchok, J.D., Hersey, P., Joseph, R.W., Weber, J.S., et al. (2013). Safety and tumor responses with lambrolizumab (anti-PD-1) in melanoma. *N. Engl. J. Med.* 369, 134–144.
- Hanahan, D., and Weinberg, R.A. (2011). Hallmarks of cancer: the next generation. *Cell* 144, 646–674.
- Hanna, N., Shepherd, F.A., Fossella, F.V., Pereira, J.R., De Marinis, F., von Pawel, J., Gatzemeier, U., Tsao, T.C., Pless, M., Muller, T., et al. (2004). Randomized phase III trial of pemetrexed versus docetaxel in patients with non-small-cell lung cancer previously treated with chemotherapy. *J. Clin. Oncol.* 22, 1589–1597.
- Hodi, F.S., Butler, M., Oble, D.A., Seiden, M.V., Haluska, F.G., Kruse, A., Macrae, S., Nelson, M., Canning, C., Lowy, I., et al. (2008). Immunologic and clinical effects of antibody blockade of cytotoxic T lymphocyte-associated antigen 4 in previously vaccinated cancer patients. *Proc. Natl. Acad. Sci. USA* 105, 3005–3010.
- Hodi, F.S., O'Day, S.J., McDermott, D.F., Weber, R.W., Sosman, J.A., Haanen, J.B., Gonzalez, R., Robert, C., Schadendorf, D., Hassel, J.C., et al. (2010). Improved survival with ipilimumab in patients with metastatic melanoma. *N. Engl. J. Med.* 363, 711–723.
- Hurwitz, A.A., Yu, T.F., Leach, D.R., and Allison, J.P. (1998). CTLA-4 blockade synergizes with tumor-derived granulocyte-macrophage colony-stimulating factor for treatment of an experimental mammary carcinoma. *Proc. Natl. Acad. Sci. USA* 95, 10067–10071.
- Ishida, Y., Agata, Y., Shibahara, K., and Honjo, T. (1992). Induced expression of PD-1, a novel member of the immunoglobulin gene superfamily, upon programmed cell death. *EMBO J.* 11, 3887–3895.
- Jenkins, M.K., and Schwartz, R.H. (1987). Antigen presentation by chemically modified splenocytes induces antigen-specific T cell unresponsiveness in vitro and in vivo. *J. Exp. Med.* 165, 302–319.
- Keir, M.E., Butte, M.J., Freeman, G.J., and Sharpe, A.H. (2008). PD-1 and its ligands in tolerance and immunity. *Annu. Rev. Immunol.* 26, 677–704.
- Knudson, A.G. (2001). Two genetic hits (more or less) to cancer. *Nat. Rev. Cancer* 1, 157–162.
- Krummel, M.F., and Allison, J.P. (1995). CD28 and CTLA-4 have opposing effects on the response of T cells to stimulation. *J. Exp. Med.* 182, 459–465.
- Kwak, E.L., Bang, Y.J., Camidge, D.R., Shaw, A.T., Solomon, B., Maki, R.G., Ou, S.H., Dezube, B.J., Jänne, P.A., Costa, D.B., et al. (2010). Anaplastic lymphoma kinase inhibition in non-small-cell lung cancer. *N. Engl. J. Med.* 363, 1693–1703.
- Kwon, E.D., Drake, C.G., Scher, H.I., Fizazi, K., Bossi, A., van den Eertwegh, A.J., Krainer, M., Houede, N., Santos, R., Mahammed, H., et al.; CA184-043 Investigators (2014). Ipilimumab versus placebo after radiotherapy in patients with metastatic castration-resistant prostate cancer that had progressed after docetaxel chemotherapy (CA184-043): a multicentre, randomised, double-blind, phase 3 trial. *Lancet Oncol.* 15, 700–712.

- Larkin, J., Ascierto, P.A., Dréno, B., Atkinson, V., Liskay, G., Maio, M., Mandalà, M., Demidov, L., Stroyakovskiy, D., Thomas, L., et al. (2014). Combined vemurafenib and cobimetinib in BRAF-mutated melanoma. *N. Engl. J. Med.* *371*, 1867–1876.
- Le Mercier, I., Chen, W., Lines, J.L., Day, M., Li, J., Sergent, P., Noelle, R.J., and Wang, L. (2014). VISTA regulates the development of protective antitumor immunity. *Cancer Res.* *74*, 1933–1944.
- Leach, D.R., Krummel, M.F., and Allison, J.P. (1996). Enhancement of anti-tumor immunity by CTLA-4 blockade. *Science* *271*, 1734–1736.
- Liakou, C.I., Kamat, A., Tang, D.N., Chen, H., Sun, J., Troncoco, P., Logothetis, C., and Sharma, P. (2008). CTLA-4 blockade increases IFN γ -producing CD4+ICOShi cells to shift the ratio of effector to regulatory T cells in cancer patients. *Proc. Natl. Acad. Sci. USA* *105*, 14987–14992.
- Linnemann, C., van Buuren, M.M., Bies, L., Verdegaal, E.M., Schotte, R., Calis, J.J., Behjati, S., Velds, A., Hilkmann, H., Atmioui, D.E., et al. (2015). High-throughput epitope discovery reveals frequent recognition of neo-antigens by CD4+ T cells in human melanoma. *Nat. Med.* *21*, 81–85.
- Martz, C.A., Ottina, K.A., Singleton, K.R., Jasper, J.S., Wardell, S.E., Perazal-Penton, A., Anderson, G.R., Winter, P.S., Wang, T., Alley, H.M., et al. (2014). Systematic identification of signaling pathways with potential to confer anti-cancer drug resistance. *Sci. Signal.* *7*, ra121.
- Melero, I., Shuford, W.W., Newby, S.A., Aruffo, A., Ledbetter, J.A., Hellström, K.E., Mittler, R.S., and Chen, L. (1997). Monoclonal antibodies against the 4-1BB T-cell activation molecule eradicate established tumors. *Nat. Med.* *3*, 682–685.
- Melero, I., Gaudernack, G., Gerritsen, W., Huber, C., Parmiani, G., Scholl, S., Thatcher, N., Wagstaff, J., Zielinski, C., Faulkner, I., and Mellstedt, H. (2014). Therapeutic vaccines for cancer: an overview of clinical trials. *Nat. Rev. Clin. Oncol.* *11*, 509–524.
- Mueller, D.L., Jenkins, M.K., and Schwartz, R.H. (1989). An accessory cell-derived costimulatory signal acts independently of protein kinase C activation to allow T cell proliferation and prevent the induction of unresponsiveness. *J. Immunol.* *142*, 2617–2628.
- Ng Tang, D., Shen, Y., Sun, J., Wen, S., Wolchok, J.D., Yuan, J., Allison, J.P., and Sharma, P. (2013). Increased frequency of ICOS+ CD4 T cells as a pharmacodynamic biomarker for anti-CTLA-4 therapy. *Cancer Immunol. Res.* *1*, 229–234.
- Pardoll, D.M. (2012). The blockade of immune checkpoints in cancer immunotherapy. *Nat. Rev. Cancer.* *12*, 252–264.
- Peggs, K.S., Quezada, S.A., Chambers, C.A., Korman, A.J., and Allison, J.P. (2009). Blockade of CTLA-4 on both effector and regulatory T cell compartments contributes to the antitumor activity of anti-CTLA-4 antibodies. *J. Exp. Med.* *206*, 1717–1725.
- Postow, M.A., Callahan, M.K., and Wolchok, J.D. (2015). Immune checkpoint blockade in cancer therapy. *J. Clin. Oncol.* Published online January 20, 2015. <http://dx.doi.org/10.1200/JCO.2014.59.4358>.
- Powles, T., Eder, J.P., Fine, G.D., Braiteh, F.S., Lortot, Y., Cruz, C., Bellmunt, J., Burris, H.A., Petrylak, D.P., Teng, S.L., et al. (2014). MPDL3280A (anti-PD-L1) treatment leads to clinical activity in metastatic bladder cancer. *Nature* *515*, 558–562.
- Quezada, S.A., Peggs, K.S., Curran, M.A., and Allison, J.P. (2006). CTLA4 blockade and GM-CSF combination immunotherapy alters the intratumor balance of effector and regulatory T cells. *J. Clin. Invest.* *116*, 1935–1945.
- Ribas, A., Hodi, F.S., Callahan, M., Konto, C., and Wolchok, J. (2013). Hepatotoxicity with combination of vemurafenib and ipilimumab. *N. Engl. J. Med.* *368*, 1365–1366.
- Robert, C., Thomas, L., Bondarenko, I., O'Day, S., Weber, J., Garbe, C., Lebbe, C., Baurain, J.F., Testori, A., Grob, J.J., et al. (2011). Ipilimumab plus dacarbazine for previously untreated metastatic melanoma. *N. Engl. J. Med.* *364*, 2517–2526.
- Robert, C., Karaszewska, B., Schachter, J., Rutkowski, P., Mackiewicz, A., Stroiakovski, D., Lichinitser, M., Dummer, R., Grange, F., Mortier, L., et al. (2015a). Improved overall survival in melanoma with combined dabrafenib and trametinib. *N. Engl. J. Med.* *372*, 30–39.
- Robert, C., Long, G.V., Brady, B., Dutriaux, C., Maio, M., Mortier, L., Hassel, J.C., Rutkowski, P., McNeil, C., Kalinka-Warzocha, E., et al. (2015b). Nivolumab in previously untreated melanoma without BRAF mutation. *N. Engl. J. Med.* *372*, 320–330.
- Rosenberg, S.A., Yang, J.C., and Restifo, N.P. (2004). Cancer immunotherapy: moving beyond current vaccines. *Nat. Med.* *10*, 909–915.
- Sakuishi, K., Apetoh, L., Sullivan, J.M., Blazar, B.R., Kuchroo, V.K., and Anderson, A.C. (2010). Targeting Tim-3 and PD-1 pathways to reverse T cell exhaustion and restore anti-tumor immunity. *J. Exp. Med.* *207*, 2187–2194.
- Schadendorf, D., Hodi, F.S., Robert, C., Weber, J.S., Margolin, K., Hamid, O., Patt, D., Chen, T.T., Berman, D.M., and Wolchok, J.D. (2015). Pooled analysis of long-term survival data from phase II and phase III trials of ipilimumab in unresectable or metastatic melanoma. *J. Clin. Oncol.* Published online February 9, 2015. <http://dx.doi.org/10.1200/JCO.2014.56.2736>.
- Segal, N.H., Parsons, D.W., Peggs, K.S., Velculescu, V., Kinzler, K.W., Vogelstein, B., and Allison, J.P. (2008). Epitope landscape in breast and colorectal cancer. *Cancer Res.* *68*, 889–892.
- Sharma, P., Wagner, K., Wolchok, J.D., and Allison, J.P. (2011). Novel cancer immunotherapy agents with survival benefit: recent successes and next steps. *Nat. Rev. Cancer* *11*, 805–812.
- Shaw, A.T., Kim, D.W., Nakagawa, K., Seto, T., Crinó, L., Ahn, M.J., De Pas, T., Besse, B., Solomon, B.J., Blackhall, F., et al. (2013). Crizotinib versus chemotherapy in advanced ALK-positive lung cancer. *N. Engl. J. Med.* *368*, 2385–2394.
- Sjöblom, T., Jones, S., Wood, L.D., Parsons, D.W., Lin, J., Barber, T.D., Mandelker, D., Leary, R.J., Ptak, J., Silliman, N., et al. (2006). The consensus coding sequences of human breast and colorectal cancers. *Science* *314*, 268–274.
- Snyder, A., Makarov, V., Merghoub, T., Yuan, J., Zaretsky, J.M., Desrichard, A., Walsh, L.A., Postow, M.A., Wong, P., Ho, T.S., et al. (2014). Genetic basis for clinical response to CTLA-4 blockade in melanoma. *N. Engl. J. Med.* *371*, 2189–2199.
- Soda, M., Choi, Y.L., Enomoto, M., Takada, S., Yamashita, Y., Ishikawa, S., Fujiwara, S., Watanabe, H., Kurashina, K., Hatanaka, H., et al. (2007). Identification of the transforming EML4-ALK fusion gene in non-small-cell lung cancer. *Nature* *448*, 561–566.
- Solomon, E., Borrow, J., and Goddard, A.D. (1991). Chromosome aberrations and cancer. *Science* *254*, 1153–1160.
- Sosman, J.A., Kim, K.B., Schuchter, L., Gonzalez, R., Pavlick, A.C., Weber, J.S., McArthur, G.A., Hutson, T.E., Moschos, S.J., Flaherty, K.T., et al. (2012). Survival in BRAF V600-mutant advanced melanoma treated with vemurafenib. *N. Engl. J. Med.* *366*, 707–714.
- Tang, C., Wang, X., Soh, H., Seyedin, S., Cortez, M.A., Krishnan, S., Massarelli, E., Hong, D., Naing, A., Diab, A., et al. (2014). Combining radiation and immunotherapy: a new systemic therapy for solid tumors? *Cancer Immunol. Res.* *2*, 831–838.
- Tivol, E.A., Borriello, F., Schweitzer, A.N., Lynch, W.P., Bluestone, J.A., and Sharpe, A.H. (1995). Loss of CTLA-4 leads to massive lymphoproliferation and fatal multiorgan tissue destruction, revealing a critical negative regulatory role of CTLA-4. *Immunity* *3*, 541–547.
- Topalian, S.L., Hodi, F.S., Brahmer, J.R., Gettinger, S.N., Smith, D.C., McDermott, D.F., Powderly, J.D., Carvajal, R.D., Sosman, J.A., Atkins, M.B., et al. (2012). Safety, activity, and immune correlates of anti-PD-1 antibody in cancer. *N. Engl. J. Med.* *366*, 2443–2454.
- Townsend, S.E., and Allison, J.P. (1993). Tumor rejection after direct costimulation of CD8+ T cells by B7-transfected melanoma cells. *Science* *259*, 368–370.
- Tran, E., Turcotte, S., Gros, A., Robbins, P.F., Lu, Y.C., Dudley, M.E., Wunderlich, J.R., Somerville, R.P., Hogan, K., Hinrichs, C.S., et al. (2014). Cancer immunotherapy based on mutation-specific CD4+ T cells in a patient with epithelial cancer. *Science* *344*, 641–645.

- Triebel, F., Jitsukawa, S., Baixeras, E., Roman-Roman, S., Genevee, C., Viegas-Pequignot, E., and Hercend, T. (1990). LAG-3, a novel lymphocyte activation gene closely related to CD4. *J. Exp. Med.* *171*, 1393–1405.
- van den Eertwegh, A.J., Versluis, J., van den Berg, H.P., Santegoets, S.J., van Moorselaar, R.J., van der Sluis, T.M., Gall, H.E., Harding, T.C., Jooss, K., Lowy, I., et al. (2012). Combined immunotherapy with granulocyte-macrophage colony-stimulating factor-transduced allogeneic prostate cancer cells and ipilimumab in patients with metastatic castration-resistant prostate cancer: a phase 1 dose-escalation trial. *Lancet Oncol.* *13*, 509–517.
- van Elsas, A., Hurwitz, A.A., and Allison, J.P. (1999). Combination immunotherapy of B16 melanoma using anti-cytotoxic T lymphocyte-associated antigen 4 (CTLA-4) and granulocyte/macrophage colony-stimulating factor (GM-CSF)-producing vaccines induces rejection of subcutaneous and metastatic tumors accompanied by autoimmune depigmentation. *J. Exp. Med.* *190*, 355–366.
- Waitz, R., Fassò, M., and Allison, J.P. (2012). CTLA-4 blockade synergizes with cryoablation to mediate tumor rejection. *Oncolimmunology* *1*, 544–546.
- Walunas, T.L., Lenschow, D.J., Bakker, C.Y., Linsley, P.S., Freeman, G.J., Green, J.M., Thompson, C.B., and Bluestone, J.A. (1994). CTLA-4 can function as a negative regulator of T cell activation. *Immunity* *1*, 405–413.
- Wang, L., Rubinstein, R., Lines, J.L., Wasiuk, A., Ahonen, C., Guo, Y., Lu, L.F., Gondek, D., Wang, Y., Fava, R.A., et al. (2011). VISTA, a novel mouse Ig superfamily ligand that negatively regulates T cell responses. *J. Exp. Med.* *208*, 577–592.
- Waterhouse, P., Penninger, J.M., Timms, E., Wakeham, A., Shahinian, A., Lee, K.P., Thompson, C.B., Griesser, H., and Mak, T.W. (1995). Lymphoproliferative disorders with early lethality in mice deficient in Ctla-4. *Science* *270*, 985–988.
- Weinberg, R.A. (1991). Tumor suppressor genes. *Science* *254*, 1138–1146.
- Wolchok, J.D., Kluger, H., Callahan, M.K., Postow, M.A., Rizvi, N.A., Lesokhin, A.M., Segal, N.H., Ariyan, C.E., Gordon, R.A., Reed, K., et al. (2013). Nivolumab plus ipilimumab in advanced melanoma. *N. Engl. J. Med.* *369*, 122–133.
- Yang, J.C., Hughes, M., Kammula, U., Royal, R., Sherry, R.M., Topalian, S.L., Suri, K.B., Levy, C., Allen, T., Mavroukakis, S., et al. (2007). Ipilimumab (anti-CTLA4 antibody) causes regression of metastatic renal cell cancer associated with enteritis and hypophysitis. *J. Immunother.* *30*, 825–830.
- Zamarin, D., Holmgard, R.B., Subudhi, S.K., Park, J.S., Mansour, M., Palese, P., Merghoub, T., Wolchok, J.D., and Allison, J.P. (2014). Localized oncolytic virotherapy overcomes systemic tumor resistance to immune checkpoint blockade immunotherapy. *Sci. Transl. Med.* *6*, 226ra32.

SOX17 Is a Critical Specifier of Human Primordial Germ Cell Fate

Naoko Irie,^{1,2,3,5} Leehee Weinberger,^{4,5} Walfred W.C. Tang,^{1,2,3,5} Toshihiro Kobayashi,^{1,2,3} Sergey Viukov,⁴ Yair S. Manor,⁴ Sabine Dietmann,³ Jacob H. Hanna,^{4,6,*} and M. Azim Surani^{1,2,3,6,*}

¹Wellcome Trust Cancer Research UK Gurdon Institute, Tennis Court Road, University of Cambridge, Cambridge CB2 1QN, UK

²Department of Physiology, Development and Neuroscience, Downing Street, University of Cambridge, Cambridge CB2 3EG, UK

³Wellcome Trust-Medical Research Council Stem Cell Institute, Tennis Court Road, University of Cambridge, Cambridge CB2 3EG, UK

⁴The Department of Molecular Genetics, Weizmann Institute of Science, Rehovot 76100, Israel

⁵Co-first author

⁶Co-senior author

*Correspondence: jacob.hanna@weizmann.ac.il (J.H.H.), a.surani@gurdon.cam.ac.uk (M.A.S.)

<http://dx.doi.org/10.1016/j.cell.2014.12.013>

This is an open access article under the CC BY license (<http://creativecommons.org/licenses/by/3.0/>).

SUMMARY

Specification of primordial germ cells (PGCs) marks the beginning of the totipotent state. However, without a tractable experimental model, the mechanism of human PGC (hPGC) specification remains unclear. Here, we demonstrate specification of hPGC-like cells (hPGCLCs) from germline competent pluripotent stem cells. The characteristics of hPGCLCs are consistent with the embryonic hPGCs and a germline seminoma that share a CD38 cell-surface marker, which collectively defines likely progression of the early human germline. Remarkably, SOX17 is the key regulator of hPGC-like fate, whereas BLIMP1 represses endodermal and other somatic genes during specification of hPGCLCs. Notable mechanistic differences between mouse and human PGC specification could be attributed to their divergent embryonic development and pluripotent states, which might affect other early cell-fate decisions. We have established a foundation for future studies on resetting of the epigenome in hPGCLCs and hPGCs for totipotency and the transmission of genetic and epigenetic information.

INTRODUCTION

Primordial germ cells (PGCs) are the precursors of sperm and eggs, which generate the totipotent state. The genetic basis of mammalian PGC specification was first established in mice (Saitou et al., 2002; Ohinata et al., 2005; Hayashi et al., 2007), which are specified from postimplantation epiblast cells on embryonic day (E)6.25 in response to bone morphogenetic protein 4 (BMP4) (Lawson et al., 1999). Subsequently, ~35 founder PGCs are detected at E7.25. Similar studies on human PGCs (hPGCs) would require E9–E16 embryos, which is not practicable. However, embryonic hPGCs at approximately week 5 to 10 of development, which correspond to mouse PGCs at E10.5–E13.5, can in principle be examined (Leitch et al., 2013). These cells retain charac-

teristic of PGCs while they undergo resetting of the epigenome and global DNA demethylation (Hackett et al., 2012).

In mice, BMP4 induces expression of BLIMP1 (encoded by *Prdm1*) and PRDM14 in the postimplantation epiblast at E6.25; together with AP2 γ (encoded by *Tfap2c*), a direct target of BLIMP1, they induce PGC fate (Magnúsdóttir et al., 2013; Nakaki et al., 2013). The tripartite genetic network acts combinatorially to repress somatic genes, induce expression of PGC genes, such as *Nanos3*, reinduce pluripotency genes, and initiate the epigenetic program (Hackett et al., 2013; Magnúsdóttir and Surani, 2014). PGC-like cells (PGCLCs) can also be induced in vitro from naive pluripotent mouse embryonic stem cells (mESCs) after they acquire competence for germ cell fate after ~48 hr culture in basic fibroblast growth factor (bFGF) and Activin A (Hayashi et al., 2011). These competent cells acquire PGC-like fate in response to either BMP4 signal or directly to *Blimp1*, *Prdm14*, and *Tfap2c*, which is similar to PGCs in vivo (Magnúsdóttir et al., 2013; Nakaki et al., 2013).

Human PGCLCs (hPGCLCs) have been generated at a low frequency by spontaneous differentiation of human ESCs (hESC) in vitro (Gkoutela et al., 2013; Kee et al., 2009), but systematic studies to characterize and identify the key regulators of hPGCs remain to be elucidated. Because there are evident differences between the regulation of mouse and human pluripotent ESCs (Hackett and Surani, 2014; Nichols and Smith, 2009) and during their early postimplantation development (de Fellici, 2013; De Miguel et al., 2010; Irie et al., 2014), this might affect the mechanism and the role of the key regulators of hPGCLC specification (Imamura et al., 2014; Pera, 2013). Once the mechanism of hPGCLC specification is established, it could provide insights on the progression of the early human germline with reference to embryonic hPGCs and seminomas that originate from human germ cells in vivo and retain key characteristics of the lineage (Looijenga et al., 2014).

We have developed a robust approach for hPGCLC specification from germ cell competent hESCs/hiPSCs (Gafni et al., 2013). We show that SOX17, a critical transcription factor for endoderm lineages, is the earliest marker of hPGCLCs and is in fact the key regulator of hPGCLC fate, which is not the case in mice (Hara et al., 2009; Kanai-Azuma et al., 2002). BLIMP1 is downstream of SOX17, and it represses endodermal and other somatic genes

during hPGCLC specification. Comparisons among hPGCLCs, embryonic hPGCs, and a seminoma indicate likely progression of the early human germline. These cells also exhibit CD38 cell surface marker, which is shared by cells with germ cell characteristics. We anticipate that genome editing approaches with our robust in vitro model for hPGCLC specification, combined with patient-specific human-induced pluripotent stem cells (hiPSCs), will lead to major advances in human germ cell biology, including on the unique germline-specific epigenetic program with potential consequences for subsequent generations.

RESULTS

Generation of hPGCLCs from Embryonic Stem Cells

First, we generated three independent hESC lines (WIS2 and LIS1 male hESC and WIBR3 female hESC line) (Gafni et al., 2013) with a NANOS3-mCherry knockin reporter (Figure S1A available online), a highly conserved PGC-specific gene (Gkoutela et al., 2013; Julaton and Reijo Pera, 2011). These hESCs maintained in bFGF and responded to BMP2/BMP4 with ~0%–5% NANOS3-mCherry positive putative hPGCLCs at day 4 (see Figure 7A). Like hESC, mouse epiblast stem cells (mEpiSC) also respond poorly to specification of PGCLCs (Hayashi and Surani, 2009). In contrast, epiblast-like cells (EpiLCs) derived from naive mESCs have a significant potential for germ cell fate (Hayashi et al., 2011). However, the approach used for mouse ESCs did not confer competence for germline fate on hESCs.

Next, we tested hESC-NANOS3-mCherry cells that were maintained in four-inhibitor-containing medium with LIF, bFGF, and TGF β (adopted and modified from NHSM conditions; see Experimental Procedures), henceforth called “4i” medium, which endows the cells with a distinct pluripotent state (Gafni et al., 2013). These hESCs were then cultured for 2 days in bFGF, TGF β , and 1% KSR medium, and thereafter, 2,000–4,000 cells were cultured in low-attachment well in the presence of BMP2 or BMP4, LIF, stem cell factor (SCF), epidermal growth factor (EGF), and Rho-kinase (ROCK) inhibitor to induce hPGCLCs (Hayashi et al., 2011; Watanabe et al., 2007) (Figure 1A). These cells aggregated to form embryoid bodies (henceforth called embryoids) and responded within 3 days with significant expression of NANOS3-mCherry and tissue-nonspecific alkaline phosphatase (TNAP), a PGC and pluripotency marker in humans and mice (Figure 1B). The intensity of the NANOS3-mCherry reporter increased progressively until day 4–5, resulting in ~27% of NANOS3/TNAP double-positive putative hPGCLCs (Figures 1B and S1B). Similar to mice, hPGCLCs do not proliferate significantly after 5 days under these conditions (Hayashi et al., 2011). The response was highly reproducible in three independent male and female NANOS3-mCherry hESC lines. Both BMP2 and/or BMP4 (with LIF, SCF, and EGF) were effective in inducing hPGCLC (Figure S1C) in a dose-dependent manner in the range of 50–500 ng/ml (Figures S1D and S1E).

The NANOS3/TNAP double-positive putative hPGCLCs also expressed key PGC genes, including *NANOS3*, *BLIMP1*, *TFAP2C*, *STELLA*, *TNAP*, *KIT*, *OCT4*, and *NANOG*, as well as *PRDM14*, albeit with reduced levels compared to hESC (Figure 1C). Remarkably, *SOX17* was significantly upregulated,

whereas *SOX2* was downregulated in the putative hPGCLCs that reflects their expression in embryonic hPGCs and seminomas (de Jong et al., 2008; see Figure 2), which is not the case in mouse PGCs. Immunofluorescence confirmed that NANOS3-mCherry expression coincided with OCT4, NANOG, and TFAP2C in day 4 embryoids (Figures 1D and S1F), as did OCT4 with BLIMP1 (Figure S1F). This suggests that the NANOS3-mCherry-positive cells are very likely nascent germ cells.

RNA-Seq Analysis of hPGCLCs: Comparison with hPGCs and Seminoma

We carried out RNA sequencing (RNA-seq) on NANOS3/TNAP double-positive cells from day 4 embryoids and compared them with the gonadal hPGCs from week 7 male human embryos (Carnegie stage 18/19), which are equivalent to mouse ~E12.5–E13.5 PGCs (Leitch et al., 2013). These hPGCs retain key characteristics of earlier hPGCs but, consistent with their more advanced state, expresses later germ cell markers such as *VASA* and *DAZL*. We also included TCam-2, a human seminoma that originates from the germline in vivo (Looijenga et al., 2014).

Unsupervised hierarchical clustering of global gene expression showed that the hPGCLCs clustered with hPGCs and TCam-2, whereas 4i hESCs and preinduced cells (4i hESCs treated with bFGF and TGF β for 2 days) clustered together in another branch away from gonadal somatic cells (soma) (Figure 2A). Consistently, hPGCs were globally more related to hPGCLCs (Pearson correlation coefficient [r] = 0.85) and TCam-2 (r = 0.818) than to 4i hESCs (r = 0.799) and preinduced cells (r = 0.773) (Figure S2A).

A heat map of mRNA expression revealed that hPGCLCs and gonadal hPGCs shared expression of early PGCs (*BLIMP1*, *TFAP2C*, *DND1*, *NANOS3*, *UTF1*, *ITGB3*, and *KIT*) and pluripotency genes (*TNAP*, *OCT4*, *NANOG*, *PRDM14*, and *LIN28A*) but with a notable lack of *SOX2* expression (Figure 2C). Early mesoderm marker *T* was detected in hPGCLCs (Figure 2C), as in mouse early PGCs (Aramaki et al., 2013). Interestingly, expression of two endodermal genes, *SOX17* and *GATA4*, was detected in hPGCLCs, embryonic hPGCs, and TCam-2, which are absent in the mouse germline. Notably, we identified *CD38* expression in hPGCLCs/hPGCs and TCam-2, but not in hESCs or soma (Figures 2C and see also Figures 3A–3C). Overall, hPGCLCs indeed have germ cell characteristics consistent with hPGCs. Late germ cell markers, however, including *DAZL*, *VASA*, and *MAEL*, were only detected in hPGCs (Figure 2C). TCam-2 gene expression was similar to hPGCLCs, albeit with lower expression levels of *NANOS3*, *ITGB3*, and *T* and upregulation of a few somatic genes, e.g., *HAND1* and *RUNX1*. Immunofluorescence analysis validated the expression of BLIMP1, TFAP2C, and OCT4 in hPGCLCs/hPGCs and TCam-2 (Figures 2E–2H). Interestingly, PRDM14 showed nuclear localization in the majority of hPGCLCs but was predominantly enriched in the cytoplasm of hPGCs (Figure 2F). Importantly, although *SOX2* was undetectable, there was significant expression of *SOX17* in hPGCLCs, hPGCs, and TCam-2 (Figures 2G and 2H).

Given the similarities of hPGCLCs, hPGCs, and TCam-2, a three-way Venn diagram was plotted to investigate their relationships (Figure 2D). Out of 972 highly upregulated genes

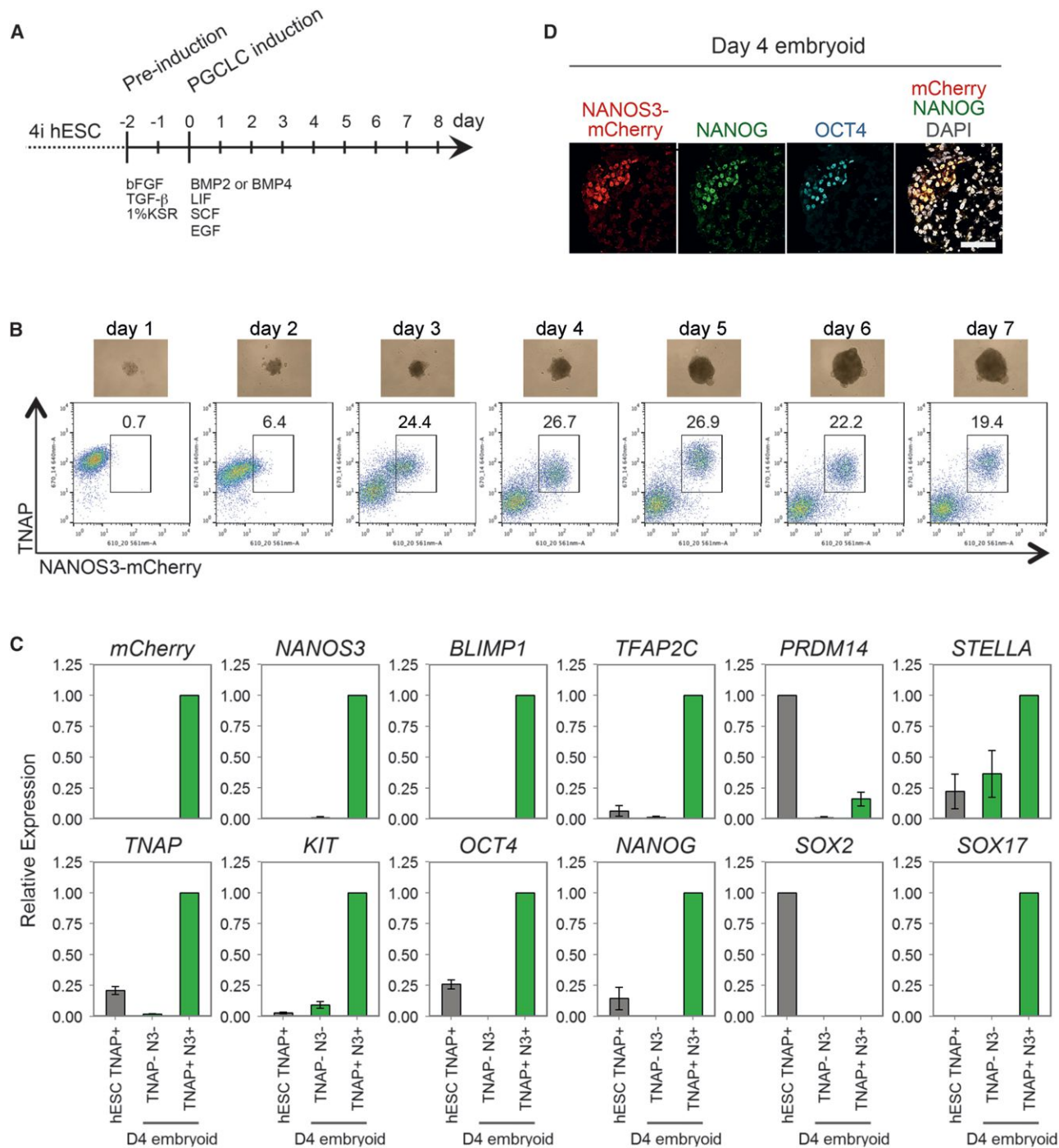


Figure 1. Specification of hPGCLCs from Human Embryonic Stem Cells

(A) Schematic protocol for hPGCLCs specification from hESCs.

(B) Development of day 1–7 embryoids derived from WIS2-NANOS3-mCherry hESCs. Top row: images of embryoids. Bottom row: FACS analysis of the dissociated embryoids with anti-TNAP-Alexa Fluor 647 and NANOS3-mCherry to detect hPGCLCs.

(C) Expression analysis by RT-qPCR of TNAP-positive 4i hESCs (hESC TNAP+), TNAP/NANOS3-mCherry-positive hPGCLCs (TNAP+N3+), and the remaining cells (TNAP-N3-) of day 4 embryoids (D4 embryoid). Relative expression levels are shown with normalization to β -ACTIN. Error bars indicate mean \pm SD from three independent biological replicates.

(D) Immunofluorescence of a day 4 embryoid showing coexpression of NANOS3-mCherry, NANOG, and OCT4 in hPGCLCs. Scale bar, 66 μ m.

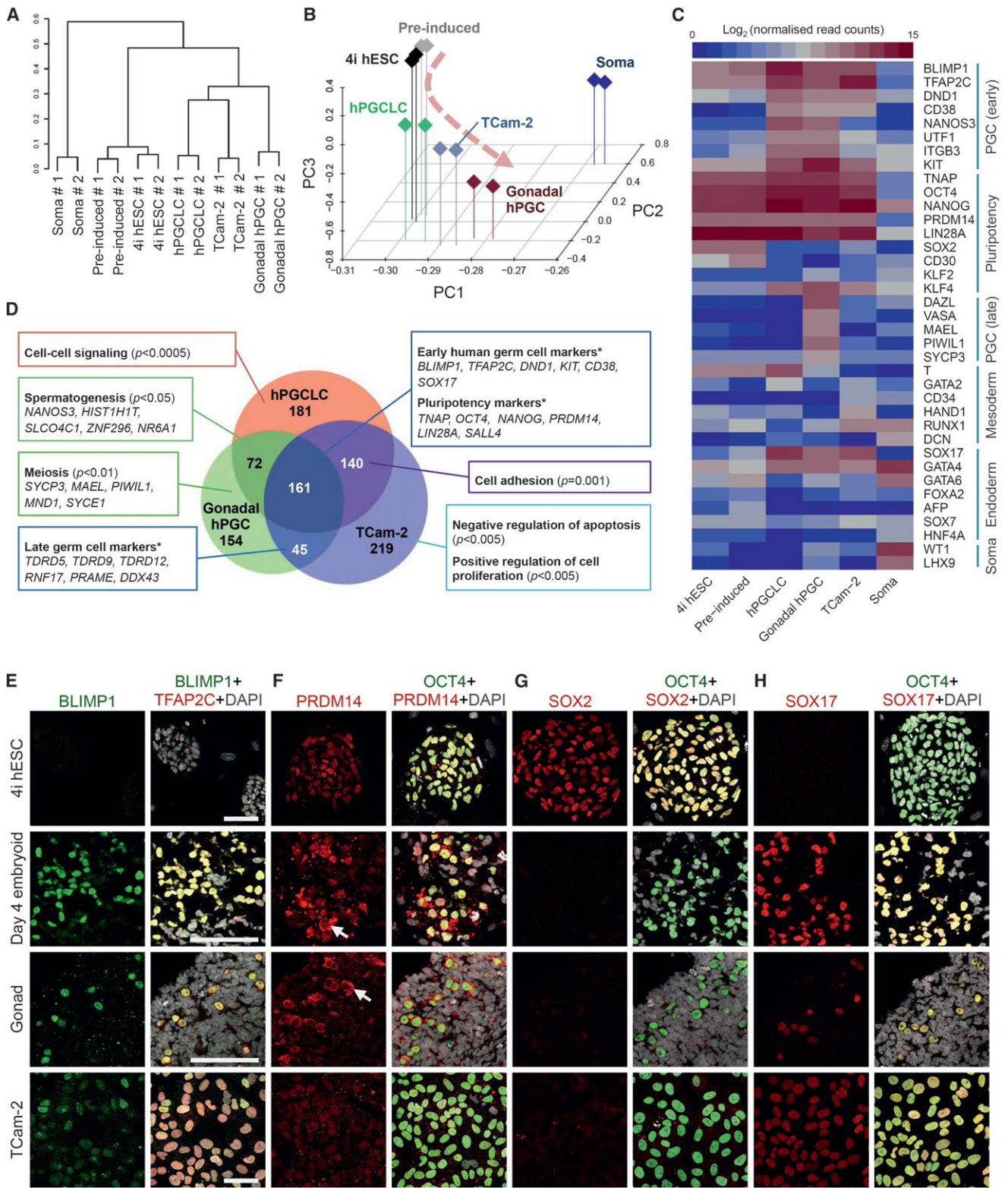


Figure 2. hPGCLC Shares Transcriptional Profile with Human Embryonic PGCs and TCam-2 Seminoma

(A) Unsupervised hierarchical clustering (UHC) of gene expression in 4i hESC, preinduced cells (Pre-induced), day 4 hPGCLCs (hPGCLC), gonadal hPGC, TCam-2, and gonadal somatic cell (Soma). RNA-seq was performed on two biological replicates (#1 and #2) for each cell type. (B) PCA of RNA-seq data. Arrowline indicates potential germline progression from 4i hESC to hPGCLC and gonadal hPGC.

(legend continued on next page)

compared to soma (Table S1), the three germline-related cell types shared expression of 161 genes, including pluripotency and germline-specific genes: *BLIMP1*, *TFAP2C*, *CD38*, *SOX17*, *OCT4*, and *NANOG* (Figure 2D). Gene ontology (GO biological process) analysis revealed (Table S1) that hPGCLCs from male cell line and male gonadal hPGCs were commonly enriched in “spermatogenesis” genes—for example, *NANOS3* and *HIST1H1T*—whereas meiosis-related *SYCP3*, *MAEL*, and *PIWIL1* genes were upregulated only in embryonic hPGCs (Figures 2C and 2D). Interestingly, TCam-2 and hPGCs revealed expression of a number of late germ cell markers, including Tudor-domain-containing *TDRD5*, *TDRD9*, and *TDRD12* genes, which have been implicated in PIWI-interacting RNA biogenesis pathway (Shoji et al., 2009) (Figure 2D). As expected, TCam-2 showed characteristics associated with cancer cells, including genes that promote cell proliferation with suppression of apoptosis genes (Figure 2D). Altogether, hPGCLCs, TCam-2, and hPGCs share key germ cell characteristics and expressed the core germ cell genes, including *CD38*, whereas the differentially expressed genes reflected their corresponding stages of development and cell identity.

Principal component analysis (PCA) further illustrates the relationships between the different cell types. PCA reduces dimensionality of whole-genome expression data by transforming into principal components (PCs), in which the variance within the dataset is maximal. A three-dimensional (3D) PCA plot of the first three PCs showed that the 4i hESC, soma, and hPGC-related cells (hPGCLCs, gonadal hPGCs, and TCam-2) settled at three discrete positions (Figure 2B). In particular, hPGCLCs, TCam-2, and gonadal hPGCs aligned together at the lower extreme of PC2, whereas 4i hESCs and preinduced cells formed a distinct cluster with medium PC2 scores and soma at the upper extreme (Figures 2B and S2B). The relative contributions (weights) of key germ cell, pluripotency, and gonadal somatic genes to PC2 and PC3 were plotted as two-dimensional (2D) loading plot alongside a corresponding 2D PCA plot (Figure S2B). Indeed, the weights of germ cell, pluripotency, and somatic genes highly overlap with the position of germ-cell-related cell types, hESCs, and soma, respectively. Germ-cell-related genes, such as *SOX17*, *CD38*, and *NANOS3* loaded heavily for lower extreme of PC2, where hPGCLCs, TCam-2, and gonadal hPGCs were aligned. There was a clear difference in weights of early germ cell genes (commonly expressed in hPGCLCs, TCam-2, and gonadal hPGCs—for example, *BLIMP1* and *TFAP2C*) and late germ cell genes (expressed only in gonadal hPGCs or TCam-2—for example, *VASA* and *DAZL*) on PC3, with the latter weighing more heavily toward low PC3 scores (Figure S2B). Notably, decreasing scores of PC3 reflected potential progression of germ cell development from hPGCLCs toward gonadal

hPGCs, whereas TCam-2 aligned between hPGCLCs and gonadal hPGCs (Figures 2B and S2B).

Taken together, hPGCLCs demonstrate germ cell characteristics that are apparently en route to hPGCs, whereas our objective analysis placed TCam-2 in an intermediate position, which reflects their origin from hPGCs in vivo. Notably, hPGCLCs evidently represent the earliest stages of the human germ cell lineage, indicating that our in vitro model provides an important opportunity to explore the mechanism of hPGC specification, which is otherwise not possible because E9–E14 postimplantation human embryos are excluded from investigations. TCam-2 and other seminomas might, however, also serve as important in vitro models of human germ cell biology (Looijenga et al., 2014; Schafer et al., 2011).

CD38: A Core Marker of Human Germ-Cell-Related Cells and Initiation of the Epigenetic Program

CD38, an established cell-surface glycoprotein on leukocytes, is a prognostic marker of leukemia (Malavasi et al., 2008). Surprisingly, we detected *CD38* expression in hPGCLCs, gonadal hPGCs, and TCam-2, but not in hESCs or gonadal somatic cells (Figure 2C). Indeed, fluorescence-activated cell sorting (FACS) analysis showed that CD38 is present on all the TNAP-positive embryonic hPGCs and on TCam-2 with some heterogeneity (Figures 3B and 3C). Although CD38 is absent on hESCs, ~50% of the NANOS3-mCherry-positive hPGCLCs were CD38 positive on day 4 (Figure 3A), which increased to ~70% by day 5 (Figure 3A). Interestingly, the NANOS3-mCherry/CD38 cells had higher expression of *NANOS3*, *BLIMP1*, *SOX17*, *OCT4*, and *NANOG* (Figure 3D). By contrast, hESCs and embryonic carcinoma cells exhibit *CD30* (also known as *TNFRSF8*) and *SOX2* (Figures 3D and 2G) (Pallesen and Hamilton-Dutoit, 1988). Thus, CD38 and CD30 could potentially be used as additional markers of germ cell tumors in vivo (Figure 7D).

The RNA-seq of hPGCLC also revealed gene expression changes that indicate initiation of the epigenetic program with downregulation of *UHRF1*, *DNMT3A*, and *DNMT3B* and upregulation of *TET1* and *TET2* (Figure S3D). Notably, we found a significant increase in 5-hydroxymethylcytosine (5hmC) in hPGCLCs, which is consistent with an increase in the expression of *TET1*, an enzyme that converts 5-methylcytosine (5mC) to 5hmC (Figures 3E–3G), together with a small but significant decline in 5mC (Figures 3G and S3A). This indicates that, as in the mouse PGCs, loss of 5mC might be coupled with the conversion of 5mC to 5hmC (Hackett et al., 2013). At the same time, we detected a decline in the expression of de novo DNA methyltransferase 3A (*DNMT3A*) and *UHRF1* in hPGCLCs compared to the neighboring somatic cells in the embryoids (Figures 3G, S3B, and S3C). *UHRF1* targets *DNMT1* to replication foci to

(C) Heat map of gene expression of key PGC-associated genes (early and late) and of pluripotency, mesoderm, endoderm, and gonadal somatic (Soma) markers. (D) Venn diagram illustrates common and differentially expressed genes. Significantly upregulated genes in hPGCLC, gonadal hPGC, and TCam-2 (with log₂ (fold change) > 3 and adjusted p value < 0.05 versus gonadal Soma, respectively) were compared. Representative genes that were exclusive to each category are indicated. Text boxes indicate gene ontology biological processes (BP) terms that were significantly enriched as indicated by p values. Asterisk denotes custom categories absent from BP annotation.

(E–H) Immunofluorescence analysis for (E) *BLIMP1*, (F) *PRDM14*, (G) *SOX2*, and (H) *SOX17* on 4i hESCs (top row), day 4 hPGCLC embryoids (second row), human week 7 male gonad (third row), and TCam-2 (bottom row). Samples were counterstained with *TFAP2C* or *OCT4* to identify hPGCLCs in embryoids and hPGCs in embryonic gonad. Arrows indicate cytoplasmic enrichment of *PRDM14* (F). Scale bars, 70 μm.

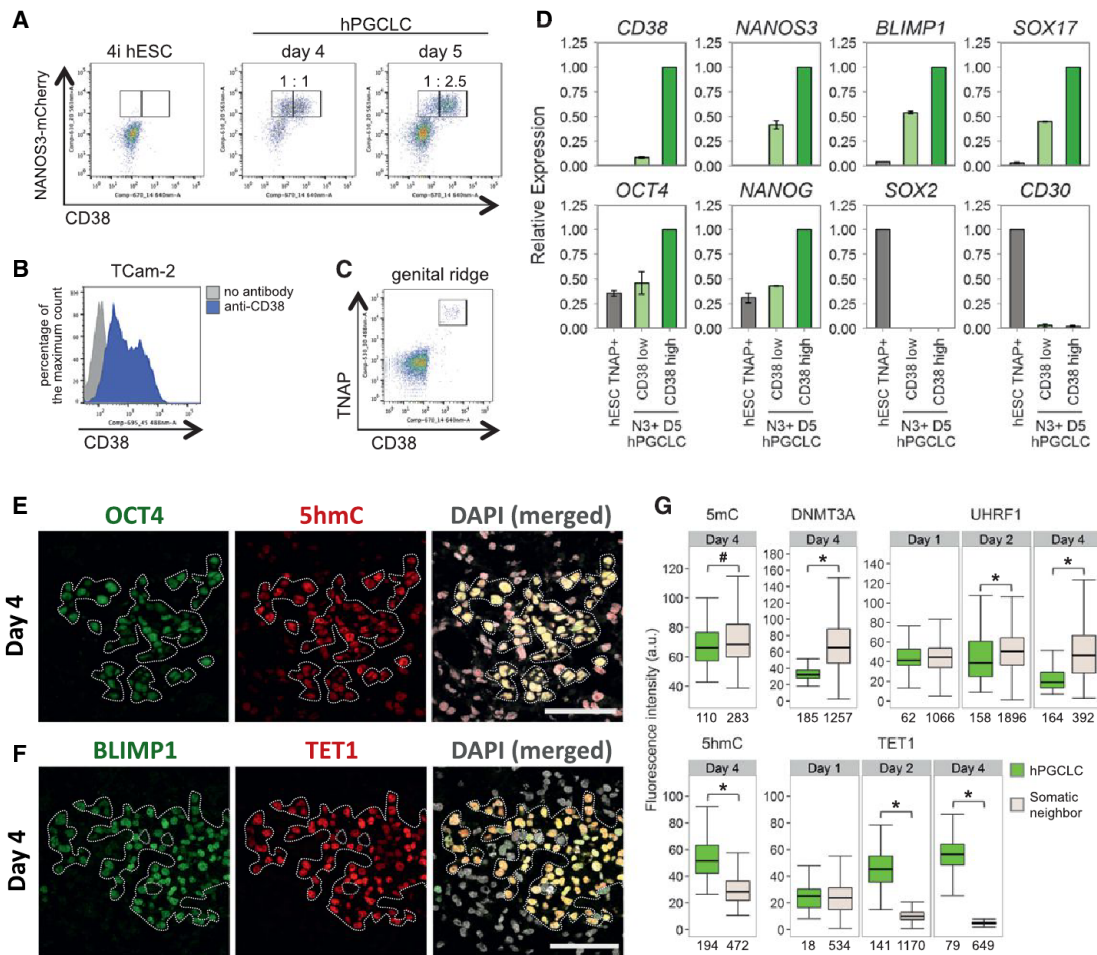


Figure 3. CD38 Expression in Human Germ-Cell-Related Cells and Epigenetic Changes in hPGCLCs

(A) FACS analysis of NANOS3-mCherry and CD38 on WIS2-NANOS3-mCherry cell line cultured in 4i medium and on day 4 and 5 embryoids following hPGCLC induction. Ratios of CD38 low and high expression in the NANOS3-mCherry-positive cells are indicated. (B) FACS histogram of CD38 low and high populations in Tcam-2. (C) FACS analysis of CD38 and TNAP on genital ridges isolated from a week 6 human embryo. (D) Expression analysis by RT-qPCR for FACS-sorted TNAP-positive 4i hESCs (TNAP+ hESC) and CD38 low or high/NANOS3-mCherry day 5 hPGCLCs. Relative expression levels are shown with normalization to β -ACTIN. Error bars indicate mean \pm SD from two independent biological replicates. (E and F) Immunofluorescence analysis for 5hmC (E) and TET1 (F) on day 4 embryoids cryosection. OCT4 or BLIMP1 were used to identify hPGCLCs (highlighted). Scale bars, 50 μ m. (G) Quantification of immunofluorescence intensity of various epigenetic marks/modifiers in hPGCLCs and somatic neighbors in day 1–4 embryoids (see also Figures S3A–S3C). For UHRF1, only KI-67-positive (proliferating) cells were used for quantification. Numbers below each box denotes number of cells analyzed. Black central line represents the median, boxes and whiskers represent the 25th and 75th, and 2.5th and 97.5th percentiles, respectively. Wilcoxon signed-rank test was used to test for statistical significance. #p < 0.05; *p < 0.0001.

confer maintenance of DNA methylation (Liu et al., 2013). The repression of UHRF1 in proliferating (KI-67-positive) hPGCLCs would allow DNA-replication-coupled loss of 5mC, which is analogous to the observations on the early mouse germline.

Taken together, day 4 hPGCLCs, which are the nascent human germ cells, already showed evidence for the initiation of epigenetic changes and DNA demethylation that are comparable to E8 mouse PGCs (Hackett et al., 2013). Notably, we also found that PRMT5, an arginine methyltransferase that was ubiquitously but weakly present in the cytoplasm of day 1 and 2 embryoids, showed enhanced expression in the nucleus of

day 4–8 hPGCLCs (Figure S3E). This is a shared characteristic with ~E8 mouse PGCs, hPGCs, and Tcam-2 seminoma (Eckert et al., 2008). The translocation of PRMT5 to the nucleus is important for the suppression of transposable elements at the onset of DNA demethylation (Kim et al., 2014).

Sequential Gene Expression during hPGCLC Specification in Embryoids

Having established similarities between hPGCLCs and the authentic hPGCs, we set out to investigate the mechanism of hPGCLC specification. First, for establishing the precise

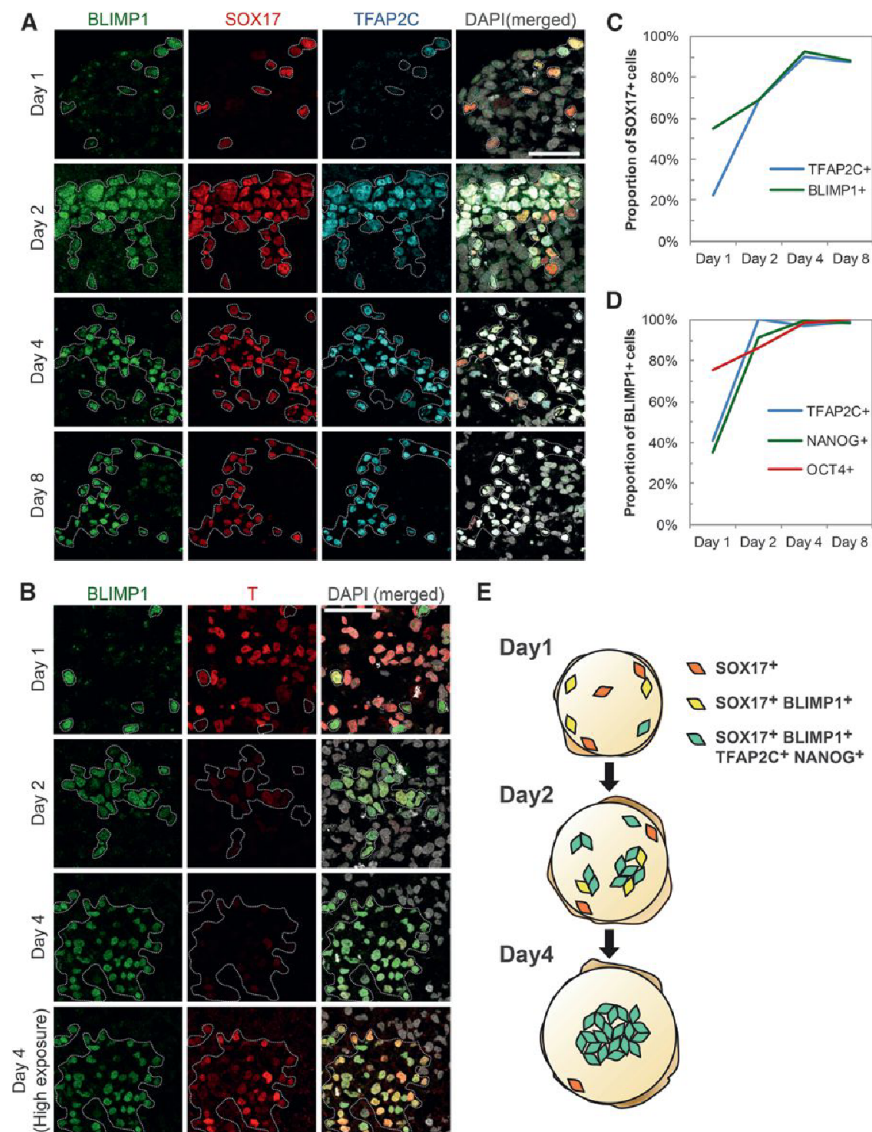


Figure 4. Sequential Expression of Germ-Cell-Related Transcription Factors in Single Cells during hPGCLC Specification

(A and B) Immunofluorescence analysis for (A) BLIMP1, SOX17, and TFAP2C and (B) BLIMP1 and T in cryosections of day 1–8 embryoids after hPGCLC induction. Bottom row in (B) shows high exposure (digital) image of T, indicating low but specific expression in hPGCLC. SOX17-positive or BLIMP1-positive cells are highlighted. Scale bars, 50 μ m.

(C) Percentage of SOX17-positive (+) cells in day 1–8 embryoids that were also TFAP2C+ or BLIMP1+. Corresponds to data in Figure 4A.

(D) Percentage of BLIMP1-positive (+) cells in day 1–8 embryoids that were TFAP2C+, NANOG+, or OCT4+. Corresponds to data in Figures 4A, S4A, and S4B.

(E) Summary model for dynamics of hPGCLC specification in embryoids. SOX17-positive cells are first scattered in day 1 embryoids. They gain expression of BLIMP1, TFAP2C, and NANOG sequentially and form a cluster from day 2 onward until the formation of nascent hPGCLC.

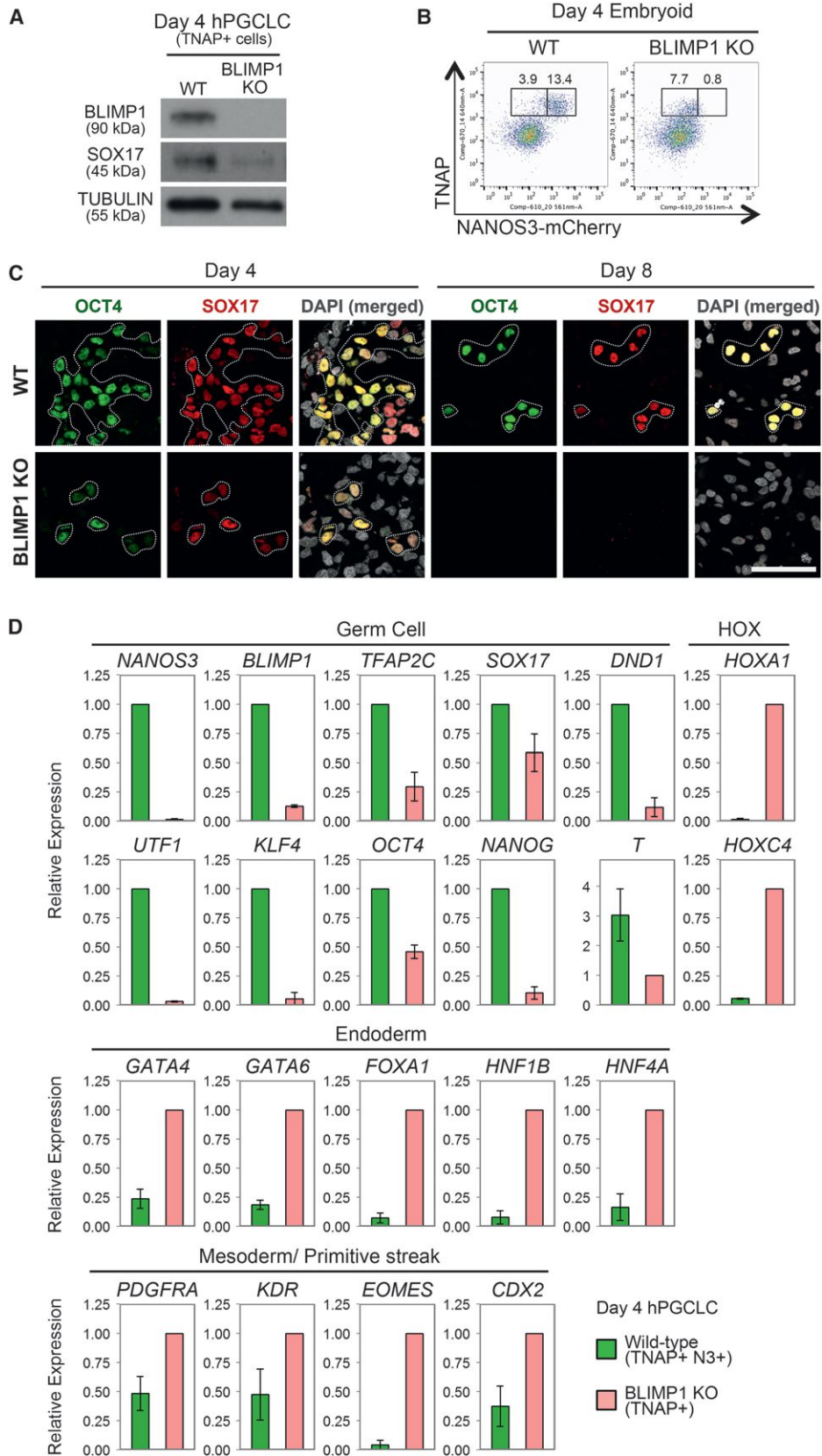
Expression of T is of particular interest, as it signifies competence for germ cell fate in mice, and BMPs can induce it in hESCs (Bernardo et al., 2011; Yu et al., 2011). Notably, expression of T was high in the majority of cells on day 1, except for most of the BLIMP1+ cells (Figure 4B). By day 2, however, T was dramatically downregulated in most cells, although now the BLIMP1+ nascent hPGCLC retained low T expression, which persisted until at least day 4 (Figure 4B), consistent with the T transcripts detected by RNA-seq (Figure 2C). It is possible that BMP signaling may initially enhance expression of T in the embryoids (Bernardo et al., 2011), and it is from this population

sequence of expression of the key hPGC-related genes at the resolution of single cells, we performed systematic time course analysis by immunofluorescence on day 1–8 embryoids after hPGCLC differentiation.

On day 1, we first detected SOX17 in a few widely scattered cells throughout the embryoids (Figures 4A and 4E). Among the SOX17-positive (+) cells, 55% were also BLIMP1+, and 22% were TFAP2C+ (Figures 4A and 4C). However, all BLIMP1+ cells coexpressed SOX17, suggesting that SOX17 is upregulated before BLIMP1. The proportion of BLIMP1+ and TFAP2C+ cells increased to ~70% on day 2 and to ~90% on days 4–8 (Figures 4A and 4C). These triple-positive cells likely represent specified hPGCLCs, as they also coexpressed other key hPGC genes. However, ~10% of single SOX17+ cells failed to undergo hPGCLC specification but persisted in day 4–8 embryoids. These may be aberrant cells or else may belong to other lineages.

that hPGCLCs are specified, which reflects the events during mouse PGC induction (Aramaki et al., 2013).

Expression of OCT4 was low but widespread in the day 1 embryoids, including 75% of the BLIMP1+ cells (Figures S4B and 4D). Although the overall OCT4 expression declined dramatically in day 2 embryoids, it was strongly expressed in ~86% of the BLIMP1+ cells. Subsequently, all BLIMP1+ cells became highly OCT4+ by day 4. By contrast, NANOG was expressed in ~35% of BLIMP1+ cells on day 1, but it was generally absent in other cells in the embryoids (Figures 4D and S4A). Thereafter, NANOG was also rapidly upregulated in the majority of BLIMP1+ cells by day 2–4. The upregulation of key pluripotency genes, such as OCT4 and NANOG, is also reminiscent of their re-expression in mouse PGCs (Magnúsdóttir et al., 2013). Although NANOS3-mCherry expression was weakly detected in 24% of OCT4+ cells at day 2 (Figure S4C), it was detected in all OCT4+ cells on day 4, confirming their PGCLC identity.



(legend on next page)

PRDM14 is a key regulator of pluripotency in mouse and human ESCs (Chia et al., 2010; Grabole et al., 2013; Ma et al., 2011; Yamaji et al., 2013) and is a key regulator of mouse PGC specification (Yamaji et al., 2008). PRDM14 was generally down-regulated in day 1–2 embryoids but was detectable in the nucleus of most BLIMP1+ cells by day 4 (Figure S4A). Notably, in a minority of BLIMP1/NANOG-positive hPGCLCs at day 8, PRDM14 was enriched in the cytoplasm (Figure S4A), which was the case in most of the gonadal hPGCs (Figure 2F). This is in marked contrast to the persistent nuclear PRDM14 expression in mouse PGCs (Grabole et al., 2013).

The SOX17/BLIMP1 double-positive cells were initially distributed randomly in day 1 embryoids (Figure 4A) but were then loosely organized in clusters and often a single cluster in day 2 embryoids. By day 4, generally one and occasionally two tight clusters of hPGCLCs were observed either at the core or periphery of each embryoid (Figure 4E). Cumulative observations suggest that SOX17/BLIMP1 might be among the key regulators of hPGCLC specification. Although OCT4 and NANOG were detected between days 1 and 2 in conjunction with NANOS3-mCherry and other PGC-specific genes from days 2–4, PRDM14 was upregulated more gradually in hPGCLCs and was subsequently detected in the cytoplasm of embryonic hPGCs. Following the early expression of SOX17 and BLIMP1 in hPGCLCs, these two transcription factors were also detected in embryonic hPGCs in vivo, as well as in Tcam-2 (Figures 2E and 2H). These observations suggest that SOX17-BLIMP1 might be among the critical determinant of hPGC specification and maintenance.

Role of BLIMP1 during hPGCLC Specification

BLIMP1 is the first and key regulator of mouse PGC, and loss of function abrogates PGC fate (Ohinata et al., 2005; Vincent et al., 2005). However, BLIMP1 expression is apparently downstream of SOX17 in hPGCLCs (Figures 4A and 4C). We examined its mechanistic role by generating *BLIMP1* knockout (KO) NANOS3-mCherry hESC line (Figure S5A). These cells showed loss of BLIMP1 by western blot (Figure 5A) and immunofluorescence (Figure S5B) on day 4 of hPGCLCs induction. Notably, there was also a loss of NANOS3-mCherry-positive cells, together with a significant reduction of NANOG, OCT4, and TFAP2C expression on day 4 (Figures 5C and S5B), indicating a failure of hPGCLC specification, and all of these cells disappeared by day 8 (Figure 5C). However, we detected ~8% of TNAP-positive cells in day 4 embryoids (Figure 5B). This observation is highly reminiscent of the effects of *Blimp1* mutation on mouse PGC specification (Ohinata et al., 2005).

We isolated and characterized the TNAP-positive cells by FACS and confirmed loss of *BLIMP1*, except for low expression

of mutant transcripts (Figure 5D). These cells also showed loss of *NANOS3*, *UTF1*, and *KLF4* and reduced expression of *TFAP2C*, *DND1*, *OCT4*, *NANOG*, and *T* (Figures 5D and S5B). In addition, they showed prominent upregulation of mesodermal/primitive streak and *HOX* genes, as well as endodermal genes, including *GATA4*, *GATA6*, *FOXA1*, *HNF1 β* , and *HNF4 α* (Figure 5D). By contrast, endodermal genes were not upregulated in *Blimp1* mutant mouse PGCs (Kurimoto et al., 2008; Vincent et al., 2005). This suggests that BLIMP1 probably suppresses endoderm and other somatic genes, which might otherwise be induced by SOX17 and BMP signaling during hPGCLCs specification (Figure 6H). Loss of *BLIMP1* and *TFAP2C* also caused upregulation of *HOX* genes in Tcam-2 (Weber et al., 2010). This suggests that one of the roles of BLIMP1 is to continually suppress the somatic program during human germline development.

SOX17 Is the Key Regulator of hPGCLCs, which Acts Upstream of BLIMP1

Expression of SOX17 among T-positive cells prior to BLIMP1 apparently marks the onset of hPGCLC specification, which is a key difference between the specification of human and mouse germline fate (see Figure 4). Notably, SOX17 and BLIMP1 are also expressed in the authentic in vivo hPGCs and in Tcam-2 (de Jong et al., 2008) (Figure 2). Knockdown of SOX17 in Tcam-2, which exhibits key germ cell characteristics (Looijenga et al., 2014) (Figure 2), induced repression of the pluripotency genes *NANOG*, as well as of the PGC-genes *BLIMP1*, *NANOS3*, *TFAP2C*, *STELLA*, and *KIT* (Figure S6A). This suggests that SOX17 might be important for regulating the established germline gene expression network.

We addressed the role of SOX17 during hPGCLC specification by generating *SOX17* KO NANOS3-mCherry hESC line (Figure S6B) and validated absence of SOX17 expression in day 4 embryoids from mutant cells by western blot and immunofluorescence (Figures 6A and S6C). Notably, we did not detect any NANOS3-mCherry or TNAP-positive cells in the embryoids from *SOX17* mutant cells (Figure 6B). Further, RT-qPCR analysis of day 4 *SOX17* null embryoids showed absence of *NANOS3*, *TFAP2C*, *DND1*, *UTF1*, *KLF4*, *OCT4*, *NANOG*, and, importantly, *BLIMP1* (Figure 6C). Instead, there was upregulation of mesodermal genes *PDGFRA*, *KDR*, and *HOXA1* (Figure 6C). Although a few TFAP2C-positive cells were detected on day 4, they were BLIMP1 negative and most likely belong to other lineages (Figure S6C).

To determine whether SOX17 acts cell autonomously, we mixed wild-type NANOS3-mCherry hESCs with the *SOX17* null hESCs in 1:1 ratio during induction of hPGCLCs by cytokines.

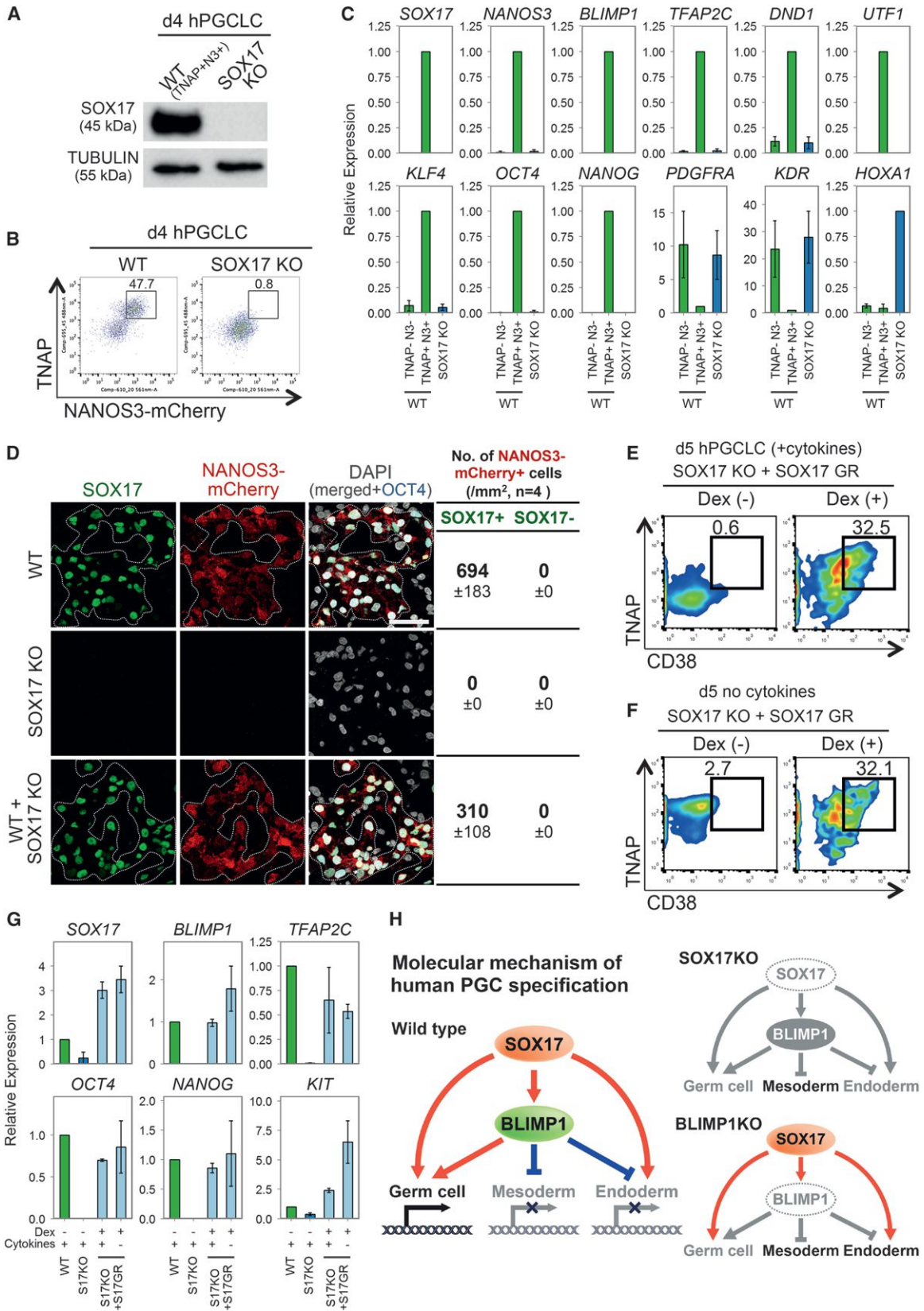
Figure 5. Role of BLIMP1 in hPGCLC Specification

(A) Western blot analysis of BLIMP1 and SOX17 in TNAP-positive (TNAP+) cells sorted from wild-type (WT) and BLIMP1 knockout (BLIMP1 KO) day 4 embryoids after hPGCLC induction. TUBULIN was used as loading control.

(B) FACS analysis of TNAP and NANOS3-mCherry on WT and BLIMP1 knockout (BLIMP1 KO) day 4 embryoids.

(C) Immunofluorescence for OCT4 and SOX17 in cryosections of WT and BLIMP1 KO day 4 and 8 embryoids. OCT4-positive cells are highlighted. Scale bar, 50 μ m.

(D) Expression analysis by RT-qPCR for WT TNAP/NANOS3-mCherry double-positive cells (WT; TNAP+N3+) and BLIMP1 KO TNAP single-positive cells (BLIMP1 KO; TNAP+) sorted from day 4 embryoids. Relative expression levels are shown with normalization to β -ACTIN. Error bars indicate mean \pm SD from two independent biological replicates.



(legend on next page)

All NANOS3-mCherry positive cells detected by immunofluorescence on day 4 were SOX17 positive (Figure 6D), indicating that SOX17 null hESCs did not undergo hPGCLC specification even in the presence of wild-type cells. The overall number of NANOS3-mCherry-positive cells in the embryoid with mixed cells was about half of that in the control consisting of wild-type cells only (Figure S6D), suggesting that SOX17 null cells did not affect PGCLC induction from wild-type cells. Thus, SOX17 null cells have intrinsic defect for hPGCLC specification.

To determine the competency of the SOX17 null hESCs, we transfected an inducible SOX17 fusion construct with human glucocorticoid receptor ligand-binding domain (GR) into the SOX17 null hESCs. This would allow dexamethasone (Dex) to activate the SOX17-GR and induce translocation of SOX17 fusion protein from the cytoplasm into the nucleus (Brocard et al., 1998). After 5 days of induction with cytokines and Dex in the SOX17 null SOX17-GR hESCs, expression of germ cell genes *BLIMP1*, *TFAP2C*, *OCT4*, *NANOG*, and *KIT* and the TNAP/CD38-positive population was restored (Figures 6E and 6G). This demonstrates that SOX17 null hESCs maintain competency for hPGCLC specification. Strikingly, activation of SOX17 alone in the absence of cytokines was sufficient to induce germ cell genes and TNAP/CD38-positive cells from 4i hESCs (Figures 6F and 6G). Taken together, SOX17 is indispensable and sufficient for hPGCLC gene induction from competent hESCs, and it acts upstream of BLIMP1 and other genes to initiate the human germ cell transcriptional network (Figure 6H). Interestingly, loss of SOX17 in TCam-2 also causes a repression of germ-cell- and pluripotency-associated genes (Figure S6A). This suggests that SOX17 might also be important for the maintenance of the germ cell state because it is also highly expressed in embryonic hPGCs.

Specification of hPGCLCs from Germ-Cell-Competent hESC/hiPSCs

Because gene expression of hESCs in 4i medium resembles that of hESC after preinduction for 2 days in bFGF/TGF β (Figures 2A, 2B, and S2A), we decided to investigate hPGCLC induction directly in hESCs maintained in 4i medium (Figure 1A). Indeed, hPGCLCs could be induced directly from 4i hESCs

with apparent enhanced response resulting in ~46% hPGCLCs (Figure 7A). These hPGCLCs showed a slightly higher intensity of NANOS3/TNAP by FACS, and a greater proportion of them were CD38 positive (Figure 7A). Notably, cells maintained for more than 2 weeks in the conventional hESC medium, regardless of whether they were initially maintained in 4i medium, showed a significantly lower numbers of hPGCLCs (~5%) with a reduced intensity of NANOS3-mCherry/TNAP and CD38 expression (Figure 7A). This demonstrates that hESCs in 4i medium are highly competent for the hPGCLC fate. Importantly, the competent state is conferred reversibly because it is gained and lost in 4i and conventional culture conditions, respectively.

Global gene expression analysis indicated overall similarities between hESCs in the conventional medium versus those in “4i” medium ($r = 0.923$) but with notable differences (Figure S7A). Although these cells showed similar expression levels of core pluripotency factors *OCT4*, *NANOG*, and *SOX2*, 4i hESCs had higher expression of mesoderm and gastrulation genes, including *T*, *RUNX1*, and *PDGFRA* (Figures S7B and S7C and Table S2). Furthermore, OCT4-positive cells in 4i hESCs had varying levels of T protein, possibly due to inhibition of GSK3 β (Chen et al., 2013), which is not the case in hESC cultured in conventional condition (Figure S7D). These differences might be relevant for the mechanism of competence of ESCs for PGCLC, which merits further investigation.

We also asked whether hiPSCs could be used to generate and isolate hPGCLCs using the combination of surface markers CD38 with TNAP (Figures 2C and 3A–3D). Using FX71.1 hiPSCs (see Experimental Procedures) maintained in 4i medium for >2 weeks that lack CD38 expression, we detected ~31% of TNAP/CD38 double-positive cells after 4 days in response to cytokines (Figure 7B). TNAP/CD38 double-positive hPGCLCs showed expression of *NANOS3*, *BLIMP1*, *TFAP2C*, *SOX17*, *STELLA*, *T*, *OCT4*, *NANOG*, and *PRDM14*, but not of *SOX2* (Figure 7C). Similar results were obtained with another hiPSC line (C1, Gafni et al., 2013). Thus, hPGCLC specification could be induced efficiently and directly in hiPSCs that are maintained in the 4i medium, which could be used for disease modeling using patient-derived iPSCs.

Figure 6. Role of SOX17 in hPGCLC Specification

(A) Western blot analysis of SOX17 expression of WT day 4 TNAP/NANOS3-mCherry-positive hPGCLCs (WT, TNAP+N3+), and whole SOX17 knockout day 4 embryoids. TUBULIN was used as loading control.

(B) FACS analysis of TNAP and NANOS3-mCherry on WT and SOX17 KO day 4 embryoids.

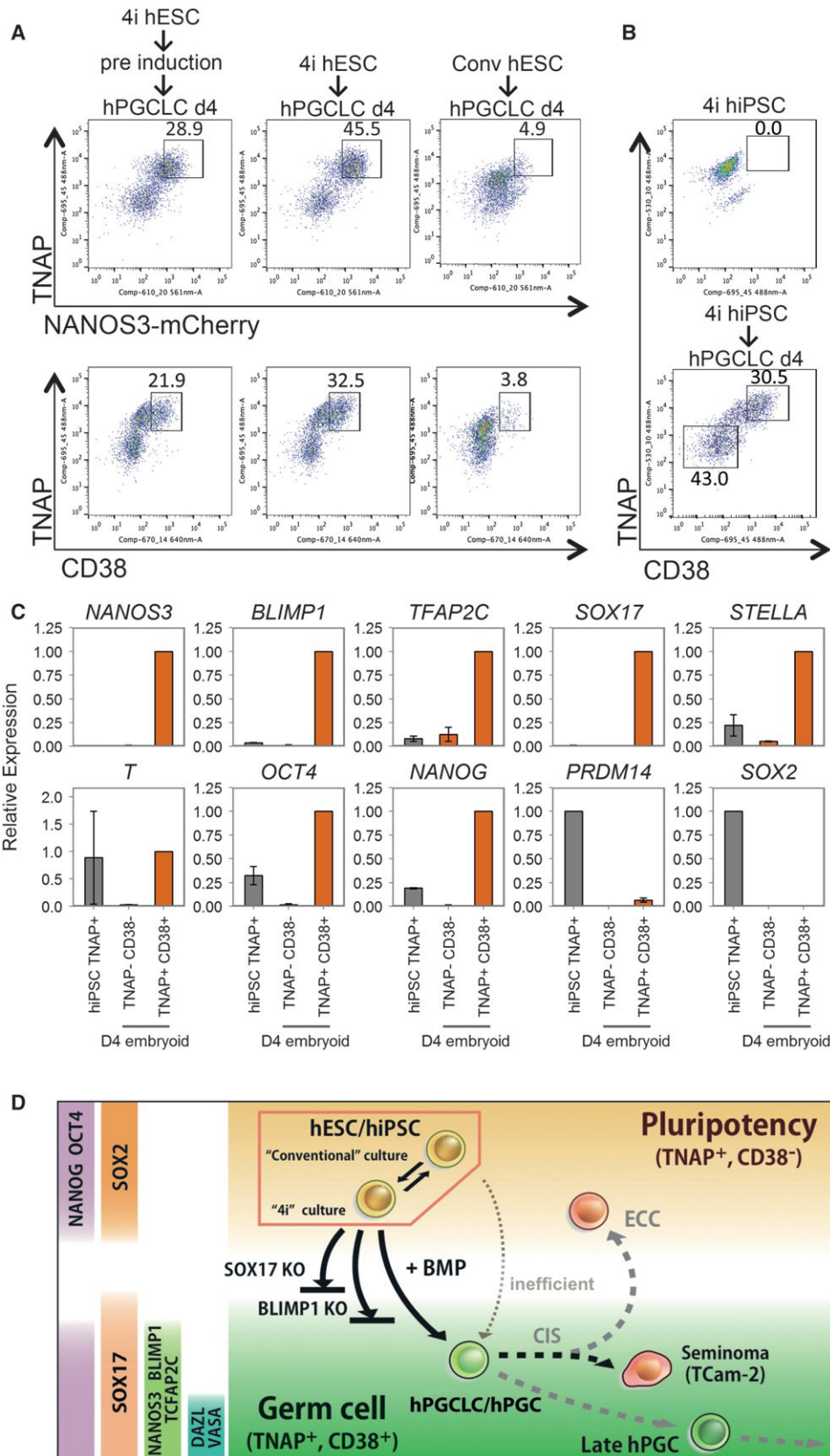
(C) RT-qPCR analysis of TNAP/NANOS3-mCherry FACS-sorted WT double-negative (TNAP-N3-) or -positive (TNAP+N3+) cells sorted from day 4 embryoids and whole SOX17 KO embryoids (SOX17 KO). Relative expression levels are shown with normalization to β -ACTIN. Error bars indicate mean \pm SD from two independent biological replicates.

(D) Immunofluorescence of day 4 embryoids derived from WT, SOX17 knockout (SOX17 KO), and from 1 to 1 mixture of WT and SOX17 KO 4i hESCs. The number of NANOS3-mCherry+ cells with or without SOX17 expression is shown. Quantification was based on seven to nine confocal images from four independent embryoids of each condition. Scale bars, 50 μ m.

(E and F) FACS analysis of TNAP and CD38 on day 5 embryoids derived from SOX17 knockout 4i hESCs containing SOX17 fusion construct with human glucocorticoid receptor ligand-binding domain (SOX17 KO+ SOX17 GR). Embryoids were derived in the presence (E) or absence (F) of cytokines with (Dex+) or without (Dex-) addition of dexamethasone.

(G) RT-qPCR analysis of day 5 hPGCLC derived from WT and SOX17 KO (S17KO) and SOX17 KO + SOX17-GR (S17KO+S17GR) hESCs with (+) or without (-) dexamethasone (Dex) and in the presence (+) or absence (-) of cytokines. FACS-sorted NANOS3-mCherry/TNAP double-positive cells or whole embryoids (for S17KO) were used. Relative expression levels are shown with normalization to *GAPDH*. Error bars indicate mean \pm SD from two biological replicates.

(H) Model for establishment of hPGC transcription network by SOX17 and BLIMP1. SOX17 induces germ cell genes and, potentially, endoderm gene. Expression of BLIMP1, downstream of SOX17, suppresses endodermal genes, as well as mesodermal genes. As a result, the SOX17-BLIMP1 axis initiates hPGC program from competent cells upon induction by BMP signaling. The hPGC specification gene network is abrogated in the absence of SOX17 or BLIMP1.



(legend on next page)

DISCUSSION

Specification of hPGCLCs from germ cell competent hESC/hiPSC provides a unique mechanistic view of the establishment of the human germline (Figure 7D). Notably, SOX17 is the key regulator of hPGCLC specification, whereas BLIMP1 represses endodermal and other somatic genes during hPGCLC specification. This was unexpected because the primary role of SOX17 is in the endoderm (D'Amour et al., 2005; Kanai-Azuma et al., 2002) and because *Sox17* has no detectable role in the specification of mouse PGCs (Hara et al., 2009; Kanai-Azuma et al., 2002). A comparison among hPGCLCs, embryonic hPGCs, and Tcam-2 seminoma (Looijenga et al., 2014; Schafer et al., 2011) also establishes the likely progression of the early human germline (Figure 2B).

During hPGCLC specification from hESCs, SOX17 was first detected in a few scattered cells in day 1 embryoids, which showed expression of T. The nascent hPGCLCs subsequently form a few or a single cluster in day 4–8 embryoids. SOX17 is indeed essential for hPGCLC specification, and this gene alone is sufficient to induce germ cell genes in the *SOX17* mutant cells, with or without cytokines from 4i hESCs. SOX17 acts cell autonomously, and the presence of mutant cells in embryoids had no effect on hPGCLC specification from wild-type cells. It will be of interest to see how SOX17, with or without BLIMP1, determines cell fates between germ cell, hematopoietic, and endodermal lineages (Nakajima-Takagi et al., 2013; Clarke et al., 2013).

Expression of BLIMP1 is intimately associated with SOX17 during hPGCLC specification. BLIMP1 represses somatic genes, including mesendodermal genes, which might allow SOX17 to function as the regulator of hPGCLCs specification. A mutation in BLIMP1 abrogates hPGCLC specification but without completely abolishing SOX17 expression. However, TNAP-positive cells were detected, in which PGC-specific genes were repressed but some endodermal and other somatic genes were upregulated. This suggests that BLIMP1 might repress them during hPGCLC specification, but not excluding its wider role in hPGCLC specification in conjunction with SOX17. In mice, BLIMP1 also represses somatic genes in PGCs (Ohinata et al., 2005; Vincent et al., 2005), but it is also a key determinant of PGC specification, together with PRDM14 and TFAP2C (Magnúsdóttir et al., 2013).

Although PRDM14 is critical for mouse PGC specification, its expression during hPGCLC specification is delayed and significantly diminished in hPGCs and is very low in Tcam-2 compared to hESCs. PRDM14 is crucial for maintaining pluripotency in human and mouse ESCs, although different signaling molecules

regulate its expression, and the genomic targets in ESCs also differ in the two species (Chia et al., 2010; Grabole et al., 2013; Ma et al., 2011; Yamaji et al., 2013). The rapid downregulation and delayed re-expression of PRDM14 at the onset of hPGCLC induction (Figures 2F and S4A) may allow exit of pluripotency from 4i hESC en route to germ cell differentiation. Interestingly, the human and mouse PRDM14 proteins have diverged, which might result in functional differences. There is expression of SOX2 in mouse PGCs, which is apparently regulated by PRDM14 (Grabole et al., 2013), whereas SOX2 is repressed in human hPGCLCs/hPGCs. BLIMP1 also apparently represses SOX2 during spontaneous differentiation of hPGCLCs from hESCs (Lin et al., 2014). By contrast, KLF4 is expressed in hPGCLCs/hPGCs (Figure 2C), but not in mouse PGCs (Kurimoto et al., 2008). The precise significance of the repression and expression of pluripotency genes, including NANOG, remains to be elucidated.

Germ cell neoplasia or carcinoma in situ (CIS) (Skakkebaek, 1972) can generate embryonal carcinoma cells that resemble hESCs or seminomas such as Tcam-2 that inherit key characteristics of germ cells (Looijenga et al., 2014; Schafer et al., 2011). Tcam-2 expresses *SOX17*, *BLIMP1*, *TFAP2C*, *KIT*, and *DND1* with low levels of *SOX2* and *PRDM14*. Knockdown of SOX17 in Tcam-2 induces repression of germ cell and pluripotency genes (Figure S6A), whereas knockdown of BLIMP1 and TFAP2C induced upregulation of somatic genes (Weber et al., 2010). These observations suggest that SOX17 and BLIMP1 might also be important for the maintenance of the early human germline. We found that CD38 is a marker of all human germline-related cells, including seminomas. Distinction between seminoma and embryonal carcinoma could therefore be made by the expression of SOX17/CD38 and SOX2/CD30, respectively (de Jong et al., 2008). Furthermore, CD38/TNAP are reliable markers for the isolation of hPGCLCs derived from hESC/hiPSC without any reporters.

The hPGCLCs also showed early signs of DNA demethylation, which is consistent with the germline-specific epigenetic program. The striking upregulation of 5hmC concomitantly with TET1 suggests that, similar to mouse, conversion of 5mC to 5hmC may contribute to DNA demethylation in hPGC (Hackett et al., 2013). Furthermore, repression of UHRF1 and DNMT3A in hPGCLCs would promote DNA-replication-coupled loss of 5mC. Indeed, there was a small but significant decline in 5mC in hPGCLCs, a trend that could lead to a significant loss of 5mC with further proliferation of hPGCLCs. Furthermore, we detected upregulation and translocation of PRMT5 to the nucleus in hPGCLC, which occurs with the onset of global DNA

Figure 7. Induction and Isolation of hPGCLCs from Competent hiPSCs/hESCs

(A) FACS analysis of TNAP and NANOS3-mCherry (top) and TNAP and CD38 (bottom) on day 4 embryoids induced from 4i hESCs after preinduction (left), directly without preinduction (middle) or from conventional hESCs (right, Conv hESC).

(B) FACS analysis of TNAP and CD38 in 4i hiPSCs (top) and day 4 embryoids derived from 4i hiPSCs after direct induction (bottom).

(C) Expression analysis by RT-qPCR in TNAP-positive hiPSCs (iPSC TNAP+), TNAP/CD38 double-negative (TNAP–CD38–) population and TNAP/CD38 double-positive population (TNAP+CD38+) on day 4 after hPGCLC induction. Relative expression levels are shown with normalization to β -ACTIN. Error bars indicate mean \pm SD from two independent biological replicates.

(D) Overview of human germline development. hESCs in 4i reversibly attains competence for germ cell fate. Exposure of 4i cells to cytokines containing BMPs results in strong induction of hPGCLCs following expression of SOX17-BLIMP1, which are among the key regulators of germ cell fate. SOX17 and BLIMP1 are detected in in vivo gonadal hPGC and Tcam-2 seminoma, indicating a likely progression of early human germ cell lineage. CD38, a cell-surface glycoprotein, is shared by all cells with germ cell characteristics, but not by hESC. Loss of *SOX17* or *BLIMP1* abrogates hPGCLC specification.

demethylation to repress transposable elements (Kim et al., 2014). Detailed analysis of the transcriptome and epigenome, together with the targets of SOX17 in hPGCLCs/hPGCs, should provide insights on the mechanism of how the epigenome is reset in the early human germline and potentially on the inheritance and consequences of transgenerational epigenetic inheritance (Heard and Martienssen, 2014).

This study shows that changes in pluripotent cell states can be induced by environmental factors with respect to gain and loss of competence for germ cell fate in hESCs in the 4i culture (Gafni et al., 2013). This competence for hPGCLCs is reversibly maintained and progressively lost in conventional culture conditions. Notably, hESCs in 4i medium show a slight upregulation of T together with HAND1 compared to conventional hESCs (Figure S7), with putative posterior primitive streak-like feature (Mendjan et al., 2014). This might explain why hESC in 4i are highly competent for hPGCLC fate. Because MAPK inhibitors may also alter the epigenetic state of pluripotent cells (Gafni et al., 2013), the precise molecular basis for competence for PGC fate remains to be elucidated in both mouse and human. Nonetheless, hESC/hiPSC can reversibly gain competence for hPGCLC specification in 4i medium, which provides a model for advances in human germ cell biology.

Mouse is the primary model organism for early mammalian development, pluripotency, and the regulation of cell fates. Post-implantation rodent embryos develop as egg cylinders with an overlying extraembryonic ectoderm, which is the source of signals, including BMP4, whereas postimplantation epiblast embryonic disc in humans is typical of many mammalian species (Barrios et al., 2013; de Fellici, 2013; Irie et al., 2014). These differences may affect the source, duration, and the nature of signaling molecules that regulate competence for cell fates in vivo. The evolutionary divergence in the pluripotent states in mouse and human might also result in differences in the mechanism of germline specification and, potentially, other cell fate decisions. If so, mechanisms of early cell fate decisions in mice cannot be safely or wholly extrapolated to specification events during early human development.

EXPERIMENTAL PROCEDURES

hESC/iPSC Culture and hPGCLC Differentiation

4i hESCs (WIS2: 46XY; WIBR3: 46XX; LIS1, 46XY) and iPSCs (FX71.1; a fragile X male patient-derived iPSC line, C1 female iPSC line) were grown in conditions adapted and modified from previously described WIS-NHSM conditions (Gafni et al., 2013). 4i cells were grown on irradiated mouse embryonic fibroblasts (MEFs) (GlobalStem) in knockout DMEM supplemented with 20% knockout serum replacement (KSR), 2 mM L-glutamine, 0.1 mM nonessential amino acids, 0.1 mM 2-mercaptoethanol (all GIBCO), 20 ng/ml human LIF (Stem Cell Institute [SCI]), 8 ng/ml bFGF (SCI), 1 ng/ml TGF- β 1 (Peprotech), 3 μ M CHIR99021 (Miltenyi Biotec), 1 μ M PD0325901 (Miltenyi Biotec), 5 μ M SB203580 (TOCRIS bioscience), and 5 μ M SP600125 (TOCRIS bioscience). Cells were passaged every 3 to 5 days using TrypLE Express (GIBCO). 10 μ M of ROCK inhibitor (Y-27632, TOCRIS bioscience) was used for 24 hr after the passage.

To preinduce, 4i hESCs were dissociated with TrypLE Express and filtered with 50 μ m cell filter (PERTEC), and 4×10^5 cells/12-well were plated on vitronectin/gelatin-coated plates (Gafni et al., 2013) in N2B27 medium (Ying et al., 2008) with 1% KSR, 10 ng/ml bFGF (SCI), 1 ng/ml TGF- β 1 (Peprotech), or 20 ng/ml Activin A (SCI) and 10 μ M ROCK inhibitor. Medium was changed on day 1. After 2 days of preinduction, the cells are dissociated with TrypLE

and plated to ultra-low cell attachment U-bottom 96-well plates (Corning, 7007) at a density of 2,000–4,000 cells/well in 200 μ l PGCLC medium. PGCLC medium is composed of Glasgow's MEM (GMEM, GIBCO), 15% KSR, 0.1 mM nonessential amino acids, 0.1 mM 2-mercaptoethanol, 100 U/ml Penicillin-0.1 mg/ml Streptomycin, 2 mM L-Glutamine, 1 mM Sodium pyruvate, and the following cytokines: 500 ng/ml BMP4 (R&D Systems) or BMP2 (SCI), 1 μ g/ml human LIF (SCI), 100 ng/ml SCF (R&D Systems), 50 ng/ml EGF (R&D Systems), and 10 μ M ROCK inhibitor.

Conventional hESCs/hiPSCs were maintained on irradiated MEFs (GlobalStem) in DMEM/F12+GlutaMAX supplemented with 20% KSR, 0.1 mM nonessential amino acids, 0.1 mM 2-mercaptoethanol (all GIBCO), and 10–20 ng/ml of bFGF (SCI). Media were replaced every day. Cells were passaged every 4 to 6 days using 1 mg/ml of Dispase (GIBCO), and 10 μ M ROCK inhibitor (Y-27632, TOCRIS bioscience) was added for 24 hr after the passage.

ACCESSION NUMBERS

The NCBI GEO accession number for the RNA-seq data reported in this paper is GSE60138.

SUPPLEMENTAL INFORMATION

Supplemental Information includes Extended Experimental Procedures, seven figures, and three tables and can be found with this article online at <http://dx.doi.org/10.1016/j.cell.2014.12.013>.

AUTHOR CONTRIBUTIONS

The study was conceived and designed by N.I., L.W., J.H.H., and M.A.S. The NANOS3-mCherry reporter hESC lines and the BLIMP1 and SOX17 knockout hESCs were generated by L.W. and S.V. hESC growth conditions were developed by L.W. and J.H.H. The PGCLC induction experiments were performed by N.I. and L.W. W.W.C.T. collected human embryos and performed immunofluorescence, RNA-seq, and bioinformatics analysis, together with S.D. and Y.M. Experiments on Tcam-2, including the knockdowns, exogenous SOX17 expression experiments, and western blot analysis, were performed by T.K. The study was supervised by M.A.S. and J.H.H. The manuscript was written by N.I., W.W.C.T., J.H.H., and M.A.S. with input from most authors.

ACKNOWLEDGMENTS

We thank Rick Livesey and his lab for help with the culture of hESCs; Sohei Kitazawa and Janet Shipley for the Tcam-2 cells; Nigel Miller and Andy Riddell for cell sorting; Roger Barker, Xiaoling He, and Pam Tyers for collection of human embryos; and Charles Bradshaw for help with bioinformatics. We thank members of the Surani and Hanna labs for important discussions and technical help. N.I. is supported by Grant-in-Aid for fellows of the JSPS and by BIRAX (the Britain Israel Research and Academic Exchange Partnership) initiative, who provided a project grant to J.H.H. and M.A.S. J.H.H. is supported by Ilana and Pascal Mantoux, the Kimmel Award, ERC (StG-2011-281906), Helmsley Charitable Trust, ISF (Bikura, Morasha, ICORE), ICRF, the Abisch Frenkel Foundation, the Fritz Thyssen Stiftung, Erica and Robert Drake, Benozio Endowment fund, and the Flight Attendant Medical Research Institute (FAMRI). J.H.H. is a New York Stem Cell Foundation Robertson Investigator. W.W.C.T. is supported by Croucher Foundation and Cambridge Trust; M.A.S. is supported by HFSP and a Wellcome Trust Investigator Award.

Received: August 8, 2014

Revised: November 13, 2014

Accepted: December 4, 2014

Published: December 24, 2014

REFERENCES

Aramaki, S., Hayashi, K., Kurimoto, K., Ohta, H., Yabuta, Y., Iwanari, H., Mochizuki, Y., Hamakubo, T., Kato, Y., Shirahige, K., and Saitou, M. (2013).

- A mesodermal factor, T, specifies mouse germ cell fate by directly activating germline determinants. *Dev. Cell* 27, 516–529.
- Barrios, F., Irie, N., and Surani, M.A. (2013). Perceiving signals, building networks, reprogramming germ cell fate. *Int. J. Dev. Biol.* 57, 123–132.
- Bernardo, A.S., Faial, T., Gardner, L., Niakan, K.K., Ortmann, D., Senner, C.E., Callery, E.M., Trotter, M.W., Hemberger, M., Smith, J.C., et al. (2011). BRACHYURY and CDX2 mediate BMP-induced differentiation of human and mouse pluripotent stem cells into embryonic and extraembryonic lineages. *Cell Stem Cell* 9, 144–155.
- Brocard, J., Feil, R., Chambon, P., and Metzger, D. (1998). A chimeric Cre recombinase inducible by synthetic, but not by natural ligands of the glucocorticoid receptor. *Nucleic Acids Res.* 26, 4086–4090.
- Chen, Y., Blair, K., and Smith, A. (2013). Robust self-renewal of rat embryonic stem cells requires fine-tuning of glycogen synthase kinase-3 inhibition. *Stem Cell Reports* 1, 209–217.
- Chia, N.Y., Chan, Y.S., Feng, B., Lu, X., Orlov, Y.L., Moreau, D., Kumar, P., Yang, L., Jiang, J., Lau, M.S., et al. (2010). A genome-wide RNAi screen reveals determinants of human embryonic stem cell identity. *Nature* 468, 316–320.
- Clarke, R.L., Yzaguirre, A.D., Yashiro-Ohtani, Y., Bondue, A., Blanpain, C., Pear, W.S., Speck, N.A., and Keller, G. (2013). The expression of Sox17 identifies and regulates haemogenic endothelium. *Nat. Cell Biol.* 15, 502–510.
- D'Amour, K.A., Agulnick, A.D., Eliazar, S., Kelly, O.G., Kroon, E., and Baetge, E.E. (2005). Efficient differentiation of human embryonic stem cells to definitive endoderm. *Nat. Biotechnol.* 23, 1534–1541.
- de Fellici, M. (2013). Origin, migration, and proliferation of human primordial germ cells. In *Oogenesis*, G. Coticchio, D.F. Albertini, and L. De Santis, eds. (London: Springer-Verlag), pp. 19–37.
- de Jong, J., Stoop, H., Gillis, A.J., van Gurp, R.J., van de Geijn, G.J., Boer, M., Hersmus, R., Saunders, P.T., Anderson, R.A., Oosterhuis, J.W., and Looijenga, L.H. (2008). Differential expression of SOX17 and SOX2 in germ cells and stem cells has biological and clinical implications. *J. Pathol.* 215, 21–30.
- De Miguel, M.P., Fuentes-Julián, S., and Alcaina, Y. (2010). Pluripotent stem cells: origin, maintenance and induction. *Stem Cell Rev.* 6, 633–649.
- Eckert, D., Biermann, K., Nettersheim, D., Gillis, A.J., Steger, K., Jäck, H.M., Müller, A.M., Looijenga, L.H., and Schorle, H. (2008). Expression of BLIMP1/PRMT5 and concurrent histone H2A/H4 arginine 3 dimethylation in fetal germ cells, CIS/IGCNU and germ cell tumors. *BMC Dev. Biol.* 8, 106.
- Gafni, O., Weinberger, L., Mansour, A.A., Manor, Y.S., Chomsky, E., Ben-Yosef, D., Kalma, Y., Viukov, S., Maza, I., Zviran, A., et al. (2013). Derivation of novel human ground state naive pluripotent stem cells. *Nature* 504, 282–286.
- Gkountela, S., Li, Z., Vincent, J.J., Zhang, K.X., Chen, A., Pellegrini, M., and Clark, A.T. (2013). The ontogeny of cKIT+ human primordial germ cells proves to be a resource for human germ line reprogramming, imprint erasure and in vitro differentiation. *Nat. Cell Biol.* 15, 113–122.
- Grabole, N., Tischler, J., Hackett, J.A., Kim, S., Tang, F., Leitch, H.G., Magnúsdóttir, E., and Surani, M.A. (2013). Prdm14 promotes germline fate and naive pluripotency by repressing FGF signalling and DNA methylation. *EMBO Rep.* 14, 629–637.
- Hackett, J.A., and Surani, M.A. (2014). Regulatory principles of pluripotency: from the ground state up. *Cell Stem Cell* 15, 416–430.
- Hackett, J.A., Zyllicz, J.J., and Surani, M.A. (2012). Parallel mechanisms of epigenetic reprogramming in the germline. *Trends Genet.* 28, 164–174.
- Hackett, J.A., Sengupta, R., Zyllicz, J.J., Murakami, K., Lee, C., Down, T.A., and Surani, M.A. (2013). Germline DNA demethylation dynamics and imprint erasure through 5-hydroxymethylcytosine. *Science* 339, 448–452.
- Hara, K., Kanai-Azuma, M., Uemura, M., Shitara, H., Taya, C., Yonekawa, H., Kawakami, H., Tsunekawa, N., Kurohmaru, M., and Kanai, Y. (2009). Evidence for crucial role of hindgut expansion in directing proper migration of primordial germ cells in mouse early embryogenesis. *Dev. Biol.* 330, 427–439.
- Hayashi, K., and Surani, M.A. (2009). Self-renewing epiblast stem cells exhibit continual delineation of germ cells with epigenetic reprogramming in vitro. *Development* 136, 3549–3556.
- Hayashi, K., de Sousa Lopes, S.M.C., and Surani, M.A. (2007). Germ cell specification in mice. *Science* 316, 394–396.
- Hayashi, K., Ohta, H., Kurimoto, K., Aramaki, S., and Saitou, M. (2011). Reconstitution of the mouse germ cell specification pathway in culture by pluripotent stem cells. *Cell* 146, 519–532.
- Heard, E., and Martienssen, R.A. (2014). Transgenerational epigenetic inheritance: myths and mechanisms. *Cell* 157, 95–109.
- Imamura, M., Hikabe, O., Lin, Z.Y., and Okano, H. (2014). Generation of germ cells in vitro in the era of induced pluripotent stem cells. *Mol. Reprod. Dev.* 81, 2–19.
- Irie, N., Tang, W.W., and Azim Surani, M. (2014). Germ cell specification and pluripotency in mammals: a perspective from early embryogenesis. *Reprod. Med. Biol.* 13, 203–215.
- Julaton, V.T., and Reijo Pera, R.A. (2011). NANOS3 function in human germ cell development. *Hum. Mol. Genet.* 20, 2238–2250.
- Kanai-Azuma, M., Kanai, Y., Gad, J.M., Tajima, Y., Taya, C., Kurohmaru, M., Sanai, Y., Yonekawa, H., Yazaki, K., Tam, P.P., and Hayashi, Y. (2002). Deletion of definitive gut endoderm in Sox17-null mutant mice. *Development* 129, 2367–2379.
- Kee, K., Angeles, V.T., Flores, M., Nguyen, H.N., and Reijo Pera, R.A. (2009). Human DAZL, DAZ and BOULE genes modulate primordial germ-cell and haploid gamete formation. *Nature* 462, 222–225.
- Kim, S., Günesdogan, U., Zyllicz, J.J., Hackett, J.A., Cougot, D., Bao, S., Lee, C., Dietmann, S., Allen, G.E., Sengupta, R., and Surani, M.A. (2014). PRMT5 Protects Genomic Integrity during Global DNA Demethylation in Primordial Germ Cells and Preimplantation Embryos. *Mol. Cell* 56, 564–579.
- Kurimoto, K., Yabuta, Y., Ohinata, Y., Shigeta, M., Yamanaka, K., and Saitou, M. (2008). Complex genome-wide transcription dynamics orchestrated by Blimp1 for the specification of the germ cell lineage in mice. *Genes Dev.* 22, 1617–1635.
- Lawson, K.A., Dunn, N.R., Roelen, B.A., Zeinstra, L.M., Davis, A.M., Wright, C.V., Korving, J.P., and Hogan, B.L. (1999). Bmp4 is required for the generation of primordial germ cells in the mouse embryo. *Genes Dev.* 13, 424–436.
- Leitch, H.G., Tang, W.W., and Surani, M.A. (2013). Primordial germ-cell development and epigenetic reprogramming in mammals. *Curr. Top. Dev. Biol.* 104, 149–187.
- Lin, I.Y., Chiu, F.L., Yeang, C.H., Chen, H.F., Chuang, C.Y., Yang, S.Y., Hou, P.S., Sintupisut, N., Ho, H.N., Kuo, H.C., and Lin, K.I. (2014). Suppression of the SOX2 neural effector gene by PRDM1 promotes human germ cell fate in embryonic stem cells. *Stem Cell Reports* 2, 189–204.
- Liu, X., Gao, Q., Li, P., Zhao, Q., Zhang, J., Li, J., Koseki, H., and Wong, J. (2013). UHRF1 targets DNMT1 for DNA methylation through cooperative binding of hemi-methylated DNA and methylated H3K9. *Nat. Commun.* 4, 1563.
- Looijenga, L.H., Stoop, H., and Biermann, K. (2014). Testicular cancer: biology and biomarkers. *Virchows Arch.* 464, 301–313.
- Ma, Z., Swigut, T., Valouev, A., Rada-Iglesias, A., and Wysocka, J. (2011). Sequence-specific regulator Prdm14 safeguards mouse ESCs from entering extraembryonic endoderm fates. *Nat. Struct. Mol. Biol.* 18, 120–127.
- Magnúsdóttir, E., and Surani, M.A. (2014). How to make a primordial germ cell. *Development* 141, 245–252.
- Magnúsdóttir, E., Dietmann, S., Murakami, K., Günesdogan, U., Tang, F., Bao, S., Diamanti, E., Lao, K., Gottgens, B., and Azim Surani, M. (2013). A tripartite transcription factor network regulates primordial germ cell specification in mice. *Nat. Cell Biol.* 15, 905–915.
- Malavasi, F., Deaglio, S., Funaro, A., Ferrero, E., Horenstein, A.L., Ortolan, E., Vaisitti, T., and Aydin, S. (2008). Evolution and function of the ADP ribosyl cyclase/CD38 gene family in physiology and pathology. *Physiol. Rev.* 88, 841–886.

- Mendjan, S., Mascetti, V.L., Ortmann, D., Ortiz, M., Karjosukarso, D.W., Ng, Y., Moreau, T., and Pedersen, R.A. (2014). NANOG and CDX2 pattern distinct subtypes of human mesoderm during exit from pluripotency. *Cell Stem Cell* 15, 310–325.
- Nakajima-Takagi, Y., Osawa, M., Oshima, M., Takagi, H., Miyagi, S., Endoh, M., Endo, T.A., Takayama, N., Eto, K., Toyoda, T., et al. (2013). Role of SOX17 in hematopoietic development from human embryonic stem cells. *Blood* 121, 447–458.
- Nakaki, F., Hayashi, K., Ohta, H., Kurimoto, K., Yabuta, Y., and Saitou, M. (2013). Induction of mouse germ-cell fate by transcription factors in vitro. *Nature* 501, 222–226.
- Nichols, J., and Smith, A. (2009). Naive and primed pluripotent states. *Cell Stem Cell* 4, 487–492.
- Ohinata, Y., Payer, B., O'Carroll, D., Ancelin, K., Ono, Y., Sano, M., Barton, S.C., Obukhanych, T., Nussenzweig, M., Tarakhovskiy, A., et al. (2005). Blimp1 is a critical determinant of the germ cell lineage in mice. *Nature* 436, 207–213.
- Pallesen, G., and Hamilton-Dutoit, S.J. (1988). Ki-1 (CD30) antigen is regularly expressed by tumor cells of embryonal carcinoma. *Am. J. Pathol.* 133, 446–450.
- Pera, R.A. (2013). Status of human germ cell differentiation from pluripotent stem cells. *Reprod. Fertil. Dev.* 25, 396–404.
- Saitou, M., Barton, S.C., and Surani, M.A. (2002). A molecular programme for the specification of germ cell fate in mice. *Nature* 418, 293–300.
- Schafer, S., Anschlag, J., Nettersheim, D., Haas, N., Pawig, L., and Schorle, H. (2011). The role of BLIMP1 and its putative downstream target TFAP2C in germ cell development and germ cell tumours. *Int. J. Androl.* 34, e152–e158, discussion e158–e159.
- Shoji, M., Tanaka, T., Hosokawa, M., Reuter, M., Stark, A., Kato, Y., Kondoh, G., Okawa, K., Chujo, T., Suzuki, T., et al. (2009). The TDRD9-MIWI2 complex is essential for piRNA-mediated retrotransposon silencing in the mouse male germline. *Dev. Cell* 17, 775–787.
- Skakkebaek, N.E. (1972). Possible carcinoma-in-situ of the testis. *Lancet* 2, 516–517.
- Vincent, S.D., Dunn, N.R., Sciammas, R., Shapiro-Shalef, M., Davis, M.M., Calame, K., Bikoff, E.K., and Robertson, E.J. (2005). The zinc finger transcriptional repressor Blimp1/Prdm1 is dispensable for early axis formation but is required for specification of primordial germ cells in the mouse. *Development* 132, 1315–1325.
- Watanabe, K., Ueno, M., Kamiya, D., Nishiyama, A., Matsumura, M., Wataya, T., Takahashi, J.B., Nishikawa, S., Nishikawa, S., Muguruma, K., and Sasai, Y. (2007). A ROCK inhibitor permits survival of dissociated human embryonic stem cells. *Nat. Biotechnol.* 25, 681–686.
- Weber, S., Eckert, D., Nettersheim, D., Gillis, A.J., Schäfer, S., Kuckenberger, P., Ehlermann, J., Werling, U., Biermann, K., Looijenga, L.H., and Schorle, H. (2010). Critical function of AP-2 gamma/TFAP2C in mouse embryonic germ cell maintenance. *Biol. Reprod.* 82, 214–223.
- Yamaji, M., Seki, Y., Kurimoto, K., Yabuta, Y., Yuasa, M., Shigeta, M., Yamana, K., Ohinata, Y., and Saitou, M. (2008). Critical function of Prdm14 for the establishment of the germ cell lineage in mice. *Nat. Genet.* 40, 1016–1022.
- Yamaji, M., Ueda, J., Hayashi, K., Ohta, H., Yabuta, Y., Kurimoto, K., Nakato, R., Yamada, Y., Shirahige, K., and Saitou, M. (2013). PRDM14 ensures naive pluripotency through dual regulation of signaling and epigenetic pathways in mouse embryonic stem cells. *Cell Stem Cell* 12, 368–382.
- Ying, Q.-L., Wray, J., Nichols, J., Battle-Morera, L., Doble, B., Woodgett, J., Cohen, P., and Smith, A. (2008). The ground state of embryonic stem cell self-renewal. *Nature* 453, 519–523.
- Yu, P., Pan, G., Yu, J., and Thomson, J.A. (2011). FGF2 sustains NANOG and switches the outcome of BMP4-induced human embryonic stem cell differentiation. *Cell Stem Cell* 8, 326–334.

Early Divergent Strains of *Yersinia pestis* in Eurasia 5,000 Years Ago

Simon Rasmussen,^{1,18} Morten Erik Allentoft,^{2,18} Kasper Nielsen,¹ Ludovic Orlando,² Martin Sikora,² Karl-Göran Sjögren,³ Anders Gorm Pedersen,¹ Mikkel Schubert,² Alex Van Dam,¹ Christian Moliin Outzen Kapel,⁴ Henrik Bjørn Nielsen,¹ Søren Brunak,^{1,5} Pavel Avetisyan,⁶ Andrey Epimakhov,⁷ Mikhail Viktorovich Khalyapin,⁸ Artak Gnuni,⁹ Aivar Kriiska,¹⁰ Irena Lasak,¹¹ Mait Metspalu,¹² Vyacheslav Moiseyev,¹³ Andrei Gromov,¹³ Dalia Pokutta,³ Lehti Saag,¹² Liivi Varul,¹⁰ Levon Yepiskoposyan,¹⁴ Thomas Sicheritz-Pontén,¹ Robert A. Foley,¹⁵ Marta Mirazón Lahr,¹⁵ Rasmus Nielsen,¹⁶ Kristian Kristiansen,³ and Eske Willerslev^{2,17,*}

¹Center for Biological Sequence Analysis, Department of Systems Biology, Technical University of Denmark, Kemitorvet, Building 208, 2800 Kongens Lyngby, Denmark

²Centre for GeoGenetics, Natural History Museum of Denmark, University of Copenhagen, Øster Voldgade 5–7, 1350 Copenhagen, Denmark

³Department of Historical Studies, University of Gothenburg, 405 30 Gothenburg, Sweden

⁴Section for Organismal Biology, Department of Plant and Environmental Sciences, University of Copenhagen, Thorvaldsensvej 40, 1871 Frederiksberg C, Denmark

⁵Novo Nordisk Foundation Center for Protein Research, University of Copenhagen, 2200 Copenhagen, Denmark

⁶Division of Armenology and Social Sciences, Institute of Archaeology and Ethnography, National Academy of Sciences, 0025 Yerevan, Republic of Armenia

⁷Institute of History and Archaeology RAS (South Ural Department), South Ural State University, 454080 Chelyabinsk, Russia

⁸Orenburg Museum of Fine Arts, 460000 Orenburg, Russia

⁹Department of Archaeology and Ethnography, Yerevan State University, 0025 Yerevan, Republic of Armenia

¹⁰Department of Archaeology, University of Tartu, 51003 Tartu, Estonia

¹¹Institute of Archaeology, University of Wrocław, 50-139 Wrocław, Poland

¹²Department of Evolutionary Biology, Estonian Biocentre and University of Tartu, 51010 Tartu, Estonia

¹³Peter the Great Museum of Anthropology and Ethnography (Kunstkamera) RAS, 199034 St. Petersburg, Russia

¹⁴Laboratory of Ethnogenomics, Institute of Molecular Biology, National Academy of Sciences, 0014 Yerevan, Armenia

¹⁵Leverhulme Centre for Human Evolutionary Studies, Department of Archaeology and Anthropology, University of Cambridge, Cambridge CB2 1QH, UK

¹⁶Center for Theoretical Evolutionary Genetics, University of California, Berkeley, California 94720-3140, USA

¹⁷Department of Zoology, University of Cambridge, Downing Street, Cambridge CB2 3EJ, UK

¹⁸Co-first author

*Correspondence: ewillerslev@snm.ku.dk

<http://dx.doi.org/10.1016/j.cell.2015.10.009>

This is an open access article under the CC BY license (<http://creativecommons.org/licenses/by/4.0/>).

SUMMARY

The bacteria *Yersinia pestis* is the etiological agent of plague and has caused human pandemics with millions of deaths in historic times. How and when it originated remains contentious. Here, we report the oldest direct evidence of *Yersinia pestis* identified by ancient DNA in human teeth from Asia and Europe dating from 2,800 to 5,000 years ago. By sequencing the genomes, we find that these ancient plague strains are basal to all known *Yersinia pestis*. We find the origins of the *Yersinia pestis* lineage to be at least two times older than previous estimates. We also identify a temporal sequence of genetic changes that lead to increased virulence and the emergence of the bubonic plague. Our results show that plague infection was endemic in the human populations of Eurasia at least 3,000 years before any historical recordings of pandemics.

INTRODUCTION

Plague is caused by the bacteria *Yersinia pestis* and is being directly transmitted through human-to-human contact (pneumonic plague) or via fleas as a common vector (bubonic or septicemic plague) (Treille and Yersin, 1894). Three historic human plague pandemics have been documented: (1) the First Pandemic, which started with the Plague of Justinian (541–544 AD), but continued intermittently until ~750 AD; (2) the Second Pandemic, which began with the Black Death in Europe (1347–1351 AD) and included successive waves, such as the Great Plague (1665–1666 AD), until the 18th century; (3) the Third Pandemic, which emerged in China in the 1850s and erupted there in a major epidemic in 1894 before spreading across the world as a series of epidemics until the middle of the 20th century (Bos et al., 2011; Cui et al., 2013; Drancourt et al., 1998; Harbeck et al., 2013; Parkhill et al., 2001; Perry and Fetherston, 1997; Wagner et al., 2014). Earlier outbreaks such as the Plague of Athens (430–427 BC) and the Antonine Plague (165–180 AD) may also have occurred, but there is no direct evidence that allows confident attribution to *Y. pestis* (Drancourt and Raoult, 2002; McNeill, 1976).

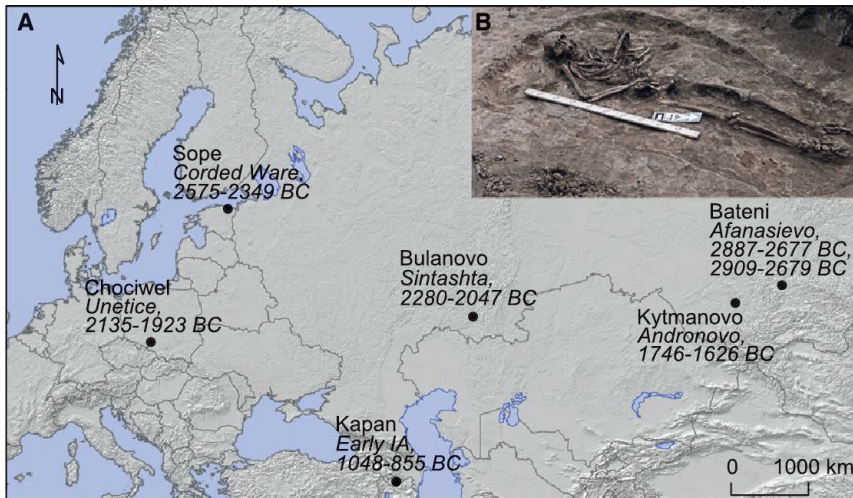


Figure 1. Archaeological Sites of Bronze Age *Yersinia pestis*

(A) Map of Eurasia indicating the position, radio-carbon dated ages and associated cultures of the samples in which *Y. pestis* were identified. Dates are given as 95% confidence interval calendar BC years. IA: Iron Age.

(B) Burial four from Bulanovo site. Picture by Mikhail V. Khalyapin. See also Table S1.

The consequences of the plague pandemics have been well-documented and the demographic impacts were dramatic (Little et al., 2007). The Black Death alone is estimated to have killed 30%–50% of the European population. Economic and political collapses have also been in part attributed to the devastating effects of the plague. The Plague of Justinian is thought to have played a major role in weakening the Byzantine Empire, and the earlier putative plagues have been associated with the decline of Classical Greece and likely undermined the strength of the Roman army.

Molecular clock estimates have suggested that *Y. pestis* diversified from the more prevalent and environmental stress-tolerant, but less pathogenic, enteric bacterium *Y. pseudotuberculosis* between 2,600 and 28,000 years ago (Achtman et al., 1999, 2004; Cui et al., 2013; Wagner et al., 2014). However, humans may potentially have been exposed to *Y. pestis* for much longer than the historical record suggests, though direct molecular evidence for *Y. pestis* has not been obtained from skeletal material older than 1,500 years (Bos et al., 2011; Wagner et al., 2014). The most basal strains of *Y. pestis* (O.PE7 clade) recorded to date were isolated from the Qinghai-Tibet Plateau in China in 1961–1962 (Cui et al., 2013).

We investigated the origin of *Y. pestis* by sequencing ancient bacterial genomes from the teeth of Bronze Age humans across Europe and Asia. Our findings suggest that the virulent, flea-borne *Y. pestis* strain that caused the historic bubonic plague pandemics evolved from a less pathogenic *Y. pestis* lineage infecting human populations long before recorded evidence of plague outbreaks.

RESULTS

Identification of *Yersinia pestis* in Bronze Age Eurasian Individuals

We screened c. 89 billion raw DNA sequence reads obtained from teeth of 101 Bronze Age individuals from Europe and Asia (Allentoft et al., 2015) and found that seven individuals carried sequences resembling *Y. pestis* (Figure 1, Table S1, Supplemental Experimental Procedures). Further sequencing allowed us to

assemble the *Y. pestis* genomes to an average depth of 0.14–29.5X, with 12%–95% of the positions in the genome covered at least once (Table 1, Table S2, S3, and S4). We also recovered the sequences of the three plasmids pCD1, pMT1, and pPCP1 (0.12 to 50.3X in average depth) the latter two of which are crucial for distinguishing *Y. pestis* from its highly similar ancestor *Y. pseudotuberculosis* (Table 1, Figure 2, Table S3) (Bercovier et al., 1980; Chain et al., 2004; Parkhill et al., 2001). The host individuals from which *Y. pestis* was recovered belong to Eurasian Late Neolithic and Bronze Age cultures (Allentoft et al., 2015), represented by the Afanasievo culture in Altai, Siberia (2782 cal BC, 2794 cal BC, n = 2), the Corded Ware culture in Estonia (2462 cal BC, n = 1), the Sintashta culture in Russia (2163 cal BC, n = 1), the Unetice culture in Poland (2029 cal BC, n = 1), the Andronovo culture in Altai, Siberia (1686 cal BC, n = 1), and an early Iron Age individual from Armenia (951 cal BC, n = 1) (Table S1).

Authentication of *Yersinia pestis* Ancient DNA

Besides applying standard precautions for working with ancient DNA (Willerslev and Cooper, 2005), the authenticity of our findings are supported by the following observations: (1) The *Y. pestis* sequences were identified in significant amounts in shotgun data from eight of 101 samples, showing that this finding is not due to a ubiquitous contaminant in our lab or in the reagents. Indeed, further analysis showed that one of these eight was most likely not *Y. pestis*. We also sequenced all negative DNA extraction controls and found no signs of *Y. pestis* DNA in these (Table S3). (2) Consistent with an ancient origin, the *Y. pestis* reads were highly fragmented, with average read lengths of 43–65 bp (Table S3) and also displayed clear signs of C-T deamination damage at the 5' termini typical of ancient DNA (Figure 3, Figure S1). Because the plasmids are central for discriminating between *Y. pestis* and *Y. pseudotuberculosis*, we tested separately for DNA damage patterns for the chromosome and for each of the plasmids. For the seven samples, we observe similar patterns of DNA damage for chromosome and plasmid sequences (Figure 3, Figure S1). (3) We observe correlated DNA degradation patterns when comparing DNA degradation in the *Y. pestis* sequences and the human sequences from the host individual. Given that DNA decay can be described as a rate process (Allentoft et al., 2012), this suggests that the DNA molecules of the pathogen and the human host have a similar age (Figure 3, Figure S1, Table S3 and Supplemental

Table 1. Overview of the *Y. pestis* Containing Samples

Sample	Country	Site	Culture	Date (cal BC)	CO92	pMT1	pPCP1	pCD1
RISE00	Estonia	Sope	Corded Ware	2575–2349	0.39	0.36	1.40	0.66
RISE139	Poland	Chociwel	Unetice	2135–1923	0.14	0.24	0.76	0.28
RISE386	Russia	Bulanovo	Sintashta	2280–2047	0.82	0.96	1.12	1.60
RISE397	Armenia	Kapan	EIA	1048–885	0.25	0.40	6.88	0.50
RISE505	Russia	Kytmanovo	Andronovo	1746–1626	8.73	9.15	34.09	17.46
RISE509	Russia	Afanasievo Gora	Afanasievo	2887–2677	29.45	16.96	31.22	50.32
RISE511	Russia	Afanasievo Gora	Afanasievo	2909–2679	0.20	0.24	1.19	0.60

The dating is direct AMS dating of bones and teeth and is given as 95% confidence interval calendar BC years (details are given in Table S1). The columns CO92, pMT1, pPCP1 and pCD1 correspond to sequencing depth. Additional information on the archaeological sites and mapping statistics can be found in the Supplemental Experimental Procedures and Table S1, S2, and S3. EIA: Early Iron Age, AMS: Accelerator Mass Spectrometry.

Experimental Procedures). (4) Because of the high sequence similarity between *Y. pestis* and *Y. pseudotuberculosis*, we mapped all reads both to the *Y. pestis* CO92 and to the *Y. pseudotuberculosis* IP32953 reference genomes (Chain et al., 2004). Consistent with being *Y. pestis*, the seven investigated samples displayed more reads matching perfectly (edit distance = 0) toward *Y. pestis* (Figure 3, Figure S2). One sample (RISE392) was most likely not *Y. pestis* based on this criterion. (5) A naive Bayesian classifier trained on known genomes predicts the seven samples to be *Y. pestis* with 100% posterior probability, while RISE392 is predicted to have 0% probability of being *Y. pestis* (Figure S2, Table S3). (6) If the DNA was from other organisms than *Y. pestis*, we would expect the reads to be more frequently associated with either highly conserved or low-complexity regions. However, we find the reads to be distributed across the entire genome (Figure S2), and comparison of actual coverage versus the coverage that would be expected from read length distributions and mappability of the reference sequences are also in agreement for the seven samples (Figure 3). (7) In a maximum likelihood phylogeny, the recovered *Y. pestis* genomic sequences of RISE505 and RISE509 are clearly within the *Y. pestis* clade and basal to all contemporary *Y. pestis* strains (Figure 4) (see below).

The Phylogenetic Position of the Bronze Age *Yersinia pestis* Strains

To determine the phylogenetic positions of the two high coverage ancient *Y. pestis* strains, RISE505 (Andronovo culture 1686 cal BC, 8.7X) and RISE509 (Afanasievo culture, 2746 cal BC, 29.7X), we mapped the reads, together with reads from strains of *Yersinia similis* (n = 5), *Y. pseudotuberculosis* (n = 25), and *Y. pestis* (n = 139), to the *Y. pseudotuberculosis* reference genome (IP32953). Only high confidence positions were extracted. To assess whether the individuals were infected with multiple strains of *Y. pestis* we investigated the genotype heterozygosity levels of the ancient genomes and found no indications of mixed infection (Figure S3). There was no decay in Linkage Disequilibrium (LD) across the chromosome (Figure S3), indicating no detectable recombination among strains. We therefore used RAxML (Stamatakis, 2014) to construct a Maximum Likelihood phylogeny from a supermatrix concatenated from 3,141 genes and a total of 3.14 Mbp (Figure 4). This contrasts with earlier phylogenies (Bos et al., 2011; Cui et al.,

2013; Morelli et al., 2010; Wagner et al., 2014), which were based on less than 2,300 nucleotides that were ascertained to be variable in *Y. pestis*, likely leading to lower statistical accuracy than with whole-genome analyses. Furthermore, the use of SNPs ascertained to be variable in *Y. pestis* would downwardly bias estimates of branch lengths in *Y. pseudotuberculosis* and lead to underestimates of the *Y. pestis* versus *Y. pseudotuberculosis* divergence time, as seen in the branch length of the *Y. pestis* clade to *Y. pseudotuberculosis* (Figure S3). The topology of our whole genome tree shows *Y. pestis* as a monophyletic group within *Y. pseudotuberculosis* with RISE505 and RISE509 (Figure 4A, black arrow, Figure S4) clustered together within the *Y. pestis* clade. The *Y. pestis* sub-tree topology (Figure 4B, Figure S4) is similar to that reported previously (Bos et al., 2011; Cui et al., 2013; Morelli et al., 2010; Wagner et al., 2014), but with the two ancient strains (RISE505 and RISE509) falling basal to all other known strains of *Y. pestis* (100% bootstrap support).

Determination of *Yersinia pestis* Divergence Dates

To determine the dates for the most recent common ancestor (MRCA) of *Y. pestis* and *Y. pseudotuberculosis*, and for all known *Y. pestis* strains, we used a Bayesian Markov Chain Monte Carlo approach implemented in BEAST2 (Bouckaert et al., 2014) on a subset of the supermatrix. We estimated the MRCA of *Y. pestis* and *Y. pseudotuberculosis* to be 54,735 years ago (95% HPD [highest posterior density] interval: 34,659–78,803 years ago) (Figure 4C, Figure S5, Table S5), which is about twice as old compared to previous estimates of 2,600–28,000 years ago (Achtman et al., 1999, 2004; Cui et al., 2013; Wagner et al., 2014). Additionally, we estimated the age of the MRCA of all known *Y. pestis* to 5,783 years ago (95% HPD interval: 5,021–7,022 years ago). This is also significantly older and with a much narrower confidence interval than previous findings of 3,337 years ago (1,505–6,409 years ago) (Cui et al., 2013).

Bronze Age *Yersinia pestis* Strains Lacking *Yersinia* Murine Toxin

For the high-depth ancient *Y. pestis* genomes, we investigated the presence of 55 genes that have been associated with the virulence of *Y. pestis* (Figure 5A, Table S6). We found all virulence genes to be present, except the *Yersinia* murine toxin (*ymt*) gene that is located at 74.4–76.2 kb on the pMT1 plasmid (Figure 2C, arrow 1). The *ymt* gene encodes a phospholipase D that protects

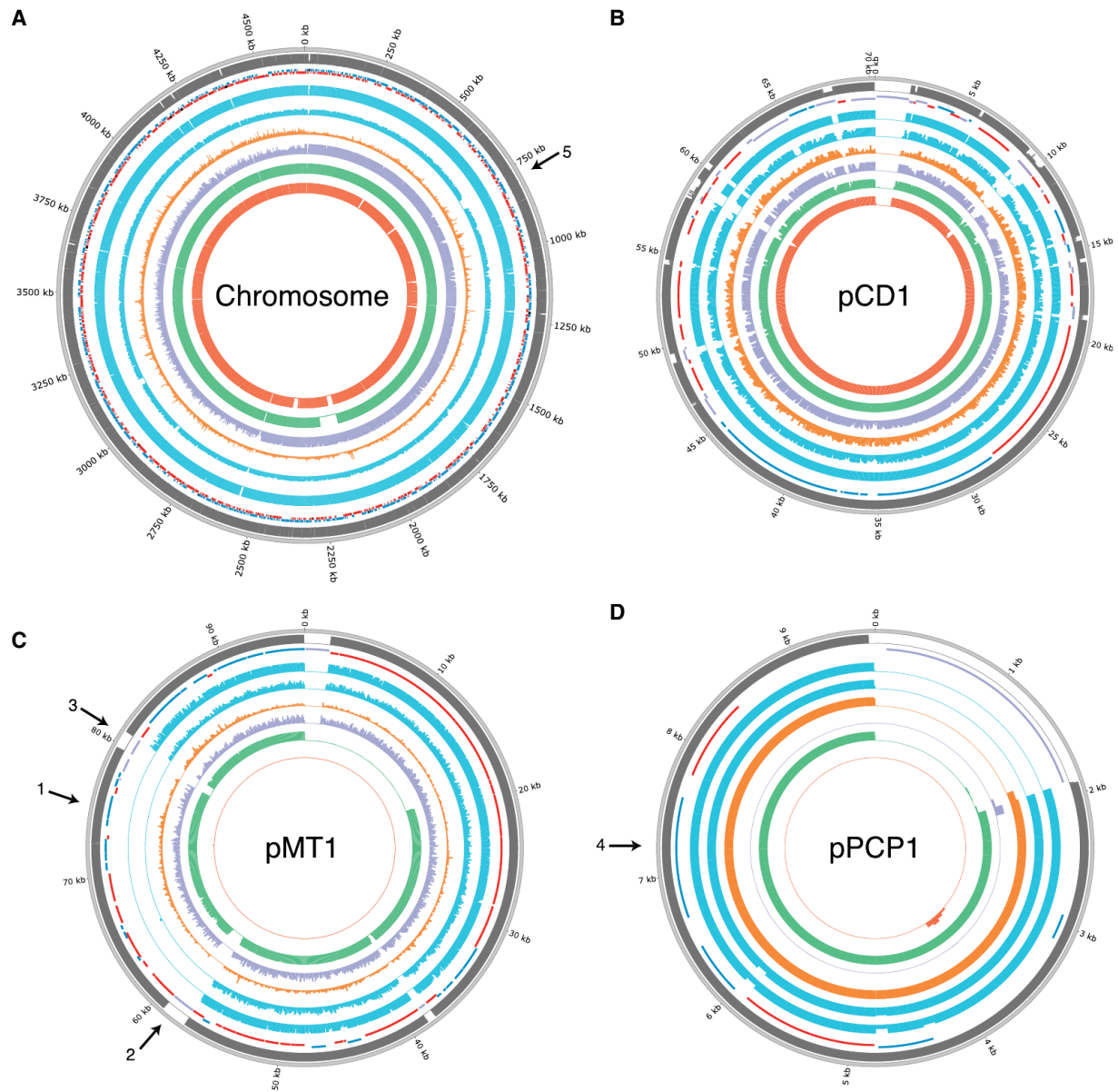


Figure 2. *Y. pestis* Depth of Coverage Plots

(A–D) Depth of coverage plots for (A) CO92 chromosome, (B) pCD1, (C) pMT1, (D) pPCP1. Outer ring: Mappability (gray), genes (RNA: black, transposon: purple, positive strand: blue, negative strand: red), RISE505 (blue), RISE509 (blue), Justinian plague (orange), Black Death plague (purple), modern *Y. pestis* D1982001 (green), *Y. pseudotuberculosis* IP32881 (red) sample. The modern *Y. pestis* and *Y. pseudotuberculosis* samples are included for reference. The histograms show sequence depth in 1 kb windows for the chromosome and 100 bp windows for the plasmids with a max of 20X depth for each ring. Arrow 1: *ymt* gene, arrow 2: transposon at start of missing region on pMT1, arrow 3: transposon at end of missing region on pMT1, arrow 4: *pla* gene, arrow 5: missing flagellin region on chromosome. The plots were generated using Circos (Krzywinski et al., 2009). See also Tables S2, S3 and S8.

Y. pestis inside the flea gut, thus enabling this enteric bacteria to use an arthropod as vector; it further allows for higher titers of *Y. pestis* and higher transmission rates (Hinnebusch, 2005; Hinnebusch et al., 2002). When investigating all seven samples for the presence of *ymt*, we identified a 19 kb region (59–78 kb, Figure 2C arrow 2–3, Figure 5B) to be missing except in the youngest sample (RISE397, 951 cal BC) (Figure 5B, Table S7). We find this region to be present in all other published *Y. pestis* strains

(modern and ancient), except three strains (5761, 945, and CA88) that are lacking the pMT1 plasmid completely.

Although larger sample sizes are needed for confirmation, our data indicate that the *ymt* gene was not present in *Y. pestis* before 1686 cal BC ($n = 6$), while after 951 cal BC, it is found in 97.8% of the strains ($n = 140$), suggesting a late and very rapid spread of *ymt*. This contrasts with previous studies arguing that the *ymt* gene was acquired early in *Y. pestis* evolution due

to its importance in its life cycle (Carniel, 2003; Hinnebusch, 2005; Hinnebusch et al., 2002; Sun et al., 2014). Interestingly, we identified two transposase elements flanking the missing 19 kb region, confirming that the *ymt* gene was acquired through horizontal gene transfer, as previously suggested (Lindler et al., 1998). Moreover, it has recently been shown that the transmission of *Y. pestis* by fleas is also dependent on loss of function mutations in the *pde2*, *pde3*, and *rcaA* genes (Sun et al., 2014). The RISE509 sample carries the promoter mutation of *pde3* and the functional *pde2* and *rcaA* alleles (Figure S6). In combination with the absence of *ymt*, these results strongly suggest that the ancestral *Y. pestis* bacteria in these early Bronze Age individuals were not transmitted by fleas.

Native Plasminogen Activator Gene Present in Bronze Age *Yersinia pestis*

Another hallmark gene of *Y. pestis* pathogenicity is the plasminogen activator gene *pla* (omptin protein family), located on the pPCP1 plasmid (6.6–7.6 kb). The gene facilitates deep tissue invasion and is essential for development of both bubonic and pneumonic plague (Sebbane et al., 2006; Sodeinde et al., 1992; Zimblet et al., 2015). We identify the gene in six of the seven genomes, but not in RISE139, the sample with the lowest overall depth of coverage (0.75X on pPCP1) (Figure 2D, arrow 4, Table S6). Recently, it has been proposed that pPCP1 was acquired after the branching of the 0.PE2 clade (Zimblet et al., 2015); however, we identified pPCP1 in our samples, including in the 0.PE7 clade (strains 620024 and CMCC05009), which diverged prior to the common ancestor of the 0.PE2 lineage (Figure 4B, Figure 5A). This shows that pPCP1 and *pla* likely were present in the most basal *Y. pestis* (RISE509), suggesting that the 0.PE2 strains lost the pPCP1 plasmid. Interestingly, three 2.ANT3 strains (5761, CMCC64001, and 735) are also missing the *pla* gene, indicating that the loss of pPCP1 occurred more than once in the evolutionary history of *Y. pestis*.

Additionally, we investigated whether RISE397, RISE505, and RISE509 had the isoleucine to threonine mutation at amino acid 259 in the Pla protein. This mutation has been shown to be essential for developing bubonic, but not pneumonic, plague (Zimblet et al., 2015). We found that these samples, in agreement with their basal phylogenetic position, carry the ancestral isoleucine residue. However, we also identified a valine to isoleucine mutation at residue 31 for RISE505 (1686 cal BC) and RISE509 (2746 cal BC). This mutation was not found in any of the other 140 *Y. pestis* strains, but was present in other omptin proteins, such as *Escherichia coli* and *Citrobacter koseri*, and very likely represents the ancestral *Y. pestis* state. The youngest of the samples, RISE397 (951 cal BC) carries the derived isoleucine residue, showing that this mutation, similar to the acquisition of *ymt*, was only observed after 1686 cal BC.

An alternative explanation to the acquisition of *ymt* and the *pla* I259T mutation, given the disparate geographical locations of our samples, could be that the Armenian strain (RISE397, 951 cal BC) containing *ymt* and the isoleucine residue in *pla* had a longer history in the Middle East and experienced an expansion during the 1st millennium BC. This would have led to its export to Eurasia and presumably the extinction of the other more ancestral and less virulent *Y. pestis* strains.

Different Region 4 Present in the Ancestral *Yersinia pestis*

Besides the 55 pathogenicity genes, we also investigated the presence of different region 4 (DFR4) that contains several genes with potential role in *Y. pestis* virulence (Radnedge et al., 2002). This region was reported as present in the Plague of Justinian and Black Death strains, having been lost in the CO92 reference genome (from the Third Pandemic) (Chain et al., 2004; Wagner et al., 2014). Consistent with the ancestral position of our samples, we find evidence that the region is present in all of our seven samples (Figure S6).

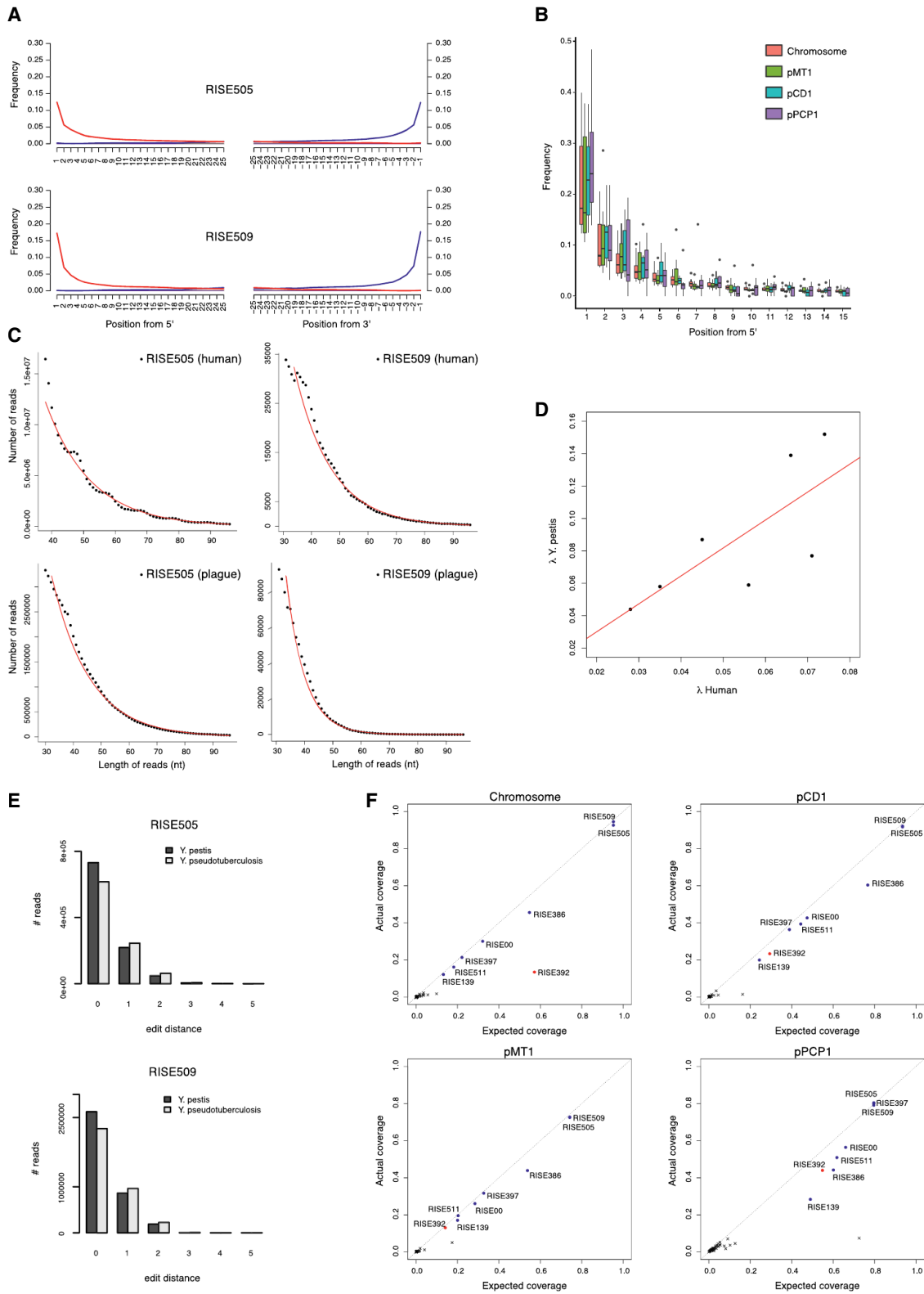
Yersinia pestis flagellar Frameshift Mutation Absent in Bronze Age Strains

Another important feature of *Y. pestis* is the ability to evade the mammalian immune system. Flagellin is a potent initiator of the mammalian innate immune system (Hayashi et al., 2001). *Y. pseudotuberculosis* is known to downregulate expression of flagellar systems in a temperature-dependent manner, and none of the known *Y. pestis* strains express flagellin due to a frameshift mutation in the *flhD* regulatory gene (Minnich and Rohde, 2007). However, we do not find this mutation in either RISE505 or RISE509, suggesting that they have fully functional *flhD* genes and that the loss of function occurred after 2746 cal BC. Interestingly, the youngest of these two *Y. pestis* genomes (RISE505, 1686 cal BC) shows partial loss of one of the two flagella systems (758–806 kb), with 39 of 49 genes deleted (Figure 2A, arrow 5, Table S8). This deletion was not found in any of the other *Y. pestis* samples ($n = 147$). This may point to selective pressure on ancestral *Y. pestis* when emerging as a mammalian pathogen, yielding variably adaptive strains.

DISCUSSION

Our calibrated molecular clock pushes the divergence dates for the early branching of *Y. pestis* back to 5,783 years ago, an additional 2,000 years compared to previous findings (Table S5, Figure S5) (Cui et al., 2013; Morelli et al., 2010). Furthermore, using the temporally stamped ancient DNA data, we are able to derive a time series for the molecular acquisition of the pathogenicity elements and immune avoidance systems that facilitated the evolution from a less virulent bacteria with zoonotic potential, such as *Y. pseudotuberculosis*, to one of the most deadly bacteria ever encountered by humans (Figure 6).

From our findings, we conclude that the ancestor of extant *Y. pestis* strains was present by the end of the 4th millennium BC and was widely spread across Eurasia from at least the early 3rd millennium BC. The occurrence of plague in the Bronze Age Eurasian individuals we sampled (7 of 101) indicates that plague infections were common at least 3,000 years earlier than recorded historically. However, based on the absence of crucial virulence genes, unlike the later *Y. pestis* strains that were responsible for the first to third pandemics, these ancient ancestral *Y. pestis* strains likely did not have the ability to cause bubonic plague, only pneumonic and septicemic plague. These early plagues may have been responsible for the suggested population declines in the late 4th millennium BC and the early 3rd millennium BC (Hinz et al., 2012; Shennan et al., 2013).



(legend on next page)

It has recently been demonstrated by ancient genomics that the Bronze Age in Europe and Asia was characterized by large-scale population movements, admixture, and replacements (Allentoft et al., 2015; Haak et al., 2015), which accompanied profound and archaeologically well-described social and economic changes (Anthony, 2007; Kristiansen and Larsson, 2005). In light of our findings, it is plausible that plague outbreaks could have facilitated—or have been facilitated by—these highly dynamic demographic events. However, our data suggest that *Y. pestis* did not fully adapt as a flea-borne mammalian pathogen until the beginning of the 1st millennium BC, which precipitated the historically recorded plagues.

EXPERIMENTAL PROCEDURES

Samples and Archaeological Sites

We initially re-analyzed the data from Allentoft et al. (Allentoft et al., 2015) and identified *Y. pestis* DNA sequences in 7 of the 101 individuals. Descriptions of the archaeological sites are given in Supplemental Experimental Procedures and Table S1.

Generation of Additional Sequence Data

In order to increase the depth of coverage on the *Y. pestis* genomes we sequenced more on these seven DNA extracts. Library construction was conducted as in (Allentoft et al., 2015). Briefly, double stranded and blunt-ended DNA libraries were prepared using the NEBNext DNA Sample Prep Master Mix Set 2 (E6070) and Illumina-specific adapters (Meyer and Kircher, 2010). The libraries were “shot-gun” sequenced in two pools on Illumina HiSeq2500 platforms using 100-bp single-read chemistry. We sequenced 32 lanes generating a total of 11.2 billion new DNA sequences for this study. Reads for the seven *Y. pestis* samples are available from ENA: PRJEB10885. Individual sample accessions numbers are available in Table S2.

Creation of Database for Identification of *Y. pestis* Reads

To identify *Y. pestis* reads in the Bronze Age dataset (Allentoft et al., 2015) we first created a database of all previously sequenced *Y. pestis* strains ($n = 140$), *Y. pseudotuberculosis* strains ($n = 30$), *Y. similis* strains ($n = 5$), and a selection of *Y. enterocolitica* strains ($n = 4$) (Supplemental Experimental Procedures and Table S2). The genomes were either downloaded from NCBI or downloaded as reads and de novo assembled using SPAdes-3.5.0 (Bankevich et al., 2012) with the `–careful` and `–cov-cutoff` auto options.

Identification and Assembly of *Y. pestis* From Ancient Samples

Raw reads were trimmed for adaptor sequences using AdapterRemoval-1.5.4 (Lindgreen, 2012). Additionally leading and trailing Ns were removed

as well as bases with quality 2 or less. Hereafter, the trimmed reads with a length of at least 30 nt were mapped using `bwa mem` (local alignment) (Li and Durbin, 2009) to the database of *Y. pestis*, *Y. pseudotuberculosis*, *Y. similis*, and *Y. enterocolitica* mentioned above. Reads with a match to any of the sequences in this database were aligned separately to three different reference genomes: *Yersinia pestis* CO92 genome including the associated plasmids pCD1, pMT1, pPCP1 (Parkhill et al., 2001); *Yersinia pseudotuberculosis* IP32953 including the associated plasmids (Chain et al., 2004); *Yersinia pestis* biovar *Microtus* 91001 and associated plasmids (Zhou et al., 2004). This alignment was performed using `bwa aln` (Li and Durbin, 2009) with the seed option disabled for better sensitivity for ancient data, enforcing global alignment of the read to the reference genome. Each sequencing run was merged to library level and duplicates removed using Picard-1.124 (<http://broadinstitute.github.io/picard/>), followed by merging to per sample alignment files. These files were filtered for a mapping quality of 30 to only retain high quality alignments and the base qualities were re-scaled for DNA damage using MapDamage 2.0 (Jónsson et al., 2013). We defined *Y. pestis* as present in a sample if the mapped depth of the CO92 reference sequence were higher or equal to 0.1X and if the reads covered at least 10% of the chromosome and each of the plasmids. The assembly of Justinian, Black Death, and the modern samples were performed similarly and is described in detail in the Supplemental Experimental Procedures.

Coverage, Depth and Mappability Analyses

We calculated the coverage of the individual sample alignments versus the *Y. pestis* CO92 reference genome using Bedtools (Quinlan and Hall, 2010) and plotted this using Circos (Krzywinski et al., 2009). For the chromosome, the coverage was calculated in 1 kbp windows and for the plasmids in 100 bp windows. Mappability was calculated using GEM-mappability library using a k-mer size of 50, which is similar to the average length of the trimmed and mapped *Y. pestis* reads (average length 43–65 bp). Statistics of the coverage and depth are given in Tables S3 and S4.

DNA Decay Rates

We investigated the molecular degradation signals obtained from the sequencing data. Based on the negative exponential relationship between frequency and sequence length, we estimated for each sample the DNA damage fraction (λ , per bond), the average fragment length ($1/\lambda$), the DNA decay rate (k , per bond per year), and the molecular half-lives of 100 bp fragments (Allentoft et al., 2012). We compared these DNA decay estimates for *Y. pestis* to the decay of endogenous human DNA from the host individuals. If the plague DNA is authentic and ancient, a correlation is expected between the rate of DNA decay in the human host and in *Y. pestis*, because the DNA has been exposed to similar environmental conditions for the same amount of time. See Supplemental Experimental Procedures for additional information.

Figure 3. Authenticity of *Y. pestis* DNA

- (A) DNA damage patterns for RISE505 and RISE509. The frequencies of all possible mismatches observed between the *Y. pestis* CO92 chromosome and the reads are reported in gray as a function of distance from 5' (left panel, first 25 nucleotides sequenced) and distance to 3' (right panel, last 25 nucleotides). The typical DNA damage mutations C>T (5') and G>A (3') are reported in red and blue, respectively.
- (B) Ancient DNA damage patterns ($n = 7$) of the reads aligned to the CO92 chromosome and the *Y. pestis* associated plasmids pMT1, pCD1 and pPCP1. The boxplots show the distribution of C-T damage in the 5' of the reads. The lower and upper hinges of the boxes correspond to the 25th and 75th percentiles, the whiskers represent the 1.5 inter-quartile range (IQR) extending from the hinges, and the dots represent outliers from these.
- (C) DNA fragment length distributions from RISE505 and RISE509 samples representing both the *Y. pestis* DNA and the DNA of the human host. The declining part of the distributions is fitted to an exponential model (red).
- (D) Linear correlation (red) between the decay constant in the DNA of the human host and the associated *Y. pestis* DNA extracted from the same individual ($R^2 = 0.55$, $p = 0.055$). The decay constant (λ) describes the damage fraction (i.e., the fraction of broken bonds on the DNA strand).
- (E) Distribution of edit distance of high quality reads from RISE505 and RISE509 samples mapped to either *Y. pestis* (dark gray) or *Y. pseudotuberculosis* (light gray) reference genomes. The reads have a higher affinity to *Y. pestis* than to *Y. pseudotuberculosis*.
- (F) Plots of actual coverage versus expected coverage for the 101 screened samples. Expected coverage was computed taking into account read length distributions, mappable fractions of reference sequences, and the deletions in pMT1 for some of the samples. Samples assumed to contain *Y. pestis* are shown in blue and RISE392 that is classified as not *Y. pestis* appears is shown in red. See also Figure S1 and S2, Table S3.

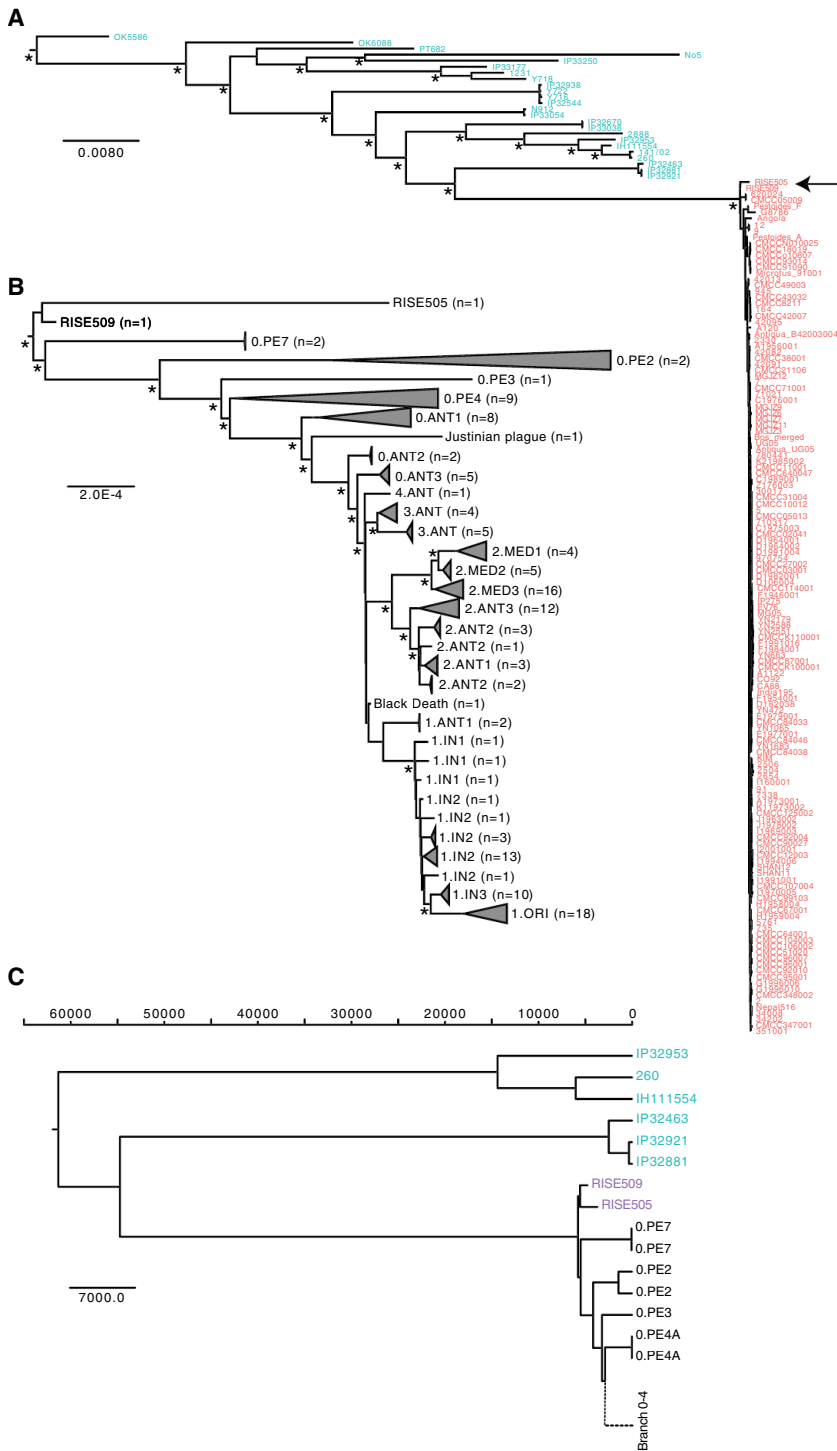


Figure 4. Phylogenetic Reconstructions

(A) Maximum Likelihood reconstruction of the phylogeny of *Y. pseudotuberculosis* (blue) and *Y. pestis* (red). The tree is rooted using *Y. similis* (not shown). The full tree including three additional *Y. pseudotuberculosis* strains (O:15 serovar) can be seen in Figure S4. Major branching nodes within *Y. pseudotuberculosis* with > 95% bootstrap support are indicated with an asterisk and branch lengths are given as substitutions per site.

(B) Maximum Likelihood reconstruction of the phylogeny in (A) showing only the *Y. pestis* clade. The clades are collapsed by population according to branches and serovars, as given in (Achtman et al., 1999, 2004; Cui et al., 2013). See Figure S4 for an uncollapsed tree and Table S2 for details on populations. Nodes with more than 95% bootstrap support are indicated with an asterisk and branch lengths are given as substitutions per site.

(C) BEAST2 maximum clade credibility tree showing median divergence dates. Branch lengths are given as years before the present (see Divergence estimations in Experimental Procedures). Only the *Y. pseudotuberculosis* (blue), the ancient *Y. pestis* samples (magenta) and the most basal branch 0 strains (black) are shown. For a full tree including all *Y. pestis* see Figure S5. See also Figure S3, S4, and S5 and Table S5.

sifier to classify whether reads were originating from *Y. pestis*, *Y. pseudotuberculosis*, or *Y. similis*. See Supplemental Experimental Procedures and Table S3.

Expected versus Actual Coverage

We estimated the expected coverage of *Y. pestis* given a specific sequencing depth and correlated that with the actual coverage of a genome per sample. Expected coverage was calculated as

$$c = 1 - \prod_{i=1}^N \left(1 - \frac{l_i}{g} \right)^{r_i}$$

where the reads have N different lengths, l_1 to l_N with counts r_1 to r_N . To account for mappability we determined the mappable fraction for each reference sequence using kmers of length 40, 50, and 60, and then used the mappability value with the k-mer length closest to the actual average read length for each sample/reference combination. For more information see Supplemental Experimental Procedures.

Genotyping For Phylogenetic Analyses

Alignments of all strains versus *Y. pseudotuberculosis* IP32953 was used as reference for genotyping the consensus sequences for all samples used in the phylogeny. The samples were genotyped individually using samtools-0.1.18 and bcftools-0.1.17 (Li et al., 2009) and hereafter filtered (Supplemental Experimental Procedures). Based on *Y. pseudotuberculosis* IP32953 gene annotations, the consensus sequences for each gene and sample were extracted. Because of the divergence between *Y. pestis* and *Y. pseudotuberculosis*, a number of gene sequences displayed high rates of missing bases and we removed genes where 20 or more modern *Y. pestis* samples had >10% missingness. This corresponded to a total of 985 genes, leaving data from 3,141 genes that were merged into

Comparison of Samples to *Y. pestis* and *Y. pseudotuberculosis* Reference Genomes

We used the alignments of several sets of reads (*Y. pestis*, *Y. pseudotuberculosis*, and *Y. similis*) to *Y. pestis* CO92 and the *Y. pseudotuberculosis* IP32953 genomes. Per sample we determined the distribution of edit-distances (mismatches) of the reads versus the particular reference genome. We used these distributions to build a Naive Bayesian clas-

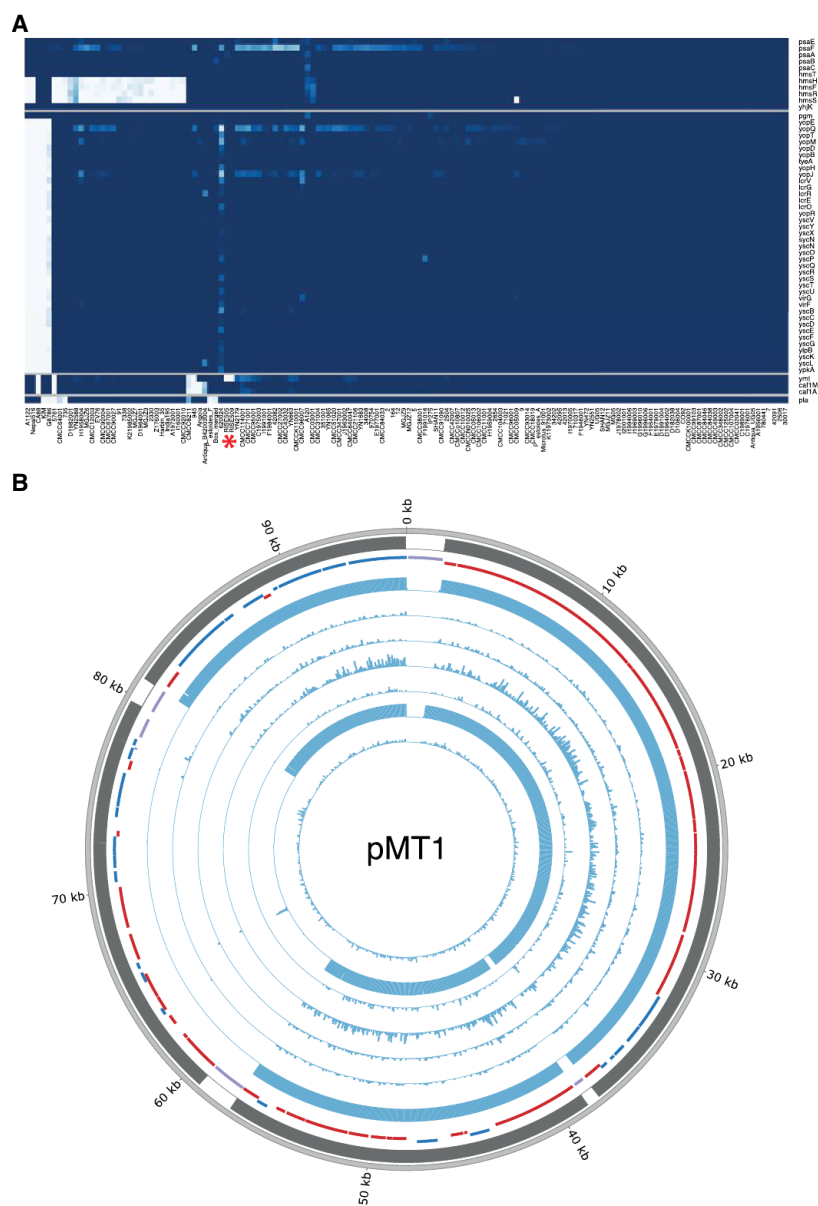


Figure 5. Identification of Virulence Genes

(A) Gene coverage heatmap of 55 virulence genes (rows) in 140 *Y. pestis* strains (columns). Sample ordering is based on hierarchical clustering (not shown) of the gene coverage distributions. RISE505 and RISE509 are marked with a red asterisk. Coloring goes from 0% gene coverage (white) to 100% gene coverage (blue).

(B) Depth of coverage of high quality reads mapping across pMT1. Outer ring is mappability (gray), genes (RNA: black, transposon: purple, positive strand: blue, negative strand: red) and then the RISE samples ordered after direct AMS dating. Sample ordering are RISE509, RISE511, RISE00, RISE386, RISE139, RISE505 and RISE397. See also Figure S6, Tables S2, S6, and S7. AMS: Accelerator Mass Spectrometry.

a supermatrix. We created two different supermatrices, one with *Y. similis*, *Y. pseudotuberculosis*, and *Y. pestis* containing 173 taxa \times 3,141 genes that was used for the initial phylogeny (Figure 4A). The second supermatrix consisted of all *Y. pestis* strains and the genomes from the two closest *Y. pseudotuberculosis* clades, which was used for the divergence time estimations.

Phylogenetics

The alignments were partitioned by codon position and analyzed with jmodeltest-2.1.7 (Darriba et al., 2012) to test for the best fitting substitution model. All decision criteria (Akaïke, Bayesian, and Decision theory) found the Generalized Time Reversible substitution model with gamma distributed rates, using four rate categories, and a proportion of invariable sites (GTR+G+I) to be the best fit for each of the three codon partitions. To test for recombination across the chromosome we estimated linkage disequilibrium (LD) using 141 *Y. pestis* strains. A total of 482 bi-allelic single nucleotide variations (SNVs), with a minor allele frequency of 5% or higher were extracted. For all pairs of the extracted

SNVs, the LD r^2 was calculated using PLINK 1.9 (Chang et al., 2015) and plotted against the physical distance between the pairs. We reconstructed the phylogeny from the codon-partitioned supermatrix using RAxML-8.1.15 (Stamatakis, 2014) with the GTR+G+I substitution model. Bootstraps were performed by generating 100 bootstrap replicates and their corresponding parsimony starting trees using RAxML. Hereafter, a standard Maximum Likelihood inference was run on each bootstrap replicate, and the resulting best trees were merged and drawn on the best ML tree. Initial phylogenies placed the *Y. pestis* Harbin strain with an unusual long branch inside the 1.ORI clade and it was excluded from further analysis. Additionally *Y. pseudotuberculosis* SP93422 (serotype O:15), *Y. pseudotuberculosis* WP-931201 (serotype O:15) and *Y. pseudotuberculosis* Y248 (serotype unknown) was in a clade with long branch lengths and were therefore also omitted (see Figure S4).

Heterozygosity Estimates

We determined heterozygosity by down-sampling the *Y. pestis* bam-files to the same average depth as the corresponding RISE samples, genotyped each of the samples and extracted heterozygote calls with a depth equal to or higher than 10. All transitions were excluded. See Supplemental Experimental Procedures for detailed information.

Divergence Estimations

To date the divergence time for *Y. pestis* and nodes within the *Y. pestis* clade we performed Bayesian Markov Chain Monte Carlo simulations using BEAST-2.3.0 (Bouckaert et al., 2014) and the BEAGLE library v2.1.2 (Ayres et al., 2012). We used the codon-partitioned supermatrix that included the two closest *Y. pseudotuberculosis* clades, with unlinked substitution models, GTR+G+I with eight gamma rate categories and unlinked clock models. Dates were set as years ago with the RISE509, RISE505, Justinian and Black Death samples set to 4,761, 3,701, 1,474, and 667 years ago, respectively. All unknown dates were set to 0 years ago. We followed previous work (Cui et al., 2013; Wagner et al., 2014) and applied a lognormal relaxed clock, assuming a constant population size. We re-rooted the ML tree from RAxML so that the root was placed between the two *Y. pseudotuberculosis* clades (IP32953, 260, IH111554) and (IP32921, IP32881, IP32463) and used this as the starting tree. Based on the ML tree we defined the closets *Y. pseudotuberculosis* clade (IP32921, IP32881, IP32463) and the *Y. pestis* clade as a monophyletic group and defined a uniform prior with 1,000 and 100,000 years as minimum and maximum bounds. We ran 20 independent parallel BEAST chains sampling every 2,000 states for between 52 and 64 million states using a total of 240,000 core hours. The chains were combined using LogCombiner discarding the initial 10 million states as burn-in. The combined post burn-in data represented 961 million states and

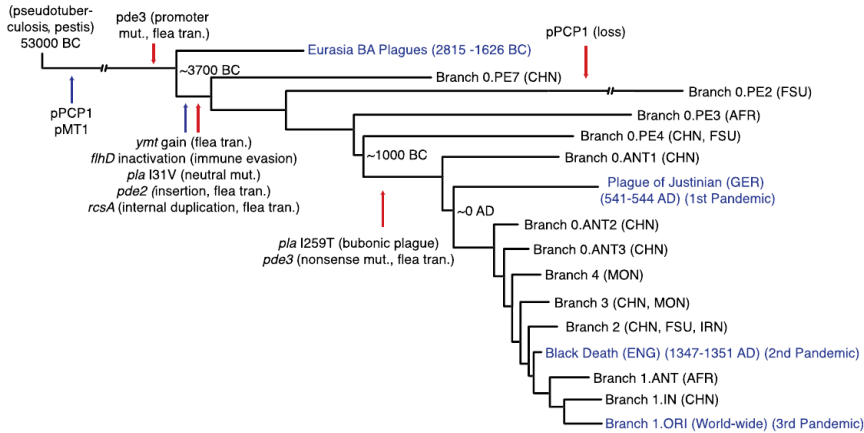


Figure 6. Schematic of *Y. pestis* Evolution
Representation of *Y. pestis* phylogeny and important evolutionary events since divergence from *Y. pseudotuberculosis*. Genetic gains (blue) and genetic loss or loss of function mutations (red) are indicated by arrows. Historical recorded pandemics are indicated in blue text. The calendric years indicates the primary outbreak of the Pandemic. Node dates are median divergence times from the BEAST analysis. The events are based on information from this study and Sun et al., 2014. We used the VCFs generated from all *Y. pestis* samples ($n = 142$) (Table S2) to verify on which branches the genetic events occurred. The figure is based on current knowledge and is subject to change with addition of new samples. See also Figure S5 and Table S5. BA: Bronze Age, CHN: China, FSU: Former Soviet Union, AFR: Africa, GER: Germany, MON: Mongolia, IRN: Iran, ENG: England, flea tran.: flea transmission, mut.: mutation.

the effective sample sizes (ESS) for the posterior was 398, for the TreeHeight 238 and for the MRCA for *Y. pseudotuberculosis* and *Y. pestis* 216. All other parameters had ESS > 125. We then sampled 1/5 of the trees from each chain and combined them for a total of 192,406 trees that were summarized using TreeAnnotator producing a maximum clade credibility tree of median heights. We additionally ran BEAST2 sampling the priors only (and disregarding sequence information) and found the posterior distribution no different than the priors used. It suggests that the posterior distributions recovered when considering full sequence alignments are driven by the sequence information and are not mere by-products of the sampling structure in our dataset (Figure S5).

Analysis of Virulence Associated Genes

To assess the potential virulence of the ancient *Y. pestis* strains, we identified 55 genes previously reported to be associated with virulence of *Y. pestis* (Supplemental Experimental Procedures and Table S6 for details). Based on the alignments to *Y. pestis* CO92 reference genome we determined the fraction of the each gene sequence that was covered by at least one read for each *Y. pestis* sample. Additionally, because the different region 4 (DFR4) (Radnedge et al., 2002) has been associated with virulence, but is not present in the CO92 genome, we used the alignments to *Y. pestis microtus* 91001 to determine the presence of this region (Supplemental Experimental Procedures). We note that the absence of KIM *pPCP1* is due to it being missing from the reference genome, but that it has been reported to be present in KIM strains (Hu et al., 1998). The genotypes were generated as described above and the variant call format (VCF) files from these analyses are available at <http://www.cbs.dtu.dk/suppl/plague/>. For detailed information on genotyping of *pde2*, *pde3*, *rscA*, *pla*, and *flhD* see Supplemental Experimental Procedures.

Identification of the Missing *ymt* Region on *pMT1*

Most of the regions that were unmapped could be associated with low mappability. However, we identified a region from 59–78 kb on *pMT1* that could not be explained by low mappability. From the depth of coverage this region was absent in all of our ancient plague genomes, except for RISE397 (Figure 5). We tested for the significance of this by comparing the distribution of gene depths within and outside of the missing region using the Wilcoxon rank-sum test (Table S7). For all samples except RISE397 the region had a median depth of 0X and the gene depth distributions were significantly different compared to the remaining *pMT1* plasmid genes (p values < $1E-9$). For the RISE397 sample, the regions had 0.43X and 0.42X median depths and there was no significant difference in the depth of the genes in the two regions (p value 0.77).

ACCESSION NUMBERS

The accession number for the reads for the seven *Y. pestis* samples reported in this paper is ENA: PRJEB10885.

SUPPLEMENTAL INFORMATION

Supplemental Information includes Supplemental Experimental Procedures, six figures, and eight tables and can be found with this article online at <http://dx.doi.org/10.1016/j.cell.2015.10.009>.

AUTHOR CONTRIBUTIONS

Conceptualization, K-G.S., R.N., K.K. and E.W.; methodology, S.R., M.E.A., A.G.P. and H.B.N.; software, S.R., K.N., M. Sikora, M. Schubert, and A.V.D.; Formal Analysis, S.R., M.E.A., K.N., M. Sikora, A.G.P., A.V.D. and M. Schubert.; Investigation, M.E.A. and K-G.S.; Resources, S.B., P.A., M.V.K., A.E., A. Gnuni, A.K., I.L., M.M., V.M., A. Gromov, D.P., L.S., L.V., L.Y. and T.S-P.; Writing – Original Draft, S.R., M.E.A., K.N., L.O., K-G.S., A.G.P., R.A.F., M.M.L., R.N., K.K. and E.W.; Writing Review & Editing, S.R., M.E.A., K.N., L.O., M. Sikora, K-G.S., A.G.P., A.V.D., C.M.O., R.A.F., M.M.L., R.N., K.K. and E.W.; Visualization, S.R. M.E.A., K-G.S. and A.G.P.; Supervision, L.O., T.S-P., R.N., K.K. and E.W.; Funding Acquisition, K.K. and E.W.

ACKNOWLEDGMENTS

The project was funded by The European Research Council (FP/2007-2013, grant 269442, The Rise), Marie Curie Actions of the European Union (FP7/2007-2013, grant 300554), The Villum Foundation (Young Investigator Programme, grant 10120), University of Copenhagen (KU2016 Programme), The Danish National Research Foundation, and The Lundbeck Foundation. A.V.D. was supported by the National Science Foundation Postdoctoral Research Fellowship in Biology under grant 1306489. S.B. was supported financially by the Novo Nordisk Foundation Grant agreement NNF14CC0001. We thank Jesper Stenderup for technical assistance and want to acknowledge the Danish national supercomputer – Computerome (computerome.cbs.dtu.dk) for the computational resources to perform the BEAST divergence estimations.

Received: August 6, 2015

Revised: September 30, 2015

Accepted: October 2, 2015

Published: October 22, 2015

REFERENCES

- Achtman, M., Zurth, K., Morelli, G., Torrea, G., Guiyoule, A., and Carniel, E. (1999). *Yersinia pestis*, the cause of plague, is a recently emerged clone of *Yersinia pseudotuberculosis*. Proc. Natl. Acad. Sci. USA 96, 14043–14048.
- Achtman, M., Morelli, G., Zhu, P., Wirth, T., Diehl, I., Kusecek, B., Vogler, A.J., Wagner, D.M., Allender, C.J., Easterday, W.R., et al. (2004). Microevolution

- and history of the plague bacillus, *Yersinia pestis*. *Proc. Natl. Acad. Sci. USA* *101*, 17837–17842.
- Allentoft, M.E., Collins, M., Harker, D., Haile, J., Oskam, C.L., Hale, M.L., Campos, P.F., Samaniego, J.A., Gilbert, M.T.P., Willerslev, E., et al. (2012). The half-life of DNA in bone: measuring decay kinetics in 158 dated fossils. *Proc. Biol. Sci.* *279*, 4724–4733.
- Allentoft, M.E., Sikora, M., Sjögren, K.-G., Rasmussen, S., Rasmussen, M., Stenderup, J., Damgaard, P.B., Schroeder, H., Ahlström, T., Vinner, L., et al. (2015). Population genomics of Bronze Age Eurasia. *Nature* *522*, 167–172.
- Anthony, D. (2007). *The Horse, The Wheel and Language. How Bronze-Age Riders from the Eurasian Steppes Shaped the Modern World* (Princeton: Princeton University Press).
- Ayres, D.L., Darling, A., Zwickl, D.J., Beerli, P., Holder, M.T., Lewis, P.O., Huelshenbeck, J.P., Ronquist, F., Swofford, D.L., Cummings, M.P., et al. (2012). BEAGLE: an application programming interface and high-performance computing library for statistical phylogenetics. *Syst. Biol.* *61*, 170–173.
- Bankevich, A., Nurk, S., Antipov, D., Gurevich, A.A., Dvorkin, M., Kulikov, A.S., Lesin, V.M., Nikolenko, S.I., Pham, S., Pribelski, A.D., et al. (2012). SPAdes: a new genome assembly algorithm and its applications to single-cell sequencing. *J. Comput. Biol.* *19*, 455–477.
- Bercovier, H., Mollaret, H.H., Alonso, J.M., Brault, J., Fanning, G.R., Steigerwalt, A.G., and Brenner, D.J. (1980). Intra- and interspecies relatedness of *Yersinia pestis* by DNA hybridization and its relationship to *Yersinia pseudotuberculosis*. *Curr. Microbiol.* *4*, 225–229.
- Bos, K.I., Schuenemann, V.J., Golding, G.B., Burbano, H.A., Waglechner, N., Coombes, B.K., McPhee, J.B., DeWitte, S.N., Meyer, M., Schmedes, S., et al. (2011). A draft genome of *Yersinia pestis* from victims of the Black Death. *Nature* *478*, 506–510.
- Bouckaert, R., Heled, J., Kühnert, D., Vaughan, T., Wu, C.-H., Xie, D., Suchard, M.A., Rambaut, A., and Drummond, A.J. (2014). BEAST 2: a software platform for Bayesian evolutionary analysis. *PLoS Comput. Biol.* *10*, e1003537.
- Carniel, E. (2003). Evolution of pathogenic *Yersinia*, some lights in the dark. In *The Genus Yersinia: Entering the Functional Genomic Era*. In *The Genus Yersinia*, M. Skurnik, J.A. Bengoechea, and K. Granfors, eds. (Boston: Springer US), pp. 3–11.
- Chain, P.S.G., Carniel, E., Larimer, F.W., Lamerdin, J., Stoutland, P.O., Regala, W.M., Georgescu, A.M., Vergez, L.M., Land, M.L., Motin, V.L., et al. (2004). Insights into the evolution of *Yersinia pestis* through whole-genome comparison with *Yersinia pseudotuberculosis*. *Proc. Natl. Acad. Sci. USA* *101*, 13826–13831.
- Chang, C.C., Chow, C.C., Tellier, L.C., Vattikuti, S., Purcell, S.M., and Lee, J.J. (2015). Second-generation PLINK: rising to the challenge of larger and richer datasets. *Gigascience* *4*, 7.
- Cui, Y., Yu, C., Yan, Y., Li, D., Li, Y., Jombart, T., Weinert, L.A., Wang, Z., Guo, Z., Xu, L., et al. (2013). Historical variations in mutation rate in an epidemic pathogen, *Yersinia pestis*. *Proc. Natl. Acad. Sci. USA* *110*, 577–582.
- Darriba, D., Taboada, G.L., Doallo, R., and Posada, D. (2012). jModelTest 2: more models, new heuristics and parallel computing. *Nat. Methods* *9*, 772.
- Drancourt, M., and Raoult, D. (2002). Molecular insights into the history of plague. *Microbes Infect.* *4*, 105–109.
- Drancourt, M., Aboudharam, G., Signoli, M., Dutour, O., and Raoult, D. (1998). Detection of 400-year-old *Yersinia pestis* DNA in human dental pulp: an approach to the diagnosis of ancient septicemia. *Proc. Natl. Acad. Sci. USA* *95*, 12637–12640.
- Haak, W., Lazaridis, I., Patterson, N., Rohland, N., Mallick, S., Llamas, B., Brandt, G., Nordenfelt, S., Harney, E., Stewardson, K., et al. (2015). Massive migration from the steppe was a source for Indo-European languages in Europe. *Nature* *522*, 207–211.
- Harbeck, M., Seifert, L., Hänsch, S., Wagner, D.M., Birdsell, D., Parise, K.L., Wiechmann, I., Grupe, G., Thomas, A., Keim, P., et al. (2013). *Yersinia pestis* DNA from skeletal remains from the 6(th) century AD reveals insights into Justinianic Plague. *PLoS Pathog.* *9*, e1003349.
- Hayashi, F., Smith, K.D., Ozinsky, A., Hawn, T.R., Yi, E.C., Goodlett, D.R., Eng, J.K., Akira, S., Underhill, D.M., and Aderem, A. (2001). The innate immune response to bacterial flagellin is mediated by Toll-like receptor 5. *Nature* *410*, 1099–1103.
- Hinnebusch, B.J. (2005). The evolution of flea-borne transmission in *Yersinia pestis*. *Curr. Issues Mol. Biol.* *7*, 197–212.
- Hinnebusch, B.J., Rudolph, A.E., Cherepanov, P., Dixon, J.E., Schwan, T.G., and Forsberg, A. (2002). Role of *Yersinia murine* toxin in survival of *Yersinia pestis* in the midgut of the flea vector. *Science* *296*, 733–735.
- Hinz, M., Feeser, I., Sjögren, K.-G., and Müller, J. (2012). Demography and the intensity of cultural activities: an evaluation of Funnel Beaker Societies (4200–2800 cal BC). *J. Archaeol. Sci.* *39*, 3331–3340.
- Hu, P., Elliott, J., McCready, P., Skowronski, E., Garnes, J., Kobayashi, A., Brubaker, R.R., and Garcia, E. (1998). Structural organization of virulence-associated plasmids of *Yersinia pestis*. *J. Bacteriol.* *180*, 5192–5202.
- Jónsson, H., Ginolhac, A., Schubert, M., Johnson, P.L.F., and Orlando, L. (2013). mapDamage2.0: fast approximate Bayesian estimates of ancient DNA damage parameters. *Bioinformatics* *29*, 1682–1684.
- Kristiansen, K., and Larsson, T.B. (2005). *The Rise of Bronze Age Society. Travels, Transmissions and Transformations* (New York: Cambridge University Press).
- Krzywinski, M., Schein, J., Birol, I., Connors, J., Gascoyne, R., Horsman, D., Jones, S.J., and Marra, M.A. (2009). CircoS: an information aesthetic for comparative genomics. *Genome Res.* *19*, 1639–1645.
- Li, H., and Durbin, R. (2009). Fast and accurate short read alignment with Burrows-Wheeler transform. *Bioinformatics* *25*, 1754–1760.
- Li, H., Handsaker, B., Wysoker, A., Fennell, T., Ruan, J., Homer, N., Marth, G., Abecasis, G., and Durbin, R.; 1000 Genome Project Data Processing Subgroup (2009). The Sequence Alignment/Map format and SAMtools. *Bioinformatics* *25*, 2078–2079.
- Lindgreen, S. (2012). AdapterRemoval: easy cleaning of next-generation sequencing reads. *BMC Res. Notes* *5*, 337.
- Lindler, L.E., Plano, G.V., Burland, V., Mayhew, G.F., and Blattner, F.R. (1998). Complete DNA sequence and detailed analysis of the *Yersinia pestis* KIM5 plasmid encoding murine toxin and capsular antigen. *Infect. Immun.* *66*, 5731–5742.
- Little, L.K., Hays, J.N., Morony, M., Kennedy, H.N., Stathakopoulos, D., Sarris, P., Stoclet, A.J., Kulikowski, M., Maddicott, J., Dooley, A., et al. (2007). Plague and the end of antiquity: The pandemic of 541–750 (Cambridge University Press).
- McNeill, W.H. (1976). *Plagues and Peoples* (New York: Anchor Books).
- Meyer, M., and Kircher, M. (2010). Illumina sequencing library preparation for highly multiplexed target capture and sequencing. *Cold Spring Harb. Protoc.* *2010*, pdb.prot5448.
- Minnich, S.A., and Rohde, H.N. (2007). A rationale for repression and/or loss of motility by pathogenic *Yersinia* in the mammalian host. *Adv. Exp. Med. Biol.* *603*, 298–310.
- Morelli, G., Song, Y., Mazzoni, C.J., Eppinger, M., Roumagnac, P., Wagner, D.M., Feldkamp, M., Kusecek, B., Vogler, A.J., Li, Y., et al. (2010). *Yersinia pestis* genome sequencing identifies patterns of global phylogenetic diversity. *Nat. Genet.* *42*, 1140–1143.
- Parkhill, J., Wren, B.W., Thomson, N.R., Titball, R.W., Holden, M.T., Prentice, M.B., Sebahia, M., James, K.D., Churcher, C., Mungall, K.L., et al. (2001). Genome sequence of *Yersinia pestis*, the causative agent of plague. *Nature* *413*, 523–527.
- Perry, R.D., and Fetherston, J.D. (1997). *Yersinia pestis*—etiologic agent of plague. *Clin. Microbiol. Rev.* *10*, 35–66.
- Quinlan, A.R., and Hall, I.M. (2010). BEDTools: a flexible suite of utilities for comparing genomic features. *Bioinformatics* *26*, 841–842.
- Radnedge, L., Agron, P.G., Worsham, P.L., and Andersen, G.L. (2002). Genome plasticity in *Yersinia pestis*. *Microbiology* *148*, 1687–1698.
- Sebbane, F., Jarrett, C.O., Gardner, D., Long, D., and Hinnebusch, B.J. (2006). Role of the *Yersinia pestis* plasminogen activator in the incidence of distinct

- septicemic and bubonic forms of flea-borne plague. *Proc. Natl. Acad. Sci. USA* *103*, 5526–5530.
- Shennan, S., Downey, S.S., Timpson, A., Edinborough, K., Colledge, S., Kerig, T., Manning, K., and Thomas, M.G. (2013). Regional population collapse followed initial agriculture booms in mid-Holocene Europe. *Nat. Commun.* *4*, 2486.
- Sodeinde, O.A., Subrahmanyam, Y.V., Stark, K., Quan, T., Bao, Y., and Goguen, J.D. (1992). A surface protease and the invasive character of plague. *Science* *258*, 1004–1007.
- Stamatakis, A. (2014). RAxML version 8: a tool for phylogenetic analysis and post-analysis of large phylogenies. *Bioinformatics* *30*, 1312–1313.
- Sun, Y.-C., Jarrett, C.O., Bosio, C.F., and Hinnebusch, B.J. (2014). Retracing the evolutionary path that led to flea-borne transmission of *Yersinia pestis*. *Cell Host Microbe* *15*, 578–586.
- Treille, G., and Yersin, A. (1894). La peste bubonique à Hong Kong. VIIIe Congrès Int. D'hygiène Démographie.
- Wagner, D.M., Klunk, J., Harbeck, M., Devault, A., Waglechner, N., Sahl, J.W., Enk, J., Birdsell, D.N., Kuch, M., Lumibao, C., et al. (2014). *Yersinia pestis* and the plague of Justinian 541–543 AD: a genomic analysis. *Lancet Infect. Dis.* *14*, 319–326.
- Willerslev, E., and Cooper, A. (2005). Ancient DNA. *Proc. Biol. Sci.* *272*, 3–16.
- Zhou, D., Tong, Z., Song, Y., Han, Y., Pei, D., Pang, X., Zhai, J., Li, M., Cui, B., Qi, Z., et al. (2004). Genetics of metabolic variations between *Yersinia pestis* biovars and the proposal of a new biovar, *microtus*. *J. Bacteriol.* *186*, 5147–5152.
- Zimble, D.L., Schroeder, J.A., Eddy, J.L., and Lathem, W.W. (2015). Early emergence of *Yersinia pestis* as a severe respiratory pathogen. *Nat. Commun.* *6*, 7487.

Personalized Nutrition by Prediction of Glycemic Responses

David Zeevi,^{1,2,8} Tal Korem,^{1,2,8} Niv Zmora,^{3,4,5,8} David Israeli,^{6,8} Daphna Rothschild,^{1,2} Adina Weinberger,^{1,2} Orly Ben-Yacov,^{1,2} Dar Lador,^{1,2} Tali Avnit-Sagi,^{1,2} Maya Lotan-Pompan,^{1,2} Jotham Suez,³ Jemal Ali Mahdi,³ Elad Matot,^{1,2} Gal Malka,^{1,2} Noa Kosower,^{1,2} Michal Rein,^{1,2} Gili Zilberman-Schapira,³ Lenka Dohnalová,³ Meirav Pevsner-Fischer,³ Rony Bikovsky,^{1,2} Zamir Halpern,^{5,7} Eran Elinav,^{3,9,*} and Eran Segal^{1,2,9,*}

¹Department of Computer Science and Applied Mathematics, Weizmann Institute of Science, Rehovot 7610001, Israel

²Department of Molecular Cell Biology, Weizmann Institute of Science, Rehovot 7610001, Israel

³Immunology Department, Weizmann Institute of Science, Rehovot 7610001, Israel

⁴Internal Medicine Department, Tel Aviv Sourasky Medical Center, Tel Aviv 6423906, Israel

⁵Research Center for Digestive Tract and Liver Diseases, Tel Aviv Sourasky Medical Center, Sackler Faculty of Medicine, Tel Aviv University, Tel Aviv 6423906, Israel

⁶Day Care Unit and the Laboratory of Imaging and Brain Stimulation, Kfar Shaul Hospital, Jerusalem Center for Mental Health, Jerusalem 9106000, Israel

⁷Digestive Center, Tel Aviv Sourasky Medical Center, Tel Aviv 6423906, Israel

⁸Co-first author

⁹Co-senior author

*Correspondence: eran.elinav@weizmann.ac.il (E.E.), eran.segal@weizmann.ac.il (E.S.)

<http://dx.doi.org/10.1016/j.cell.2015.11.001>

SUMMARY

Elevated postprandial blood glucose levels constitute a global epidemic and a major risk factor for prediabetes and type II diabetes, but existing dietary methods for controlling them have limited efficacy. Here, we continuously monitored week-long glucose levels in an 800-person cohort, measured responses to 46,898 meals, and found high variability in the response to identical meals, suggesting that universal dietary recommendations may have limited utility. We devised a machine-learning algorithm that integrates blood parameters, dietary habits, anthropometrics, physical activity, and gut microbiota measured in this cohort and showed that it accurately predicts personalized postprandial glycemic response to real-life meals. We validated these predictions in an independent 100-person cohort. Finally, a blinded randomized controlled dietary intervention based on this algorithm resulted in significantly lower postprandial responses and consistent alterations to gut microbiota configuration. Together, our results suggest that personalized diets may successfully modify elevated postprandial blood glucose and its metabolic consequences.

INTRODUCTION

Blood glucose levels are rapidly increasing in the population, as evident by the sharp incline in the prevalence of prediabetes and impaired glucose tolerance estimated to affect, in the U.S. alone, 37% of the adult population (Bansal, 2015). Prediabetes, charac-

terized by chronically impaired blood glucose responses, is a significant risk factor for type II diabetes mellitus (T2DM), with up to 70% of prediabetics eventually developing the disease (Nathan et al., 2007). It is also linked to other manifestations, collectively termed the metabolic syndrome, including obesity, hypertension, non-alcoholic fatty liver disease, hypertriglyceridemia, and cardiovascular disease (Grundy, 2012). Thus, maintaining normal blood glucose levels is considered critical for preventing and controlling the metabolic syndrome (Riccardi and Rivellese, 2000).

Dietary intake is a central determinant of blood glucose levels, and thus, in order to achieve normal glucose levels it is imperative to make food choices that induce normal postprandial (post-meal) glycemic responses (PPGR; Gallwitz, 2009). Postprandial hyperglycemia is an independent risk factor for the development of T2DM (American Diabetes Association., 2015a), cardiovascular disease (Gallwitz, 2009), and liver cirrhosis (Nishida et al., 2006) and is associated with obesity (Blaak et al., 2012), and enhanced all-cause mortality in both T2DM (Cavalot et al., 2011) and cancer (Lamkin et al., 2009).

Despite their importance, no method exists for predicting PPGRs to food. The current practice is to use the meal carbohydrate content (American Diabetes Association., 2015b; Bao et al., 2011), even though it is a poor predictor of the PPGR (Conn and Newburgh, 1936). Other methods aimed at estimating PPGRs are the glycemic index, which quantifies PPGR to consumption of a single tested food type, and the derived glycemic load (Jenkins et al., 1981). It thus has limited applicability in assessing the PPGR to real-life meals consisting of arbitrary food combinations and varying quantities (Dodd et al., 2011), consumed at different times of the day and at different proximity to physical activity and other meals. Indeed, studies examining the effect of diets with a low glycemic index on T2DM risk, weight loss, and cardiovascular risk factors yielded mixed results (Greenwood et al., 2013; Kristo et al., 2013; Schwingshackl and Hoffmann, 2013).

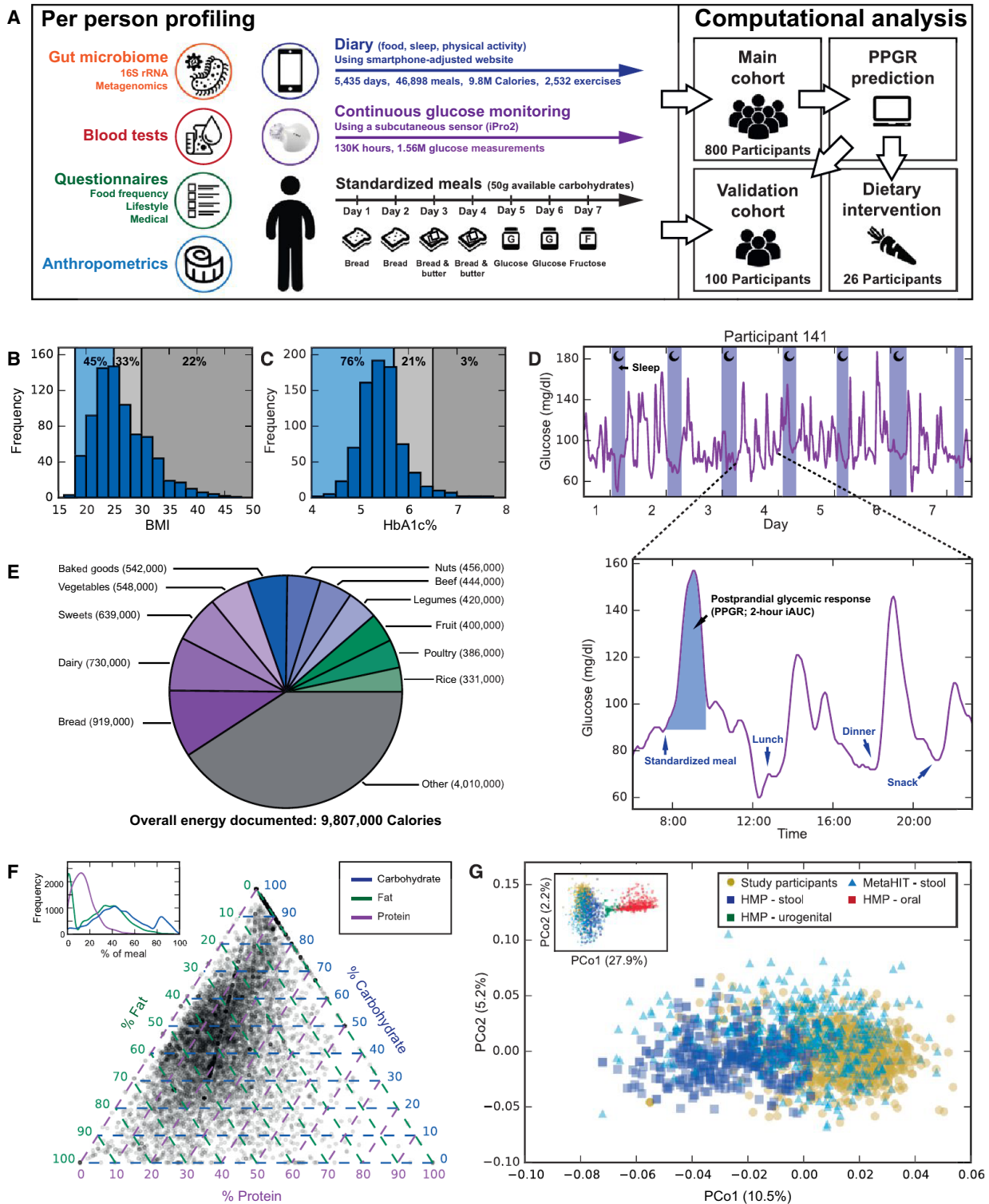


Figure 1. Profiling of Postprandial Glycemic Responses, Clinical Data, and Gut Microbiome

(A) Illustration of our experimental design.

(B and C) Distribution of BMI and glycated hemoglobin (HbA1c%) in our cohort. Thresholds for overweight (BMI ≥ 25 kg/m²), obese (BMI ≥ 30 kg/m²), prediabetes (HbA1c% $\geq 5.7\%$) and T1DM ($\geq 6.5\%$) are shown.

(legend continued on next page)

Table 1. Cohorts Description

	Main Cohort	Validation Cohort	KS p Value
Number of participants (n)	800	100	
Sex (% female)	60%	60%	1
Age (y) Mean \pm SD	43.3 \pm 13.1	42.4 \pm 12.6	0.972
BMI (kg/m ²) Mean \pm SD	26.4 \pm 5.1	26.5 \pm 4.8	0.867
BMI \geq 25	428 (54%)	50 (50%)	
BMI \geq 30	173 (22%)	18 (18%)	
HbA1c% Mean \pm SD	5.43 \pm 0.45	5.50 \pm 0.55	0.492
HbA1c% \geq 5.7	189 (24%)	31 (31%)	
HbA1c% \geq 6.5	23 (3%)	3 (3%)	
Total cholesterol (non-fasting, mg/dl) Mean \pm SD	186.8 \pm 37.5	182.7 \pm 35.7	0.231
HDL cholesterol (non-fasting, mg/dl) Mean \pm SD	59.0 \pm 17.8	55.0 \pm 16.1	0.371
Waist-to-hip circumference ratio Mean \pm SD	0.83 \pm 0.12	0.84 \pm 0.07	0.818

KS - Kolmogorov-Smirnov test. See also Figure S1.

More broadly, ascribing a single PPGR to each food assumes that the response is solely an intrinsic property of the consumed food. However, the few small-scale ($n = 23\text{--}40$) studies that examined interpersonal differences in PPGRs found high variability in the response of different people to the same food (Vega-López et al., 2007; Vrolix and Mensink, 2010), but the factors underlying this variability have not been systematically studied.

Factors that may affect interpersonal differences in PPGRs include genetics (Carpenter et al., 2015), lifestyle (Dunstan et al., 2012), insulin sensitivity (Himsworth, 1934), and exocrine pancreatic and glucose transporters activity levels (Gibbs et al., 1995). Another factor that may be involved is the gut microbiota. Pioneering work by Jeffrey Gordon and colleagues previously showed that it associates with the propensity for obesity and its complications, and later works also demonstrated associations with glucose intolerance, T1DM, hyperlipidemia, and insulin resistance (Le Chatelier et al., 2013; Karlsson et al., 2013; Qin et al., 2012; Suez et al., 2014; Turnbaugh et al., 2006; Zhang et al., 2013). However, little is known about the association of gut microbiota with PPGRs.

Here, we set out to quantitatively measure individualized PPGRs, characterize their variability across people, and identify factors associated with this variability. To this end, we continuously monitored glucose levels during an entire week in a cohort of 800 healthy and prediabetic individuals and also measured

blood parameters, anthropometrics, physical activity, and self-reported lifestyle behaviors, as well as gut microbiota composition and function. Our results demonstrate high interpersonal variability in PPGRs to the same food. We devised a machine learning algorithm that integrates these multi-dimensional data and accurately predicts personalized PPGRs, which we further validated in an independently collected 100-person cohort. Moreover, we show that personally tailored dietary interventions based on these predictions result in significantly improved PPGRs accompanied by consistent alterations to the gut microbiota.

RESULTS

Measurements of Postprandial Responses, Clinical Data, and Gut Microbiome

To comprehensively characterize PPGRs, we recruited 800 individuals aged 18–70 not previously diagnosed with T1DM (Figure 1A, Table 1). The cohort is representative of the adult non-diabetic Israeli population (Israeli Center for Disease Control, 2014), with 54% overweight (BMI ≥ 25 kg/m²) and 22% obese (BMI ≥ 30 kg/m², Figures 1B, 1C, and S1). These properties are also characteristic of the Western adult non-diabetic population (World Health Organization, 2008).

Each participant was connected to a continuous glucose monitor (CGM), which measures interstitial fluid glucose every 5 min for 7 full days (the “connection week”), using subcutaneous sensors (Figure 1D). CGMs estimate blood glucose levels with high accuracy (Bailey et al., 2014) and previous studies found no significant differences between PPGRs extracted from CGMs and those obtained from either venous or capillary blood (Vrolix and Mensink, 2010). We used blinded CGMs and thus participants were unaware of their CGM levels during the connection week. Together, we recorded over 1.5 million glucose measurements from 5,435 days.

While connected to the CGM, participants were instructed to log their activities in real-time, including food intake, exercise and sleep, using a smartphone-adjusted website (www.personalnutrition.org) that we developed (Figure S2A). Each food item within every meal was logged along with its weight by selecting it from a database of 6,401 foods with full nutritional values based on the Israeli Ministry of Health database that we further improved and expanded with additional items from certified sources. To increase compliance, participants were informed that accurate logging is crucial for them to receive an accurate analysis of their PPGRs to food (ultimately provided to each of them). During the connection week, participants were asked to follow their normal daily routine and dietary habits, except for the first meal of every day, which we provided as one of four different types of standardized meals, each consisting of 50 g of available carbohydrates. This resulted in a total of 46,898 real-life meals with close-to or full nutritional values (median of 54

(D) Example of continuous glucose monitoring (CGM) for one participant during an entire week. Colored area within zoom-in shows the incremental area under the glucose curve (IAUC) which we use to quantify the meal's PPGR.

(E) Major food components consumed by energy intake.

(F) Distribution of meals (dots) by macronutrient content. Inset shows histogram of meals per macronutrient.

(G) Bray-Curtis based PCoA of metagenome-based bacterial abundances of stool samples in our cohort and in the U.S. HMP and European MetaHIT cohorts. Inset shows PCoA when samples from other HMP body sites are added. See also Figure S2.

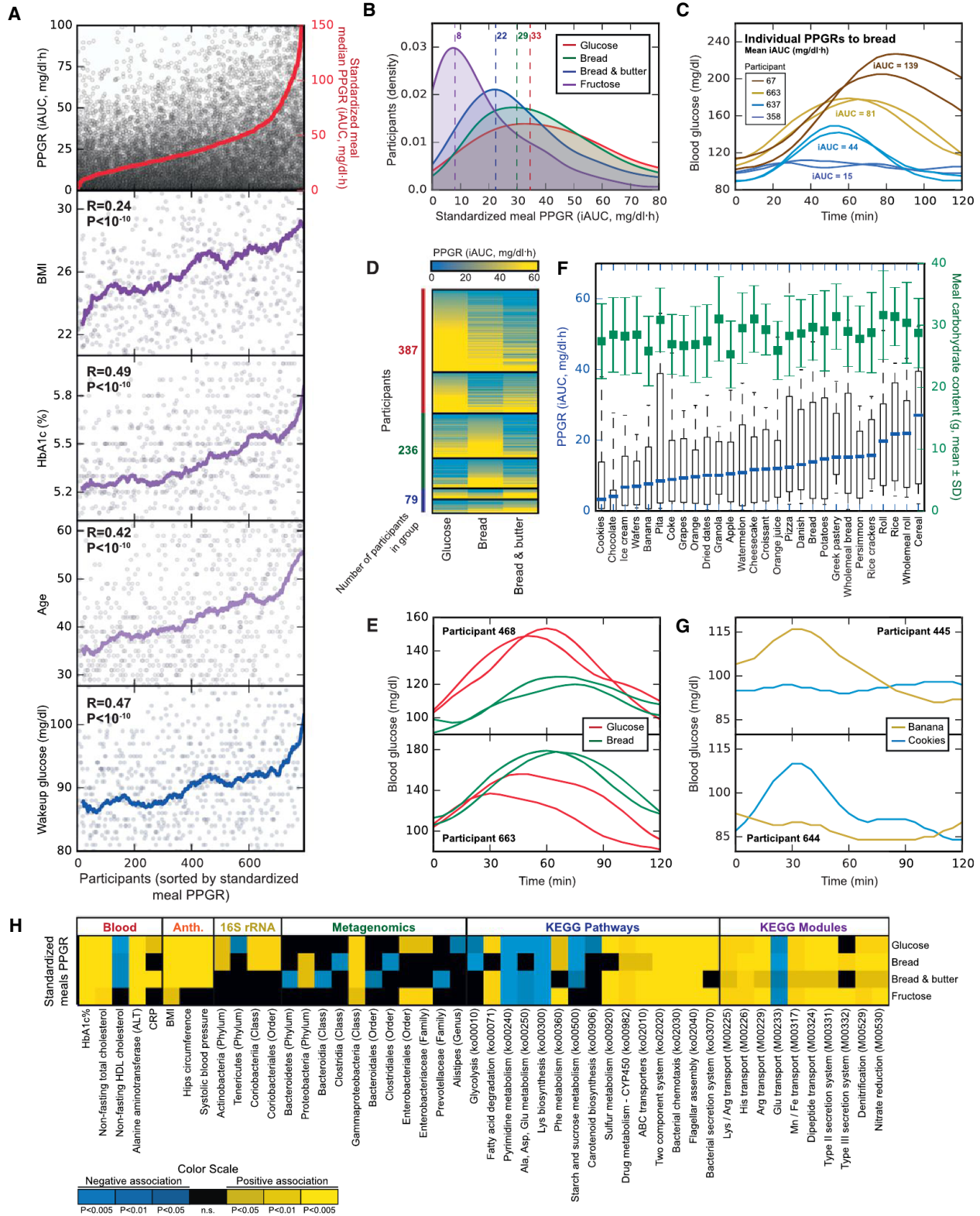


Figure 2. High Interpersonal Variability in the Postprandial Glycemic Response to the Same Meal

(A) PPGRs associate with risk factors. Shown are PPGRs, BMI, HbA1c%, age, and wakeup glucose of all participants, sorted by median standardized meal PPGR (top, red dots). Correlation of factors with the median PPGRs to standardized meals is shown along with a moving average line.

(legend continued on next page)

meals per participant) and 5,107 standardized meals. The PPGR of each meal was calculated by combining reported meal time with CGM data and computing the incremental area under the glucose curve in the 2 hr after the meal (iAUC; Wolever and Jenkins, 1986; Figure 1D).

Prior to CGM connection, a comprehensive profile was collected from each participant, including: food frequency, lifestyle, and medical background questionnaires; anthropometric measures (e.g., height, hip circumference); a panel of blood tests; and a single stool sample, used for microbiota profiling by both 16S rRNA and metagenomic sequencing.

With a total of ~10,000,000 Calories logged, our data provide a global view into the cohort's dietary habits, showing the fraction that each food source contributes to the cohort's overall energy intake (e.g., dairy, 7%; sweets, 6%; Figure 1E), and macronutrient intake (Figures S2B–S2D). Analysis of the caloric breakdown of every meal by macronutrients revealed that protein intake varies relatively little across meals (80% of meals have 5%–35% protein), while fat and carbohydrates have a wide and bimodal distribution, where one of the modes corresponds to fat-free meals and constitutes 18% of all meals (Figure 1F).

Principal coordinates analysis (PCoA) on the Bray-Curtis dissimilarity between metagenome-based relative abundances (RA) revealed a similar degree of variability in the microbiomes of our cohort and stool samples of the US HMP (Human Microbiome Project Consortium, 2012) and European MetaHIT (Nielsen et al., 2014) cohorts (Figure 1G). The first two principal coordinates show some distinction between our cohort and the other cohorts, but when HMP samples from other body sites are added to the PCoA, stool samples from all three cohorts cluster together and separate from the rest, indicative of overall similarity in the gut microbiota composition of individuals from these three distinct geographical regions (Figure 1G).

Postprandial Glycemic Responses Associate with Multiple Risk Factors

Our data replicate known associations of PPGRs with risk factors, as the median standardized meal PPGR was significantly correlated with several known risk factors including BMI ($R = 0.24$, $p < 10^{-10}$), glycated hemoglobin (HbA1c%, $R = 0.49$, $p < 10^{-10}$), wakeup glucose ($R = 0.47$, $p < 10^{-10}$), and age ($R = 0.42$, $p < 10^{-10}$, Figure 2A). These associations are not confined to extreme values but persist along the entire range of PPGR values, suggesting that the reduction in levels of risk factors is continuous across all postprandial values, with lower values associated with lower levels of risk factors even within the normal value ranges (Figure 2A).

Utilizing the continuous nature of the CGMs, we also examined the association between risk factors and the glucose level of each participant at different percentiles (0–100) with respect to all glucose measurements from the connection week. These levels are affected by the PPGRs while also reflecting the general glycemic control state of the participant. All percentiles significantly associated with risk factors (wakeup glucose, BMI, HbA1c%, and age; Figures S3A–S3D). The percentile at which the glucose level correlation was highest varied across risk factors. For example, BMI had the highest correlation with the 40th glucose value percentile, whereas for HbA1c% percentile 95 had the highest correlation (Figures S3A and S3C). These results suggest that the entire range of glucose levels of an individual may have clinical relevance, with different percentiles being more relevant for particular risk factors.

High Interpersonal Variability in the Postprandial Response to Identical Meals

Next, we examined intra- and interpersonal variability in the PPGR to the same food. First, we assessed the extent to which PPGRs to three types of standardized meals that were given twice to every participant (Figure 1A), are reproducible within the same person. Indeed, the two replicates showed high agreement ($R = 0.77$ for glucose, $R = 0.77$ for bread with butter, $R = 0.71$ for bread, $p < 10^{-10}$ in all cases), demonstrating that the PPGR to identical meals is reproducible within the same person and that our experimental system reliably measures this reproducibility. However, when comparing the PPGRs of different people to the same meal, we found high interpersonal variability, with the PPGRs of every meal type (except fructose) spanning the entire range of PPGRs measured in our cohort (Figures 2B, 2C, and S3E–S3H). For example, the average PPGR to bread across 795 people was 44 ± 31 mg/dl*h (mean \pm SD), with the bottom 10% of participants exhibiting an average PPGR below 15 mg/dl*h and the top 10% of participants exhibiting an average PPGR above 79 mg/dl*h. The large interpersonal differences in PPGRs are also evident in that the type of meal that induced the highest PPGR differs across participants and that different participants might have opposite PPGRs to pairs of different standardized meals (Figures 2D and 2E).

Interpersonal variability was not merely a result of participants having high PPGRs to all meals, since high variability was also observed when the PPGR of each participant was normalized to his/her own PPGR to glucose (Figures S3I–S3K). For white bread and fructose, for which such normalized PPGRs were previously measured, the mode of the PPGR distribution in our cohort had excellent agreement with published values (Foster-Powell et al.,

(B) Kernel density estimation (KDE) smoothed histogram of the PPGR to four types of standardized meals provided to participants (each with 50 g of available carbohydrates). Dashed lines represent histogram modes (See also Figure S3).

(C) Example of high interpersonal variability and low intra-personal variability in the PPGR to bread across four participants (two replicates per participant consumed on two different mornings).

(D) Heatmap of PPGR (average of two replicates) of participants (rows) to three types of standardized meals (columns) consumed in replicates. Clustering is by each participant's relative rankings of the three meal types.

(E) Example of two replicates of the PPGR to two standardized meals for two participants exhibiting reproducible yet opposite PPGRs.

(F) Box plot (box, IQR; whiskers, 10–90 percentiles) of the PPGR to different real-life meals along with amount of carbohydrates consumed (green; mean \pm std).

(G) Same as (E), for a pair of real-life meals, each containing 20 g of carbohydrates.

(H) Heatmap (subset) of statistically significant associations ($p < 0.05$, FDR corrected) between participants' standardized meals PPGRs and participants' clinical and microbiome data (See also Figure S4 for the full heatmap).

2002), further validating the accuracy of our data (bread: 65 versus 71; fructose: 15 versus 19, Figures S3I and S3K).

Next, we examined variability in the PPGRs to the multiple real-life meals reported by our participants. Since real-life meals vary in amounts and may each contain several different food components, we only examined meals that contained 20–40 g of carbohydrates and had a single dominant food component whose carbohydrate content exceeded 50% of the meal's carbohydrate content. We then ranked the resulting dominant foods that had at least 20 meal instances by their population-average PPGR (Figure 2F). For foods with a published glycemic index, our population-average PPGRs agreed with published values ($R = 0.69$, $p < 0.0005$), further supporting our data (Table S1). For example, the average PPGR to rice and potatoes was relatively high, whereas that for ice cream, beer, and dark chocolate was relatively low, in agreement with published data (Atkinson et al., 2008; Foster-Powell et al., 2002). Similar to standardized meals, PPGRs to self-reported meals highly varied across individuals, with both low and high responders noted for each type of meal (Figures 2F and 2G).

Postprandial Variability Is Associated with Clinical and Microbiome Profiles

We found multiple significant associations between the standardized meal PPGRs of participants and both their clinical and gut microbiome data (Figures 2H and S4). Notably, the T1DM and metabolic syndrome risk factors HbA1c%, BMI, systolic blood pressure, and alanine aminotransferase (ALT) activity are all positively associated with PPGRs to all types of standardized meals, reinforcing the medical relevance of PPGRs. In most standardized meals, PPGRs also exhibit a positive correlation with CRP, whose levels rise in response to inflammation (Figure 2H).

With respect to microbiome features, the phylogenetically related Proteobacteria and Enterobacteriaceae both exhibit positive associations with a few of the standardized meals PPGR (Figure 2H). These taxa have reported associations with poor glycemic control, and with components of the metabolic syndrome including obesity, insulin resistance, and impaired lipid profile (Xiao et al., 2014). RAs of Actinobacteria are positively associated with the PPGR to both glucose and bread, which is intriguing since high levels of this phylum were reported to associate with a high-fat, low-fiber diet (Wu et al., 2011).

At the functional level, the KEGG pathways of bacterial chemotaxis and of flagellar assembly, reported to increase in mice fed high-fat diets and decrease upon prebiotics administration (Everard et al., 2014), exhibit positive associations with several standardized meal PPGRs (Figure 2H). The KEGG pathway of ABC transporters, reported to be positively associated with T1DM (Karlsson et al., 2013) and with a Western high-fat/high-sugar diet (Turnbaugh et al., 2009), also exhibits positive association with several standardized meal PPGRs (Figure 2H). Several bacterial secretion systems, including both type II and type III secretion systems that are instrumental in bacterial infection and quorum sensing (Sandkvist, 2001) are positively associated with most standardized meal PPGRs (Figure 2H). Finally, KEGG modules for transport of the positively charged amino acids lysine and arginine are associated with high PPGR to standardized foods, while transport of the negatively charged

amino acid glutamate is associated with low PPGRs to these foods.

Taken together, these results show that PPGRs vary greatly across different people and associate with multiple person-specific clinical and microbiome factors.

Prediction of Personalized Postprandial Glycemic Responses

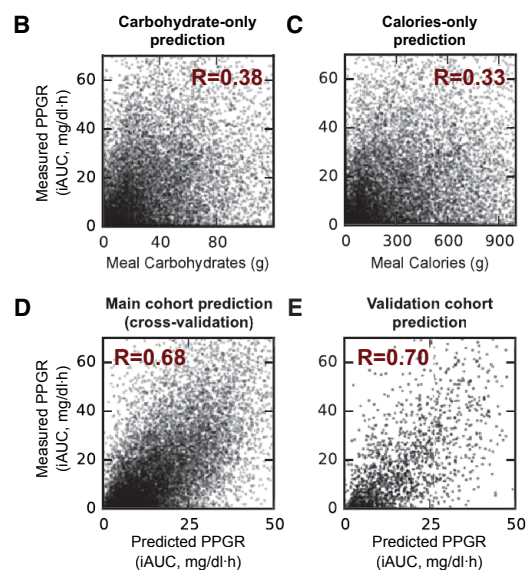
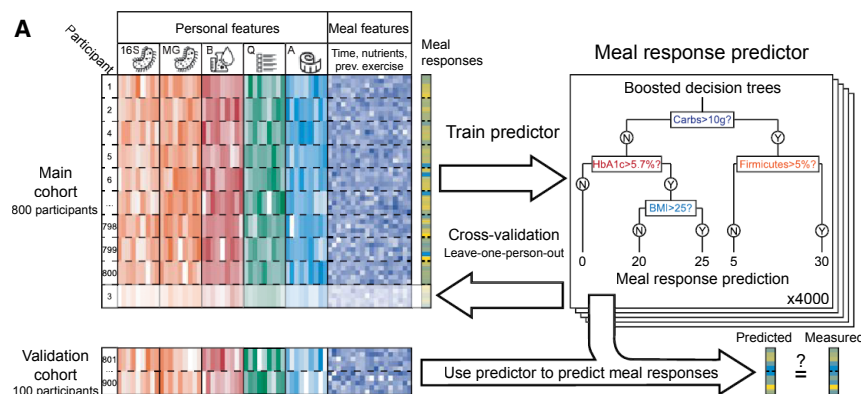
We next asked whether clinical and microbiome factors could be integrated into an algorithm that predicts individualized PPGRs. To this end, we employed a two-phase approach. In the first, discovery phase, the algorithm was developed on the main cohort of 800 participants, and performance was evaluated using a standard leave-one-out cross validation scheme, whereby PPGRs of each participant were predicted using a model trained on the data of all other participants. In the second, validation phase, an independent cohort of 100 participants was recruited and profiled, and their PPGRs were predicted using the model trained only on the main cohort (Figure 3A).

Given non-linear relationships between PPGRs and the different factors, we devised a model based on gradient boosting regression (Friedman, 2001). This model predicts PPGRs using the sum of thousands of different decision trees. Trees are inferred sequentially, with each tree trained on the residual of all previous trees and making a small contribution to the overall prediction (Figure 3A). The features within each tree are selected by an inference procedure from a pool of 137 features representing meal content (e.g., energy, macronutrients, micronutrients); daily activity (e.g., meals, exercises, sleep times); blood parameters (e.g., HbA1c%, HDL cholesterol); CGM-derived features; questionnaires; and microbiome features (16S rRNA and metagenomic RAs, KEGG pathway and module RAs and bacterial growth dynamics - PTRs; Korem et al., 2015).

As a baseline reference, we used the "carbohydrate counting" model, as it is the current gold standard for predicting PPGRs (American Diabetes Association., 2015b; Bao et al., 2011). On our data, this model that consists of a single explanatory variable representing the meal's carbohydrate amount achieves a modest yet statistically significant correlation with PPGRs ($R = 0.38$, $p < 10^{-10}$, Figure 3B). A model using only meal Caloric content performs worse ($R = 0.33$, $p < 10^{-10}$, Figure 3C). Our predictor that integrates the above person-specific factors predicts the held-out PPGRs of individuals with a significantly higher correlation ($R = 0.68$, $p < 10^{-10}$, Figure 3D). This correlation approaches the presumed upper bound limit set by the 0.71–0.77 correlation that we observed between the PPGR of the same person to two replicates of the same standardized meal.

Validation of Personalized Postprandial Glycemic Response Predictions on an Independent Cohort

We further validated our model on an independent cohort of 100 individuals that we recruited separately. Data from this additional cohort were not available to us while developing the algorithm. Participants in this cohort underwent the same profiling as in the main 800-person cohort. No significant differences were found between the main and validation cohorts in key parameters, including age, BMI, non-fasting total and HDL cholesterol, and HbA1c% (Table 1, Figure S1).



Notably, our algorithm, derived solely using the main 800 participants cohort, achieved similar performance on the 100 participants of the validation cohort ($R = 0.68$ and $R = 0.70$ on the main and validation cohorts, respectively, Figures 3D and 3E). The reference carbohydrate counting model achieved the same performance as in the main cohort ($R = 0.38$). This result further supports the ability of our algorithm to provide personalized PPGR predictions.

Factors Underlying Personalized Predictions

To gain insight into the contribution of the different features in the algorithm's predictions, we examined partial dependence plots (PDP), commonly used to study functional relations between features used in predictors such as our gradient boosting regressor and an outcome (PPGRs in our case; Hastie et al., 2008). PDPs graphically visualize the marginal effect of a given feature on prediction outcome after accounting for the average effect of all other features. While this effect may be indicative of feature importance, it may also be misleading due to higher-order interactions (Hastie et al., 2008). Nonetheless, PDPs are commonly used for knowledge discovery in large datasets such as ours.

Figure 3. Accurate Predictions of Personalized Postprandial Glycemic Responses

(A) Illustration of our machine-learning scheme for predicting PPGRs.

(B–E) PPGR predictions. Dots represent predicted (x axis) and CGM-measured PPGR (y axis) for meals, for a model based: only on the meal's carbohydrate content (B); only on the meal's Caloric content (C); our predictor evaluated in leave-one-person-out cross validation on the main 800-person cohort (D); and our predictor evaluated on the independent 100-person validation cohort (E). Pearson correlation of predicted and measured PPGRs is indicated.

As expected, the PDP of carbohydrates (Figure 4A) shows that as the meal carbohydrate content increases, our algorithm predicts, on average, a higher PPGR. We term this relation, of higher predicted PPGR with increasing feature value, as non-beneficial (with respect to prediction), and the opposite relation, of lower predicted PPGR with increasing feature value, as beneficial (also with respect to prediction; see PDP legend in Figure 4). However, since PDPs display the overall contribution of each feature across the entire cohort, we asked whether the relationship between carbohydrate amount and PPGRs varies across people. To this end, for each participant we computed the slope of the linear regression between the PPGR and carbohydrate amount of all his/her meals. As expected, this slope was

positive for nearly all (95.1%) participants, reflective of higher PPGRs in meals richer in carbohydrates. However, the magnitude of this slope varies greatly across the cohort, with the PPGR of some people correlating well with the carbohydrate content (i.e., carbohydrates "sensitive") and that of others exhibiting equally high PPGRs but little relationship to the amount of carbohydrates (carbohydrate "insensitive"; Figure 4B). This result suggests that carbohydrate sensitivity is also person specific.

The PDP of fat exhibits a beneficial effect for fat since our algorithm predicts, on average, lower PPGR as the meal's ratio of fat to carbohydrates (Figure 4C) or total fat content (Figure S5A) increases, consistent with studies showing that adding fat to meals may reduce the PPGR (Cunningham and Read, 1989). However, here too, we found that the effect of fat varies across people. We compared the explanatory power of a linear regression between each participant's PPGR and meal carbohydrates, with that of regression using both fat and carbohydrates. We then used the difference in Pearson R between the two models as a quantitative measure of the added contribution of fat (Figure 4D). For some participants we observed a reduction in PPGR with the addition of fat, while for others meal fat content

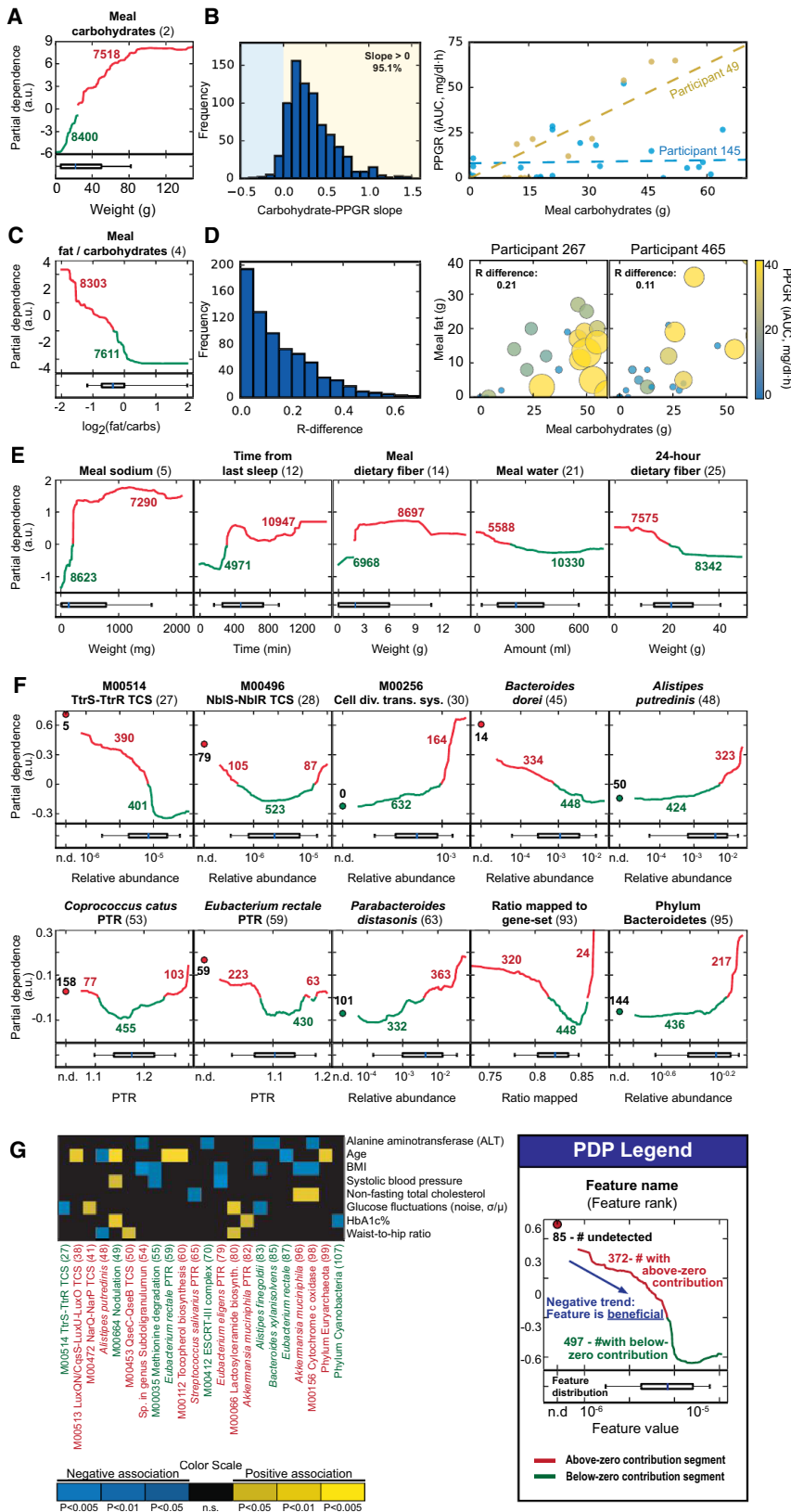


Figure 4. Factors Underlying the Prediction of Postprandial Glycemic Responses

(A) Partial dependence plot (PDP) showing the marginal contribution of the meal's carbohydrate content to the predicted PPGR (y axis, arbitrary units) at each amount of meal carbohydrates (x axis). Red and green indicate above and below zero contributions, respectively (number indicate meals). Boxplots (bottom) indicate the carbohydrates content at which different percentiles (10, 25, 50, 75, and 90) of the distribution of all meals across the cohort are located. See PDP legend.

(B) Histogram of the slope (computed per participant) of a linear regression between the carbohydrate content and the PPGR of all meals. Also shown is an example of one participant with a low slope and another with a high slope.

(C) Meal fat/carbohydrate ratio PDP.

(D) Histogram of the difference (computed per participant) between the Pearson R correlation of two linear regression models, one between the PPGR and the meal carbohydrate content and another when adding fat and carbohydrate*fat content. Also shown is an example of the carbohydrate and fat content of all meals of one participant with a relatively low R difference (carb alone correlates well with PPGR) and another with a relatively high difference (meals with high fat content have lower PPGRs). Dot color and size correspond to the meal's PPGR.

(E) Additional PDPs.

(F) Microbiome PDPs. The number of participants in which the microbiome feature was not detected is indicated (left, n.d.). Boxplots (box, IQR; whiskers 10–90 percentiles) based only on detected values.

(G) Heatmap of statistically significant correlations (Pearson) between microbiome features termed beneficial (green) or non-beneficial (red) and several risk factors and glucose parameters. See also Figure S5.

did not add much to the explanatory power of the regressor based only on the meal's carbohydrates content (Figure 4D).

Interestingly, while dietary fibers in the meal increase the predicted PPGR, their long-term effect is beneficial as higher amount of fibers consumed in the 24 hr prior to the meal reduces the predicted PPGR (Figure 4E). The meal's sodium content, the time that passed since last sleeping, and a person's cholesterol levels or age all exhibit non-beneficial PDPs, while the PDPs of the meal's alcohol and water content display beneficial effects (Figures 4E and S5A). As expected, the PDP of HbA1c% shows a non-beneficial effect with increased PPGR at higher HbA1c% values; intriguingly, higher PPGRs are predicted, on average, for individuals with HbA1c% above ~5.5%, which is very close to the prediabetes threshold of 5.7% (Figure S5A).

The 72 PDPs of the microbiome-based features used in our predictor were either beneficial (21 factors), non-beneficial (28), or non-decisive (23) in that they mostly decreased, increased, or neither, as a function of the microbiome feature. The resulting PDPs had several intriguing trends. For example, growth of *Eubacterium rectale* was mostly beneficial, as in 430 participants with high inferred growth for *E. rectale* it associates with a lower PPGR (Figure 4F). Notably, *E. rectale* can ferment dietary carbohydrates and fibers to produce metabolites useful to the host (Duncan et al., 2007), and was associated with improved postprandial glycemic and insulinemic responses (Martinez et al., 2013), as well as negatively associated with T1DM (Qin et al., 2012). RAs of *Parabacteroides distasonis* were found non-beneficial by our predictor (Figure 4F) and this species was also suggested to have a positive association with obesity (Ridaura et al., 2013). As another example, the KEGG module of cell-division transport system (M00256) was non-beneficial, and in the 164 participants with the highest levels for it, it associates with a higher PPGR (Figure 4F). *Bacteroides thetaiotaomicron* was non-beneficial (Figure S5B), and it was associated with obesity and was suggested to have increased capacity for energy harvest (Turnbaugh et al., 2006). In the case of *Alistipes putredinis* and the Bacteroidetes phylum, the non-beneficial classification that our predictor assigns to both of them is inconsistent with previous studies that found them to be negatively associated with obesity (Ridaura et al., 2013; Turnbaugh et al., 2006). This may reflect limitations of the PDP analysis or result from a more complex relationship between these features, obesity, and PPGRs.

To assess the clinical relevance of the microbiome-based PDPs, we computed the correlation between several risk factors and overall glucose parameters, and the factors with beneficial and non-beneficial PDPs across the entire 800-person cohort. We found 20 statistically significant correlations ($p < 0.05$, FDR corrected) where microbiome factors termed non-beneficial correlated with risk factors, and those termed beneficial exhibited an anti-correlation (Figure 4G). For example, higher levels of the beneficial methionine degradation KEGG module (M00035) resulted in lower PPGRs in our algorithm, and across the cohort, this module anti-correlates with systolic blood pressure and with BMI (Figure 4G). Similarly, fluctuations in glucose levels across the connection week correlates with nitrate respiration two-component regulatory system (M00472) and with lactosylceramide biosynthesis (M00066), which were both termed

non-beneficial. Glucose fluctuations also anti-correlate with levels of the tetrathionate respiration two-component regulatory system (M00514) and with RAs of *Alistipes fingoldii*, both termed beneficial (Figure 4G). In 14 other cases, factors with beneficial or non-beneficial PDPs were correlated and anti-correlated with risk factors, respectively.

These results suggest that PPGRs are associated with multiple and diverse factors, including factors unrelated to meal content.

Personally Tailored Dietary Interventions Improve Postprandial Responses

Next, we asked whether personally tailored dietary interventions based on our algorithm could improve PPGRs. We designed a two-arm blinded randomized controlled trial and recruited 26 new participants. A clinical dietitian met each participant and compiled 4–6 distinct isocaloric options for each type of meal (breakfast, lunch, dinner, and up to two intermediate meals), accommodating the participant's regular diet, eating preferences, and dietary constraints. Participants then underwent the same 1-week profiling of our main 800-person cohort (except that they consumed the meals compiled by the dietitian), thus providing the inputs (microbiome, blood parameters, CGM, etc.) that our algorithm needs for predicting their PPGRs.

Participants were then blindly assigned to one of two arms (Figure 5A). In the first, "prediction arm," we applied our algorithm in a leave-one-out scheme to rank every meal of each participant in the profiling week (i.e., the PPGR to each predicted meal was hidden from the predictor). We then used these rankings to design two 1-week diets: (1) a diet composed of the meals predicted by the algorithm to have low PPGRs (the "good" diet); and (2) a diet composed of the meals with high predicted PPGRs (the "bad" diet). Every participant then followed each of the two diets for a full week, during which they were connected to a CGM and a daily stool sample was collected (if available). The order of the 2 diet weeks was randomized for each participant and the identity of the intervention weeks (i.e., whether they are "good" or "bad") was kept blinded from CRAs, dietitians and participants.

The second, "expert arm," was used as a gold standard for comparison. Participants in this arm underwent the same process as the prediction arm except that instead of using our predictor for selecting their "good" and "bad" diets a clinical dietitian and a researcher experienced in analyzing CGM data (collectively termed "expert") selected them based on their measured PPGRs to all meals during the profiling week. Specifically, meals that according to the expert's analysis of their CGM had low and high PPGRs in the profiling week were selected for the "good" and "bad" diets, respectively. Thus, to the extent that PPGRs are reproducible within the same person, this expert-based arm should result in the largest differences between the "good" and "bad" diets because the selection of meals in the intervention weeks is based on their CGM data.

Notably, for 10 of the 12 participants of the predictor-based arm, PPGRs in the "bad" diet were significantly higher than in the "good" diet ($p < 0.05$, Figure 5C). Differences between the two diets are also evident in fewer glucose spikes and fewer fluctuations in the raw week-long CGM data (Figure 5B). The

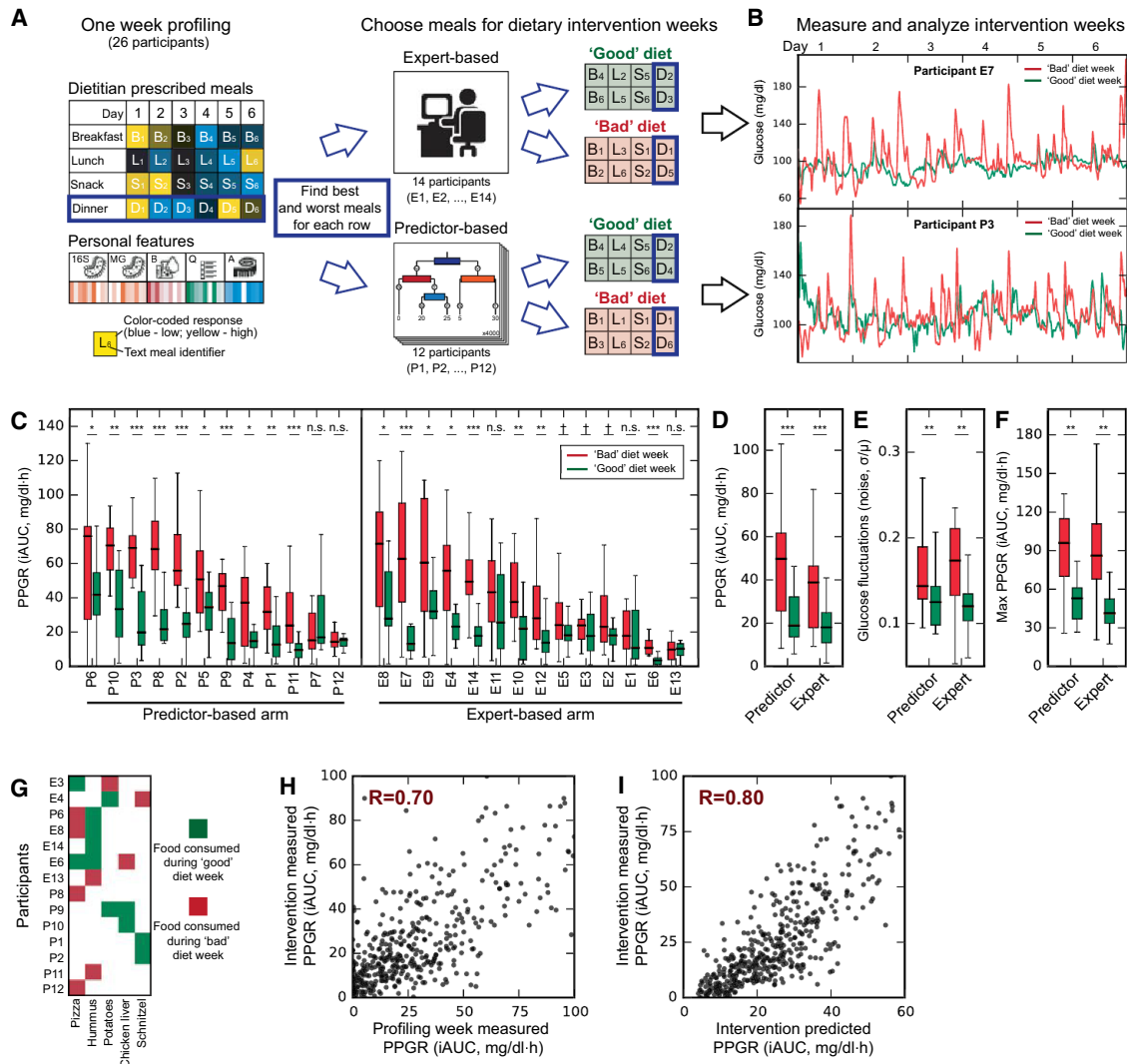


Figure 5. Personally Tailored Dietary Interventions Improve Postprandial Glycemic Responses

(A) Illustration of the experimental design of our two-arm blinded randomized controlled trial.

(B) Continuous glucose measurements of one participant from the expert arm (top) and another from the predictor arm (bottom) across their “good” (green) and “bad” (red) diet weeks.

(C) Boxplot of meal PPGRs during the “bad” (red) and “good” (green) diet weeks for participants in both the predictor (left) and expert (right) arms. Statistical significance is marked (Mann-Whitney *U*-test, ****p* < 0.001, ***p* < 0.01, **p* < 0.05, †*p* < 0.1, n.s. not significant).

(D) As in (C), but for a grouping of all meals of all participants in each study arm (*p*, Wilcoxon signed-rank test).

(E) Boxplot of the blood glucose fluctuations (noise) of participants in both the “bad” (red) and “good” (green) diet weeks for both study arms. Blood glucose fluctuations per participant are defined as the ratio between the standard deviation and mean of his/her weeklong blood glucose levels (*p*, Wilcoxon signed-rank test).

(F) As in (E), but for the maximum PPGR of each participant.

(G) Subset of dominant food components prescribed in the “good” (green) diet of some participants and in the “bad” (red) diet of other participants. See also Figure S6 for the full matrix.

(H) Dot plot between the CGM-measured PPGR of meals during the profiling week (*x* axis) and the average CGM-measured PPGR of the same meals during the dietary intervention weeks (*y* axis). Meals of all participants in both study arms are shown.

(I) As in (H), but when PPGRs in the dietary intervention weeks are predicted by our predictor using only the first profiling week data of each participant. Boxplots - box, IQR; whiskers 1.5*IQR.

success of the predictor was comparable to that of the expert-based arm, in which significantly lower PPGRs in the “good” versus the “bad” diet were observed for 8 of its 14 participants (*p* < 0.05, 11 of 14 participants with *p* < 0.1, Figure 5C).

When combining the data across all participants, the “good” diet exhibited significantly lower PPGRs than the “bad” diet (*p* < 0.05, Figure 5D) as well as improvement in other measures of blood glucose metabolism in both study arms, specifically,

lower fluctuations in glucose levels across the CGM connection week ($p < 0.05$, Figure 5E), and a lower maximal PPGR ($p < 0.05$, Figure 5F) in the “good” diet.

Both study arms constitute personalized nutritional interventions and thus demonstrate the efficacy of this approach in lowering PPGRs. However, the predictor-based approach has broader applicability since it can predict PPGRs to arbitrary unseen meals, whereas the “expert”-based approach will always require CGM measurements of the meals it prescribes.

Post hoc examination of the prescribed diets revealed the personalized aspect of the diets in both arms in that multiple dominant food components (as in Figure 2F) prescribed in the “good” diet of some participants were prescribed in the “bad” diet of others (Figures 5G and S6). This occurs when components induced opposite CGM-measured PPGRs across participants (expert arm) or were predicted to have opposite PPGRs (predictor arm).

The correlation between the measured PPGR of meals during the profiling week and the average CGM-measured PPGR of the same meals during the dietary intervention was 0.70 (Figure 5H), which is similar to the reproducibility observed for standardized meals ($R = 0.71\text{--}0.77$). Thus, as in the case of standardized meals, a meal’s PPGR during the profiling week was not identical to its PPGR in the dietary intervention week. Notably, using only the first profiling week data of each participant, our algorithm predicted the average PPGRs of meals in the dietary intervention weeks with an even higher correlation ($R = 0.80$, Figure 5I). Since our predictor also incorporates context-specific factors (e.g., previous meal content, time since sleep), this result also suggests that such factors may be important determinants of PPGRs.

Taken together, these results show the utility of personally tailored dietary interventions for improving PPGRs in a short-term intervention period, and the ability of our algorithm to devise such interventions.

Alterations in Gut Microbiota Following Personally Tailored Dietary Interventions

Finally, we used the daily microbiome samples collected during the intervention weeks to ask whether the interventions induced significant changes in the gut microbiota. Previous studies showed that even short-term dietary interventions of several days may significantly alter the gut microbiota (David et al., 2014; Korem et al., 2015).

We detected changes following the dietary interventions that were significant relative to a null hypothesis of no change derived from the first week, in which there was no intervention, across all participants (Figures 6A and 6B). While many of these significant changes were person-specific, several taxa changed consistently in most participants ($p < 0.05$, FDR corrected, Figure 6C and S7). Moreover, in most cases in which the consistently changing taxa had reported associations in the literature, the direction of change in RA following the “good” diet was in agreement with reported beneficial associations. For example, *Bifidobacterium adolescentis*, for which low levels were reported to be associated with greater weight loss (Santacruz et al., 2009), generally decrease in RA following the “good” diet and increase following the “bad” diet (Figure 6C,D). Similarly, T1DM has been associated with low levels of *Roseburia inulinivorans* (Qin et al.,

2012; Figure 6E), *Eubacterium eligens* (Karlsson et al., 2013), and *Bacteroides vulgatus* (Ridaura et al., 2013), and all these bacteria increase following the “good” diet and decrease following the “bad” diet (Figure 6C). The Bacteroidetes phylum, for which low levels associate with obesity and high fasting glucose (Turnbaugh et al., 2009), increases following the “good” diet and decreases following the “bad” diet (Figure 6C). Low levels of *Anaerostipes* associate with improved glucose tolerance and reduced plasma triglyceride levels in mice (Everard et al., 2011) and indeed these bacteria decrease following the “good” diet and increase following the “bad” diet (Figure 6C). Finally, low levels of *Alistipes putredinis* associate with obesity (Ridaura et al., 2013) and this bacteria increased following the “good” diet (Figure 6C).

These findings demonstrate that while both baseline microbiota composition and personalized dietary intervention vary between individuals, several consistent microbial changes may be induced by dietary intervention with a consistent effect on PPGR.

DISCUSSION

In this work we measured 46,898 PPGRs to meals in a population-based cohort of 800 participants. We demonstrate that PPGRs are highly variable across individuals even when they consume the same standardized meals. We further show that an algorithm that integrates clinical and microbiome features can accurately predict personalized PPGRs to complex, real-life meals even in a second independently collected validation cohort of 100 participants. Finally, personalized dietary interventions based on this algorithm induced lower PPGRs and were accompanied by consistent gut microbiota alterations.

Our study focused on PPGRs, as they were shown to be important in achieving proper glycemic control, and when disturbed are considered an independent disease risk factor (American Diabetes Association., 2015a; Gallwitz, 2009). PPGRs in our study also associated with several risk factors, including BMI, HbA1c%, and wakeup glucose. In addition to its centrality in glucose homeostasis, PPGRs serves as a convenient and accurate endpoint, enabling continuous “point-of-care” collection of dozens of quantitative measurements per person during a relatively short follow up period. Such continuous assessment of PPGRs is complementary to other equally important clinical parameters such as BMI and HbA1c%, for which changes typically occur over longer timescales and are thus difficult to correlate to nutritional responses in real time.

In line with few small-scale studies that previously examined individual PPGRs (Vega-López et al., 2007; Vrolix and Mensink, 2010), we demonstrate on 800 individuals that the PPGR of different people to the same food can greatly vary. The most compelling evidence for this observation is the controlled setting of standardized meals, provided to all participants in replicates. This high interpersonal variability suggests that at least with regard to PPGRs, approaches that grade dietary ingredients as universally “good” or “bad” based on their average PPGR in the population may have limited utility for an individual.

We report several associations between microbiome features and variability in PPGRs across people. In some cases, such as for Actinobacteria, Proteobacteria, and Enterobacteriaceae, the

direction of our associations are consistent with previous associations reported between these taxa and higher-level phenotypes such as dietary habits, obesity and overall glycemic control (Wu et al., 2011; Xiao et al., 2014), raising testable hypotheses about how these taxa may mediate these host metabolic effects. However, in most other cases we identify yet unknown associations with particular biosynthesis pathways or transport and secretion systems, which may be contributed by different taxa in different individuals. These correlations thus provide concrete new pointers for further mechanistic research, aimed at establishing causal roles for these bacterial taxa and functional pathways in determining PPGRs.

Our study further attempts to analyze real-life meals that are consumed in complex food combinations, at different times of the day, and in varying proximity to previous meals, physical activity, and sleep. While clearly of higher translational relevance, the use of “real-life” nutritional input also introduces noise into the meal composition data. Despite that, our results show that predictions for such meals can be made informative by integrating data from a large cohort into a carefully structured predictor. Even better predictions can likely be achieved with further research.

Our algorithm takes as input a comprehensive clinical and microbiome profile and employs a data-driven unbiased approach to infer the major factors that are predictive of PPGRs. Inspecting the resulting algorithm shows that its predictions integrate multiple diverse features that are unrelated to the content of the meal itself. These include contents of previous meals, time since sleep, proximity to exercise, and several microbiome-based factors. With respect to microbiome factors, our algorithm identifies multiple functional pathways and bacterial taxa as either beneficial or non-beneficial, such that in participants with increasing levels for these factors the algorithm predicts a lower or higher PPGR, respectively. In many such cases, microbiome factors found to be beneficial with respect to PPGRs are also negatively associated with risk factors such as HbA1c% and cholesterol levels.

Dietary interventions based on our predictor showed significant improvements in multiple aspects of glucose metabolism, including lower PPGRs and lower fluctuations in blood glucose levels within a short 1-week intervention period. It will be interesting to evaluate the utility of such personalized intervention over prolonged periods of several months and even years. If successful, prolonged individualized dietary control of the PPGR may be useful in controlling, ameliorating, or preventing a set of disorders associated with chronically impaired glucose control, including obesity, prediabetes, T1DM, and non-alcoholic fatty liver disease (Grundy, 2012). These intriguing possibilities, and the microbiome changes that accompany them, merit further studies. Of equal interest and importance, our individualized nutritional study protocols may be applicable to address other clinically relevant issues involving nutritional modifications,

such as T1DM and T2DM patient-specific determination of medication (e.g., insulin and oral hypoglycemics) dosing and timing.

Employing similar individualized prediction of nutritional effects on disease development and progression may also be valuable in rationally designing nutritional interventions in a variety of inflammatory, metabolic, and neoplastic multi-factorial disorders. More broadly, accurate personalized predictions of nutritional effects in these scenarios may be of great practical value, as they will integrate nutritional modifications more extensively into the clinical decision-making scheme.

EXPERIMENTAL PROCEDURES

Human Cohorts

Approved by Tel Aviv Sourasky Medical Center Institutional Review Board (IRB), approval numbers TLV-0658-12, TLV-0050-13 and TLV-0522-10; Kfar Shaul Hospital IRB, approval number 0-73; and Weizmann Institute of Science Bioethics and Embryonic Stem Cell Research oversight committee. Reported to <http://clinicaltrials.gov/>, NCT: NCT01892956.

Study Design

Study participants were healthy individuals aged 18–70 able to provide informed consent and operate a glucometer. Prior to the study, participants filled medical, lifestyle, and nutritional questionnaires. At connection week start, anthropometric, blood pressure and heart-rate measurements were taken by a CRA or a certified nurse, as well as a blood test. Glucose was measured for 7 days using the iPro2 CGM with Enlite sensors (Medtronic, MN, USA), independently calibrated with the Contour BGM (Bayer AG, Leverkusen, Germany) as required. During that week participants were instructed to record all daily activities, including standardized and real-life meals, in real-time using their smartphones; meals were recorded with exact components and weights. Full inclusion and exclusion criteria are detailed in Supplemental Experimental Procedures. Questionnaires used can be found in Data S1.

Standardized Meals

Participants were given standardized meals (glucose, bread, bread and butter, bread and chocolate, and fructose), calculated to have 50 g of available carbohydrates. Participants were instructed to consume these meals immediately after their night fast, not to modify the meal, and to refrain from eating or performing strenuous physical activity before, and for 2 hr following consumption.

Stool Sample Collection

Participants sampled their stool following detailed printed instructions. Sampling was done using a swab ($n = 776$) or both a swab and an OMNIgene-GUT (OMR-200; DNA Genotek) stool collection kit ($n = 413$, relative abundances (RA) for the same person are highly correlated ($R = 0.99$ $p < 10^{-10}$) between swabs and OMNIgene-GUT collection methods). Collected samples were immediately stored in a home freezer (-20°C), and transferred in a provided cooler to our facilities where it was stored at -80°C (-20°C for OMNIgene-GUT kits) until DNA extraction. All samples were taken within 3 days of connection week start.

Genomic DNA Extraction and Filtering

Genomic DNA was purified using PowerMag Soil DNA isolation kit (MoBio) optimized for Tecan automated platform. For shotgun sequencing, 100 ng of purified DNA was sheared with a Covaris E220X sonicator. Illumina compatible libraries were prepared as described (Suez et al., 2014). For 16S rRNA sequencing, PCR amplification of the V3/4 region using the 515F/806R 16S

(D) For *Bifidobacterium adolescentis*, which decreased significantly following the “good” diet interventions (see panel C), shown is the average and standard deviation of the (log) fold change of all participants in each day of the “good” (top) diet week relative to days 0–3 of the “good” week. Same for the “bad” diet week (bottom) in which *B. adolescentis* increases significantly (see panel C). Grey lines show fold changes (log) in individual participants.

(E) As in (D), for *Roseburia inulinivorans*.

rRNA gene primers was performed followed by 500 bp paired-end sequencing (Illumina MiSeq).

Microbial Analysis

We used USEARCH8.0 (Edgar, 2013) to obtain RA from 16S rRNA reads. We filtered metagenomic reads containing Illumina adapters, filtered low quality reads and trimmed low quality read edges. We detected host DNA by mapping with GEM (Marco-Sola et al., 2012) to the Human genome with inclusive parameters, and removed those reads. We obtained RA from metagenomic sequencing via MetaPhlan2 (Truong et al., 2015) with default parameters. We assigned length-normalized RA of genes, obtained by similar mapping with GEM to the reference catalog of (Li et al., 2014), to KEGG Orthology (KO) entries (Kanehisa and Goto, 2000), and these were then normalized to a sum of 1. We calculated RA of KEGG modules and pathways by summation. We considered only samples with >10K reads of 16S rRNA, and >10 M metagenomic reads (>1.5 M for daily samples in diet intervention cohort).

Associating PPGRs with Risk Factors and Microbiome Profile

We calculated the median PPGR to standardized meals for each participant who consumed at least four of the standardized meals and correlated it with clinical parameters (Pearson). We also calculated the mean PPGR of replicates of each standardized meal (if performed) and correlated (Pearson) these values with (a) blood tests; (b) anthropometric measurements; (c) 16S rRNA RA at the species to phylum levels; (d) MetaPhlan tag-level RA; and (e) RA of KEGG genes. We capped RA at a minimum of $1e-4$ (16S rRNA), $1e-5$ (MetaPhlan) and $2e-7$ (KEGG gene). For 16S rRNA analysis we removed taxa present in less than 20% of participants. Correlations on RAs were performed in logspace.

Enrichment analysis of higher phylogenetic levels (d) and KEGG pathways and modules (e) was performed by Mann-Whitney *U*-test between $-\log(p \text{ value}) \cdot \text{sign}(R)$ of above correlations (d, e) of tags or genes contained in the higher order groups and $-\log(p \text{ value}) \cdot \text{sign}(R)$ of the correlations of the rest of the tags or genes.

FDR Correction

FDR was employed at the rate of 0.15, per tested variable (e.g., glucose standardized PPGR) per association test (e.g., with blood tests) for analyses in Figure 2G and Figure S4; per phylogenetic level in Figure 6 and Figure S7; and on the entire association matrix in Figure 4G.

Meal Preprocessing

We merged meals logged less than 30 min apart and removed meals logged within 90 min of other meals. We also removed very small (<15 g and <70 Calories) meals and meals with very large (>1 kg) components, meals with incomplete logging and meals consumed at the first and last 12 hr of the connection week.

PPGR Predictor

Microbiome derived features were selected according to number of estimators using them in an additional predictor run on training data. For detailed feature list see Supplemental Experimental Procedures. We predicted PPGRs using stochastic gradient boosting regression, such that 80% of the samples and 40% of the features were randomly sampled for each estimator. The depth of the tree at each estimator was not limited, but leaves were restricted to have at least 60 instances (meals). We used 4000 estimators with a learning rate of 0.002.

Microbiome Changes during Dietary Intervention

We determined the significantly changing taxa of each participant by a *Z* test of fold-change in RA between the beginning and end of each intervention week against a null hypothesis of no change and standard deviation calculated from at least 25-fold changes across the first profiling week (no intervention) of corresponding taxa from all participants with similar initial RA. We checked whether a change was consistent across the cohort for each taxa by performing Mann-Whitney *U*-test between the *Z* statistics of the “good” intervention weeks and those of the “bad” intervention weeks across all participants.

A detailed description of methods used in this paper can be found in the Supplemental Experimental Procedures.

ACCESSION NUMBERS

The accession number for the data reported in this paper is ENA: PRJEB11532.

SUPPLEMENTAL INFORMATION

Supplemental Information includes Supplemental Experimental Procedures, seven figures, one table and one dataset and can be found with this article online at <http://dx.doi.org/10.1016/j.cell.2015.11.001>.

AUTHOR CONTRIBUTIONS

T.K. and D.Z. conceived the project, designed and conducted all analyses, interpreted the results, wrote the manuscript and are listed in random order. D.R. conceived and directed the dietary intervention (DI) study and designed and conducted analyses. T.K., D.Z., and A.W. designed protocols and supervised data collection. N.Z., D.I., Z.H., and E.E. coordinated and supervised clinical aspects of data collection. T.K., D.Z., N.Z. and D.I. equally contributed to this work. A.W. conceived the project, developed protocols, directed and performed sample sequencing. M.R. and O.B.-Y. supervised the DI study. O.B.-Y. conducted analyses and wrote the manuscript. D.L. conducted analyses, interpreted results and advised nutritional decisions. T.A.-S. and M.L.-P. developed protocols and together with E.M. performed metagenomic extraction and sequencing. N.Z., J.S., J.A.M., G.Z.-S., L.D., and M.P.-F. developed protocols and performed 16S sequencing. G.M., N.K. and R.B. coordinated and designed data collection. Z.H. conceived the project and provided infrastructure. E.E. and E.S. conceived and directed the project and analyses, designed data collection protocols, designed and conducted the analyses, interpreted the results, and wrote the manuscript.

ACKNOWLEDGMENTS

We thank the Segal and Elinav group members for fruitful discussions; Keren Segal, Yuval Dor, Tali Raveh-Sadka, Michal Levo, and Leeat Keren for fruitful discussions and critical insights to the manuscript; Guy Raz and Ran Chen for website development; Shira Zelber-Sagi for discussions; and Noya Horowitz for writing and submitting documents for review by IRBs. This research was supported by the Weizmann Institute of Science. T.K., D.Z., and D.R. are supported by the Ministry of Science, Technology, and Space, Israel. T.K. is supported by the Foulkes Foundation. E.E. is supported by Yael and Rami Ungar, Israel; Leona M. and Harry B. Helmsley Charitable Trust; the Gurwin Family Fund for Scientific Research; Crown Endowment Fund for Immunological Research; estate of Jack Gitlitz; estate of Lydia Hershkovich; the Benozio Endowment Fund for the Advancement of Science; John L. and Vera Schwartz, Pacific Palisades; Alan Markovitz, Canada; Cynthia Adelson, Canada; estate of Samuel and Alwyn J. Weber; Mr. and Mrs. Donald L. Schwarz, Sherman Oaks; grants funded by the European Research Council (ERC); the Israel Science Foundation (ISF); E.E. is the incumbent of the Rina Gudinski Career Development Chair. E.S. is supported by a research grant from Jack N. Halpern, and Mr. and Mrs. Donald L. Schwarz and by grants from the ERC and the ISF.

Received: October 5, 2015

Revised: October 29, 2015

Accepted: October 30, 2015

Published: November 19, 2015

REFERENCES

- American Diabetes Association (2015a). (5) Prevention or delay of type 2 diabetes. *Diabetes Care* 38 (Suppl), S31–S32.
- American Diabetes Association (2015b). (4) Foundations of care: education, nutrition, physical activity, smoking cessation, psychosocial care, and immunization. *Diabetes Care* 38 (Suppl), S20–S30.

- Atkinson, F.S., Foster-Powell, K., and Brand-Miller, J.C. (2008). International tables of glycemic index and glycemic load values: 2008. *Diabetes Care* 31, 2281–2283.
- Bailey, T.S., Ahmann, A., Brazg, R., Christiansen, M., Garg, S., Watkins, E., Welsh, J.B., and Lee, S.W. (2014). Accuracy and acceptability of the 6-day Enlite continuous subcutaneous glucose sensor. *Diabetes Technol. Ther.* 16, 277–283.
- Bansal, N. (2015). Prediabetes diagnosis and treatment: A review. *World J. Diabetes* 6, 296–303.
- Bao, J., Gilbertson, H.R., Gray, R., Munns, D., Howard, G., Petocz, P., Colagiuri, S., and Brand-Miller, J.C. (2011). Improving the estimation of mealtime insulin dose in adults with type 1 diabetes: the Normal Insulin Demand for Dose Adjustment (NIDDA) study. *Diabetes Care* 34, 2146–2151.
- Blaak, E.E., Antoine, J.-M., Benton, D., Björck, I., Bozzetto, L., Brouns, F., Diamant, M., Dye, L., Hulshof, T., Holst, J.J., et al. (2012). Impact of postprandial glycaemia on health and prevention of disease. *Obes. Rev.* 13, 923–984.
- Carpenter, D., Dhar, S., Mitchell, L.M., Fu, B., Tyson, J., Shwan, N.A.A., Yang, F., Thomas, M.G., and Armour, J.A.L. (2015). Obesity, starch digestion and amylase: association between copy number variants at human salivary (AMY1) and pancreatic (AMY2) amylase genes. *Hum. Mol. Genet.* 24, 3472–3480.
- Cavalot, F., Pagliarino, A., Valle, M., Di Martino, L., Bonomo, K., Massucco, P., Anfossi, G., and Trovati, M. (2011). Postprandial blood glucose predicts cardiovascular events and all-cause mortality in type 2 diabetes in a 14-year follow-up: lessons from the San Luigi Gonzaga Diabetes Study. *Diabetes Care* 34, 2237–2243.
- Conn, J.W., and Newburgh, L.H. (1936). The glycemic response to isoglucogenic quantities of protein and carbohydrate. *J. Clin. Invest.* 15, 665–671.
- Cunningham, K.M., and Read, N.W. (1989). The effect of incorporating fat into different components of a meal on gastric emptying and postprandial blood glucose and insulin responses. *Br. J. Nutr.* 61, 285–290.
- David, L.A., Maurice, C.F., Carmody, R.N., Gootenberg, D.B., Button, J.E., Wolfe, B.E., Ling, A.V., Devlin, A.S., Varma, Y., Fischbach, M.A., et al. (2014). Diet rapidly and reproducibly alters the human gut microbiome. *Nature* 505, 559–563.
- Dodd, H., Williams, S., Brown, R., and Venn, B. (2011). Calculating meal glycemic index by using measured and published food values compared with directly measured meal glycemic index. *Am. J. Clin. Nutr.* 94, 992–996.
- Duncan, S.H., Belongue, A., Holtrop, G., Johnstone, A.M., Flint, H.J., and Lobley, G.E. (2007). Reduced dietary intake of carbohydrates by obese subjects results in decreased concentrations of butyrate and butyrate-producing bacteria in feces. *Appl. Environ. Microbiol.* 73, 1073–1078.
- Dunstan, D.W., Kingwell, B.A., Larsen, R., Healy, G.N., Cerin, E., Hamilton, M.T., Shaw, J.E., Bertovic, D.A., Zimmet, P.Z., Salmon, J., and Owen, N. (2012). Breaking up prolonged sitting reduces postprandial glucose and insulin responses. *Diabetes Care* 35, 976–983.
- Edgar, R.C. (2013). UPARSE: highly accurate OTU sequences from microbial amplicon reads. *Nat. Methods* 10, 996–998.
- Everard, A., Lazarevic, V., Derrien, M., Girard, M., Muccioli, G.G., Neyrinck, A.M., Possemiers, S., Van Holle, A., François, P., de Vos, W.M., et al. (2011). Responses of gut microbiota and glucose and lipid metabolism to prebiotics in genetic obese and diet-induced leptin-resistant mice. *Diabetes* 60, 2775–2786.
- Everard, A., Lazarevic, V., Gaïa, N., Johansson, M., Ståhlman, M., Backhed, F., Delzenne, N.M., Schrenzel, J., François, P., and Cani, P.D. (2014). Microbiome of prebiotic-treated mice reveals novel targets involved in host response during obesity. *ISME J.* 8, 2116–2130.
- Foster-Powell, K., Holt, S.H.A., and Brand-Miller, J.C. (2002). International table of glycemic index and glycemic load values: 2002. *Am. J. Clin. Nutr.* 76, 5–56.
- Friedman, J.H. (2001). Greedy Function Approximation: A Gradient Boosting Machine. *Ann. Stat.* 29, 1189–1232.
- Gallwitz, B. (2009). Implications of postprandial glucose and weight control in people with type 2 diabetes: understanding and implementing the International Diabetes Federation guidelines. *Diabetes Care* 32 (Suppl 2), S322–S325.
- Gibbs, E.M., Stock, J.L., McCoid, S.C., Stukenbrok, H.A., Pessin, J.E., Stevenson, R.W., Milici, A.J., and McNeish, J.D. (1995). Glycemic improvement in diabetic db/db mice by overexpression of the human insulin-regulatable glucose transporter (GLUT4). *J. Clin. Invest.* 95, 1512–1518.
- Greenwood, D.C., Threapleton, D.E., Evans, C.E.L., Cleghorn, C.L., Nykjaer, C., Woodhead, C., and Burley, V.J. (2013). Glycemic index, glycemic load, carbohydrates, and type 2 diabetes: systematic review and dose-response meta-analysis of prospective studies. *Diabetes Care* 36, 4166–4171.
- Grundy, S.M. (2012). Pre-diabetes, metabolic syndrome, and cardiovascular risk. *J. Am. Coll. Cardiol.* 59, 635–643.
- Hastie, T., Tibshirani, R., and Friedman, J. (2008). *The Elements of Statistical Learning: Data Mining, Inference and Prediction* (Stanford: Springer).
- Himsworth, H.P. (1934). Dietetic factors influencing the glucose tolerance and the activity of insulin. *J. Physiol.* 81, 29–48.
- Human Microbiome Project Consortium (2012). Structure, function and diversity of the healthy human microbiome. *Nature* 486, 207–214.
- Israeli Center for Disease Control (2014). *Health 2013* (Jerusalem: Israeli Ministry of Health).
- Jenkins, D.J., Wolever, T.M., Taylor, R.H., Barker, H., Fielden, H., Baldwin, J.M., Bowling, A.C., Newman, H.C., Jenkins, A.L., and Goff, D.V. (1981). Glycemic index of foods: a physiological basis for carbohydrate exchange. *Am. J. Clin. Nutr.* 34, 362–366.
- Kanehisa, M., and Goto, S. (2000). KEGG: kyoto encyclopedia of genes and genomes. *Nucleic Acids Res.* 28, 27–30.
- Karlsson, F.H., Tremaroli, V., Nookaew, I., Bergström, G., Behre, C.J., Fagerberg, B., Nielsen, J., and Bäckhed, F. (2013). Gut metagenome in European women with normal, impaired and diabetic glucose control. *Nature* 498, 99–103.
- Korem, T., Zeevi, D., Suez, J., Weinberger, A., Avnit-Sagi, T., Pompan-Lotan, M., Matot, E., Jona, G., Harmelin, A., Cohen, N., et al. (2015). Growth dynamics of gut microbiota in health and disease inferred from single metagenomic samples. *Science* 349, 1101–1106.
- Kristo, A.S., Matthan, N.R., and Lichtenstein, A.H. (2013). Effect of diets differing in glycemic index and glycemic load on cardiovascular risk factors: review of randomized controlled-feeding trials. *Nutrients* 5, 1071–1080.
- Lamkin, D.M., Spitz, D.R., Shahzad, M.M.K., Zimmerman, B., Lenihan, D.J., Degeest, K., Lubaroff, D.M., Shinn, E.H., Sood, A.K., and Lutgendorf, S.K. (2009). Glucose as a prognostic factor in ovarian carcinoma. *Cancer* 115, 1021–1027.
- Le Chatelier, E., Nielsen, T., Qin, J., Prifti, E., Hildebrand, F., Falony, G., Almeida, M., Arumugam, M., Batto, J.-M., Kennedy, S., et al.; MetaHIT consortium (2013). Richness of human gut microbiome correlates with metabolic markers. *Nature* 500, 541–546.
- Li, J., Jia, H., Cai, X., Zhong, H., Feng, Q., Sunagawa, S., Arumugam, M., Kultima, J.R., Prifti, E., Nielsen, T., et al.; MetaHIT Consortium; MetaHIT Consortium (2014). An integrated catalog of reference genes in the human gut microbiome. *Nat. Biotechnol.* 32, 834–841.
- Marco-Sola, S., Sammeth, M., Guigó, R., and Ribeca, P. (2012). The GEM mapper: fast, accurate and versatile alignment by filtration. *Nat. Methods* 9, 1185–1188.
- Martinez, I., Lattimer, J.M., Hubach, K.L., Case, J.A., Yang, J., Weber, C.G., Louk, J.A., Rose, D.J., Kyureghian, G., Peterson, D.A., et al. (2013). Gut microbiome composition is linked to whole grain-induced immunological improvements. *ISME J.* 7, 269–280.
- Nathan, D.M., Davidson, M.B., DeFronzo, R.A., Heine, R.J., Henry, R.R., Pratley, R., and Zinman, B.; American Diabetes Association (2007). Impaired fasting glucose and impaired glucose tolerance: implications for care. *Diabetes Care* 30, 753–759.
- Nielsen, H.B., Almeida, M., Juncker, A.S., Rasmussen, S., Li, J., Sunagawa, S., Plichta, D.R., Gautier, L., Pedersen, A.G., Le Chatelier, E., et al.; MetaHIT

- Consortium; MetaHIT Consortium (2014). Identification and assembly of genomes and genetic elements in complex metagenomic samples without using reference genomes. *Nat. Biotechnol.* *32*, 822–828.
- Nishida, T., Tsuji, S., Tsujii, M., Arimitsu, S., Haruna, Y., Imano, E., Suzuki, M., Kanda, T., Kawano, S., Hiramoto, N., et al. (2006). Oral glucose tolerance test predicts prognosis of patients with liver cirrhosis. *Am. J. Gastroenterol.* *101*, 70–75.
- Qin, J., Li, Y., Cai, Z., Li, S., Zhu, J., Zhang, F., Liang, S., Zhang, W., Guan, Y., Shen, D., et al. (2012). A metagenome-wide association study of gut microbiota in type 2 diabetes. *Nature* *490*, 55–60.
- Riccardi, G., and Rivellese, A.A. (2000). Dietary treatment of the metabolic syndrome—the optimal diet. *Br. J. Nutr.* *83* (Suppl 1), S143–S148.
- Ridaura, V.K., Faith, J.J., Rey, F.E., Cheng, J., Duncan, A.E., Kau, A.L., Griffin, N.W., Lombard, V., Henrissat, B., Bain, J.R., et al. (2013). Gut microbiota from twins discordant for obesity modulate metabolism in mice. *Science* *341*, 1241214.
- Sandkvist, M. (2001). Type II secretion and pathogenesis. *Infect. Immun.* *69*, 3523–3535.
- Santacruz, A., Marcos, A., Wärnberg, J., Martí, A., Martín-Matillas, M., Campoy, C., Moreno, L.A., Veiga, O., Redondo-Figuero, C., Garagorri, J.M., et al.; EVASYON Study Group (2009). Interplay between weight loss and gut microbiota composition in overweight adolescents. *Obesity* (Silver Spring) *17*, 1906–1915.
- Schwingshackl, L., and Hoffmann, G. (2013). Long-term effects of low glycemic index/load vs. high glycemic index/load diets on parameters of obesity and obesity-associated risks: a systematic review and meta-analysis. *Nutr. Metab. Cardiovasc. Dis.* *23*, 699–706.
- Suez, J., Korem, T., Zeevi, D., Silberman-Schapiro, G., Thaiss, C.A., Maza, O., Israeli, D., Zmora, N., Gilad, S., Weinberger, A., et al. (2014). Artificial sweeteners induce glucose intolerance by altering the gut microbiota. *Nature* *514*, 181–186.
- Truong, D.T., Franzosa, E.A., Tickle, T.L., Scholz, M., Weingart, G., Pasolli, E., Tett, A., Huttenhower, C., and Segata, N. (2015). MetaPhlan2 for enhanced metagenomic taxonomic profiling. *Nat. Methods* *12*, 902–903.
- Turnbaugh, P.J., Ley, R.E., Mahowald, M.A., Magrini, V., Mardis, E.R., and Gordon, J.I. (2006). An obesity-associated gut microbiome with increased capacity for energy harvest. *Nature* *444*, 1027–1031.
- Turnbaugh, P.J., Hamady, M., Yatsunenkov, T., Cantarel, B.L., Duncan, A., Ley, R.E., Sogin, M.L., Jones, W.J., Roe, B.A., Affourtit, J.P., et al. (2009). A core gut microbiome in obese and lean twins. *Nature* *457*, 480–484.
- Vega-López, S., Ausman, L.M., Griffith, J.L., and Lichtenstein, A.H. (2007). Interindividual variability and intra-individual reproducibility of glycemic index values for commercial white bread. *Diabetes Care* *30*, 1412–1417.
- Vrolix, R., and Mensink, R.P. (2010). Variability of the glycemic response to single food products in healthy subjects. *Contemp. Clin. Trials* *31*, 5–11.
- Wolever, T.M., and Jenkins, D.J. (1986). The use of the glycemic index in predicting the blood glucose response to mixed meals. *Am. J. Clin. Nutr.* *43*, 167–172.
- World Health Organization (2008). Global Health Observatory Data Repository (Disease and Injury Country Estimates).
- Wu, G.D., Chen, J., Hoffmann, C., Bittinger, K., Chen, Y.-Y., Keilbaugh, S.A., Bewtra, M., Knights, D., Walters, W.A., Knight, R., et al. (2011). Linking long-term dietary patterns with gut microbial enterotypes. *Science* *334*, 105–108.
- Xiao, S., Fei, N., Pang, X., Shen, J., Wang, L., Zhang, B., Zhang, M., Zhang, X., Zhang, C., Li, M., et al. (2014). A gut microbiota-targeted dietary intervention for amelioration of chronic inflammation underlying metabolic syndrome. *FEMS Microbiol. Ecol.* *87*, 357–367.
- Zhang, X., Shen, D., Fang, Z., Jie, Z., Qiu, X., Zhang, C., Chen, Y., and Ji, L. (2013). Human gut microbiota changes reveal the progression of glucose intolerance. *PLoS ONE* *8*, e71108.

Variation in the Human Immune System Is Largely Driven by Non-Heritable Influences

Petter Brodin,^{1,2,3,11} Vladimir Jojic,^{4,11} Tianxiang Gao,⁴ Sanchita Bhattacharya,³ Cesar J. Lopez Angel,^{2,3} David Furman,^{2,3} Shai Shen-Orr,⁵ Cornelia L. Dekker,⁶ Gary E. Swan,⁷ Atul J. Butte,^{6,8} Holden T. Maecker,^{3,9} and Mark M. Davis^{2,3,10,*}

¹Science for Life Laboratory, Department of Medicine, Solna, Karolinska Institutet, 17121 Solna, Sweden

²Department of Microbiology and Immunology, Stanford University School of Medicine, Stanford, CA 94304, USA

³Institute of Immunity, Transplantation and Infection, Stanford University School of Medicine, Stanford, CA 94304, USA

⁴Department of Computer Science, University of North Carolina at Chapel Hill, Chapel Hill, NC 27599, USA

⁵Department of Immunology, Faculty of Medicine, Technion, Haifa 31096, Israel

⁶Department of Pediatrics, Stanford University School of Medicine, Stanford, CA 94304, USA

⁷Stanford Prevention Research Center, Department of Medicine, Stanford University School of Medicine, Stanford, CA 94304, USA

⁸Center for Pediatric Bioinformatics, Lucille Packard Children's Hospital, Stanford University, Stanford, CA 94304, USA

⁹Human Immune Monitoring Center, Stanford University School of Medicine, Stanford, CA 94304, USA

¹⁰Howard Hughes Medical Institute, Stanford University School of Medicine, Stanford, CA 94304, USA

¹¹Co-first author

*Correspondence: mmdavis@stanford.edu

<http://dx.doi.org/10.1016/j.cell.2014.12.020>

SUMMARY

There is considerable heterogeneity in immunological parameters between individuals, but its sources are largely unknown. To assess the relative contribution of heritable versus non-heritable factors, we have performed a systems-level analysis of 210 healthy twins between 8 and 82 years of age. We measured 204 different parameters, including cell population frequencies, cytokine responses, and serum proteins, and found that 77% of these are dominated (>50% of variance) and 58% almost completely determined (>80% of variance) by non-heritable influences. In addition, some of these parameters become more variable with age, suggesting the cumulative influence of environmental exposure. Similarly, the serological responses to seasonal influenza vaccination are also determined largely by non-heritable factors, likely due to repeated exposure to different strains. Lastly, in MZ twins discordant for cytomegalovirus infection, more than half of all parameters are affected. These results highlight the largely reactive and adaptive nature of the immune system in healthy individuals.

INTRODUCTION

The study of monozygotic (MZ) and dizygotic (DZ) twin pairs has provided a powerful means for separating heritable from non-heritable influences on measured traits for almost 100 years (Jablonski, 1922). Such studies have been used to study autoimmune diseases, vaccine responses (Jacobson et al., 2007), serum cytokines (de Craen et al., 2005), or the frequencies of major immune cell populations (Clementi et al., 1999; Evans et al., 2004). Most of these studies have found that both heritable

and non-heritable factors contribute to the resulting phenotype. Recent advances in technology now allow much more comprehensive surveys to be conducted across the many different components of the immune system, and thus we performed a very broad “systems-level” study in which we measured 51 serum cytokines, chemokines, and growth factors; the frequencies of 95 different immune cell subsets; and cellular responses to cytokine stimulation (Figure 1A). Our results show that these functional units of immunity vary across individuals primarily as a consequence of non-heritable factors, with a generally limited influence of heritable ones. This indicates that the immune system of healthy individuals is very much shaped by the environment and most likely by the many different microbes that an individual encounters in their lifetime.

RESULTS

A Systems-Level Analysis of the Immune System in Healthy Twins

Our study cohort was recruited from the Twin Research Registry at SRI International (Krasnow et al., 2013) in the years 2009–2011, with demographic data detailed in Table S1 (available online). The subjects were all apparently healthy, without any symptoms of disease (Experimental Procedures, “Twin Cohort”). To minimize biological variability, the time between blood sampling of each twin in a pair was kept to a minimum (Experimental Procedures, “Blood Sampling, PBMC Preparation, and Zygosity Testing”). Immunological assays were performed by the Human Immune Monitoring Center, where assays are continually benchmarked to minimize technical variability (<http://iti.stanford.edu/himc/>) (Maecker et al., 2005). However, some technical variability is inevitable, and thus we corrected for this in all of our models. We did this by analyzing aliquots of the same control sample many (>17) times to estimate the technical variance and subtracted this from our estimates of heritability (Experimental Procedures, “Correction of Model Estimates for Technical Variability”). We also analyzed longitudinal samples in an unrelated cohort over 2–5



Figure 1. Systems-Level Analysis of Healthy Human Twins

(A) Overview of data collected covering the functional units of the immune system, the cells, and proteins in circulation.

(B) Summary of all heritability estimates for 72 immune cell population frequencies as determined by flow (2009) and mass cytometry (2010–2011) (Experimental Procedures, section 3). See also Table S3.

(C) Heritability estimates of 43 serum proteins as determined by a fluorescent bead assay. See also Table S4. Error bars represent 95% confidence intervals for the heritability estimate. Gray area is heritability < 0.2, our detection limit.

consecutive, yearly samplings and found that the variation was largely due to technical variability (Table S2). A total of 204 different immune measurements were included in our analyses.

Estimating Heritable and Non-Heritable Influences

Heritability for each parameter was estimated by comparing observed MZ and DZ covariance matrices to the expected

values based on a structural equation model that partitioned the observed variance into three components: heritable (A), shared (C), and unique (E) non-heritable factors. This model is based on the assumptions that: (1) heritable factors correlate perfectly between MZ twins ($r_{MZ} = 1$) but only to 50% between DZ twins ($r_{DZ} = 0.5$) and (2) that shared non-heritable influences are equally similar ($r_{MZ} = r_{DZ}$) between MZ and DZ twin pairs

(Experimental Procedures, “Structural Equation Modeling to Estimate Heritable and Non-Heritable Influences”). For each measurement, we subtracted the technical variance estimate from the e-component prior to normalization to correct for noise (Experimental Procedures, “Correction of Model Estimates for Technical Variability”). We also corrected all measurements for the effects of age (Dorshkind et al., 2009) and gender (Furman et al., 2014) by regressing out such effects and using only residual variance for estimating heritability. Finally, we performed jackknife bootstrapping tests to obtain 95% confidence intervals (Experimental Procedures, “Structural Equation Modeling to Estimate Heritable and Non-Heritable Influences”). Importantly, as our model estimates heritability by comparing MZ and DZ twins, heritable influences include genomic and shared epigenetic traits (Bell and Spector, 2011), and non-heritable influences include environmental factors and stochastic epigenetic changes (Fraga et al., 2005).

We first ran a simulation experiment to verify that our cohort size of 210 twins (78 MZ and 27 DZ pairs) would be enough to test our hypothesis that most immunological traits are explained more by non-heritable than by heritable influences. We found this to be the case, and we estimate 20% heritability to be our detection limit, under which we cannot distinguish small heritable influences from zero (Figure S1).

Most Cell Population Frequencies and Serum Proteins Are Dominated by Non-Heritable Influences

Although it is well known that the frequencies of different types of immune cells in blood often vary widely between individuals, in most cases it is not known how much of this can be attributed to heritable or non-heritable factors, respectively. To address this question, we used antibodies against cell surface markers to quantify 95 different cell subset frequencies but used the 72 most non-redundant ones and estimated the influence of heritable and non-heritable factors on their variation (Experimental Procedures, “Immune Cell Phenotyping by Mass Cytometry and Flow Cytometry”). Among these, a few had very strong influences from heritable factors, especially naive, CD27⁺, and central memory CD4⁺ T cells (Figure 1B and Table S3), but for most, non-heritable influences were clearly dominant. In fact, for 61% of all cell populations, the influence of heritable factors was undetectable (<20% of the total variation) (Figure 1B and Table S3). This was true of both adaptive (T and B cells) and innate cell types (granulocytes, monocytes, and NK-cells).

Serum cytokines and chemokines also have important functions as immune mediators and biomarkers of disease (Villeda and Wyss-Coray, 2013), and thus we measured 51 serum proteins but eliminated eight that were often at or below the limits of detection (Experimental Procedures, “Serum Protein Quantification”). This left 24 cytokines, 10 chemokines, 6 growth factors, and 3 other serum proteins for which we estimated the influences of heritable and non-heritable factors (Figure 1C and Table S4). Some cytokines were particularly heritable, such as IL-12p40 (Figure 1C and Table S4). Interestingly, variants in the IL12B gene that contribute to the IL-12p40 protein have been associated with immune-mediated diseases such as psoriasis (Nair et al., 2009) and asthma (Morahan et al., 2002). In the latter condition, the susceptibility locus was also associated with a

reduced serum concentration of IL-12p40 (Morahan et al., 2002). For many other measurements, such as IL-10 and a group of chemokines, the heritable influence was low (Figure 1C and Table S4).

Homeostatic Cytokine Responses Are Largely Heritable, whereas Most Other Cell Responses Are Highly Non-Heritable

Because these serum proteins often regulate immune cells, we assessed the responses of eight different cell populations stimulated *in vitro* with seven different cytokines for the phosphorylation of three important transcription factors, STAT1, 3, and 5, using phospho-specific antibodies in flow cytometry (Krutzik and Nolan, 2006). We performed a total of 192 different measurements but focused on the 24 baseline measurements and the 65 strongest induced responses (Experimental Procedures, “Immune Cell Signaling Experiments”). Baseline measurements were generally driven by non-heritable factors, with possible minor contributions from heritable factors (Figure 2A). The important homeostatic cytokines IL-2 and IL-7, known to stimulate the proliferation and differentiation of T cells, were found to induce STAT5 phosphorylation in both CD4⁺ and CD8⁺ T cell populations, and these responses were highly heritable (Figure 2A and Table S5). In contrast, most signaling responses such as interferon-induced STAT1 phosphorylation and, in particular, the IL-6-, IL-21-, and regulatory IL-10-induced phosphorylation of STAT3, were dominated by non-heritable influences (Figure 2A and Table S5). In total, 69% of all signaling responses had no detectable heritable influence (e.g., <20%) (Figure 2A and Table S5). This lack of heritability was not related to the strength of responses or explained by a bias toward weak and variable responses (Figure S2).

Non-Heritable Influences Are Major Factors Determining Immune Variation

Taken together, these results show that variation in blood cell frequencies and functions and soluble factors is largely driven by non-heritable factors, with 58% of all measurements having <20% of their total variance explained by heritable influences (Figure 2B). There was no relationship between the absolute degree of measurement variability in the cohort and estimated heritability (Figure S3), and we could also rule out any underestimation of heritability due to the skewed ratio of MZ/DZ twin pairs in our cohort by a resampling test. In brief, by creating 1,000 synthetic data sets with uniform heritability and the same MZ/DZ ratio as in our cohort, we estimated heritability and found that none of the 1,000 data sets ever had >40% of measurements with an estimated heritability < 0.2 ($p < 0.001$) (Figure 2C), thus suggesting that the low heritability estimates obtained are not a result of study design or overall measurement variation in the cohort.

Heritable and Non-Heritable Measurements Are Interrelated in the Immune Network

Our analysis also allowed us to analyze the interrelationships between the different components of the immune system. To construct such a network model, we calculated a precision matrix derived from a Spearman correlation matrix (Liu et al., 2012).

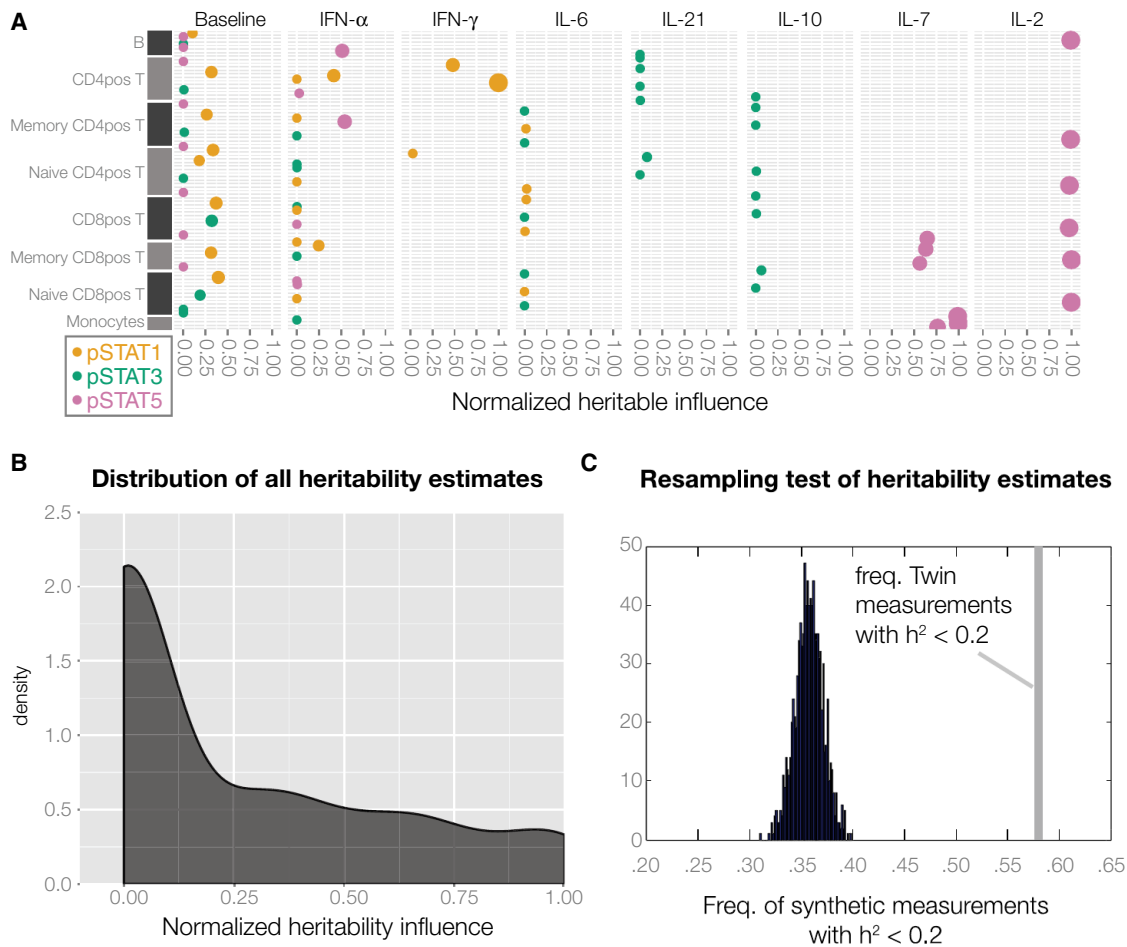


Figure 2. Heritable Factors Explain Only a Fraction of the Variation for Most Immune Measurements

(A) Heritability estimates for immune cell signaling states upon stimulation with the indicated cytokines. Only unstimulated controls and induced responses >1.5 -fold are shown. See also Table S5.

(B) The overall distribution of heritability for all 204 measurements.

(C) The maximum number of measurements with heritability <0.2 across 1,000 synthetic data sets with the same MZ/DZ ratio as in our twin cohort is $<40\%$, significantly less than our results of 58% of measurements with heritability $<20\%$ (gray bar). $p < 0.001$.

A matrix of this type captures partial correlations between variables and avoids spurious, indirect interactions that might occur in standard correlation analyses. By penalizing non-zero entries in this matrix (Friedman et al., 2008), we could pursue what is referred to as a sparse (rather than dense) network model, making it more interpretable. After removing unconnected nodes and validating the edges by a permutation test (Experimental Procedures, “Identification of Pairwise Dependencies between Measurements and the Creation of an Immune Network Model”), this model consists of 126 nodes and 142 edges (Figure 3A and Table S6). An interactive version is available online (<http://www.brodinlab.com/twins.html>). We found that heritable nodes (yellow) were generally connected to non-heritable nodes (purple) throughout the network (Figure 3A). One example shows how the weakly heritable cytokine IL-10 and CD161⁺CD45RA⁺ regulatory T cells are connected to the strongly heritable frequency of naive CD4⁺ T cells (Figure 3B). We found that all hubs in the network were dominated by non-heritable influences,

like the network as a whole, showing that heritable factors are not isolated by themselves but are buffered by connected non-heritable ones (Figure 3A and 3B). This may explain why the many gene polymorphisms found (for example, CTLA4 [Gregersen et al., 2009]) outside of the HLA locus that are associated with immune-mediated disease only explain a small fraction of the total disease risk (Todd, 2010).

With Age, Genetically Identical Twins Diverge as a Consequence of Non-Heritable Influences

As a major source of non-heritable influence is likely to be environmental, particularly microbial exposure, we reasoned that such influences would increase with time. To this end, we compared twin-twin correlations for all immune measurements between the oldest (>60 years; median, 72 years) and the youngest (<20 years; median, 13 years) MZ pairs in our cohort. Here, we also note that twins in the younger (<20 years) cohort are in most cases living together, whereas the older (>60 years) twins

Network of Immune measurements

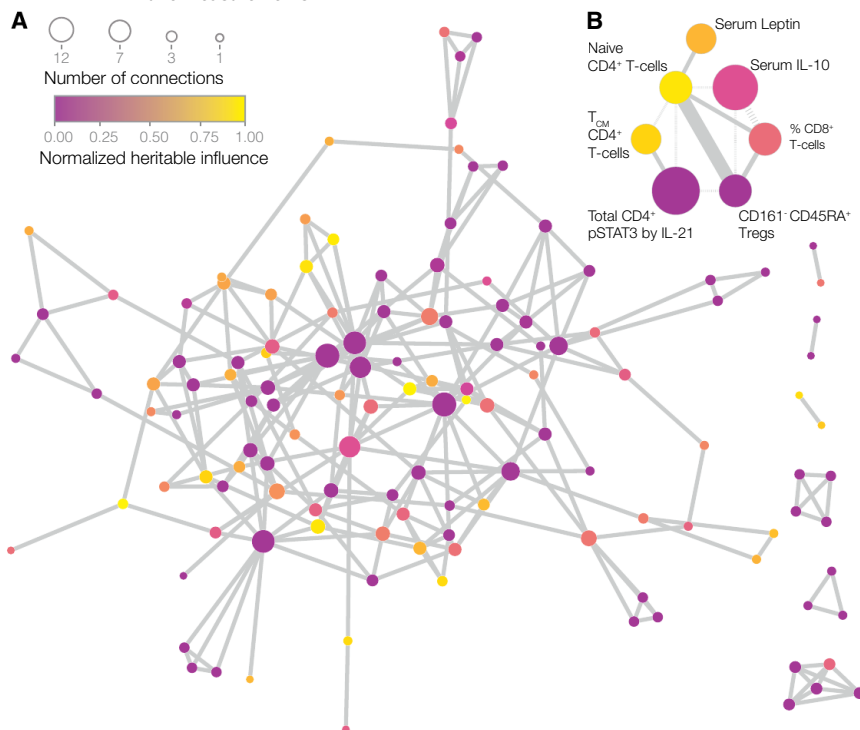


Figure 3. Network of Dependencies between Immune Measurements

(A) Undirected network model of the healthy human immune system showing 126 nodes (measurements), connected by 142 undirected edges illustrating conditional measurement dependencies. Nodes are colored by their estimated heritability and sized by their number of edges.

(B) Subnetwork exemplifying direct relationships between heritable and non-heritable nodes. Solid edges represent positive relationships, and dashed edges represent negative relationships. The edge weight represents the strength of relationships.

See also Table S6.

have lived apart for decades, so concordance can also be a result of either shared environment and/or shared exposure, in addition to genetic similarity. For several cell population frequencies, we found much reduced correlations with age (Figure 4A). In the most striking example, the frequency of Tregs between the youngest MZ twins correlated very strongly at 0.78 but was highly uncorrelated at 0.24 between the oldest MZ twin pairs (Figure 4A). Similarly, several serum proteins showed remarkably reduced correlations between older as compared to younger MZ twins (Figure 4B). In particular, the chemokine CXCL10/IP10 showed a strong correlation (0.79) between the youngest MZ twins but was greatly reduced (0.18) in the older MZ twins (Figure 4B). Similar patterns were found for many cell signaling responses (data not shown), suggesting that this immune divergence between genetically identical twins with age is a common phenomenon, consistent with a major role for environmental exposure in driving variation, although some epigenetic changes could also contribute (Fraga et al., 2005).

Cytomegalovirus Infection Has a Broad Influence on Immune Variation

As we postulate that microbial exposure is a likely driver of immune variation with age, a particularly interesting example is cytomegalovirus (CMV), a lifelong viral infection that has striking effects on the immune phenotypes of both humans and rhesus macaques (Sylwester et al., 2005). In our twin cohort, 16 MZ pairs were discordant for CMV seropositivity, and we compared their twin-twin correlations for all measurements to those of 26 CMV concordant (negative) MZ pairs. Here, we found that the CMV discordant MZ twins showed greatly reduced correlations

for many immune cell frequencies such as effector CD8⁺ and gamma-delta T cells (Figure 5A), as compared to CMV-negative MZ twins. The same was true for cell signaling responses, especially in response to IL-10 and IL-6 stimulation (Figure 5B), as well as the concentrations of these same cytokines in serum (Figure 5C). In general, the influence of CMV was very broad, affecting 119 of all 204 measurements (58%) dispersed throughout the immune network (Figure 5D) and illustrating how at least one type of microbial exposure can dramatically modulate the overall immune profile of healthy individuals.

Antibody Responses to Seasonal Flu Vaccines in Adults Have No Detectable Heritable Component

Finally, we immunized all of the subjects with seasonal flu vaccines in the year of participation (2009, 2010, or 2011) and assessed antibody responses using a standard hemagglutination inhibition (HAI) assay (Experimental Procedures, “Hemagglutination Inhibition Assays”). We were surprised to find no detectable contribution from heritable factors on any of these vaccine responses (Table 1). As pre-existing antibodies are known to influence flu vaccine responses (Sasaki et al., 2008), we excluded subjects with a pre-vaccination titer above 40 but were still unable to find any heritable influences (Table 1). Though preliminary due to a small sample size, this result suggests that responses to seasonal flu vaccines in healthy adults (median age, 44 years) are dominantly influenced by non-heritable factors, likely due to multiple previous vaccinations and/or infections involving this pathogen (Table 1).

In summary, our findings strongly suggest that a healthy human immune system adapts to non-heritable influences such as pathogens, nutritional factors, and more and that this overshadows the influences of most, although not all, heritable factors.

DISCUSSION

The vertebrate immune system consist of thousands of different components, and the application of systems biology (Davis,

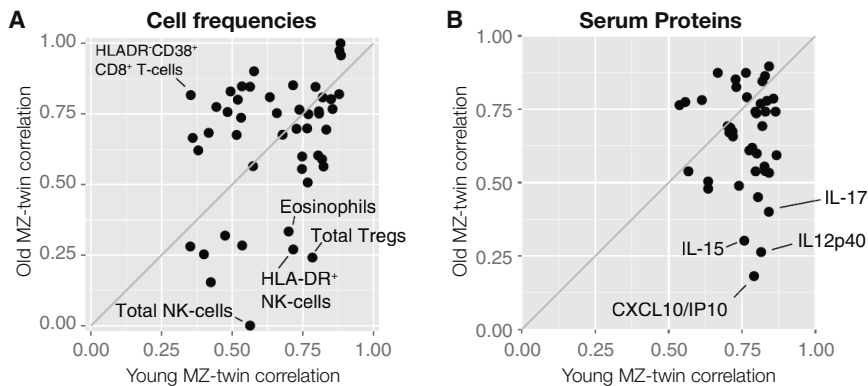


Figure 4. Increased Variability in the Immune System with Age

(A) Twin-twin correlations (Spearman's rank) for all cell frequencies within the youngest MZ twin pairs (≤ 20 years; median, 13.5; $n = 25$ pairs), and the oldest MZ twin pairs (≥ 60 years; median, 72 years; $n = 16$).

(B) Twin-twin correlations (Spearman's rank) for all serum protein concentrations within the youngest MZ twin pairs (≤ 20 years; median, 13 years; $n = 26$) and the oldest MZ twin pairs (≥ 60 years; median, 73 years; $n = 13$).

2008; Duffy et al., 2014; Li et al., 2014; Querec et al., 2009; Sekaly, 2008; Tsang et al., 2014) holds great promise as a way to understand the interactions between these during immune health and disease. Here, we combine a classical twin study approach with the most recent advances in immune monitoring technologies to assess the balance between heritable and non-heritable influences on the functional units of the immune system, namely serum proteins and cell populations. In every category, we find that non-heritable influences dominantly influence 77% of all measurements ($>50\%$ of variance) and almost exclusively drive 58% of the measurements ($>80\%$ of the variance). Because most measurements made in this study focus on the adaptive immune system, partly due to the availability of reagents, one possibility is that these low levels of heritability are related to the stochastic nature of antigen receptor recombination. Indeed, previous work has shown that there are significant differences in the immunoglobulin-sequence repertoires of MZ twins (Glanville et al., 2011). But this is unlikely, as we find low heritability estimates also for many innate immune cell frequencies (NK cells, monocytes, and granulocytes [Figure 1B]) and differences within and between CD4⁺ and CD8⁺ subsets of T cells, which share the same antigen receptor apparatus.

Although this study is not powered to completely rule out all heritable influences on any of the measurements made, the overall dominance of non-heritable factors is independent of this. The low estimates of heritable influences are also not explained by technical noise, as this is rigorously corrected for in our models (Figure S6A). We are also able to rule out that measurement variability over time is an important source of bias (Figure S6B). Therefore, the low heritability estimates for the majority of measurements cannot be explained by either technical noise or biological variability over time.

Given the concordance rates for common autoimmune diseases between 25% and 50% (Cooper et al., 1999) and the many studies finding associations between specific genetic variants and immunological traits and disorders, we were surprised to find such a dominance by non-heritable factors on these functional units of the immune system. Several large population studies have associated specific loci with white blood cell counts, showing some heritable influence though the amount of variation explained is typically low (Okada et al., 2011; Reiner et al., 2011). A recent study by Orrù et al. estimated the heritability of 272 immune cell traits from a non-twin cohort of healthy in-

dividuals on the island of Sardinia. They found that 220 of these ($\sim 81\%$) had an estimated heritability lower than 50% (Orrù et al., 2013), which is comparable to our results. Although all the most heritable subpopulations identified by Orrù et al. expressed the marker CD39, which was not analyzed in our study, a number of the cell populations gave quite similar values, although others were different, such as NKT cells and central memory CD8⁺ T cells (Table S7), possibly reflecting different environments (Bell and Spector, 2011) or a more diverse Palo Alto cohort versus a less diverse Sardinian one.

It is important to note that the twins in our cohort are healthy and without any known immunological deficiencies. Interestingly, two serious immunodeficiency syndromes are caused by defects in the genes IRAK-4 and MyD88 and are associated with invasive bacterial infections due to defects in TLR or IL-1R signaling (von Bernuth et al., 2008; Ku et al., 2007). Despite being associated with severe and often lethal infections in young children, both of these conditions improve significantly with age, starting in late childhood (von Bernuth et al., 2008; Ku et al., 2007). Although this could be explained by developmental immaturity, an alternative explanation for the improvement with age could be that these children's immune systems become more capable with greater environmental exposure.

A striking example of how broad the influence from one non-heritable factor can be is shown here for CMV, influencing 58% of all parameters measured in discordant MZ twins. These striking differences illustrate how non-heritable factors, alone or in combination, can affect the immune system broadly. We suggest that repeated environmental influences like herpes viruses and other pathogens, vaccinations, and nutritional factors cause shifts in immune cell frequencies and other parameters and, with time, outweigh most heritable factors. As an example, the life-long need to control CMV seems to cause a broad shift in the magnitude and complexity of many cell subsets (Chidrawar et al., 2009; Wills et al., 2011), and $\sim 10\%$ of all T cells in CMV⁺ individuals can be directed against this virus (Sylwester et al., 2005). The microbiome also clearly has a major influence on the immune system (Hooper et al., 2012; Mazmanian et al., 2005), and shifts in its composition might cause significant changes in the immune system. Also interesting in the context of how infectious disease exposure can shape subsequent immunity are the influenza vaccine results, in which we could not detect any heritable influence on the antibody responses to

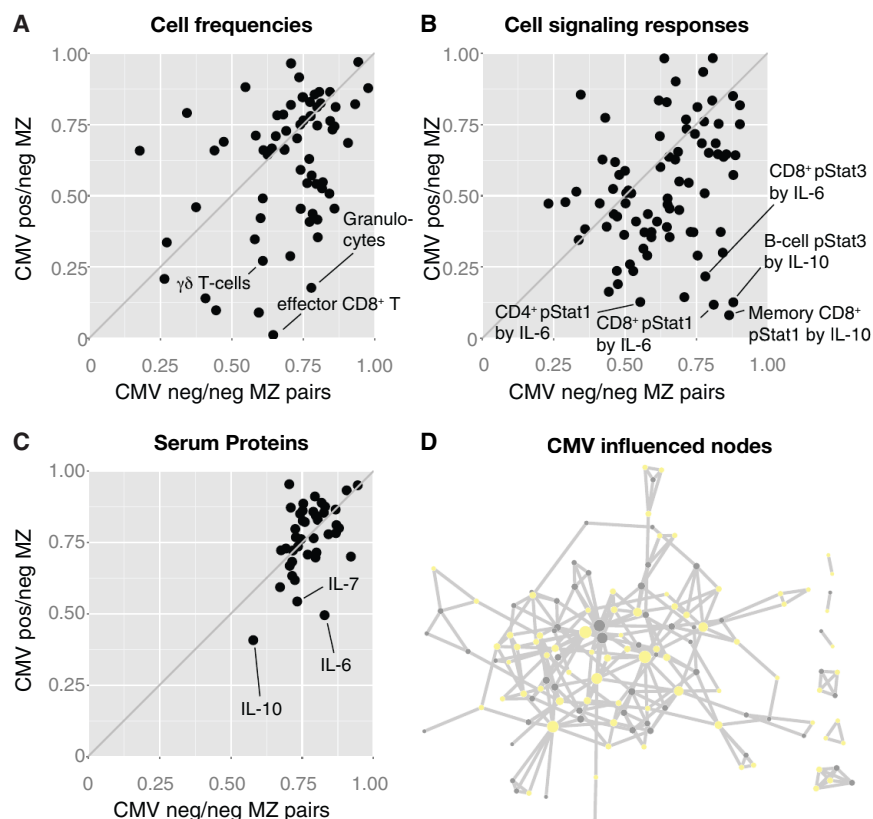


Figure 5. Broad Non-Heritable Influences in the Healthy Immune System

(A) Twin-twin correlations (Spearman's rank) for all cell frequency measurements made in CMV concordant negative (neg/neg) MZ twin pairs ($n = 26$ pairs) and CMV discordant (pos/neg) MZ twin pairs ($n = 16$ pairs).

(B and C) (B) Twin-twin correlations (Spearman's rank) for cell signaling responses to cytokine stimulation and (C) serum protein measurements between CMV neg/neg and CMV pos/neg MZ twin pairs.

(D) 58% of all 126 nodes in the immune network model with reduced correlations in CMV pos/neg as compared to CMV neg/neg MZ twin pairs.

influenza vaccination (Table 1). This recalls the “original antigenic sin” hypothesis (Francis, 1960), wherein it was postulated that previous encounters with influenza strains strongly impact the response to a novel strain. But our finding contrasts with other vaccine studies in twins, most often performed in very young children and involving vaccines against pathogens less frequently encountered in the population (Table 1) (Jacobson et al., 2007). Specifically, vaccines against mumps, measles, rubella (Tan et al., 2001), oral polio, tetanus, and diphtheria vaccines (Newport et al., 2004) have all been shown to be strongly heritable (Table 1) in studies with young children. The one study that we know of from adult twins is a study of hepatitis A/B vaccine responses and was conducted across a similar age range (18–65 years) as ours and reported a heritable influence of 36% for hepatitis A and 61% for hepatitis B antibody responses (Table 1). However, two other studies of hepatitis B vaccine responses performed in young children showed much higher estimates of heritability of 91% (Yan et al., 2013) and 77% (Newport et al., 2004), respectively. In addition, responses to vaccines given at birth (oral polio vaccine [OPV] and Bacillus Calmette–Guérin [BCG]) are more heritable than even those administered only 2 months later (diphtheria and tetanus) (Newport et al., 2004; O'Connor and Pollard, 2013). In addition, Evans et al. analyzed 12-year-old twins in Australia (Evans et al., 1999). Although there are only six broad categories of immune cell subsets that can be compared with our study and those of Orrù et al., it is interesting that, in all cases, the estimates of heritability in the 12-year-old twins were higher than either ours or Orrù et al., in

which the mean age is about 38 and 40 years, respectively (Table S7). These observations are consistent with our data (Figure 4), showing an increasing non-heritable influence on many variables with age, and suggest quite strongly that many if not most of the less heritable traits that we measure here in our mostly adult population may be much more heritable if measured in young children.

Before the advent of childhood vaccines, antibiotics, and improvements in human hygiene, almost half of all children younger than 5 years of age died of infectious diseases. Casanova and colleagues have proposed a genetic theory of infectious disease to account for the interindividual differences in susceptibility (Alcais et al., 2009). Our data and the vaccine studies cited here suggest that such genetic predisposition would be most pronounced in young children but that, later on, the adaptive nature of the immune system is able to overcome many defects. This is similar to the hypothesis proposed by Alcais and colleagues to explain the discrepancies in genetic lesions underlying the susceptibility to primary and secondary infections, respectively (Alcais et al., 2010). Adaptations of the immune system with time could be the result of well-known immune mechanisms, such as specific antibodies and T cells or cross-reactive immunity (Su et al., 2013), or some as yet to be defined maturational process. We would also speculate that the immune system may have feedback mechanisms that allow it to skew its mix of cell types and functional properties in order to compensate for a given individual's particular mix of gene polymorphisms and microbial exposures.

In summary, we find that, in an examination of many of the component parts of the immune system, as well as some response metrics, much of the considerable variation in human beings is driven by non-heritable influences. This variation increases with age and is likely due in large part to exposure to pathogens and other microbes, as we see for CMV discordant MZ twins and in the responses to influenza vaccination. Lastly, we expect that other complex systems in higher organisms, such as the nervous system, will also show this pronounced

Table 1. Influenza Vaccine Responses in Adults Are Determined Mainly by Non-Heritable Factors

Vaccine Response	Age at Vaccination	Heritability	Comment
Measles	1–6 years ^a	89%	(Tan et al., 2001)
Polio (oral vaccine)	<1 year	60%	(Newport et al., 2004)
H. influenzae b	<1 year	51%	(Lee et al., 2006)
Diphtheria	<1 year	49%	(Newport et al., 2004)
Rubella	1–6 years ^a	46%	(Tan et al., 2001)
Tetanus	<1 year	44%	(Newport et al., 2004)
Mumps	1–6 years ^a	39%	(Tan et al., 2001)
Combined hepatitis A/B	18–65 years	36% (HAV)/61% (HBsAg)	(Höhler et al., 2002)
Hepatitis B virus	<1 year	77%/91%	(Newport et al., 2004; Yan et al., 2013)
B/Brisbane/60/2008	12–82 years (median, 45)	0% (<20%)	
A/Cal/07/2009 (H1N1)	12–82 years (median, 44)	0% (<20%)	
A/Perth/16/2009 (H3N2)	12–82 years (median, 44)	0% (<20%)	
B/Brisbane/60/2008	13–77 years (median, 49)	0% (<20%)	Pre-vaccine titer < 40
A/Cal/07/2009 (H1N1)	12–76 years (median, 45)	0% (<20%)	Pre-vaccine titer < 40
A/Perth/16/2009 (H3N2)	12–82 years (median, 44)	0% (<20%)	Pre-vaccine titer < 40

Table of published heritability estimates for vaccine responses to various vaccines as well as the seasonal influenza vaccine responses analyzed in this study with or without the removal of subjects with a pre-vaccine antibody titer ≥ 40 .

^aVaccine responses analyzed between 2 and 18 years of age.

influence of non-heritable factors, as there is also a need (and ability) of such systems to adapt to environmental stimuli.

EXPERIMENTAL PROCEDURES

Twin Cohort

In collaboration with the Twin Research Registry at SRI International (Krasnow et al., 2013), 105 healthy twin pairs were recruited over the years 2009, 2010, and 2011. The study protocol was approved by the Stanford University Administrative Panels on Human Subjects in Medical Research, and written informed consent was obtained from all participants. We excluded anyone having received the seasonal influenza vaccine in the last 6 months, anyone with known or suspected impairment of immunologic function, with clinically significant liver disease, diabetes mellitus treated with insulin, moderate to severe renal disease, or any other chronic disorder, including autoimmune diseases or severe hypertension. We also excluded anyone who had received blood products in the last 6 months and pregnant or lactating women. The complete inclusion/exclusion criteria are available (Data S1).

Blood Sampling, PBMC Preparation, and Zygosity Testing

Blood samples were collected in heparinized vacutainer tubes by venipuncture at day 0 (and day +28 for HAI responses after seasonal influenza vaccination) at the Clinical and Translational Research Unit, Stanford University Hospital. Whole blood collected in sodium heparin tubes was either analyzed immediately using our whole-blood flow cytometry protocol below or enriched for PBMCs using 15 ml of Ficoll-Paque PLUS (GE Health Care) and frozen at -80°C overnight, transferred to liquid nitrogen, and stored until further analysis. Zygosity was determined by comparing 384 SNP loci using a discriminatory DNA polymerase and ligase assay (GoldenGate genotyping Assay, Illumina) and were performed by IGenix. Twins were considered fraternal if similarities in DNA markers were below 99.0%. Twins of the same pair were almost exclusively analyzed in the same experimental batch, irrespective of technology used in order to minimize technical variation.

Immune Cell Phenotyping by Mass Cytometry and Flow Cytometry

All experiments were performed by the Human Immune Monitoring Center at Stanford University. For years 2010 and 2011, 2 million thawed PBMCs were stained without prior resting or fixation using a panel of 26 different metal-

tagged probes to surface antigens and DNA (Data S2A). After repeated washes, cells were analyzed by mass cytometry (CyTOF, Fluidigm) with the following instrument settings: high-resolution mode analysis with cell length set to 10–75 pushes, a lower deconvolution threshold of 10, and instrument run in dual-count detection mode and noise reduction turned off. FCS3.0 files were manually analyzed using FlowJo v9.3 (TreeStar), as shown in Figure S4. Year 2009 PBMC samples were similarly processed but were instead analyzed using a set of custom-made Lyoplates (BD Biosciences) covering seven different antibody panels of fluorescently labeled antibodies (Data S2B and S2C). These samples were acquired using a LSRII flow cytometer (BD Biosciences) and were similarly analyzed manually using the same FlowJo v9.3 (TreeStar).

Immune Cell Signaling Experiments

PBMCs were thawed in warm media, washed twice, and resuspended at 0.5×10^6 viable cells/microliter. 200 μl of cells were plated per well in 96-well deep-well plates. After resting for 1 hr at 37°C , cells were stimulated by addition of 50 μl solutions of cytokines: IFN α , IFN γ , IL-6, IL-7, IL-10, IL-2, or IL-21 (Data S2D), respectively, and incubated at 37°C for 15 min. Cells were then immediately fixed in 1.6% paraformaldehyde, permeabilized with 100% cold methanol, and kept at -80°C overnight. Each well was barcoded by a unique combination of Pacific Orange and Alexa-750 dye concentrations (Invitrogen/Life Technologies), and the cells were washed with FACS buffer (PBS supplemented with 2% FBS and 0.1% sodium azide) and stained with our phospho-Flow antibody panel (Data S2E). Finally, cells were washed and resuspended in FACS buffer, and 100,000 cells per stimulation condition were collected using DIVA 6.0 software on an LSRII flow cytometer (BD Biosciences). Data analysis was performed using FlowJo v9.3 (TreeStar), as shown in Figure S5, and the mean fluorescence intensity (MFI) of the 90th percentile was used for downstream analysis. All stimulated samples were compared to unstimulated control (baseline) samples, and fold changes were calculated. Responses above 1.5 fold change as well as baseline MFI values were used for heritability estimates.

Serum Protein Quantification

Blood samples were centrifuged and stored at -80°C awaiting analysis. Human 51-plex were purchased from Affymetrix and were used according to the manufacturer's recommendations with modifications as described below. In brief, samples were mixed with antibody-linked polystyrene beads

on 96-well filter-bottom plates and incubated at room temperature for 2 hr followed by overnight incubation at 4°C. Room temperature incubation steps were performed on an orbital shaker at 500–600 rpm. Plates were vacuum filtered and washed twice with wash buffer and were then incubated with biotinylated detection antibody for 2 hr at room temperature. Samples were then filtered and washed twice as above and were resuspended in streptavidin-PE. After incubation for 40 min at room temperature, two additional vacuum washes were performed and the samples resuspended in reading buffer. Each sample was measured in duplicate. Plates were read using a Luminex 200 instrument with a lower bound of 100 beads per sample per protein. Each sample was measured in duplicate. Plates were read using a Luminex LabMap200 instrument with a lower bound of 100 beads per sample per protein per well. The Luminex LabMap200 outputs the fluorescence intensity of a given protein in a sample. For each well, we considered the median fluorescence intensity (MFI) for a serum protein as its abundance and averaged the MFI of these replicates. To ignore low-abundance proteins, only measurements with mean concentrations higher than a negative control serum were included in our analysis.

Hemagglutination Inhibition Assays

The HAI assay was performed on sera from day 0 and day 28 post influenza vaccination. Fold changes day 28/day 0 were used for analyses. In one analysis, subjects with a pre-vaccination titer of 40 or more were excluded (Table 1). Serially diluted 25 μ l aliquots of serum samples in PBS were mixed with 25 μ l aliquots of virus, corresponding to four HA units, in V-bottom 96-well plates (Nunc). These were then incubated for 15 min at room temperature. At the end of the incubation, 50 μ l of 0.5% chicken red blood cells (cRBC) were added and the plate incubated for 1 hr at room temperature, and HAI activity was read as follows: (1) positive result: hemagglutination is present, the well is hazy with no cRBC button or (2) negative result: hemagglutination is absent, the well is relatively clear with cRBC button. The HAI titer is defined as the reciprocal of dilution of the last well that inhibits hemagglutination.

Structural Equation Modeling to Estimate Heritable and Non-Heritable Influences

For all of the measurements made, a structural equation modeling approach was used to estimate heritability (Rijsdijk and Sham, 2002). This classical twin modeling approach is based on the assumption that MZ twins are genetically identical, whereas DZ twins share ~50% of their polymorphic genes and that MZ and DZ twin pairs are equally similar with respect to their shared environmental influence. The covariance matrix for each measurement made in MZ and DZ twin pairs can then be decomposed into three parameters: (1) additive genetic parameter, (2) common environmental parameter, and (3) environmental parameter unique to one twin. A linear ACE model then estimates the contribution of each of these parameters by maximum likelihood. After correcting the E-parameter for technical measurement errors, as described in detail below, all parameters were scaled as a proportion of the total variance (A+C+E). All data was corrected for age and gender prior to ACE modeling. We performed resampling tests on all heritability estimates, using a jackknife resampling approach leaving one twin pair out of the calculation in each iteration and using the mean values of all such iterations as our final estimate with 95% confidence intervals. All calculations were performed using both our own implementation of ACE fitting in MATLAB, version 8.3 and the openMX library version 1.4 running in R version 3.0.3. Both platforms were used in order to prevent any bias due to the software used.

Correction of Model Estimates for Technical Variability

For all measurements, standard samples were analyzed repeatedly (>17 times). These were either PBMC aliquots frozen at the same time and thawed for every experiment or pooled serum used as standards for Luminex and HAI assays. By calculating pooled variance estimates for these technical replicates and subtracting this from the E-component in our ACE models prior to normalization, we prevented the underestimation of heritability due to such stochastic measurement errors. This procedure overestimates the technical noise level of the actual twin samples by being collected across multiple batches, whereas twin samples compared were always analyzed within the same batch, and after correction, no relationship between technical variability and heritability

estimates is seen (Figure S6A). We also assessed the biological variability over time in an unrelated cohort by calculating coefficients of variance (CVs) from longitudinal samples drawn once yearly for 2–5 years. No relationship between longitudinal CVs and estimated heritability was found (Figure S6B).

Identification of Pairwise Dependencies between Measurements and the Creation of an Immune Network Model

To identify meaningful relationships between measurements, we used the recently developed non-paranormal SKEPTIC approach (Liu et al., 2012), with a transformed Spearman/rank correlation matrix as input. To make the network model interpretable, we pursued sparse precision matrices with a graphical lasso approach penalizing non-zero entries in the matrix (Friedman et al., 2008). A zero entry in the precision matrix encodes conditional independencies of pairs of measurements given the state of all other measurements and is less sensitive to spurious indirect connections as compared to simple correlation analyses. To validate the inferred structural relationships, two tests were performed. (1) A permutation of samples on per phenotype basis was done to obtain null distributions for entries of the precision matrix. By repeatedly producing permuted samples and running our procedure on those samples, we obtain a distribution of precision matrices that is mostly dominated by very sparse, diagonal matrices but that also has occurrences of precision matrices that have non-zero entries. The non-zero entries thus obtained were false positive, and hence we can estimate which entries obtained on the actual data exceed the size of these false positives. (2) Given relative infrequent occurrences of non-zero entries when fitting sparse precision matrices, we opted to estimate confidence intervals for each entry in the precision matrix. We deemed entries whose confidence interval contained 0 insignificant. To obtain these confidence intervals, we performed bootstrap analysis by resampling the real samples.

CMV Serology

CMV serology was determined using a commercially available ELISA kit (CMV IgG, Gold Standard Diagnostics) as per manufacturer's instructions. In brief, sera stored at -80°C were thawed to room temperature ($20\text{--}25^{\circ}\text{C}$) and diluted 1:51 in kit diluent. Diluted samples were added to wells coated with CMV antigen from strain AD169 and were incubated at room temperature for 30 min. Wells were washed and drained, followed by the addition of goat anti-human IgG antibodies labeled with calf alkaline phosphatase, and incubated at room temperature for 30 min. Wells were again washed and drained, followed by addition of p-nitrophenyl phosphate substrate, and incubated at room temperature for 30 min. After the addition of 0.5 M trisodium phosphate stop solution, the absorbance of each well at 405 nm was read and results analyzed using the manufacturer's instructions.

MZ Twin-Twin Correlations

All measurements performed in the youngest set of MZ twin pairs (<20 years) and oldest MZ twin pairs (>60 years) was extracted, and Spearman's rank correlation coefficients were calculated and compared between these independent groups for every measurement made. Similarly, CMV serologically negative/negative MZ-twin pairs were compared to CMV positive/negative (discordant twins).

SUPPLEMENTAL INFORMATION

Supplemental Information includes six figures, seven tables, and two data files and can be found with this article online at <http://dx.doi.org/10.1016/j.cell.2014.12.020>.

AUTHOR CONTRIBUTIONS

P.B. and V.J. performed all analyses. T.G. helped with the network analysis. S.B. and S.S.-O. provided input on heritability estimates. All data was generated by the Human Immune Monitoring Center under the direction of H.T.M. except for the 2009 HAI data generated by D.F. and CMV serology by C.J.L.A. G.E.S. directs the twin registry and provided input on the twin analyses, and C.L.D. was responsible for regulatory approvals, protocol design,

study conduct, and clinical data management. P.B. and M.M.D. wrote the paper with input from co-authors.

ACKNOWLEDGMENTS

The authors thank all members of the Davis and Y. Chien labs for inspiring discussions and the staff at the Human Immune Monitoring Center and the Stanford-LPCH Vaccine Program for sample collection and data generation. Thanks also to Rob Tibshirani and Chiara Sabatti for input on statistical analyses. Twins were recruited from Twin Research Registry at SRI International, Menlo Park, CA and the authors wish to thank the following individuals: Mary McElroy, Lisa Jack, Ruth Krasnow, Jill Rubin, Dina Basin, Lucia Panini, and Marty Ritchey. The Stanford-LPCH program thanks Project Manager Sally Mackey; Research Nurses Susan Swope, Tony Trela, and Cynthia Walsh; phlebotomist Michele Ugur; and CRAs Ashima Goel, Thu Quan, Kyrsten Spann, Sushil Batra, Isaac Chang, and Raquel Fleischmann. The authors also wish to thank the contributions and commitment to science provided by the twins through their ongoing participation in the Registry and various research studies. This work was supported by NIH grants U19 AI090019, U19 AI057229 and the Howard Hughes Medical Institute to M.M.D. Additional support was provided by the Wenner-Gren Foundation and Sweden-America Foundation to P.B, funds to the Twin Registry were provided through SRI's Center for Health Sciences and through grants from the NIH including DA011170, DA023063, AI090019 and ES022153. The Clinical and Translational Research Unit at Stanford University Hospital was supported by an NIH/NCRR CTSA award number UL1 RR025744.

Received: June 26, 2014

Revised: October 20, 2014

Accepted: November 14, 2014

Published: January 15, 2015

REFERENCES

- Alcaïs, A., Abel, L., and Casanova, J.-L. (2009). Human genetics of infectious diseases: between proof of principle and paradigm. *J. Clin. Invest.* *119*, 2506–2514.
- Alcaïs, A., Quintana-Murci, L., Thaler, D.S., Schurr, E., Abel, L., and Casanova, J.-L. (2010). Life-threatening infectious diseases of childhood: single-gene inborn errors of immunity? *Ann. N Y Acad. Sci.* *1214*, 18–33.
- Bell, J.T., and Spector, T.D. (2011). A twin approach to unraveling epigenetics. *Trends Genet.* *27*, 116–125.
- Chidrawar, S., Khan, N., Wei, W., McLarnon, A., Smith, N., Nayak, L., and Moss, P. (2009). Cytomegalovirus-seropositivity has a profound influence on the magnitude of major lymphoid subsets within healthy individuals. *Clin. Exp. Immunol.* *155*, 423–432.
- Clementi, M., Forabosco, P., Amadori, A., Zamarchi, R., De Silvestro, G., Di Gianantonio, E., Chieco-Bianchi, L., and Tenconi, R. (1999). CD4 and CD8 T lymphocyte inheritance. Evidence for major autosomal recessive genes. *Hum. Genet.* *105*, 337–342.
- Cooper, G.S., Miller, F.W., and Pandey, J.P. (1999). The role of genetic factors in autoimmune disease: implications for environmental research. *Environ. Health Perspect.* *107* (Suppl 5), 693–700.
- Davis, M.M. (2008). A prescription for human immunology. *Immunity* *29*, 835–838.
- de Craen, A.J.M., Posthuma, D., Remarque, E.J., van den Biggelaar, A.H.J., Westendorp, R.G.J., and Boomsma, D.I. (2005). Heritability estimates of innate immunity: an extended twin study. *Genes Immun.* *6*, 167–170.
- Dorshkind, K., Montecino-Rodriguez, E., and Signer, R.A.J. (2009). The ageing immune system: is it ever too old to become young again? *Nat. Rev. Immunol.* *9*, 57–62.
- Duffy, D., Rouilly, V., Libri, V., Hasan, M., Beitz, B., David, M., Urrutia, A., Bissiaux, A., Labrie, S.T., Dubois, A., et al.; Milieu Intérieur Consortium (2014). Functional analysis via standardized whole-blood stimulation systems defines the boundaries of a healthy immune response to complex stimuli. *Immunity* *40*, 436–450.
- Evans, D.M., Frazer, I.H., and Martin, N.G. (1999). Genetic and environmental causes of variation in basal levels of blood cells. *Twin Res.* *2*, 250–257.
- Evans, D.M., Zhu, G., Duffy, D.L., Frazer, I.H., Montgomery, G.W., and Martin, N.G. (2004). A major quantitative trait locus for CD4-CD8 ratio is located on chromosome 11. *Genes Immun.* *5*, 548–552.
- Fraga, M.F., Ballestar, E., Paz, M.F., Ropero, S., Setien, F., Ballestar, M.L., Heine-Suñer, D., Cigudosa, J.C., Urioste, M., Benitez, J., et al. (2005). Epigenetic differences arise during the lifetime of monozygotic twins. *Proc. Natl. Acad. Sci. USA* *102*, 10604–10609.
- Francis, T.J. (1960). On the doctrine of original antigenic sin. *Proc. Am. Philos. Soc.* *104*, 572–578.
- Friedman, J., Hastie, T., and Tibshirani, R. (2008). Sparse inverse covariance estimation with the graphical lasso. *Biostatistics* *9*, 432–441.
- Furman, D., Hejblum, B.P., Simon, N., Jojic, V., Dekker, C.L., Thiébaud, R., Tibshirani, R.J., and Davis, M.M. (2014). Systems analysis of sex differences reveals an immunosuppressive role for testosterone in the response to influenza vaccination. *Proc. Natl. Acad. Sci. USA* *111*, 869–874.
- Glanville, J., Kuo, T.C., von Büdingen, H.C., Guey, L., Berka, J., Sundar, P.D., Huerta, G., Mehta, G.R., Oksenberg, J.R., Hauser, S.L., et al. (2011). Naive antibody gene-segment frequencies are heritable and unaltered by chronic lymphocyte ablation. *Proc. Natl. Acad. Sci. USA* *108*, 20066–20071.
- Gregersen, P.K., Amos, C.I., Lee, A.T., Lu, Y., Remmers, E.F., Kastner, D.L., Seldin, M.F., Criswell, L.A., Plenge, R.M., Holers, V.M., et al. (2009). REL, encoding a member of the NF-kappaB family of transcription factors, is a newly defined risk locus for rheumatoid arthritis. *Nat. Genet.* *41*, 820–823.
- Höhler, T., Reuss, E., Evers, N., Dietrich, E., Rittner, C., Freitag, C.M., Vollmar, J., Schneider, P.M., and Fimmers, R. (2002). Differential genetic determination of immune responsiveness to hepatitis B surface antigen and to hepatitis A virus: a vaccination study in twins. *Lancet* *360*, 991–995.
- Hooper, L.V., Littman, D.R., and Macpherson, A.J. (2012). Interactions between the microbiota and the immune system. *Science* *336*, 1268–1273.
- Jablonski, W. (1922). A contribution to the heredity of refraction in human eyes. *Arch. Augenheilk.* *91*, 308–328.
- Jacobson, R.M., Ovsyannikova, I.G., Targonski, P.V., and Poland, G.A. (2007). Studies of twins in vaccinology. *Vaccine* *25*, 3160–3164.
- Krasnow, R.E., Jack, L.M., Lessov-Schlaggar, C.N., Bergen, A.W., and Swan, G.E. (2013). The Twin Research Registry at SRI International. *Twin Res. Hum. Genet.* *16*, 463–470.
- Krutzik, P.O., and Nolan, G.P. (2006). Fluorescent cell barcoding in flow cytometry allows high-throughput drug screening and signaling profiling. *Nat. Methods* *3*, 361–368.
- Ku, C.-L., von Bernuth, H., Picard, C., Zhang, S.Y., Chang, H.H., Yang, K., Chrabieh, M., Issekutz, A.C., Cunningham, C.K., Gallin, J., et al. (2007). Selective predisposition to bacterial infections in IRAK-4-deficient children: IRAK-4-dependent TLRs are otherwise redundant in protective immunity. *J. Exp. Med.* *204*, 2407–2422.
- Lee, Y.C., Newport, M.J., Goetghebuer, T., Siegrist, C.-A., Weiss, H.A., Pollard, A.J., and Marchant, A.; MRC Twin Study Group (2006). Influence of genetic and environmental factors on the immunogenicity of Hib vaccine in Gambian twins. *Vaccine* *24*, 5335–5340.
- Li, S., Roupael, N., Duraisingham, S., Romero-Steiner, S., Presnell, S., Davis, C., Schmidt, D.S., Johnson, S.E., Milton, A., Rajam, G., et al. (2014). Molecular signatures of antibody responses derived from a systems biology study of five human vaccines. *Nat. Immunol.* *15*, 195–204.
- Liu, H., Han, F., Yuan, M., Lafferty, J., and Wasserman, L. (2012). High-dimensional semiparametric Gaussian copula graphical models. *Ann. Stat.* *40*, 2293–2326.
- Maecker, H.T., Rinfret, A., D'Souza, P., Darden, J., Roig, E., Landry, C., Hayes, P., Birungi, J., Anzala, O., Garcia, M., et al. (2005). Standardization of cytokine flow cytometry assays. *BMC Immunol.* *6*, 13.

- Mazmanian, S.K., Liu, C.H., Tzianabos, A.O., and Kasper, D.L. (2005). An immunomodulatory molecule of symbiotic bacteria directs maturation of the host immune system. *Cell* 122, 107–118.
- Morahan, G., Huang, D., Wu, M., Holt, B.J., White, G.P., Kendall, G.E., Sly, P.D., and Holt, P.G. (2002). Association of IL12B promoter polymorphism with severity of atopic and non-atopic asthma in children. *Lancet* 360, 455–459.
- Nair, R.P., Duffin, K.C., Helms, C., Ding, J., Stuart, P.E., Goldgar, D., Gudjonsson, J.E., Li, Y., Tejasvi, T., Feng, B.-J., et al.; Collaborative Association Study of Psoriasis (2009). Genome-wide scan reveals association of psoriasis with IL-23 and NF-kappaB pathways. *Nat. Genet.* 41, 199–204.
- Newport, M.J., Goetghebuer, T., Weiss, H.A., Whittle, H., Siegrist, C.-A., and Marchant, A.; MRC Gambia Twin Study Group (2004). Genetic regulation of immune responses to vaccines in early life. *Genes Immun.* 5, 122–129.
- O'Connor, D., and Pollard, A.J. (2013). Characterizing vaccine responses using host genomic and transcriptomic analysis. *Clin. Infect. Dis.* 57, 860–869.
- Okada, Y., Hirota, T., Kamatani, Y., Takahashi, A., Ohmiya, H., Kumasaka, N., Higasa, K., Yamaguchi-Kabata, Y., Hosono, N., Nalls, M.A., et al. (2011). Identification of nine novel loci associated with white blood cell subtypes in a Japanese population. *PLoS Genet.* 7, e1002067.
- Orrù, V., Steri, M., Sole, G., Sidore, C., Viridis, F., Dei, M., Lai, S., Zoledziewska, M., Busonero, F., Mulas, A., et al. (2013). Genetic variants regulating immune cell levels in health and disease. *Cell* 155, 242–256.
- Querec, T.D., Akondy, R.S., Lee, E.K., Cao, W., Nakaya, H.I., Teuwen, D., Pirani, A., Gernert, K., Deng, J., Marzolf, B., et al. (2009). Systems biology approach predicts immunogenicity of the yellow fever vaccine in humans. *Nat. Immunol.* 10, 116–125.
- Reiner, A.P., Lettre, G., Nalls, M.A., Ganesh, S.K., Mathias, R., Austin, M.A., Dean, E., Arepalli, S., Britton, A., Chen, Z., et al. (2011). Genome-wide association study of white blood cell count in 16,388 African Americans: the continental origins and genetic epidemiology network (COGENT). *PLoS Genet.* 7, e1002108.
- Rijsdijk, F.V., and Sham, P.C. (2002). Analytic approaches to twin data using structural equation models. *Brief. Bioinform.* 3, 119–133.
- Sasaki, S., He, X.-S., Holmes, T.H., Dekker, C.L., Kemble, G.W., Arvin, A.M., and Greenberg, H.B. (2008). Influence of prior influenza vaccination on antibody and B-cell responses. *PLoS ONE* 3, e2975.
- Sekaly, R.-P. (2008). The failed HIV Merck vaccine study: a step back or a launching point for future vaccine development? *J. Exp. Med.* 205, 7–12.
- Su, L.F., Kidd, B.A., Han, A., Kotzin, J.J., and Davis, M.M. (2013). Virus-specific CD4(+) memory-phenotype T cells are abundant in unexposed adults. *Immunity* 38, 373–383.
- Sylwester, A.W., Mitchell, B.L., Edgar, J.B., Taormina, C., Pelte, C., Ruchti, F., Sleath, P.R., Grabstein, K.H., Hosken, N.A., Kern, F., et al. (2005). Broadly targeted human cytomegalovirus-specific CD4+ and CD8+ T cells dominate the memory compartments of exposed subjects. *J. Exp. Med.* 202, 673–685.
- Tan, P.-L., Jacobson, R.M., Poland, G.A., Jacobsen, S.J., and Pankratz, V.S. (2001). Twin studies of immunogenicity—determining the genetic contribution to vaccine failure. *Vaccine* 19, 2434–2439.
- Todd, J.A. (2010). Etiology of type 1 diabetes. *Immunity* 32, 457–467.
- Tsang, J.S., Schwartzberg, P.L., Kotliarov, Y., Biancotto, A., Xie, Z., Germain, R.N., Wang, E., Olnes, M.J., Narayanan, M., Golding, H., et al.; Baylor HIPC Center; CHI Consortium (2014). Global analyses of human immune variation reveal baseline predictors of postvaccination responses. *Cell* 157, 499–513.
- Villeda, S.A., and Wyss-Coray, T. (2013). The circulatory systemic environment as a modulator of neurogenesis and brain aging. *Autoimmun. Rev.* 12, 674–677.
- von Bernuth, H., Picard, C., Jin, Z., Pankla, R., Xiao, H., Ku, C.L., Chrabieh, M., Mustapha, I.B., Ghandil, P., Camcioglu, Y., et al. (2008). Pyogenic bacterial infections in humans with MyD88 deficiency. *Science* 321, 691–696.
- Wills, M., Akbar, A., Beswick, M., Bosch, J.A., Caruso, C., Colonna-Romano, G., Dutta, A., Franceschi, C., Fülöp, T., Gkrania-Klotsas, E., et al. (2011). Report from the second cytomegalovirus and immunosenescence workshop. *Immun. Ageing* 8, 10.
- Yan, K., Cai, W., Cao, F., Sun, H., Chen, S., Xu, R., Wei, X., Shi, X., and Yan, W. (2013). Genetic effects have a dominant role on poor responses to infant vaccination to hepatitis B virus. *J. Hum. Genet.* 58, 293–297.

Saturated Reconstruction of a Volume of Neocortex

Narayanan Kasthuri,^{1,8,*} Kenneth Jeffrey Hayworth,^{1,9} Daniel Raimund Berger,^{1,6} Richard Lee Schalek,¹ José Angel Conchello,¹ Seymour Knowles-Barley,¹ Dongil Lee,¹ Amelio Vázquez-Reina,² Verena Kaynig,² Thouis Raymond Jones,^{1,2} Mike Roberts,^{2,10} Josh Lyskowski Morgan,¹ Juan Carlos Tapia,^{1,11} H. Sebastian Seung,^{6,12} William Gray Roncal,^{3,13} Joshua Tzvi Vogelstein,^{7,14} Randal Burns,³ Daniel Lewis Sussman,⁴ Carey Eldin Priebe,⁵ Hanspeter Pfister,² and Jeff William Lichtman^{1,*}

¹Department of Molecular and Cellular Biology and Center for Brain Science, Harvard University, Cambridge, MA 02138, USA

²School of Engineering and Applied Sciences, Harvard University, Cambridge, MA 02138, USA

³Department of Computer Science, Johns Hopkins University, Baltimore, MD 21218-2128, USA

⁴Department of Statistics, Harvard University, Cambridge, MA 02138, USA

⁵Department of Applied Mathematics and Statistics, Johns Hopkins University, Baltimore, MD 21218-2682, USA

⁶Department of Brain and Cognitive Sciences, Massachusetts Institute of Technology, Cambridge, MA 02139, USA

⁷Department of Statistical Science and Neurobiology, Duke University, Durham, NC 27708, USA

⁸Present address: Department of Anatomy and Neurobiology, Boston University School of Medicine, Boston, MA 02118, USA

⁹Present address: Janelia Farm Research Campus, Ashburn, VA 20147, USA

¹⁰Present address: Department of Computer Science, Stanford University, Stanford, CA 94305, USA

¹¹Present address: Department of Neuroscience, Columbia University, New York, NY 10032, USA

¹²Present address: Princeton Neuroscience Institute and Department of Computer Science, Princeton University, Princeton, NJ 08544, USA

¹³Present address: Johns Hopkins University Applied Physics Laboratory, Laurel, MD 20723, USA

¹⁴Present address: Department of Biomedical Engineering and the Institute for Computational Medicine, Johns Hopkins University, Baltimore, MD 21218-2682, USA

*Correspondence: bobby.kasthuri@gmail.com (N.K.), jeff@mcb.harvard.edu (J.W.L.)

<http://dx.doi.org/10.1016/j.cell.2015.06.054>

SUMMARY

We describe automated technologies to probe the structure of neural tissue at nanometer resolution and use them to generate a saturated reconstruction of a sub-volume of mouse neocortex in which all cellular objects (axons, dendrites, and glia) and many sub-cellular components (synapses, synaptic vesicles, spines, spine apparatus, postsynaptic densities, and mitochondria) are rendered and itemized in a database. We explore these data to study physical properties of brain tissue. For example, by tracing the trajectories of all excitatory axons and noting their juxtapositions, both synaptic and non-synaptic, with every dendritic spine we refute the idea that physical proximity is sufficient to predict synaptic connectivity (the so-called Peters' rule). This online minable database provides general access to the intrinsic complexity of the neocortex and enables further data-driven inquiries.

INTRODUCTION

The cellular organization of the mammalian brain is more complicated than that of any other known biological tissue. As a result, much of the nervous system's fine cellular structure is unexplored. While it has been known for more than a century that a directional network interconnects many kinds of nerve cells (Cajal, 1899), and that this network underlies behaviors (Sherrington, 1906), for the most part, the precise relationships between the

brain's many cellular components are not known. Several laboratories are now beginning to generate such data in mammals using electron microscopy (EM). This work has provided new insights into the visual system (Anderson et al., 2011; Helmstaedter et al., 2011; Kim et al., 2014; Briggman et al., 2011; Bock et al., 2011; see also Takemura et al., 2013; Mishchenko et al., 2010). Descriptions of neuronal network structure could also be important if derangements in networks underlie psychiatric or developmental disorders and/or if modifications to these networks store learned information (i.e., memories). Exploring such possibilities may require methods for obtaining detailed synaptic-level connectomic data.

A reconstruction effort on the scale of mammalian brains, however, would be enormously expensive and difficult to justify without assurances that this kind of information would be of value (Marblestone et al., 2013; Plaza et al., 2014; Lichtman et al., 2014). Substantial savings in effort could come if the connectivity of the cerebral cortex could be ascertained without looking at every single synapse. For example, if the overlap of axons and dendrites at light microscope resolution provides sufficient information to infer connectivity (Hill et al., 2012), huge data sets of EM images of cerebral cortex might be superfluous. We thus decided to reconstruct all the connectivity within a very small piece of neocortical tissue (1,500 μm^3 at a resolution allowing identification of every synaptic vesicle) to be in a better position to decide whether or not obtaining complete brain maps at such a fine level of resolution reveals interesting properties that cannot be inferred from either lower resolution or more sparse analyses.

Previous connectomic studies of retina and hippocampus concluded that connectivity was not entirely predictable from the proximity of presynaptic elements to postsynaptic targets (Briggman et al., 2011; Mishchenko et al., 2010; Helmstaedter

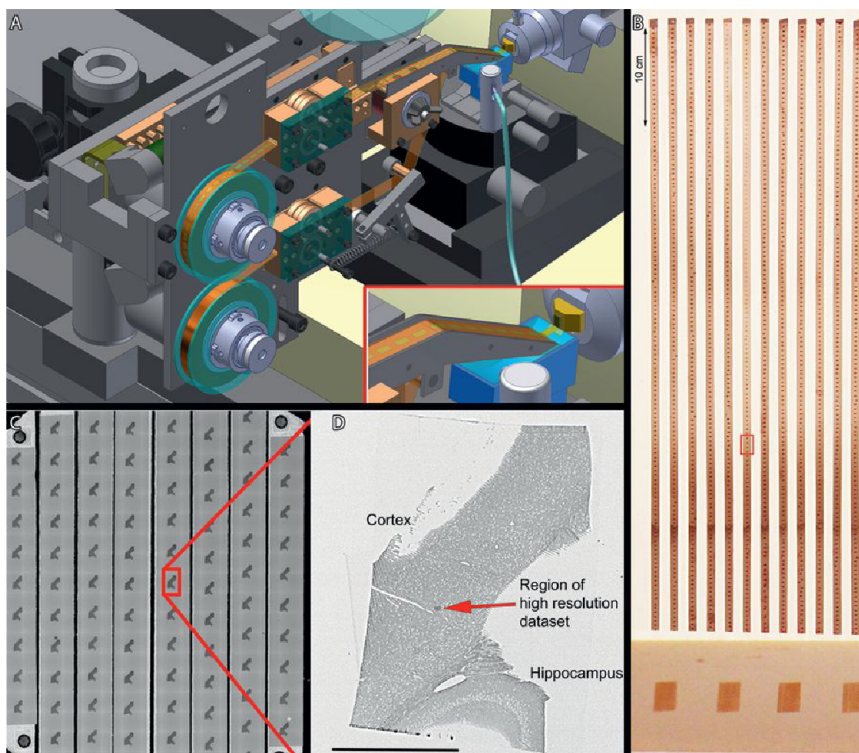


Figure 1. Automatic Tape Collection of Ultrathin Brain Sections

(A) Diagram of the automated tape-collecting ultramicrotome (ATUM). The bottom reel of the ATUM contains a plastic tape that is fed into the knife boat of a diamond knife mounted on a commercial ultramicrotome. The tape is collected on a take up reel (top). (Red inset) Close-up view of the tape conveyor positioned in the knife boat. The diamond knife boat (dark blue) is filled with water (light blue). The diamond knife (green rectangle) is at the opposite end of the knife boat from the taping mechanism. It cuts serial ultrathin sections from tissue embedded in a plastic block. The sections then float on the surface of the water in the knife boat until they adhere to the moving tape (see Movie S1).

(B) ~ 10 m of Kapton tape with $\sim 2,000$ sections collected. Four of the 29-nm sections (red rectangle) are shown at a higher magnification at the bottom of the panel.

(C) The reel of tape is then cut into individual strips and mounted on silicon wafers for poststaining and/or carbon coating. A low-power scanning electron microscopy image of part of a wafer containing 85 brain sections is shown. One of the sections (red rectangle) is shown at a higher magnification in the next panel.

(D) One 29-nm section containing neocortex and hippocampus. The region that was studied at high resolution is the dark-looking box (red arrow).

Scale bar, 1 mm.

See also Movie S1.

et al., 2013). We wished to examine this question again but now in neocortex for several reasons. First, a large effort is underway to model and simulate neocortical processing based on stochastic connectivity based on spatial overlap of axons and dendrites (Markram et al., 2012). Second, the retina and the hippocampus (archicortex) are phylogenetically older than neocortex and may have evolved deterministic targeting mechanisms that could explain why overlap is insufficient to predict connectivity in those regions. In neocortex, however, less is known and it remains possible that spatial overlap is sufficient to explain synaptic connections between particular pairs of axons and dendrites. Third, in analyzing our data, we have found significant redundancies in the synaptic connections and wanted to know if these were accidental. For all these reasons, we have attempted to analyze the connectivity of each of many axons and dendrites by looking at not only the synapses each axon establishes but also the occurrences when axons and dendrites get close with potential postsynaptic targets but do not establish synapses.

Even for such a small volume, however, we found considerable technical challenges standing in the way of doing such an analysis. After “saturating” the segmentation of a sub-region in the middle of the imaged volume in which all intracellular space was assigned to one or another cellular entity, we then needed to catalog all the connectivity and structural information into a minable database before analyses. Surprisingly, analysis of the connectomic data turned out to be even more challenging than creating the image data or annotating it.

This “omics” approach provided a wealth of data for potential analysis. Here, we investigate aspects of the connectivity of

excitatory axons and find interesting patterns that would have been difficult to detect with lower resolution methods. To assist readers who wish to examine the data in detail, we serve out the images and their segmentations and annotated databases that link to the image data, as well as all the software we developed for the display and analysis (described herein <http://openconnecto.me/Kasthurietal2014/>).

RESULTS

The results are divided into two parts. We first describe the technical approaches for acquiring and analyzing this data and then turn to some of the biological findings.

TECHNICAL DETAILS

Collecting Serial Brain Tissue Sections on Tape

We built an automatic tape-collecting ultramicrotome (ATUM) that retrieves brain sections from the water boat of a diamond knife immediately as they are cut via a continuous submerged conveyor belt (Figure 1A; Movie S1). The tape’s pulling motion and its adhesiveness cause the caught sections to lie flat on the tape’s surface (Figure 1A, inset). To generate the cerebral cortex image dataset in this paper, we collected 2,250 29-nm coronal brain slices (each section ~ 1 mm², total volume 0.13 mm³) from somatosensory cortex of a young adult mouse on ~ 6.5 m of Kapton tape (Figure 1B). We generated 1,000 sections per 24 hr. We chose 29 nm as section thickness in order to trace the finest neuronal wires (Mishchenko, 2009), and with a

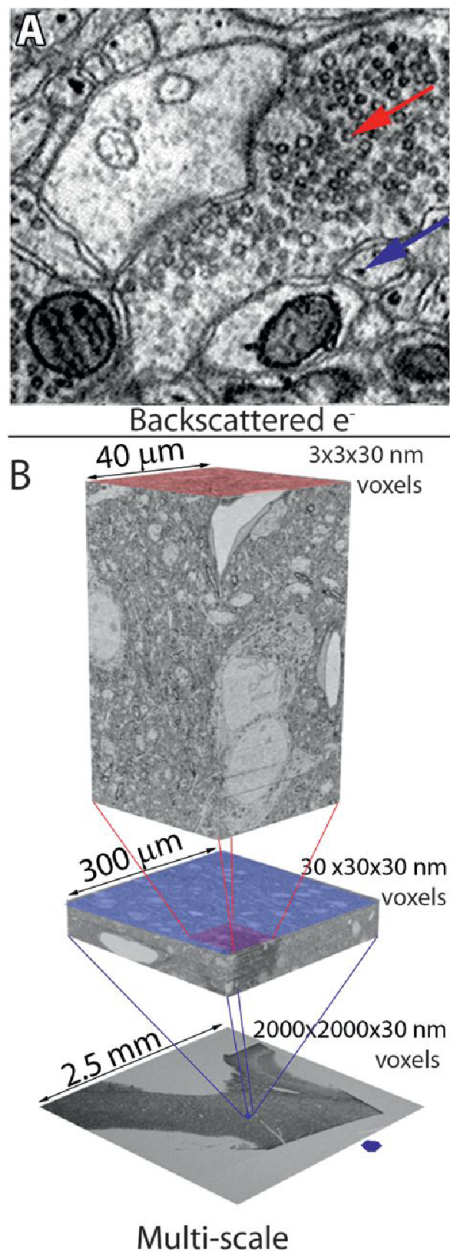


Figure 2. Imaging Brain Sections on Tape

(A) A section of somatosensory neocortex imaged in a scanning electron microscope. The red arrow shows synaptic vesicles. The blue arrow shows a strongly labeled membranous tube found in unmyelinated axons.

(B) The strategy for placing high-resolution images in a larger anatomical context by re-imaging sections at multiple resolutions. The sections used for all of the subsequent analysis in this paper are ~ 2.5 mm².

See also Figure S1 and Movies S2, S3, S4, and S5.

sharp knife we have successfully sectioned >10,000 sections from a small block without missing a cut and importantly manual segmentation is nearly flawless at this thickness (see below). Following section collection, the tape was cut into strips and placed on silicon wafers that were then photographed (Figure 1C). The wafer image was used to map the positions of the

sections on the wafer for automated EM (Hayworth et al., 2014). Once mapped, the wafers constitute an ultrathin section library for repeated imaging of the sections at a range of resolutions (Figures 1D and 2; Movies S2, S3, S4, and S5).

Image Acquisition

Sections were imaged with a scanning electron microscope using backscattered electron detection (9–10 keV incident electron energy), which had sufficient resolution and contrast to detect individual synaptic vesicles (red arrows, Figure 2A). In this study, reduced osmium tetroxide-thiocarbohydrazide (TCH)-osmium (ROTO) was used as stain (Friedman and Ellisman, 1981; Tapia et al., 2012). The ROTO stain highlights a tubular organelle coursing through most unmyelinated axons, aiding in reconstruction of fine processes (blue arrows, Figure 2A) (Sinha et al., 2013; Movies S4 and S5). The plasma membranes with this staining protocol were 6–8 nm in width. We acquired high-resolution images with 3-nm pixels, ensuring that membrane boundaries would be oversampled for easier reconstruction. The same sample was imaged at lower resolutions (30 or 2,000 nm) to rapidly acquire images of larger tissue volumes (Figure 2B). Image acquisition scan rate was 1 M pixels per s. Time is also spent moving the stage from one section to another and automatic focusing each successive section, roughly halving the overall throughput.

Speed-up can be achieved in several ways, including imaging different wafers in parallel on multiple microscopes, use of secondary electron detection (with 1.5–3 keV incident electron energy and speeds of up to 40 M pixels per s; Figure S1A), and by imaging in a new microscope that parallelizes imaging by use of multiple scanning beams (Eberle et al., 2015; Figure S1B).

Generating a Multi-Scale Dataset from Cerebral Cortex

We created a multi-scale digital volume in order to provide tissue context surrounding the region in which we did circuit reconstruction. We first imaged all the sections in their entirety at low resolution (2 μ m/pixel). We also imaged a sub-volume (a radial strip of cerebral cortex extending from the pia to white matter, 500 μ m wide and 1 mm long) at 29 nm/pixel and finally we imaged an $\sim 80,000$ μ m³ box (40 \times 40 \times 50 μ m³) that transected the apical dendritic bundle of a cortical mini-column (Krieger et al., 2007) at high resolution (3 nm/pixel) (Figure 2B; Movies S4 and S5).

VAST

A manual tool to segment neuronal processes in the image data: we developed a computer-assisted manual space-filling segmentation and annotation program (“VAST,” <http://openconnecto.me/Kasthurietal2014/Code/VAST/>). VAST allowed us to work with EM images online, avoiding the need for their local storage, to “color” the images in at multiple scales of resolution, to organize the results in a flexible annotation framework, to export results for 3D visualization and analysis, and to do these tasks without being limited by working memory. We tested the accuracy of this manual tracing approach, by analyzing saturated segmentations in which every membrane-bound object in every section was colored in. We used

a Matlab script (<http://openconnecto.me/Kasthurietal2014/Code/findOrphans>) to find “orphans” (i.e., segmented objects that were not connected to parent axons and dendrites; see the Supplemental Experimental Procedures for details). The analysis found that in a $\sim 500 \mu\text{m}^3$ cylinder surrounding an apical dendrite (see below), there were no axonal or dendritic orphans in the volume, which included a total of 568 spines and 601 terminal axon branches. With the VAST manual reconstructions, miswiring errors (e.g., connecting the spine head or terminal axon varicosity to the wrong parent process) were also apparently rare because there was substantial agreement between two experienced tracers working independently in the assignment of the finest processes to their parent dendrites or axons (spine necks >99%; 565/568 agreement and axonal terminal branches >99%; 598/601 agreement). In the six cases of disagreement, the two tracers reached consensus once they compared results, meaning there were no places in which the axonal and dendritic data were actually ambiguous. However, for the astrocytic cytoplasm (Figure 3J), there were many glial fragments for which experts could not agree on how they were connected.

RhoANA

Suite of automatic tracing tools: based on the tracing, we found 6.4 profiles per μm^2 in a section and estimated that in the $64,000 \mu\text{m}^3$ high-resolution volume there are 13.7 million cell profiles in its 1,850 sections. Experienced tracers require about 15 min to trace the ~ 200 cell profiles in $1 \mu\text{m}^3$ so about two people-years of 24/7 tracing would be required to segment out all the profiles in this volume. We therefore developed ways to generate more rapid and automated segmentation of neural processes (details and software are available at <http://www.rhoana.org/>). To aid this effort, we manually traced all of the cellular objects in several small volumes ($\sim 150 \mu\text{m}^3$) and used this “stained glass” segmented image data (Figure 3B) to train automated reconstruction methods (Fusion: Vazquez-Reina et al., 2011; Kaynig et al., 2013; GALA: Nunez-Iglesias et al., 2014). Based on this training, we produced automated segmentations of all the cellular processes within a high-resolution volume with dimensions of $30.7 \times 30.7 \times 33.7 \mu\text{m}$ (via the RhoANA pipeline using random forest membrane probabilities and graph-cut segmentations with the Fusion segmentation algorithm). In a sub-volume of the cube centered on the “red” neuron’s apical dendrite (see below), we produced a different segmentation (via RhoANA using the Maxout deep-learning convolutional neural network for membrane probabilities and the GALA segment agglomeration algorithm). These automatically segmented volumes are available at http://openconnecto.me/Kasthurietal2014/data/automatic_segmentation (Figure 3C; Movie S7).

We found that although fully automated methods are improving rapidly, they are still only first passes and require human assistance to correct merge and split errors. In single images, we found that 92.6% of the pixels or 87.6% (of 92,747) of the profiles were correctly segmented with a fully automated segmentation algorithm (RhoANA with Maxout and GALA; Figures S2A and S2B). However, despite the appearance of largely correct two-dimensional data, when we analyzed cellular profiles

in three dimensions, we estimated the need for ~ 0.9 split operations (to correct inappropriate mergers) and 5.8 merge operations (to correct splits) per μm^3 (Figure S2C; Movie S8). We did these corrections for a sub-volume of the full segmented dataset (cylinder 3; see below), with a newly developed tool for computer-assisted editing and rendering (Mojo and an online version for this tool “Dojo”; Haehn et al., 2014; available at <http://www.rhoana.org/>). The most important metric for automated reconstruction is the accuracy of the resulting connectivity matrix, but we concluded that at present it is premature to generate fully automated connectivity matrices.

Biological Analysis of the Serial EM Images of Cerebral Cortex

In the medium resolution volume, we identified neuronal somata in order to locate the cortical layer boundaries (Figure 3A) and reconstructed the shapes of a subset of cells running in a cortical mini-column (Figure 3A; Movie S6). Most ($\sim 70\%$, 21/30) of these cells were pyramidal and the rest fell into several different categories, including putative interneurons, atypical excitatory cells, and glial cells. We then fully annotated a sub-volume of somatosensory cortex within this same volume (Movie S9; <http://openconnecto.me/Kasthurietal2014/data/segments>). Building on work done previously in the hippocampus (Mishchenko et al., 2010; Stepanyants and Chklovskii, 2005), we itemized all the neuronal and non-neuronal cells in three cylindrical volumes that encompass apical dendrite segments of two cortical pyramidal cells, including their spines (Movie S10). We selected these particular apical dendrites because they ran very close to each other (see pink arrow in Figures 3A and 3D) and originated from nearby neuronal somata (in upper layer 6; red and green arrows in Figures 3A and 3D). Thus, they appeared to be in the same mini-column and perhaps participated in the same neural processing unit (Mountcastle, 1997). The three cylinder site was in layer 5, $100 \mu\text{m}$ and $135 \mu\text{m}$ superficial to the pseudo-colored “red” and “green” neuronal somata, respectively. Cross-sections of the annotations of two cylinders are shown in Figures 3B and 3D; reconstruction of the three cylinders is shown in Figure 3E; and the location of all three cylinders in the full volume is shown with pink arrows in Figures 3A, 3D, and 3O. These three slightly overlapping $\sim 600 \mu\text{m}^3$ cylinders, two of which (cylinders 1 and 3) are centered on the “red” neuron’s apical dendrite and one (cylinder 2) on the “green” apical dendrite, provided a total reconstructed volume of $1,500 \mu\text{m}^3$. In cylinder 3, rather than tracing the objects manually, we edited the computer-segmented data (Figure 3C). All of the 193 dendrites in this volume were traced out into the surrounding high-resolution cube, and some were traced onto the medium resolution data to locate somata ($n = 30$; Figure 3O).

Parts List: 3 Cylinder Volume

The $1,500 \mu\text{m}^3$ 3 cylinder volume contains parts of many cells (Movies S10 and S11) and of a variety of types (Figures 3E–3N; Movie S11), including 193 dendrites, 92% spiny, the rest relatively smooth (Figures 3K and 3N), and 1,407 unmyelinated axons. Based on synapse appearance, 93% of the axons are excitatory (Figure 3I), and most of the remainder are inhibitory (Figure 3L). A few axons (5; $\sim 0.5\%$), despite possessing vesicle-filled varicosities, did not establish classic close synaptic

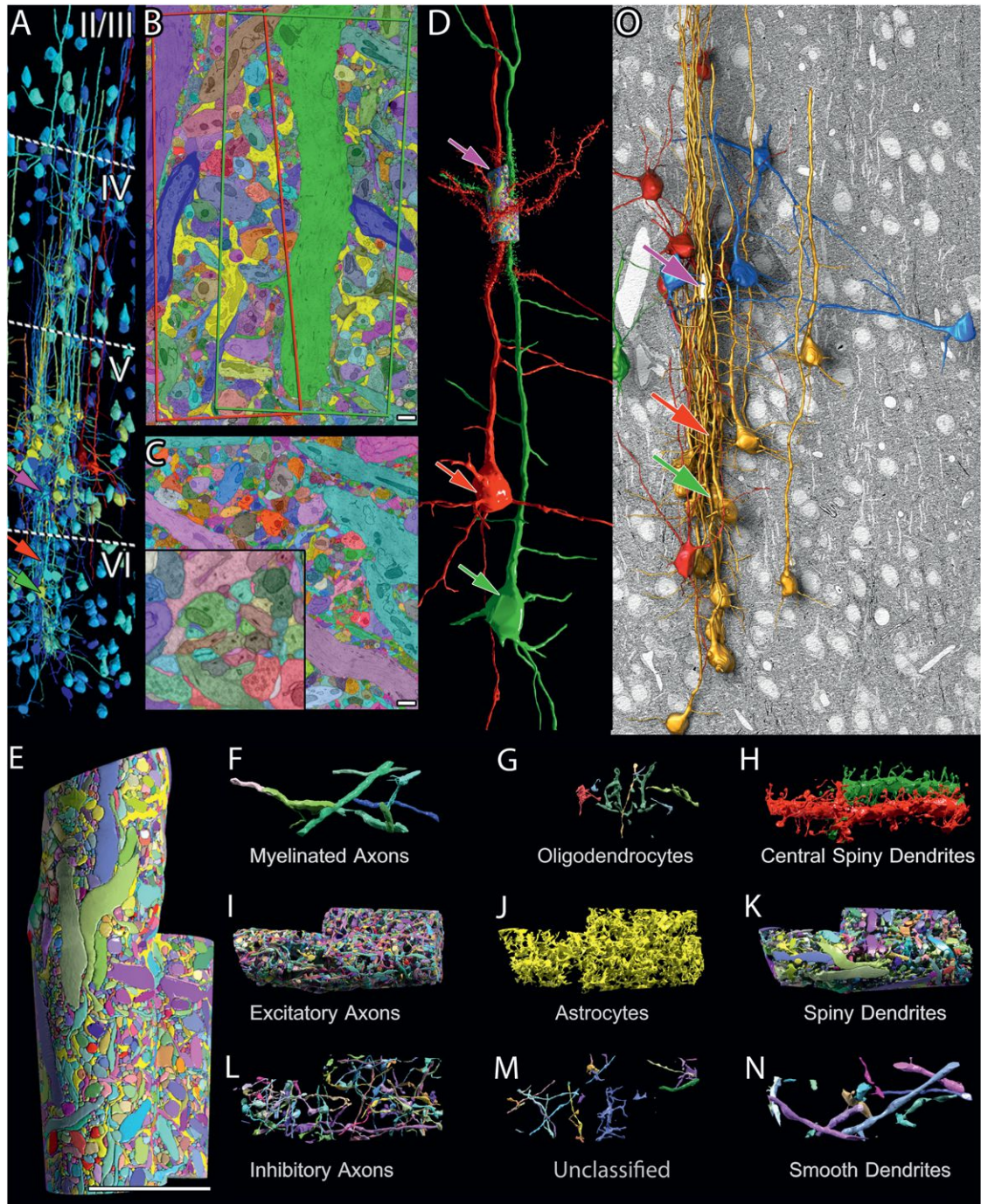


Figure 3. Multi-Scale Reconstruction in Neocortex

(A) Cortical neuronal somata reconstruction to aid in cortical layer boundaries (dotted lines) based on cell number and size. Large neurons are labeled red; intermediate ones are labeled yellow; and small ones are labeled blue. The site of the saturated segmentation is in layer V (pink arrow). These two layer VI pyramidal cell somata (red and green arrows) give rise to the apical dendrites that form the core of the saturated cylinders.

(B) A single section of the manually saturated reconstruction of the high-resolution data. The borders of the cylinders encompassing the “red” and “green” apical dendrites are outlined in this section as red and green quadrilaterals. This section runs through the center of the “green” apical dendrite (full data stack in Movie S9).

(C) A single section of a fully automated saturated reconstruction of the high-resolution data (full data stack in Movie S7). Higher magnification view (lower left inset) shows 2D merge and split errors (for 3D errors see; Figure S1).

(D) The two pyramidal cells (red and green arrows) whose apical dendrites lie in the centers of the saturated reconstructions. Dendritic spines reconstructed in the high-resolution image stack only.

(legend continued on next page)

junctions with postsynaptic cells. In total, there were 1,700 synapses at a density of one synapse per $1.13 \mu\text{m}^3$ (Table S1). We also observed astrocytic processes (Figure 3J), myelinated axons (Figure 3F), oligodendrocyte processes (Figure 3G), and about 20 entities that we could not as easily classify (Figure 3M). Neuronal processes (axons and dendrites) occupy 92% of the cellular volume with glial processes, occupying much of the remaining 8% (Movies S9 and S10). The non-cellular (extracellular) space accounts for 6% of the total volume, less than half the extracellular space estimates from living brains, probably because of fixation-induced swelling (Vanharreveld et al., 1965).

The ~7-fold disparity between the number of axons and dendrites (1,407 versus 193) likely reflects a real difference in the numbers of pre- and postsynaptic cells that send processes into the volume. We analyzed the shape of the 660 excitatory axons that entered cylinder 1 and found that only three of them (0.5%) established branches that were non-terminal within the volume (Figure S3). To estimate the number of axons that branched outside the cylinders and sent more than one branch in, we analyzed axonal arbors from light microscopy reconstructions of mouse neocortical pyramidal neurons (NeuroMorpho.org; see the Methods) by superimposing them on the cylindrical volumes at random locations. The result of this analysis argues that only ~8 of the 1,308 excitatory axons (< 1%) in the volume are likely to be branches originating from the same parent neuron. Also, the dendrites in the cylinder only rarely originated from the same neuron: we found two dendritic shafts in cylinder 1 that were from the same neuron (out of 100). Presumably, therefore, axons extend into a 7-fold greater volume than dendrites, on average. The ~1,600 different neurons within this small region of mammalian brain (several billionths of the volume of a whole brain) is more than five times as many neurons as are contained within the entire nervous system of a *Caenorhabditis elegans* (White et al., 1986).

Synapses in the Reconstructed Volume

We created a spreadsheet of the 1,700 synaptic connections in the volume, providing the location of each, its pre- and postsynaptic partners, and a wide variety of other information (Table S1; <http://openconnecto.me/Kasthurietal2014/view/highResAnnotated>; <http://openconnecto.me/Kasthurietal2014/data/synapses>).

The spreadsheet shows that the connectivity is highly skewed toward excitatory elements: 92% (177/193) of the dendrites are spiny and purportedly excitatory (Figure 3K; DeFelipe and Fariñas, 1992), and 93% (1,308/1,407) of the axons are excitatory. Looking at each presynaptic varicosity, we found that 95% (1,610/1,700) of them also meet the criteria for being excitatory. Each excitatory axon establishes slightly more synapses in the volume than each inhibitory axon (~1.2 synapses/excitatory

axon versus ~0.9 synapses/inhibitory). The excitatory-to-inhibitory-synapse ratio (van Vreeswijk and Sompolinsky, 1996; Wehr and Zador, 2003) is 20.2 for the dendrites of excitatory neurons (1,494 excitatory synapses versus 74 inhibitory synapses), whereas the ratio is only 9.7 (116 excitatory synapses and 12 inhibitory synapses) for the input to inhibitory dendrites. These ratios are in line with what has been described in hippocampal studies (Gulyás et al., 1999; Megias et al., 2001).

Most (71%; $n = 1,207/1,700$) of the synapses in the volume derive from varicosities along axons (en passant synapses), and the rest are at the end of short branches (terminal synapses). 18% of excitatory, and 43% of the inhibitory, axonal varicosities are presynaptic to multiple partners (Figure 4A). Multi-synaptic excitatory varicosities were previously described in the hippocampus (Chicurel and Harris, 1992; Popov and Stewart, 2009). The most extreme example in this dataset is a large excitatory en passant bouton innervating five different postsynaptic targets (Figure 4B). Tracing ten randomly chosen axons (with 78 varicosities) into the larger surrounding volume showed all but one axon had at least one multi-synaptic varicosity, suggesting that axons in general establish both mono- and multi-synaptic varicosities. Excitatory axons establish synapses mostly on spines (94%; $n = 1,406/1,700$), and inhibitory axons establish mostly on shafts (81%, $n = 70/86$). A few (1%; $n = 7$) of the unmyelinated axons, despite having vesicle-filled varicosities, do not make traditional close synaptic contacts with any target cell within the volume (listed as “2” in column 12 in Table S1). Some of these axons have relatively large vesicles that match the description of cortical aminergic axons (see, for example, <http://openconnecto.me/Kasthurietal2014/view/bigVesicles>) (Smiley and Goldman-Rakic, 1993). We also notice that glial processes associate with synapses in an uneven way (Figure 3J; Movies S9 and S10): ~50% of synapses were not adjacent to any glial process.

We did not find evidence of electrical connections in the three cylinder volume. Gap junction proteins are seen in inhibitory neurons in layers 4 and 6, but not so much in layer 5, where this study was carried out (Deans et al., 2007).

Synaptic Vesicles

In cylinder 1, we identified the location of each synaptic vesicle at 774 synapses (Figures 4A, 4B, 5A, and 5B; Table S1; <http://openconnecto.me/Kasthurietal2014/view/highResAnnotated>; <http://openconnecto.me/Kasthurietal2014/data/vesicles>). The counts were similar ($\pm 4.6\%$) when two expert tracers independently counted the same synapses, and they likely reflect the actual number per synapses (Figure S4). The number of vesicles per synaptic varicosity range from 2 to 1,366 for varicosities with one postsynaptic target (mean = 153 ± 127), with significantly greater numbers of vesicles at multi-synaptic varicosities (mean = 200 ± 173 ; Wilcoxon rank-sum test; $p = 0.0005$). The

(E) The saturated reconstruction volume.

(F–N) The “parts list” of the saturated volume.

(O) Reconstruction of 30 dendrites contained within cylinder 1 (pink arrow) that were traced back to their cell bodies. These dendrites were predominantly apical dendrites of pyramidal cells (gold), several basal dendrites of pyramidal cells (blue), and in one case both a branch of the apical and a basal dendrite branch of the same pyramidal cell entered the volume (green) and a small number of non-pyramidal cell dendrites (red). The somata of the red and green apical dendrites that lie at the centers of saturated reconstruction are shown at red and green arrows. Scale bars, 1 μm for (B) and (C) and 7 μm for (E).

See also Figures S2 and S3 and Movies S6, S7, S8, S9, S10, and S11.

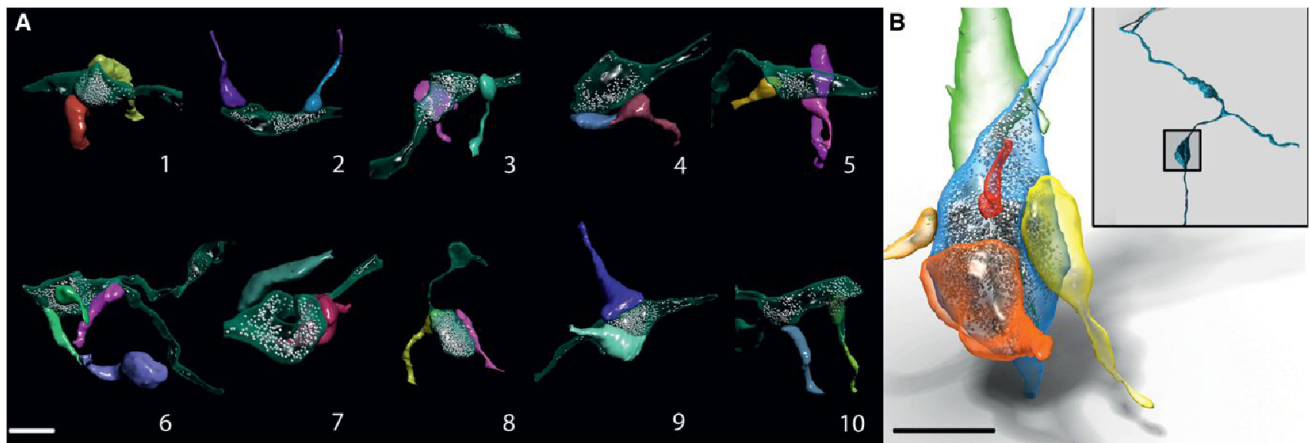


Figure 4. Multi-Synaptic Varicosities Are Commonplace in the Reconstructed Volume of Neocortex

(A) Ten axonal varicosities, which were presynaptic to multiple dendritic spines, are shown. In most cases a single large cluster of vesicles served the multiple synapses. In some cases two spines from the same dendrite were postsynaptic to the same varicosity (e.g., the two purple spines in #5).

(B) An axonal varicosity (blue) that was presynaptic to four dendritic spines (red, orange, yellow, and gold) and one dendritic shaft (green). Inset shows that this was an en passant varicosity of an axon. Scale bar, 1 μm in (A) and (B).

number of vesicles is not significantly different in excitatory and inhibitory synapses.

Mitochondria Size and Density in Different Cells

We also identified 607 mitochondria in cylinder 1 with a density of $\sim 1/\mu\text{m}^3$ (Figure 5C; mitochondrial dataset available <http://openconnecto.me/Kasthurietal2014/view/highResAnnotated> and <http://openconnecto.me/Kasthurietal2014/data/mitochondria>). Mitochondria occupy twice as much volume in inhibitory dendrites than in excitatory dendrites, perhaps related to the metabolic demands associated with greater levels of activity (Beierlein et al., 2003). In addition, mitochondria are present in axonal varicosities, most typically varicosities that had large numbers of vesicles (Table S1). Only very rarely ($n = 3/1,425$) do mitochondria reside in dendritic spines, a surprising result given the fact that mitochondria are transported to spines with intense stimulation (Li et al., 2004). Among the three mitochondria that enter spines, two were continuations of mitochondria in the parent dendrite (<http://openconnecto.me/Kasthurietal2014/view/spineMito1>; <http://openconnecto.me/Kasthurietal2014/view/spineMito2>; <http://openconnecto.me/Kasthurietal2014/view/spineMito3>).

Spine Numbers and Sizes

We itemized 1,425 dendritic spines in the 3 cylinder volume. They occupy $\sim 9\%$ percent of the intracellular space. Although each of the three cylinders was constructed around a single apical dendrite to capture nearly all of its spines, there were many more spines from other dendrites that invaded this territory, i.e., the central “red” dendrite contributes only 12%; $n = 77/628$ of the spines in cylinder 1. Furthermore, the central dendrite’s spines were completely intermingled with the spines of other dendrites (see Figure 7A; Movie S12).

In general, spines appear more densely packed (~ 51 spines per 10 μm dendritic length for the red dendrite in cylinder 1) and often of greater length (mean $\sim 1.8 \pm 0.6 \mu\text{m}$ and longest $\sim 3.8 \mu\text{m}$; $n = 77$) than expected in mouse cortex based on previous reports (Benavides-Piccione et al., 2002). Perhaps this is a

consequence of the saturated method of reconstruction, where no spine could be overlooked. The long neck lengths could mean that some of these spines are electrically invisible to the soma (Araya et al., 2006). Larger spine volumes were positively correlated with spine apparatus ($r = 0.36$; $p < 0.000001$), larger postsynaptic densities ($r = 0.77$; $p < 0.000001$), larger numbers of presynaptic vesicles ($r = 0.58$; $p < 0.000001$), and presynaptic mitochondria ($r = 0.141$; $p = 0.007$).

Approximately 5% (39/780) of spines belonging to the central dendrite were not innervated by an axon. They appeared longer and thinner than spines that were innervated and often did not terminate in “heads” (Figure S5). These are termed filopodia (Purpura, 1975). Individual filopodia occupied less volume ($0.03 \pm 0.02 \mu\text{m}^3$) than innervated spines ($0.10 \pm 0.08 \mu\text{m}^3$) and only $\sim 30\%$ of them have spine apparatus versus 60% of innervated spines.

Connectivity Patterns of Excitatory Axons

We examined excitatory axonal input to dendritic spines that account for three-quarters of the synapses ($n = 1,286/1,700$) in the 3 cylinder volume and quickly found by mining the data in the synapse spread sheet (Table S1) a potential anatomical correlate of the physiological finding that different excitatory axons can have strikingly different strength connections with the same dendrite (Markram et al., 1998; Song et al., 2005). There were many instances in which the same axon innervated the same dendrite at multiple different spines. Such multiple contacts have been described in the hippocampus (Chicurel and Harris, 1992) and inferred from light microscopy of cortex (Markram et al., 1997). In cylinder 1, the 77 excitatory spine synapses onto its central (red) apical dendrite came from only 63 different axons because eight axons innervated two spines each and three axons innervated three spines (Movie S13). In cylinder 2, 12 of a total of 84 axons innervated two spines of the green dendrite, accounting for 22% of that dendrite’s spines. Such multiple contacts were not restricted to apical dendrites because the most extreme example was an axon that innervated

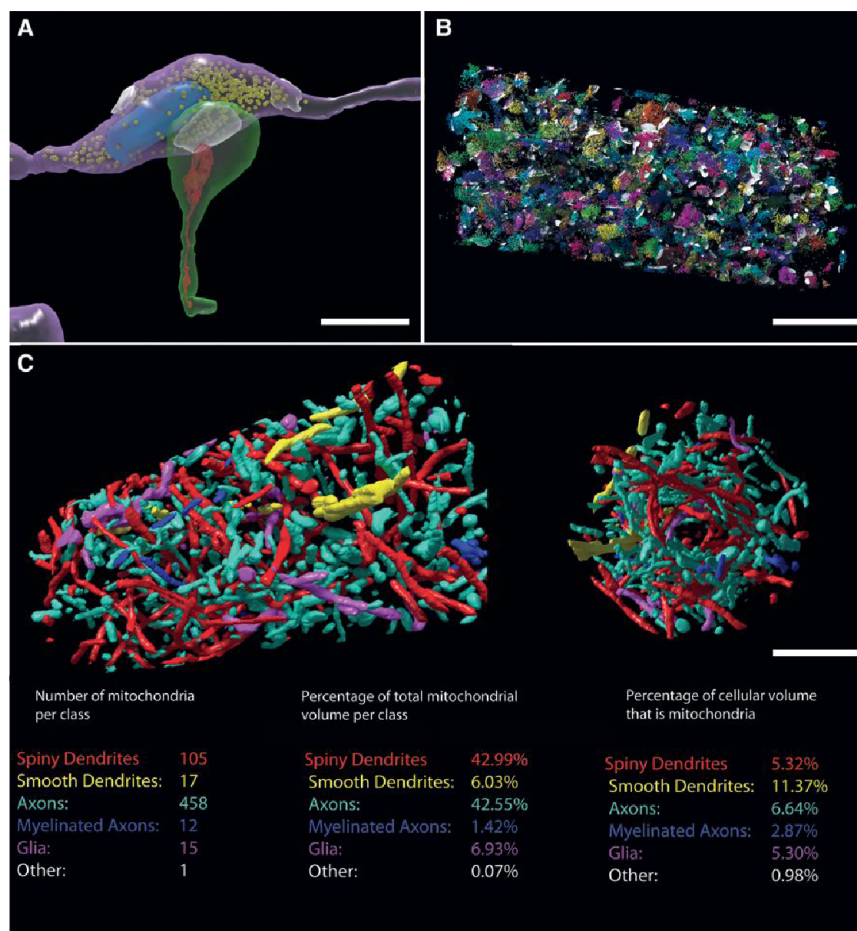


Figure 5. Reconstruction of Subcellular Organelles

(A) A reconstruction of a single synapse showing the innervating excitatory axon and its en passant varicosity (purple), postsynaptic dendritic spine (green), synaptic vesicles (yellow), a presynaptic mitochondrion (blue), the postsynaptic density (white), and spine apparatus (red).

(B) All of the synaptic vesicles in cylinder 1 ($n = 162,259$) and their corresponding postsynaptic densities (white) are shown. Vesicles with the same color belong to the same axon (full data at <http://openconnecto.me/Kasthurietal2014/view/highResAnnotated>).

(C) All of the mitochondria ($n = 635$) contained in cylinder 1 from side view of the cylinder (left) and end-on view (right). Three tables show mitochondrial metrics for cell and process types. Colors of mitochondria in the rendering refer to the classes listed. Scale bars, $1 \mu\text{m}$ for (A), $7 \mu\text{m}$ for (B), and $3 \mu\text{m}$ for (C).

See also Figure S4.

five different spines of a basal pyramidal dendrite (Figure 6). The spines innervated by the same axon were not by rule adjacent either in terms of the location of the spine heads or their origins from the dendritic shaft (Figure 6). In cylinder 1 there were 34 instances in which an axon established synapses on two spines of the same dendrite, 4 instances in which an axon innervated three spines on the same dendrite, and the 1 instance of five just mentioned. Therefore, 46 synapses were “redundant” in the sense that these synapses replicated synaptic connections that were already established by a different synapse of the same axon on the same target cell. For all spines in cylinders 1–3, we counted 97 redundant synapses. However, given the shape of the volume, only the red and green dendrites had all their spines assayed, and thus the measured redundancy almost certainly underestimates the actual amount.

Next, we consider potential reasons for why multiple spine synapses between an axon and a dendrite exist. One idea is that, by virtue of having substantially more branches or a more convoluted path through the volume, some axons have a greater opportunity to establish multiple synapses with the same dendrite than simpler axons. However, there was only a weak correlation between the total length of excitatory axons that crossed through cylinder 1 and the number of synapses they established with its central dendrite ($n = 63$ axons, 77 synapses;

correlation = 0.16; Figure S6A). Alternatively, some axons may have a strong affinity to run near the spines of particular dendrites. We therefore looked at the trajectory of each excitatory axon in greater detail to see if we could discover any differences between the axons that innervated the central (“red”) dendrite in cylinder 1 and a cohort of excitatory axons that did not innervate the central dendrite in the cylinder but at least passed immediately adjacent to at least one of its spines (contacts we call “touches,” see the Methods for details). Many axons touched each spine (8.9 ± 4.3 excitatory axons touched each spine), but in almost all cases ($\sim 99\%$) only one excitatory axon innervated each (Figure 7B; Movie S14; <http://openconnecto.me/Kasthurietal2014/data/touchSynapse>). The analysis of axons making touches and those that innervated the central dendrite argues against the idea that the trajectory axons predict their synaptic connectivity. First, for the 77 dendritic spines of the central dendrite in cylinder 1, we found little correlation (correlation coefficient = 0.0001) between the number of these spines that an excitatory axon touches versus the number of synapses it establishes on these spines, as would be expected if synapse probability is just related to the number of opportunities based on proximity to spines (Figure S6B). Second, we found no evidence to support the idea that axons that established the synapses with the central dendrite grew in closer proximity to that dendrite than the axons that touched but did not establish synapses. We compared the length of axons that entered the cylinder and touched a spine of the central dendrite without establishing any synapses with it to the lengths of axons that established synapses with the central dendrite. The axons that touched, but did not establish synapses with the central dendrite, were on average slightly longer in the volume than the axons that established

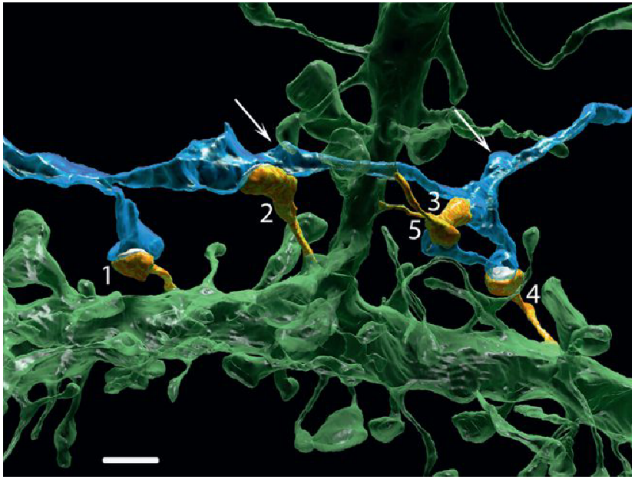


Figure 6. Multiple Synapses of the Same Axon Innervate Multiple Spines of the Same Postsynaptic Cell

An extreme example in which one axon (blue) innervates five dendritic spines (orange, labeled 1–5) of a basal dendrite (green) is shown. Arrows point to other varicosities of this axon that are innervating dendritic spines of other neurons (data not shown). Scale bar, 2 μm .

synapses (mean $9.9 \pm 6.6 \mu\text{m}$ synapsing versus mean $10.8 \pm 5.18 \mu\text{m}$ touching), providing no support for the idea that innervating axons had a greater affinity to grow along the central dendrite than axons that passed by but did not innervate it (Stepanyants et al., 2004).

We tested whether the axon-spine connectivity observed could be based on purely stochastic mechanisms. Specifically, did redundant excitatory synapses originate by synapse formation among a random subset of the close encounters (i.e., touches) between excitatory axons and dendritic spines? This analysis tests a high-resolution version of the so called Peters' rule (see discussion). We analyzed the 7,505 spine touches and 1,037 synapses between all the excitatory axons ($n = 916$) with dendritic spines ($n = 1,036$) in cylinders 1 and 2. For each axon we itemized all the spines that it touched and the subset of these that were actual synapses (Figure 7C). If synaptic connections occurred randomly among the close encounters of axons and spines then a randomization of the synapses among the spine touches should not significantly change the number of times the same axon innervates a dendrite more than once. To assure that each axon in the randomization still established the identical number of synapses as it did in the actual data and that each spine was still innervated by only one excitatory axon (or in 10 cases, two excitatory axons), we developed an algorithm that essentially solved a Sudoku matrix of axons and spines in that it kept the numbers of synapses in the rows and columns unchanged from the actual data (<http://openconnecto.me/Kasthuri2014/Code/touchSynapse>; see also the Methods). In this randomization, both the quantitative aspects of the synaptic connectivity of each axon and each dendrite and the spatial overlap of all axons and dendrites are identical to the actual data. The only change made is the particular identity of which of the close axon-spine touches are

synaptic. We calculated for each randomization the number of redundant synapses. In a run of 80,000 randomization trials, none of the randomized connectivity patterns had as many redundant synapses as the 78 found in the actual dataset of cylinder 1+2 (simulation median = 52 redundant synapses; $p < 0.00001$; Figure 7D). Thus axon-dendrite adjacency, while of course necessary for synapses to form, is insufficient to explain why some axons establish multiple synapses on some dendrites and not others. This is an explicit refutation of Peters' rule. Rather this result argues that there are different probabilities for synapses between particular dendrites and particular excitatory axons.

To further explore this idea that excitatory axons show preferences in terms of the dendritic spines they innervate (and those they don't) among the larger population of dendritic spines with which they come into close proximity, we carried out an additional test. We analyzed two cohorts of axons from cylinder 1: the 63 axons that innervated the central dendrite's spines within the cylinder (cohort 1) and 63 different excitatory axons that touched the same number of its spines, but did not innervate the central dendrite's spines in the cylinder (cohort 2). Inside the cylinder, the 63 axons in cohort 1 as already described, innervated multiple spines on the central dendrite whereas axons in cohort 2 did not innervate any spines of the central dendrite (by definition) despite both groups having the same access to that dendrite's spines. We then traced these two sets of axons into the surrounding high-resolution volume to see if their synaptic preferences within the cylinder predicted their connectivity preferences outside the cylinder. The results were clear: axons in cohort 1 continued to innervate the central dendrite in the large surrounding volume, adding an additional 11 synapses onto its spines. Axons in cohort 2 however, added only 1 synapse on the central dendrite (Figures 7E and 7F; $p \sim 0.003$; from the binomial distribution, see the Methods). These data show that axons have intrinsic preferences for the spines of some dendrites as opposed to others. However, even among those axons that innervate the central dendrite in the cylinder, some appear better matched to it than others based on their behavior outside the cylinder. Among the axons innervating the central dendrite in the cylinder their likelihood to form additional synapses with it outside the cylindrical volume was in rough proportion to the number of synapses they formed with it in the cylinder. The cohort of axons that established one synapse with the central dendrite in cylinder 1 ($n = 52$) add 0.13 synapses per axon with it in the larger volume (i.e., excluding the cylinder); those that established two synapses on the central dendrite in the cylinder ($n = 8$) added 0.38 additional synapses per axon and those axons that established three synapses with the central dendrite in the cylinder ($n = 3$) added 0.67 additional synapses per axon. Importantly however, these three groups of axons did not differ in their tendency to establish synapses on the sum of all their other dendritic targets indicating that the different synapse biases related to the central dendrite was not accounted for by intrinsically different tendencies to establish synapses among these three cohorts. When all the 63 axons that innervated the central dendrite were considered as a single population $\sim 30\%$ (18/63) of them innervate the central dendrite multiple times. Thus in this region of cortex at least, axons forming multiple synapses

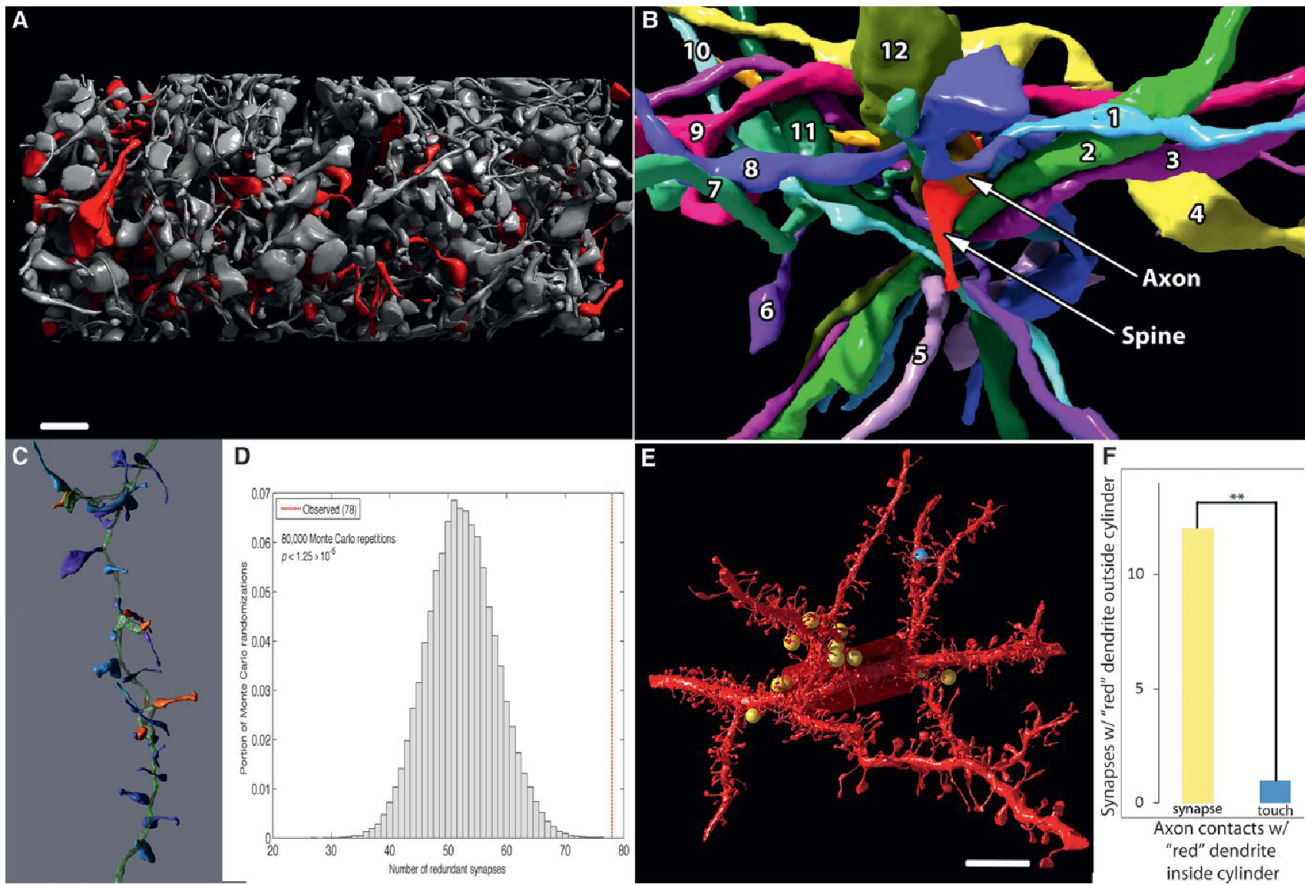


Figure 7. Specificity of Spine Innervation by Excitatory Axons

(A) A rendering demonstrating the high density and intermixing of spines from the red dendrite (red) and many other dendrites (gray) in the cylinder surrounding the "red" apical dendrite. See also Movie S13.

(B) A reconstruction showing 12 additional excitatory axons in the immediate vicinity of a dendritic spine (arrow) and its innervating axon (arrow). See also Movie S14.

(C) A reconstruction showing the nine spines (blue) that "touch" one excitatory axon (green) and the three spines (orange) that are innervated by it.

(D) A histogram showing the number of redundant synapses (see text) in 80,000 randomizations of the synapses among the touches of each axon. In none of these trials was the number of redundant synapses equal to, or greater than, the actual number (red line).

(E) Sites in which the axons that form synapses with the "red" dendrite's spines inside the cylinder establish 11 additional synapses with this dendrite outside the cylinder (yellow spheres). Axons that only touched the "red" dendrite spines in the cylinder form only one synapse with it outside of the cylinder (blue sphere).

(F) A graph showing the result described in (E) ($p = 0.003$). Scale bars, 2 μm for (A) and 15 μm for (E). See also Figures S5 and S6 and Movies S12, S13, and S14.

on the same dendrite are commonplace and the tendency appears to be graded: some axons consistently avoid synapses with some dendrites, and among those that do form synapses with a dendrite, there appear to be a range of tendencies from weak to strong.

Synapses with Identical Activity

The high incidence of multiple synapses of one axon on one dendrite offers an opportunity to study spine synapses with nearly identical pre- and postsynaptic activity patterns. Are structural properties of synapses regulated by activity patterns? Such tests have been carried out in the hippocampus suggesting that they do (Sorra et al., 1998) and here we examine if the trends are the same in neocortex. We use the synapse dataset (Table S1) to compare five structural features of pairs of synap-

ses established by the same axon on pairs of dendritic spines of the same dendrite. To assess whether synapses of the same axon on the same dendrite show more similarity than would be expected if synapse structures at each site are independently and randomly determined, we compared the measured values between the actual pairs with randomly chosen pairs from the same cohort by doing a permutation test.

The overall conclusion we reach is that pairs of excitatory synapses that have identical pre- and postsynaptic partners tend to be more similar than randomly chosen pairs from the same cohort for 4 of the 5 metrics (mitochondria in the synaptic terminal being the exception) but that for our data sample, this only reaches statistical significance for measures of the volume of dendritic spines. The evidence for similarity is stronger at pairs

sharing both the same axon and the same dendrite than pairs sharing either just the same axon (on different dendrites) or just the same dendrite (but from different axons).

DISCUSSION

The aim of this work was to turn EM images of brain into a minable dataset for multiple analyses without the need for new image data for each question (Figure S7). The vast majority of our effort occurred after generating the segmented images as we learned how to transform images into a database and analyze it. The synapse database (Table S1) provides such a resource for the connections within the volume as demonstrated by some of the queries and results in this paper.

In the last few years there have been a number of detailed analyses of neural ultrastructure and its relation to functional properties of neurons. In this paper we depart from this approach in that there were no antecedent functional studies to focus our analysis. The goal rather was to see what could be learned from a saturated connectomic analysis per se in neocortex. Part of the motivation was to explicitly consider the fact that connectomics can reveal structure where functional information is not available in analogy to the way genomics reveals sequences of genes whose function are not yet known. To allow for further inquiries and analyses in the high-resolution volume (80,000 μm^3) we provide access to all the image data via the Open Connectome Project (<http://openconnectome.me/Kasthuri2014/>), the 2D and 3D visualization, tracing, and editing tools, many of which were developed specifically for this project. Moreover, much of the analytic software developed for this project is also available (<http://openconnectome.me/Kasthuri2014/Code>).

We analyzed the synapses of excitatory axons with dendritic spines, the most plentiful synapses in the saturated volume to learn if their connectivity could be predicted by simply knowing the degree of physical overlap of axons and dendrites. This idea underpins theoretical approaches to understanding the brain (Braitenberg and Schuz, 1998; da Costa and Martin, 2013). Explaining synaptic connectivity by physical overlap is an attractive idea because of the obviously laminated organization of many regions of the brain including the cerebral cortex. Evidence supports the idea that molecular cues guide innervating terminal axon branches and perhaps postsynaptic dendrites to particular regions where they can form synapses with each other (Williams et al., 2010). It is thus possible that synaptic specificity in the cortex is explained in large part by axon and dendrite guidance mechanisms that put pre- and postsynaptic elements in close proximity (i.e., the same layer or sub-layer). If so, this would simplify the analysis of cortical connectivity and support models based largely on areal projections of axons and the classes of dendrites in their terminal fields. Such statistical approaches potentially provide a way to model brains without requiring knowing the exact details of every neuron's connections (Binzegger et al., 2004; Hill et al., 2012). This concept, called Peters' Rule, after Alan Peters (despite his insistence that he disputes it—A. Peters, personal communication) has been examined in retina and hippocampus. In retina some data support the idea that, to at least some degree, the contacts

(probably synapses) between neurons can be accounted for by their proximity, in support of Peters' Rule (Kim et al., 2014). However even that work found the numbers of contacts were skewed from what one would expect if proximity were the only factor guiding contacts. In a different piece of work from the same serial dataset the directional selectivity of individual amacrine dendrites looked to be arranged in a way that was incompatible with random contacts (Briggman et al., 2011). In hippocampus, support for the idea that connectivity was not explicable simply by proximity has also been obtained (Mishchenko et al., 2010; Druckmann et al., 2014). The previous results do not explicitly test the degree to which actual proximity of each individual axon to all the postsynaptic sites in a volume explains the connectivity patterns observed.

We therefore used the saturated reconstruction to identify each place each excitatory axon comes within touching distance to a dendritic spine. We discovered that each spine is closely apposed by about nine different axons (of which typically only one establishes a synapse). This means that one must use some caution in light microscopy when claiming an axon and a nearby dendritic spine are making synaptic contact. Our results argue for the idea that cellular identity, and not proximity, guides the connections between excitatory axons and dendritic spines. The best predictor of whether an axon would establish a synapse with a particular dendrite was its synaptic connectivity with that dendrite at other sites. An excitatory axon that established a spine synapse with a dendrite, had a 40% probability of establishing another synapse on the same dendrite whereas excitatory axons that only came adjacent to, but did not innervate, a dendrite's spine had a 25-fold lower probability ($\sim 1.6\%$) of establishing a synapse with that dendrite at another site. Thus while physical overlap of axons and dendrites is necessary, it is not sufficient to generate the pattern of synaptic connections in this region of cerebral cortex, refuting Peters' rule.

The abundance of multiple spine synapses of the same excitatory axon on the same dendrite suggests that the strength of excitatory connections here, as elsewhere in the brain, is based on the number of synapses between them and can range from zero to a potentially large number. Changes in the number of spine synapses between an axon and a dendrite could be downstream of short term alterations in synaptic efficacy (such as by changes in neurotransmitter receptor number or spine shape at individual synapses). In distinction to synaptic efficacy, such numerical changes in connectivity may be longer lasting and may be less reversible. Indeed, developmental synapse elimination in the peripheral nervous system occurs in this way: changes in efficacy are followed by addition of new synaptic sites (Colman et al., 1997). If comparable developmental processes of synapse elimination and compensatory synapse addition that are known to occur in the peripheral nervous system, and some parts of the CNS (Hashimoto and Kano, 2005; Walsh and Lichtman, 2003), are also occurring in the cerebral cortex, then the pattern of connectivity seen here might occur as a consequence of similar activity-dependent mechanisms. In particular, if synapse elimination removes some of the axonal input converging on a pyramidal cell, then remaining inputs might locally sprout to occupy vacated spines in much the same way remaining motor axons takeover sites vacated by eliminated axons at

the developing neuromuscular junction (Walsh and Lichtman, 2003; Turney and Lichtman, 2012). Saturated reconstructions of neural circuits in younger cerebral cortex may therefore be informative.

Finally, given the many challenges we encountered and those that remain in doing saturated connectomics, we think it is fair to question whether the results justify the effort expended. What after all have we gained from all this high density reconstruction of such a small volume? In our view, aside from the realization that connectivity is not going to be easy to explain by looking at overlap of axons and dendrites (a central premise of the Human Brain Project (Markram et al., 2012), we think that this “omics” effort lays bare the magnitude of the problem confronting neuroscientists who seek to understand the brain. Although technologies, such as the ones described in this paper, seek to provide a more complete description of the complexity of a system, they do not necessarily make understanding the system any easier. Rather, this work challenges the notion that the only thing that stands in the way of fundamental mechanistic insights is lack of data. The numbers of different neurons interacting within each miniscule portion of the cortex is greater than the total number of different neurons in many behaving animals. Some may therefore read this work as a cautionary tale that the task is impossible. Our view is more sanguine; in the nascent field of connectomics there is no reason to stop doing it until the results are boring.

EXPERIMENTAL PROCEDURES

A detailed description is available in the Supplemental Experimental Procedures.

Data Acquisition

An anesthetized adult mouse was perfused transcardially with a fixative solution containing glutaraldehyde, paraformaldehyde, and CaCl_2 in cacodylate buffer. The brain was removed and maintained overnight at 4°C in the same fixative solution. A 200- μm vibratome section encompassing part of the somatosensory cortex was then removed, washed, and stained with reduced osmium tetroxide-thiocarbohydrazide (TCH)-osmium (“ROTO”) and infiltrated with Epon (for details, see Tapia et al., 2012). The cured block was trimmed to a 2 × 3 mm rectangle and a depth of 200 μm and then readied for automated serial sectioning. The automated, unattended collection of 29.4-nm serial sections was accomplished using a custom tape collection device attached to a commercial ultramicrotome (ATUM). The sections were collected on plasma-treated polyamide (Kapton, Sheldahl) 8-mm-wide tape. The tape was then cut into strips and attached to silicon wafers (Figure 1). The wafers with sections were then coated with ~10 nm of carbon to ensure conductivity. An automated protocol to locate and image sections on the wafers was used (Hayworth et al., 2014; see also Tomassy et al., 2014) with a Sigma scanning electron microscope (Carl Zeiss), equipped with the ATLAS software (Fibics). The serial section images were acquired using backscattered electron detection. Single images using secondary electron detection were acquired using the FEI Magellan thru-the-lens detector or the Zeiss MultiSEM 505. Sections collected on carbon-coated Kapton were required for secondary electron detection.

For the medium- and high-resolution data sets, alignment was accomplished by affine image transformations using custom Matlab scripts. The high-resolution image stack (1,850 images) was aligned using a single affine transformation per image. The aligned images were then manually segmented using a custom Direct3D-based Windows volume annotation and segmentation tool (VAST; <http://openconnectome.me/Kasthurietal2014/Code/VAST>). The segmented images and metadata were processed for data analysis with Matlab scripts and 3D rendering with Matlab scripts for computation of surface meshes and 3 dsMax (Autodesk) for the rendering steps. We also developed

RhoANA, a processing pipeline, to generate automatic segmentations, and Mojo, a proofreading tool. All code is open source and available online at <http://www.rhoana.org/>. In order to scale to large data sets, we designed the processing pipeline to run on a computer cluster.

Data Analysis

Excitatory (E) and inhibitory (I) synapses were classified according to established criteria (Peters et al., 1991). If a particular synapse was ambiguous, additional synapses of the same axon were found and analyzed until a clear assignment could be made. In any section synaptic vesicles were only counted that showed a clear center, and this is an accurate measure of the total number of vesicles (Figure S4). We utilized the Open Connectome Project, which has developed the Reusable Annotation Markup for Open connectomics (RAMON), a spatial database to store large-scale images and co-registered annotation datasets (Burns et al., 2013). To assess whether the observed number of “redundant” synapses (defined as the number of synapses in excess of one that an axon and dendrite “share”), we used Monte Carlo reassignment of the synapses (the Sudoku algorithm) among all the close contacts each axon established with dendritic spines described in detail in the Supplemental Experimental Procedures. To estimate the number of objects within the cylinder that are likely to be branches of the same axon, we used a set of cortical axon skeletons available at the NeuroMorpho web site (Ascoli et al., 2007) and a Monte Carlo simulation in which the cylinder is randomly translated so that at least one branch overlaps, and we count the number of times a second branch is also in the cylinder. To assess the similarity of pairs of synapses made by the same axon on the same dendrite, we select all the pairs of synapses shared by the same axon and same dendrite (SASD) from the spreadsheet in Table S1 and use the values of five morphological metrics for statistical analysis.

SUPPLEMENTAL INFORMATION

Supplemental Information includes Supplemental Experimental Procedures, 7 figures, 1 table, and 14 movies and can be found with this article online at <http://dx.doi.org/10.1016/j.cell.2015.06.054>.

AUTHOR CONTRIBUTIONS

ATUM, N.K., K.J.H., R.L.S., N.K. J.C.T., and J.W.L.; sample preparation, N.K., R.L.S., J.C.T., and J.W.L.; optimization of scanning electron microscope and imaging (tape substrates, wafer creation, etc.), N.K., R.L.S., J.C.T., and J.W.L.; semi-automatic acquisition of data, N.K., D.R.B., R.L.S., and J.W.L.; alignment, D.R.B.; VAST, D.R.B., and H.S.S.; manual segmentation, N.K., D.R.B., and D.L.; automatic segmentation pipeline (RhoANA, Mojo, etc.), S.K.B., A.V.R., V.K., T.R.J., M.R., H.P., and J.W.L. statistical analyses, N.K., D.R.B., J.A.C., T.R.J., J.L.M., W.G.R., J.T.V., D.L.S., C.E.P., and J.W.L.; 3D renderings, D.R.B. and N.K.; online database management (openconnectome, etc.), W.G.R., J.T.V., and R.B.; writing, N.K., D.R.B., R.L.S., J.C.T., H.S.S., and J.W.L.

ACKNOWLEDGMENTS

We gratefully acknowledged support from the NIH/NINDS (1DP2OD006514-01, TR01 1R01NS076467-01, and 1U01NS090449-01), Conte (1P50MH094271-01), MURI Army Research Office (contract no. W911NF1210594 and IIS-1447786), CRCNS 1R01EB016411), NSF (OIA-1125087 and IIS-1110955), DARPA (HR0011-14-2-0004), the Human Frontier Science Program (RGP0051/2014), the JHU Applied Physics Laboratory, the Research Program for Applied Neuroscience, the Howard Hughes Medical Institute, Nvidia, Intel, and Google. We are also grateful to the Center for the Developing Child at Harvard University for providing tracers, Masconomet Regional High School, and Priya Manavalan and Kunal Lillaney at the Open Connectome Project for help with data management.

Received: October 19, 2014

Revised: March 10, 2015

Accepted: June 1, 2015

Published: July 30, 2015

REFERENCES

- Anderson, J.R., Jones, B.W., Watt, C.B., Shaw, M.V., Yang, J.H., Demill, D., Lauritzen, J.S., Lin, Y., Rapp, K.D., Mastronarde, D., et al. (2011). Exploring the retinal connectome. *Mol. Vis.* *17*, 355–379.
- Araya, R., Jiang, J., Eisenthal, K.B., and Yuste, R. (2006). The spine neck filters membrane potentials. *Proc. Natl. Acad. Sci. USA* *103*, 17961–17966.
- Ascoli, G.A., Donohue, D.E., and Halavi, M. (2007). NeuroMorpho.org: a central resource for neuronal morphologies. *J. Neurosci.* *27*, 9247–9251.
- Beierlein, M., Gibson, J.R., and Connors, B.W. (2003). Two dynamically distinct inhibitory networks in layer 4 of the neocortex. *J. Neurophysiol.* *90*, 2987–3000.
- Benavides-Piccione, R., Ballesteros-Yáñez, I., DeFelipe, J., and Yuste, R. (2002). Cortical area and species differences in dendritic spine morphology. *J. Neurocytol.* *31*, 337–346.
- Binzegger, T., Douglas, R.J., and Martin, K.A. (2004). A quantitative map of the circuit of cat primary visual cortex. *J. Neurosci.* *24*, 8441–8453.
- Bock, D.D., Lee, W.C., Kerlin, A.M., Andermann, M.L., Hood, G., Wetzel, A.W., Yurgenson, S., Soucy, E.R., Kim, H.S., and Reid, R.C. (2011). Network anatomy and in vivo physiology of visual cortical neurons. *Nature* *471*, 177–182.
- Braitenberg, V., and Schuz, A. (1998). *Cortex: Statistics and Geometry of Neuronal Connectivity* (Berlin: Springer).
- Briggman, K.L., Helmstaedter, M., and Denk, W. (2011). Wiring specificity in the direction-selectivity circuit of the retina. *Nature* *471*, 183–188.
- Burns, R., Roncal, W.G., Kleissas, D., Lillaney, K., Manavalan, P., Perlman, E., Berger, D.R., Bock, D.D., Chung, K., Grosenick, L., et al. (2013). The open connectome project data cluster: Scalable analysis and vision for high-throughput neuroscience. A. Szalay, T. Budavari, M. Balazinska, A. Meliou, and A. Sacan, eds. *Proceedings of the 25th International Conference on Scientific and Statistical Database Management*.
- Cajal, R.S. (1899). *Textura del sistema nervioso del hombre y de los vertebrados* (Madrid: Moya).
- Chicurel, M.E., and Harris, K.M. (1992). Three-dimensional analysis of the structure and composition of CA3 branched dendritic spines and their synaptic relationships with mossy fiber boutons in the rat hippocampus. *J. Comp. Neurol.* *325*, 169–182.
- Colman, H., Nabekura, J., and Lichtman, J.W. (1997). Alterations in synaptic strength preceding axon withdrawal. *Science* *275*, 356–361.
- da Costa, N.M., and Martin, K.A. (2013). Sparse reconstruction of brain circuits: or, how to survive without a microscopic connectome. *Neuroimage* *80*, 27–36.
- Deans, J.K., Powell, A.D., and Jefferys, J.G. (2007). Sensitivity of coherent oscillations in rat hippocampus to AC electric fields. *J. Physiol.* *583*, 555–565.
- DeFelipe, J., and Fariñas, I. (1992). The pyramidal neuron of the cerebral cortex: morphological and chemical characteristics of the synaptic inputs. *Prog. Neurobiol.* *39*, 563–607.
- Druckmann, S., Feng, L., Lee, B., Yook, C., Zhao, T., Magee, J.C., and Kim, J. (2014). Structured synaptic connectivity between hippocampal regions. *Neuron* *81*, 629–640.
- Eberle, A.L., Mikula, S., Schalek, R., Lichtman, J.W., Tate, M.L., and Zeidler, D. (2015). High-resolution, high-throughput imaging with a multibeam scanning electron microscope. *J. Microsc.* Published online January 27, 2015. <http://dx.doi.org/10.1111/jmi.12224>.
- Friedman, P.L., and Ellisman, M.H. (1981). Enhanced visualization of peripheral nerve and sensory receptors in the scanning electron microscope using cryofracture and osmium-thiocarbonylhydrazide-osmium impregnation. *J. Neurocytol.* *10*, 111–131.
- Gulyás, A.I., Megias, M., Emri, Z., and Freund, T.F. (1999). Total number and ratio of excitatory and inhibitory synapses converging onto single interneurons of different types in the CA1 area of the rat hippocampus. *J. Neurosci.* *19*, 10082–10097.
- Haehn, D., Knowles-Barley, S., Roberts, M., Beyer, J., Kasthuri, N., Lichtman, J.W., and Pfister, H. (2014). Design and evaluation of interactive proofreading tools for connectomics. *Proceedings of IEEE Transactions on Visualization and Computer Graphics*.
- Hashimoto, K., and Kano, M. (2005). Postnatal development and synapse elimination of climbing fiber to Purkinje cell projection in the cerebellum. *Neurosci. Res.* *53*, 221–228.
- Hayworth, K.J., Morgan, J.L., Schalek, R., Berger, D.R., Hildebrand, D.G., and Lichtman, J.W. (2014). Imaging ATUM ultrathin section libraries with WaferMapper: a multi-scale approach to EM reconstruction of neural circuits. *Front. Neural Circuits* *8*, 68.
- Helmstaedter, M., Briggman, K.L., and Denk, W. (2011). High-accuracy neurite reconstruction for high-throughput neuroanatomy. *Nat. Neurosci.* *14*, 1081–1088.
- Helmstaedter, M., Briggman, K.L., Turaga, S.C., Jain, V., Seung, H.S., and Denk, W. (2013). Connectomic reconstruction of the inner plexiform layer in the mouse retina. *Nature* *500*, 168–174.
- Hill, S.L., Wang, Y., Riachi, I., Schürmann, F., and Markram, H. (2012). Statistical connectivity provides a sufficient foundation for specific functional connectivity in neocortical neural microcircuits. *Proc. Natl. Acad. Sci. USA* *109*, E2885–E2894.
- Kaynig, V., Vazquez-Reina, A., Knowles-Barley, S., Roberts, M., Jones, T.R., Kasthuri, N., Miller, E., Lichtman, J.W., and Pfister, H. (2013). Large scale automatic reconstruction of neuronal processes from electron microscopy images. *arXiv*, arXiv:1303.7186, <http://arxiv.org/abs/1303.7186>.
- Kim, J.S., Greene, M.J., Zlateski, A., Lee, K., Richardson, M., Turaga, S.C., Purcaro, M., Balkam, M., Robinson, A., Behabadi, B.F., et al.; EyeWires (2014). Space-time wiring specificity supports direction selectivity in the retina. *Nature* *509*, 331–336.
- Krieger, P., Kuner, T., and Sakmann, B. (2007). Synaptic connections between layer 5B pyramidal neurons in mouse somatosensory cortex are independent of apical dendrite bundling. *J. Neurosci.* *27*, 11473–11482.
- Li, Z., Okamoto, K., Hayashi, Y., and Sheng, M. (2004). The importance of dendritic mitochondria in the morphogenesis and plasticity of spines and synapses. *Cell* *119*, 873–887.
- Lichtman, J.W., Pfister, H., and Shavit, N. (2014). The big data challenges of connectomics. *Nat. Neurosci.* *17*, 1448–1454. <http://dx.doi.org/10.1038/nn.3837>.
- Marblestone, A., Daugharthy, E., Kalhor, R., Peikon, I., Kechschul, J., Shipman, S., Mishchenko, Y., Dalrymple, D., Zamft, B., Kording, K., Boyden, E., Zador, A., and Church, G. (2013). *Conneconomics: The economics of large-scale neural connectomics*. <http://dx.doi.org/10.1101/001214>.
- Markram, H., Lubke, J., Frotscher, M., Roth, A., and Sakmann, B. (1997). Physiology and anatomy of synaptic connections between thick tufted pyramidal neurones in the developing rat neocortex. *J. Physiol.* *500* (Pt 2), 409–440.
- Markram, H., Wang, Y., and Tsodyks, M. (1998). Differential signaling via the same axon of neocortical pyramidal neurons. *Proc. Natl. Acad. Sci. USA* *95*, 5323–5328.
- Markram, H., Ailamaki A., Alvandpour A., Amunts K., Andreoni W., Ashburner J., Axer M., Baaden M., Badia R., Bartolome J., et al. (2012). *The human brain project: A report to the European Commission*. https://www.humanbrainproject.eu/documents/10180/17648/TheHBPreport_LR.pdf/18e5747e-10af-4bec-9806-d03aead57655.
- Megias, M., Emri, Z., Freund, T.F., and Gulyás, A.I. (2001). Total number and distribution of inhibitory and excitatory synapses on hippocampal CA1 pyramidal cells. *Neuroscience* *102*, 527–540.
- Mishchenko, Y. (2009). Automation of 3D reconstruction of neural tissue from large volume of conventional serial section transmission electron micrographs. *J. Neurosci. Methods* *176*, 276–289.
- Mishchenko, Y., Hu, T., Spacek, J., Mendenhall, J., Harris, K.M., and Chklovskii, D.B. (2010). Ultrastructural analysis of hippocampal neuropil from the connectomics perspective. *Neuron* *67*, 1009–1020.

- Mountcastle, V.B. (1997). The columnar organization of the neocortex. *Brain* 120, 701–722.
- Nunez-Iglesias, J., Kennedy, R., Plaza, S.M., Chakraborty, A., and Katz, W.T. (2014). Graph-based active learning of agglomeration (GALA): a Python library to segment 2D and 3D neuroimages. *Front. Neuroinform.* 8, 34.
- Peters, A., Josephson, K., and Vincent, S.L. (1991). Effects of aging on the neuroglial cells and pericytes within area 17 of the rhesus monkey cerebral cortex. *Anat. Rec.* 229, 384–398.
- Plaza, S.M., Scheffer, L.K., and Chklovskii, D.B. (2014). Toward large-scale connectome reconstructions. *Curr. Opin. Neurobiol.* 25, 201–210.
- Popov, V.I., and Stewart, M.G. (2009). Complexity of contacts between synaptic boutons and dendritic spines in adult rat hippocampus: three-dimensional reconstructions from serial ultrathin sections in vivo. *Synapse* 63, 369–377.
- Purpura, D.P. (1975). Dendritic differentiation in human cerebral cortex: normal and aberrant developmental patterns. *Adv. Neurol.* 12, 91–134.
- Sherrington, C. (1906). *The Integrative Action of the Nervous System* (Yale: Yale University Press).
- Sinha, A., Roncal, W.G., Kasthuri, N., Lichtman, J.W., Burns, R., and Kazhdan, M. (2013). Automatic annotation of axoplasmic reticula in pursuit of connectomes using high resolution neural EM data. 3rd Annual Hopkins Imaging Conference.
- Smiley, J.F., and Goldman-Rakic, P.S. (1993). Heterogeneous targets of dopamine synapses in monkey prefrontal cortex demonstrated by serial section electron microscopy: a laminar analysis using the silver-enhanced diaminobenzidine sulfide (SEDS) immunolabeling technique. *Cereb. Cortex* 3, 223–238.
- Song, S., Sjöström, P.J., Reigl, M., Nelson, S., and Chklovskii, D.B. (2005). Highly nonrandom features of synaptic connectivity in local cortical circuits. *PLoS Biol.* 3, e68.
- Sorra, K.E., Fiala, J.C., and Harris, K.M. (1998). Critical assessment of the involvement of perforations, spinules, and spine branching in hippocampal synapse formation. *J. Comp. Neurol.* 398, 225–240.
- Stepanyants, A., and Chklovskii, D.B. (2005). Neurogeometry and potential synaptic connectivity. *Trends Neurosci.* 28, 387–394.
- Stepanyants, A., Tamás, G., and Chklovskii, D.B. (2004). Class-specific features of neuronal wiring. *Neuron* 43, 251–259.
- Takemura, S.Y., Bharioke, A., Lu, Z., Nern, A., Vitaladevuni, S., Rivlin, P.K., Katz, W.T., Olbris, D.J., Plaza, S.M., Winston, P., et al. (2013). A visual motion detection circuit suggested by *Drosophila* connectomics. *Nature* 500, 175–181.
- Tapia, J.C., Kasthuri, N., Hayworth, K.J., Schalek, R., Lichtman, J.W., Smith, S.J., and Buchanan, J. (2012). High-contrast en bloc staining of neuronal tissue for field emission scanning electron microscopy. *Nat. Protoc.* 7, 193–206.
- Tomassy, G.S., Berger, D.R., Chen, H.H., Kasthuri, N., Hayworth, K.J., Vercelli, A., Seung, H.S., Lichtman, J.W., and Arlotta, P. (2014). Distinct profiles of myelin distribution along single axons of pyramidal neurons in the neocortex. *Science* 344, 319–324.
- Turney, S.G., and Lichtman, J.W. (2012). Reversing the outcome of synapse elimination at developing neuromuscular junctions in vivo: evidence for synaptic competition and its mechanism. *PLoS Biol.* 10, e1001352.
- van Vreeswijk, C., and Sompolinsky, H. (1996). Chaos in neuronal networks with balanced excitatory and inhibitory activity. *Science* 274, 1724–1726.
- Vanharreveld, A., Crowell, J., and Malhotra, S.K. (1965). A study of extracellular space in central nervous tissue by freeze-substitution. *J. Cell Biol.* 25, 117–137.
- Vazquez-Reina, A., Gelbart, M., Huang, D., Lichtman, J., Miller, E.L., Pfister, H. (2011). Segmentation fusion for connectomics. *Proceedings of IEEE International Conference on Computer Vision*, 177–184.
- Walsh, M.K., and Lichtman, J.W. (2003). In vivo time-lapse imaging of synaptic takeover associated with naturally occurring synapse elimination. *Neuron* 37, 67–73.
- Wehr, M., and Zador, A.M. (2003). Balanced inhibition underlies tuning and sharpens spike timing in auditory cortex. *Nature* 426, 442–446.
- White, J.G., Southgate, E., Thomson, J.N., and Brenner, S. (1986). The structure of the nervous system of the nematode *Caenorhabditis elegans*. *Philos. Trans. R. Soc. Lond. B Biol. Sci.* 314, 1–340.
- Williams, M.E., de Wit, J., and Ghosh, A. (2010). Molecular mechanisms of synaptic specificity in developing neural circuits. *Neuron* 68, 9–18.

Genome-wide CRISPR Screen in a Mouse Model of Tumor Growth and Metastasis

Sidi Chen,^{1,2,3,10} Neville E. Sanjana,^{3,4,5,6,7,10} Kaijie Zheng,^{3,4} Ophir Shalem,^{3,4} Kyunghoon Lee,⁸ Xi Shi,^{3,4} David A. Scott,^{3,4} Jun Song,⁸ Jen Q. Pan,^{3,4} Ralph Weissleder,^{8,9} Hakho Lee,⁸ Feng Zhang,^{3,4,5,6,7,*} and Phillip A. Sharp^{1,2,*}

¹David H. Koch Institute for Integrative Cancer Research, Cambridge, MA 02139, USA

²Department of Biology, Massachusetts Institute of Technology, Cambridge, MA 02139, USA

³Broad Institute of MIT and Harvard, Cambridge, MA 02142, USA

⁴Stanley Center for Psychiatric Research, Cambridge, MA 02142, USA

⁵McGovern Institute for Brain Research

⁶Department of Brain and Cognitive Sciences

⁷Department of Biological Engineering

Massachusetts Institute of Technology, Cambridge, MA 02139, USA

⁸Center for Systems Biology, Massachusetts General Hospital, Boston, MA 02114, USA

⁹Department of Systems Biology, Harvard Medical School, Boston, MA 02115, USA

¹⁰Co-first author

*Correspondence: zhang@broadinstitute.org (F.Z.), sharp@mit.edu (P.A.S.)

<http://dx.doi.org/10.1016/j.cell.2015.02.038>

SUMMARY

Genetic screens are powerful tools for identifying genes responsible for diverse phenotypes. Here we describe a genome-wide CRISPR/Cas9-mediated loss-of-function screen in tumor growth and metastasis. We mutagenized a non-metastatic mouse cancer cell line using a genome-scale library with 67,405 single-guide RNAs (sgRNAs). The mutant cell pool rapidly generates metastases when transplanted into immunocompromised mice. Enriched sgRNAs in lung metastases and late-stage primary tumors were found to target a small set of genes, suggesting that specific loss-of-function mutations drive tumor growth and metastasis. Individual sgRNAs and a small pool of 624 sgRNAs targeting the top-scoring genes from the primary screen dramatically accelerate metastasis. In all of these experiments, the effect of mutations on primary tumor growth positively correlates with the development of metastases. Our study demonstrates Cas9-based screening as a robust method to systematically assay gene phenotypes in cancer evolution *in vivo*.

INTRODUCTION

Cancer genomes have complex landscapes of mutations and diverse types of genetic aberrations (Lawrence et al., 2013; Weinberg, 2007). A major challenge in understanding the cancer genome is to disentangle alterations that are driving the processes of tumor evolution from passenger mutations (Garraway and Lander, 2013). Primary tumor growth and metastasis are distinct yet linked processes in the progression of solid tumors (Nguyen et al., 2009; Valastyan and Weinberg, 2011; Vanharanta and Massagué, 2013). It has been observed in the clinic that the

probability of detecting metastases in a patient correlates positively with the size of a primary tumor (Heimann and Hellman, 1998). Several possible explanations have been suggested: metastatic properties may only be acquired in late-stage tumors, larger tumors may seed proportionally more cells into circulation that eventually migrate to other sites, or cells with a strong ability to proliferate may also have enhanced ability to metastasize (Weinberg, 2007). In early studies using random insertional mutagenesis, it was observed that metastatic cell subpopulations overgrow to complete dominance in the primary tumor, suggesting progressive selection at both sites (Korczak et al., 1988; Waghorne et al., 1988).

Genetic screens are powerful tools for assaying phenotypes and identifying causal genes in various hallmarks of cancer progression (Hanahan and Weinberg, 2011). RNAi and overexpression of open reading frames (ORFs) have been utilized for screening cancer genes in several models of oncogenesis in mice (Schramek et al., 2014; Shao et al., 2014; Zender et al., 2008). Recently, the Cas9 nuclease (Barrangou et al., 2007; Bolotin et al., 2005; Chylinski et al., 2013, 2014; Deltcheva et al., 2011; Garneau et al., 2010; Gasiunas et al., 2012; Jinek et al., 2012; Sapranaukas et al., 2011) from the microbial type II CRISPR (clustered regularly interspaced short palindromic repeats) system has been harnessed to facilitate loss-of-function mutations in eukaryotic cells (Cong et al., 2013; Mali et al., 2013). When the Cas9 nuclease is targeted to specific locations in the genome, DNA cleavage results in double-stranded breaks (DSBs), which are repaired via non-homologous end-joining (NHEJ) (Rouet et al., 1994). NHEJ repair results in insertion or deletion (indel) mutations that can cause loss of function if the DSB occurs in a coding exon. The Cas9 nuclease can be guided to its DNA target by a single-guide RNA (sgRNA) (Jinek et al., 2012), a synthetic fusion between the CRISPR RNA (crRNA) and *trans*-activating crRNA (tracrRNA) (Deltcheva et al., 2011). In cells, Cas9-mediated gene disruption requires the full-length tracrRNA (Cong et al., 2013; Mali et al., 2013), in which secondary structures at the 3' end of tracrRNA are

critical for Cas9-mediated genome modification (Cong et al., 2013; Hsu et al., 2013).

Screens utilizing Cas9 have identified genes that are essential for cell survival and genes involved in drug resistance in various cell lines (Shalem et al., 2014; Wang et al., 2014; Koike-Yusa et al., 2014; Zhou et al., 2014). In vivo pooled screens are challenging due to many factors, such as the complexity of the library, limitations of virus delivery and/or cell transplantation, uniformity of viral transduction at a low MOI, and the complex dynamics and interactions of cells in animals. In this study, we report a genome-wide Cas9 knockout screen in a mouse model of tumor evolution. This screen provides a systematic phenotypic measurement of loss-of-function mutations in primary tumor growth and metastasis.

RESULTS

CRISPR/Cas9 Library-Mediated Mutagenesis Promotes Metastasis

We derived and cloned a cell line (Chen et al., 2014) from a mouse non-small-cell lung cancer (NSCLC) (Kumar et al., 2009). This cell line possesses an oncogenic *Kras* in conjunction with homozygous *p53* and heterozygous *Dicer1* loss of function (*Kras*^{G12D/+}; *p53*^{-/-}; *Dicer1*^{+/-}, denoted KPD) and is capable of inducing tumors when transplanted into immunocompromised mice (Chen et al., 2014; Kumar et al., 2009). We transduced this cell line with a lentivirus carrying a Cas9 transgene fused to a GFP and generated clonal cell lines (Cas9-GFP KPD) (Experimental Procedures) (Figures S1A and S1B). A clonal Cas9-GFP KPD cell line (clone 5) was selected to provide genetic and cellular homogeneity for subsequent screens.

We utilized a pooled genome-wide mouse sgRNA library (termed mouse genome-scale CRISPR knockout library A, or mGeCKOa) containing 67,405 sgRNAs targeting 20,611 protein-coding genes and 1,175 microRNA precursors in the mouse genome (Sanjana et al., 2014). The library also contains 1,000 control sgRNAs (termed non-targeting sgRNAs) designed to have minimal homology to sequences in the mouse genome (Sanjana et al., 2014; Shalem et al., 2014). We transduced the Cas9-GFP KPD cell line with the mGeCKOa library in three independent infection replicate experiments; for each replicate, the library representation (cells per lentiviral CRISPR construct) was greater than 400× (Figure 1A) (Experimental Procedures).

After in vitro culture for 1 week, we subcutaneously transplanted 3×10^7 cells into the flanks of immunocompromised *Nu/Nu* mice (Figure 1A). We transplanted the cells from each infection replicate into four mice, using one mouse for early tumor sequencing and three mice for sequencing of late-stage primary tumor and metastases (Figure 1A). Both mGeCKOa-transduced and untransduced Cas9-GFP KPD cells formed tumors at the injection site (Figure 1B). Like most subcutaneously transplanted tumors, these tumors were poorly differentiated. The primary tumors induced by mGeCKOa-transduced cells grew slightly faster than tumors from the untransduced cells at an early stage (Figure 1C) (2 weeks post-transplantation) (paired two-tailed t test, $p = 0.05$), but at late stages all tumors were similar in size (paired two-tailed t test, $p = 0.18$ for data at 4 weeks, $p = 0.6$ for data at 6 weeks) (Figure 1C).

At 6 weeks post-transplantation, we imaged the mice using micro-computed tomography (μ CT) and found tumors in the lungs of the mice transplanted with mGeCKOa-transduced Cas9-GFP KPD cells (mGeCKOa mice), but not in the mice transplanted with untransduced Cas9-GFP KPD cells (control mice) (Figure 1D, Figure S1C). Mice were sacrificed and examined for metastases in various organs. Under a fluorescent stereoscope at 6× magnification, metastases were visually detected in the lung in 89% (8/9) of the mGeCKOa mice (Figure S1D). The mGeCKOa mice on average had 80% of their lung lobes positive for metastases (Figure 1E). In contrast, none (0/3) of the control mice developed detectable metastases in the lung (Figure 1E). At this time, metastases were not detected in the liver, kidney, or spleen in either group (Figure 1F). These data indicated that mGeCKOa library transduction enhanced the ability of the Cas9-GFP KPD cells to form metastases in the lung.

Dynamic Evolution of sgRNA Library Representation during Tumor Growth and Metastasis

To investigate the sgRNA representation through different stages of tumor evolution and to identify genes where loss of function confers a proliferative or metastatic phenotype, we used deep sequencing to readout the sgRNA representation (see Data S1 in Dataset S1). At 6 weeks post transplantation, we sequenced the late-stage primary tumor and three random lobes from the lung of each of the nine mGeCKOa mice (Figure 1A) (Experimental Procedures). In parallel, we also sequenced the mGeCKOa input plasmid library, the pre-transplantation mGeCKOa-transduced Cas9-GFP KPD cells (cultured in vitro for 7 days after transduction), and early-stage primary tumors (2 weeks post transplantation, one mouse from each infection replicate). In the cell samples, the sgRNA representations showed high concordance between technical replicates (correlation, $\rho = 0.95$ on average, $n = 3$) and biological infection replicates (correlation, $\rho = 0.84$ on average, $n = 3$) (Figures 2A, S2A, S2B, and S2E). The sgRNA representation of cell samples correlates highly with the plasmid representation (correlation, $\rho = 0.93$ on average, $n = 3$) (Figures 2A, S2C, and S2E). Furthermore, different sgRNAs that target the same gene are correlated in terms of rank change (correlation, $\rho = 0.49$ on average, $n = 3$) (Figure S2D). Using gene set enrichment analysis (GSEA), we found that the sgRNAs with significantly decreased abundance in cells compared to plasmid are enriched for genes involved in fundamental cellular processes, such as ribosomal proteins, translation factors, RNA splicing factors, and RNA processing factors, indicating selection against the loss of these genes after 1 week in culture (Figure S2F).

To investigate the sgRNA library dynamics in different sample types (plasmid, pre-transplantation cells, early primary tumor, late primary tumor, and lung metastases), we compared the overall distributions of sgRNAs from all samples sequenced. Cell samples clustered tightly with each other and the plasmid, forming a cell-plasmid clade (Figures 2A and S2E). Early primary tumor samples also clustered with each other and then with the cell-plasmid clade, whereas late tumors and lung metastases clustered together in a distinct group (Figures 2A and S2E). The overlap of detected sgRNAs between different pre-transplantation infection replicates is over 95% (Figure S3A). The detected sgRNAs in the three infection replicates of early tumor

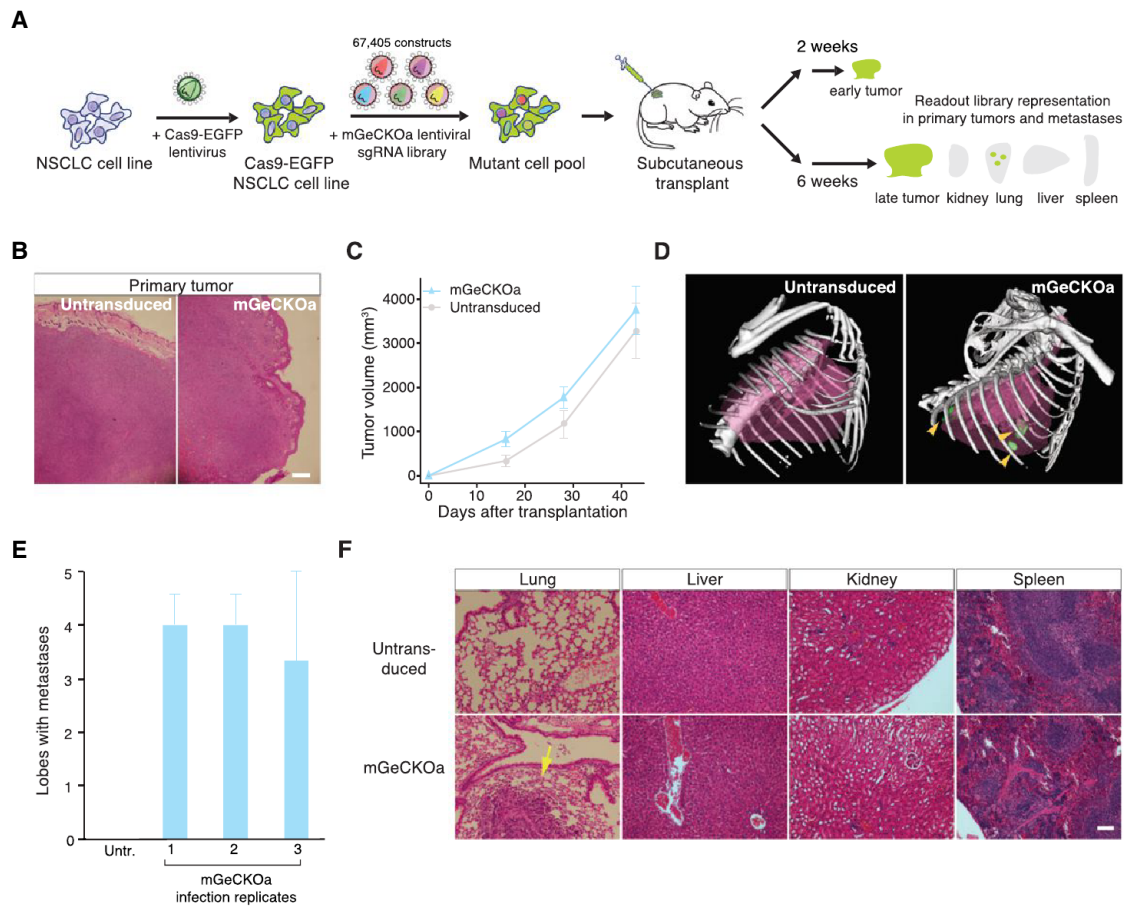


Figure 1. Tumor Growth and Metastasis in Transplanted Cas9-GFP KPD Cells with mGeCKOa Library

(A) Schematic representation of the loss-of-function metastasis screen using the mouse genome-scale CRISPR/Cas9 knockout library (mGeCKOa). (B) Representative H&E stains of primary tumor from *Nu/Nu* mice subcutaneously transplanted with a Cas9-GFP *Kras*^{G12D/+}; *p53*^{-/-}; *Dicer1*^{+/-} (KPD) NSCLC cell line that was either untransduced or transduced with the mGeCKOa lentiviral library. Scale bar, 200 μ m. (C) Primary tumor growth curve of *Nu/Nu* mice transplanted with untransduced cells (n = 3 mice) or mGeCKOa-transduced Cas9-GFP KPD cells (n = 9 mice). Error bars indicate SEM. (D) MicroCT 3D reconstruction of the lungs of representative mice transplanted with control (untransduced) and mGeCKOa-transduced (mGeCKOa) cell pools. Lung metastases were identified and traced in each 2D section (green). (E) Percent of lobes with metastases visible after dissection under a fluorescence stereoscope in *Nu/Nu* mice transplanted with untransduced Cas9-GFP KPD cells (n = 3 mice) or mGeCKOa-transduced Cas9-GFP KPD cells with three independent infection replicate experiments (1, 2, and 3; n = 3 mice per replicate). Error bars indicate SEM. (F) Representative H&E stains from various organs of *Nu/Nu* mice subcutaneously transplanted with untransduced and mGeCKOa-transduced Cas9-GFP KPD cells. Yellow arrow indicates a lung metastasis. Scale bar, 40 μ m. See also Figure S1.

samples overlap 63%–76% with each other (Figure S3B). Early primary tumors retained less than half (32%–49%) of the sgRNAs found in the transplanted cell populations (Figures 2B, 2C, S3C, and S3D). Compared to the cell populations, sgRNAs whose targets are genes involved in fundamental cellular processes are further depleted in early tumors (Table S1).

Interestingly, only a small fraction of sgRNAs (less than 4% of all sgRNAs, or less than 8% of sgRNAs in the early primary tumor of the corresponding replicate) were detected in the late-stage primary tumor samples (Figures 2B, 2C, S3C, and S3D). The sgRNA diversity (i.e., number of different sgRNAs detected) further decreased in samples from lung metastases (Figures

2B, 2C, S3C, and S3D). The lung samples retained $\leq 0.4\%$ of all sgRNAs in the mGeCKOa library, or $\leq 1.1\%$ of sgRNAs found in the early primary tumor of the corresponding replicate, with a subset of highly enriched sgRNAs (Figures 2B, 2C, S3C, and S3D). The global patterns of sgRNA distributions in different sample types are distinct, as is evident in the strong shifts in the respective cumulative distribution functions (Kolmogorov-Smirnov [KS] test, $p < 10^{-15}$ for all pairwise comparisons) (Figure 2D).

Enriched sgRNAs in Primary Tumors

Late primary tumors retain few sgRNAs (on average 813 ± 264 sgRNAs, n = 9 mice), with even fewer at high frequencies

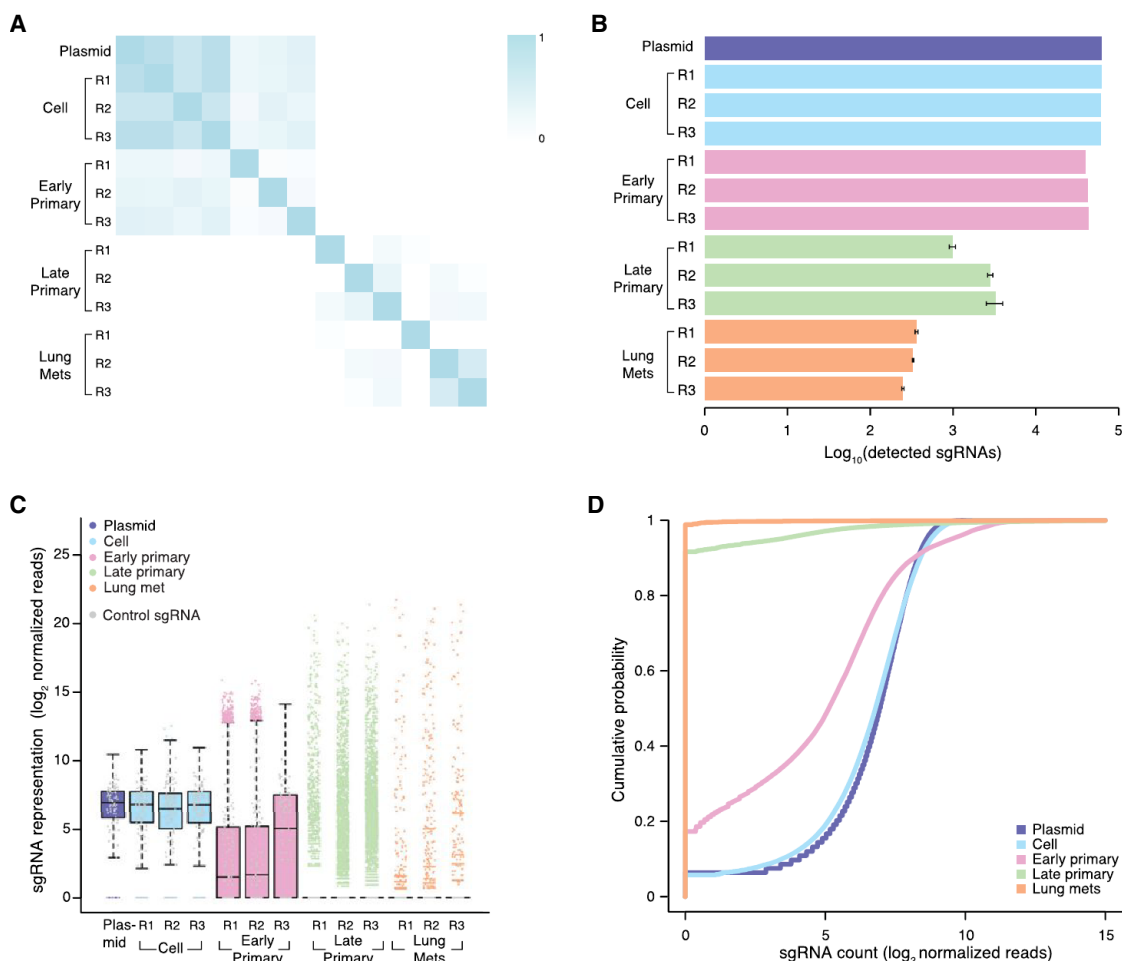


Figure 2. Representation of mGeCKOa Library at Different Stages of Tumor Growth and Metastasis

(A) Pearson correlation coefficient of the normalized sgRNA read counts from the mGeCKOa plasmid library, transduced cells before transplantation (day 7 after spinfection), early primary tumors (~2 weeks after transplantation), late primary tumors (~6 weeks after transplantation), and lung metastases (~6 weeks after transplantation). For each biological sample type, three independent infection replicates (R1, R2, and R3) are shown. $n = 1$ mouse per infection replicate for early primary tumors; $n = 3$ mice per infection replicate for late primary tumors and lung samples.

(B) Number of unique sgRNAs in the plasmid, cells before transplantation, early and late primary tumors, and lung metastases as in (A). Error bars for late primary tumors and lung metastases denote SEM for $n = 3$ mice per infection replicate.

(C) Boxplot of the sgRNA normalized read counts for the mGeCKOa plasmid pool, cells before transplantation, early and late primary tumors, and lung metastases as in (A). Outliers are shown as colored dots for each respective sample. Gray dots overlaid on each boxplot indicate read counts for the 1,000 control (non-targeting) sgRNAs in the mGeCKOa library. Distributions for late primary tumors and lung metastases are averaged across individual mice from the same infection replication.

(D) Cumulative probability distribution of library sgRNAs in the plasmid, cells before transplantation, early and late primary tumors, and lung metastases as in (A). Distributions for each sample type are averaged across individual mice and infection replications.

See also Figures S2 and S3.

(4 ± 1 sgRNAs with $>5\%$ of total reads) in each mouse (Figures 2B, 2C, S2C, S2D, 3A, and S4H). We used three methods to identify enriched sgRNAs in late primary tumors: (1) sgRNAs above a certain threshold, (2) top-ranked sgRNAs in the tumor of each mouse, and (3) using false discovery rate (FDR), i.e., sgRNAs enriched compared to the distribution of the 1,000 non-targeting sgRNAs. All three methods generated similar results (Figure S4A). Taking the results from (3) as an example, a total of 935 sgRNAs (targeting 909 genes) are enriched over the non-targeting controls (FDR cutoff = 0.2%) in the late primary

tumor of one or more mice (Figures 3B and 3C). These sgRNAs are targeting genes highly enriched in apoptosis pathways (Table S2), with many of them being pro-apoptotic, such as BH3 interacting-domain death agonist (*Bid*), phosphatase and tensin homolog (*Pten*), cyclin-dependent kinase inhibitor 2a (*Cdkn2a*), and O-6-methylguanine-DNA methyltransferase (*Mgmt*), suggesting strong selection for mutations that inactivate apoptosis in primary tumor cells.

We identified 24 candidate genes that were targeted by two or more independent sgRNAs enriched in late primary tumors

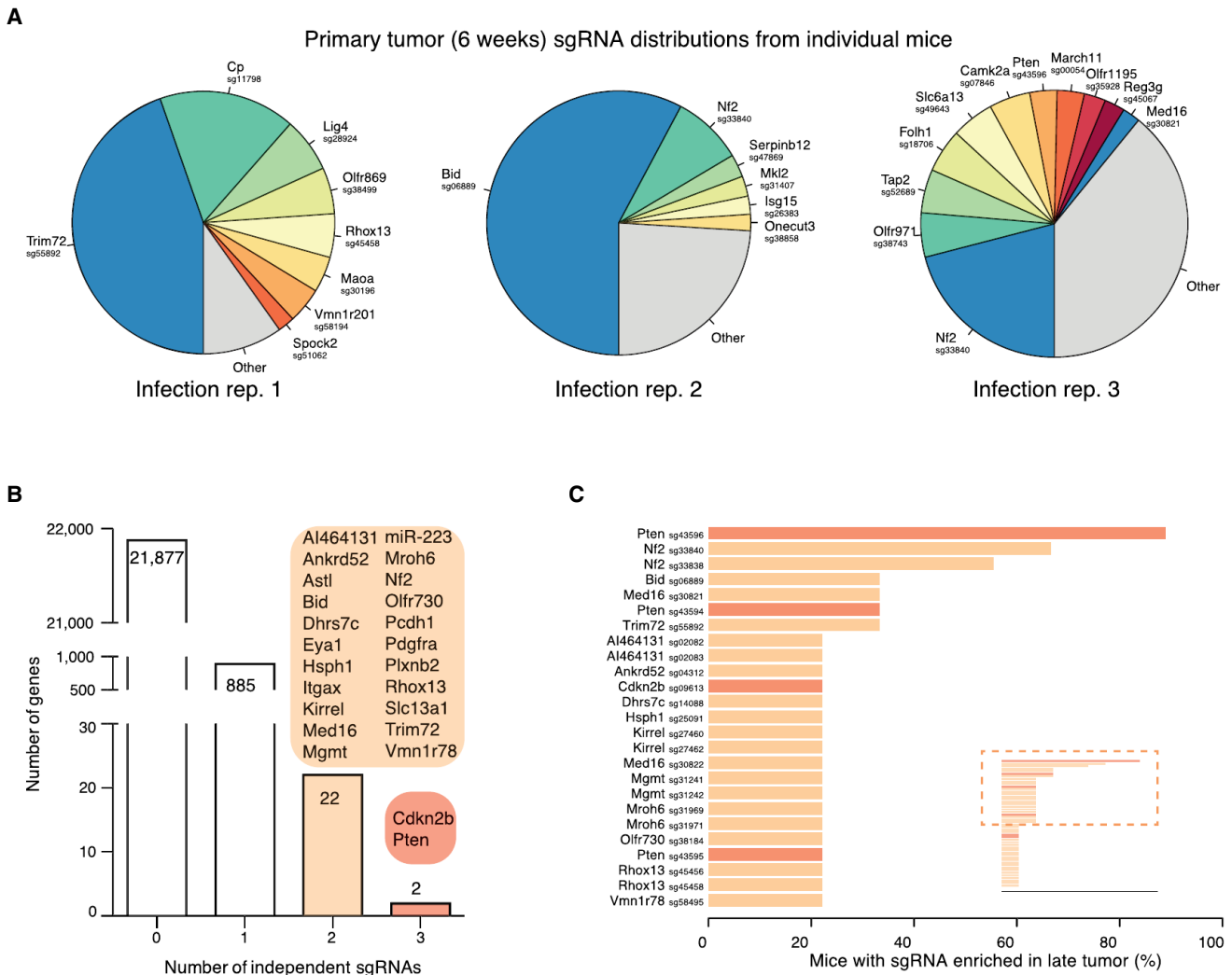


Figure 3. Enriched sgRNAs from the mGeCKOa Screen in Primary Tumors

(A) Pie charts of the most abundant sgRNAs in the primary tumors (at ~6 weeks post-transplantation) of three representative mice (one from each replicate mGeCKOa infection). The area for each sgRNA corresponds to the fraction of total reads from the primary tumor for the sgRNA. All sgRNAs with $\geq 2\%$ of total reads are plotted individually.

(B) Number of genes with 0, 1, 2, or 3 significantly enriched (FDR < 0.2% for at least one mouse) mGeCKOa sgRNAs targeting that gene. For genes/miRs with 2 or more enriched sgRNAs, genes/miRs are categorized by how many sgRNAs targeting that gene/miR are enriched as indicated in the colored bubbles adjacent to each bar.

(C) Inset: waterfall plot of sgRNAs where multiple sgRNAs targeting the same gene are significantly enriched in primary tumors. Each sgRNA is ranked by the percent of mice in which it is enriched. Only sgRNAs enriched in two or more mice are shown in the main panel. Main panel: enlargement and gene labels for sgRNAs at the top of the list from the inset (boxed region).

See also Figures S3, S4, and S5.

(Figures 3B and 3C). These genes were found to be mutated in patients in many previously reported cancer sequencing studies curated by cBioPortal (Cerami et al., 2012; Gao et al., 2013) (Figure S5A). For example, in somatic mutations identified by The Cancer Genome Atlas (TCGA) for NSCLC, including adenocarcinoma (LUAD) (Cancer Genome Atlas Research Network, 2014) and lung squamous cell carcinoma (LUSC) (Cancer Genome Atlas Research Network, 2012), 36% (107/407) of patients have one or more of these 24 genes mutated (Figures S5B and S5C). Several candidates were well-known tumor suppressors,

such as *Pten*, cyclin-dependent kinase inhibitor 2b (*Cdkn2b*), neurofibromin 2 (*Nf2/Merlin*), alpha-type platelet-derived growth factor receptor (*Pdgfra*), and integrin alpha X (*Itgax*).

Enriched sgRNAs in Metastases

We also sequenced the sgRNA distributions from three lung lobes for each mouse transplanted with mGeCKOa-transduced Cas9-GFP KPD cells. In each lobe, the sgRNA representation is dominated by one or a few sgRNAs (Figures 4A, S3D, and S4I). In each mouse, the lung sgRNA representation (average of

normalized sgRNA representations from three lobes) is also dominated by a small number of sgRNAs (on average, 3.4 ± 0.4 sgRNAs with $>5\%$ of total reads) (Figure 4B), suggesting that metastases were seeded by a small set of cells, which grew to dominance over this timescale. Non-targeting sgRNAs were occasionally detected in the metastases but were never observed at high frequency ($<0.1\%$ of total reads in any lobe; Figures 2C, 4A and 4B, and S4I). These observations are consistent with our finding that untransduced tumors are not metastatic (Figure 1E), suggesting that specific sgRNA-mediated mutations led to metastasis.

The sgRNA representations in the lung metastases are similar to those in the late-stage primary tumors in several ways. First, the detected sgRNAs in lung samples overlap significantly with those in late tumor samples (chi-square test, $p < 10^{-15}$) (Figure S3E). Second, the number of sgRNAs detected in lung samples correlates, albeit weakly, with the number of sgRNAs detected in late primary tumor samples ($\rho = 0.42$, F test, $p = 0.097$) (Figure S3F). Third, the abundance (number of reads) of sgRNAs in the lung correlates positively with that in the late primary tumors of the same mouse (correlation, $\rho = 0.18$ on average, F test, $p < 0.01$, $n = 9$) (Figure S3G). Fourth, in most mice (8/9), the lung metastasis enriched sgRNAs also occupy a large fraction of reads in the late primary tumor of the same mouse (Figure 4C, left panel), significantly larger than a random sampling of the same number of sgRNAs from the mGeCKOa library (Figure 4C, right panel). These data indicate that mutants with preferential ability to proliferate in late primary tumors are more likely to dominate the metastases.

The three methods (threshold, rank, or FDR) of finding enriched sgRNAs in the lung metastases yield similar results (Figure S4B). Using the non-targeting sgRNA distribution to set a FDR-based cutoff for enrichment, the enriched sgRNAs in different lobes of the same mouse overlap with each other by $62\% \pm 5\%$ (chi-square test, $p < 10^{-15}$) (Figure S4C), while different mice show greater variability while still overlapping significantly ($29\% \pm 3\%$, chi-square test, $p < 10^{-15}$) (Figure S4D). The overlap between sgRNAs in different biological/infection replicate experiments when pooling enriched sgRNAs from all mice in the same replicate is 54% (chi-square test, $p < 10^{-15}$) (Figure S4E), suggesting that pooling sgRNAs from mice in the same experiment facilitates the identification of shared hits. These data suggest that the three independent experiments reproducibly captured a common set of hits and provide a picture for in vivo experimental variation between different lobes, different animals, and different infection replicates.

We found 147 sgRNAs enriched in more than one lobe, and 105 sgRNAs enriched in the lung of more than one mouse (Figures 4D and 4E). These include sgRNAs targeting *Nf2*, *Pten*, tripartite motif-containing protein 72 (*Trim72*), fibrinogen alpha chain (*Fga*), *Bid*, cyclin-dependent kinase inhibitor 2a (*Cdkn2a*), zinc finger FYVE domain-containing 28 (*Zfyve28*), reproductive homeobox 13 (*Rhox13*), and BRISC and BRCA1 A complex member 1 (*Babam1*), as well as microRNA genes *miR-152* and *miR-345*. Intriguingly, a few sgRNAs targeting the Pol II subunits and olfactory receptor are also enriched in the lung, possibly due to off-target effects or unknown roles of these genes. For most sgRNAs detected in lung metastases, the relative abundance in metastases is lower than that in the late primary tumor of the

same mouse, with a metastasis-primary ratio (MPR) less than 1 (Figure S4F), likely due to more skewed distributions of sgRNAs in the metastases compared to those in the late primary tumors. A small subset of sgRNAs, however, are more abundant in metastases than in primary tumors (MPR > 1) in multiple mice, e.g., sgRNAs targeting *Nf2*, *Trim72*, prostaglandin E synthase 2 (*Ptges2*), or ubiquitin-conjugating enzyme E2G 2 (*Ube2g2*) (Figure 4F).

For four genes, *Nf2*, *Pten*, *Trim72*, and *Zfyve28*, two independent sgRNAs targeting different regions of the same gene were enriched in lung metastases (Figure 4G). One of the *Zfyve28*-targeting sgRNAs, however, is enriched in only one mouse, whereas *Nf2*, *Pten*, and *Trim72* all have two sgRNAs enriched in multiple mice (Figure 4H). These three genes, several representative genes with one frequently enriched sgRNA (*Cdkn2a*, *Fga*, and *Cryba4*), and the two top-scoring microRNAs (*miR-152* and *miR-345*) were chosen to assay individually for primary tumor growth and metastases formation.

Validation In Vivo Using Individual sgRNAs

For these eight genes (*Nf2*, *Pten*, *Trim72*, *Cdkn2a*, *Fga*, *Cryba4*, *miR-152*, and *miR-345*), we cloned multiple sgRNAs targeting each of them into the lentiGuide-Puro vector and transduced them into the Cas9-GFP KPD cell line (Figure 5A) (Experimental Procedures). As expected, these sgRNAs generated a broad distribution of NHEJ-mediated indels at the target site when examined 3 days post-transduction, with a bias toward deletions (Figure 5B). For protein-coding genes, the majority ($>80\%$) of indels are out of frame, which potentially disrupts the protein functions. For *miR-152* and *miR-345*, the sgRNAs generated mostly deletions ($>90\%$ of indels are deletions, average indel size -7 bp) (Figure 5B), overlapping with the loop or mature microRNA sequences in the hairpins, which are structures required for maturation of microRNAs. For proteins where specific antibodies are available (*Nf2* and *Pten*), we found that the majority of the protein products were significantly reduced 1 week after lentiviral sgRNA infection (Figure S6A).

When these single-sgRNA-transduced cells were transplanted into the flanks of immunocompromised mice, they all formed tumors in situ. With two mice injected per sgRNA and three sgRNAs per gene, all genes tested showed increased lung metastasis formation compared to controls (untransduced and non-targeting sgRNAs), with the most significant ones being *Nf2*, *Pten*, and *Cdkn2a* (Fisher's exact test, one-tailed, $p < 10^{-3}$) (Figures 5C and 5D). *Fga* and *Trim72* also have effects on metastasis acceleration (*Fga* $p = 0.001$, *Trim72* $p = 0.046$). *Cryba4* is not statistically different from controls ($p = 0.1$). sgRNAs targeting *miR-345* or *miR-152* significantly increased the rate of metastasis (*miR-345* $p = 0.01$, *miR-152* $p = 0.046$). These data suggest that loss-of-function mutations in any of *Nf2*, *Pten*, *Cdkn2a*, *Trim72*, *Fga*, *miR345*, or *miR-152* are sufficient to accelerate the rate of metastasis formation in this genetic background.

Most genes targeted by single sgRNAs also contributed to accelerated primary tumor growth compared to controls (Figure 5E). *Nf2* and *Pten* loss of function dramatically speed up tumor growth (KS test, $p < 0.001$) (Figure 5E); *Cdkn2a*-, *Trim72*-, and *Fga*-targeting sgRNAs slightly accelerate primary tumor growth (KS test, $p = 0.003$ – 0.01); *Cryba4* has a marginal effect

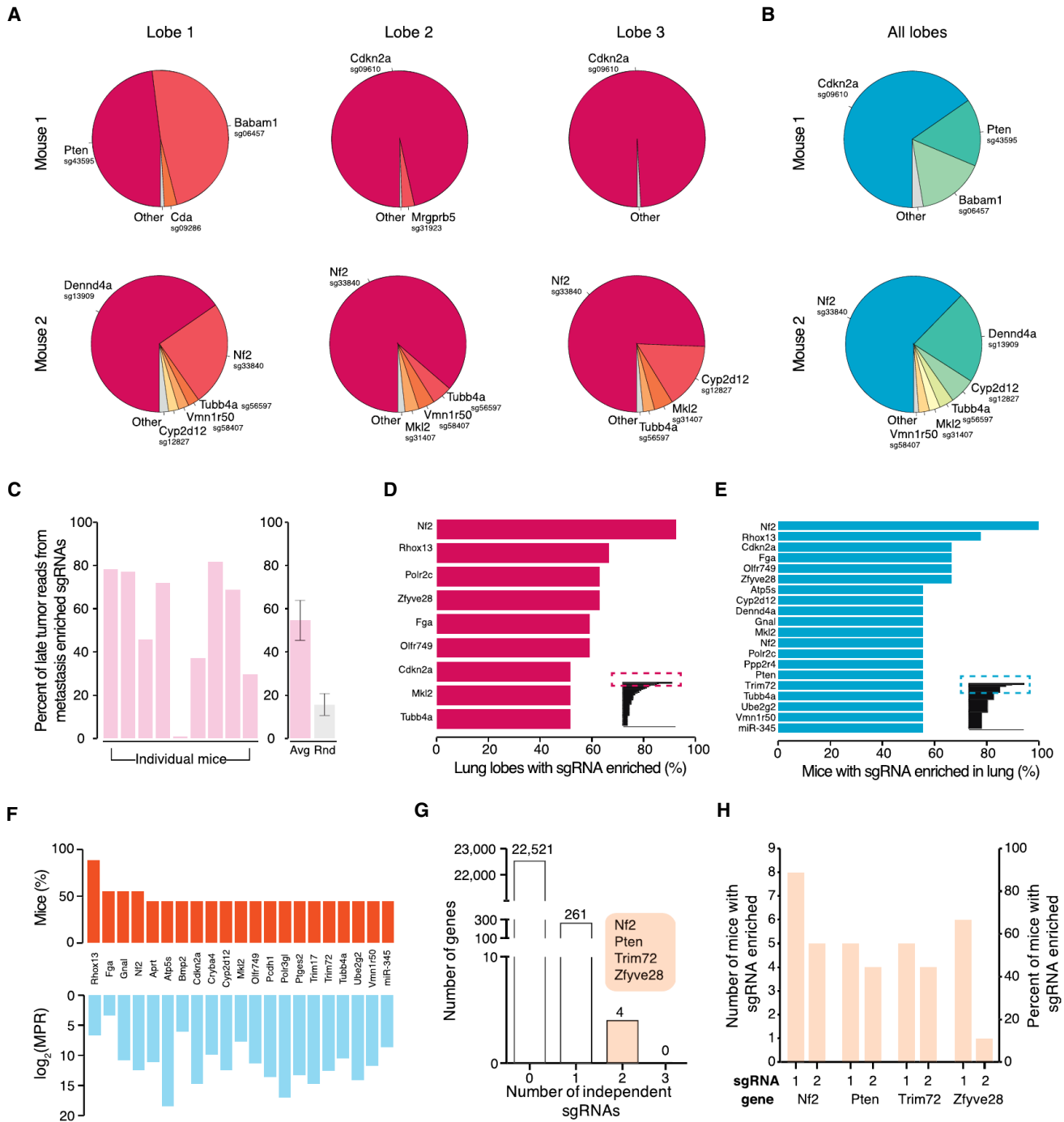


Figure 4. Enriched sgRNAs from the mGeCKOa Screen in Lung Metastases

(A) Pie charts of the most abundant sgRNAs in three individual lobes of the lungs of two representative mice transplanted with mGeCKOa-transduced cells. The area for each sgRNA corresponds to the fraction of total reads from the lobe for the sgRNA. All sgRNAs with $\geq 2\%$ of total reads are plotted individually.

(B) Pie charts of the most abundant sgRNAs in the lung (averaged across three individual lobes) for the two mice shown in (A). All sgRNAs with $\geq 2\%$ of average reads are plotted individually.

(C) Left: percentage of late tumor reads for the significantly enriched ($FDR < 0.2\%$) mGeCKOa sgRNAs found in the lung metastases (averaged across three dissected lobes). Right: in purple, the percentage of late tumor reads for the significantly enriched ($FDR < 0.2\%$) mGeCKOa sgRNAs found in the lung metastases (average across all mice, $n = 9$ mice). In gray, the percentage of late tumor reads for random, size-matched samplings of sgRNAs present in the late tumor ($n = 100$ samplings). Error bars indicate SD.

(legend continued on next page)

(KS test, $p = 0.08$); and neither *miR-152*- nor *miR-345*-targeting sgRNAs promote primary tumor growth (KS test, $p > 0.1$). Overall, for the targets we examined using individual sgRNAs, the number of lobes with lung metastases strongly correlates with the terminal volume of the late primary tumor (or average primary tumor growth rate) (correlation, $\rho = 0.83$, F test, $p < 0.01$) (Figure 5F), indicating at a single-gene level that mutant cells with a stronger ability to promote primary tumor growth generate metastases faster.

To analyze blood samples for the presence of circulating tumor cells (CTCs), we designed a microfluidic device based on the physical size of the Cas9-GFP KPD cells (Figures S6B and S6C). We performed CTC capture with terminal blood samples from mice injected with Cas9-GFP KPD cells transduced with sgRNAs targeting *Nf2*, *Pten*, *Trim72*, *Cdkn2a*, and *miR-152* and from mice injected with Cas9-GFP KPD control cells (untransduced or non-targeting sgRNA) (Figures S6C and S6D). Mice transplanted with cells transduced with sgRNAs targeting *Nf2*, *Pten*, *Trim72*, or *Cdkn2a* had a higher concentration of CTCs as compared to controls (Figures S6D–S6G), consistent with the higher rate of lung metastasis formation.

Competitive Dynamics of Top Hits Assessed Using an sgRNA Minipool

To better understand the relative metastatic potential of multiple genes from our genome-wide screen, we designed a targeted pooled screen with a smaller library. This small library (termed validation minipool) contains 524 sgRNAs targeting 53 genes that had highly enriched sgRNAs in lung metastases in the genome-wide screen (ten sgRNAs per gene for most genes) plus 100 non-targeting sgRNAs. We also created a size-matched library containing 624 non-targeting sgRNAs (termed control minipool) (Figure 6A). Lentiviruses from these two pools were used to transduce the Cas9-GFP KPD cells, which were cultured in vitro for 1 week and then transplanted into *Nu/Nu* mice (Figure 6A). Both validation minipool- and control minipool-transduced cells induced primary tumor growth at a similar rate (Figure 6B). However, mice transplanted with validation minipool cells had a dramatically elevated rate of lung metastasis formation (Figure 6C).

We sequenced the validation minipool plasmid library and the transduced cells pre-transplantation, as well as the late-stage primary tumors and whole lungs of the mice at 5 weeks post-transplantation (see Data S2 in Dataset S1). The sgRNA representations correlate strongly between technical replicates of

the transduced cell pool, late primary tumors, and lung metastases (Figures S7A and S7D). The sgRNA representation in the cell sample strongly correlated with the plasmid (correlation, $\rho = 0.91$) (Figures S7B and S7D). Almost all (99.4%) sgRNAs were recovered in the plasmid and the cell population (Figure S7C). The late primary tumors retained less than half of the sgRNAs, and the metastases in the whole lung retained only a small fraction (2%–7%) of all sgRNAs (Figure S7C). Enriched sgRNAs from lung metastases clustered with each other and with late primary tumors (Figure S7D). Similar to the genome-wide library, in this validation minipool, the plasmid and cell samples had a unimodal distribution of sgRNAs, whereas the late primary tumors and lung metastases contained a bimodal distribution, with the majority of sgRNAs being absent and a small fraction spanning a large range of non-zero read counts (Figure 6D). Intriguingly, two mice retained relatively high sgRNA diversity in late primary tumors (Figure 6D), likely due to dormant or slowly proliferating cells that remained in low numbers during tumor growth. Similar to the genome-wide library, large shifts in the sgRNA distribution exist between different sample types (KS test, $p < 10^{-15}$ for pairwise comparisons between the cell, primary tumor, and lung metastases, $p = 0.02$ between plasmid and cell) (Figure 6E).

In the validation minipool, the sgRNAs detected in the late primary tumors or the lungs of five different mice significantly overlap with each other (Figures S7E and S7F). The late primary tumors and lung metastases are dominated by a few sgRNAs (Figures 7A and S7G–S7I), suggesting that these sgRNAs outcompete others during tumor growth and metastasis. With the validation library, the sgRNA representations are highly correlated between late primary tumors and lung metastases (correlation, $\rho = 0.55$ on average, F test, $p < 0.01$, $n = 5$) (Figure 7B). The late primary tumors and lung metastases have dozens of sgRNAs at moderate to high frequencies (Figures 7B and 7C). Several genes have multiple independent sgRNAs that are enriched in the lung over the primary tumor (MPR > 1), such as *Nf2* (eight sgRNAs), *Pten* (four sgRNAs), *Trim72* (three sgRNAs), *Ube2g2* (three sgRNAs), *Ptges2* (two sgRNAs), and ATP-dependent DNA ligase IV (*Lig4*) (two sgRNAs) (Figures 7C and 7D). Two *Cdkn2a* sgRNAs were present in both late primary tumors and lung metastases in two mice, but with MPR < 1. *Fga*-, *Cryba4*-, *miR-152*-, and *miR-345*-targeting sgRNAs were not found at high frequency in either late primary tumors or lung metastases, suggesting that they are outcompeted by other loss-of-function mutations (such as *Nf2*), which agrees with the relatively reduced metastasis formation of these genes in the

(D) Inset: all sgRNAs found in individual lung lobes, ordered by the percent of lobes in which a particular sgRNA was among the significantly enriched (FDR < 0.2%) sgRNAs for that lobe. Only sgRNAs enriched in two or more lobes are shown. Main panel: enlargement and gene labels for sgRNAs at the top of the list from the inset (boxed region).

(E) Inset: all sgRNAs found in individual mice (averaged across three dissected lobes), ordered by the percent of mice in which a particular sgRNA was among the significantly enriched (FDR < 0.2%) sgRNAs for that mouse. Only sgRNAs enriched in two or more mice are shown. Main panel: enlargement and gene labels for sgRNAs at the top of the list from the inset (boxed region).

(F) Bottom: metastasis primary ratio (MPR) for the sgRNAs in mGeCKOa with enrichment in metastases over late tumors (MPR > 1) observed in at least three mice. The sgRNAs are sorted by the number of mice in which the MPR for the sgRNA is greater than 1. Top: number of mice in which the MPR for this sgRNA is greater than 1. In both panels, individual sgRNAs are labeled by gene target.

(G) Number of genes with 0, 1, 2, or 3 significantly enriched (FDR < 0.2% for at least one mouse) mGeCKOa sgRNAs in the lung metastases. For genes with 2 enriched sgRNAs, gene names are indicated in the colored bubble adjacent to the bar.

(H) Number of mice and percentage of mice in which each sgRNA was enriched in the lung metastases for all genes with multiple enriched sgRNAs. See also Figures S4 and S5.

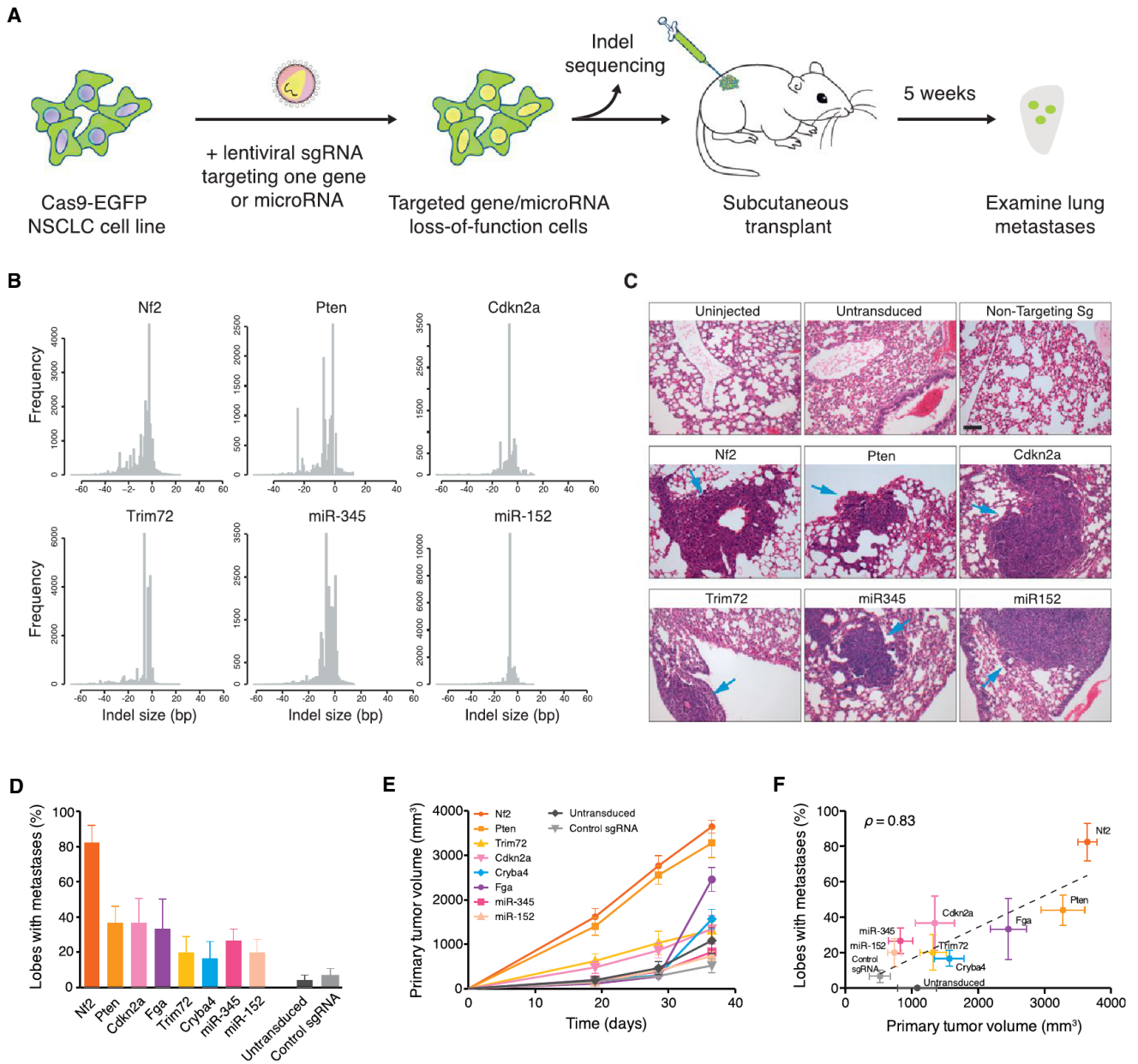


Figure 5. Validation of Target Genes and MicroRNAs from mGeCKOa Screen Using Individual sgRNAs

(A) Schematic representation of lentiviral transduction of Cas9-GFP KPD cells with single sgRNAs designed to target one gene or miR. After puromycin selection, the cell population was transplanted into *Nu/Nu* mice and also deep sequenced to examine the distribution of indels at the target site. After 5 weeks, the primary tumor and lungs were examined.

(B) Histograms of indel sizes at the genomic locus targeted by a representative sgRNA for each gene/miR after 3 days of puromycin selection. Indels from sgRNAs targeting the same gene were pooled (6 sgRNAs for each protein-coding gene; 4 sgRNAs for each miR).

(C) Representative H&E staining of lung lobes from uninjected mice ($n = 3$ mice), mice transplanted with cells transduced with Cas9 only ($n = 5$), and mice transplanted with cells containing Cas9 and a single sgRNA ($n = 6$). Single sgRNAs are either control/non-targeting sgRNAs ($n = 6$ mice for control sgRNAs, 3 distinct control sgRNAs with 2 mice each) or targeting sgRNAs ($n = 6$ mice for each gene/miR target, 3 sgRNAs per target with 2 mice each). Blue arrows indicate lung metastases. Scale bar, 10 μm .

(D) Percent of lung lobes with metastases after 6 weeks for the mice in (C). Error bars indicate SEM.

(E) Primary tumor growth curve of *Nu/Nu* mice transplanted with NSCLC cells transduced with Cas9 only ($n = 5$) or single sgRNAs ($n = 6$ mice per gene/miR target, 3 sgRNAs per target with 2 mice each; $n = 6$ mice for control sgRNAs, 3 control sgRNAs with 2 mice each). Error bars indicate SEM.

(F) Correlation between primary tumor volume and percent of lobes with metastases for each gene in (D) and (E). Error bars indicate SEM.

See also Figure S6.

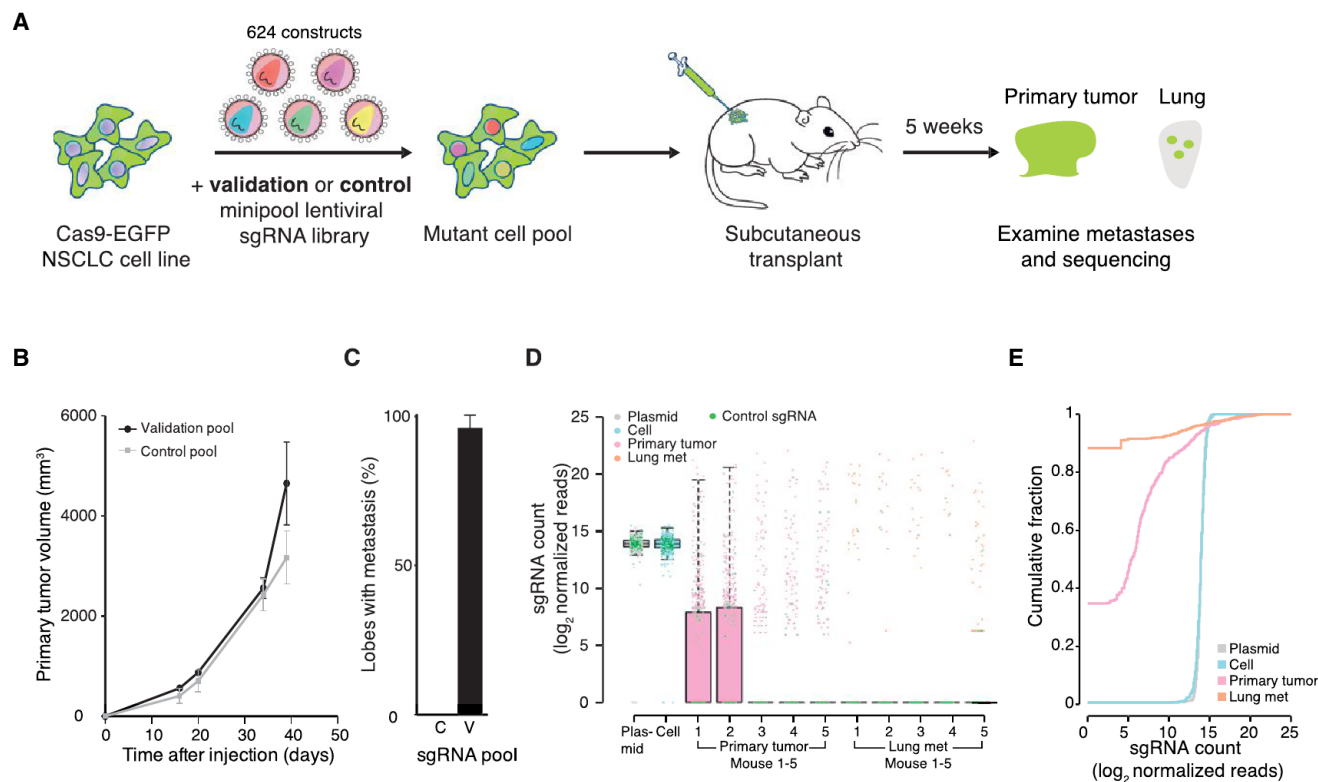


Figure 6. Tumor Evolution and Library Representation in Transplanted Cas9-GFP KPD Cells with Minipool Libraries

(A) Schematic representation of the loss-of-function metastasis minipool screen. Briefly, Cas9-GFP KPD cells were transduced with either validation minipool (524 gene-targeting + 100 non-targeting sgRNAs) or control minipool (624 non-targeting sgRNAs). After puromycin selection, the cell pools were transplanted into *Nu/Nu* mice. After 5 weeks, validation minipool sgRNAs were sequenced from primary tumor and lung samples.

(B) Primary tumor growth curve of *Nu/Nu* mice transplanted with Cas9 vector + validation minipool cells ($n = 5$ mice) or Cas9 + control minipool cells ($n = 5$ mice). Error bars indicate SEM.

(C) Percent of lung lobes with metastases after 6 weeks for the mice in (B). C, control minipool; V, validation minipool. Error bars indicate SEM.

(D) Boxplot of the sgRNA normalized read counts for the plasmid library, cells before transplantation, primary tumors, and lung metastases using the validation minipool.

(E) Cumulative probability distribution of library sgRNAs in the validation plasmid pool, cells before transplantation, primary tumors, and lung metastases. Distributions of primary tumor and lung metastases are averaged across five mice.

See also Figure S7.

individual sgRNA validation. These results further validate several of the top hits from the primary screen, using either sgRNA dominance (e.g., *Nf2*, *Pten*, *Trim72*) or MPR (e.g., *Nf2*, *Trim72*, *Ube2g2*, *Ptges2*). This validation minipool reveals the dynamics of multiple competing mutants chosen from the primary screen hits and indicates that mutants with strong pro-growth effects tend to enhance metastasis (Figure 7E).

TCGA Gene Expression of Screen Hits in Human Lung Cancer

To assess the relevance of our mGeCKOa and validation minipool screen hits (genes targeted by sgRNAs enriched in lung metastases) to pathological metastasis in human cancer, we performed gene expression analysis of the human orthologs of these genes. We compared mRNA levels in metastatic compared to non-metastatic primary tumors in patient samples using TCGA mRNA sequencing data. We found that most (61%–75%) of these genes are downregulated in metastatic tumors in

NSCLC patients (Figures S5D and S5E; Table S6). These data suggest that downregulation of these genes is selected for in metastatic tumors from patients.

DISCUSSION

Pooled Mutagenesis in a Metastasis Model

Distal metastases develop as primary tumors shed CTCs into the circulation, from which CTCs travel to the destination site, move out of the blood or lymphatic vessels, and initiate clonal growth (Valastyan and Weinberg, 2011; Vanharanta and Massagué, 2013; Weinberg, 2007). In this study, cancer cells transplanted into the flanks of mice form primary tumors in situ, and cells from this mass undergo the intravasation-circulation-extravasation-clonal growth cascade to form distal metastases (Francia et al., 2011). The initial lung cancer cell line has little capacity to form metastases; in contrast, after being mutagenized with the mGeCKOa genome-scale Cas9 knockout library, the cell

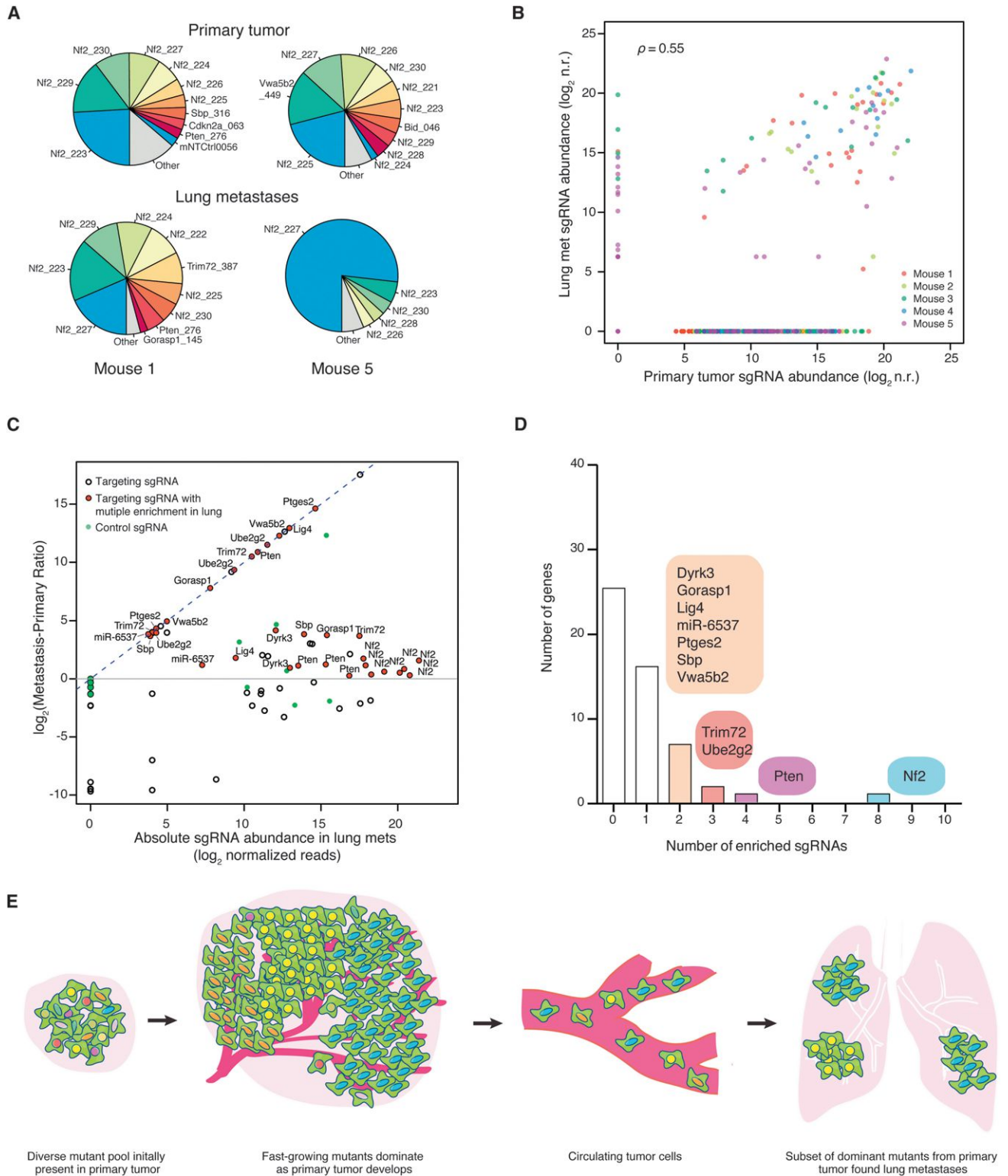


Figure 7. Enriched sgRNAs from the Validation Minipool Screen in Primary Tumors and Lung Metastases

(A) Pie charts of the most abundant sgRNAs in the primary tumor and the whole lung of two representative mice transplanted with validation minipool-transduced Cas9-GFP KPD cells. The area for each sgRNA corresponds to the fraction of total reads from the tissue (primary tumor or lung metastases) for the sgRNA. All sgRNAs with $\geq 2\%$ of total reads are plotted individually.

(legend continued on next page)

population forms highly metastatic tumors. Thus, these mutations, acting in simple or complex pleiotropic ways, accelerate metastasis. In this model, the effect of mutations on metastasis strongly correlates with their abundance in late-stage primary tumors.

sgRNA Dynamics during Tumor Evolution

The dynamics of the sgRNA population changed dramatically over the course of tumor development and metastasis, reflecting the selection and bottlenecks of cellular evolution *in vitro* and *in vivo*. After a week in culture, cells retained most of the sgRNAs present in the plasmid library, with decreases in sgRNAs targeting genes involved in fundamental cellular processes. The distribution of non-targeting control sgRNAs is almost identical to those targeting genes, suggesting that the selective pressure of *in vitro* culture alone does not radically alter sgRNA representation, similar to previous observations in human melanoma cells (Shalem et al., 2014).

In contrast, less than half of the sgRNAs survive in an early-stage primary tumor. This loss of representation occurs with both gene-targeting sgRNAs and non-targeting control sgRNAs, suggesting that random sampling influences sgRNA dynamics during the transplantation and tumor initiation processes, although we cannot exclude that some of the non-targeting sgRNAs might have detrimental or pro-growth effects. We also detected further dropout of genes involved in fundamental cellular processes in early tumor samples compared to cell samples. Thus, it is likely that the sgRNA dynamics are influenced by a combination of selection and random sampling during transplantation and tumor initiation.

As primary tumors grow, the mutant cells proliferate and compete as a pool. This creates strong selection for sgRNAs targeting anti-apoptotic genes and other tumor suppressors. The majority of the genetic diversity in early tumors is lost during the subsequent 4 weeks of primary tumor growth in mice. Accordingly, sequencing revealed a smaller set of dominant sgRNAs, usually on the order of hundreds to a few thousand per mouse. In addition, almost all of non-targeting sgRNAs are lost during primary tumor growth, which is consistent with selection for cells with special growth and survival properties. This observation is also consistent with earlier transplantation studies by Kerbel and colleagues using small pools of randomly mutagenized cells, which found that the majority of clonal variants detectable by Southern blot disappeared within 6 weeks of primary tumor growth, leaving one dominant clone (Korcak et al., 1988; Waghorne et al., 1988).

Each step toward metastasis has a bottleneck effect. In the lung metastases, we detected very few sgRNAs at high abun-

dance. As with the primary tumor, we found only a few non-targeting sgRNAs at low frequencies in metastases. Their presence could be due to unknown off-target effects of these sgRNAs, random shedding of CTCs in the primary tumor, or clustering together with other strongly selected CTCs during metastasis (Aceto et al., 2014).

Relevance of Screen Hits to Human Cancer

Several of the genes enriched in late-stage primary tumors are associated with cancer, but their functions in tumor growth are poorly understood. For example, *Mgmt*, a gene with two enriched sgRNAs, is required for DNA repair and is thus crucial for genome stability (Tano et al., 1990). Mutation, silencing, or promoter methylation of *MGMT* is associated with primary glioblastomas (Jesien-Lewandowicz et al., 2009). *Med16*, another gene with two enriched sgRNAs, encodes a subunit of the mediator complex of transcription regulation, which has been recently implicated in cancer (Huang et al., 2012; Schiano et al., 2014).

We found that the genes that are significantly enriched in lung metastases largely overlap with those found in abundance in the late primary tumor. Several of these hits were validated *in vivo* using multiple individual sgRNAs, including *Nf2*, *Pten*, *Cdkn2a*, *Trim72*, *Fga*, *miR-152*, and *miR-345*. *Nf2*, *Pten*, and *Cdkn2a* are well-known tumor suppressor genes. Intriguingly, the *NF2* locus is mutated at only 1% frequency in primary tumors of human NSCLC patients (LUAD and/or LUSC) (Cancer Genome Atlas Research Network, 2012, 2014). *Nf2* mutant mice develop a range of highly metastatic tumors (McClatchey et al., 1998). It is possible that *NF2* mutations influence metastases to a greater degree than primary tumor growth, but this awaits metastasis genomics from patient samples. *Pten* mutations are also associated with advanced stages of tumor progression in a mouse model of lung cancer (McFadden et al., 2014), and *PTEN* was found to be mutated at 8% in adenocarcinoma patients (LUAD). *CDKN2A* has been shown to be often inactivated in lung cancer (Kaczmarczyk et al., 2012; Yokota et al., 2003). *Fga* encodes fibrinogen, an extracellular matrix protein involved in blood clot formation. *Fga* mutations have been found in various cancer types in TCGA (Lawrence et al. 2013), as well as circulating tumor cells (Lohr et al., 2014). *Trim72* is an E3 ubiquitin ligase, and its role in cancer metastasis is largely unknown. Studies have shown that *miR-152* and *miR-345* are associated with cancer and metastasis (Cheng et al., 2014; Tang et al., 2011). *FGF2* and *BAG3*, which promote metastasis, were predicted targets of *miR-152* and *miR-345*; thus, loss of these

(B) Scatterplot of normalized sgRNA read counts in primary tumor and lung metastases for all sgRNAs in the validation minipool for each mouse (different color dots indicate sgRNAs from different mice). \log_2 n.r., \log_2 normalized reads.

(C) \log_2 ratio of sgRNA abundance in the lung metastases over the primary tumor (MPR) plotted against the abundance in the lung metastases ($n = 5$ mice per sgRNA). Green dots are the 100 control sgRNAs. Dots with black outlines are non-control sgRNAs that target genes or miRs. Red dots indicate non-control sgRNAs for which more than one sgRNA targeting the same gene/miR is enriched in the lung metastases over the primary tumor (i.e., $\log_2(\text{MPR}) > 0$) and are labeled with the gene/miR targeted. The lung-primary ratio is calculated for individual mice, and these quantities are averaged across mice.

(D) Number of genes with 0 to 10 significantly enriched validation minipool sgRNAs in lung metastases. For genes/miRs with 2 or more enriched sgRNAs, genes/miRs are categorized by how many sgRNAs targeting that gene/miRs are enriched, as indicated in the colored bubbles adjacent to each bar.

(E) Schematic illustration of tumor growth and metastasis in the library-transduced NSCLC transplant model. The initially diverse set of loss-of-function mutations in the subcutaneously transplanted pool is selected over time for mutations that promote growth of the primary tumor. A subset of these mutants also dominate lung metastases.

See also Figure S7.

microRNAs may lead to acceleration of metastases, likely due to de-repression of these genes (Cheng et al., 2014; Tang et al., 2011).

In our own analysis of TCGA samples from lung cancer patients, we observed downregulation of the human orthologs of the genes identified in the genome-wide and validation minipool screens at the mRNA level in metastatic tumors compared to non-metastatic tumors, suggesting that these genes may also be inactivated during pathological metastasis. Human orthologs of these genes are often found to be mutated in cancers. Moreover, these genes have been implicated in various pathways and biological processes in tumorigenesis and/or metastasis in human cancer (Tables S7A–S7C). However, most cancer sequencing studies involve samples from primary tumors of patients. In the clinic, metastases are rarely sampled. Future patient sequencing directly from metastases may further connect genes identified in the mouse model to those mutated or silenced in clinical metastases.

Future In Vivo Functional Genomic Screens

Our study provides a roadmap for in vivo Cas9 screens, and future studies can take advantage of this model to explore other oncogenotypes, delivery methods, or metastasis target organs. Genome-scale CRISPR screening is feasible using a transplant model with virtually any cell line or genetic background (e.g., mutations in *EGFR*, *KRAS*, *ALK*, etc.), including a large repertoire of human cell lines from diverse cancer types (Barretina et al., 2012). Other cell delivery methods, such as intravenous injection or orthotopic transplantation, may help identify genes regulating extravasation and clonalization. Examining samples from other stages or sites, such as CTCs or metastases to other organs, can provide a more refined picture of tumor evolution.

In addition to these parameters, several aspects of the screen perturbations themselves can also be modified. Targeted drug therapies or immunotherapies can be applied in conjunction with the in vivo screening strategy to identify genes involved in acquired resistance. Other screening technologies, such as Cas9-mediated activation (Gilbert et al., 2014; Konermann et al., 2015), can identify metastasis-regulating factors that act in a gain-of-function manner. Activation screens that identify oncogenes, as well as dropout screens that identify genetic dependencies, may facilitate identification of novel therapeutic targets. Targeted subpool strategies can be used to reduce the library size and facilitate further confirmation of primary screens. In a customized library, genes can be chosen based on genomic analysis, pathways, or clinical relevance for focused screening libraries. Additionally, application of pooled sgRNA libraries using individually barcoded cells will allow quantitative assessment of the robustness and significance of each candidate hit and will enable analysis of the competitive dynamics among different perturbations. With these promising future directions and the results of our study, Cas9-based in vivo screening establishes a new platform for functional genomics discovery.

EXPERIMENTAL PROCEDURES

Generation of Cas9-GFP Expression Vector

A lentiviral vector, lenti-Cas9-NLS-FLAG-2A-EGFP (lentiCas9-EGFP), was generated by subcloning Cas9 into a lentiviral vector.

Pooled Guide-Only Library Cloning and Viral Production

The Cas9-GFP KPD cell line was transduced at a MOI of ~ 0.4 with lentivirus produced from a genome-wide lentiviral mouse CRISPR knockout guide-only library (Sanjana et al., 2014) containing 67,405 sgRNAs (mGeCKOa, Addgene 1000000053) with at least 400-fold representation (cells per construct) in each infection replicate. A detailed viral production and infection protocol can be found in Extended Experimental Procedures.

Animal Work Statement

All animal work was performed under the guidelines of the MIT Division of Comparative Medicine, with protocols (0411-040-14, 0414-024-17, 0911-098-11, 0911-098-14, and 0914-091-17) approved by the MIT Committee for Animal Care, and were consistent with the Guide for the Care and Use of Laboratory Animals, National Research Council, 1996 (institutional animal welfare assurance no. A-3125-01).

Mice, Tumor Transplant, and Metastasis Analysis in the Primary Screen

Untransduced or mGeCKOa-transduced Cas9-GFP KPD cells were injected subcutaneously into the right side flank of *Nu/Nu* mice at 3×10^7 cells per mouse. Transplanted primary tumor sizes were measured by caliper. At 6 weeks post-transplantation, mice were sacrificed and several organs (liver, lung, kidney, and spleen) were dissected for examination of metastases under a fluorescence stereoscope.

Mouse Tissue Collection

Primary tumors and other organs were dissected manually. For molecular biology, tissues were flash frozen with liquid nitrogen and ground in 24-well polyethylene vials with metal beads in a GenoGrinder machine (OPS Diagnostics). Homogenized tissues were used for DNA/RNA/protein extractions using standard molecular biology protocols. Tissues for histology were then fixed in 4% formaldehyde or 10% formalin overnight, embedded in paraffin, and sectioned at 6 μ m with a microtome as described previously (Chen et al., 2014). Slices were subjected to H&E staining as described previously (Chen et al., 2014).

Genomic DNA Extraction from Cells and Mouse Tissues

Genomic DNA from cells and tissues (primary tumors and lungs) was extracted using a homemade modified salt precipitation method similar to the Puregene (QIAGEN/Gentra) procedure. The sgRNA cassette was amplified and prepared for Illumina sequencing as described previously (Shalem et al., 2014). A detailed readout protocol can be found in Extended Experimental Procedures.

Individual Gene and MicroRNA Validation

Six sgRNAs per protein-coding gene and four sgRNAs per microRNA gene were chosen for validation using individual sgRNAs (Table S4). For protein-coding genes, we cloned both the three sgRNAs from the mGeCKOa library and three additional sgRNAs to target each gene. For microRNAs, we used all four sgRNAs from the mGeCKOa library.

Validation and Control Minipool Synthesis and In Vivo Transplantation

Validation and control minipools (Table S5) were synthesized using array oligonucleotide synthesis (CustomArray) and transduced at $>1,000$ -fold representation in Cas9-GFP KPD cells. After 7 days in culture, Cas9-GFP KPD cells transduced with the validation minipool or control minipool were injected subcutaneously into the right side flank of *Nu/Nu* mice at 3×10^7 cells per mouse with five replicate mice. After 5 weeks, mice were sacrificed, and primary tumors and lungs were dissected.

ACCESSION NUMBERS

Genomic sequencing data have been deposited in the NCBI Sequence Read Archive under accession number PRJNA273894. Plasmids and pooled libraries have been deposited in Addgene (LentiCas9-EGFP: 63592, Metastasis Validation Minipool library: 63594, Mouse Non-targeting Control Minipool: 63595).

SUPPLEMENTAL INFORMATION

Supplemental Information includes Extended Experimental Procedures, seven figures, seven tables, and a dataset and can be found with this article online at <http://dx.doi.org/10.1016/j.cell.2015.02.038>.

AUTHOR CONTRIBUTIONS

S.C., N.E.S., O.S., F.Z., and P.A.S. conceived and designed the study. S.C., N.E.S., and K.Z. performed all screening and validation experiments. S.C., N.E.S., O.S., and D.A.S. analyzed the data. K.L., J.S., R.W., and H.L. designed the CTC chip and performed CTC analysis. X.S. and J.Q.P. performed western blots. S.C., N.E.S., F.Z., and P.A.S. wrote the manuscript with the input from all authors. P.A.S. and F.Z. supervised the work.

ACKNOWLEDGMENTS

We thank R. Weinberg and R. Kerbel for critically reading the manuscript; the entire P.A.S. lab and F.Z. lab, L. Cong, T. Kelly, X. Ni, M. Nobel, J. Boehm, A. Tsherniak, S. Levine, M. Cornwall-Brady, S. Malstrom, M. Jennings, E. Vasile, C. Whittaker, K. Cormier, R. Bronson, and colleagues at the Koch Institute, Broad Institute, McGovern Institute, and Department of Biology for technical assistance and/or discussion; the Swanson Biotechnology Center for technical support (Genomics, Animal Imaging and Preclinical Testing, Bioinformatics and Computing, Microscopy, Flow Cytometry, Microscopy, and Histology, in particular). This work is supported by grants to P.A.S., including a United States Public Health Service grant R01-CA133404 from the NIH, an MIT-Harvard Center for Cancer Nanotechnology Excellence Grant U54 CA151884 from the National Cancer Institute, a generous gift from the Marie D. and Pierre Casimir-Lambert Fund, an SKTech/MIT Initiative Grant from the Skolkovo Foundation, and the Koch Institute Support (core) grant P30-CA14051 from the National Cancer Institute. F.Z. is supported by the NIH through NIMH grant 5DP1-MH100706 and NIDDK grant 5R01-DK097768; a Waterman Award from the National Science Foundation; the Keck, New York Stem Cell, Damon Runyon, Searle Scholars, Merkin, and Vallee foundations; and Bob Metcalfe. F.Z. is a New York Stem Cell Foundation Robertson Investigator. S.C. is a Damon Runyon Cancer Research Fellow (DRG-2117-12) and also supported by the Dale Frey Award for Breakthrough Scientists. N.E.S. is supported by a Simons Center for the Social Brain Postdoctoral Fellowship and NIH NHGRI award K99-HG008171. O.S. is a fellow of the Klarman Cell Observatory. R.W. is supported by NIH grant U54 CA151884. D.A.S. is supported by a NSF Graduate Research Fellowship. H.L. is supported by Department of Defense grant OCRP W81XWH-14-1-0279. CRISPR reagents (plasmids and libraries) are available to the academic community through Addgene. F.Z. is a co-founder of Editas Medicine and a scientific advisor for Editas Medicine and Horizon Discovery.

Received: December 30, 2014

Revised: February 3, 2015

Accepted: February 18, 2015

Published: March 5, 2015

REFERENCES

Aceto, N., Bardia, A., Miyamoto, D.T., Donaldson, M.C., Wittner, B.S., Spencer, J.A., Yu, M., Pely, A., Engstrom, A., Zhu, H., et al. (2014). Circulating tumor cell clusters are oligoclonal precursors of breast cancer metastasis. *Cell* **158**, 1110–1122.

Barrangou, R., Fremaux, C., Deveau, H., Richards, M., Boyaval, P., Moineau, S., Romero, D.A., and Horvath, P. (2007). CRISPR provides acquired resistance against viruses in prokaryotes. *Science* **315**, 1709–1712.

Barretina, J., Caponigro, G., Stransky, N., Venkatesan, K., Margolin, A.A., Kim, S., Wilson, C.J., Lehár, J., Kryukov, G.V., Sonkin, D., et al. (2012). The Cancer Cell Line Encyclopedia enables predictive modelling of anticancer drug sensitivity. *Nature* **483**, 603–607.

Bolotin, A., Quinquis, B., Sorokin, A., and Ehrlich, S.D. (2005). Clustered regularly interspaced short palindrome repeats (CRISPRs) have spacers of extrachromosomal origin. *Microbiology* **151**, 2551–2561.

Cancer Genome Atlas Research Network (2012). Comprehensive genomic characterization of squamous cell lung cancers. *Nature* **489**, 519–525.

Cancer Genome Atlas Research Network (2014). Comprehensive molecular profiling of lung adenocarcinoma. *Nature* **511**, 543–550.

Cerami, E., Gao, J., Dogrusoz, U., Gross, B.E., Sumer, S.O., Aksoy, B.A., Jacobsen, A., Byrne, C.J., Heuer, M.L., Larsson, E., et al. (2012). The cBio cancer genomics portal: an open platform for exploring multidimensional cancer genomics data. *Cancer Discovery* **2**, 401–404.

Chen, S., Xue, Y., Wu, X., Le, C., Bhutkar, A., Bell, E.L., Zhang, F., Langer, R., and Sharp, P.A. (2014). Global microRNA depletion suppresses tumor angiogenesis. *Genes Dev.* **28**, 1054–1067.

Cheng, Z., Ma, R., Tan, W., and Zhang, L. (2014). MiR-152 suppresses the proliferation and invasion of NSCLC cells by inhibiting FGF2. *Exp. Mol. Med.* **46**, e112.

Chylinski, K., Le Rhun, A., and Charpentier, E. (2013). The tracrRNA and Cas9 families of type II CRISPR-Cas immunity systems. *RNA Biol.* **10**, 726–737.

Chylinski, K., Makarova, K.S., Charpentier, E., and Koonin, E.V. (2014). Classification and evolution of type II CRISPR-Cas systems. *Nucleic Acids Res.* **42**, 6091–6105.

Cong, L., Ran, F.A., Cox, D., Lin, S., Barretto, R., Habib, N., Hsu, P.D., Wu, X., Jiang, W., Marraffini, L.A., and Zhang, F. (2013). Multiplex genome engineering using CRISPR/Cas systems. *Science* **339**, 819–823.

Deltcheva, E., Chylinski, K., Sharma, C.M., Gonzales, K., Chao, Y., Pirzada, Z.A., Eckert, M.R., Vogel, J., and Charpentier, E. (2011). CRISPR RNA maturation by trans-encoded small RNA and host factor RNase III. *Nature* **471**, 602–607.

Francia, G., Cruz-Munoz, W., Man, S., Xu, P., and Kerbel, R.S. (2011). Mouse models of advanced spontaneous metastasis for experimental therapeutics. *Nat. Rev. Cancer* **11**, 135–141.

Gao, J., Aksoy, B.A., Dogrusoz, U., Dresdner, G., Gross, B., Sumer, S.O., Sun, Y., Jacobsen, A., Sinha, R., Larsson, E., et al. (2013). Integrative analysis of complex cancer genomics and clinical profiles using the cBioPortal. *Sci. Signal.* **6**, p11.

Garneau, J.E., Dupuis, M.E., Villion, M., Romero, D.A., Barrangou, R., Boyaval, P., Fremaux, C., Horvath, P., Magadán, A.H., and Moineau, S. (2010). The CRISPR/Cas bacterial immune system cleaves bacteriophage and plasmid DNA. *Nature* **468**, 67–71.

Garraway, L.A., and Lander, E.S. (2013). Lessons from the cancer genome. *Cell* **153**, 17–37.

Gasiunas, G., Barrangou, R., Horvath, P., and Siksnys, V. (2012). Cas9-crRNA ribonucleoprotein complex mediates specific DNA cleavage for adaptive immunity in bacteria. *Proc. Natl. Acad. Sci. USA* **109**, E2579–E2586.

Gilbert, L.A., Horlbeck, M.A., Adamson, B., Villalta, J.E., Chen, Y., Whitehead, E.H., Guimaraes, C., Panning, B., Ploegh, H.L., Bassik, M.C., et al. (2014). Genome-scale CRISPR-mediated control of gene repression and activation. *Cell* **159**, 647–661.

Hanahan, D., and Weinberg, R.A. (2011). Hallmarks of cancer: the next generation. *Cell* **144**, 646–674.

Heimann, R., and Hellman, S. (1998). Aging, progression, and phenotype in breast cancer. *J. Clin. Oncol.* **16**, 2686–2692.

Hsu, P.D., Scott, D.A., Weinstein, J.A., Ran, F.A., Konermann, S., Agarwala, V., Li, Y., Fine, E.J., Wu, X., Shalem, O., et al. (2013). DNA targeting specificity of RNA-guided Cas9 nucleases. *Nat. Biotechnol.* **31**, 827–832.

Huang, S., Hölzel, M., Knijnenburg, T., Schlicker, A., Roepman, P., McDermott, U., Garnett, M., Grenrum, W., Sun, C., Prahallad, A., et al. (2012). MED12 controls the response to multiple cancer drugs through regulation of TGF- β receptor signaling. *Cell* **151**, 937–950.

Jesien-Lewandowicz, E., Jesionek-Kupnicka, D., Zawlik, I., Szybka, M., Kulczycka-Wojdala, D., Rieske, P., Sieruta, M., Jaskolski, D., Och, W., Skowronski,

- W., et al. (2009). High incidence of MGMT promoter methylation in primary glioblastomas without correlation with TP53 gene mutations. *Cancer Genet. Cytogenet.* *188*, 77–82.
- Jinek, M., Chylinski, K., Fonfara, I., Hauer, M., Doudna, J.A., and Charpentier, E. (2012). A programmable dual-RNA-guided DNA endonuclease in adaptive bacterial immunity. *Science* *337*, 816–821.
- Kaczmarczyk, G., Lewandowski, R., Trautsolt, W., Ziótkowski, A., and Kozielski, J. (2012). Cytological examination of pleural cavity lavage accompanied by the study of gene promoter hypermethylation of p16 and O6-methylguanine-DNA-methyltransferase genes in diagnostics of non-small cell lung cancer metastatic changes into pleura. *Contemp Oncol (Pozn)* *16*, 322–327.
- Koike-Yusa, H., Li, Y., Tan, E.P., Velasco-Herrera, Mdel.C., and Yusa, K. (2014). Genome-wide recessive genetic screening in mammalian cells with a lentiviral CRISPR-guide RNA library. *Nat. Biotechnol.* *32*, 267–273.
- Konermann, S., Brigham, M.D., Trevino, A.E., Joung, J., Abudayyeh, O.O., Barcena, C., Hsu, P.D., Habib, N., Gootenberg, J.S., Nishimasu, H., et al. (2015). Genome-scale transcriptional activation by an engineered CRISPR-Cas9 complex. *Nature* *517*, 583–588.
- Korczak, B., Robson, I.B., Lamarche, C., Bernstein, A., and Kerbel, R.S. (1988). Genetic tagging of tumor cells with retrovirus vectors: clonal analysis of tumor growth and metastasis in vivo. *Mol. Cell. Biol.* *8*, 3143–3149.
- Kumar, M.S., Pester, R.E., Chen, C.Y., Lane, K., Chin, C., Lu, J., Kirsch, D.G., Golub, T.R., and Jacks, T. (2009). Dicer1 functions as a haploinsufficient tumor suppressor. *Genes Dev.* *23*, 2700–2704.
- Lawrence, M.S., Stojanov, P., Polak, P., Kryukov, G.V., Cibulskis, K., Sivachenko, A., Carter, S.L., Stewart, C., Mermel, C.H., Roberts, S.A., et al. (2013). Mutational heterogeneity in cancer and the search for new cancer-associated genes. *Nature* *499*, 214–218.
- Lohr, J.G., Adalsteinsson, V.A., Cibulskis, K., Choudhury, A.D., Rosenberg, M., Cruz-Gordillo, P., Francis, J.M., Zhang, C.Z., Shalek, A.K., Satija, R., et al. (2014). Whole-exome sequencing of circulating tumor cells provides a window into metastatic prostate cancer. *Nat. Biotechnol.* *32*, 479–484.
- Mali, P., Yang, L., Esvelt, K.M., Aach, J., Guell, M., DiCarlo, J.E., Norville, J.E., and Church, G.M. (2013). RNA-guided human genome engineering via Cas9. *Science* *339*, 823–826.
- McClatchey, A.I., Saotome, I., Mercer, K., Crowley, D., Gusella, J.F., Bronson, R.T., and Jacks, T. (1998). Mice heterozygous for a mutation at the Nf2 tumor suppressor locus develop a range of highly metastatic tumors. *Genes Dev.* *12*, 1121–1133.
- McFadden, D.G., Papagiannakopoulos, T., Taylor-Weiner, A., Stewart, C., Carter, S.L., Cibulskis, K., Bhutkar, A., McKenna, A., Dooley, A., Vernon, A., et al. (2014). Genetic and clonal dissection of murine small cell lung carcinoma progression by genome sequencing. *Cell* *156*, 1298–1311.
- Nguyen, D.X., Bos, P.D., and Massagué, J. (2009). Metastasis: from dissemination to organ-specific colonization. *Nat. Rev. Cancer* *9*, 274–284.
- Rouet, P., Smih, F., and Jasin, M. (1994). Introduction of double-strand breaks into the genome of mouse cells by expression of a rare-cutting endonuclease. *Mol. Cell. Biol.* *14*, 8096–8106.
- Sanjana, N.E., Shalem, O., and Zhang, F. (2014). Improved vectors and genome-wide libraries for CRISPR screening. *Nat. Methods* *11*, 783–784.
- Sapranauskas, R., Gasiunas, G., Fremaux, C., Barrangou, R., Horvath, P., and Siksnys, V. (2011). The *Streptococcus thermophilus* CRISPR/Cas system provides immunity in *Escherichia coli*. *Nucleic Acids Res.* *39*, 9275–9282.
- Schiano, C., Casamassimi, A., Rienzo, M., de Nigris, F., Sommese, L., and Napoli, C. (2014). Involvement of Mediator complex in malignancy. *Biochim. Biophys. Acta* *1845*, 66–83.
- Schramek, D., Sendoel, A., Segal, J.P., Beronja, S., Heller, E., Oristian, D., Reva, B., and Fuchs, E. (2014). Direct in vivo RNAi screen unveils myosin IIa as a tumor suppressor of squamous cell carcinomas. *Science* *343*, 309–313.
- Shalem, O., Sanjana, N.E., Hartenian, E., Shi, X., Scott, D.A., Mikkelsen, T.S., Heckl, D., Ebert, B.L., Root, D.E., Doench, J.G., and Zhang, F. (2014). Genome-scale CRISPR-Cas9 knockout screening in human cells. *Science* *343*, 84–87.
- Shao, D.D., Xue, W., Krall, E.B., Bhutkar, A., Piccioni, F., Wang, X., Schinzel, A.C., Sood, S., Rosenbluh, J., Kim, J.W., et al. (2014). KRAS and YAP1 converge to regulate EMT and tumor survival. *Cell* *158*, 171–184.
- Tang, J.T., Wang, J.L., Du, W., Hong, J., Zhao, S.L., Wang, Y.C., Xiong, H., Chen, H.M., and Fang, J.Y. (2011). MicroRNA 345, a methylation-sensitive microRNA is involved in cell proliferation and invasion in human colorectal cancer. *Carcinogenesis* *32*, 1207–1215.
- Tano, K., Shiota, S., Collier, J., Foote, R.S., and Mitra, S. (1990). Isolation and structural characterization of a cDNA clone encoding the human DNA repair protein for O6-alkylguanine. *Proc. Natl. Acad. Sci. USA* *87*, 686–690.
- Valastyan, S., and Weinberg, R.A. (2011). Tumor metastasis: molecular insights and evolving paradigms. *Cell* *147*, 275–292.
- Vanharanta, S., and Massagué, J. (2013). Origins of metastatic traits. *Cancer Cell* *24*, 410–421.
- Waghorne, C., Thomas, M., Lagarde, A., Kerbel, R.S., and Breitman, M.L. (1988). Genetic evidence for progressive selection and overgrowth of primary tumors by metastatic cell subpopulations. *Cancer Res.* *48*, 6109–6114.
- Wang, T., Wei, J.J., Sabatini, D.M., and Lander, E.S. (2014). Genetic screens in human cells using the CRISPR-Cas9 system. *Science* *343*, 80–84.
- Weinberg, R.A. (2007). *The Biology of Cancer* (Garland Science).
- Yokota, J., Nishioka, M., Tani, M., and Kohno, T. (2003). Genetic alterations responsible for metastatic phenotypes of lung cancer cells. *Clin. Exp. Metastasis* *20*, 189–193.
- Zender, L., Xue, W., Zuber, J., Semighini, C.P., Krasnitz, A., Ma, B., Zender, P., Kubicka, S., Luk, J.M., Schirmacher, P., et al. (2008). An oncogenomics-based in vivo RNAi screen identifies tumor suppressors in liver cancer. *Cell* *135*, 852–864.
- Zhou, Y., Zhu, S., Cai, C., Yuan, P., Li, C., Huang, Y., and Wei, W. (2014). High-throughput screening of a CRISPR/Cas9 library for functional genomics in human cells. *Nature* *509*, 487–491.

A 3D Map of the Human Genome at Kilobase Resolution Reveals Principles of Chromatin Looping

Suhas S.P. Rao,^{1,2,3,4,10} Miriam H. Huntley,^{1,2,3,4,5,10} Neva C. Durand,^{1,2,3,4} Elena K. Stamenova,^{1,2,3,4} Ivan D. Bochkov,^{1,2,3} James T. Robinson,^{1,4} Adrian L. Sanborn,^{1,2,3,6} Ido Machol,^{1,2,3} Arina D. Omer,^{1,2,3} Eric S. Lander,^{4,7,8,*} and Erez Lieberman Aiden^{1,2,3,4,9,*}

¹The Center for Genome Architecture, Baylor College of Medicine, Houston, TX 77030, USA

²Department of Molecular and Human Genetics, Baylor College of Medicine, Houston, TX 77030, USA

³Department of Computer Science, Department of Computational and Applied Mathematics, Rice University, Houston, TX 77005, USA

⁴Broad Institute of MIT and Harvard, Cambridge, MA 02139, USA

⁵School of Engineering and Applied Sciences, Harvard University, Cambridge, MA 02138, USA

⁶Department of Computer Science, Stanford University, Stanford, CA 94305, USA

⁷Department of Biology, Massachusetts Institute of Technology (MIT), Cambridge, MA 02139, USA

⁸Department of Systems Biology, Harvard Medical School, Boston, MA 02115, USA

⁹Center for Theoretical Biological Physics, Rice University, Houston, TX 77030, USA

¹⁰Co-first author

*Correspondence: lander@broadinstitute.org (E.S.L.), erez@erez.com (E.L.A.)

<http://dx.doi.org/10.1016/j.cell.2014.11.021>

SUMMARY

We use in situ Hi-C to probe the 3D architecture of genomes, constructing haploid and diploid maps of nine cell types. The densest, in human lymphoblastoid cells, contains 4.9 billion contacts, achieving 1 kb resolution. We find that genomes are partitioned into contact domains (median length, 185 kb), which are associated with distinct patterns of histone marks and segregate into six subcompartments. We identify ~10,000 loops. These loops frequently link promoters and enhancers, correlate with gene activation, and show conservation across cell types and species. Loop anchors typically occur at domain boundaries and bind CTCF. CTCF sites at loop anchors occur predominantly (>90%) in a convergent orientation, with the asymmetric motifs “facing” one another. The inactive X chromosome splits into two massive domains and contains large loops anchored at CTCF-binding repeats.

INTRODUCTION

The spatial organization of the human genome is known to play an important role in the transcriptional control of genes (Cremer and Cremer, 2001; Sexton et al., 2007; Bickmore, 2013). Yet important questions remain, like how distal regulatory elements, such as enhancers, affect promoters, and how insulators can abrogate these effects (Banerji et al., 1981; Blackwood and Kadonaga, 1998; Gaszner and Felsenfeld, 2006). Both phenomena are thought to involve the formation of protein-mediated “loops” that bring pairs of genomic sites that lie far apart along the linear genome into proximity (Schleif, 1992).

Various methods have emerged to assess the 3D architecture of the nucleus. In one seminal study, the binding of a protein to sites at opposite ends of a restriction fragment created a loop, which was detectable because it promoted the formation of DNA circles in the presence of ligase. Removal of the protein or either of its binding sites disrupted the loop, eliminating this “cyclization enhancement” (Mukherjee et al., 1988). Subsequent adaptations of cyclization enhancement made it possible to analyze chromatin folding in vivo, including nuclear ligation assay (Cullen et al., 1993) and chromosome conformation capture (Dekker et al., 2002), which analyze contacts made by a single locus, extensions such as 5C for examining several loci simultaneously (Dostie et al., 2006), and methods such as ChIA-PET for examining all loci bound by a specific protein (Fullwood et al., 2009).

To interrogate all loci at once, we developed Hi-C, which combines DNA proximity ligation with high-throughput sequencing in a genome-wide fashion (Lieberman-Aiden et al., 2009). We used Hi-C to demonstrate that the genome is partitioned into numerous domains that fall into two distinct compartments. Subsequent analyses have suggested the presence of smaller domains and have led to the important proposal that compartments are partitioned into condensed structures ~1 Mb in size, dubbed “topologically associated domains” (TADs) (Dixon et al., 2012; Nora et al., 2012). In principle, Hi-C could also be used to detect loops across the entire genome. To achieve this, however, extremely large data sets and rigorous computational methods are needed. Recent efforts have suggested that this is an increasingly plausible goal (Sexton et al., 2012; Jin et al., 2013).

Here, we report the results of an effort to comprehensively map chromatin contacts genome-wide, using in situ Hi-C, in which DNA-DNA proximity ligation is performed in intact nuclei. The protocol facilitates the generation of much denser Hi-C maps. The maps reported here comprise over 5 Tb of sequence

data recording over 15 billion distinct contacts, an order of magnitude larger than all published Hi-C data sets combined. Using these maps, we are able to clearly discern domain structure, compartmentalization, and thousands of chromatin loops. In addition to haploid maps, we were also able to create diploid maps analyzing each chromosomal homolog separately. The maps provide a picture of genomic architecture with resolution down to 1 kb.

RESULTS

In Situ Hi-C Methodology and Maps

Our in situ Hi-C protocol combines our original Hi-C protocol (here called dilution Hi-C) with nuclear ligation assay (Cullen et al., 1993), in which DNA is digested using a restriction enzyme, DNA-DNA proximity ligation is performed in intact nuclei, and the resulting ligation junctions are quantified. Our in situ Hi-C protocol involves crosslinking cells with formaldehyde, permeabilizing them with nuclei intact, digesting DNA with a suitable 4-cutter restriction enzyme (such as Mbol), filling the 5'-overhangs while incorporating a biotinylated nucleotide, ligating the resulting blunt-end fragments, shearing the DNA, capturing the biotinylated ligation junctions with streptavidin beads, and analyzing the resulting fragments with paired-end sequencing (Figure 1A). This protocol resembles a recently published single-cell Hi-C protocol (Nagano et al., 2013), which also performed DNA-DNA proximity ligation inside nuclei to study nuclear architecture in individual cells. Our updated protocol has three major advantages over dilution Hi-C. First, in situ ligation reduces the frequency of spurious contacts due to random ligation in dilute solution—as evidenced by a lower frequency of junctions between mitochondrial and nuclear DNA in the captured fragments and by the higher frequency of random ligations observed when the supernatant is sequenced (Extended Experimental Procedures available online). This is consistent with a recent study showing that ligation junctions formed in solution are far less meaningful (Gavrilov et al., 2013). Second, the protocol is faster, requiring 3 days instead of 7 (Extended Experimental Procedures). Third, it enables higher resolution and more efficient cutting of chromatinized DNA, for instance, through the use of a 4-cutter rather than a 6-cutter (Data S1, I).

A Hi-C map is a list of DNA-DNA contacts produced by a Hi-C experiment. By partitioning the linear genome into “loci” of fixed size (e.g., bins of 1 Mb or 1 kb), the Hi-C map can be represented as a “contact matrix” M , where the entry $M_{i,j}$ is the number of contacts observed between locus L_i and locus L_j . (A “contact” is a read pair that remains after we exclude reads that are duplicates, that correspond to unligated fragments, or that do not align uniquely to the genome.) The contact matrix can be visualized as a heatmap, whose entries we call “pixels.” An “interval” refers to a set of consecutive loci; the contacts between two intervals thus form a “rectangle” or “square” in the contact matrix. We define the “matrix resolution” of a Hi-C map as the locus size used to construct a particular contact matrix and the “map resolution” as the smallest locus size such that 80% of loci have at least 1,000 contacts. The map resolution is meant to reflect the finest scale at which one can reliably discern local features.

Contact Maps Spanning Nine Cell Lines Containing over 15 Billion Contacts

We constructed in situ Hi-C maps of nine cell lines in human and mouse (Table S1). Whereas our original Hi-C experiments had a map resolution of 1 Mb, these maps have a resolution of 1 kb or 5 kb. Our largest map, in human GM12878 B-lymphoblastoid cells, contains 4.9 billion pairwise contacts and has a map resolution of 950 bp (“kilobase resolution”) (Table S2). We also generated eight in situ Hi-C maps at 5 kb resolution, using cell lines representing all human germ layers (IMR90, HMEC, NHEK, K562, HUVEC, HeLa, and KBM7) as well as mouse B-lymphoblasts (CH12-LX) (Table S1). Each map contains between 395 M and 1.1 B contacts.

When we used our original dilution Hi-C protocol to generate maps of GM12878, IMR90, HMEC, NHEK, HUVEC, and CH12-LX, we found that, as expected, in situ Hi-C maps were superior at high resolutions, but closely resembled dilution Hi-C at lower resolutions. For instance, our dilution map of GM12878 (3.2 billion contacts) correlated highly with our in situ map at 500, 50, and 25 kb resolutions ($R > 0.96, 0.90, \text{ and } 0.87$, respectively) (Data S1, I; Figure S1).

We also performed 112 supplementary Hi-C experiments using three different protocols (in situ Hi-C, dilution Hi-C, and Tethered Conformation Capture) while varying a wide array of conditions such as extent of crosslinking, restriction enzyme, ligation volume/time, and biotinylated nucleotide. These include several in situ Hi-C experiments in which the formaldehyde crosslinking step was omitted, which demonstrate that the structural features we observe cannot be due to the crosslinking procedure. In total, 201 independent Hi-C experiments were successfully performed, many of which are presented in Data S1 and S2.

To account for nonuniformities in coverage due to the number of restriction sites at a locus or the accessibility of those sites to cutting (Lieberman-Aiden et al., 2009; Yaffe and Tanay, 2011) we use a matrix-balancing algorithm due to Knight and Ruiz (2012) (Extended Experimental Procedures).

Adequate tools for visualization of these large data sets are essential. We have therefore created the “Juicebox” visualization system that enables users to explore contact matrices, zoom in and out, compare Hi-C matrices to 1D tracks, superimpose all features reported in this paper onto the data, and contrast different Hi-C maps. All contact data and feature sets reported here can be explored interactively via Juicebox at <http://www.aidenlab.org/juicebox/>.

The Genome Is Partitioned into Small Domains Whose Median Length Is 185 kb

We began by probing the 3D partitioning of the genome. In our earlier experiments at 1 Mb map resolution (Lieberman-Aiden et al., 2009), we saw large squares of enhanced contact frequency tiling the diagonal of the contact matrices. These squares partitioned the genome into 5–20 Mb intervals, which we call “megadomains.”

We also found that individual 1 Mb loci could be assigned to one of two long-range contact patterns, which we called compartments A and B, with loci in the same compartment showing more frequent interaction. Megadomains—and the associated squares along the diagonal—arise when all of the 1 Mb loci in

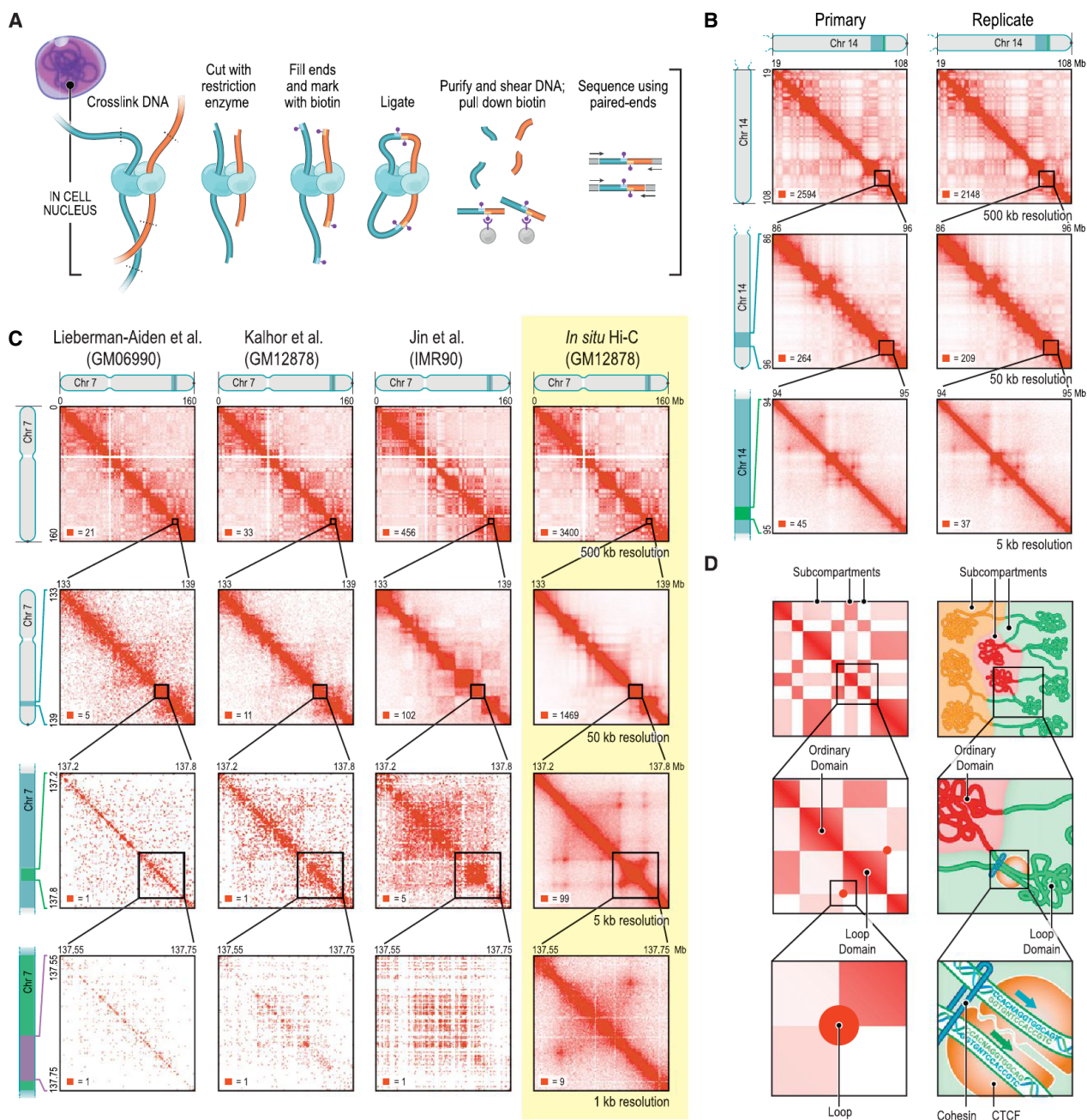


Figure 1. We Used In Situ Hi-C to Map over 15 Billion Chromatin Contacts across Nine Cell Types in Human and Mouse, Achieving 1 kb Resolution in Human Lymphoblastoid Cells

(A) During in situ Hi-C, DNA-DNA proximity ligation is performed in intact nuclei.

(B) Contact matrices from chromosome 14: the whole chromosome, at 500 kb resolution (top); 86–96 Mb/50 kb resolution (middle); 94–95 Mb/5 kb resolution (bottom). Left: GM12878, primary experiment; Right: biological replicate. The 1D regions corresponding to a contact matrix are indicated in the diagrams above and at left. The intensity of each pixel represents the normalized number of contacts between a pair of loci. Maximum intensity is indicated in the lower left of each panel.

(C) We compare our map of chromosome 7 in GM12878 (last column) to earlier Hi-C maps: Lieberman-Aiden et al. (2009), Kalhor et al. (2012), and Jin et al. (2013). (D) Overview of features revealed by our Hi-C maps. Top: the long-range contact pattern of a locus (left) indicates its nuclear neighborhood (right). We detect at least six subcompartments, each bearing a distinctive pattern of epigenetic features. Middle: squares of enhanced contact frequency along the diagonal (left) indicate the presence of small domains of condensed chromatin, whose median length is 185 kb (right). Bottom: peaks in the contact map (left) indicate the presence of loops (right). These domains tend to lie at domain boundaries and bind CTCF in a convergent orientation.

See also Figure S1, Data S1, I–II, and Tables S1 and S2.

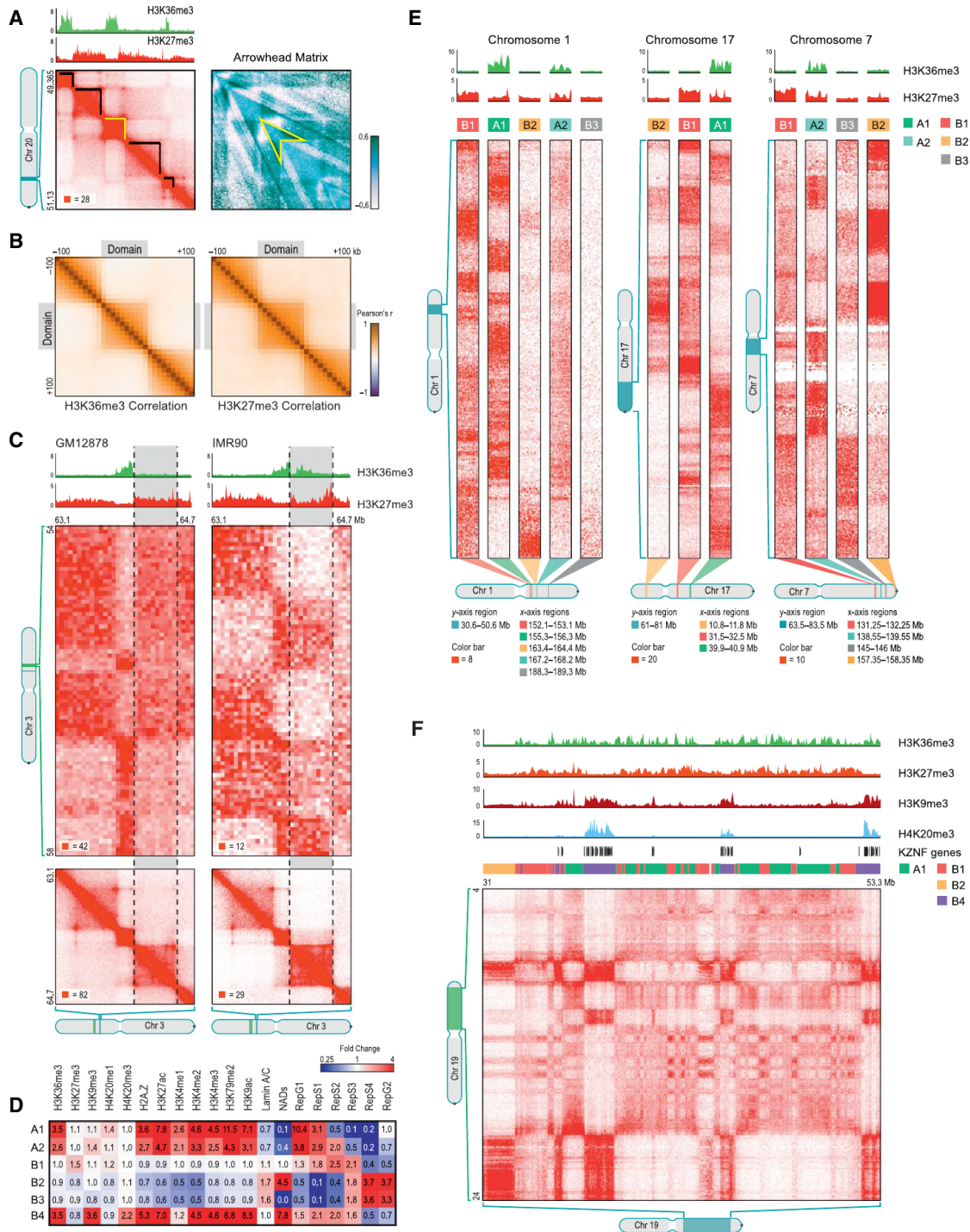


Figure 2. The Genome Is Partitioned into Contact Domains that Segregate into Nuclear Subcompartments Corresponding to Different Patterns of Histone Modifications

(A) We annotate thousands of domains across the genome (left, black highlight). To do so, we define an arrowhead matrix A (right) such that $A_{i,i+d} = (M^*_{i,i-d} - M^*_{i,i+d}) / (M^*_{i,i-d} + M^*_{i,i+d})$, where M^* is the normalized contact matrix. This transformation replaces domains with an arrowhead-shaped motif pointing toward the domain's upper-left corner (example in yellow); we identify these arrowheads using dynamic programming. See Experimental Procedures.

(B) Pearson correlation matrices of the histone mark signal between pairs of loci inside and within 100 kb of a domain. Left: H3K36me3; Right: H3K27me3.

(C) Conserved contact domains on chromosome 3 in GM12878 (left) and IMR90 (right). In GM12878, the highlighted domain (gray) is enriched for H3K27me3 and depleted for H3K36me3. In IMR90, the situation is reversed. Marks at flanking domains are the same in both: the domain to the left is enriched for H3K36me3 and the domain to the right is enriched for H3K27me3. The flanking domains have long-range contact patterns that differ from one another and are preserved in both

(legend continued on next page)

an interval exhibit the same genome-wide contact pattern. Compartment A is highly enriched for open chromatin; compartment B is enriched for closed chromatin (Lieberman-Aiden et al., 2009; Kalhor et al., 2012; Sexton et al., 2012).

In our new, higher resolution maps (200- to 1,000-fold more contacts), we observe many small squares of enhanced contact frequency that tile the diagonal of each contact matrix (Figure 2A). We used the Arrowhead algorithm (see Experimental Procedures) to annotate these contact domains genome-wide. The observed domains ranged in size from 40 kb to 3 Mb (median size 185 kb). As with megadomains, there is an abrupt drop in contact frequency (33%) for pairs of loci on opposite sides of the domain boundary (Figure S2G). Contact domains are often preserved across cell types (Figures S3A and S3B).

The presence of smaller domains in Hi-C maps is consistent with several other recent studies (Dixon et al., 2012; Nora et al., 2012; Sexton et al., 2012). We explore the relationship between the domains we annotate and those annotated in prior studies in the Discussion.

Contact Domains Exhibit Consistent Histone Marks Whose Changes Are Associated with Changes in Long-Range Contact Pattern

Loci within a contact domain show correlated histone modifications for eight different factors (H3K36me3, H3K27me3, H3K4me1, H3K4me2, H3K4me3, H3K9me3, H3K79me2, and H4K20me1) based on data from the ENCODE project in GM12878 cells (ENCODE Project Consortium, 2012). By contrast, loci at comparable distance but residing in different domains showed much less correlation in chromatin state (Figures 2B, S2I, and S2K; Extended Experimental Procedures). Strikingly, changes in a domain's chromatin state are often accompanied by changes in the long-range contact pattern of domain loci (i.e., the pattern of contacts between loci in the domain and other loci genome-wide), indicating that changes in chromatin pattern are accompanied by shifts in a domain's nuclear neighborhood (Figures 2C and S3C–S3E; Extended Experimental Procedures). This observation is consistent with microscopy studies associating changes in gene expression with changes in nuclear localization (Finlan et al., 2008).

There Are at Least Six Nuclear Subcompartments with Distinct Patterns of Histone Modifications

Next, we partitioned loci into categories based on long-range contact patterns alone, using four independent approaches: manual annotation and three unsupervised clustering algorithms (HMM, K-means, Hierarchical). All gave similar results (Figure S4B; Extended Experimental Procedures). We then investigated the biological meaning of these categories.

When we analyzed the data at low matrix resolution (1 Mb), we reproduced our earlier finding of two compartments (A and B). At high resolution (25 kb), we found evidence for at least five “subcompartments” defined by their long-range interaction patterns, both within and between chromosomes. These findings expand on earlier reports suggesting three compartments in human cells (Yaffe and Tanay, 2011). We found that the median length of an interval lying completely within a subcompartment is 300 kb. Although the subcompartments are defined solely based on their Hi-C interaction patterns, they exhibit distinct genomic and epigenomic content.

Two of the five interaction patterns are correlated with loci in compartment A (Figure S4E). We label the loci exhibiting these patterns as belonging to subcompartments A1 and A2. Both A1 and A2 are gene dense, have highly expressed genes, harbor activating chromatin marks such as H3K36me3, H3K79me2, H3K27ac, and H3K4me1 and are depleted at the nuclear lamina and at nucleolus-associated domains (NADs) (Figures 2D, 2E, and S4I; Table S3). While both A1 and A2 exhibit early replication times, A1 finishes replicating at the beginning of S phase, whereas A2 continues replicating into the middle of S phase. A2 is more strongly associated with the presence of H3K9me3 than A1, has lower GC content, and contains longer genes (2.4-fold).

The other three interaction patterns (labeled B1, B2, and B3) are correlated with loci in compartment B (Figure S4E) and show very different properties. Subcompartment B1 correlates positively with H3K27me3 and negatively with H3K36me3, suggestive of facultative heterochromatin (Figures 2D and 2E). Replication of this subcompartment peaks during the middle of S phase. Subcompartments B2 and B3 tend to lack all of the above-noted marks and do not replicate until the end of S phase (see Figure 2D). Subcompartment B2 includes 62% of pericentromeric heterochromatin (3.8-fold enrichment) and is enriched at the nuclear lamina (1.8-fold) and at NADs (4.6-fold). Subcompartment B3 is enriched at the nuclear lamina (1.6-fold), but strongly depleted at NADs (76-fold).

Upon closer visual examination, we noticed the presence of a sixth pattern on chromosome 19 (Figure 2F). Our genome-wide clustering algorithm missed this pattern because it spans only 11 Mb, or 0.3% of the genome. When we repeated the algorithm on chromosome 19 alone, the additional pattern was detected. Because this sixth pattern correlates with the Compartment B pattern, we labeled it B4. Subcompartment B4 comprises a handful of regions, each of which contains many KRAB-ZNF superfamily genes. (B4 contains 130 of the 278 KRAB-ZNF genes in the genome, a 65-fold enrichment). As noted in previous studies (Vogel et al., 2006; Hahn et al., 2011), these regions exhibit a highly distinctive chromatin pattern, with strong enrichment for

cell types. In IMR90, the highlighted domain is marked by H3K36me3 and its long-range contact pattern matches the similarly-marked domain on the left. In GM12878, it is decorated with H3K27me3, and the long-range pattern switches, matching the similarly-marked domain to the right. Diagonal submatrices, 10 kb resolution; long-range interaction matrices, 50 kb resolution.

(D) Each of the six long-range contact patterns we observe exhibits a distinct epigenetic profile (data sources are listed in Table S3). Each subcompartment also has a visually distinctive contact pattern.

(E) Each example shows part of the long-range contact patterns for several nearby genomic intervals lying in different subcompartments.

(F) A large contiguous region on chromosome 19 contains intervals in subcompartments A1, B1, B2, and B4.

See also Figures S2, S3, and S4 and Data S1, III–IV.

both activating chromatin marks, such as H3K36me3, and heterochromatin-associated marks, such as H3K9me3 and H4K20me3.

Approximately 10,000 Peaks Mark the Position of Chromatin Loops

We next sought to identify the positions of chromatin loops by using an algorithm to search for pairs of loci that show significantly closer proximity with one another than with the loci lying between them (Figure 3A). Such pairs correspond to pixels with higher contact frequency than typical pixels in their neighborhood. We refer to these pixels as “peaks” in the Hi-C contact matrix and to the corresponding pair of loci as “peak loci.” Peaks reflect the presence of chromatin loops, with the peak loci being the anchor points of the chromatin loop. (Because contact frequencies vary across the genome, we define peak pixels relative to the local background. We note that some papers [Sanyal et al., 2012; Jin et al., 2013] have sought to define peaks relative to a genome-wide average. This choice is problematic because, for example, many pixels within a domain may be reported as peaks despite showing no locally distinctive proximity; see Discussion.)

Our algorithm detected 9,448 peaks in the in situ Hi-C map for GM12878 at 5 kb matrix resolution. These peaks are associated with a total of 12,903 distinct peak loci (some peak loci are associated with more than one peak). The vast majority of peaks (98%) reflected loops between loci that are <2 Mb apart.

These findings were reproducible across all of our high-resolution Hi-C maps. Examining the primary and replicate maps separately, we found 8,054 peaks in the former and 7,484 peaks in the latter, with 5,403 in both lists (see Figures 3A and 3B; Data S1, V; Table S4). The differences were almost always the result of our conservative peak-calling criteria (Extended Experimental Procedures). We also called peaks using our GM12878 dilution Hi-C experiment. Because the map is sparser and thus noisier, we called only 3,073 peaks. Nonetheless, 65% of these peaks were also present in the list of peaks from our in situ Hi-C data set, again reflecting high interreplicate reproducibility.

To independently confirm that peak loci are closer than neighboring locus pairs, we performed 3D-FISH (Beliveau et al., 2012) on four loops (Table S5). In each case, we compared two peak loci, *L1* and *L2*, with a control locus, *L3*, that lies an equal genomic distance away from *L2* but on the opposite side (Figures 3C and S5B). In all cases, the 3D-distance between *L1* and *L2* was consistently shorter than the 3D-distance between *L2* and *L3* (Extended Experimental Procedures).

We also confirmed that our list of peaks was consistent with previously published Hi-C maps. Although earlier maps contained too few contacts to reliably call individual peaks, we developed a method called Aggregate Peak Analysis (APA) that compares the aggregate enrichment of our peak set in these low-resolution maps to the enrichment seen when our peak set is translated in any direction (Experimental Procedures). APA

showed strong consistency between our loop calls and all six previously published Hi-C experiments in lymphoblastoid cell lines (Lieberman-Aiden et al., 2009; Kalhor et al., 2012) (Figure 3D; Data S2, I,E; Table S6).

Finally, we demonstrated that the peaks observed were robust to particular protocol conditions by performing APA on our GM12878 dilution Hi-C map and on our 112 supplemental Hi-C experiments exploring a wide range of protocol variants. Enrichment was seen in every experiment. Notably, these include five experiments (HIC043-HIC047; Table S1) in which the Hi-C protocol was performed without crosslinking, demonstrating that the peaks observed in our experiments cannot be byproducts of the formaldehyde-crosslinking procedure.

Conservation of Peaks among Human Cell Lines and across Evolution

We also identified peaks in the other seven human cell lines (Table S1). Because these maps contain fewer contacts, sensitivity is reduced, and fewer peaks are observed (ranging from 2,634 to 8,040). APA confirmed that these peak calls were consistent with the dilution Hi-C maps reported here (in IMR90, HMEC, HUVEC, and NHEK), as well as with all previously published Hi-C maps in these cell types (Lieberman-Aiden et al., 2009; Dixon et al., 2012; Jin et al., 2013) (Data S2, I,F).

We found that peaks were often conserved across cell types (Figure 4A): between 55% and 75% of the peaks found in any given cell type were also found in GM12878 (Figure S5D).

Next, we compared peaks across species. In CH12-LX mouse B-lymphoblasts, we identified 2,927 high-confidence contact domains and 3,331 peaks. When we examined orthologous regions in GM12878, we found that 50% of peaks and 45% of domains called in mouse were also called in humans. This suggests substantial conservation of 3D genome structure across the mammals (Figures 4B–4E).

Loops Anchored at a Promoter Are Associated with Enhancers and Increased Gene Activation

Various lines of evidence indicate that many of the observed loops are associated with gene regulation.

First, our peaks frequently have a known promoter at one peak locus (as annotated by ENCODE’s ChromHMM) (Hoffman et al., 2013) and a known enhancer at the other (Figure 5A). For instance, 2,854 of the 9,448 peaks in our GM12878 map bring together known promoters and known enhancers (30% versus 7% expected by chance). The peaks include classic promoter-enhancer loops, such as at *MYC* (chr8:128.35–128.75 Mb, in HMEC) and alpha-globin (chr16:0.15–0.22 Mb, in K562). Second, genes whose promoters are associated with a loop are much more highly expressed than genes whose promoters are not associated with a loop (6-fold).

Third, the presence of cell type-specific peaks is associated with changes in expression. When we examined RNA sequencing (RNA-seq) data produced by ENCODE, we found

(D) APA plot shows the aggregate signal from the 9,448 GM12878 loops we report by summing submatrices surrounding each peak in a low-resolution GM12878 Hi-C map due to Kalhor et al. (2012). Although individual peaks cannot be seen in the Kalhor et al. (2012) data (that contains 42 M contacts), the peak at the center of the APA plot indicates that the aggregate signal from our peak set as a whole can be clearly discerned using their data set. See also Figure S5, Data S1, V, and Data S2,I, and Tables S4, S5, and S6.

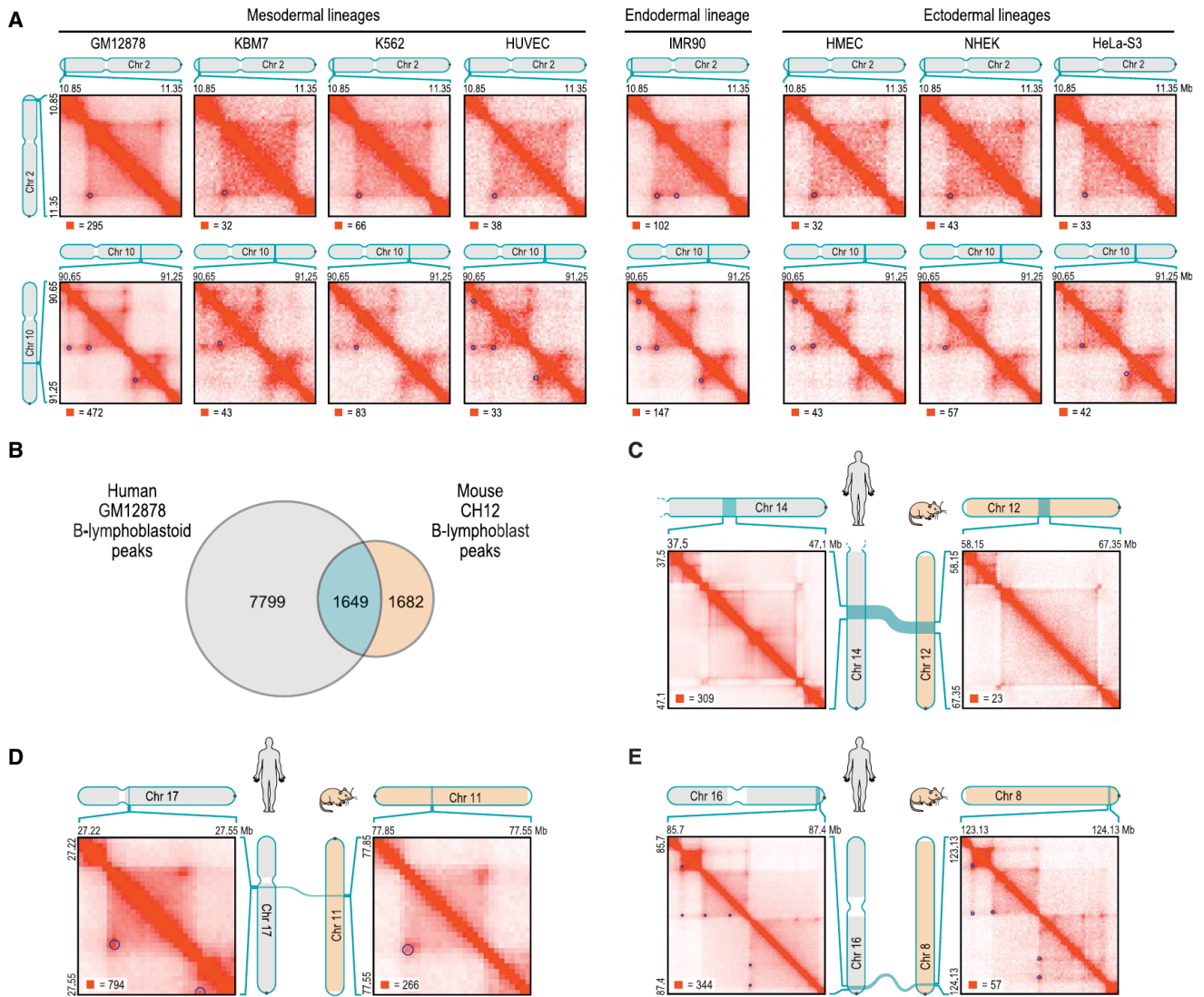


Figure 4. Loops Are Often Preserved across Cell Types and from Human to Mouse

(A) Examples of peak and domain preservation across cell types. Annotated peaks are circled in blue. All annotations are completely independent.

(B) Of the 3,331 loops we annotate in mouse CH12-LX, 1,649 (50%) are orthologous to loops in human GM12878.

(C–E) Conservation of 3D structure in syntenic blocks. The contact matrices in (C) are shown at 25 kb resolution. (D) and (E) are shown at 10 kb resolution.

that the appearance of a loop in a cell type was frequently accompanied by the activation of a gene whose promoter overlapped one of the peak loci. For example, a cell-type-specific loop is anchored at the promoter of the gene encoding L-selectin (*SELL*), which is expressed in GM12878 (where the loop is present), but not in IMR90 (where the loop is absent, Figure 5B). Genome-wide, we observed 557 loops in GM12878 that were clearly absent in IMR90. The corresponding peak loci overlapped the promoters of 43 genes that were markedly upregulated (>50-fold) in GM12878, but of only one gene that was markedly upregulated in IMR90. Conversely, we found 510 loops in IMR90 that were clearly absent in GM12878. The corresponding peak loci overlapped the promoters of 94 genes that were markedly upregulated in IMR90, but of only three genes that were

markedly upregulated in GM12878. When we compared GM12878 to the five other human cell types for which ENCODE RNA-seq data were available, the results were very similar (Figure 5C; Table S7).

Occasionally, gene activation is accompanied by the emergence of a cell-type-specific network of peaks. Figure 5D illustrates the case of *ADAMTS1*, which encodes a protein involved in fibroblast migration. The gene is expressed in IMR90, where its promoter is involved in six loops. In GM12878, it is not expressed, and the promoter is involved in only two loops. Many of the IMR90 peak loci form transitive peaks with one another (see discussion of “transitivity” below), suggesting that the *ADAMTS1* promoter and the six distal sites may all be located at a single spatial hub.

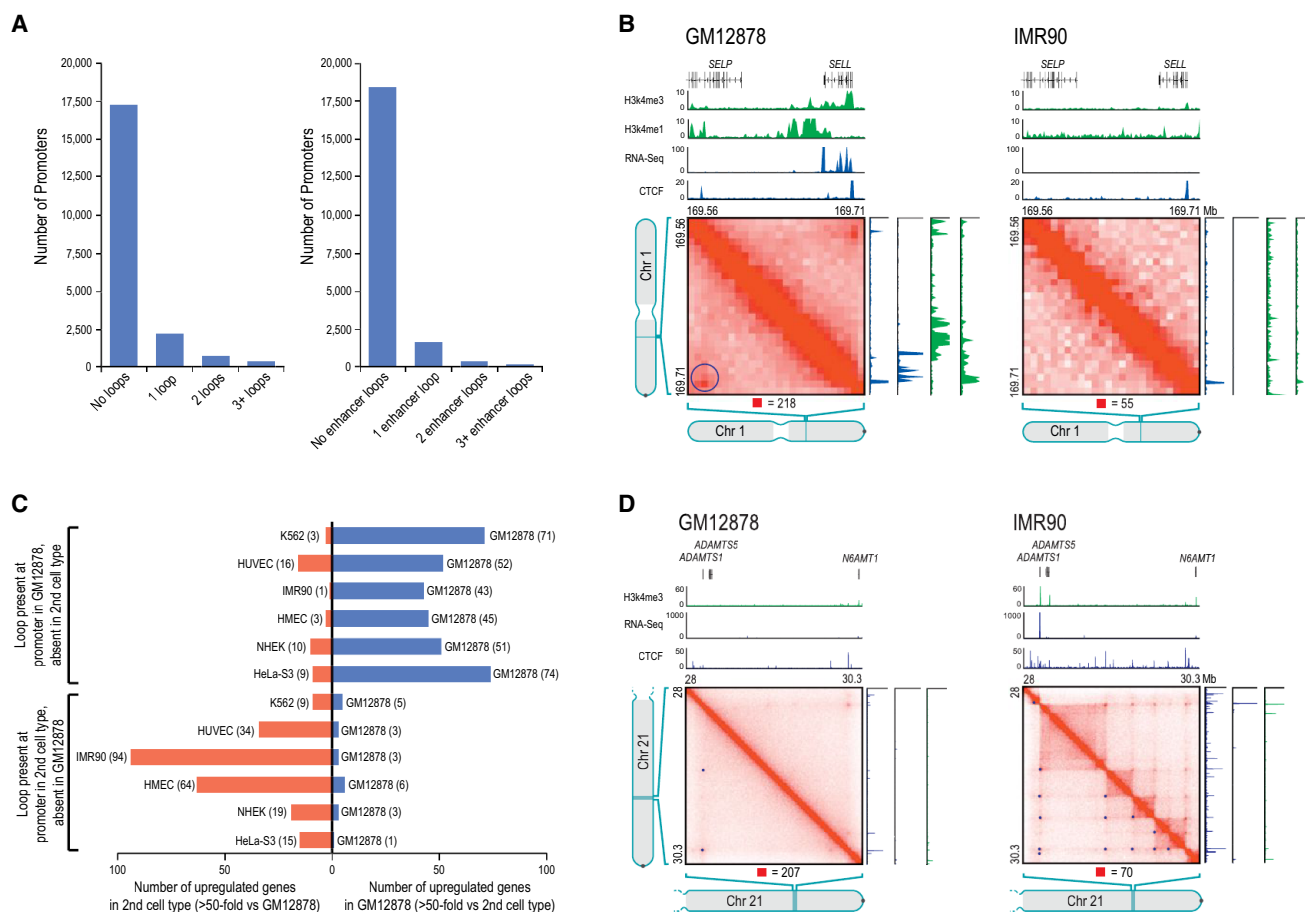


Figure 5. Loops between Promoters and Enhancers Are Strongly Associated with Gene Activation

(A) Histogram showing loop count at promoters (left); restricted to loops where the distal peak locus contains an enhancer (right).

(B) Left: a loop in GM12878, with one anchor at the *SELL* promoter and the other at a distal enhancer. The gene is on. Right: the loop is absent in IMR90, where the gene is off.

(C) Genes whose promoters participate in a loop in GM12878 but not in a second cell type are frequently upregulated in GM12878 and vice versa.

(D) Left: two loops in GM12878 are anchored at the promoter of the inactive *ADAMTS1* gene. Right: a series of loops and domains appear, along with transitive looping. *ADAMTS1* is on.

See also Data S1, VI and Table S7.

These observations are consistent with the classic model in which looping between a promoter and enhancer activates a target gene (Tolhuis et al., 2002; Amano et al., 2009; Ahmadiyeh et al., 2010).

Loops Frequently Delineate the Boundaries of Contact Domains

A large fraction of peaks (38%) coincide with the corners of a contact domain—that is, the peak loci are located at domain boundaries (Figures 6A and S6). Conversely, a large fraction of domains (39%) had peaks in their corner. Moreover, the appearance of a loop is usually (in 65% of cases) associated with the appearance of a domain demarcated by the loop. Because this configuration is so common, we use the term “loop domain” to refer to contact domains whose endpoints form a chromatin loop.

In some cases, adjacent loop domains (bounded by peak loci *L1-L2* and *L2-L3*, respectively) exhibit transitivity—that is, *L1* and

L3 also correspond to a peak. This may indicate that the three loci simultaneously collocate at a single spatial position. However, many peaks do not exhibit transitivity, suggesting that the corresponding loci do not collocate. Figure 6B shows a region on chromosome 4 exhibiting both configurations.

We also found that overlapping loops are strongly disfavored: pairs of loops *L1-L3* and *L2-L4* (where *L1*, *L2*, *L3* and *L4* occur consecutively in the genome) are found 4-fold less often than expected under a random model (Extended Experimental Procedures).

The Vast Majority of Loops Are Associated with Pairs of CTCF Motifs in a Convergent Orientation

We next wondered whether peaks are associated with specific proteins. We examined the results of 86 chromatin immunoprecipitation sequencing (ChIP-seq) experiments performed by ENCODE in GM12878. We found that the vast majority of peak

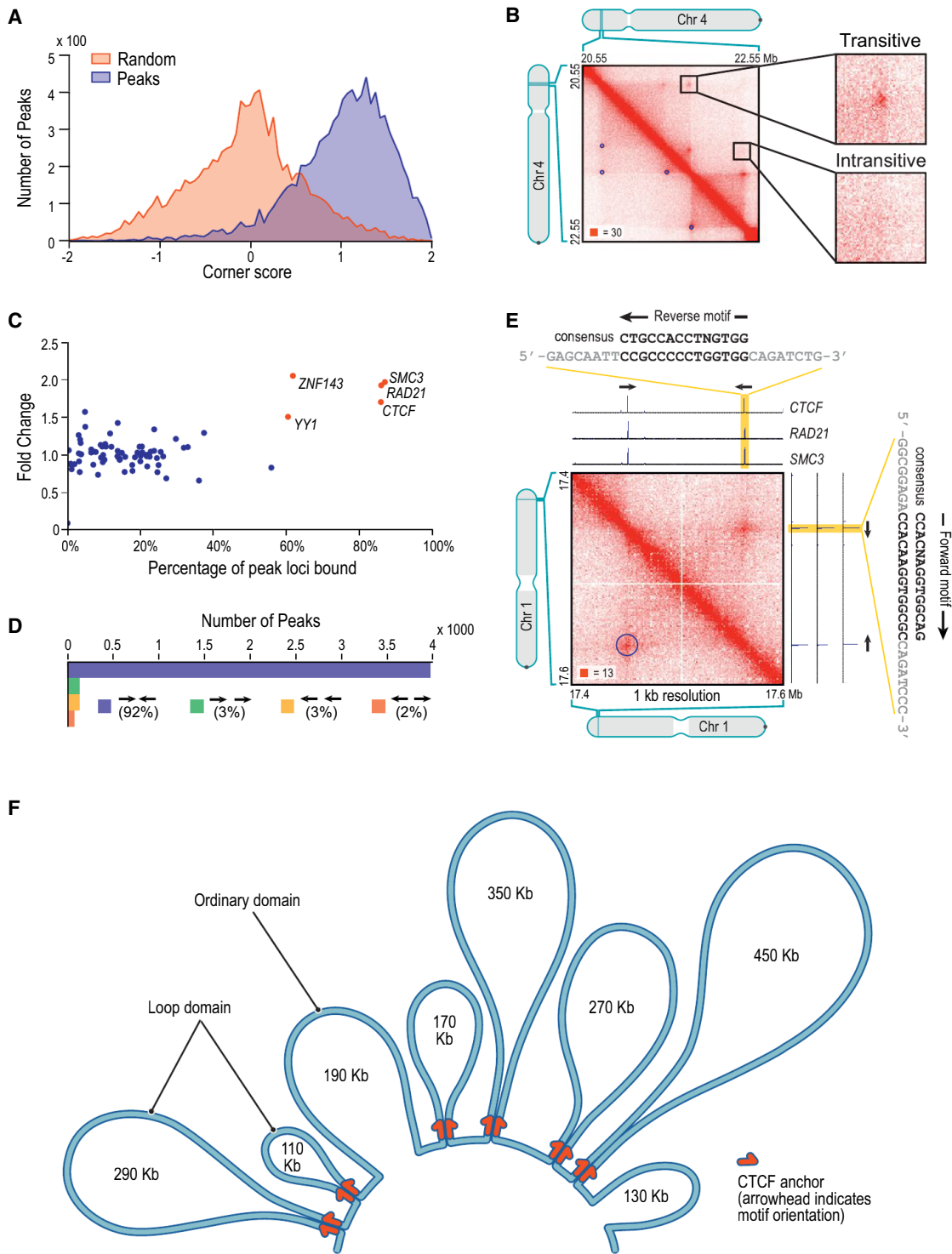


Figure 6. Many Loops Demarcate Contact Domains; The Vast Majority of Loops Are Anchored at a Pair of Convergent CTCF/RAD21/SMC3 Binding Sites

(A) Histograms of corner scores for peak pixels versus random pixels with an identical distance distribution.
 (B) Contact matrix for chr4:20.55 Mb–22.55 Mb in GM12878, showing examples of transitive and intransitive looping behavior.
 (C) Percent of peak loci bound versus fold enrichment for 76 DNA-binding proteins.
 (D) The pairs of CTCF motifs that anchor a loop are nearly all found in the convergent orientation.

(legend continued on next page)

loci are bound by the insulator protein CTCF (86%) and the cohesin subunits RAD21 (86%) and SMC3 (87%) (Figure 6C). This is consistent with numerous reports, using a variety of experimental modalities, that suggest a role for CTCF and cohesin in mediating DNA loops (Splinter et al., 2006; Hou et al., 2008; Phillips and Corces, 2009). Because many of our loops demarcate domains, this observation is also consistent with studies suggesting that CTCF delimits structural and regulatory domains (Xie et al., 2007; Cuddapah et al., 2009; Dixon et al., 2012).

We found that most peak loci encompass a unique DNA site containing a CTCF-binding motif, to which all three proteins (CTCF, SMC3, and RAD21) were bound (5-fold enrichment). We were thus able to associate most of the peak loci (6,991 of 12,903, or 54%) with a specific CTCF-motif “anchor.”

The consensus DNA sequence for CTCF-binding sites is typically written as 5'-CCACNAGGTGGCAG-3'. Because the sequence is not palindromic, each CTCF motif has an orientation; we designate the consensus motif above as the “forward” orientation. Thus, a pair of CTCF sites on the same chromosome can have four possible orientations: (1) same direction on one strand, (2) same direction on the other strand, (3) convergent on opposite strands, and (4) divergent on opposite strands.

If CTCF sites were randomly oriented, one would expect all four orientations to occur equally often. But when we examined the 4,322 peaks in GM12878 where the two corresponding peak loci each contained a single CTCF-binding motif, we found that the vast majority (92%) of motif pairs are convergent (Figures 6D and 6E). Overall, the presence, at pairs of peak loci, of bound CTCF sites in the convergent orientation was enriched 102-fold over random expectation (Extended Experimental Procedures). The convergent orientation was overwhelmingly more frequent than the divergent orientation, despite the fact that divergent motifs also lie on opposing strands: in GM12878, the counts were 3,971-78 (51-fold enrichment, convergent versus divergent); in IMR90, 1,456-5 (291-fold); in HMEC, 968-11 (88-fold); in K562, 723-2 (362-fold); in HUVEC, 671-4 (168-fold); in HeLa, 301-3 (100-fold); in NHEK, 556-9 (62-fold); and in CH12-LX, 625-8 (78-fold). This pattern suggests that a pair of CTCF sites in the convergent orientation is required for the formation of a loop.

The observation that looped CTCF sites occur in the convergent orientation also allows us to analyze peak loci containing multiple CTCF-bound motifs to predict which motif instance plays a role in a given loop. In this way, we can associate nearly two-thirds of peak loci (8,175 of 12,903, or 63.4%) with a single CTCF-binding motif.

The specific orientation of CTCF sites at observed peaks provides evidence that our peak calls are biologically correct. Because randomly chosen CTCF pairs would exhibit each of the four orientations with equal probability, the near-perfect as-

sociation between our loop calls and the convergent orientation could not occur by chance ($p < 10^{-1,900}$, binomial distribution).

In addition, the presence of CTCF and RAD21 sites at many of our peaks provides an opportunity to compare our results to three recent ChIA-PET experiments reported by the ENCODE Consortium (in GM12878 and K562) in which ligation junctions bound to CTCF (or RAD21) were isolated and analyzed. We found strong concordance with our results in all three cases (Li et al., 2012; Heidari et al., 2014) (Extended Experimental Procedures).

The CTCF-Binding Exapted SINEB2 Repeat in Mouse Shows Preferential Orientation with Respect to Loops

In mouse, we found that 7% of peak anchors lie within SINEB2 repeat elements containing a CTCF motif, which has been exapted to be functional. (The spread of CTCF binding via retrotransposition of this element, which contains a CTCF motif in its consensus sequence, has been documented in prior studies [Bourque et al., 2008; Schmidt et al., 2012].) The CTCF motifs at peak anchors in SINEB2 elements show the same strong bias toward convergent orientation seen throughout the genome (89% are oriented toward the opposing loop anchor versus 94% genome-wide). The orientation of these CTCF motifs is aligned with the orientation of the SINEB2 consensus sequence in 97% of cases. This suggests that exaptation of a CTCF in a SINEB2 element is more likely when the orientation of the inserted SINEB2 is compatible with local loop structure.

Diploid Hi-C Maps Reveal Homolog-Specific Features, Including Imprinting-Specific Loops and Massive Domains and Loops on the Inactive X Chromosome

Because many of our reads overlap SNPs, it is possible to use GM12878 phasing data (McKenna et al., 2010; 1000 Genomes Project Consortium et al., 2012) to assign contacts to specific chromosomal homologs (Figure 7A; Table S8). Using these assignments, we constructed a “diploid” Hi-C map of GM12878 comprising both maternal (238 M contacts) and paternal (240 M) maps.

For autosomes, the maternal and paternal homologs exhibit very similar inter- and intrachromosomal contact profiles (Pearson's $R > 0.998$). One interchromosomal difference was notable: an elevated contact frequency between the paternal homologs of chromosome 6 and 11 that is consistent with an unbalanced translocation fusing chr11q:73.5 Mb and all distal loci (a stretch of over 60 Mb) to the telomere of chromosome 6p (Figures 7B and S7B). The signal intensity suggests that the translocation is present in between 1.2% and 5.6% of our cells (Extended Experimental Procedures). We tested this prediction by karyotyping 100 GM12878 cells using Giemsa staining and found three abnormal chromosomes, each showing the predicted

(E) A peak on chromosome 1 and corresponding ChIP-seq tracks. Both peak loci contain a single site bound by CTCF, RAD21, and SMC3. The CTCF motifs at the anchors exhibit a convergent orientation.

(F) A schematic rendering of a 2.1 Mb region on chromosome 20 (48.78–50.88 Mb). Eight domains tile the region, ranging in size from 110 kb to 450 kb; 95% of the region is contained inside a domain (contour lengths are shown to scale). Six of the eight domains are demarcated by loops between convergent CTCF-binding sites located at the domain boundaries. The other two domains are not demarcated by loops. The motif orientation is indicated by the direction of the arrow. Note that not every CTCF-binding site is shown.

See also Figure S6.

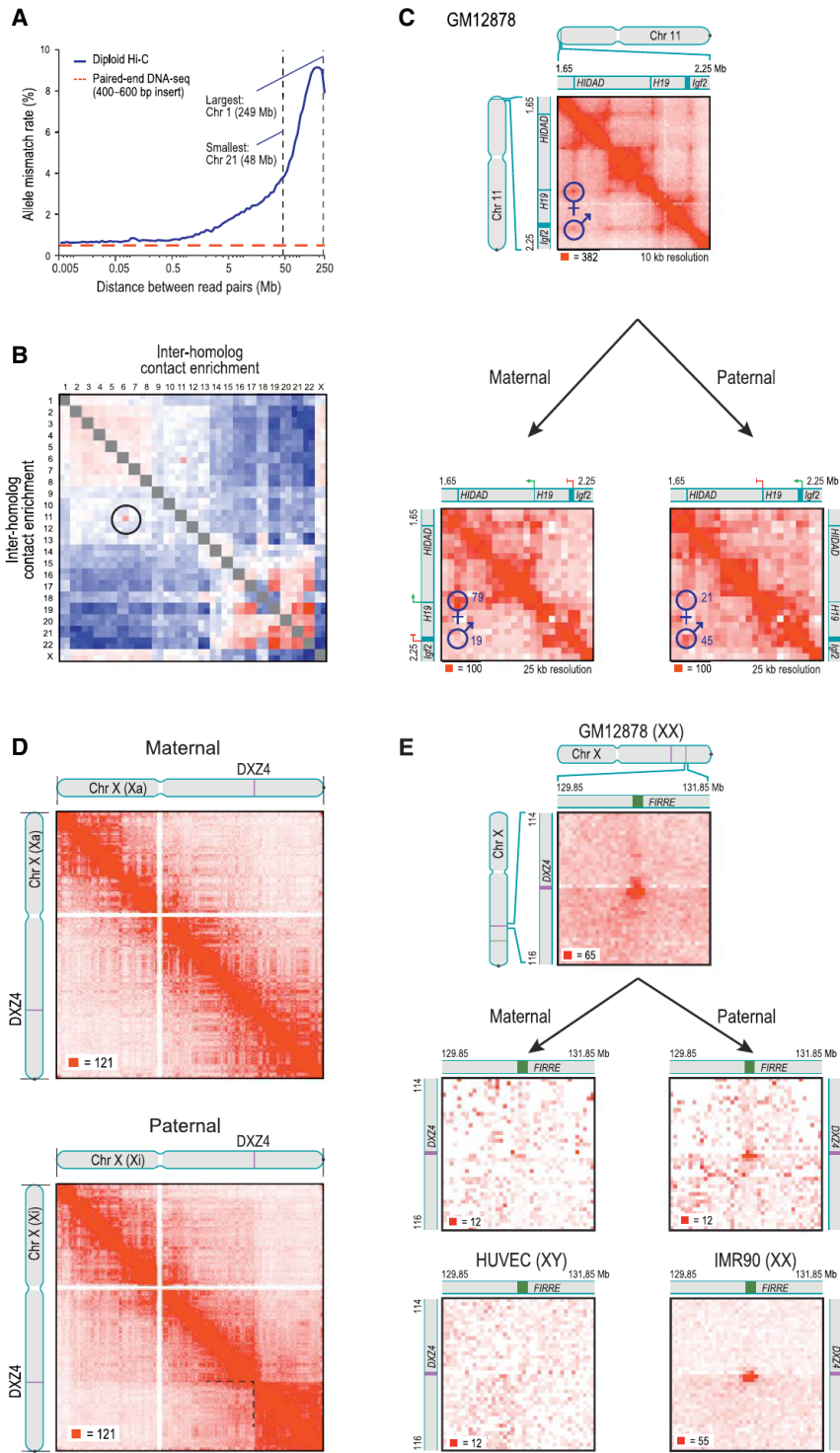


Figure 7. Diploid Hi-C Maps Reveal Superdomains and Superloops Anchored at CTCF-Binding Tandem Repeats on the Inactive X Chromosome

(A) The frequency of mismatch (maternal-paternal) in SNP allele assignment versus distance between two paired read alignments. Intrachromosomal read pairs are overwhelmingly intramolecular. (B) Preferential interactions between homologs. Left/top is maternal; right/bottom is paternal. The aberrant contact frequency between 6/paternal and 11/paternal (circle) reveals a translocation. (C) Top: in our unphased Hi-C map of GM12878, we observe two loops joining both the promoter of the maternally-expressed *H19* and the promoter of the paternally-expressed *Igf2* to a distal locus, HIDAD. Using diploid Hi-C maps, we phase these loops: the HIDAD-*H19* loop is present only on the maternal homolog (left) and the HIDAD-*Igf2* loop is present only on the paternal homolog (right). (D) The inactive (paternal) copy of chromosome X (bottom) is partitioned into two massive “superdomains” not seen in the active (maternal) copy (top). *DXZ4* lies at the boundary. Contact matrices are shown at 500 kb resolution. (E) The “superloop” between *FIRRE* and *DXZ4* is present in the unphased GM12878 map (top), in the paternal GM12878 map (middle right), and in the map of the female cell line IMR90 (bottom right); it is absent from the maternal GM12878 map (middle left) and the map of the male HUVEC cell line (bottom left). Contact matrices are shown at 50 kb resolution. See also Figure S7 and Table S8.

of genomic imprinting. In our unphased maps, we clearly see two loops from a single distal locus at 1.72 Mb (that binds CTCF in the forward orientation) to loci located near the promoters of both *H19* and *Igf2* (both of which bind CTCF in the reverse orientation, i.e., the above consensus motif lies on the opposite strand; see Figure 7C). We refer to this distal locus as the *H19/Igf2* Distal Anchor Domain (HIDAD). Our diploid maps reveal that the loop to the *H19* region is present on the maternal chromosome (from which *H19* is expressed), but the loop to the *Igf2* region is absent or greatly attenuated. The opposite pattern is found on the paternal chromosome (from which *Igf2* is expressed).

Pronounced differences were seen on the diploid intrachromosomal maps of chromosome X. The paternal X chromosome, which is usually inactive in GM12878, is partitioned into two massive domains (0–115 Mb and 115–155.3 Mb). These “superdomains” are not seen in the active, maternal X (Figure 7D). When we examined the unphased maps of chromosome X for the karyotypically normal female cell lines in our study (GM12878, IMR90, HMEC,

translocation, der(6)t(6,11)(pter;q) (Figures S7C–S7F). The Hi-C data reveal that the translocation involves the paternal homologs, which cannot be determined with ordinary cytogenetic methods.

We also observed differences in loop structure between homologous autosomes at some imprinted loci. For instance, the *H19/Igf2* locus on chromosome 11 is a well-characterized case

NHEK), the superdomains on X were evident, although the signal was attenuated due to the superposition of signals from active and inactive X chromosomes. When we examined the male HUVEC cell line and the haploid KBM7 cell line, we saw no evidence of superdomains (Figure S7G).

Interestingly, the boundary between the superdomains (ChrX: 115 Mb \pm 500 kb) lies near the macrosatellite repeat *DXZ4* (ChrX: 114,867,433–114,919,088) near the middle of Xq. *DXZ4* is a CpG-rich tandem repeat that is conserved across primates and monkeys and encodes a long noncoding RNA. In males and on the active X, *DXZ4* is heterochromatic, hypermethylated and does not bind CTCF. On the inactive X, *DXZ4* is euchromatic, hypomethylated, and binds CTCF. *DXZ4* has been hypothesized to play a role in reorganizing chromatin during X inactivation (Chadwick, 2008).

There were also significant differences in loop structure between the chromosome X homologs. We observed 27 large “superloops,” each spanning between 7 and 74 Mb, present only on the inactive X chromosome in the diploid map (Figure 7E). The superloops were also seen in all four unphased maps from karyotypically normal XX cells, but were absent in unphased maps from X0 and XY cells (Figure S7I). Two of the superloops (chrX:56.8 Mb-*DXZ4* and *DXZ4*-130.9 Mb) were reported previously in a locus-specific study (Horakova et al., 2012).

Like the peak loci of most other loops, nearly all the superloop anchors bind CTCF (23 of 24). The six anchor regions most frequently associated with superloops are large (up to 200 kb). Four of these anchor regions contain whole long noncoding RNA (lncRNA) genes: *loc550643*, *XIST*, *DXZ4*, and *FIRRE*. Three (*loc550643*, *DXZ4*, and *FIRRE*) contain CTCF-binding tandem repeats that only bind CTCF on the inactive homolog.

DISCUSSION

Using the in situ Hi-C protocol, we probed genomic architecture with high resolution; in the case of GM12878 lymphoblastoid cells, better than 1 kb. We observe the presence of contact domains that were too small (median length = 185 kb) to be seen in previous maps. Loci within a domain interact frequently with one another, have similar patterns of chromatin modifications, and exhibit similar long-range contact patterns. Domains tend to be conserved across cell types and between human and mouse. When the pattern of chromatin modifications associated with a domain changes, the domain’s long-range contact pattern also changes. Domains exhibit at least six distinct patterns of long-range contacts (subcompartments), which subdivide the two compartments that we previously reported based on low resolution data. The subcompartments are each associated with distinct chromatin patterns. It is possible that the chromatin patterns play a role in bringing about the long-range contact patterns, or vice versa.

Our data also make it possible to create a genome-wide catalog of chromatin loops. We identified loops by looking for pairs of loci that have significantly more contacts with one another than they do with other nearby loci. In our densest map (GM12878), we observe 9,448 loops.

The loops reported here have many interesting properties. Most loops are short (<2 Mb) and strongly conserved across

cell types and between human and mouse. Promoter-enhancer loops are common and associated with gene activation. Loops tend not to overlap; they often demarcate contact domains, and may establish them. CTCF and the cohesin subunits RAD21 and SMC3 associate with loops; each of these proteins is found at over 86% of loop anchors.

The most striking property of loops is that the pair of CTCF motifs present at the loop anchors occurs in a convergent orientation in >90% of cases (versus 25% expected by chance). The importance of motif orientation between loci that are separated by, on average, 360 kb is surprising and must bear on the mechanism by which CTCF and cohesin form loops, which seems likely to involve CTCF dimerization. Experiments in which the presence or orientation of CTCF sites is altered may enable the engineering of loops, domains, and other chromatin structures.

It is interesting to compare our results to those seen in previous reports. The contact domains we observe are similar in size to the “physical domains” that have been reported in Hi-C maps of *Drosophila* (Sexton et al., 2012) and to the “topologically constrained domains” (mean length: 220 kb) whose existence was demonstrated in the 1970s and 1980s in structural studies of human chromatin (Cook and Brazell, 1975; Vogelstein et al., 1980; Zehnbauser and Vogelstein, 1985). On the other hand, the domains we observe are much smaller than the TADs (1 Mb) (Dixon et al., 2012) that have been reported in humans and mice on the basis of lower-resolution contact maps. This is because detecting TADs involves detection of domain boundaries. With higher resolution data, it is possible to detect additional boundaries beyond those seen in previous maps. Interestingly, nearly all the boundaries we observe are associated with either a subcompartment transition (that occur approximately every 300 kb), or a loop (that occur approximately every 200 kb); and many are associated with both.

Our annotation identifies many fewer loops than were reported in several recent high-throughput studies, despite the fact that we have more data. The key reason is that we call peaks only when a pair of loci shows elevated contact frequency relative to the local background—that is, when the peak pixel is enriched as compared to other pixels in its neighborhood. In contrast, prior studies have defined peaks by comparing the contact frequency at a pixel to the genome-wide average (Sanyal et al., 2012; Jin et al., 2013). This latter definition is problematic because many pixels within a domain can be annotated as peaks despite showing no local increase in contact frequency. Papers using the latter definition imply the existence of more than 100,000 loops (1,187 loops were reported in 1% of the genome [Sanyal et al., 2012]) or even more than 1 million loops (reported in a genome-wide Hi-C study [Jin et al., 2013]). The vast majority of the loops annotated by these papers show no enrichment relative to the local background when examined one-by-one and no enrichment with respect to any published Hi-C data set when analyzed using APA (see Extended Experimental Procedures; Figure S8; Data S2). This suggests that these peak annotations may correspond to pairs of loci that lie in the same domain or compartment, but rarely correspond to loops.

We created diploid Hi-C maps by using polymorphisms to assign contacts to distinct chromosomal homologs. We found that the inactive X chromosome is partitioned into two large

superdomains whose boundary lies near the locus of the lncRNA *DXZ4*. We also detect a network of long-range superloops, the strongest of which are anchored at locations containing lncRNA genes (*loc550643*, *XIST*, *DXZ4*, and *FIRRE*). With the exception of *XIST*, all of these lncRNAs contain CTCF-binding tandem repeats that bind CTCF only on the inactive X.

In our original report on Hi-C, we observed that Hi-C maps can be used to study physical models of genome folding, and we proposed a fractal globule model for genome folding at the megabase scale. The kilobase-scale maps reported here allow the physical properties of genome folding to be probed at much higher resolution. We will report such studies elsewhere.

Just as loops bring distant DNA loci into close spatial proximity, we find that they bring disparate aspects of DNA biology—domains, compartments, chromatin marks, and genetic regulation—into close conceptual proximity. As our understanding of the physical connections between DNA loci continues to improve, our understanding of the relationships between these broader phenomena will deepen.

EXPERIMENTAL PROCEDURES

In Situ Hi-C Protocol

All cell lines were cultured following the manufacturer's recommendations. Two to five million cells were crosslinked with 1% formaldehyde for 10 min at room temperature. Nuclei were permeabilized. DNA was digested with 100 units of Mbol, and the ends of restriction fragments were labeled using biotinylated nucleotides and ligated in a small volume. After reversal of crosslinks, ligated DNA was purified and sheared to a length of ~400 bp, at which point ligation junctions were pulled down with streptavidin beads and prepped for Illumina sequencing. Dilution Hi-C was performed as in Lieberman-Aiden et al. (2009).

3D-FISH

3D DNA-FISH was performed as in Beliveau et al. (2012) with minor modifications.

Hi-C Data Pipeline

All sequence data were produced using Illumina paired-end sequencing. We processed data using a custom pipeline that was optimized for parallel computation on a cluster. The pipeline uses BWA (Li and Durbin, 2010) to map each read end separately to the b37 or mm9 reference genomes; removes duplicate and near-duplicate reads; removes reads that map to the same fragment; and filters the remaining reads based on mapping quality score. Contact matrices were generated at base pair delimited resolutions of 2.5 Mb, 1 Mb, 500 kb, 250 kb, 100 kb, 50 kb, 25 kb, 10 kb, and 5 kb, as well as fragment-delimited resolutions of 500 f, 200 f, 100 f, 50 f, 20 f, 5 f, 2 f, and 1 f. For our largest maps, we also generated a 1 kb contact matrix. Normalized contact matrices are produced at all resolutions using Knight and Ruiz (2012).

Annotation of Domains: Arrowhead

To annotate domains, we apply an "arrowhead" transformation, defined as $A_{i,i+d} = (M_{i,i+d}^* - M_{i,i+d}^e) / (M_{i,i-d}^* + M_{i,i+d}^*)$. M^* denotes the normalized contact matrix (see Figures S2A–S2F). This is equivalent to calculating a matrix equal to $-1 \times (\text{observed/expected} - 1)$, where the expected model controls for local background and distance from the diagonal in the simplest possible way: the "expected" value at $i, i + d$ is simply the mean of the observed values at $i, i - d$ and $i, i + d$. $A_{i,i+d}$ will be strongly positive if locus $i - d$ is inside a domain and locus $i + d$ is not. If the reverse is true, $A_{i,i+d}$ will be strongly negative. If the loci are both inside or both outside a domain, $A_{i,i+d}$ will be close to zero. Consequently, if there is a domain at $[a,b]$, we find that A takes on very negative values inside a triangle whose vertices lie at $[a,a]$, $[a,b]$, and $[(a + b)/2, b]$ and very positive values inside a triangle whose vertices lie at $[(a + b)/2, b]$, $[b,b]$, and $[b, 2b - a]$. The size and positioning of these triangles creates the arrow-

head-shaped feature that replaces each domain in M^* . A "corner score" matrix, indicating each pixel's likelihood of lying at the corner of a domain, is efficiently calculated from the arrowhead matrix using dynamic programming.

Assigning Loci to Subcompartments

To cluster loci based on long-range contact patterns, we constructed a 100 kb resolution interchromosomal contact matrix such that loci from odd chromosomes appeared on the rows, and loci from even chromosomes appeared on the columns. (Intrachromosomal data and data involving chromosome X were excluded.) We cluster this matrix using the Python package *scikit*. For subcompartment B4, the 100 kb interchromosomal matrix for chromosome 19 was constructed and clustered separately, using the same procedure.

Annotation of Peaks: HiCCUPS

Our peak-calling algorithm examines each pixel in a Hi-C contact matrix and compares the number of contacts in the pixel to the number of contacts in a series of regions surrounding the pixel. The algorithm thus identifies "enriched pixels" $M_{i,j}^*$ where the contact frequency is higher than expected and where this enrichment is not the result of a larger structural feature. For instance, we rule out the possibility that the enrichment of pixel $M_{i,j}^*$ is the result of L_i and L_j lying in the same domain by comparing the pixel's contact count to an expected model derived by examining the "lower-left" neighborhood. (The "lower-left" neighborhood samples pixels $M_{i',j'}$ where $i \leq i' \leq j' \leq j$; if a pixel is in a domain, these pixels will necessarily be in the same domain.) We require that the pixel being tested contain at least 50% more contacts than expected based on the lower-left neighborhood and the enrichment be statistically significant after correcting for multiple hypothesis testing (False Discovery Rate < 10%). The same criteria are applied to three other neighborhoods. Thus, to be labeled an enriched pixel, a pixel must be significantly enriched relative to four neighborhoods: (1) pixels to its lower-left, (2) pixels to its left and right, (3) pixels above and below, and (4) a donut surrounding the pixel of interest (Figure 3A). The resulting enriched pixels tend to form contiguous interaction regions comprising 5–20 pixels each. We define the "peak pixel" (or simply the "peak") to be the pixel in an interaction region with the most contacts.

Because of the enormous number of pixels that must be examined, this calculation requires weeks of central processing unit (CPU) time to execute. (For instance, at a matrix resolution of 5 kb, the algorithm must be run on 20 billion pixels.) To accelerate it, we created a highly parallelized implementation using general-purpose graphical processing units resulting in a 200-fold speedup.

Aggregate Peak Analysis

We perform APA on 10 kb resolution contact matrices. To measure the aggregate enrichment of a set of putative peaks in a contact matrix, we plot the sum of a series of submatrices derived from that contact matrix. Each of these submatrices is a 210 kb \times 210 kb square centered at a single putative peak in the upper triangle of the contact matrix. The resulting APA plot displays the total number of contacts that lie within the entire putative peak set at the center of the matrix; the entry immediately to the right of center corresponds to the total number of contacts in the pixel set obtained by shifting the peak set 10 kb to the right; the entry two positions above center corresponds to an upward shift of 20 kb and so on. Focal enrichment across the peak set in aggregate manifests as larger values at the center of the APA plot. The APA plots shown only include peaks whose loci are at least 300 kb apart.

ACCESSION NUMBERS

The Gene Expression Omnibus (GEO) accession number for the data sets reported in this paper is GSE63525. The dbGaP accession number for the HeLa data reported in this paper is phs000640.

SUPPLEMENTAL INFORMATION

Supplemental Information includes Extended Experimental Procedures, eight figures, two data files, and eight tables and can be found with this article online at <http://dx.doi.org/10.1016/j.cell.2014.11.021>.

AUTHOR CONTRIBUTIONS

E.L.A. conceived this project. S.S.P.R., M.H.H., E.K.S., and E.L.A. designed experiments. S.S.P.R., E.K.S., I.D.B., A.D.O., and M.H.H. performed Hi-C experiments. E.K.S. and I.D.B. performed 3D-FISH experiments. N.C.D. built the computational pipeline for Hi-C data. N.C.D. and J.T.R. built the visualization system for Hi-C data. S.S.P.R., M.H.H., N.C.D., A.L.S., I.M., E.S.L., and E.L.A. analyzed data. S.S.P.R., M.H.H., N.C.D., E.S.L., and E.L.A. prepared the manuscript.

ACKNOWLEDGMENTS

This paper is dedicated to the memory of Aharon Lieberman. Our work was supported by an NSF Graduate Research Fellowship (DGE0946799 and DGE1144152) to M.H.H., an NIH New Innovator Award (OD008540-01), an NSF Physics Frontier Center (PHY-1427654, Center for Theoretical Biological Physics), an NHGRI CEGS (HG006193), NVIDIA, IBM, Google, a CPRIT Scholar Award (R1304), a McNair Medical Institute Scholar Award, and the President's Early Career Award in Science and Engineering to E.L.A., and an NHGRI grant (HG003067) to E.S.L. We thank Leslie Gaffney, Lauren Solomon, and Bang Wong for assistance with figures; BCM's Integrated Microscopy Core, Michael Mancini, Justin Demmerle, Wendy Salmon, Fabio Stossi, Radhika Dandekar, Sanjay Krishna, and especially Asha Multani for microscopy assistance; Aharon Lieberman, Aviva Presser Aiden, Nicholas Christakis, James Lupski, José Onuchic, Mitchell Guttman, Andreas Gnirke, Louise Williams, Chad Nusbaum, John Bohannon, Olga Dudchenko, and the Aiden laboratory for discussions; and Robbyn Issner and Broad's ENCODE group for several cell lines. The Center for Genome Architecture is grateful to Janice, Robert, and Cary McNair for support. A provisional patent covering in situ Hi-C and related methods has been filed. All sequence data reported in this paper that were not derived from HeLa cells have been deposited at GEO (<http://www.ncbi.nlm.nih.gov/geo/>) (GSE63525). Some of the genome sequences described in this research were derived from a HeLa cell line. Henrietta Lacks, and the HeLa cell line that was established from her tumor cells without her knowledge or consent in 1951, have made significant contributions to scientific progress and advances in human health. We are grateful to Henrietta Lacks, now deceased, and to her surviving family members for their contributions to biomedical research. The HeLa data generated from this research were submitted to the database of Genotypes and Phenotypes (dbGaP) as a substudy under accession number phs000640.

Received: October 12, 2014

Revised: November 5, 2014

Accepted: November 13, 2014

Published: December 11, 2014

REFERENCES

- Ahmadiyah, N., Pomerantz, M.M., Grisanzio, C., Herman, P., Jia, L., Almendro, V., He, H.H., Brown, M., Liu, X.S., Davis, M., et al. (2010). 8q24 prostate, breast, and colon cancer risk loci show tissue-specific long-range interaction with MYC. *Proc. Natl. Acad. Sci. USA* *107*, 9742–9746.
- Amano, T., Sagai, T., Tanabe, H., Mizushima, Y., Nakazawa, H., and Shiroishi, T. (2009). Chromosomal dynamics at the Shh locus: limb bud-specific differential regulation of competence and active transcription. *Dev. Cell* *16*, 47–57.
- Banerji, J., Rusconi, S., and Schaffner, W. (1981). Expression of a beta-globin gene is enhanced by remote SV40 DNA sequences. *Cell* *27*, 299–308.
- Beliveau, B.J., Joyce, E.F., Apostolopoulos, N., Yilmaz, F., Fonseka, C.Y., McCole, R.B., Chang, Y., Li, J.B., Senaratne, T.N., Williams, B.R., et al. (2012). Versatile design and synthesis platform for visualizing genomes with Oligopaint FISH probes. *Proc. Natl. Acad. Sci. USA* *109*, 21301–21306.
- Bickmore, W.A. (2013). The spatial organization of the human genome. *Annu. Rev. Genomics Hum. Genet.* *14*, 67–84.
- Blackwood, E.M., and Kadonaga, J.T. (1998). Going the distance: a current view of enhancer action. *Science* *281*, 60–63.
- Bourque, G., Leong, B., Vega, V.B., Chen, X., Lee, Y.L., Srinivasan, K.G., Chew, J.-L.L., Ruan, Y., Wei, C.-L.L., Ng, H.H., and Liu, E.T. (2008). Evolution of the mammalian transcription factor binding repertoire via transposable elements. *Genome Res.* *18*, 1752–1762.
- Chadwick, B.P. (2008). DXZ4 chromatin adopts an opposing conformation to that of the surrounding chromosome and acquires a novel inactive X-specific role involving CTCF and antisense transcripts. *Genome Res.* *18*, 1259–1269.
- Cook, P.R., and Brazzel, I.A. (1975). Supercoils in human DNA. *J. Cell Sci.* *19*, 261–279.
- Cremer, T., and Cremer, C. (2001). Chromosome territories, nuclear architecture and gene regulation in mammalian cells. *Nat. Rev. Genet.* *2*, 292–301.
- Cuddapah, S., Jothi, R., Schones, D.E., Roh, T.-Y., Cui, K., and Zhao, K. (2009). Global analysis of the insulator binding protein CTCF in chromatin barrier regions reveals demarcation of active and repressive domains. *Genome Res.* *19*, 24–32.
- Cullen, K.E., Kladde, M.P., and Seyfred, M.A. (1993). Interaction between transcription regulatory regions of prolactin chromatin. *Science* *261*, 203–206.
- Dekker, J., Rippe, K., Dekker, M., and Kleckner, N. (2002). Capturing chromosome conformation. *Science* *295*, 1306–1311.
- Dixon, J.R., Selvaraj, S., Yue, F., Kim, A., Li, Y., Shen, Y., Hu, M., Liu, J.S., and Ren, B. (2012). Topological domains in mammalian genomes identified by analysis of chromatin interactions. *Nature* *485*, 376–380.
- Dostie, J., Richmond, T.A., Arnaout, R.A., Selzer, R.R., Lee, W.L., Honan, T.A., Rubio, E.D., Krumm, A., Lamb, J., Nusbaum, C., et al. (2006). Chromosome Conformation Capture Carbon Copy (5C): a massively parallel solution for mapping interactions between genomic elements. *Genome Res.* *16*, 1299–1309.
- ENCODE Project Consortium (2012). An integrated encyclopedia of DNA elements in the human genome. *Nature* *489*, 57–74.
- Finlan, L.E., Sproul, D., Thomson, I., Boyle, K., Kerr, E., Perry, P., Ylstra, B., Chubb, J.R., and Bickmore, W.A. (2008). Recruitment to the nuclear periphery can alter expression of genes in human cells. *PLoS Genet.* *4*, e1000039.
- Fullwood, M.J., Liu, M.H., Pan, Y.F., Liu, J., Xu, H., Mohamed, Y.B., Orlov, Y.L., Velkov, S., Ho, A., Mei, P.H., et al. (2009). An oestrogen-receptor-alpha-bound human chromatin interactome. *Nature* *462*, 58–64.
- Gaszner, M., and Felsenfeld, G. (2006). Insulators: exploiting transcriptional and epigenetic mechanisms. *Nat. Rev. Genet.* *7*, 703–713.
- Gavrilov, A.A., Gushchanskaya, E.S., Strelkova, O., Zhironkina, O., Kireev, I.I., Iarovaia, O.V., and Razin, S.V. (2013). Disclosure of a structural milieu for the proximity ligation reveals the elusive nature of an active chromatin hub. *Nucleic Acids Res.* *41*, 3563–3575.
- Hahn, M.A., Wu, X., Li, A.X., Hahn, T., and Pfeifer, G.P. (2011). Relationship between gene body DNA methylation and intragenic H3K9me3 and H3K36me3 chromatin marks. *PLoS ONE* *6*, e18844.
- Heidari, N., Phanstiel, D.H., He, C., Grubert, F., Jahanbani, F., Kasowski, M., Zhang, M.Q., and Snyder, M.P. (2014). Genome-wide map of regulatory interactions in the human genome. *Genome Res.* Published online September 16, 2014. <http://dx.doi.org/10.1101/gr.176586.114>.
- Hoffman, M.M., Ernst, J., Wilder, S.P., Kundaje, A., Harris, R.S., Libbrecht, M., Giardine, B., Ellenbogen, P.M., Bilmes, J.A., Birney, E., et al. (2013). Integrative annotation of chromatin elements from ENCODE data. *Nucleic Acids Res.* *41*, 827–841.
- Horakova, A.H., Moseley, S.C., McLaughlin, C.R., Tremblay, D.C., and Chadwick, B.P. (2012). The macrosatellite DXZ4 mediates CTCF-dependent long-range intrachromosomal interactions on the human inactive X chromosome. *Hum. Mol. Genet.* *21*, 4367–4377.
- Hou, C., Zhao, H., Tanimoto, K., and Dean, A. (2008). CTCF-dependent enhancer-blocking by alternative chromatin loop formation. *Proc. Natl. Acad. Sci. USA* *105*, 20398–20403.
- Jin, F., Li, Y., Dixon, J.R., Selvaraj, S., Ye, Z., Lee, A.Y., Yen, C.-A., Schmitt, A.D., Espinoza, C.A., and Ren, B. (2013). A high-resolution map of the three-dimensional chromatin interactome in human cells. *Nature* *503*, 290–294.

- Kalhor, R., Tjong, H., Jayathilaka, N., Alber, F., and Chen, L. (2012). Genome architectures revealed by tethered chromosome conformation capture and population-based modeling. *Nat. Biotechnol.* *30*, 90–98.
- Knight, P., and Ruiz, D. (2012). A fast algorithm for matrix balancing. *IMA J. Numer. Anal.* Published online October 26, 2012. <http://dx.doi.org/10.1093/imanum/drs019>.
- Li, H., and Durbin, R. (2010). Fast and accurate long-read alignment with Burrows-Wheeler transform. *Bioinformatics* *26*, 589–595.
- Li, G., Ruan, X., Auerbach, R.K., Sandhu, K.S., Zheng, M., Wang, P., Poh, H.M., Goh, Y., Lim, J., Zhang, J., et al. (2012). Extensive promoter-centered chromatin interactions provide a topological basis for transcription regulation. *Cell* *148*, 84–98.
- Lieberman-Aiden, E., van Berkum, N.L., Williams, L., Imakaev, M., Ragooczy, T., Telling, A., Amit, I., Lajoie, B.R., Sabo, P.J., Dorschner, M.O., et al. (2009). Comprehensive mapping of long-range interactions reveals folding principles of the human genome. *Science* *326*, 289–293.
- McKenna, A., Hanna, M., Banks, E., Sivachenko, A., Cibulskis, K., Kernysky, A., Garimella, K., Altshuler, D., Gabriel, S., Daly, M., and DePristo, M.A. (2010). The Genome Analysis Toolkit: a MapReduce framework for analyzing next-generation DNA sequencing data. *Genome Res.* *20*, 1297–1303.
- Mukherjee, S., Erickson, H., and Bastia, D. (1988). Enhancer-origin interaction in plasmid R6K involves a DNA loop mediated by initiator protein. *Cell* *52*, 375–383.
- Nagano, T., Lubling, Y., Stevens, T.J., Schoenfelder, S., Yaffe, E., Dean, W., Laue, E.D., Tanay, A., and Fraser, P. (2013). Single-cell Hi-C reveals cell-to-cell variability in chromosome structure. *Nature* *502*, 59–64.
- Nora, E.P., Lajoie, B.R., Schulz, E.G., Giorgetti, L., Okamoto, I., Servant, N., Piolot, T., van Berkum, N.L., Meisig, J., Sedat, J., et al. (2012). Spatial partitioning of the regulatory landscape of the X-inactivation centre. *Nature* *485*, 381–385.
- 1000 Genomes Project Consortium, Abecasis, G.R., Auton, A., Brooks, L.D., DePristo, M.A., Durbin, R.M., Handsaker, R.E., Kang, H.M., Marth, G.T., and McVean, G.A. (2012). An integrated map of genetic variation from 1,092 human genomes. *Nature* *491*, 56–65.
- Phillips, J.E., and Corces, V.G. (2009). CTCF: master weaver of the genome. *Cell* *137*, 1194–1211.
- Sanyal, A., Lajoie, B.R., Jain, G., and Dekker, J. (2012). The long-range interaction landscape of gene promoters. *Nature* *489*, 109–113.
- Schleif, R. (1992). DNA looping. *Annu. Rev. Biochem.* *61*, 199–223.
- Schmidt, D., Schwalie, P.C., Wilson, M.D., Ballester, B., Gonçalves, A., Kutter, C., Brown, G.D., Marshall, A., Fliecek, P., and Odom, D.T. (2012). Waves of retrotransposon expansion remodel genome organization and CTCF binding in multiple mammalian lineages. *Cell* *148*, 335–348.
- Sexton, T., Schober, H., Fraser, P., and Gasser, S.M. (2007). Gene regulation through nuclear organization. *Nat. Struct. Mol. Biol.* *14*, 1049–1055.
- Sexton, T., Yaffe, E., Kenigsberg, E., Bantignies, F., Leblanc, B., Hoichman, M., Parrinello, H., Tanay, A., and Cavalli, G. (2012). Three-dimensional folding and functional organization principles of the *Drosophila* genome. *Cell* *148*, 458–472.
- Splinter, E., Heath, H., Kooren, J., Palstra, R.-J., Klous, P., Grosveld, F., Galjart, N., and de Laat, W. (2006). CTCF mediates long-range chromatin looping and local histone modification in the beta-globin locus. *Genes Dev.* *20*, 2349–2354.
- Tolhuis, B., Palstra, R.J., Splinter, E., Grosveld, F., and de Laat, W. (2002). Looping and interaction between hypersensitive sites in the active beta-globin locus. *Mol. Cell* *10*, 1453–1465.
- Vogel, M.J., Guelen, L., de Wit, E., Peric-Hupkes, D., Lodén, M., Talhout, W., Feenstra, M., Abbas, B., Classen, A.K., and van Steensel, B. (2006). Human heterochromatin proteins form large domains containing KRAB-ZNF genes. *Genome Res.* *16*, 1493–1504.
- Vogelstein, B., Pardoll, D.M., and Coffey, D.S. (1980). Supercoiled loops and eucaryotic DNA replicaton. *Cell* *22*, 79–85.
- Xie, X., Mikkelsen, T.S., Gnirke, A., Lindblad-Toh, K., Kellis, M., and Lander, E.S. (2007). Systematic discovery of regulatory motifs in conserved regions of the human genome, including thousands of CTCF insulator sites. *Proc. Natl. Acad. Sci. USA* *104*, 7145–7150.
- Yaffe, E., and Tanay, A. (2011). Probabilistic modeling of Hi-C contact maps eliminates systematic biases to characterize global chromosomal architecture. *Nat. Genet.* *43*, 1059–1065.
- Zehnbaauer, B.A., and Vogelstein, B. (1985). Supercoiled loops and the organization of replication and transcription in eukaryotes. *BioEssays* *2*, 52–54.

COLD1 Confers Chilling Tolerance in Rice

Yun Ma,^{1,7} Xiaoyan Dai,^{1,7} Yunyuan Xu,^{1,7} Wei Luo,^{1,7} Xiaoming Zheng,² Dali Zeng,³ Yajun Pan,⁴ Xiaoli Lin,¹ Huanhuan Liu,¹ Dajian Zhang,¹ Jun Xiao,¹ Xiaoyu Guo,¹ Shujuan Xu,¹ Yuda Niu,¹ Jingbo Jin,¹ Hui Zhang,¹ Xun Xu,⁵ Legong Li,⁴ Wen Wang,⁵ Qian Qian,³ Song Ge,² and Kang Chong^{1,6,*}

¹Key Laboratory of Plant Molecular Physiology, Institute of Botany, Chinese Academy of Sciences, Beijing 100093, China

²State Key Laboratory of Systematic and Evolutionary Botany, Institute of Botany, Chinese Academy of Sciences, Beijing 100093, China

³State Key Laboratory of Rice Biology, China National Rice Research Institute, Chinese Academy of Agricultural Sciences, Hangzhou 310006, China

⁴College of Life Science, Capital Normal University, Beijing 100048, China

⁵State Key Laboratory of Genetic Resources and Evolution, Kunming Institute of Zoology, Chinese Academy of Sciences, Kunming 650223, China

⁶National Center for Plant Gene Research, Beijing 100093, China

⁷Co-first author

*Correspondence: chongk@ibcas.ac.cn

<http://dx.doi.org/10.1016/j.cell.2015.01.046>

SUMMARY

Rice is sensitive to cold and can be grown only in certain climate zones. Human selection of *japonica* rice has extended its growth zone to regions with lower temperature, while the molecular basis of this adaptation remains unknown. Here, we identify the quantitative trait locus *COLD1* that confers chilling tolerance in *japonica* rice. Overexpression of *COLD1^{jap}* significantly enhances chilling tolerance, whereas rice lines with deficiency or downregulation of *COLD1^{jap}* are sensitive to cold. *COLD1* encodes a regulator of G-protein signaling that localizes on plasma membrane and endoplasmic reticulum (ER). It interacts with the G-protein α subunit to activate the Ca^{2+} channel for sensing low temperature and to accelerate G-protein GTPase activity. We further identify that a SNP in *COLD1*, SNP2, originated from Chinese *Oryza rufipogon*, is responsible for the ability of *COLD^{jap/ind}* to confer chilling tolerance, supporting the importance of *COLD1* in plant adaptation.

INTRODUCTION

Rice, which is both a model plant and one that feeds more than half of the world's population (Sasaki and Burr, 2000), evolved in tropical and subtropical areas and is sensitive to chilling stress (Kovach et al., 2007; Saito et al., 2001; Sang and Ge, 2007). Extreme temperature thus represents a key factor limiting global rice plant distribution. Super hybrid rice cultivars produce high yields in tropical or subtropical climates but are frequently harmed by chilling. Therefore, molecular genetic tools have been urgently sought to improve rice chilling tolerance in order to maintain rice production in current regions and expand it into northern areas with lower yearly temperatures.

Asian cultivated rice (*Oryza sativa*) was domesticated from its wild relatives *Oryza nivara* and *O. rufipogon*. It consists of two

major subspecies, *indica* (*O. sativa* ssp. *indica*) and *japonica* (*O. sativa* ssp. *japonica*) (Kovach et al., 2007; Sang and Ge, 2007). Typical *japonica* cultivars, called *temperate japonica*, are grown in regions with lower yearly temperatures and generally exhibit stronger chilling tolerance than do *indica* cultivars. By contrast, some *japonica* cultivars that moved southwest to southeast Asia became tropical ecotypes, referred to as *javanica* or *tropical japonica*. Divergence between *indica* and *japonica* was driven by divergent natural selection imposed by contrasting environmental temperatures (Kovach et al., 2007; Sang and Ge, 2007). During human selection, cultivated rice has undergone significant changes in agricultural traits, such as grain yield, as well as environmental tolerance (Huang et al., 2012; Xu et al., 2012). Several developmental trait-related genes, such as *SH4* and *PROG1*, with signatures of domestication in cultivated rice have been identified using genetic mapping for quantitative trait loci (QTLs) and genome-wide association studies (GWAS) (Huang et al., 2012; Xu et al., 2012). The QTLs responsible for chilling tolerance in rice were mapped, revealing that the corresponding genes affect either seed germination or male sterility (Saito et al., 2001, 2010; Fujino et al., 2008; Koseki et al., 2010), but less is known about the molecular basis of the divergence between the two subspecies in terms of adaptation to the environment and geographical distribution.

Plant cellular adaptations to temperature differences are dependent on specific molecular cellular pathways including Ca^{2+} -mediated signal transduction. Cyclic nucleotide-gated channels (CNGCs) are nonspecific cation channels; in *Arabidopsis*, CNGCs form a family with 20 members and contribute to Ca^{2+} fluxes in various stress responses (Finka et al., 2012; Steinhorst and Kudla, 2013; Swarbreck et al., 2013). In mammals, Ca^{2+} channels interact with heterotrimeric guanine nucleotide-binding protein (G protein) complexes to function in stress responses (Wang and Chong, 2010). The transition of the mammalian G-protein α subunit between an activated state and an inactivated is regulated by G-protein-coupled receptors (GPCRs), which mediate exchange (GDP release and GTP binding), and by regulator of G-protein signaling (RGS), which promotes GTP hydrolysis. Unlike animal G proteins, plant

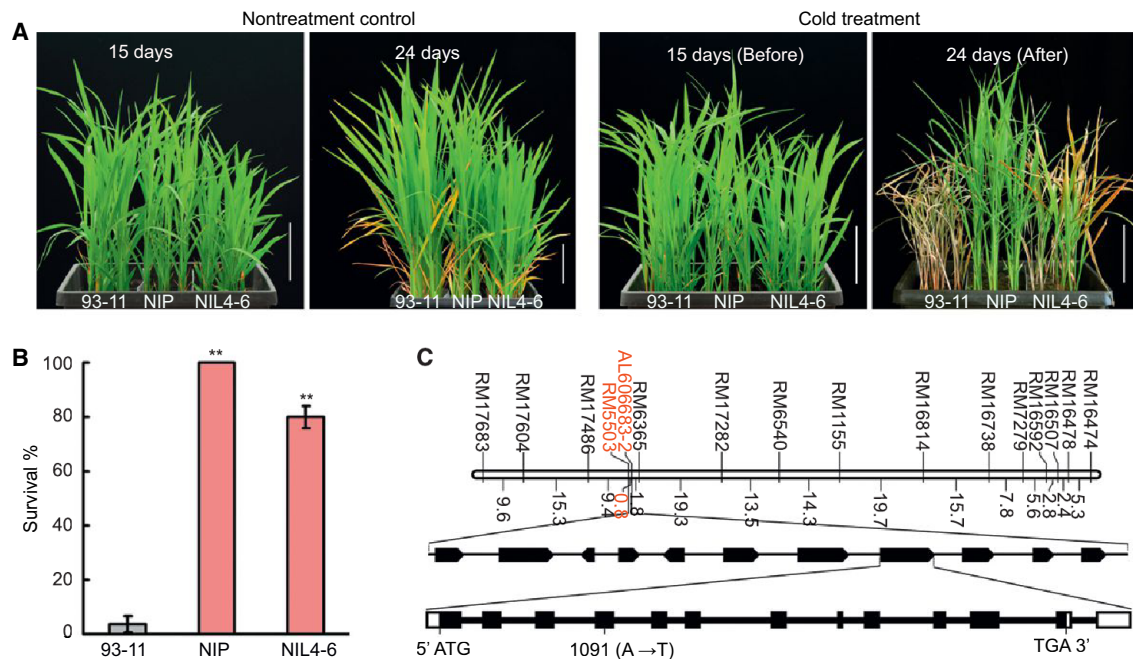


Figure 1. Map-Based Cloning of *COLD1*

(A) Phenotypic response to chilling in 93-11, Nipponbare (NIP), and the homozygote NIL4-6. Scale bars, 5 cm.

(B) The survival rate of 93-11, NIL4-6, and NIP after chilling treatment (96 hr). Values are expressed as mean \pm SD, n = 3, **p < 0.01. See also Figure S1.

(C) The *COLD1* gene was mapped to the interval between the molecular markers AL606683-2 and RM5503 in chromosome 4. The gene was further delimited to a 77.33-kb genomic region on a BAC. Black arrows represent predicted genes. Black rectangles represent exons of *COLD1*.

See also Table S1 and Figure S1.

heterotrimeric G proteins are self-activating and do not utilize GPCRs in converting to the GTP-binding state (Urano et al., 2013). Instead, the RGS with activity of GTPase-accelerating protein (GAP) activity for GTP hydrolysis is more important for G-protein signaling in plant cells. In response to mild heating shock, Ca^{2+} -permeable channels mediate signals that lead to an influx of Ca^{2+} into plant cells (Saidi et al., 2009). Ca^{2+} signaling in plant cells also occurs during cold shock (Knight et al., 1996), although less is known about how the cold shock is linked to Ca^{2+} signaling. Overall, it is well established that Ca^{2+} signaling pathways and the resultant changes in gene transcription are involved in responses to altered temperature in plant cells (Dai et al., 2007; Lee et al., 2009; Ma et al., 2009). However, it is unknown how the signaling pathway in response to cold stimulation evolved during the divergence between rice subspecies *indica* and *japonica*.

Here, we provide evidence that a QTL gene, *CHILLING-TOLERANCE DIVERGENCE 1* (*COLD1*), is associated with divergence in chilling tolerance of rice cultivars. We further demonstrate that a single-nucleotide mutation at *COLD1* confers adaptation of *japonica* rice to chilling and originated from the Chinese wild populations of *O. rufipogon*. *COLD1* localized at the plasma membrane, and endoplasmic reticulum (ER) is involved in sensing cold to trigger Ca^{2+} signaling for chilling tolerance. These findings reveal the importance of *COLD1* in plant adaptation and its great potential for rice molecular breeding.

RESULTS

COLD1 Confers Chilling Tolerance in Rice

Chilling tolerance of rice cultivars is regulated by QTLs derived from the subspecies *japonica* (Saito et al., 2001). To identify the genes involved in the increased chilling tolerance found in cultivars from growth regions with low yearly temperatures, we carried out a QTL analysis for *chilling-tolerance divergence* (*COLD*) in recombinant inbred lines (RILs) generated from a cross between chilling-tolerant Nipponbare (*japonica*) and chilling-sensitive 93-11 (*indica*) cultivars, testing for chilling sensitivity using the cold treatment (4°C) (Figure 1A). Using 151 RILs, we detected five QTLs, on chromosomes 1, 2, 4, 6, and 8 (Table S1). One of them, *COLD1*, was defined between markers RM6365 and RM5503 on the long arm of chromosome 4 (Figure 1C; Table S1). This locus explained 7.23% of the variance in chilling tolerance and shared the same locus with the QTL *Ctb2* despite slight differences in the crossed populations (Saito et al., 2001). The *COLD1* locus displayed much lower interaction with other QTLs for chilling tolerance ($p = 0.0363, 0.0242$) than did the other loci, such as *COLD4* ($p = 0.0002$) and *COLD5* ($p = 0.0006$) (Table S1).

To evaluate whether the Nipponbare (NIP) locus, *COLD1*^{NIP}, contributes to chilling tolerance, we generated three near-isogenic lines (NILs) containing the *COLD1*^{NIP} locus in the 93-11 genetic background, which is one of the parental lines of the Chinese super hybrid rice. The homozygous *COLD1*^{NIP/NIP} lines NIL4-1 and NIL4-6 showed remarkably higher tolerance

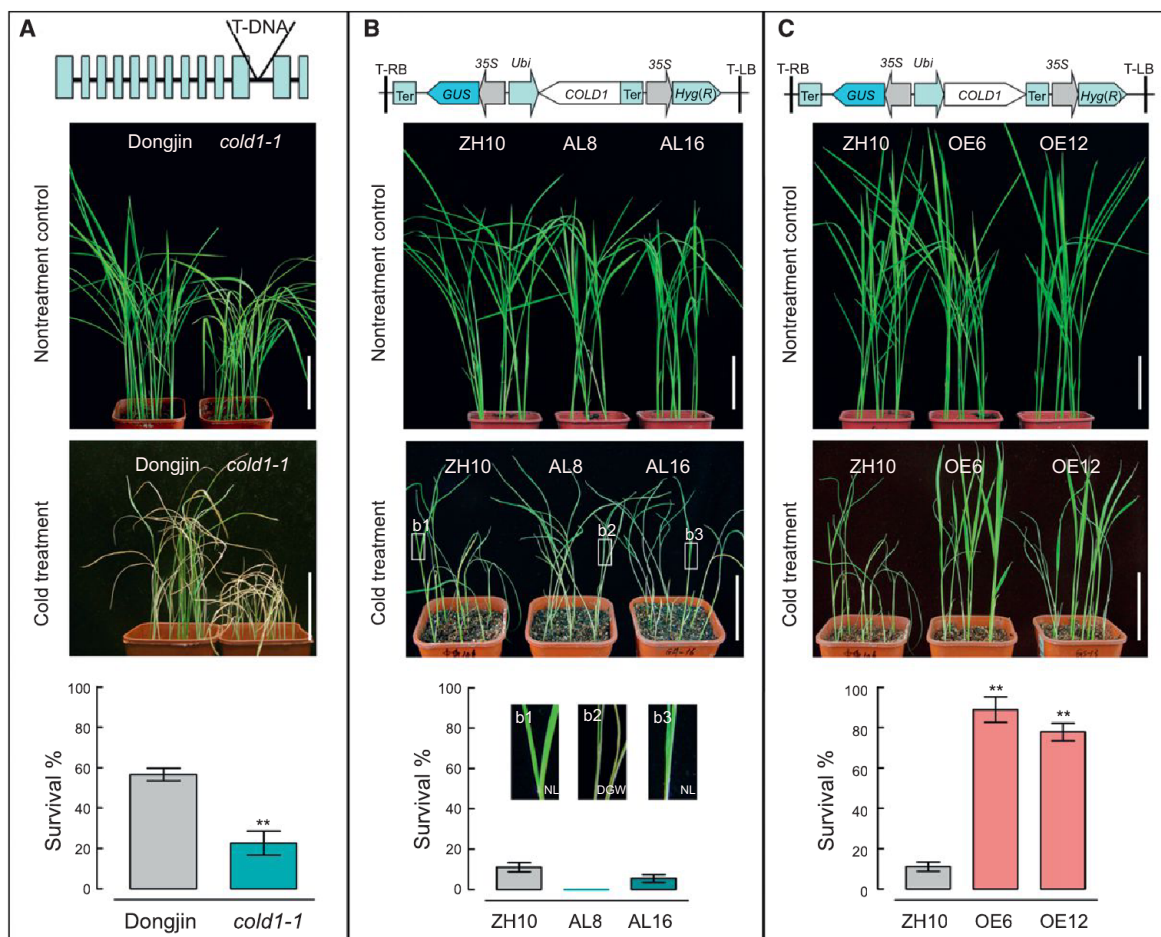


Figure 2. *COLD1* Is Essential for Chilling Tolerance

(A) The *cold1-1* mutant showed chilling sensitivity. The survival rate was determined after treatment at 4°C for 96 hr and subsequent recovery at 30°C for 7 days. (B) The antisense transgenic rice lines (AL8 and AL16) showed chilling sensitivity. The survival rate was determined after treatment at 2°C–3°C for 96 hr and subsequent recovery at 30°C for 4 days. Panes are enlargements of plants showing live seedlings with new leaves (NL) and dead seedlings with dry green and white leaves (DGW).

(C) The overexpression transgenic lines (OE6 and OE12) showed chilling tolerance. The survival rate was determined after treatment at 2°C–3°C for 96 hr and subsequent recovery at 30°C for 4 days. The upper diagrams represent the T-DNA insertion or the transgenes used to generate the lines.

35S, CaV 35S promoter; Ubi, maize ubiquitin promoter; T-RB, T-DNA, right border; T-LB, T-DNA, left border; GUS, β-glucuronidase; Hyg (R), Hygromycin B resistance, Ter, terminator. Values are means ± SD, n = 3. Scale bars, 5 cm. **<0.01. See also Figures S2 and S3.

to chilling compared to 93-11 (Figures 1B and S1). A dominance assay on the heterozygote *COLD1*^{NIP/93-11} NIL2-5 showed that its chilling tolerance was similar to that of NIL4-1 and NIL4-6 (Figure S1). To fine-map *COLD1*, we analyzed 8,368 F₂ plants generated from NIL2-5 and narrowed the candidate region to 77.33 kb between AL606683-2 and RM5503. This region contains 11 predicted genes or open reading frames (Figure 1C; Table S1). Genomic DNA sequence comparisons between the candidate regions of the parents NIP and 93-11 showed that one single-nucleotide mutation at 15th nucleotide in the fourth exon of *COLD1* (A in NIP was changed into T in 93-11) (LOC_Os04 g51180, MSU Rice Genome Annotation (Osa1) release 7. <http://rice.plantbiology.msu.edu>) caused a change in an encoded amino acid (Lys in NIP was changed into Met in 93-11) (Figure 1).

To determine whether the *COLD1* gene underlies the QTL, we constructed *COLD1*^{jap}-overexpression (OE) and antisense (AL) transgenic rice lines in *japonica* cultivar Zhonghua 10 (ZH10) (Figures 2 and S2), and examined their chilling tolerance. In addition, we analyzed the *cold1-1* mutant, which has a T-DNA insertion in the 11th intron of *COLD1*, +3,707 bp downstream from the ATG in the *japonica* rice Dongjin (DJ) background, and which lacks the full-length transcript (Figure S2). Seedlings were exposed to chilling temperature (4°C) and subsequently returned to 30°C. Rice plants with chilling tolerance were defined as those that could re-differentiate new leaves or continue growing leaves when returned normal conditions after treatment with chilling stress. Clear phenotypic differences in the survival rate (percentage alive seedlings of the total tested plants) were observed among these lines (Figures 2 and S2). Seedlings of the *cold1-1*

mutant, as well as of the antisense lines (AL5, AL6, AL8, and AL16) were chilling sensitive compared to the wild-type (WT). By contrast, *COLD1*^{iap}-overexpression lines, such as OE6, OE12, OE1, and OE2, showed higher chilling tolerance than WT. The findings suggest that *COLD1* modulates chilling tolerance in rice.

SNP2 Is Associated with Chilling Tolerance

To test for association between *COLD1* alleles and chilling tolerance, we examined the chilling tolerance of 5 *indica* and 20 *japonica* cultivars, as well as 2 accessions of wild rice (Table S2). All *japonica* cultivars and 2 *O. rufipogon* accessions showed stronger chilling tolerance than did all *indica* cultivars (Figure 3A; Table S2). We then sequenced the full-length *COLD1* gene of 4.78 kb including the 5' and 3' untranslated regions in these samples and identified seven SNPs (Figure 3A), including a synonymous polymorphism in the first exon (SNP1), a nonsynonymous polymorphism only in the fourth exon (SNP2), and five substitutions in introns (SNP3, 4, 5, 6, and 7). We grouped the cultivars based on chilling sensitivity and examined whether chilling tolerance was associated with allelic differences (SNPs) in *COLD1*. Strikingly, all accessions with confirmed chilling tolerance, including 20 *japonica* cultivars and 2 *O. rufipogon* accessions, differed from the *indica* cultivars that lacked the chilling tolerance by the SNP in the fourth exon (SNP2). The nucleotide polymorphism of T/C versus A in the fourth exon resulted in Met¹⁸⁷/Thr¹⁸⁷ in *indica* compared to Lys¹⁸⁷ in *japonica* cultivars. At the remaining SNP sites, polymorphic nucleotides were found in cultivars both with and without chilling tolerance (Figure 3A and Table S3).

To determine whether SNP2 led to alteration of chilling tolerance, we generated transgenic lines overexpressing the gene from *indica* plants (SNP2^{ind(T)}) in the *japonica* ZH11 background (Figures 3 and S3). The *COLD1*^{ind} transgenic lines were more sensitive to chilling compared to ZH11. In addition, the transgenic lines of *COLD1*^{ind} (SNP2^{ind(T)}) in the *cold1-1* mutant background showed a similar chilling tolerance as *cold1-1*, but significantly weaker tolerance than wild-type DJ. By contrast, the transgenic lines of *COLD1*^{iap} (SNP2^{iap(A)}) in the *cold1-1* background showed similar tolerance as wild-type after cold treatment (Figures 3B and S3). Together with the enhanced chilling tolerance observed in the *COLD1*^{iap} (SNP2^{iap(A)}) transgenic lines in wild-type background and that in the *cold1-1* background for the genetic complementation (Figure 2C), this suggests that SNP2, resulting in a change of encoded amino acid, is responsible for chilling tolerance in *japonica* rice.

SNP2 Arose during *japonica* Domestication

To examine the evolutionary origin of the alleles, we sequenced the full-length *COLD1* gene in an additional 100 accessions of cultivated and wild rice, including 36 *indica*, 15 *japonica*, and 15 *javanica* accessions, and 14 *O. nivara* and 19 *O. rufipogon* individuals as well as one *O. barthii* individual (Table S2). All *japonica* accessions, except for two samples displaying heterozygosity, had nucleotide A at the SNP2 site, whereas the *indica* accessions had either T or C, and *javanica* had A or T or C at this site. The five *O. rufipogon* samples originated from China

had A at this site, and one *O. rufipogon* sample from Hainan province in China had W, whereas the remaining wild rice samples including 15 *O. rufipogon* samples from outside of China, 14 *O. nivara* samples and one *O. barthii* sample had either T or C (Table S2).

Geographically, 33 *japonica* cultivars, one *javanica* and the Chinese *O. rufipogon* samples with A at SNP2 were distributed in the northern area of China, Japan, Korea, and the United States, or at higher elevations of the southeast zone of Asia (Figure 3C). By contrast, all samples without A at SNP2, including 41 *indica* and 15 *O. rufipogon* samples from outside of China, were distributed in southern and southeastern Asia, regions with higher yearly temperatures. For *javanica*, 14 samples with nucleotide diversities at the site were distributed in regions of higher yearly temperature, such as southern area of China and the Philippines. Phylogenetic analysis of the *COLD1* sequences of the 72 accessions sampled (Table S2) indicated that all *japonica* accessions and the Chinese *O. rufipogon* samples carrying the chilling-tolerance SNP2^A were grouped together with 60% bootstrap support (Figure 3D). These observations indicate that the *COLD1* allele with the mutation at SNP2^A is likely to have originated from Chinese *O. rufipogon* during *japonica* rice domestication.

To examine whether selection has acted on *COLD1*, we analyzed nucleotide diversity across the sequenced region in 72 accessions (Table S2), including the original 27 accessions tested for chilling tolerance. A comparison of the nucleotide diversity among *indica*, *japonica*, *javanica*, *O. nivara*, and *O. rufipogon* indicated that on average, *japonica* exhibited much lower diversity ($\theta = 0.0004$; $\pi = 0.0002$) than *indica* ($\theta = 0.0014$; $\pi = 0.0013$), *javanica* ($\theta = 0.0025$; $\pi = 0.0017$), and the two wild rice species ($\theta = 0.0014$ – 0.0022 ; $\pi = 0.0010$ – 0.0020). Significantly negative Tajima's *D* values were observed only for *japonica* cultivars (Table S3), consistent with selection at the *COLD1* locus.

To determine further whether the reduction in nucleotide diversity in *japonica* rice could be caused by artificial selection, we conducted MLHKA tests on *COLD1* sequences for all six taxa (Table S3) in reference to seven neutral genes (Zhu et al., 2007). We found a significant value for *japonica* rice ($p = 0.001$), indicative of strong artificial selection on the *COLD1* locus during *japonica* domestication. To exclude the potential impact of demography on diversity reduction at *COLD1*, we further examined the nucleotide diversity for the ten genes within 400-kb region surrounding the *COLD1* locus in 43 accessions (Tables S2 and S3) because selection might lead to a selective sweep in the flanking region of the selected genes (Asano et al., 2011). As expected, we found that the average nucleotide diversity of the ten genes in *japonica* ($\pi = 0.0003$) was much lower than those of all other rice groups ($\pi = 0.0027$ for *indica*; $\pi = 0.0020$ for *javanica*; $\pi = 0.0057$ for wild rice) (Table S3), consistent with the selective sweep argument. A coalescent simulation using the ten surrounding genes revealed a significant lower *K* value (the severity of the bottleneck) in *japonica* ($K = 0.06$) than that of neutral genes ($K = 0.2$) ($p = 0.0097$) (Table S3) (Zhu et al., 2007), indicating that the reduced diversity at the genes surrounding *COLD1* in *japonica* cannot be explained by a domestication bottleneck alone. Taken together, our data

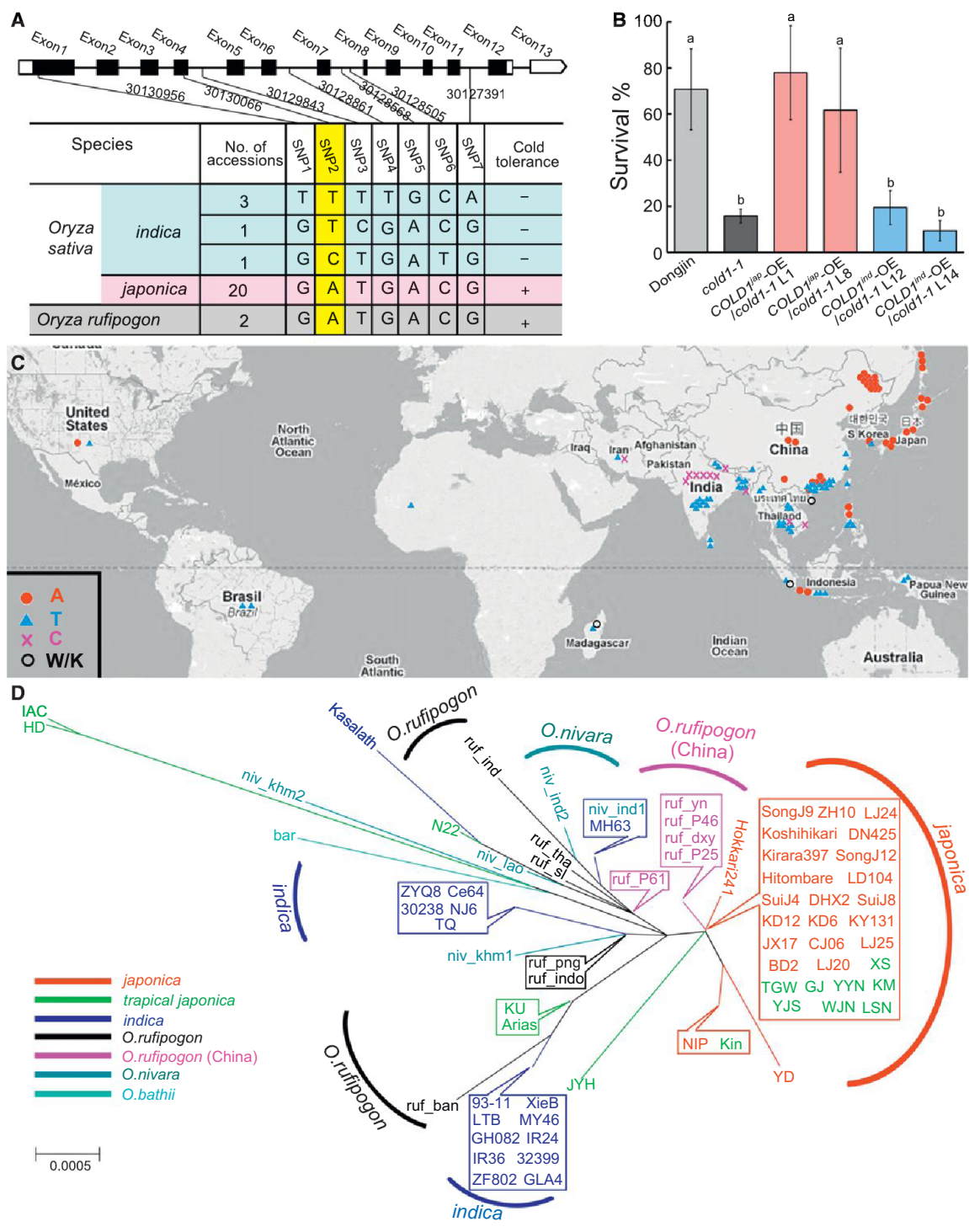
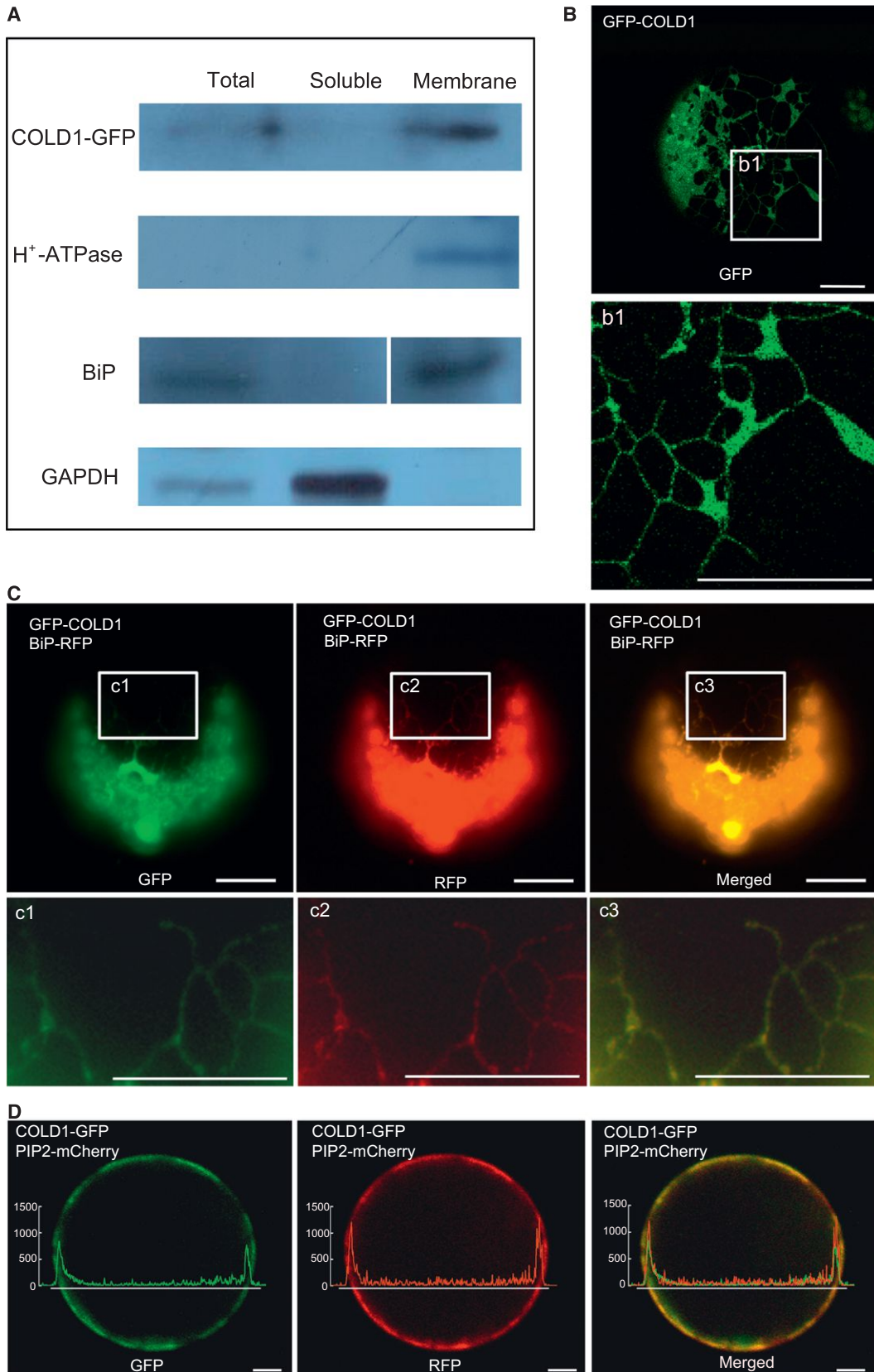


Figure 3. Association of SNPs in *COLD1* with Chilling Tolerance and Their Geographic and Phylogenetic Origins

(A) SNPs and chilling tolerance in 27 accessions.
 (B) Chilling tolerance response of *COLD1* complementation lines in the *cold1-1* genetic background. Values are expressed as means \pm SD, n = 3. Statistically different values (p < 0.05) are indicated by different letters.
 (C) Geographic distribution of 127 accessions tested (Table S2). The *japonica* and *O. rufipogon* samples carrying A at the SNP2 site are represented by red circles. The *indica* cultivars with T/C are denoted by blue triangles/purple crosses, respectively. The heterozygous cultivars [W (A or T)/K (G or T)] are represented by black rings.
 (D) Neighbor-joining tree. Bootstrap values over 60% are given on the branches.
 See also Tables S2 and S3.



(legend on next page)

show that the A at the functional SNP2 of *COLD1* is associated with the development of chilling tolerance in cultivated rice and might represent an ancient allele preserved in the Chinese populations of *O. rufipogon* and selected during domestication of *japonica* rice.

COLD1 Localizes to the ER and Plasma Membrane

COLD1 was predicted to encode a 53-kDa protein with nine transmembrane domains. As expected, it was grouped with its orthologs from the monocotyledons in a phylogenetic tree (Figure S4). Immunoblotting assays on tissues expressing a *COLD1-GFP* fusion transgene showed signal from an anti-GFP antibody only in the membrane protein fraction, similar to the control membrane proteins H⁺-ATPase and BiP, a marker of the endoplasmic reticulum (ER). No signal for *COLD1-GFP* was found in the soluble fractions, although the soluble control of glyceraldehyde-3-phosphate dehydrogenase (GAPDH) protein did show a signal (Figure 4A). Under microscopy, fluorescence of GFP-*COLD1* overlapped with that of BiP-RFP at the ER (Figures 4B, 4C, and S4D) and with that of PIP2-mCherry, a marker for the plasma membrane and ER (Lee et al., 2009), at the plasma membrane (Figure S4E). Similarly, the signal of *COLD1-GFP* co-localized with that of PIP2-mCherry at ER with a reticular pattern and at the plasma membrane (Figures S4F, S4G, and 4D). The plasma membrane localization was independent on the myristoylation of G2 in the N-terminal motif M1-G2-W3 of *COLD1* (Figures S4H and S4I) (Batistic et al., 2008; Yamauchi et al., 2010). These results suggest that *COLD1* is mainly localized to the ER and plasma membrane.

COLD1 Interacts with G-Protein α Subunit

Based on hidden Markov model (Krogh et al., 2001) predictions, *COLD1* contains nine transmembrane domains with a preferred orientation of an extracellular N terminus and an intracellular terminus, similar to the pattern of its *Arabidopsis* orthologs (Figures S4 and S5), GTG1/2, which interact with G-protein α subunit. We confirmed the interaction between *COLD1* and the rice G-protein α subunit 1 (RGA1) (Ludewig et al., 2003; Stagljar et al., 1998) in vitro and in vivo. Yeast cells co-transformed either with *COLD1^{jap}* or *COLD1^{ind}* or *COLD1^{Δjap}* and RGA1 grew well on medium lacking His and Ade and showed X-gal staining, in contrast to the negative controls (Figure S5). In co-immunoprecipitation (Co-IP) assays, GFP-*COLD1* was detected in complexes immunoprecipitated with the anti-FLAG antibody from leaves of transgenic plants expressing GFP-*COLD1* and FLAG-RGA1 (Figure 5A). Bimolecular fluorescence complementation (BiFC) assays revealed reconstituted YFP fluorescence in the

plasma membrane of transgenic lines harboring *COLD1-YFP^C* and *RGA1-YFP^N* (Figure 5B). By contrast, no fluorescence was detected in the negative controls *OsBAK1-YFP^C* and *RGA1-YFP^N*. These data demonstrate that *COLD1* can physically interact with RGA1 in plant cells.

COLD1 Functions as a GTPase-Accelerating Factor on RGA1

Biochemical activity assays confirmed that RGA1 instead of *COLD1* alone had GTPase activity, dependent on Mg²⁺ concentration in the reaction (Figures 5C, 5D, and S5D). RGA1 GTPase activity was accelerated in the presence of *COLD1^{jap}* (SNP^{*jap(A)*}). By contrast, *COLD1^{ind}* (SNP^{*ind(A)*}), as well as the truncated protein *COLD1^{Δjap}* from *cold1-1*, suppressed RGA1 GTPase activity over the course of the assay (Figure 5C). The *COLD1^{jap}*-induced acceleration of RGA1 GTPase activity was impaired by inclusion of *COLD1^{ind}* in the reaction (Figure 5D), which may explain the tolerance differences between *COLD1^{ind}* and *COLD1^{jap}* transgenic lines on the *japonica* background, as well decreased tolerance of *cold1-1* (Figure S3). A time-course assay for the tolerance showed that the RGA1 mutant *d1* was significantly more sensitive to chilling for survival compared with wild-type Shikari (Figure 5E). This is consistent with that the *COLD1* and RGA1 complex is required for the tolerance.

We used an electrode voltage clamp approach to record the currents of oocytes co-expressing *COLD1* and RGA1 (Figure 5F). Upon cold treatment, an inward current was significantly activated in the cells co-expressing *COLD1^{jap}* and RGA1 compared with expression alone, which was in contrast to their patterns showing no response to heat stimulation (40°C) (Figure S5) (Finka et al., 2012). The cold-activated response lagged by several seconds and returned rapidly to baseline levels after removal of cold stimulation. The cold-stimulated inward current was 588 ± 90 nA. By contrast, control cells and oocytes co-expressing *COLD1^{ind}* and RGA1 generated background currents of 373 ± 36 and 246 ± 41 nA, respectively. Co-expression of the truncated gene *COLD1^{Δjap}* and RGA1 led to a weaker inward current in response to cold stimulation than that of *COLD1^{jap}*. This suggests that the cold-stimulated inward current signal is dependent on interaction between *COLD1* and RGA1 in the presence of Ca²⁺. Probably, a complex of *COLD1* that has a GTPase-accelerating on RGA1 may affect influx of cations (such as Ca²⁺) to cause changes of the membrane currents in oocyte cells. The *japonica* allele *COLD1^{jap}* showed a stronger response with RGA1 on the cold-stimulated inward current signal than did the *indica* allele *COLD1^{ind}*.

Figure 4. COLD1 Localization

(A) Immunoblotting assay showing GFP antibody recognized GFP-tagged *COLD1* in the membrane protein fraction from transgenic tobacco. H⁺-ATPase, membrane protein control; BiP, ER marker control; GAPDH, glyceraldehydes-3-phosphate hydrogenase soluble protein control.
 (B) ER localization of *COLD1* in *Arabidopsis* protoplast cells. The b1 images (lower) show enlargements of the regions framed in white (upper).
 (C) Co-localization of *COLD1* with ER marker. GFP-*COLD1* signal was merged with that of the RFP-tagged BiP marker in *Arabidopsis* mesophyll protoplasts. The images with labels c1, c2, and c3 (lower) are enlargements of the regions framed in white (upper). Scale bars, 10 μm.
 (D) Plasma membrane localization of *COLD1* in cells. *COLD1-GFP* signal was merged with that of the PIP2-mCherry (an intrinsic plasma membrane protein) marker in Tobacco mesophyll protoplasts. The fluorescence intensity was scanned with the ImageJ plot profile tool (ImageJ v.1.47; <http://rsbweb.nih.gov/ij/download.html>). y axes are relative pixel intensity. Scale bar, 10 μm.
 All experiments were performed with at least three biological replicates. See also Figure S4.

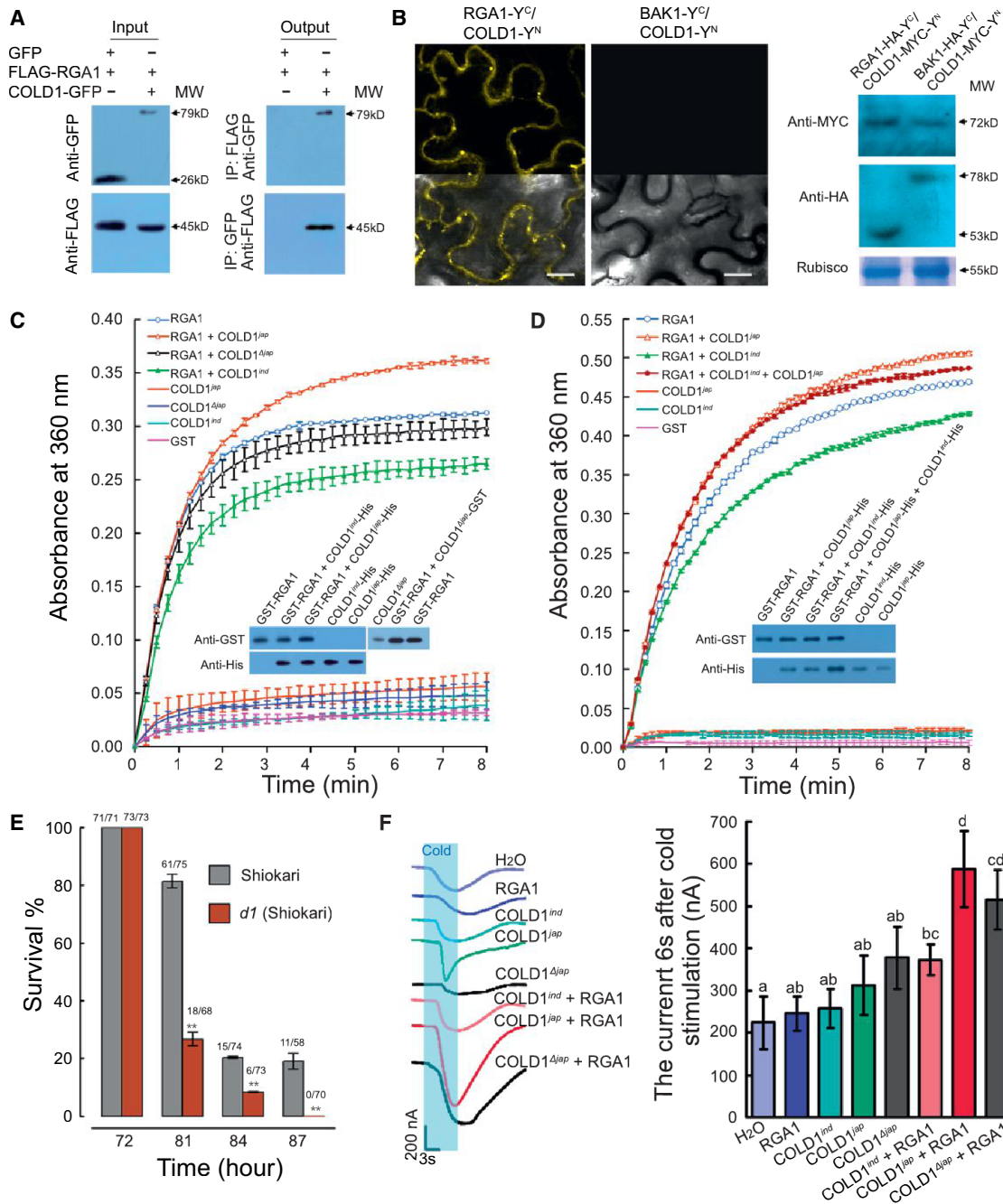


Figure 5. COL1D1 Interacts with RGA1

(A) Co-immunoprecipitation assays confirming the interaction between COL1D1 and RGA1. Co-expressed FLAG-RGA1 and COL1D1-GFP in tobacco leaves were immunoprecipitated by anti-FLAG or -GFP. Blots were probed with by anti-GFP or -FLAG.

(B) BiFC assays showing that the proteins interact in vivo. The bottom ones are the merged images. Immunoblots (right) confirmed the expression of the interaction proteins in the transgenic leaf tissues used in the BiFC assay. Y^N, YN173; Y^C, YCM. Scale bars, 20 μm.

(C) Intrinsic GTPase activity of RGA1 was accelerated by COL1D1^{Δiap} but impaired by COL1D1^{ind} or COL1D1^{Δiap}. The molar ratio of RGA1/COL1D1 was 4.8. Values are expressed as mean ± SD, n = 3. The immunoblots show amount of proteins in the reaction.

(D) Acceleration of RGA1 GTPase activity by COL1D1^{Δiap} was inhibited by addition of COL1D1^{ind} in vitro. The molar ratio of RGA1/COL1D1 was 4.8. Values are expressed as mean ± SD, n = 3. The immunoblots show amount of proteins in the reaction.

(E) Time course of chilling tolerance showing that the *d1* mutant is sensitive to cold treatment. The numbers above the bars are alive and total plants. Values are expressed as mean ± SD, n = 3; **p < 0.01.

(F) Electrophysiological characterization of *Xenopus* oocytes co-expressing COL1D1 and RGA1, as well as the control RGA1 only. The blue background represents a duration for cold treatment in solution. The holding potential was -110 mV.

Values are expressed as means ± SD, n = 7. Statistically different values (p < 0.05) are indicated by different letters. See also Figure S5.

(legend continued on next page)

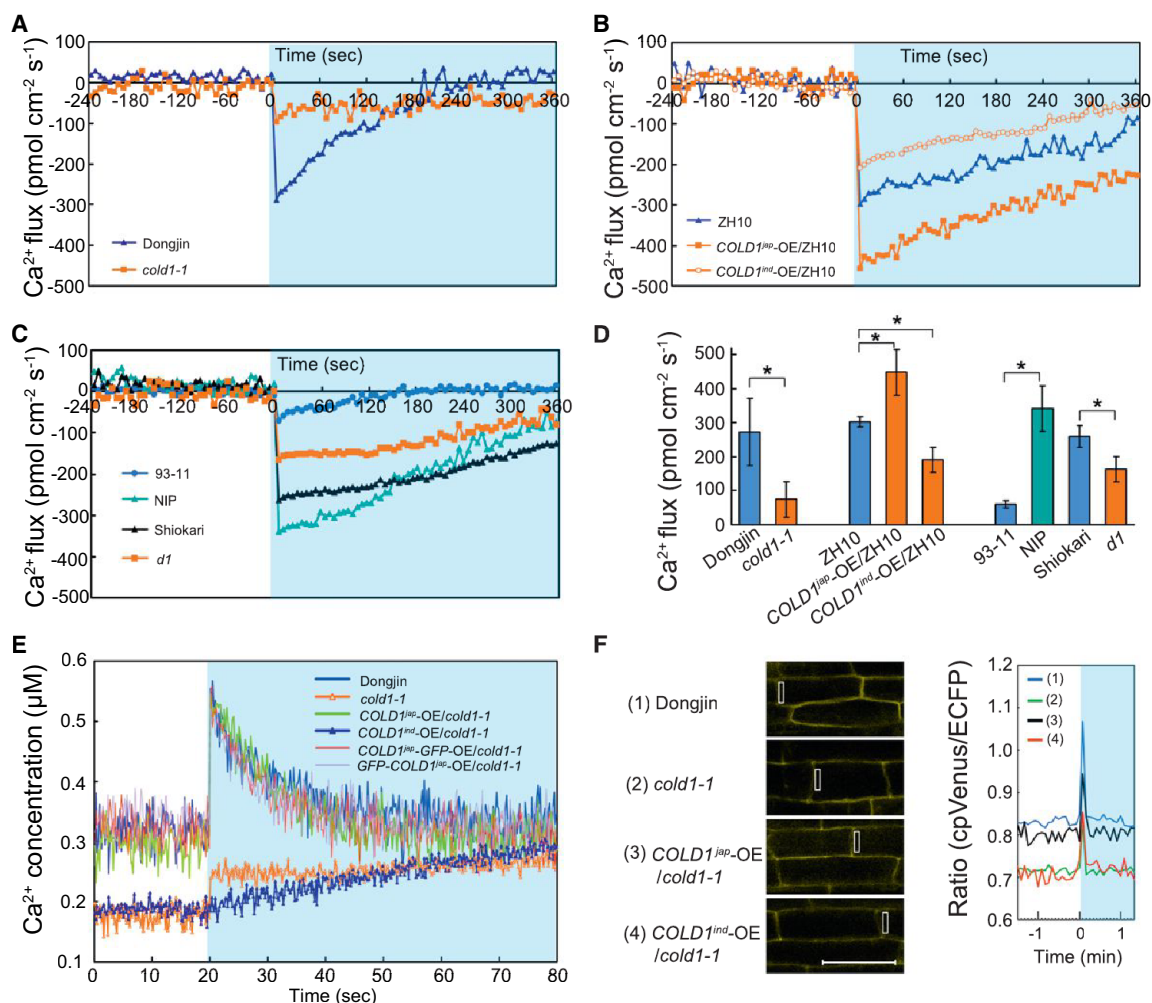


Figure 6. Ca^{2+} Signaling upon Cold Shock in Rice Plants

(A–C) SIET measurements show extracellular Ca^{2+} influx upon cold shock in live roots of various genetic backgrounds ($n > 6$).

(D) Significance testing of the mean maximal Ca^{2+} influxes. Values are expressed as mean \pm SD, $n > 6$, Student's *t* test, * $p < 0.05$.

(E) $[\text{Ca}^{2+}]_{\text{cyt}}$ monitored with aequorin in response to cold shock in wild-type Dongjin and the *cold1-1* mutant ($n > 6$).

(F) Cold response of $[\text{Ca}^{2+}]_{\text{cyt}}$ in live root cells using Yellow Cameleon (NES-YC3.6). Scale bars, 50 μm . The rectangles represent regions of interest (ROIs) considered for ratiometric measurements. The numbers used for ratiometric measurements are indicated in the boxes. The experiments were replicated at least three times. The blue background represents a duration for cold treatment.

See also Figure S6.

COLD1 Is Essential for Changes in Ca^{2+} Influx upon Cold Treatment

To examine Ca^{2+} flux in response to cold shock, we used the scanning ion-selective electrode technique (SIET) on rice roots (Ludewig et al., 2003). Upon cold stimulation, there was a significant influx of extracellular Ca^{2+} with a minus peak in wild-type Dongjin roots (Figures 6A and S6). By contrast, *cold1-1* showed no remarkable changes in SIET signals under the same conditions. Compared with wild-type ZH10, the *COLD1^{ind}-OE* transgenic line exhibited more Ca^{2+} influx in response to cold treatment, but the *COLD1^{ind}-OE* transgenic line displayed less (Figure 6B). Nipponbare, *japonica* rice, showed a stronger response than did *indica* 93-11 (Figure 6C). In addition, the *d1* mutant of *RGA1* showed less Ca^{2+} influx than did wild-type Shiohari. The mean

maximal influxes of cold shock between *cold1-1* or transgenic lines and wild-type were significantly different (Figure 6D). In response to salt stress, by contrast, the overlapped SIET patterns between *cold1-1* and DJ indicated that salt stimulation signaling may be independent to *COLD1* (Figure S6). The extracellular Ca^{2+} influx peaks in response to cold shock hint that the net cytoplasm $[\text{Ca}^{2+}]_{\text{cyt}}$ derived from bulk extracellular Ca^{2+} might be substantially increased.

We also monitored Ca^{2+} concentration in the cytoplasm ($[\text{Ca}^{2+}]_{\text{cyt}}$) using cytosolic aequorin. Immediately upon the onset of cold treatment, Dongjin showed a significant $[\text{Ca}^{2+}]_{\text{cyt}}$ peak up to $0.554 \pm 0.013 \mu\text{M}$ from $0.319 \pm 0.029 \mu\text{M}$ ($n = 7$), which then decreased (Figure 6E). By contrast, *cold1-1* showed a much smaller increase in $[\text{Ca}^{2+}]_{\text{cyt}}$ from 0.177 ± 0.014 to

0.240 ± 0.040 μM (n = 9) and subsequently maintained a nearly stable level under the same conditions (Figure 6E). With regard to calcium level, the cold shock pattern of $[Ca^{2+}]_{cyt}$ in the *COLD1-jap*-complemented lines (harboring either *COLD1^{jap}-GFP* or *GFP-COLD1^{jap}*) (0.545 ± 0.042 μM [n = 6]) nearly overlapped with that of wild-type, whereas the *COLD1^{ind}* transgenic line on *cold1-1* (0.186 ± 0.011 μM [n = 6]) showed similar pattern as *cold1-1* (Figure 6E).

We used the Cameleon technique to further confirm the genetic complementation effect on Ca^{2+} elevation (Krebs et al., 2012). The root cells of DJ showed a remarkable cytoplasm Ca^{2+} peak after cold treatment, while *cold1-1* had a weaker peak, as well as a relatively low basal level (Figure 6F). The complemented lines of *COLD1^{jap}* almost completely rescued the cold-stimulated Ca^{2+} elevation in the *cold1-1* background. It is also notable that the recovered Ca^{2+} patterns of *COLD1^{jap}* included the basal elevation compared to *cold1-1*. By contrast, overexpression *COLD1^{ind}* in *cold1-1* did not rescue Ca^{2+} response in either the peak or basal level. In addition, the trends on fluorescence dyeing data for $[Ca^{2+}]_{cyt}$ cold responses were in accord with these results (Figure S6).

In addition, the genetic complementation lines of *COLD1^{jap}* in *cold1-1* background showed more remarkable cold-induced expression patterns for the stress-specific downstream genes, such as *OsAP2*, *OsDREB1A*, *OsDREB1B*, and *OsDREB1C* than did the overexpression of *COLD1^{ind}* line (Figure S6). Thus, the findings on both the extracellular Ca^{2+} influx and the net cytoplasm $[Ca^{2+}]_{cyt}$ signaling are consistent with the idea that *COLD1* is essential for cold shock-dependent intracellular Ca^{2+} changes in rice.

DISCUSSION

In this work, we identified the QTL *COLD1*, which is required for chilling tolerance in *japonica* rice during the seedling stage. The *COLD1* locus enhanced chilling tolerance in near-isogenic lines NIL4-1 and NIL4-6 from the background cultivar *indica* 93-11 (Figure S1). It is worth noting that mature rice plants of both NILs with chilling tolerance displayed increased seed number per panicle and maintained grain yield per plant compared with 93-11, which is one of the desirable parental lines of the Chinese super hybrid rice. Thus, these NILs could potentially be used as parents of super hybrid rice, conferring chilling tolerance without negative effects on grain yield. This finding, along with the enhanced tolerance of the *COLD1^{jap}* overexpression lines, emphasizes the potential of either genetic or transgenic approaches to improve chilling tolerance for rice breeding.

Chilling tolerance, i.e., the capacity to reestablish differentiation and growth under normal conditions after cold exposure, is a complex trait in seedlings that is controlled by multiple QTLs. Most of the QTLs genetically interacted with each other, resulting in a higher genetic contribution to chilling tolerance in the population. For instance, the *COLD2* QTL interacted genetically either with *COLD4* or *COLD5* resulting in an overall contribution to chilling tolerance of more than 16.8% (Table S1). By contrast, *COLD1* did not genetically interact with other QTLs and already alone contributed 7.23% to overall chilling tolerance. Nucleotide diversity analysis suggested that there was

strong artificial selection on the *COLD1* locus during *japonica* domestication (Tables S2 and S3).

COLD1's topology, localization and interaction with RGA1, as well as its regulatory effects on RGA1 GTPase activity, support the idea that *COLD1* is a RGS with GTPase-accelerating activity, similar to AtRGS1 (Chen et al., 2003; Johnston et al., 2007; Shabala and Newman., 2000; Stagljar et al., 1998; Urano et al., 2012). The subcellular localization pattern of *COLD1* on the ER and plasma membrane partially overlaps those of its *Arabidopsis* orthologs GTG1/2 (Johnston et al., 2007; Pandey et al., 2009), but *COLD1* is different from those GTG1/2 in intrinsic GTPase activity (Jaffé et al., 2012; Pandey et al., 2009). *COLD1* is predicted to contain a Ras GTPase-activating protein domain in the third cytoplasmic loop, and our biochemical data support this. Correspondingly, SNP2^{jap(A)} versus ind(T/C) in fourth exon would cause an amino acid substitution in the third loop (Dong et al., 2007). Genetic complementation of *COLD1^{jap}* instead of *COLD1^{ind}* in *cold1-1* suggests that SNP2 functions in chilling tolerance (Figure 3B). The specific domain involved (i.e., the loop containing a predicted GTPase-activating protein domain) and its effects on GTPase activity, as well as Ca^{2+} signaling and electrophysiological response, are consistent with a *COLD1* biochemical function associated with G-protein signaling. We found that the substitution of Met¹⁸⁷/Thr¹⁸⁷ for Lys¹⁸⁷ in *japonica* cultivars conferred stronger tolerance to chilling. Overexpression of *COLD1^{jap}* also conferred enhanced tolerance. By contrast, the *COLD1^{ind}* transgenic lines exhibited decreased tolerance, which could be explained by competition between *COLD1^{ind}* and *COLD1^{jap}* in interaction with RGA1 for regulation in $[Ca^{2+}]_{cyt}$ level and GTPase activity (Figures 5 and 6).

Our genetic and biochemical analyses of *COLD1* revealed several similarities to mammalian cold receptors and plant heat sensors that lead us to hypothesize that *COLD1* is involved in sensing cold. (1) *COLD1* has broad tissue expression and is plasma- and ER-membrane localized, with nine predicted TM domains. (2) *COLD1* acts as a RGS to accelerate RGA1's GTPase activity and has phenotypic effects on chilling tolerance. (3) Cold-induced changes in Ca^{2+} influx and $[Ca^{2+}]_{cyt}$ are mediated by *COLD1*. (4) Interaction between *COLD1* and RGA1 is required for the cold-induced specific electrophysiological response. (5) Differences in chilling tolerance are observed in *cold1-1*, in transgenic lines harboring various alleles from *japonica* and *indica*, and in the *RGA1* mutant, *d1*.

Cold temperature may be sensed through direct alteration of a sensor's structure and membrane fluidity to trigger cations influx for signaling. Notably, changes on Ca^{2+} signal involve both the resting level in the cytoplasm and the temporal elevation. The *cold1-1* showed lower resting levels of Ca^{2+} , which was genetically rescued by *COLD1^{jap}* (Figure 6). This finding may hint that *COLD1* itself possibly represents a potential calcium permeable channel or a subunit of such a channel. Consequently, changes of this channel function would affect resting $[Ca^{2+}]_{cyt}$, which would influence the amplitudes of Ca^{2+} signals. The potential function of *COLD1* as a cold sensor could be simply explained by the lack of a significant Ca^{2+} gradient in *cold1-1* plants and *COLD1^{ind}*-OE lines in Ca^{2+} resting levels that does not allow the formation of an appropriate Ca^{2+} signal. Therefore, it is appealing to speculate that *COLD1* is involved in sensing cold and that changes in

COLD1 protein structure and membrane fluidity in response to cold might initiate signaling through COLD1's physical interaction with RGA1, leading to Ca^{2+} influx into cytoplasm, which would then trigger downstream responses to chilling stress. Subsequently, accelerated GTPase activity of RGA1 by COLD1 might induce a regression shift on equilibrium between GDP- and GTP-bound states of RGA1 (Urano et al., 2012) (Figure S6).

The strong phenotype of plants with the *COLD1* QTL could result from tight functional interaction of COLD1 with important hormonal pathways. Consequently, an imbalance in COLD1 function likely affects multiple response pathways in this way aggravating the effects of its modulated temperature dependent functionality and thereby leading to significant decreased ability to re-assume growth after chilling stress. In this regard, COLD1 is functionally interconnected with the key gibberellin signaling component D1/RGA1 (Ueguchi-Tanaka et al., 2000) and brassinosteroid signaling, which are involved in regulation of plant height (Hu et al., 2013; Wang et al., 2006). Moreover, D1/RGA1 also affects TUD1, which mediates brassinosteroid signaling to regulate cell proliferation for plant growth and development (Hu et al., 2013; Wang et al., 2006). In addition D1/RGA1 is functionally dependent on SLR of GA signaling pathway for cell elongation (Ueguchi-Tanaka et al., 2000). In fact, our *cold1-1* significantly showed a decrease in plant height compared with wild-type, while plant height of the complemented lines of *cold1-1* with *COLD1* was recovered (Figure S3). Therefore, it is likely that COLD1 exhibits this strong impact on chilling tolerance via the RGA1 by disturbing multiple pathways, such as GA and/or BR signaling pathways (Hu et al., 2013; Wang et al., 2006).

We show here that a SNP of *COLD1* endows *japonica* rice with chilling tolerance, and that the mutation in the coding region of *COLD1* has been fixed in chilling-tolerant *japonica* cultivars. Our phylogenetic and population genetic analyses based on the large number of SNPs identified by resequencing 50 accessions of cultivated and wild rice (Huang et al., 2012; Xu et al., 2012) demonstrate that the chilling-tolerant allele originated from the Chinese *O. rufipogon* populations and was subject to strong human selection during *japonica* domestication, similar to the case of the *SD1* gene for *japonica* domestication (Asano et al., 2011). Therefore, genomic segments bearing agronomic traits can originate in one population and spread across all cultivars through artificial selection (He et al., 2011). Our findings are consistent with archaeological and genetic evidence that *japonica* rice was domesticated in China (Fuller et al., 2009; Huang et al., 2012; Londo et al., 2006; Xu et al., 2012). Importantly, our work demonstrates that the process of rice domestication was associated with fixation and extension of favored alleles or mutations that enhanced chilling tolerance for growth in regions with lower yearly temperatures. The *COLD1* allele and SNPs identified in this work have great potential for improving rice chilling tolerance via molecular breeding techniques.

EXPERIMENTAL PROCEDURES

Genetic Population and Plant Materials

Oryza sativa recombinant inbred lines (RIL) were developed by crossing *japonica* variety Nipponbare (NIP) and *indica* variety 93-11. The F_2 generation from NIP × 93-11 was subjected to more than six rounds of self-pollination to

generate the RILs. For QTL genetic assay, the RILs were randomly selected. The near-isogenic lines were generated by backcrossing the NIP × 93-11 lines to 93-11 five times to generate BC₅F₂.

The T-DNA insertion mutant *cold1-1* was obtained from Dr G. An. *O. sativa* ssp. *japonica* cv. ZH10/11 and DJ were used for transformation to create the transgenic lines (Jeong et al., 2002). Mutant *cold1-1* was transformed with *COLD1* for a genetic complementation. The primers used for PCR are listed in Table S4.

Chilling Treatment

To test chilling tolerance, the seedlings were treated at 2°C–4°C for various times based on the genetic background. Subsequently, they were moved to a temperature-controlled greenhouse with 28°C–30°C/25°C day/night cycles for recovery. After 3–7 days, the survival rate was determined as the percentage of the total seedlings that were alive (Ma et al., 2009).

SNP Identification, Phylogenetic Analysis, Genetic Diversity, and Neutrality Tests

Full-length *COLD1* gene was sequenced using the tiling format. The primer sequences are listed in Table S4. The gene sequences from 127 samples were aligned using MEGA 5.0 software. A phylogenetic tree was constructed using the neighbor-joining method in MEGA5 (Tamura et al., 2011).

Estimates of nucleotide diversity and population genetic analyses were performed for each group using DnaSP 5.1 (Librado and Rozas, 2009). Tajima's D (Tajima, 1989) and maximum likelihood Hudson-Kreitman-Aguade (MLHKA) (Wright and Charlesworth, 2004) tests were used to examine the departure of *COLD1* polymorphisms from neutrality with a set of known neutral genes, namely, *Adh1*, *GBSSII*, *Ks1*, *Lhs1*, *Os0053*, *SSII1*, and *TFIIA γ -1* (Zhu et al., 2007), as controls. The genome-wide controls with 400-kb regions around *COLD1* in 43 accessions were used for interpret the Tajima's statistics. The coalescent simulation analysis was carried out according to Wu et al. (2013). Details are in Supplemental Information.

Subcellular Localization of COLD1

GFP was fused to COLD1 either at the N or C terminus. Its colocalization assays with marker proteins were carried out in protoplast (*Arabidopsis*, or Tobacco) cells as described previously (Lee et al., 2009). The transformed protoplast cells were examined by a confocal microscopy. See details in Supplemental Information.

Coimmunoprecipitation Assay

Briefly, the recombinant plasmids were co-transformed into tobacco leaves according to Liu et al. (2007). The extracts were incubated with anti-FLAG M2 affinity gel (Sigma) or anti-GFP antibody at 4°C overnight. The antigen-antibody complex was collected. Then the sample was separated on SDS/PAGE gels for immunoblots. See details in Supplemental Information.

Bimolecular Fluorescence Complementation

BIFC experiments and gene transformation were performed as described previously (Stagljar et al., 1998; Waadt et al., 2008; Wang et al., 2009). The vectors were from Dr. J. Kudla. See details in Supplemental Information.

Expression and Purification in *Spodoptera frugiperda*

Protein expression and purification of COLD1 in the cells of *Spodoptera frugiperda* (Sf9) were performed as previously described (Wu et al., 2010). Affinity chromatography was used in protein purification. See details in Supplemental Information.

GTPase Activity Assay

The GTPase activity of RGA1 was monitored with the Enzcheck Phosphate Assay Kit as described previously (Dong et al., 2007). The amount of the tested protein (RGA1/COLD1 = 10/1 μg) was measured and confirmed in immunoblots using the FLAG antibodies. Amounts loaded were 1/0.1 μg (RGA1/COLD1) for the blot. Details are in Supplemental Information.

Electrophysiological Assay

For electrophysiological analysis, complementary RNA was prepared using the RNA Capping Kit (Stratagene). *Xenopus* oocytes were injected with

cRNA for *COLD1* and *RGA1*, mixed, and used for voltage-clamp experiments. Details are in Supplemental Information.

Extracellular Ca²⁺ Flux and [Ca²⁺]_{cyt} Monitoring

The roots of 3-day-old seedlings were used to monitor Ca²⁺ flux with scanning ion-selective electrode technique (SIET) (Ludewig et al., 2003). The solution of 25°C was replaced with that of 0°C for the cold treatment. [Ca²⁺]_{cyt} in callus was monitored by the cytosolic aequorin method (Saidi et al., 2009). The remaining aequorin was discharged by 1 M CaCl₂ and 10% ethanol. Calibration of cytosolic Ca²⁺ concentration was according to Knight et al. (1996).

For monitoring Ca²⁺ elevation using Yellow Cameleon (YC3.6), whole plants were infected rice (GV3101) containing NES-YC3.6. Roots were used to monitor [Ca²⁺]_{cyt} according to the method described by Krebs et al. (2012). Details are in Supplemental Information.

SUPPLEMENTAL INFORMATION

Supplemental Information includes Extended Experimental Procedures, six figures, and four tables and can be found with this article online at <http://dx.doi.org/10.1016/j.cell.2015.01.046>.

AUTHOR CONTRIBUTIONS

Y.M. performed experiments on phenotypic and biochemical assays. X.D. worked on the transgenic lines. Y.X. designed the experiments, analyzed data, and prepared the manuscript. W.L. performed genetic and evolution experiments. In Q.Q.'s lab, Q.Q. and D.Z. created the genetic population. In S.G.'s lab, S.G. and X.Z. performed analysis of molecular evolution. In W.W.'s lab, W.W. and X.X. performed SNP analysis. In L.L.'s lab, L.L. and Y.P. performed the electrical physiological assay. In J.J.'s lab, J.J. and X.L. performed the protein localization. H.L., D.Z., J.X., X.G., and S.X. performed some experiments on calcium and localization. H.Z. joined in calcium analysis. Y.N. performed gene transformation. K.C. designed all experiments, analyzed data, and wrote the manuscript.

ACKNOWLEDGMENTS

The authors appreciate Dr. Qiang Zhao and Dr. B. Wu for their friendly help with purification of the membrane proteins. We are grateful to Dr. Joerg Kudla for his helpful comments and the kind gifts of constructs. We thank Dr. Gynheung An for the mutant line, and Ms. Rongxi Jiang, and Ms. Yuan Zhao, as well as Mr. Bo Wang for assistance with either gene transformation or molecular assay. We thank Dr. Yongbiao Xue, Dr. Bin Han, and Dr. Zhiyong Wang for their useful comments and help on the project. This work was supported by the Major State Basic Research Program of China (2013CBA01403) and the National Nature Science Foundation (30821007), as well as CAS grants (XDA08010205) to K.C.

Received: November 15, 2014

Revised: December 31, 2014

Accepted: January 14, 2015

Published: February 26, 2015

REFERENCES

Asano, K., Yamasaki, M., Takuno, S., Miura, K., Katagiri, S., Ito, T., Doi, K., Wu, J., Ebana, K., Matsumoto, T., et al. (2011). Artificial selection for a green revolution gene during japonica rice domestication. *Proc. Natl. Acad. Sci. USA* *108*, 11034–11039.

Batistic, O., Sorek, N., Schültke, S., Yalovsky, S., and Kudla, J. (2008). Dual fatty acyl modification determines the localization and plasma membrane targeting of CBL/CIPK Ca²⁺ signaling complexes in *Arabidopsis*. *Plant Cell* *20*, 1346–1362.

Chen, J.G., Willard, F.S., Huang, J., Liang, J., Chasse, S.A., Jones, A.M., and Siderovski, D.P. (2003). A seven-transmembrane RGS protein that modulates plant cell proliferation. *Science* *301*, 1728–1731.

Dai, X., Xu, Y., Ma, Q., Xu, W., Wang, T., Xue, Y., and Chong, K. (2007). Overexpression of an R1R2R3 MYB gene, *OsMYB3R-2*, increases tolerance to freezing, drought, and salt stress in transgenic *Arabidopsis*. *Plant Physiol.* *143*, 1739–1751.

Dong, G., Medkova, M., Novick, P., and Reinisch, K.M. (2007). A catalytic coiled coil: structural insights into the activation of the Rab GTPase Sec4p by Sec2p. *Mol. Cell* *25*, 455–462.

Finka, A., Cuendet, A.F., Maathuis, F.J., Saidi, Y., and Goloubinoff, P. (2012). Plasma membrane cyclic nucleotide gated calcium channels control land plant thermal sensing and acquired thermotolerance. *Plant Cell* *24*, 3333–3348.

Fujino, K., Sekiguchi, H., Matsuda, Y., Sugimoto, K., Ono, K., and Yano, M. (2008). Molecular identification of a major quantitative trait locus, *qLTG3-1*, controlling low-temperature germinability in rice. *Proc. Natl. Acad. Sci. USA* *105*, 12623–12628.

Fuller, D.Q., Qin, L., Zheng, Y., Zhao, Z., Chen, X., Hosoya, L.A., and Sun, G.P. (2009). The domestication process and domestication rate in rice: spikelet bases from the Lower Yangtze. *Science* *323*, 1607–1610.

He, Z., Zhai, W., Wen, H., Tang, T., Wang, Y., Lu, X., Greenberg, A.J., Hudson, R.R., Wu, C.I., and Shi, S. (2011). Two evolutionary histories in the genome of rice: the roles of domestication genes. *PLoS Genet.* *7*, e1002100.

Hu, X., Qian, Q., Xu, T., Zhang, Y., Dong, G., Gao, T., Xie, Q., and Xue, Y. (2013). The U-box E3 ubiquitin ligase TUD1 functions with a heterotrimeric G α subunit to regulate Brassinosteroid-mediated growth in rice. *PLoS Genet.* *9*, e1003391.

Huang, X., Kurata, N., Wei, X., Wang, Z.X., Wang, A., Zhao, Q., Zhao, Y., Liu, K., Lu, H., Li, W., et al. (2012). A map of rice genome variation reveals the origin of cultivated rice. *Nature* *490*, 497–501.

Jaffé, F.W., Freschet, G.E., Valdes, B.M., Runions, J., Terry, M.J., and Williams, L.E. (2012). G protein-coupled receptor-type G proteins are required for light-dependent seedling growth and fertility in *Arabidopsis*. *Plant Cell* *24*, 3649–3668.

Jeong, D.H., An, S., Kang, H.G., Moon, S., Han, J.J., Park, S., Lee, H.S., An, K., and An, G. (2002). T-DNA insertional mutagenesis for activation tagging in rice. *Plant Physiol.* *130*, 1636–1644.

Johnston, C.A., Taylor, J.P., Gao, Y., Kimple, A.J., Grigston, J.C., Chen, J.G., Siderovski, D.P., Jones, A.M., and Willard, F.S. (2007). GTPase acceleration as the rate-limiting step in *Arabidopsis* G protein-coupled sugar signaling. *Proc. Natl. Acad. Sci. USA* *104*, 17317–17322.

Knight, H., Trewavas, A.J., and Knight, M.R. (1996). Cold calcium signaling in *Arabidopsis* involves two cellular pools and a change in calcium signature after acclimation. *Plant Cell* *8*, 489–503.

Koseki, M., Kitazawa, N., Yonebayashi, S., Maehara, Y., Wang, Z.X., and Minobe, Y. (2010). Identification and fine mapping of a major quantitative trait locus originating from wild rice, controlling cold tolerance at the seedling stage. *Mol. Genet. Genomics* *284*, 45–54.

Kovach, M.J., Sweeney, M.T., and McCouch, S.R. (2007). New insights into the history of rice domestication. *Trends Genet.* *23*, 578–587.

Krebs, M., Held, K., Binder, A., Hashimoto, K., Den Herder, G., Parniske, M., Kudla, J., and Schumacher, K. (2012). FRET-based genetically encoded sensors allow high-resolution live cell imaging of Ca²⁺ dynamics. *Plant J.* *69*, 181–192.

Krogh, A., Larsson, B., von Heijne, G., and Sonnhammer, E.L. (2001). Predicting transmembrane protein topology with a hidden Markov model: application to complete genomes. *J. Mol. Biol.* *305*, 567–580.

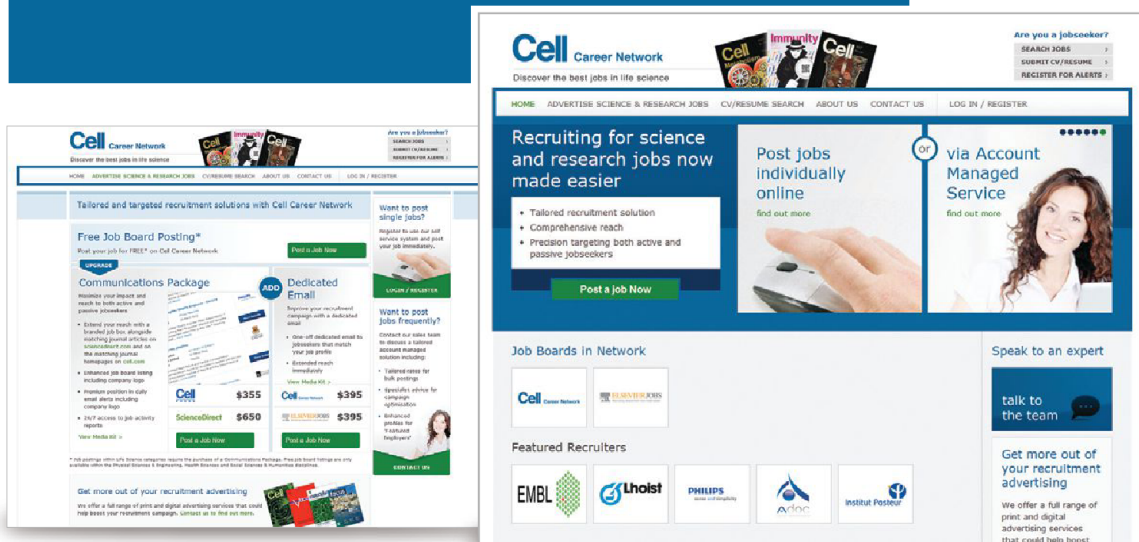
Lee, H.K., Cho, S.K., Son, O., Xu, Z., Hwang, I., and Kim, W.T. (2009). Drought stress-induced Rma1H1, a RING membrane-anchor E3 ubiquitin ligase homolog, regulates aquaporin levels via ubiquitination in transgenic *Arabidopsis* plants. *Plant Cell* *21*, 622–641.

Librado, P., and Rozas, J. (2009). DnaSP v5: a software for comprehensive analysis of DNA polymorphism data. *Bioinformatics* *25*, 1451–1452.

Liu, X., Yue, Y., Li, B., Nie, Y., Li, W., Wu, W.H., and Ma, L. (2007). A G protein-coupled receptor is a plasma membrane receptor for the plant hormone abscisic acid. *Science* *315*, 1712–1716.

- Londo, J.P., Chiang, Y.C., Hung, K.H., Chiang, T.Y., and Schaal, B.A. (2006). Phylogeography of Asian wild rice, *Oryza rufipogon*, reveals multiple independent domestications of cultivated rice, *Oryza sativa*. *Proc. Natl. Acad. Sci. USA* *103*, 9578–9583.
- Ludewig, U., Wilken, S., Wu, B., Jost, W., Obrdlík, P., El Bakkoury, M., Marini, A.M., André, B., Hamacher, T., Boles, E., et al. (2003). Homo- and hetero-oligomerization of ammonium transporter-1 NH₄⁺ uniporters. *J. Biol. Chem.* *278*, 45603–45610.
- Ma, Q., Dai, X., Xu, Y., Guo, J., Liu, Y., Chen, N., Xiao, J., Zhang, D., Xu, Z., Zhang, X., and Chong, K. (2009). Enhanced tolerance to chilling stress in *Os-MYB3R-2* transgenic rice is mediated by alteration in cell cycle and ectopic expression of stress genes. *Plant Physiol.* *150*, 244–256.
- Pandey, S., Nelson, D.C., and Assmann, S.M. (2009). Two novel GPCR-type G proteins are abscisic acid receptors in *Arabidopsis*. *Cell* *136*, 136–148.
- Saidi, Y., Finka, A., Muriset, M., Bromberg, Z., Weiss, Y.G., Maathuis, F.J., and Goloubinoff, P. (2009). The heat shock response in moss plants is regulated by specific calcium-permeable channels in the plasma membrane. *Plant Cell* *21*, 2829–2843.
- Saito, K., Miura, K., Nagano, K., Hayano-Saito, Y., Araki, H., and Kato, A. (2001). Identification of two closely linked quantitative trait loci for cold tolerance on chromosome 4 of rice and their association with anther length. *Theor. Appl. Genet.* *103*, 862–868.
- Saito, K., Hayano-Saito, Y., Kuroki, M., and Sato, Y. (2010). Map-based cloning of the rice cold tolerance gene *Ctb1*. *Plant Sci.* *179*, 97–102.
- Sang, T., and Ge, S. (2007). Genetics and phylogenetics of rice domestication. *Curr. Opin. Genet. Dev.* *17*, 533–538.
- Sasaki, T., and Burr, B. (2000). International Rice Genome Sequencing Project: the effort to completely sequence the rice genome. *Curr. Opin. Plant Biol.* *3*, 138–141.
- Shabala, S., and Newman, I. (2000). Salinity effects on the activity of plasma membrane H⁺ and Ca²⁺ transporters in bean leaf mesophyll: Masking role of the cell wall. *Ann. Bot. (Lond.)* *85*, 681–686.
- Stagljar, I., Korostensky, C., Johnsson, N., and te Heesen, S. (1998). A genetic system based on split-ubiquitin for the analysis of interactions between membrane proteins in vivo. *Proc. Natl. Acad. Sci. USA* *95*, 5187–5192.
- Steinhorst, L., and Kudla, J. (2013). Calcium and reactive oxygen species rule the waves of signaling. *Plant Physiol.* *163*, 471–485.
- Swarbreck, S.M., Colaço, R., and Davies, J.M. (2013). Plant calcium-permeable channels. *Plant Physiol.* *163*, 514–522.
- Tajima, F. (1989). Statistical method for testing the neutral mutation hypothesis by DNA polymorphism. *Genetics* *123*, 585–595.
- Tamura, K., Peterson, D., Peterson, N., Stecher, G., Nei, M., and Kumar, S. (2011). MEGA5: molecular evolutionary genetics analysis using maximum likelihood, evolutionary distance, and maximum parsimony methods. *Mol. Biol. Evol.* *28*, 2731–2739.
- Ueguchi-Tanaka, M., Fujisawa, Y., Kobayashi, M., Ashikari, M., Iwasaki, Y., Kitano, H., and Matsuoka, M. (2000). Rice dwarf mutant d1, which is defective in the alpha subunit of the heterotrimeric G protein, affects gibberellin signal transduction. *Proc. Natl. Acad. Sci. USA* *97*, 11638–11643.
- Urano, D., Phan, N., Jones, J.C., Yang, J., Huang, J., Grigston, J., Taylor, J.P., and Jones, A.M. (2012). Endocytosis of the seven-transmembrane RGS1 protein activates G-protein-coupled signalling in *Arabidopsis*. *Nat. Cell Biol.* *14*, 1079–1088.
- Urano, D., Chen, J.G., Botella, J.R., and Jones, A.M. (2013). Heterotrimeric G protein signalling in the plant kingdom. *Open Biol.* *3*, 120186.
- Waadt, R., Schmidt, L.K., Lohse, M., Hashimoto, K., Bock, R., and Kudla, J. (2008). Multicolor bimolecular fluorescence complementation reveals simultaneous formation of alternative CBL/CIPK complexes in planta. *Plant J.* *56*, 505–516.
- Wang, L., and Chong, K. (2010). Signaling and communication in plants. In *Integrated G Proteins Signaling in Plants*, S. Yalovsky, F. Baluska, and A. Jones, eds. (Springer), pp. 1–25.
- Wang, L., Xu, Y.Y., Ma, Q.B., Li, D., Xu, Z.H., and Chong, K. (2006). Heterotrimeric G protein alpha subunit is involved in rice brassinosteroid response. *Cell Res.* *16*, 916–922.
- Wang, L., Wang, Z., Xu, Y., Joo, S.H., Kim, S.K., Xue, Z., Xu, Z., Wang, Z., and Chong, K. (2009). OsGSR1 is involved in crosstalk between gibberellins and brassinosteroids in rice. *Plant J.* *57*, 498–510.
- Wright, S.I., and Charlesworth, B. (2004). The HKA test revisited: a maximum-likelihood-ratio test of the standard neutral model. *Genetics* *168*, 1071–1076.
- Wu, B., Chien, E.Y., Mol, C.D., Fenalti, G., Liu, W., Katritch, V., Abagyan, R., Brooun, A., Wells, P., Bi, F.C., et al. (2010). Structures of the CXCR4 chemokine GPCR with small-molecule and cyclic peptide antagonists. *Science* *330*, 1066–1071.
- Wu, W., Zheng, X.M., Lu, G., Zhong, Z., Gao, H., Chen, L., Wu, C., Wang, H.J., Wang, Q., Zhou, K., et al. (2013). Association of functional nucleotide polymorphisms at DTH2 with the northward expansion of rice cultivation in Asia. *Proc. Natl. Acad. Sci. USA* *110*, 2775–2780.
- Xu, X., Liu, X., Ge, S., Jensen, J.D., Hu, F., Li, X., Dong, Y., Gutenkunst, R.N., Fang, L., Huang, L., et al. (2012). Resequencing 50 accessions of cultivated and wild rice yields markers for identifying agronomically important genes. *Nat. Biotechnol.* *30*, 105–111.
- Yamauchi, S., Fusada, N., Hayashi, H., Utsumi, T., Uozumi, N., Endo, Y., and Tozawa, Y. (2010). The consensus motif for N-myristoylation of plant proteins in a wheat germ cell-free translation system. *FEBS J.* *277*, 3596–3607.
- Zhu, Q., Zheng, X., Luo, J., Gaut, B.S., and Ge, S. (2007). Multilocus analysis of nucleotide variation of *Oryza sativa* and its wild relatives: severe bottleneck during domestication of rice. *Mol. Biol. Evol.* *24*, 875–888.

Cell Career Network just got better!



- Additional reach via extended network
- Post a job within 5 minutes via self service
- More intuitive feel and easier navigation
- New vacancy packages and pricing

Your recruitment process just became even easier.
Get started today!

careers.cell.com/recruiters



Cell
PRESS

Prospective Derivation of a Living Organoid Biobank of Colorectal Cancer Patients

Marc van de Wetering,^{1,2,12} Hayley E. Francies,^{3,12} Joshua M. Francis,^{4,5,12} Gergana Bounova,⁶ Francesco Iorio,⁷ Apollo Pronk,⁸ Winan van Houdt,⁸ Joost van Gorp,⁹ Amaro Taylor-Weiner,⁴ Lennart Kester,¹ Anne McLaren-Douglas,³ Joyce Blokker,^{1,2} Sridevi Jaksani,^{1,2} Sina Bartfeld,¹ Richard Volckman,¹⁰ Peter van Sluis,¹⁰ Vivian S.W. Li,¹¹ Sara Seepo,⁴ Chandra Sekhar Pedamallu,^{4,5} Kristian Cibulskis,⁴ Scott L. Carter,^{4,5} Aaron McKenna,⁴ Michael S. Lawrence,⁴ Lee Lichtenstein,⁴ Chip Stewart,⁴ Jan Koster,¹⁰ Rogier Versteeg,¹⁰ Alexander van Oudenaarden,¹ Julio Saez-Rodriguez,⁷ Robert G.J. Vries,^{1,2} Gad Getz,^{4,5} Lodewyk Wessels,⁶ Michael R. Stratton,³ Ultan McDermott,³ Matthew Meyerson,^{4,5} Mathew J. Garnett,^{3,*} and Hans Clevers^{1,2,*}

¹Hubrecht Institute, Royal Netherlands Academy of Arts and Sciences (KNAW), Cancer Genomics and University Medical Center, 3584 CT Utrecht, the Netherlands

²Foundation Hubrecht Organoid Technology (HUB), 3584 CT Utrecht, the Netherlands

³Wellcome Trust Sanger Institute, Wellcome Trust Genome Campus, Hinxton, Cambridgeshire CB10 1SA, UK

⁴The Broad Institute of MIT and Harvard, Cambridge, MA 02142, USA

⁵Department of Medical Oncology, Dana-Farber Cancer Institute, Boston, MA 02115, USA

⁶Computational Cancer Biology, Netherlands Cancer Institute, 1066 CX Amsterdam, the Netherlands

⁷European Molecular Biology Laboratory, European Bioinformatics Institute, Wellcome Trust Genome Campus, Cambridge CB10 1SA, UK

⁸Department of Surgery, Diakonessenhuis, 3582 KE Utrecht, the Netherlands

⁹Department of Pathology, Diakonessenhuis, 3582 KE Utrecht, the Netherlands

¹⁰Department of Oncogenomics, Academic Medical Center, University of Amsterdam, 1105 AZ Amsterdam, the Netherlands

¹¹Division of Stem Cell Biology and Developmental Genetics, MRC National Institute for Medical Research, The Ridgeway, Mill Hill, London NW7 1AA, UK

¹²Co-first author

*Correspondence: mg12@sanger.ac.uk (M.J.G.), h.clevers@hubrecht.eu (H.C.)

<http://dx.doi.org/10.1016/j.cell.2015.03.053>

SUMMARY

In R-spondin-based 3D cultures, *Lgr5* stem cells from multiple organs form ever-expanding epithelial organoids that retain their tissue identity. We report the establishment of tumor organoid cultures from 20 consecutive colorectal carcinoma (CRC) patients. For most, organoids were also generated from adjacent normal tissue. Organoids closely recapitulate several properties of the original tumor. The spectrum of genetic changes within the “living biobank” agrees well with previous large-scale mutational analyses of CRC. Gene expression analysis indicates that the major CRC molecular subtypes are represented. Tumor organoids are amenable to high-throughput drug screens allowing detection of gene-drug associations. As an example, a single organoid culture was exquisitely sensitive to Wnt secretion (porcupine) inhibitors and carried a mutation in the negative Wnt feedback regulator *RNF43*, rather than in *APC*. Organoid technology may fill the gap between cancer genetics and patient trials, complement cell-line- and xenograft-based drug studies, and allow personalized therapy design.

INTRODUCTION

Colorectal carcinoma (CRC) represents one of the major forms of cancer. Seminal studies have revealed a series of molecular

pathways that are critical to the pathogenesis of CRC, including WNT, RAS-MAPK, PI3K, P53, TGF- β , and DNA mismatch repair (Fearon, 2011; Fearon and Vogelstein, 1990). Large-scale sequencing analyses have dramatically extended the list of recurrently mutated genes and chromosomal translocations (Garraway and Lander, 2013; Vogelstein et al., 2013). CRC cases are characterized by either microsatellite instability (MSI) (associated with a hyper-mutator phenotype), or as microsatellite-stable (MSS) but chromosomally unstable (CIN) (Lengauer et al., 1997). The absolute number and combination of genetic alterations in CRC confounds our ability to unravel the functional contribution of each of these potential cancer genes. Thus, while genome changes in tumors of individual patients can be assessed in great detail and at low cost, these data are difficult to interpret in terms of prognosis, drug response, or patient outcome, necessitating model systems for analysis of genotype-to-phenotype correlations.

Self-renewal of the intestinal epithelium is driven by *Lgr5* stem cells located in crypts (Barker et al., 2007). We have recently developed a long-term culture system that maintains basic crypt physiology (Sato et al., 2009). Wnt signals are required for the maintenance of active crypt stem cells (Korinek et al., 1998; Kuhnert et al., 2004; Pinto et al., 2003). Indeed, the Wnt agonist R-spondin1 induces dramatic crypt hyperplasia in vivo (Kim et al., 2005). R-spondin-1 is the ligand for *Lgr5* (Carmon et al., 2011; de Lau et al., 2011). Epidermal growth factor (EGF) signaling is associated with intestinal proliferation (Wong et al., 2012), while transgenic expression of Noggin induces a dramatic increase in crypt numbers (Haramis et al., 2004). The combination of R-spondin-1, EGF, and Noggin in

Basement Membrane Extract (BME) sustains ever-expanding small intestinal organoids, which display all hallmarks of the original tissue in terms of architecture, cell-type composition, and self-renewal dynamics. We adapted the culture condition for long-term expansion of human colonic epithelium and primary colonic adenocarcinoma, by adding nicotinamide, A83-01 (Alk inhibitor), Prostaglandin E2, and the p38 inhibitor SB202190 (Sato et al., 2011). Of note, a 2D culture method for cells from normal and malignant primary tissue has been described by Liu et al. (2012).

Here, we explore organoid technology to routinely establish and phenotypically annotate “paired organoids” derived from adjacent tumor and healthy epithelium from CRC patients.

RESULTS

Establishment of a Living CRC Biobank

Surgically resected tissue was obtained from previously untreated CRC patients. Tissue from rectal cancer patients was excluded because they routinely undergo irradiation before surgery. For multiple tissues, we observe that normal tissue-derived organoids outcompete tumor organoids under the optimized culture conditions, presumably due to genomic instability and resulting apoptosis in the latter. Combination of Wnt3A and the Wnt amplifier R-spondin1 is essential to grow organoids from normal epithelium. Over 90% of CRC cases harbor mutations that aberrantly activate the Wnt signaling pathway (Cancer Genome Atlas Network, 2012), so we exploited the Wnt-dependency of normal colonic stem cells to selectively expand tumor organoids. A total of 22 tumor organoid cultures and 19 normal-adjacent organoid cultures were derived from 20 patients (P19 and P24 each carried two primary tumors separated by >10 cm; Figure 1A). We successfully generated organoid cultures from 22 of 27 tumor samples. For one, we never observed growth. Four were lost due to bacterial/yeast infection. Since then, we have added next-generation antibiotics (see Experimental Procedures) and currently observe an ~90% success rate.

The number of primary tumor organoids varied between patient samples, with some tumors rendering thousands of primary organoids whereas others yielded only 10–20 primary organoids. This difference in derivation likely reflects the heterogeneous composition of tumors, with proliferative areas intermingled with regions of differentiated cells, stromal cells or necrosis. The growth rate of the organoids from patients 5 and 27 decreased over time, which prohibited their inclusion in the drug screen. All other organoids could be readily expanded and frozen to create a master cell bank. Upon thawing, cell survival was typically >80%. Unlike healthy tissue-derived organoids, tumor-derived organoids presented with a range of patient-specific morphologies, ranging from thin-walled cystic structures to compact organoids devoid of a lumen. H&E staining on primary tumors and the corresponding organoids revealed that the “cystic versus solid”-organization of the epithelium was generally preserved. Yet, marker expression analysis (KI67, OLFM4, KRT 20, Alcian blue) revealed heterogeneity both between patients and individual organoids within each culture (Figure 1B; Data S1).

Genomic Characterization of Tumor-Derived Organoids

Genomic DNA was isolated from tumor and matched normal organoid cultures for whole-exome sequencing in order to identify tumor-specific somatic mutations (Cancer Genome Atlas Network, 2012). Genomic DNA from the corresponding biopsy specimens were available for comparative analysis for 16 of these cases (Table S1A). The mutation rates per Mb varied widely for different tumor organoids (range 2.0–77.9), with a median value of 3.7 in the tumor organoids, similar to the median rate of 3.6 in the biopsy samples (Figure 2A; Table S1B). Mutations were predominantly CpG to T transitions, consistent with results from large-scale CRC sequencing (Figures S1A and S1B; Table S1C). Of the 22 tumor organoids, six displayed hypermutation (>10 mutations/Mb): P7, P10 and the organoids from the two patients with two tumors each (P19a and P19b, P24a and P24b). Interestingly, the P19a and P19b tumors share TP53 R273C and BRAF V600E alterations, suggesting they arose from the same somatically altered progenitor cell but then diverged to acquire independent secondary alterations (Figures S1C and S1D). In contrast, the P24a and P24b tumors share 80% (469/590) of somatic alterations but then have discordant driving alterations in *APC* and *TP53*, indicating that the hypermutator phenotype may have been present prior to the acquisition of growth promoting mutations (Figures S1E and S1F). The frequency of hypermutated organoid cultures in our patient panel (20%; 4 of 20) agreed with the reported frequency in a much larger cohort of clinical samples and display comparable somatic copy number alterations (SCNAs) (Figure 2B; Table S1D) (Bass et al., 2011; Cancer Genome Atlas Network, 2012). The successful derivation of both hypermutated and non-hypermutated organoids implies an absence of culture-based bias.

Somatic variants within the coding regions in organoid cultures were highly concordant with the corresponding biopsy specimen for both hypermutated and non-hypermutated patients (median = 0.88 frequency of concordance, range 0.62–1.00) (Figure 3A; Table S1E). Indeed, combined analysis of SCNAs and single nucleotide variants (SNVs) to infer Cancer Cell Fractions (CCF) (Carter et al., 2012; Landau et al., 2013) in the biopsy and tumor organoids, revealed that the common CRC driver mutations were maintained in culture. In 13 out of 14 organoid-biopsy pairs tested, tumor subclones sharing common CRC drivers were detected in the biopsy. In 50% of the organoids, a dominant subclone from the biopsy was present, likely representing sampling during derivation but it could also indicate loss in culture (Figures S2A and S2B; Tables S1F and S1G). Transcriptome analysis of single organoids showed subtle differences in gene expression within an organoid culture, confirming their heterogeneous composition. The differences in overall gene expression were more pronounced in the organoids derived from the hypermutant tumors (Figure S2C).

Discordant mutations were assessed for their likely biological significance in cancer, based on Cancer Gene Census and data reported from the PanCancer analysis of 5,000 whole exomes (Futreal et al., 2004; Lawrence et al., 2014). Only 4% (27/679) of discordant mutations found in organoids affected cancer-related genes, including a third hit to *APC*, which was already biallelically inactivated in P14, *SMAD4* mutation in P16, and *POLE* mutation in P19b (Table S1H). Cancer-significant genes

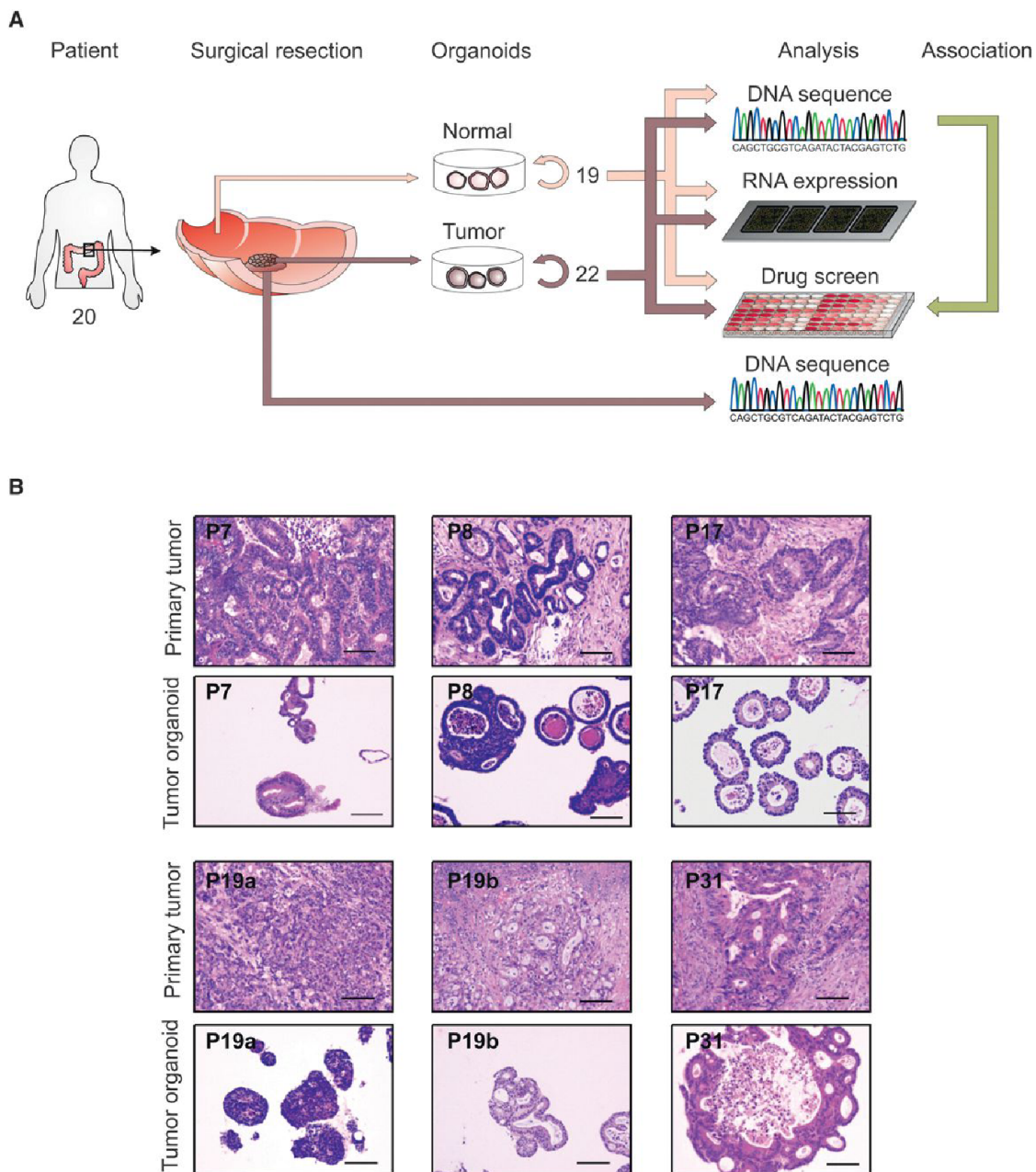


Figure 1. Derivation of Organoids from Primary Tissue

(A) Overview of the procedure. A total of 22 tumor organoids and 19 normal control organoids were derived and analyzed by exome-sequencing, RNA expression analysis and high-throughput drug screening. To determine the concordance between tumor organoids and primary tumor, DNA from the primary tumor was also isolated.

(B) Organoids architecture resembles primary tumor epithelium. H&E staining of primary tumor and the tumor organoids derived of these. A feature of most organoids is the presence of one or more lumens, resembling the tubular structures of the primary tumor (e.g., P8 and P19b). Tumors devoid of lumen give rise to compact organoids without lumen (P19a). Scale bar, 100 μ M.

See also Data S1.

that were discordant in the biopsy represented 4.4% (12/271) (Table S1H). The discordant mutations had a mean allelic frequency of 10.3% and 34.1% for the biopsy and organoids, respectively. This could represent the enrichment or depletion of a sub-clonal population in the organoid culture present within

the original tumor, as well as acquisition of additional mutations during derivation or propagation.

The most commonly altered genes in CRC (Bass et al., 2011; Cancer Genome Atlas Network, 2012; Lawrence et al., 2014) were well represented in the organoid cultures (Figure 3B;

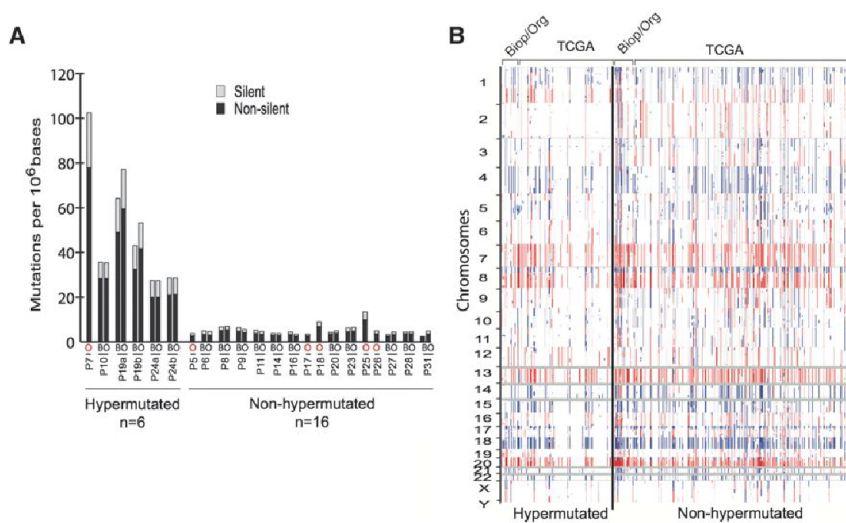


Figure 2. CRC Subtypes Are Present in Organoid Cultures

(A) Whole exome sequencing of the tumor and corresponding biopsy, when available, revealed the presence of hypermutated (>10 mutations/Mb) and non-hypermutated subtypes within the organoids. Comparable rates of mutations were observed in the tumor organoid (O) and tumor biopsy (B). Organoids without corresponding biopsy are indicated in with red (O).

(B) Comparison of somatic copy-number alterations found in the biopsies and corresponding organoids (Biop/Org) and TCGA CRC in hypermutated and non-hypermutated samples. See also Figure S1 and Tables S1A–S1D.

Tables S1I and S1J). Inactivating alterations to the tumor suppressors *APC*, *TP53*, *FBXW7*, and *SMAD4*, as well as activating mutations in *KRAS* (codon 12 and 146) and *PIK3CA* (codon 545 and 1047) were observed. Activating mutations in *BRAF* and *TGFBR1/2* mutations were observed in the hypermutated organoids, consistent with previous reports for primary CRC (Cancer Genome Atlas Network, 2012).

Mutations of genes in DNA mismatch repair (MMR)-associated pathways are associated with a hypermutated phenotype (Boland and Goel, 2010). Consistent with their classification as hypermutated CRC cases (Cancer Genome Atlas Network, 2012), missense mutations were present in *MSH3* in P7, and *POLE* mutations were detected in P10, P19a, and P19b. We did not observe mutations in MMR-associated genes in P24a and P24b and expression analysis showed normal levels of the pertinent genes. The culprit for hyper mutability thus remains to be identified for P24. The limited cohort size did not allow a statistical analysis for somatic copy number alterations to identify significant regions of amplification and deletions. However, manual inspection of the top regions identified by TCGA did reveal the presence of *ERBB2*-, *MYC*-, and *IGF2*-amplified organoids, as well as a reported gain of 13q in the non-hypermutated group (Figure 3C). In aggregate, these analyses demonstrate that organoid cultures faithfully capture the genomic features of the primary tumor from which they derive and much of the genomic diversity of CRC.

Most CRC cases carry activating mutations in the WNT pathway: inactivation mutations in *APC*, *FBXW7*, *AXIN2*, and *FAM123B*, or activating mutations in *CTNNB1* (Cancer Genome Atlas Network, 2012). Gene fusions involving the Wnt-agonistic *RSPO2* and *RSPO3* genes have been observed in 5%–10% of CRC (Seshagiri et al., 2012). *RNF43* encodes a negative regulator of the Wnt pathway, which serves to remove the Wnt receptor FZ in a negative feedback loop (Hao et al., 2012; Koo et al., 2012, de Lau et al., 2014). Recent sequencing efforts of gastric, ovary, and pancreatic neoplasias identified *RNF43* mutations (Jiao et al., 2014; Ryland et al., 2013; Wang et al., 2014), and *RNF43* mutations have been observed in

CRC (Giannakis et al., 2014; Ivanov et al., 2007; Koo et al., 2012)

We found *APC* alterations in all but four of the organoids (P11, P19a/b, P28). Western blotting revealed P11 to express a truncated APC protein, pointing to a mutational event not covered by our exome-sequencing (Figure S3). The wtAPC organoid P28 carries an activating mutation in *CTNNB1* (T41A). In both P19a and P19b, we detected *RNF43* mutations: frameshifts at aa positions 659 and 355, respectively. Only the latter is predicted to affect protein function.

RNA Analysis of Normal and Tumor-Derived Organoids

Organoid cultures consist purely of epithelial cells. Therefore, the system allows for direct gene expression analysis without a contamination from mesenchyme, blood vessels, immune cells, etc. Normal colon-derived and tumor-derived organoids were plated under identical conditions in complete medium (+Wnt). After 3 days, RNA was analyzed using Affymetrix single transcript arrays. Figure 4A shows the correlation heatmap of the organoid samples. Normal colon-derived organoids clustered tightly together, while the tumor-derived organoids exhibited much more heterogeneity. Next, we searched for genes differentially expressed between normal and tumor organoids. Normal colon-derived organoids (Figure 4B) expressed genes of differentiated cells (e.g., the goblet cell markers *MUC1* and *MUC4* and the colonocyte marker *CA2*). Genes enriched in tumor organoids included cancer-associated genes such as *PROX1*, *BAMBI*, and *PTCH1* and the Wnt target gene *APCDD1* (Takahashi et al., 2002).

Several CRC classifications have been proposed based on RNA expression. We combined expression data from organoid samples and TCGA tissue samples and classified these in subtypes using the gene signatures by Sadanandam et al. (2013). Figure 4C displays the subtyping of the 22 organoid samples and 431 TCGA RNA sequencing (RNA-seq) tumor tissue samples. The heatmap shows the normalized scores of genes by samples, both sorted by subtype (see Experimental Procedures). Organoid samples were spread across the subtypes, with the transit-amplifying (TA) subtype being most frequently represented. The enterocyte subtype was not represented. In addition, the RNA expression data allowed expression analysis

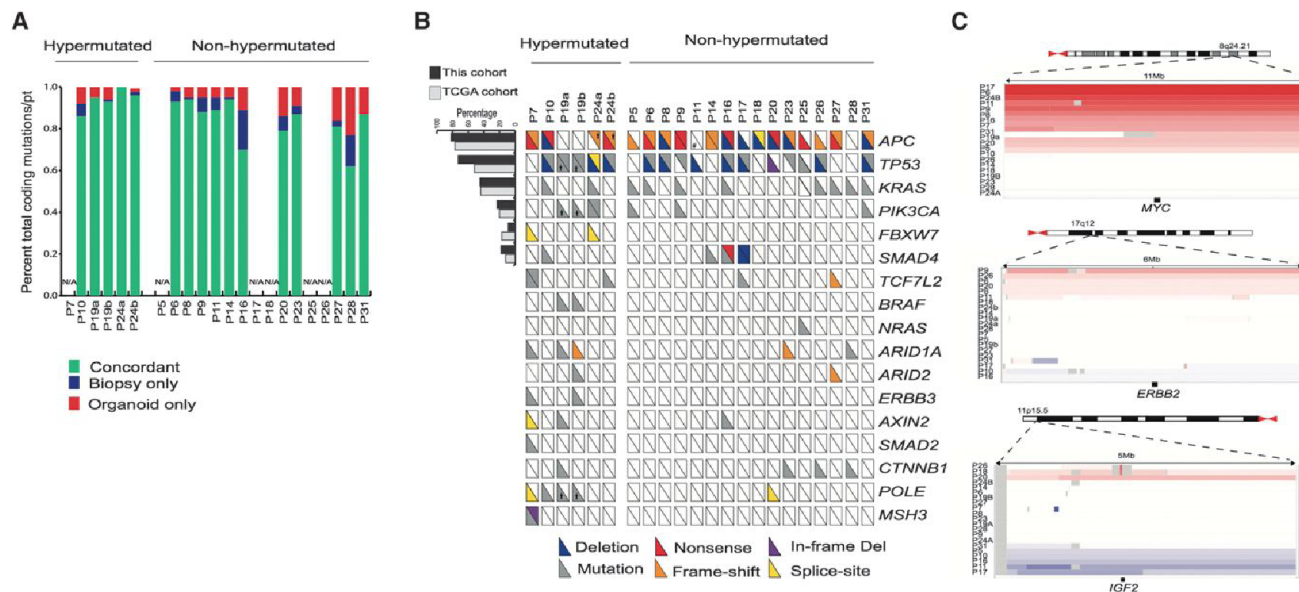


Figure 3. Genomic Alterations Found in CRC Are Represented in Organoid Cultures

(A) Concordance of somatic mutations detected in organoid and corresponding biopsies. Bar graph represents the proportion of coding alterations that are concordant between the biopsy and the corresponding organoid culture and those that are found only in organoid or biopsy specimen. N/A indicates cases in which exome-sequencing was not performed on the corresponding biopsy.

(B) Overview of the mutations found in the tumor organoids. The hash-mark in each box represents each allele and whether it was subject to deletion, mutation, frame-shift alteration, nonsense mutation or splice site mutation. Those alterations present in >10% of cases are compared to the percentage of cases reported by the TCGA CRC. *Indicates discordant mutations targeting the same gene between the two sites in P19 and P24. See also Tables S11 and S1J.

(C) Somatic copy-number alterations in organoids among commonly amplified genes identified in TCGA CRC.

See also Figures S2 and S3 and Tables S1D–S1J.

of individual genes in organoids. *MLH1* expression was absent from two tumor organoids from patient 19 as well as from patient 7 (that is also mutant in *MSH3*) (Figure S4). In the two tumor organoids from P24, we did not detect expression changes in *MLH1* or any other MSI-associated gene.

Effect of Porcupine Inhibitor on *RNF43* Mutant Organoids

Unlike most other WNT pathway mutations, *RNF43* mutations yield a cell that is hypersensitive to—yet still dependent on—secreted WNT. Array data confirmed the expression of several WNTs by the organoids (Figure S5A). The O-acyltransferase Porcupine is required for the secretion of WNTs and its inhibition prevents autocrine/paracrine activation of the pathway (Kadowaki et al., 1996). The small molecule porcupine inhibitor IWP2 (Chen et al., 2009) was tested on a small panel of the tumor organoids and strongly affected the *RNF43* mutant P19b organoid (Figure 5A). This observation implied that porcupine inhibition may be evaluated for treatment of the small subset of cancer patients mutant in *RNF43*.

Organoid Proof-of-Concept Drug Screen

Prompted by this, we developed a robotized drug sensitivity screen in 3D-organoid culture and correlated drug sensitivity with genomic features to identify molecular signatures associated with altered drug response. Organoid cultures were gently disrupted and plated on BME-coated 384-well plates in a 2%

BME solution. Organoids were left overnight before being drugged and left for 6 days before measuring cell number using CellTiter-Glo reagent. Drug sensitivity was represented by the half-maximal inhibitory concentration (IC_{50}), the slope of the dose-response curve, and area under the dose-response curve (AUC).

A bespoke 83 compound library was assembled for screening, including drugs in clinical use ($n = 25$), chemotherapeutics ($n = 10$), drugs previously investigated in or currently undergoing studies in clinical trials ($n = 29$), and experimental compounds to a diverse range of cancer targets ($n = 29$) (Table S2A). The library included the anti-EGFR antibody cetuximab, used clinically for *KRAS/NRAS/BRAF* wild-type CRC, as well as oxaliplatin and 5-FU, first line chemotherapeutics for CRC treatment. In total, 19 of 20 tumor organoids (from 18 different patients) were successfully screened in experimental triplicate, generating >5,000 measurements of organoid-drug interactions (Table S2B).

We incorporated a number of controls into the assay design. The median Z factor score, a measure of assay plate quality, across all screening plates was 0.62 ($n = 119$; upper and lower quartile = 0.85 and 0.3, respectively), consistent with an experimentally robust assay. We did observe some unexplained organoid-specific variation in assay plate quality. Dose-response measurements were performed in experimental triplicate or duplicate (on separate plates) and replicate AUC values were highly correlated (Pearson correlation [R_p] > 0.87) (Figure 5B).

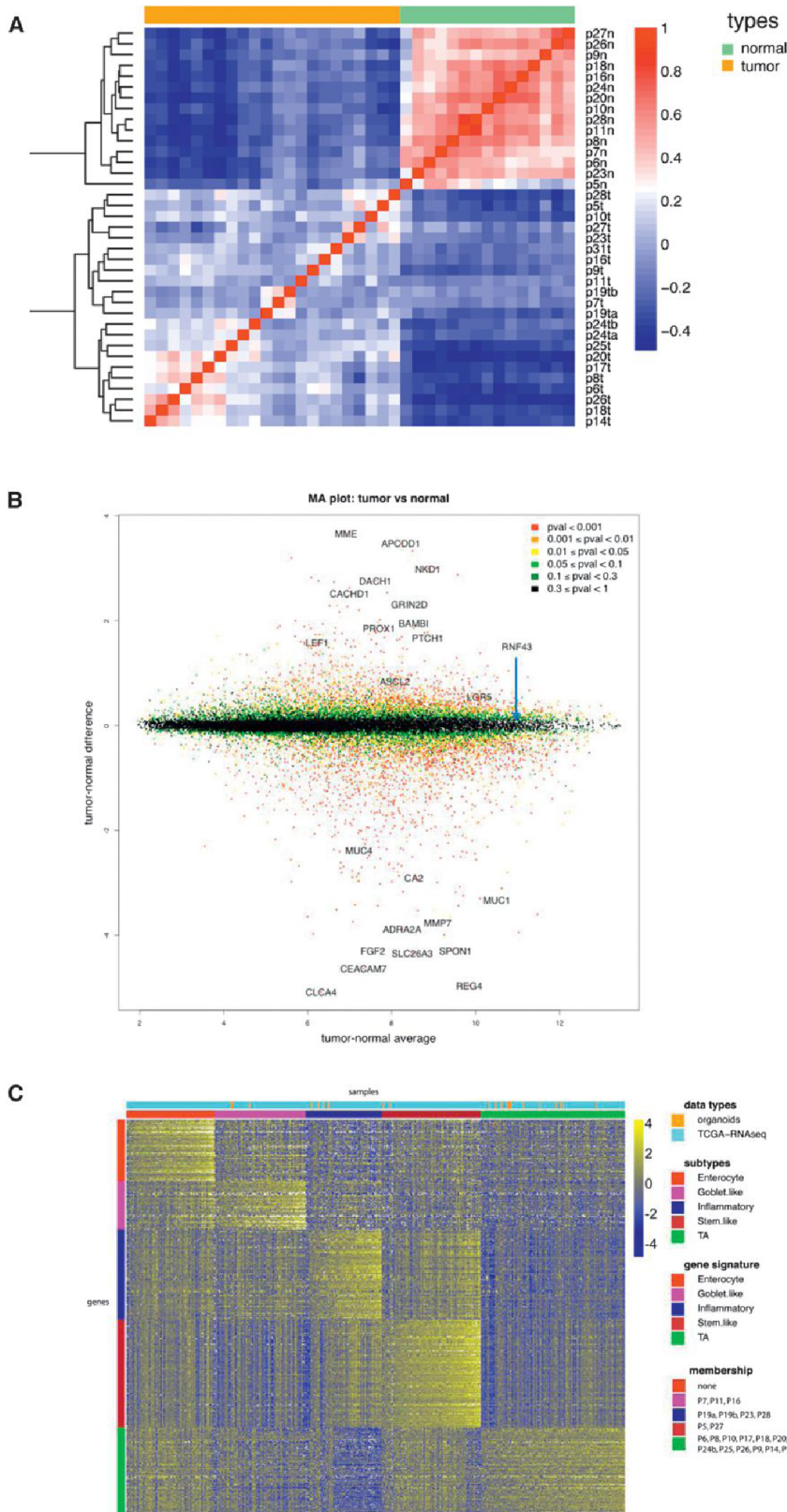


Figure 4. RNA Expression Analysis

(A) Correlation heat map of normal organoids versus tumor organoids based on 2,186 genes (the top 10% of genes in terms of SD). The normal organoids are very highly correlated with each other, whereas the tumor samples exhibit more heterogeneity. The colors represent pairwise Pearson correlations after the expression values have been logged and mean-centered for every gene. The hierarchical clustering is based on one minus correlation distance. The affix N = normal, T = tumor.

(B) MA plot of logged normal versus tumor gene expression. p values are computed with the R package limma, by comparing normal versus tumor gene expression. Cancer-associated genes (e.g., *APCDD1*, *PROX1*, and *PTCH1*) are shown in the top half.

(C) CRC molecular subtypes are represented by the organoid panel. Genes by samples heat map of normalized gene expression of 22 organoid samples and 431 TCGA RNA-seq tumor tissue samples, organized by subtype. Within each subtype, samples are sorted by their mean gene expression for the signature genes associated with that specific subtype.

See also Figure S4.

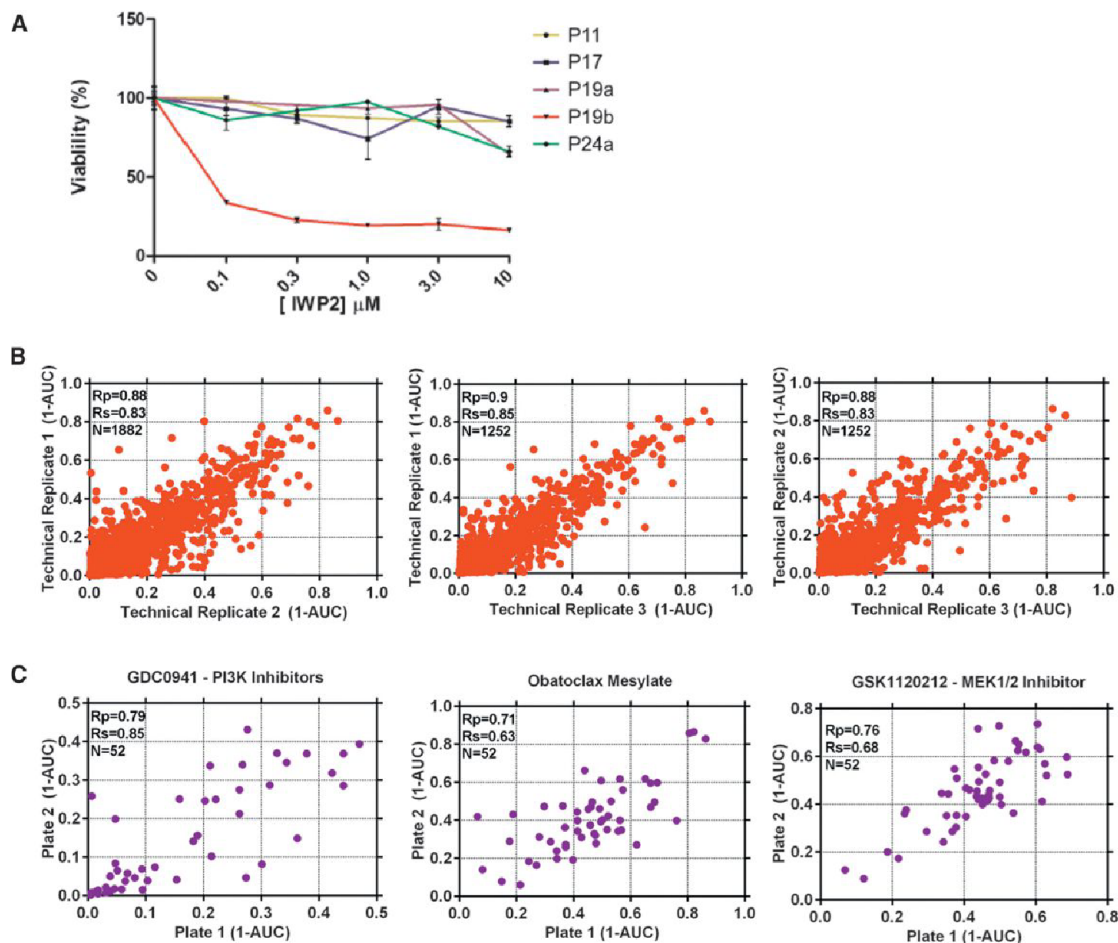


Figure 5. Development of a High-Throughput Drug Screening Assay Utilizing Organoid Models

(A) Autocrine/paracrine WNT signaling in P19b. A small panel of tumor organoids was incubated with increasing amounts of the Porcupine inhibitor IWP2. Growth of the *RNF43* mutant P19b was inhibited, indicative of dependency on autocrine/paracrine WNT signaling. Error bars indicate the SD of triplicate measurements. See also Figure S5.

(B) Scatterplot of (1-AUC) values for all technical replicates of drug screening data. Plots show the correlation between the three different technical replicates and each data point represents the (1-AUC) value for an individual organoid.

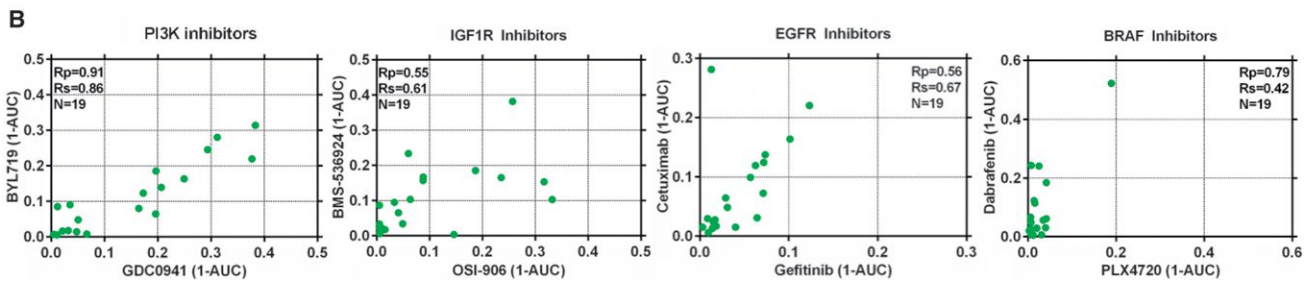
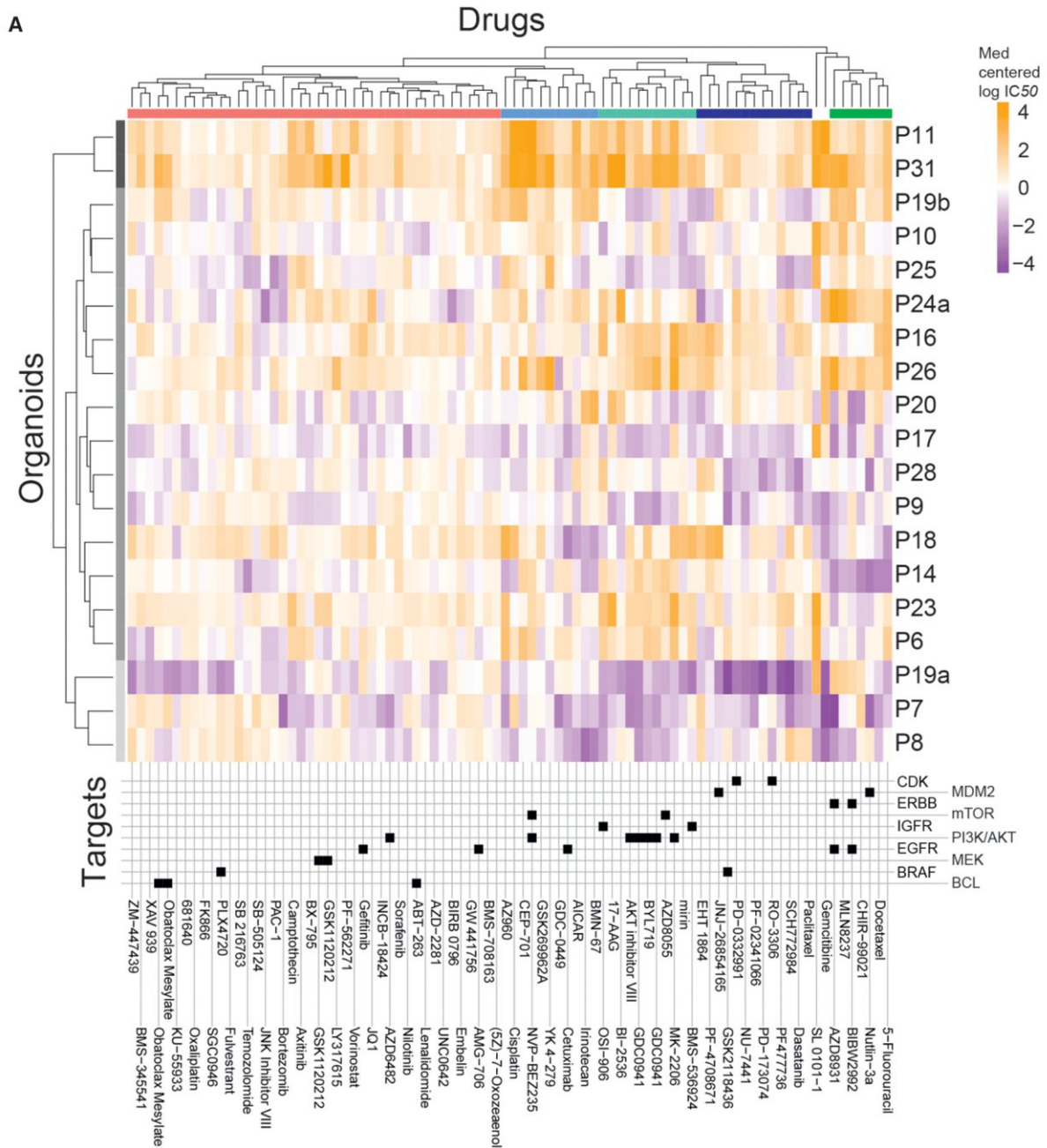
(C) Scatterplots of the correlation in (1-AUC) values for three compounds (GDC0941, obatoclox mesylate, and trametinib) screened twice during every screening run. Values are the mean of three technical replicates.

Furthermore, the compounds trametinib, GDC0941, and obatoclox mesylate were screened twice independently on separate assay plates and a good correlation was observed between the experimentally determined AUC values ($R_p = 0.79$, 0.71 , and 0.76 , respectively) (Figure 5C).

As a first validation, the only tumor organoid in the panel that was sensitive to the Porcupine inhibitor LGK974 was P19b (Figure S5B), confirming the observations made with IWP2 (Figure 5A). The clustering of compounds based on their IC_{50} values demonstrated a diverse range of sensitivities across the organoids and identified three major sub-groups (Figure 6A). One group was associated with sensitivity to a majority of the compounds (organoids P8, P7, and P19a), in contrast to the cluster (P31, P11) exhibiting insensitivity. The remaining organoids had intermediate sensitivity. Interestingly, the multifocal tumors P19a and P19b, derived from the same patient and

both carrying the BRAF V600E mutation, differed in their overall drug response profile. We observed clustering of drugs that inhibit the IGF1R and PI3K-AKT signaling pathways (Figure 6A), and compounds with similar nominal targets had comparable activity across the organoid collection. For example, a similar sensitivity pattern was observed for the PI3K inhibitors GDC0941 and BYL719 (α -selective), the IGF1R inhibitors OSI-906 and BMS-536924, EGFR inhibitors cetuximab and gefitinib, and the BRAF inhibitors dabrafenib and PLX4720 (Figure 6B). All but one of the organoids displayed a lack of sensitivity to BRAF inhibition. P19a, a BRAF V600E mutant organoid, displayed partial sensitivity to dabrafenib with an IC_{50} of $0.5 \mu\text{M}$, comparable to IC_{50} values of BRAF V600E colorectal cancer cell lines (range 0.004 – $2.55 \mu\text{M}$; average $0.96 \mu\text{M}$).

To identify genetic correlates between individual oncogenic mutations and drug response, we performed a multivariate



(legend on next page)

analysis of variance (MANOVA) incorporating IC_{50} values and slopes of the corresponding dose-response curves, with MSI-status as a covariate. Complete drug sensitivity and genomic data sets were available for 18 organoids and used for this analysis. The analysis included 16 genes identified as mutated, amplified, or deleted in CRC (referred to as mutant genes) as described by Lawrence et al. (2014) (Table S3). The MANOVA identified a subset (12 of 864, ~1%) of gene-drug associations as statistically significant ($p < 0.005$, incorporating a 30% false discovery rate [FDR]) (Table S4). These results were further filtered based on the magnitude of the effect size on the IC_{50} values of wild-type versus mutant cell line populations (effect size >2 ; Cohen's D), and correlations identified due to a singlet outlier organoids were removed. This resulted in the identification of one high confidence gene-drug association already reported in the literature (Vassilev et al., 2004). Loss-of-function mutations of the tumor suppressor TP53 were associated with resistance to nutlin-3a ($p = 0.0018$), an inhibitor of MDM2 (Figure 7A). Of the four organoids that were wild-type for TP53 by DNA sequencing, only P18 was (unexpectedly) insensitive to nutlin-3a. However, immunohistochemistry of p53 in P18 revealed the protein to be stabilized, indicative of functional inactivation of the p53 pathway (Figure 7B).

We could also readily detect resistance to the anti-EGFR inhibitors cetuximab and BIBW2992 (afatinib) in the setting of KRAS mutant organoids ($p = 0.008$ /FDR 37% and $p = 0.029$ /FDR 54%, respectively), although these associations were below statistical significance when considering an FDR $<30\%$ (Figures 7C and S6). Of the KRAS wild-type organoids, a subset 2/10 was insensitive to cetuximab, including P19b that has a BRAF mutation, a known mediator of cetuximab resistance (Di Nicolantonio et al., 2008). For the remaining organoid, further mechanisms beyond mutated KRAS/NRAS/BRAF are likely to be involved in cetuximab resistance (De Roock et al., 2010; Vecchione, 2014).

We also identified a number of compounds with differential activity in the absence of an apparent genetic biomarker (Figure 7D). For example, a subset of organoids was exquisitely sensitive to the AKT1/2 inhibitor MK2206. Similarly, we observed distinct subsets of organoids that are exquisitely sensitive to the pan-ERBB inhibitor AZD8931 and the chemotherapeutic gemcitabine. We also performed a validation screen with 11 of the original 83 compounds across the organoid panel and compared the measured responses (Figure S7; Table S5). We observed positive correlation for all compounds and nine exhibited good to fair reproducibility as indicated by an Rp of 0.5 or greater (Figures 7E and 7F). Variation within the assay was likely due to inherent technical noise, biological variation, and sensitivity to outlier data points due to the small number of organoids.

In summary, the successful application of organoids in a systematic and unbiased high-throughput drug screen to

identify clinically relevant biomarkers demonstrates the feasibility and utility of organoid technology for investigating the molecular basis of drug response. Furthermore, the identification of putative novel molecular markers has opened avenues for further investigation of drug sensitivity in CRC. The current analysis is still constrained by the relatively small number of patients. The derivation of a significantly larger organoid collection would increase the representation of rare genotypes and the statistical power to detect molecular markers of drug response.

DISCUSSION

Cancer cell lines have served for many years as the workhorse model in cancer research. Recent studies have exploited high-throughput screening of large panels of cancer cell lines to identify drug-sensitivity patterns and to correlate drug sensitivity to genomic alterations (Barretina et al., 2012; Garnett et al., 2012). From these high-throughput cell-line-based studies, a picture emerges of a complex network of biological factors that affect sensitivity to the majority of cancer drugs. For instance, no direct relationship may exist between sensitivity to a certain drug and a single genomic alteration. Instead, difficult-to-find, complex interactions between multiple genomic alterations may determine drug sensitivity outcome. Thus, with currently available insights, it remains a challenge to develop algorithms that accurately predict the drug sensitivity of a patient's tumor based on the spectrum of genomic alterations present, in the context of the unique genetic background.

Two approaches to determine directly the drug sensitivity in a patient-derived sample have been quite widely exploited, namely the short-term culture of tumor sections (Centenera et al., 2013), and xeno-transplantation of the tumor into immunodeficient mice (Jin et al., 2010; Tentler et al., 2012). Short-term culture allows for in vitro screening at a reasonably large scale, but is constrained by the limited proliferative capacity of the cultures. Xenotransplantation allows for in vivo screening but is resource-intensive due to the need for large mouse colonies. It thus appears of interest to develop additional technologies that allow the combination of sequencing and high-throughput drug screening in patient-derived samples. Here, we demonstrate that the organoid culture platform can be exploited for genomic and functional studies at the level of the individual patient at a scale that cannot be achieved by existing approaches. Our organoid drug screening assay generates reproducible high quality drug sensitivity data, positive correlation of biological replicates, and reproducible activity of compounds inhibiting the same target. By connecting genetic and drug sensitivity data, we were able to confirm the activity of cetuximab in a subset of KRAS wild-type organoids reflecting observations made in the clinic (De Roock et al., 2010) as well as Nutlin-3a effectiveness in TP53 wild-type organoids. Furthermore, we describe

Figure 6. Heatmap of IC_{50} s of All 85 Compounds against 19 Colorectal Cancer Organoids

(A) Organoids have been clustered based on their IC_{50} values across the drug panel. The drug names and their nominal target(s) are provided in the bottom panel. (B) Drugs with the same nominal targets have similar activity profiles across the organoid panel. (1-AUC) values are plotted for inhibitor of PI3K (GDC0941 and BYL719), IGF1R (OSI-906 and BMS-536924), EGFR (cetuximab and gefitinib), and BRAF (PLX4720 and dabrafenib). See also Tables S2A and S2B.

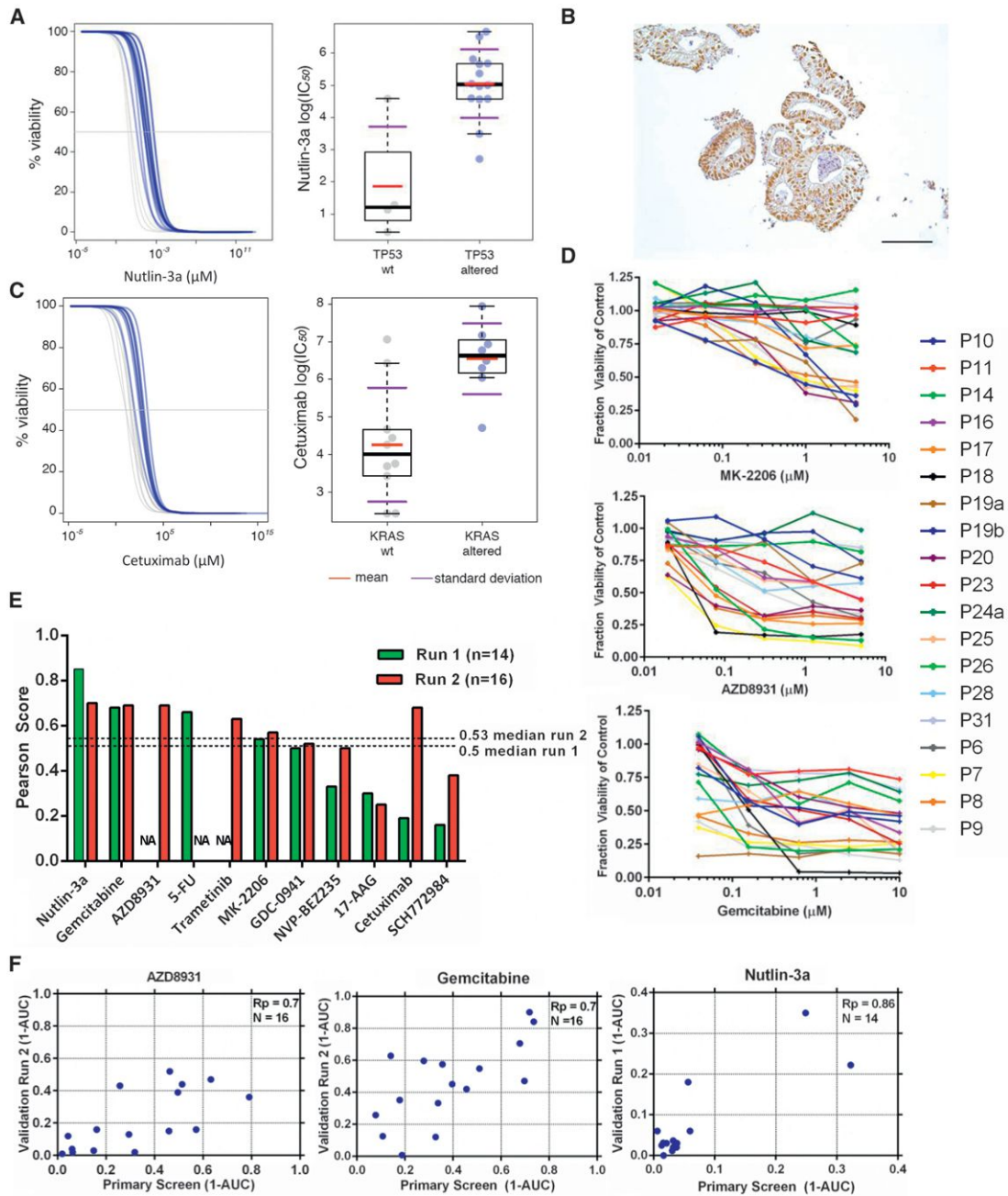


Figure 7. Gene-Drug Associations and Differential Drug Sensitivity Profiles of Interest

(A) Association of *TP53* mutational status with nutlin-3a response. Viability response curves of the altered (blue) and wild-type organoids (gray) as well as scatter plots of cell line IC_{50} (μM) values are shown. IC_{50} values are on a natural logarithmic scale. Each circle represents one cell line, red bars indicate geometric means of IC_{50} values and black bold bars indicate median $\log IC_{50}$ values. Box top/low bounds indicate upper/lower quartiles, and whiskers (indicated by the dashed lines) extend to extreme values (minimal and maximal) excluding outliers (i.e., whose value is more than 3/2 times the upper quartile and less than 3/2 times the lower quartile). Purple bar positions on the y axis indicate means $\pm \log IC_{50}$ SD.

(B) Immunohistochemical staining showing stabilization of TP53 in organoid P18. Scale bar, 100 μM .

(C) Association of *KRAS* status and cetuximab response. Colors and symbols coding is the same as (A).

(D) Dose-response curves after 6 days treatment with MK2206, AZD8931, and gemcitabine.

(E) Reproducibility of drug response profiles for 11 drugs. The Pearson correlation score of (1-AUC) values from the primary screen compared to (1-AUC) values from validation screens are used for comparison. The validation screen was performed twice (run 1 and 2) with >1 month elapsed between each screen. NA, data unavailable for this drug.

(F) The correlation of 1-AUC values from the primary and validation screens for AZD8931, gemcitabine, and nutlin-3a.

See also Figures S6 and S7 and Tables S3, S4, and S5.

the differential activity of a handful of clinical and preclinical compounds (gemcitabine, MK2206, and AZD8941).

Tumors are composed of a mixture of sub-clones that coevolve through a Darwinian selection process. This cellular heterogeneity and phenotypic variation allows the emergence of a complex clonal architecture, which underpins important features such as drug resistance and metastatic potential (Burrell et al., 2013). Our CCF analysis of clonal structure determined that almost all of the biopsies were polyclonal at the time of resection, and this is reflected to varying extent in the corresponding organoid culture. The ability to capture sub-clonal populations in *in vitro* organoid culture should enable more predictive modeling of patient responses to therapy. In many respects, the clonal selection and heterogeneity observed in organoids is similar to PDX models of cancers (Eirew et al., 2015). For both models, understanding the factors that affect tumor heterogeneity and evolution, and how heterogeneity impacts on drug response, will be important to fully exploit their potential for predicting patient responses.

We perceive patient-derived organoids to be used to directly test drug sensitivity of the tumor in a personalized treatment approach. For this, we envision organoids to be tested against a limited number of clinically approved drugs within weeks after derivation. While building this pilot biobank, we observed that normal epithelial tissue always yield good numbers of organoids within weeks, while significant differences in “take rates” were observed between patients’ tumor organoids. Crucial for this approach to be effective, is to decrease the time needed to derive and expand the organoids. In conclusion, tumor organoids may fill the gap between cancer genetics and patient trials, complement cell-line- and xenograft-based drug studies, and allow personalized therapy design.

EXPERIMENTAL PROCEDURES

Human Tissues

Colonic tissues were obtained from The Diaconessen Hospital Utrecht with informed consent and the study was approved by the ethical committee. All patients were diagnosed with colorectal cancer. From the resected colon segment, normal as well as tumor tissue was isolated. The isolation of healthy crypts and tumor epithelium was performed essentially as described by Sato et al. (2011).

Organoid Culture

Healthy tissue-derived organoids were cultured in Human Intestinal Stem Cell medium (HISC). The composition of HISC is: Basal culture medium with 50% Wnt conditioned medium, 20% R-Spondin conditioned medium, 10% Noggin conditioned medium, 1× B27, 1,25 mM n-Acetyl Cysteine, 10 mM Nicotinamide, 50 ng/ml human EGF, 10 nM Gastrin, 500 nM A83-01, 3 μ M SB202190, 10 nM Prostaglandin E2, and 100 μ g/ml Primocin (Vivogen). Tumor organoids were cultured in HICS minus Wnt. See the Extended Experimental Procedures for a detailed description.

Whole-Exome Sequencing and Copy-Number Analysis

For each sample, ~250 ng of DNA was sheared and subject to whole-exome sequencing using the Agilent v2 capture probe set and sequenced by HiSeq2500 using 76 base pair reads, as previously described (Fisher et al., 2011; Imielinski et al., 2012). A median 9.6 Gb of unique sequence was generated for each sample (Table S1A).

Sequence data were locally realigned to improve sensitivity and reduce alignment artifacts prior to identification of mutations, insertions, and deletions

as previously described (Cibulskis et al., 2013; DePristo et al., 2011; Ojesina et al., 2014).

Somatic copy-number analysis was performed using segmented copy-number profiles generated from whole-exome sequencing using the SegSeq algorithm (Table S1D) (Chiang et al., 2009). The procedure is described in detail in the Extended Experimental Procedures.

Organoid Data Processing

RNA from 22 organoid tumor samples and 15 paired normal samples was hybridized on Affymetrix Human Gene 2.0 ST arrays. The raw CEL files were processed with Affymetrix Power Tools using the Hg19 genome build and NetAffx annotation dating from 09-30-2012. Between-array normalization was performed using *rma-sketch*, within APT. This resulted in an intensity matrix of 21,681 genes by 37 samples. For analysis of individual genes, data were analyzed using the R2 web application, which is freely available at <http://r2.amc.nl>.

To subtype the samples, we used the gene signature published by Sadanandam et al. (2013). The procedure is described in detail in the Extended Experimental Procedures.

Organoid Viability Assays

Eight microliters of ~7 mg/ml BME was dispensed in to 384-well microplates and allowed to polymerize. Organoids were mechanically dissociated by pipetting before being resuspended in 2% BME/growth media (15–20,000 organoids/ml) and dispensed into drug wells. The following day a 5-point 4-fold dilution series of each compound was dispensed using liquid handling robotics and cell viability assayed using CellTiter-Glo (Promega) following 6 days of drug incubation. All screening plates were subjected to stringent quality control measures and a Z factor score comparing negative and positive control wells calculated. Dose-response curves were fitted to the luminescent signal intensities utilizing a method previously described (Garrett et al., 2012). Further information of the compounds used, data-fitting algorithm, and validation screen can be found in the Extended Experimental Procedures.

Systematic Multivariate Analysis of Variance

We excluded from the analysis drugs with no IC₅₀ values falling within the range of tested concentrations. For each of the remaining drugs, we assembled an 18 × 2 matrix Y composed by two vectors of length n = 18, containing IC₅₀ values and dose-response curve slopes β , respectively, obtained by treating 18 organoids with the drug under consideration. A multivariate analysis of variance (MANOVA) model was then fitted to this drug response data matrix with factors including the microsatellite stability status of the organoids and the status (altered or wild-type) of 16 genomic features (Extended Experimental Procedures). Significance and effect size scores were obtained for each of the genomic-feature/drug pairs. Q values were subsequently obtained by correcting the MANOVA p values for multiple hypotheses testing, and a threshold of 30% of positive false discovery rate, IC₅₀, and effect size >2 (as quantified by the Cohen’s D) was used to identify significant associations.

ACCESSION NUMBERS

The accession number for the healthy and tumor organoid array data reported in this paper is GEO: GSE64392. The accession number for the single organoid RNA-seq data is GEO: GSE65253.

SUPPLEMENTAL INFORMATION

Supplemental Information includes Extended Experimental Procedures, seven figures, five tables, and one data file and can be found with this article online at <http://dx.doi.org/10.1016/j.cell.2015.03.053>.

AUTHOR CONTRIBUTIONS

M.v.d.W. derived, maintained, and analyzed organoid cultures. H.E.F. developed, performed, and analyzed the organoid drug screen. J.M.F. analyzed

sequencing data. G.B. analyzed RNA expression data. R.G.J.V. organized ethical approval. F.I. performed analyses and statistical inferences on the drug screening data supervised by J.S.R. A.P. and W.v.H. performed surgery. J.v.G. isolated tumor and normal tissue from resected material. A.T.M. performed cancer cell fraction analysis. L.K. performed single organoid transcriptomics supervised by A.v.O. A.M. assisted in drug screening. J.B. performed immunostainings and assisted in culturing organoids together with S.J. and S.B. P.v.d.S. and R.V. processed and analyzed RNA, supervised by R.V. V.S.W.L. performed APC western analysis. S.S. processed DNA samples for exome sequencing. C.S.P., K.C., S.L.C., A.M., M.S.L., L.L., and C.S. helped in processing and analyzing sequencing data. G.G. and M.M. supervised the sequencing and analysis. L.W. supervised the RNA analysis. M.R.S., U.M., M.G., and H.C. participated in the development of the project concept. M.G. aided in drug data analysis. M.v.d.W. and H.E.F. participated in data analysis and project design. M.v.d.W., H.E.F., J.M.F., M.M., M.J.G., and H.C. wrote the manuscript.

ACKNOWLEDGMENTS

Thanks to the Broad Institute Genomics Platform for processing and generating the sequence data, the cell line screening, and analysis team at the Sanger Institute, Liliene Wijnaendts and Joost Oudejans for help with tumor dissections, Harry Begthel and Jeroen Korving for histology, Sepideh Darakhshan for help with organoids, and the members of the M.M., M.J.G., and H.C. laboratories for support. M.v.d.W. is supported by Stichting Virtutis Opus and Stichting Vrienden van het Hubrecht. R.G.J.V., S.J., and J.B. are supported by a Grant from Alpe d'Huizes/KWF. This work was supported with a grant from the Dutch Cancer Society to M.S. (H1/2014-6919). The organoids are available for academic research upon evaluation of a research proposal by the Medical Ethical Comity. M.M. received a commercial research grant from Bayer and has ownership interest (including patents) in and is a consultant/advisory board member for Foundation Medicine.

Received: October 29, 2014

Revised: January 20, 2015

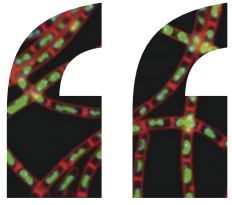
Accepted: March 18, 2015

Published: May 7, 2015

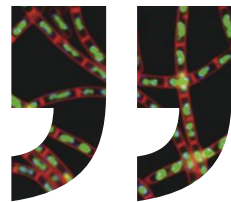
REFERENCES

- Barker, N., van Es, J.H., Kuipers, J., Kujala, P., van den Born, M., Cozijnsen, M., Haegerbarth, A., Korving, J., Begthel, H., Peters, P.J., and Clevers, H. (2007). Identification of stem cells in small intestine and colon by marker gene *Lgr5*. *Nature* *449*, 1003–1007.
- Barretina, J., Caponigro, G., Stransky, N., Venkatesan, K., Margolin, A.A., Kim, S., Wilson, C.J., Lehár, J., Kryukov, G.V., Sonkin, D., et al. (2012). The Cancer Cell Line Encyclopedia enables predictive modelling of anticancer drug sensitivity. *Nature* *483*, 603–607.
- Bass, A.J., Lawrence, M.S., Brace, L.E., Ramos, A.H., Drier, Y., Cibulskis, K., Sougnez, C., Voet, D., Saksena, G., Sivachenko, A., et al. (2011). Genomic sequencing of colorectal adenocarcinomas identifies a recurrent *VT1A-TCF7L2* fusion. *Nat. Genet.* *43*, 964–968.
- Boland, C.R., and Goel, A. (2010). Microsatellite instability in colorectal cancer. *Gastroenterology* *138*, 2073–2087.
- Burrell, R.A., McGranahan, N., Bartek, J., and Swanton, C. (2013). The causes and consequences of genetic heterogeneity in cancer evolution. *Nature* *501*, 338–345.
- Cancer Genome Atlas Network (2012). Comprehensive molecular characterization of human colon and rectal cancer. *Nature* *487*, 330–337.
- Carmon, K.S., Gong, X., Lin, Q., Thomas, A., and Liu, Q. (2011). R-spondins function as ligands of the orphan receptors *LGR4* and *LGR5* to regulate *Wnt*/ β -catenin signaling. *Proc. Natl. Acad. Sci. USA* *108*, 11452–11457.
- Carter, S.L., Cibulskis, K., Helman, E., McKenna, A., Shen, H., Zack, T., Laird, P.W., Onofrio, R.C., Winckler, W., Weir, B.A., et al. (2012). Absolute quantification of somatic DNA alterations in human cancer. *Nat. Biotechnol.* *30*, 413–421.
- Centenera, M.M., Raj, G.V., Knudsen, K.E., Tilley, W.D., and Butler, L.M. (2013). Ex vivo culture of human prostate tissue and drug development. *Nat. Rev. Urol.* *10*, 483–487.
- Chen, B., Dodge, M.E., Tang, W., Lu, J., Ma, Z., Fan, C.-W., Wei, S., Hao, W., Kilgore, J., Williams, N.S., et al. (2009). Small molecule-mediated disruption of *Wnt*-dependent signaling in tissue regeneration and cancer. *Nat. Chem. Biol.* *5*, 100–107.
- Chiang, D.Y., Getz, G., Jaffe, D.B., O'Kelly, M.J.T., Zhao, X., Carter, S.L., Russ, C., Nusbaum, C., Meyerson, M., and Lander, E.S. (2009). High-resolution mapping of copy-number alterations with massively parallel sequencing. *Nat. Methods* *6*, 99–103.
- Cibulskis, K., Lawrence, M.S., Carter, S.L., Sivachenko, A., Jaffe, D., Sougnez, C., Gabriel, S., Meyerson, M., Lander, E.S., and Getz, G. (2013). Sensitive detection of somatic point mutations in impure and heterogeneous cancer samples. *Nat. Biotechnol.* *31*, 213–219.
- de Lau, W., Barker, N., Low, T.Y., Koo, B.-K., Li, V.S.W., Teunissen, H., Kujala, P., Haegerbarth, A., Peters, P.J., van de Wetering, M., et al. (2011). *Lgr5* homologues associate with *Wnt* receptors and mediate R-spondin signalling. *Nature* *476*, 293–297.
- de Lau, W., Peng, W.C., Gros, P., and Clevers, H. (2014). The R-spondin/*Lgr5*/*Rnf43* module: regulator of *Wnt* signal strength. *Genes Dev.* *28*, 305–316.
- De Roock, W., Claes, B., Bernasconi, D., De Schutter, J., Biesmans, B., Fountzilas, G., Kalogerias, K.T., Kotoula, V., Papamichael, D., Laurent-Puig, P., et al. (2010). Effects of *KRAS*, *BRAF*, *NRAS*, and *PIK3CA* mutations on the efficacy of cetuximab plus chemotherapy in chemotherapy-refractory metastatic colorectal cancer: a retrospective consortium analysis. *Lancet Oncol.* *11*, 753–762.
- DePristo, M.A., Banks, E., Poplin, R., Garimella, K.V., Maguire, J.R., Hartl, C., Philippakis, A.A., del Angel, G., Rivas, M.A., Hanna, M., et al. (2011). A framework for variation discovery and genotyping using next-generation DNA sequencing data. *Nat. Genet.* *43*, 491–498.
- Di Nicolantonio, F., Martini, M., Molinari, F., Sartore-Bianchi, A., Arena, S., Saletti, P., De Dosso, S., Mazzucchelli, L., Frattini, M., Siena, S., and Bardelli, A. (2008). Wild-type *BRAF* is required for response to panitumumab or cetuximab in metastatic colorectal cancer. *J. Clin. Oncol.* *26*, 5705–5712.
- Eirew, P., Steif, A., Khattri, J., Ha, G., Yap, D., Farahani, H., Gelmon, K., Chia, S., Mar, C., Wan, A., et al. (2015). Dynamics of genomic clones in breast cancer patient xenografts at single-cell resolution. *Nature* *518*, 422–426.
- Fearon, E.R. (2011). Molecular genetics of colorectal cancer. *Annu. Rev. Pathol.* *6*, 479–507.
- Fearon, E.R., and Vogelstein, B. (1990). A genetic model for colorectal tumorigenesis. *Cell* *61*, 759–767.
- Fisher, S., Barry, A., Abreu, J., Minie, B., Nolan, J., Delorey, T.M., Young, G., Fennell, T.J., Allen, A., Ambrogio, L., et al. (2011). A scalable, fully automated process for construction of sequence-ready human exome targeted capture libraries. *Genome Biol.* *12*, R1.
- Futreal, P.A., Coin, L., Marshall, M., Down, T., Hubbard, T., Wooster, R., Rahman, N., and Stratton, M.R. (2004). A census of human cancer genes. *Nat. Rev. Cancer* *4*, 177–183.
- Garnett, M.J., Edelman, E.J., Heidorn, S.J., Greenman, C.D., Dastur, A., Lau, K.W., Greninger, P., Thompson, I.R., Luo, X., Soares, J., et al. (2012). Systematic identification of genomic markers of drug sensitivity in cancer cells. *Nature* *483*, 570–575.
- Garraway, L.A., and Lander, E.S. (2013). Lessons from the cancer genome. *Cell* *153*, 17–37.
- Giannakis, M., Hodis, E., Jasmine Mu, X., Yamauchi, M., Rosenbluh, J., Cibulskis, K., Saksena, G., Lawrence, M.S., Qian, Z.R., Nishihara, R., et al. (2014). *RNF43* is frequently mutated in colorectal and endometrial cancers. *Nat. Genet.* *46*, 1264–1266.

- Hao, H.-X., Xie, Y., Zhang, Y., Charlat, O., Oster, E., Avello, M., Lei, H., Mickanin, C., Liu, D., Ruffner, H., et al. (2012). ZNRF3 promotes Wnt receptor turnover in an R-spondin-sensitive manner. *Nature* *485*, 195–200.
- Haramis, A.-P.G., Begthel, H., van den Born, M., van Es, J., Jonkheer, S., Offerhaus, G.J.A., and Clevers, H. (2004). De novo crypt formation and juvenile polyposis on BMP inhibition in mouse intestine. *Science* *303*, 1684–1686.
- Imielinski, M., Berger, A.H., Hammerman, P.S., Hernandez, B., Pugh, T.J., Hodis, E., Cho, J., Suh, J., Capelletti, M., Sivachenko, A., et al. (2012). Mapping the hallmarks of lung adenocarcinoma with massively parallel sequencing. *Cell* *150*, 1107–1120.
- Ivanov, I., Lo, K.C., Hawthorn, L., Cowell, J.K., and Ionov, Y. (2007). Identifying candidate colon cancer tumor suppressor genes using inhibition of nonsense-mediated mRNA decay in colon cancer cells. *Oncogene* *26*, 2873–2884.
- Jiao, Y., Yonescu, R., Offerhaus, G.J.A., Klimstra, D.S., Maitra, A., Eshleman, J.R., Herman, J.G., Poh, W., Pelosof, L., Wolfgang, C.L., et al. (2014). Whole-exome sequencing of pancreatic neoplasms with acinar differentiation. *J. Pathol.* *232*, 428–435.
- Jin, K., Teng, L., Shen, Y., He, K., Xu, Z., and Li, G. (2010). Patient-derived human tumour tissue xenografts in immunodeficient mice: a systematic review. *Clin. Transl. Oncol.* *12*, 473–480.
- Kadowaki, T., Wilder, E., Klingensmith, J., Zachary, K., and Perrimon, N. (1996). The segment polarity gene *porcupine* encodes a putative multitransmembrane protein involved in Wingless processing. *Genes Dev.* *10*, 3116–3128.
- Kim, K.-A., Kakitani, M., Zhao, J., Oshima, T., Tang, T., Binnerts, M., Liu, Y., Boyle, B., Park, E., Emtage, P., et al. (2005). Mitogenic influence of human R-spondin1 on the intestinal epithelium. *Science* *309*, 1256–1259.
- Koo, B.-K., Spit, M., Jordens, I., Low, T.Y., Stange, D.E., van de Wetering, M., van Es, J.H., Mohammed, S., Heck, A.J.R., Maurice, M.M., and Clevers, H. (2012). Tumour suppressor RNF43 is a stem-cell E3 ligase that induces endocytosis of Wnt receptors. *Nature* *488*, 665–669.
- Korinek, V., Barker, N., Moerer, P., van Donselaar, E., Huls, G., Peters, P.J., and Clevers, H. (1998). Depletion of epithelial stem-cell compartments in the small intestine of mice lacking Tcf-4. *Nat. Genet.* *19*, 379–383.
- Kuhnert, F., Davis, C.R., Wang, H.-T., Chu, P., Lee, M., Yuan, J., Nusse, R., and Kuo, C.J. (2004). Essential requirement for Wnt signaling in proliferation of adult small intestine and colon revealed by adenoviral expression of Dickkopf-1. *Proc. Natl. Acad. Sci. USA* *101*, 266–271.
- Landau, D.A., Carter, S.L., Stojanov, P., McKenna, A., Stevenson, K., Lawrence, M.S., Sougnez, C., Stewart, C., Sivachenko, A., Wang, L., et al. (2013). Evolution and impact of subclonal mutations in chronic lymphocytic leukemia. *Cell* *152*, 714–726.
- Lawrence, M.S., Stojanov, P., Mermel, C.H., Robinson, J.T., Garraway, L.A., Golub, T.R., Meyerson, M., Gabriel, S.B., Lander, E.S., and Getz, G. (2014). Discovery and saturation analysis of cancer genes across 21 tumour types. *Nature* *505*, 495–501.
- Lengauer, C., Kinzler, K.W., and Vogelstein, B. (1997). Genetic instability in colorectal cancers. *Nature* *386*, 623–627.
- Liu, X., Ory, V., Chapman, S., Yuan, H., Albanese, C., Kallakury, B., Timofeeva, O.A., Nealon, C., Dakic, A., Simic, V., et al. (2012). ROCK inhibitor and feeder cells induce the conditional reprogramming of epithelial cells. *Am. J. Pathol.* *180*, 599–607.
- Ojesina, A.I., Lichtenstein, L., Freeman, S.S., Pedamallu, C.S., Imaz-Rosshandler, I., Pugh, T.J., Cherniack, A.D., Ambrogio, L., Cibulskis, K., Bertelsen, B., et al. (2014). Landscape of genomic alterations in cervical carcinomas. *Nature* *506*, 371–375.
- Pinto, D., Gregorieff, A., Begthel, H., and Clevers, H. (2003). Canonical Wnt signals are essential for homeostasis of the intestinal epithelium. *Genes Dev.* *17*, 1709–1713.
- Ryland, G.L., Hunter, S.M., Doyle, M.A., Rowley, S.M., Christie, M., Allan, P.E., Bowtell, D.D.L., Gorringe, K.L., and Campbell, I.G.; Australian Ovarian Cancer Study Group (2013). RNF43 is a tumour suppressor gene mutated in mucinous tumours of the ovary. *J. Pathol.* *229*, 469–476.
- Sadanandam, A., Lyssiotis, C.A., Homicsko, K., Collisson, E.A., Gibb, W.J., Wullschlegel, S., Ostos, L.C.G., Lannon, W.A., Grotzinger, C., Del Rio, M., et al. (2013). A colorectal cancer classification system that associates cellular phenotype and responses to therapy. *Nat. Med.* *19*, 619–625.
- Sato, T., Vries, R.G., Snippert, H.J., van de Wetering, M., Barker, N., Stange, D.E., van Es, J.H., Abo, A., Kujala, P., Peters, P.J., and Clevers, H. (2009). Single Lgr5 stem cells build crypt-villus structures in vitro without a mesenchymal niche. *Nature* *459*, 262–265.
- Sato, T., Stange, D.E., Ferrante, M., Vries, R.G.J., Van Es, J.H., Van den Brink, S., Van Houdt, W.J., Pronk, A., Van Gorp, J., Siersema, P.D., and Clevers, H. (2011). Long-term expansion of epithelial organoids from human colon, adenoma, adenocarcinoma, and Barrett's epithelium. *Gastroenterology* *141*, 1762–1772.
- Seshagiri, S., Stawiski, E.W., Durinck, S., Modrusan, Z., Storm, E.E., Conboy, C.B., Chaudhuri, S., Guan, Y., Janakiraman, V., Jaiswal, B.S., et al. (2012). Recurrent R-spondin fusions in colon cancer. *Nature* *488*, 660–664.
- Takahashi, M., Fujita, M., Furukawa, Y., Hamamoto, R., Shimokawa, T., Miwa, N., Ogawa, M., and Nakamura, Y. (2002). Isolation of a novel human gene, APCDD1, as a direct target of the beta-Catenin/T-cell factor 4 complex with probable involvement in colorectal carcinogenesis. *Cancer Res.* *62*, 5651–5656.
- Tentler, J.J., Tan, A.C., Weekes, C.D., Jimeno, A., Leong, S., Pitts, T.M., Arcaroli, J.J., Messersmith, W.A., and Eckhardt, S.G. (2012). Patient-derived tumour xenografts as models for oncology drug development. *Nat. Rev. Clin. Oncol.* *9*, 338–350.
- Vassilev, L.T., Vu, B.T., Graves, B., Carvajal, D., Podlaski, F., Filipovic, Z., Kong, N., Kammlott, U., Lukacs, C., Klein, C., et al. (2004). In vivo activation of the p53 pathway by small-molecule antagonists of MDM2. *Science* *303*, 844–848.
- Vecchione, L. (2014). Optimization of anti-EGFR treatment of advanced colorectal cancer. *Curr. Colorectal Cancer Rep.* *10*, 263–271.
- Vogelstein, B., Papadopoulos, N., Velculescu, V.E., Zhou, S., Diaz, L.A., Jr., and Kinzler, K.W. (2013). Cancer genome landscapes. *Science* *339*, 1546–1558.
- Wang, K., Yuen, S.T., Xu, J., Lee, S.P., Yan, H.H.N., Shi, S.T., Siu, H.C., Deng, S., Chu, K.M., Law, S., et al. (2014). Whole-genome sequencing and comprehensive molecular profiling identify new driver mutations in gastric cancer. *Nat. Genet.* *46*, 573–582.
- Wong, V.W.Y., Stange, D.E., Page, M.E., Buczacck, S., Wabik, A., Itami, S., van de Wetering, M., Poulsom, R., Wright, N.A., Trotter, M.W.B., et al. (2012). Lrig1 controls intestinal stem-cell homeostasis by negative regulation of ErbB signalling. *Nat. Cell Biol.* *14*, 401–408.



We are editors and scientists too.



We are in your lab, at meetings and talking by phone to get to know as many of you as possible in all corners of the world and at all points of your career.

When you choose Cell Press you get the attention you deserve.

For more information visit: www.cell.com/values

Your **work** is our **life**



Selective Elimination of Mitochondrial Mutations in the Germline by Genome Editing

Pradeep Reddy,^{1,14} Alejandro Ocampo,^{1,14} Keiichiro Suzuki,¹ Jinping Luo,¹ Sandra R. Bacman,² Sion L. Williams,² Atsushi Sugawara,¹ Daiji Okamura,¹ Yuji Tsunekawa,³ Jun Wu,¹ David Lam,¹ Xiong Xiong,⁴ Nuria Montserrat,⁵ Concepcion Rodriguez Esteban,¹ Guang-Hui Liu,^{6,7,8} Ignacio Sancho-Martinez,¹ Dolors Manau,⁹ Salva Civico,⁹ Francesc Cardellach,¹⁰ Maria del Mar O'Callaghan,¹¹ Jaime Campistol,¹¹ Huimin Zhao,⁴ Josep M. Campistol,¹² Carlos T. Moraes,^{2,13} and Juan Carlos Izpisua Belmonte^{1,*}

¹Gene Expression Laboratory, Salk Institute for Biological Studies, La Jolla, CA 92037, USA

²Department of Neurology, University of Miami Miller School of Medicine, Miami, FL 33136, USA

³Laboratory for Cell Asymmetry, RIKEN Center for Developmental Biology, Kobe, Hyogo 650-0047, Japan

⁴Department of Chemical and Biomolecular Engineering, University of Illinois at Urbana-Champaign, Urbana, IL 61801, USA

⁵Pluripotent Stem Cells and Organ Regeneration, Institute for Bioengineering of Catalonia (IBEC), Barcelona 08028, Spain

⁶National Laboratory of Biomacromolecules, Institute of Biophysics, Chinese Academy of Sciences, Beijing 100101, China

⁷Center for Molecular and Translational Medicine (CMTM), Beijing 100101, China

⁸Beijing Institute for Brain Disorders, Beijing 100069, China

⁹Institut Clínic of Gynecology, Obstetrics and Neonatology (ICGON), Hospital Clinic, University of Barcelona, Barcelona 08036, Spain

¹⁰Mitochondrial Research Laboratory, IDIBAPS/CIBER on Rare Diseases, University of Barcelona and Internal Medicine Department, Hospital Clínic, University of Barcelona, Barcelona 08036, Spain

¹¹Neuropediatric Department/CIBERER, Hospital Universitari Sant Joan de Déu, Esplugues de Llobregat 08950, Spain

¹²Renal Division, Hospital Clinic, University of Barcelona, IDIBAPS, Barcelona 08036, Spain

¹³Department of Cell Biology, University of Miami Miller School of Medicine, Miami, FL 33136, USA

¹⁴Co-first author

*Correspondence: belmonte@salk.edu

<http://dx.doi.org/10.1016/j.cell.2015.03.051>

SUMMARY

Mitochondrial diseases include a group of maternally inherited genetic disorders caused by mutations in mtDNA. In most of these patients, mutated mtDNA coexists with wild-type mtDNA, a situation known as mtDNA heteroplasmy. Here, we report on a strategy toward preventing germline transmission of mitochondrial diseases by inducing mtDNA heteroplasmy shift through the selective elimination of mutated mtDNA. As a proof of concept, we took advantage of NZB/BALB heteroplasmic mice, which contain two mtDNA haplotypes, BALB and NZB, and selectively prevented their germline transmission using either mitochondria-targeted restriction endonucleases or TALENs. In addition, we successfully reduced human mutated mtDNA levels responsible for Leber's hereditary optic neuropathy (LHON), and neurogenic muscle weakness, ataxia, and retinitis pigmentosa (NARP), in mammalian oocytes using mitochondria-targeted TALEN (mito-TALENs). Our approaches represent a potential therapeutic avenue for preventing the transgenerational transmission of human mitochondrial diseases caused by mutations in mtDNA.

INTRODUCTION

Mitochondria are double-membrane cellular organelles of bacterial origin that play fundamental roles in multiple cellular

processes including energy production, calcium homeostasis, cellular signaling, and apoptosis (Dyall et al., 2004). Mitochondria contain their own mtDNA encoding 13 polypeptides of the mitochondrial respiratory chain as well as tRNAs and rRNAs necessary for their synthesis (Anderson et al., 1981). mtDNA is present in multiple copies per cell, ranging from approximately 1,000 copies in somatic cells to several 100,000 copies in oocytes, with an average 1–10 copies per organelle (Shoubridge and Wai, 2007). In contrast to nuclear DNA, mtDNA is exclusively transmitted through maternal inheritance. Diseases resulting from mitochondrial dysfunction caused by mtDNA mutations affect 1 in 5,000 children (Haas et al., 2007), and it is estimated that 1 in 200 women could be a mitochondrial disease carrier. Due to the fundamental role of mitochondria in energy production, mitochondrial diseases correlate with degeneration of tissues and organs with high-energy demands. This leads to myopathies, cardiomyopathies, and encephalopathies, among other phenotypes (Taylor and Turnbull, 2005). Currently, there is no cure for mitochondrial diseases. Genetic counseling and pre-implantation genetic diagnosis (PGD) represent the only therapeutic options for preventing transmission of mitochondrial diseases caused by mtDNA mutations. However, due to the non-Mendelian segregation of mtDNA, PGD can only partially reduce the risk of transmitting the disease (Brown et al., 2006). Moreover, analysis of multiple blastomeres may compromise embryo viability. Recently, mitochondrial replacement techniques by spindle, pronuclear, or polar body genome transfer into healthy enucleated donor oocytes or embryos have been reported (Craven et al., 2010; Paull et al., 2013; Tachibana et al., 2013; Wang et al., 2014). Application of these techniques implies combining genetic material from three different individuals, which has

raised ethical, safety, and medical concerns (Hayden, 2013; Vogel, 2014). Therefore, alternative and complementary approaches that alleviate or eliminate these concerns should be investigated when devising feasible clinical paths toward preventing the transmission of mitochondrial diseases caused by mtDNA mutations.

Due to the thousands of copies of mtDNA contained within a cell, the levels of mutated mtDNA can vary. The term homoplasmy refers to the presence of a single mtDNA haplotype in the cell, whereas heteroplasmy refers to the coexistence of more than one mtDNA haplotype. When the percentage of mutated mtDNA molecules exceeds a threshold that compromises mitochondrial function, a disease state may ensue (Taylor and Turnbull, 2005; Wallace and Chalkia, 2013). Threshold levels for biochemical and clinical defects are generally in the range of 60%–95% mutated mtDNA depending on the severity of the mutation (Russell and Turnbull, 2014). Changes in the relative levels of heteroplasmic mtDNA can be referred to as mtDNA heteroplasmy shifts. Despite the fact that mitochondria possess all the necessary machinery for homologous recombination and non-homologous end joining, they do not seem to represent the major pathway for mtDNA repair in mammalian mitochondria (Alexeyev et al., 2013). Previous studies have demonstrated that the relative levels of mutated and wild-type mtDNA can be altered in patient somatic cells containing the m.8993T>G mtDNA mutation responsible for the NARP and MILS syndromes, where elimination of mutated mtDNA led to the restoration of normal mitochondrial function (Alexeyev et al., 2008). Similarly, using the heteroplasmic NZB/BALB mouse model that carries two different mtDNA haplotypes (NZB and BALB), BALB mtDNA, which contains a unique ApaLI site, has been specifically reduced *in vivo* using a mitochondria-targeted ApaLI (Bacman et al., 2012; 2010). Recently, transcription activator-like effector nucleases (TALENs) and zinc finger nucleases (ZFNs) targeted to mitochondria have been utilized for the specific elimination of mitochondrial genomes carrying mutations responsible for mitochondrial diseases (Bacman et al., 2013; Gammage et al., 2014; Minczuk et al., 2006; 2008). These novel approaches allow for the targeting of a wider spectrum of mutations against which restriction endonucleases could not be used. However, these approaches do not provide mechanisms for preventing the transmission of mutated mtDNA nor do they allow for a complete systemic clearance of mtDNA mutations in subsequent generations.

Here, we report on the specific reduction of mitochondrial genomes in the germline for preventing transmission of mitochondrial diseases. As a proof of concept, and by using the heteroplasmic NZB/BALB mouse model, we specifically reduced BALB or NZB mitochondrial genomes in the germline using mitochondria-targeted restriction endonucleases and TALENs and prevented their transmission to the next generation. Moreover, we successfully reduced mutated mitochondrial genomes responsible for human mitochondrial diseases in mouse oocytes using mitochondria-targeted nucleases. The approaches presented here may be applied and developed to prevent the transgenerational transmission of human mitochondrial diseases.

RESULTS

Specific Reduction of Mitochondrial Genomes in Oocytes and Embryos Using Restriction Endonucleases

With the goal of establishing an alternative therapeutic approach for preventing the germline transmission of mitochondrial diseases caused by mtDNA mutations, we tested the specific elimination of BALB mtDNA in NZB/BALB oocytes and one-cell embryos. For this purpose, we generated a mammalian codon optimized ApaLI targeted to mitochondria by the ATP5B mitochondria targeting sequence and the ATP5B 5' and 3' UTRs to promote co-translational import from mitochondrial associated ribosomes (Marc et al., 2002). An enhanced GFP (EGFP) reporter was also included in the construct to monitor expression (Figure 1A). First, we tested the mitochondrial localization of the ApaLI protein generated from the construct by immunostaining in NZB/BALB tail tip fibroblasts (TTFs) and observed robust co-localization of mitochondria-targeted ApaLI (mito-ApaLI) with the mitochondrial dye Mitotracker (Figure S1A). In contrast, we failed to observe mitochondrial localization of non-mitochondria-targeted ApaLI (Figure S1A). Analysis of mtDNA by “last-cycle hot” PCR and restriction fragment length polymorphism (RFLP) demonstrated induction of heteroplasmy shift by specific reduction of BALB mtDNA in cells transfected with mito-ApaLI compared to control cells transfected with mito-GFP after 72 hr (Figure S1B). In addition, we found normal mtDNA copy number in mito-ApaLI transfected cells, which resulted from the replication of the remaining NZB mtDNA that compensated for the reduction of BALB mtDNA (Figure S1C).

We next decided to test whether a similar approach could be used in oocytes to specifically eliminate BALB mtDNA (Figure 1A). First, we confirmed the mitochondrial localization of mito-ApaLI in NZB/BALB metaphase II (MII) oocytes injected with mRNA encoding mito-ApaLI by immunostaining (Figure 1B). As expected, mito-ApaLI co-localized with Mitotracker in MII oocytes (Figure 1B). RFLP analysis 48 hr after mito-ApaLI mRNA injection demonstrated the specific reduction of BALB mtDNA and a consequential increase in the relative NZB mtDNA levels (Figure 1C). In agreement with the lack of mtDNA replication in mature oocytes and pre-implantation embryos (Wai et al., 2010), analysis of mtDNA copy number by qPCR revealed a decrease in mtDNA copy number following mito-ApaLI injection proportional to the initial levels of BALB mtDNA (Figure 1D). To verify the reduction of BALB mtDNA, we performed RFLP and qPCR analyses by amplification of an independent region of the mtDNA containing a unique HindIII site, exclusively present in BALB mtDNA. These analyses confirmed the specific reduction of BALB mtDNA upon injection of mito-ApaLI in NZB/BALB MII oocytes (Figure S1D and S1E). Injection of mito-ApaLI in BALB or NZB single haplotype oocytes resulted in complete depletion of mtDNA in BALB oocytes and did not affect mtDNA levels in NZB oocytes reinforcing the specificity of mito-ApaLI (Figure S1F). Collectively, these results suggest the potential of this approach for the specific reduction of mtDNA in the germline.

In addition to oocytes, we tested whether mtDNA heteroplasmy shift could be applied to one-cell embryos without affecting their normal development until the blastocyst stage (Figure 2A). For this purpose, NZB/BALB one-cell embryos

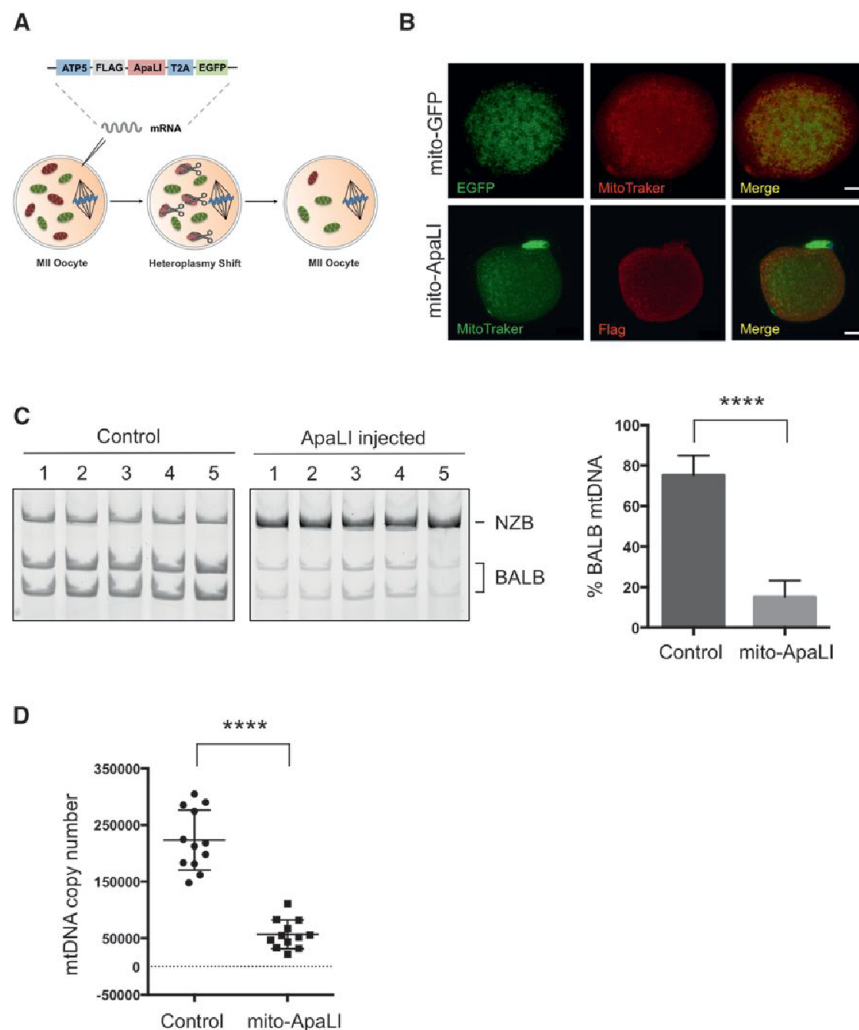


Figure 1. Heteroplasmy Shift in NZB/BALB MII Oocytes Using mito-ApaLI

(A) Injection of mito-ApaLI mRNA in oocytes for induction of heteroplasmy shift.

(B) Mitochondrial co-localization of mito-GFP and mito-ApaLI with MitoTracker in injected oocytes by immunofluorescence. Scale bars, 10 μ m.

(C) RFLP analysis and quantification of mtDNA heteroplasmy in control and mito-ApaLI injected MII oocytes after 48 hr (Control n = 16; mito-ApaLI n = 12). Representative gel.

(D) Quantification of mtDNA copy number by qPCR in control and mito-ApaLI-injected oocytes MII after 48 hr (Control n = 12; mito-ApaLI n = 12).

Error bars represent \pm SEM. ****p < 0.0001. See also Figure S1.

were injected with mito-ApaLI mRNA. Time-lapse fluorescent microscopy images revealed the expression of mito-ApaLI indicated by EGFP expression, and more importantly, normal development of mito-ApaLI-injected embryos through the different developmental stages analyzed (Figure 2B). Similarly to the results observed in oocytes, RFLP analysis of mito-ApaLI blastocysts demonstrated specific reduction of BALB mtDNA and an increase in the relative levels of NZB mtDNA (Figure 2C). Moreover, due to the lack of mtDNA replication until the blastocyst stage (Wai et al., 2010), analysis of mtDNA copy number by qPCR showed a decrease in mtDNA levels proportional to the BALB mtDNA levels (Figure 2D). RFLP and qPCR analyses at the HindIII region confirmed the specific reduction of BALB mtDNA upon injection of mito-ApaLI in NZB/BALB embryos (Figures S2A and S2B).

Preventing the Transmission of Mitochondrial Genomes Using Mitochondria-Targeted Restriction Endonucleases

Next, we investigated whether induction of mtDNA heteroplasmy shift could be utilized for preventing the transmission of mito-

chondrial diseases to the next generation. NZB/BALB one-cell embryos injected with mito-ApaLI mRNA were cultured in vitro until the blastocyst stage and transferred to pseudopregnant mice (Figure 3A). After a standard gestation period, pseudopregnant mice gave birth to live pups through natural delivery (Figure 3B). Most importantly, RFLP analysis of total DNA from F1 mito-ApaLI animals revealed a significant reduction of BALB mtDNA (Figure 3C). Further analysis demonstrated reduction of BALB mtDNA in the brain, muscle, heart, and liver. These data indicate the systemic clearance of a specific mtDNA in the offspring of heteroplasmic mothers (Figure 3D). Similarly, analysis at the HindIII region confirmed the specific reduction of BALB mtDNA in F1 mito-ApaLI animals

(Figures S3A and S3B). Furthermore, analysis of mtDNA copy number showed normal mtDNA levels resulting from NZB mtDNA replication upon embryo implantation (Figure 3E). Comprehensive characterization of mito-ApaLI animals, both males and females, showed normal development, weight gain (Figure 4A), complete blood count (Table S1) as well as normal blood levels of glucose and lactate, all potential indicators of mitochondrial dysfunction (Haas et al., 2007) (Figure 4B). Moreover, typical behavioral studies indicative of CNS defects (Ross et al., 2013), including open field, rotor-rod, grip strength, and sensory neuron screening, showed normal performance of mito-ApaLI animals (Figures 4C–4E).

To assess potential off-target effects on the nuclear genome, we performed comparative hybridization genomic (CHG) array and exome sequencing. CGH array indicated normal genomic integrity of mito-ApaLI animals (Figure S3C). Confirming this result, exome sequencing demonstrated variant rates in ApaLI containing exomic regions comparable to non-ApaLI exomic regions, excluding the possibility of off-target effects of mito-ApaLI (0.0014 versus 0.0047 variants per hundred base pairs, respectively). Furthermore, mito-ApaLI animals were fertile, and RFLP

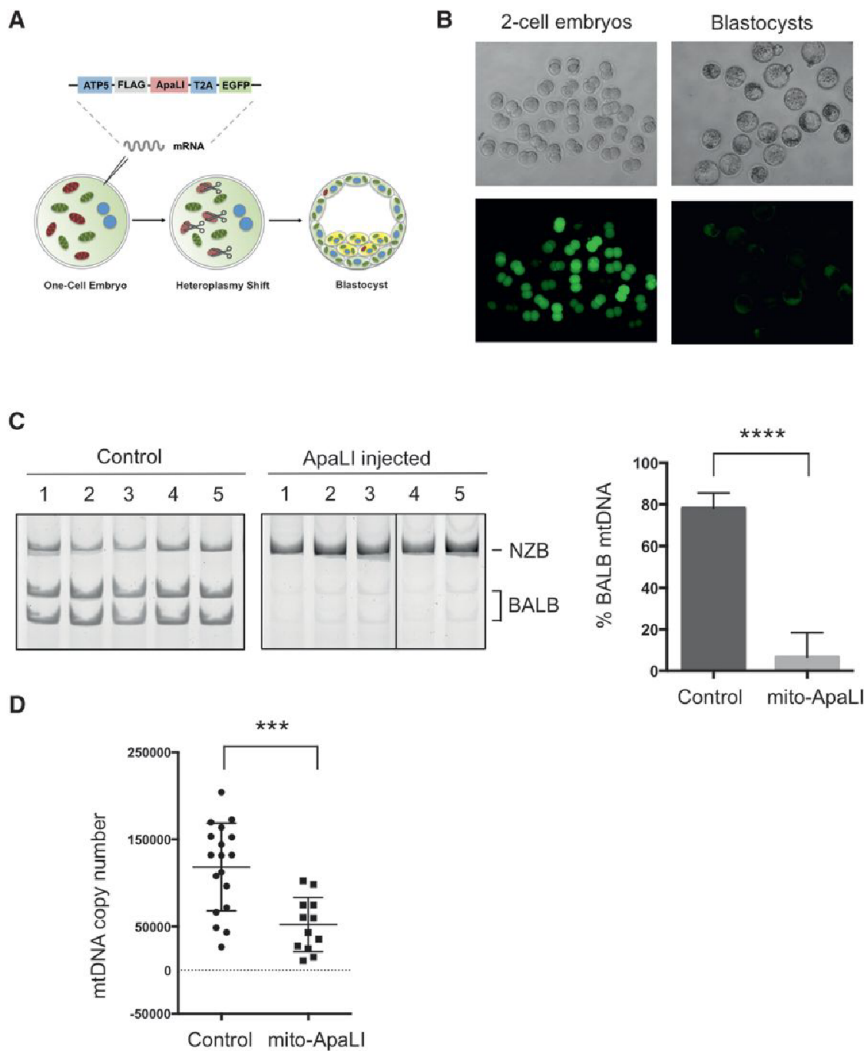


Figure 2. Heteroplasmy Shift in NZB/BALB Embryos Using mito-ApaLI

(A) Injection of mito-ApaLI mRNA in one-cell embryos for induction of heteroplasmy shift.

(B) In vitro development of mito-ApaLI-injected embryos to blastocyst stage. Time-lapse images of EGFP reporter expression at different developmental stages.

(C) RFLP analysis and quantification of mtDNA heteroplasmy in control and mito-ApaLI-injected embryos (Control n = 10; mito-ApaLI n = 8). Representative gel.

(D) Quantification of mtDNA copy number by qPCR in control and mito-ApaLI-injected embryos (Control n = 18; mito-ApaLI n = 12).

Error bars represent \pm SEM. ***p < 0.001. ****p < 0.0001. See also Figure S2.

2008). In order to evaluate the use of mito-TALENs to prevent the transmission of mitochondrial diseases, we tested the specific elimination of NZB mtDNA in NZB/BALB oocytes. For this purpose, we first generated a collection of TALENs against NZB mtDNA and screened for a TALEN with the highest specificity against NZB mtDNA (Figures S5A–S5C). Under our design, the left monomer of the TALEN will bind to the common sequence of NZB and BALB mtDNA while the right monomer will preferentially recognize and bind to NZB mtDNA, dictating the specific cleavage of NZB mtDNA upon dimerization of the FokI nuclease (Figure S5A). NZB TALEN monomers were targeted to mitochondria by the human ATP5B and SOD2 mitochondria targeting sequence and the ATP5B and SOD2 5'

and 3' UTRs to promote co-translational import from mitochondrial associated ribosomes (Marc et al., 2002). In addition, an EGFP or mCherry reporter was also included in the constructs encoding each TALEN monomer (Figure 5A). Once again, we tested the mitochondrial localization of the NZB TALEN by immunostaining in NZB/BALB tail tip fibroblasts (TTFs) and observed robust co-localization of mitochondria-targeted NZB TALEN monomers (hereafter NZB mito-TALEN) with the Mitotracker (Figure S5D). Analysis of mtDNA by RFLP demonstrated induction of heteroplasmy shift in NZB/BALB cells by a specific reduction of NZB mtDNA after 72 hr in cells transfected with NZB mito-TALENs compared to control cells transfected with mito-GFP (Figure S5E). In addition, similar to mito-ApaLI, we found normal mtDNA copy number in NZB mito-TALEN transfected cells resulting from the replication of the remaining BALB mtDNA that compensated for the reduction of NZB mtDNA (Figure S5F).

Preventing the Transmission of Mitochondrial Genomes Using Mito-TALENs

Despite the broad range of over 200 mtDNA mutations associated with mitochondrial diseases, only the human mutation m8993T>G responsible for two mitochondrial diseases: neurogenic muscle weakness, ataxia, and retinitis pigmentosa (NARP) and maternally inherited Leigh syndrome (MILS) generates a unique restriction site that can be targeted using the naturally occurring restriction endonuclease XmaI. For these reasons, alternative approaches to induce heteroplasmy shift based on the use of mitochondria-targeted transcription activator-like effector nucleases (TALENs) and zinc finger nucleases (ZFNs), which could be designed against virtually any mutation, have been recently developed by us and other groups (Bacman et al., 2013; Gammage et al., 2014; Minczuk et al., 2006;

and 3' UTRs to promote co-translational import from mitochondrial associated ribosomes (Marc et al., 2002). In addition, an EGFP or mCherry reporter was also included in the constructs encoding each TALEN monomer (Figure 5A). Once again, we tested the mitochondrial localization of the NZB TALEN by immunostaining in NZB/BALB tail tip fibroblasts (TTFs) and observed robust co-localization of mitochondria-targeted NZB TALEN monomers (hereafter NZB mito-TALEN) with the Mitotracker (Figure S5D). Analysis of mtDNA by RFLP demonstrated induction of heteroplasmy shift in NZB/BALB cells by a specific reduction of NZB mtDNA after 72 hr in cells transfected with NZB mito-TALENs compared to control cells transfected with mito-GFP (Figure S5E). In addition, similar to mito-ApaLI, we found normal mtDNA copy number in NZB mito-TALEN transfected cells resulting from the replication of the remaining BALB mtDNA that compensated for the reduction of NZB mtDNA (Figure S5F).

We next decided to test whether mito-TALENs could be used in oocytes to specifically eliminate NZB mtDNA (Figure 5A). Fluorescent microscopy images revealed the expression of both

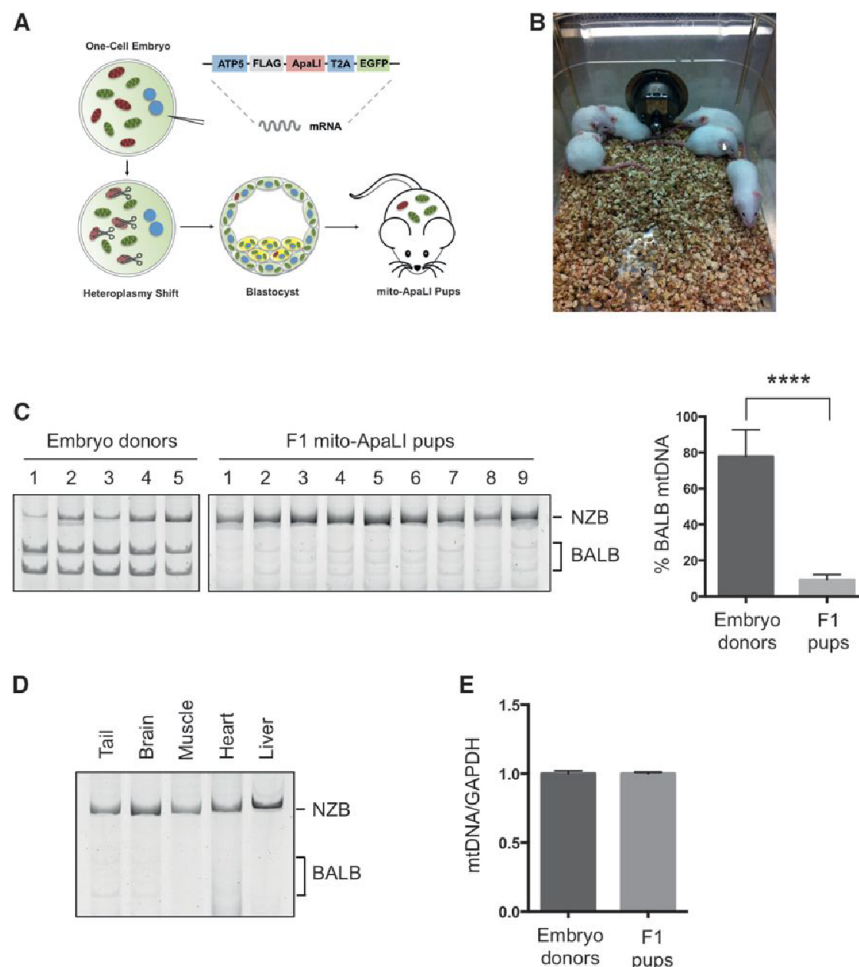


Figure 3. Generation of Live Animals after Induction of Heteroplasmy Shift in NZB/BALB Embryos Using mito-ApaLI

(A) Outline for the generation of live animals after injection of mito-ApaLI mRNA in one-cell embryos. (B) Representative photograph of F1 mito-ApaLI mice.

(C) RFLP analysis and quantification of mtDNA heteroplasmy in tail tip biopsies of embryo donors and generated F1 mito-ApaLI pups. (Donor n = 10; mito-ApaLI n = 9).

(D) RFLP analysis and quantification of mtDNA heteroplasmy in tail, brain, muscle, heart, and liver of F1 mito-ApaLI mice.

(E) Quantification of mtDNA copy number by qPCR in F1 mito-ApaLI pups (Donor n = 10; F1 mito-ApaLI n = 9).

Error bars represent \pm SEM. ****p < 0.0001. See also Figure S3.

(LHOND) and NARP (Jun et al., 1994; Taylor and Turnbull, 2005). Due to the limited number of available patients and the difficulty in obtaining oocytes from these patients, we generated artificial mammalian oocytes carrying mutated genomes by cellular fusion of patient cells and mouse oocytes using Sendai virus (Figure 6A). Although this model has limitations compared to patient oocytes, it helped us to test the potential of our methodology for the specific elimination of pathogenic human mtDNAs in mammalian oocytes.

For this purpose, we first tested the fusion of 143B osteosarcoma cybrid cells

NZB mito-TALEN monomers as indicated by EGFP and mCherry expression in oocytes (Figure 5B). RFLP analysis 48 hr after NZB mito-TALEN mRNA injection demonstrated the specific decrease of NZB mtDNA and a consequential increase in the relative BALB mtDNA levels (Figure 5C). RFLP analysis at the HindIII region confirmed the specific reduction of NZB mtDNA upon injection of NZB mito-TALEN in NZB/BALB MII oocytes (Figure S5G). Analysis of mtDNA copy number by qPCR revealed a decrease in mtDNA copy number following NZB mito-TALEN injection in oocytes in agreement with the lack of mtDNA replication in oocytes (Figure 5D). These results demonstrate the potential of custom designed mito-TALENs for the specific elimination of mitochondrial genomes in the germline aimed at preventing the transmission of mitochondrial diseases.

Specific Reduction of Human Mutated Mitochondrial Genomes Responsible for Mitochondrial Diseases in Mammalian Oocytes

In order to evaluate the potential of our approach to prevent the transmission of human mitochondrial diseases we decided to test the use of mitochondria-targeted nucleases against mutated mitochondrial genomes responsible for two mitochondrial diseases: Leber's hereditary optic neuropathy and dystonia

harboring the LHOND m.14459G>A mutation to mouse MII oocytes (Figure 6B). After 3 hr, complete fusion was observed and no individual cells were detected under the zona pellucida of oocytes (Figure 6B). LHOND-fused oocytes were incubated for 48 hr and collected for analysis. PCR analysis using primers specific against the human mtDNA region containing the LHOND m.14459G>A mutation allowed for the detection of LHOND mtDNA in fused oocytes (Figure S6A). Next, we tested whether the LHOND mito-TALEN that we have recently reported could be used for the specific elimination of LHOND mtDNA in oocytes (Bacman et al., 2013). For this purpose, MII oocytes harboring LHOND mtDNA were injected with mRNA encoding the LHOND mito-TALEN 3 hr after cell fusion. Fluorescent microscopy images revealed the expression of both LHOND mito-TALEN monomers as indicated by EGFP and mCherry expression (Figure S6B). RFLP analysis 48 hr after mRNA injection demonstrated the specific reduction of LHOND mtDNA in fused oocytes (Figure 6C). Analysis of mtDNA copy number by qPCR confirmed a significant reduction of human mutated LHOND mtDNA upon injection of LHOND mito-TALENs in fused oocytes (Figure 6D). Finally, to demonstrate the potential of this approach against other mitochondrial diseases we decided to use a similar strategy to test the elimination of human mitochondrial genomes

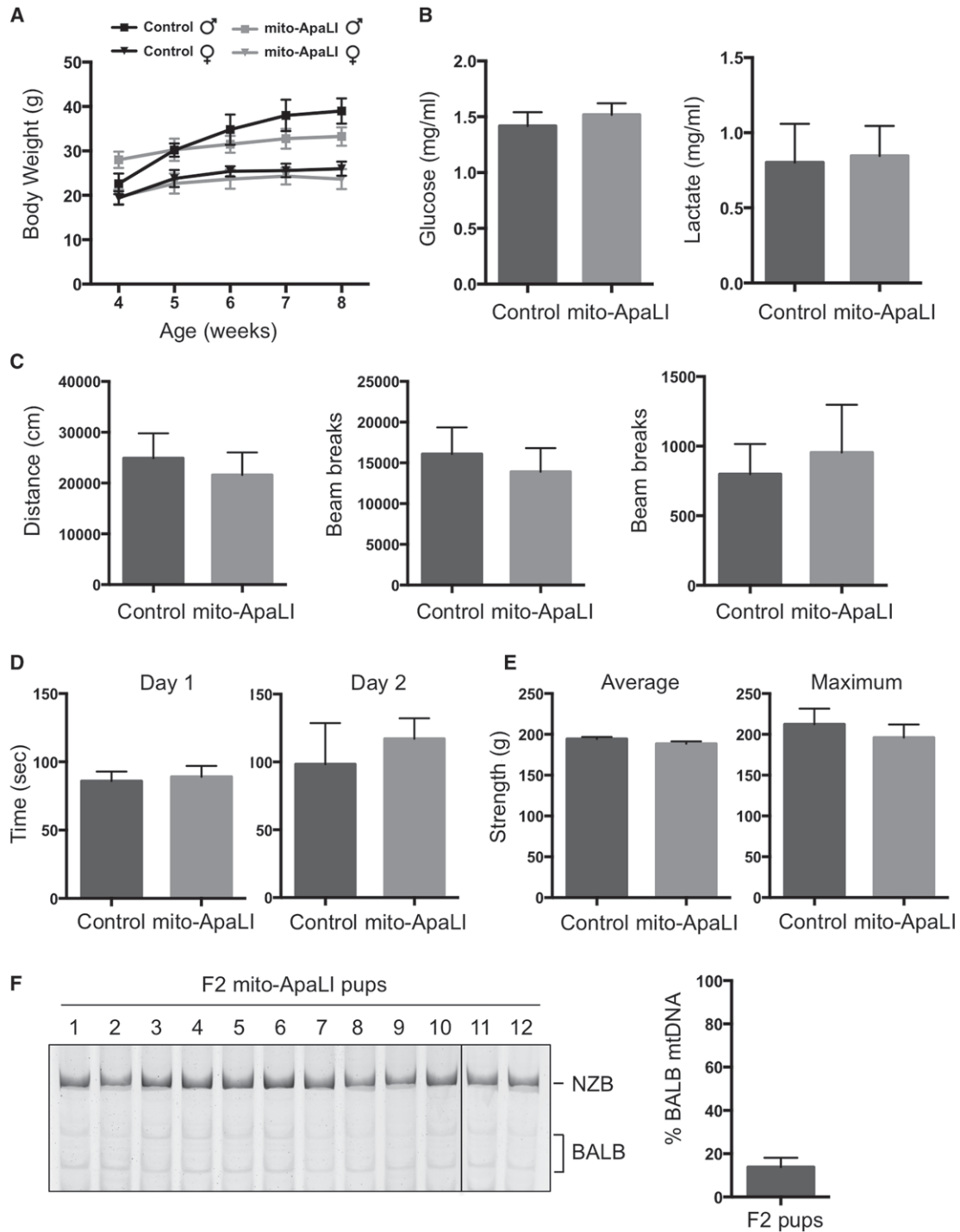


Figure 4. Characterization of F1 mito-ApaLI Mice

(A) Body weight of mito-ApaLI males (Control n = 5 and mito-ApaLI n = 3) and mito-ApaLI females (Control n = 5 and mito-ApaLI n = 6) at different time points. ns, non-significant.

(B) Biochemical analysis of glucose and lactate in blood of control (n = 10) and mito-ApaLI (n = 9) mice. ns, non-significant.

(C) Open field test measuring baseline levels of locomotor activity in freely moving mice quantifying distance traveled, ambulatory counts, and vertical counts.

(D) Rotarod test evaluating locomotor coordination based on the latency at which a fall occurs on a gradually accelerating spinning rod.

(E) Grip strength test measuring average and maximum grip force in the forelimbs.

(F) RFLP analysis and quantification of mtDNA heteroplasmy in tail tip biopsies of F2 mito-ApaLI pups. (F2 mito-ApaLI n = 12).

Error bars represent ± SEM. See also Figure S4 and Table S1.

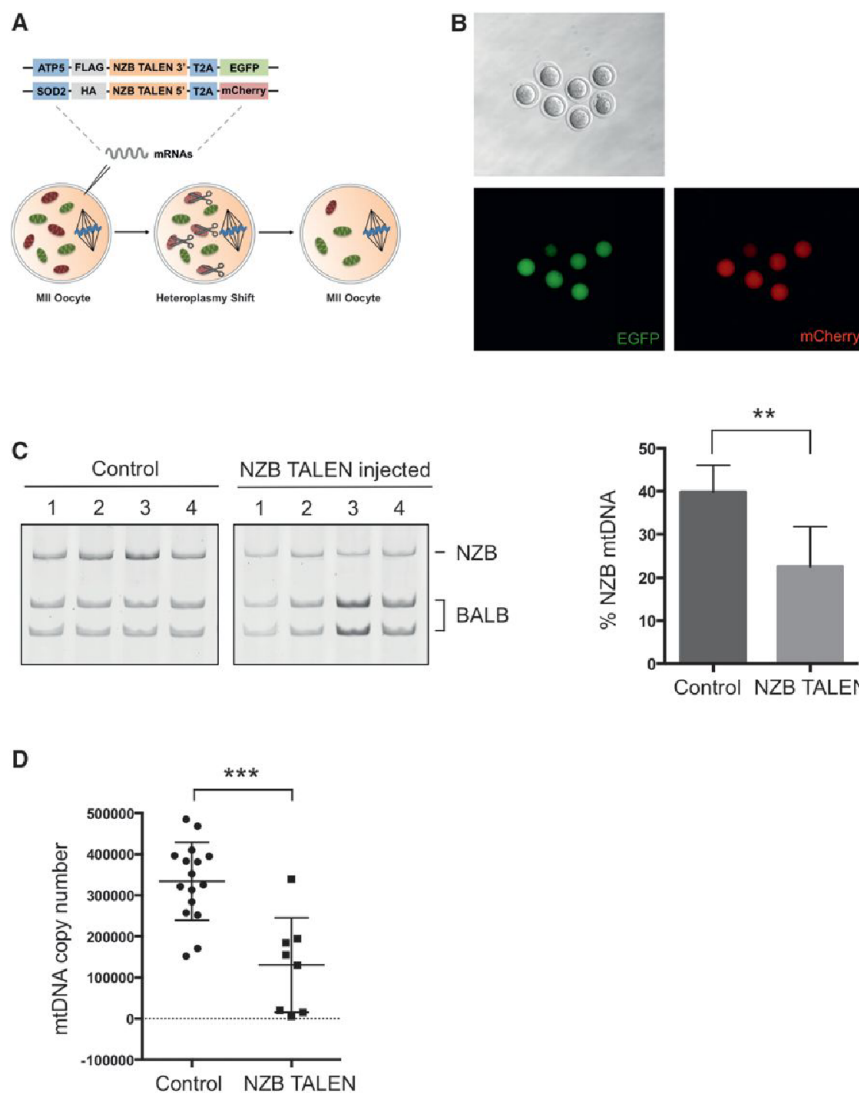


Figure 5. Heteroplasmy Shift in NZB/BALB MII Oocytes Using NZB Mito-TALEN

(A) Injection of NZB mito-TALEN mRNA in oocytes for induction of heteroplasmy shift.

(B) Expression of fluorescent reporters of NZB TALEN monomer in MII oocytes.

(C) RFLP analysis and quantification of mtDNA heteroplasmy in control and NZB TALEN-injected oocytes after 48 hr (Control $n = 9$; NZB TALEN $n = 7$). Representative gel.

(D) Quantification of mtDNA copy number by qPCR in control and NZB TALEN-injected oocytes after 48 hr (Control $n = 16$; NZB TALEN $n = 8$).

Error bars represent \pm SEM. ** $p < 0.01$. *** $p < 0.001$. See also Figure S5.

NARP mitochondrial genomes in oocytes. As before, patient cells harboring the NARP m.9176T>C mutation were fused to MII oocytes using Sendai virus and injected with NARP mito-TALEN 3 hr after fusion. Fluorescent reporters for both NARP mito-TALEN monomers were observed in oocytes as indicated by EGFP and mCherry expression (Figure S6I). RFLP analysis 48 hr after mRNA injection demonstrated the specific reduction of NARP mtDNA in fused oocytes (Figure 6E). Analysis of mtDNA copy number by qPCR confirmed a significant reduction of human mutated NARP mtDNA upon injection of NARP mito-TALENs in fused oocytes (Figure 6F). We speculate that the low levels of wild-type mtDNA carried by the NARP patient cells, together with the lack of mtDNA replication in oocytes, might be the reason why we fail to detect a significant increase in wild-type human mtDNA upon NARP

mito-TALEN injection. Collectively, these results confirm the potential of custom-designed mito-TALENs for the specific elimination of clinically relevant mutated mitochondrial genomes responsible for human mitochondrial diseases in the germline.

carrying the mutation NARP m.9176T>C. For this purpose, we first generated a collection of TALENs against NARP mtDNA and screened for a TALEN with the highest specificity against the mutation NARP m.9176T>C (Figures S6C–S6E). NARP mito-TALEN monomers were targeted to mitochondria by the ATP5B and SOD2 mitochondria targeting sequence and the ATP5B and SOD2 5' and 3' UTRs (Figure 6A). Immunostaining in NARP patient cells revealed a robust co-localization of mitochondria-targeted NARP mito-TALEN monomers with the mitochondrial dye Mitotracker (Figure S6F). Subsequently, we tested the induction of heteroplasmy shift by NARP mito-TALEN using immortalized NARP patient cells. Analysis of mtDNA by RFLP demonstrated induction of heteroplasmy shift in NARP cells with a reduction in NARP mtDNA after 72 hr in cells transfected with the NARP mito-TALEN compared to cells transfected with mito-GFP (Figure S6G). In addition, we found normal mtDNA copy numbers in NARP mito-TALEN transfected cells resulting from the replication of the remaining mtDNA (Figure S6H). Next, similar to LHOND, we tested the specific elimination of

mito-TALEN injection. Collectively, these results confirm the potential of custom-designed mito-TALENs for the specific elimination of clinically relevant mutated mitochondrial genomes responsible for human mitochondrial diseases in the germline.

DISCUSSION

In summary, we report here on novel strategies for preventing germline transmission of mitochondrial diseases through the induction of mtDNA heteroplasmy shift in oocytes and embryos. As a proof of concept, we used a heteroplasmic mouse model carrying two different mtDNA haplotypes: NZB and BALB. First, we demonstrated that injection of mRNA encoding mitochondria-targeted ApaI restriction enzyme into oocytes, as well as into one-cell embryos, led to the generation of live animals with significantly reduced levels of the BALB mtDNA haplotype. These animals displayed normal behavior, development, gross genomic integrity and fertility. Moreover, their progeny (F2 generation) maintained significantly reduced levels of BALB mtDNA. These results

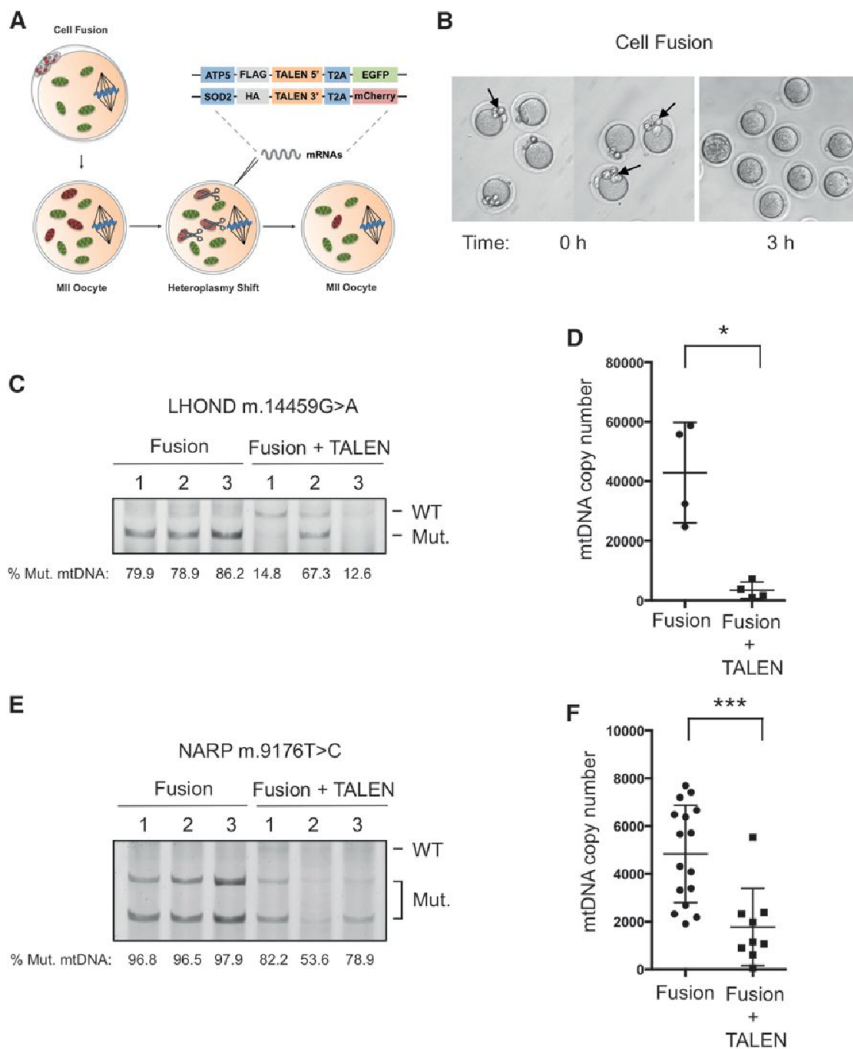


Figure 6. Specific Elimination of Human LHOND m.14459G>A and NARP m.9176T>C Mutations in Mammalian Oocytes Using Mito-TALENs

(A) Fusion of human cells harboring LHOND m.14459G>A and NARP m.9176T>C mutations with mouse MII oocytes followed by the injection of mito-TALENs for induction of heteroplasmy shift. (B) Representative images of MII oocytes before and after cell fusion. (C) RFLP analysis and quantification of LHOND heteroplasmy in individual MII oocytes with and without LHOND TALEN injection after 48 hr (Fusion n = 3; Fusion + TALEN n = 3). (D) Quantification of human mtDNA copy number by qPCR in individual MII oocytes with and without LHOND TALEN injection after 48 hr (Fusion n = 4; Fusion + TALEN n = 4). (E) RFLP analysis and quantification of NARP heteroplasmy in individual MII oocytes with and without NARP TALEN injection after 48 hr (Fusion n = 7; Fusion + TALEN n = 3). (F) Quantification of human mtDNA copy number by qPCR in individual MII oocytes with and without NARP TALEN injection after 48 hr (Fusion n = 17; Fusion + TALEN n = 9). Error bars represent ± SEM. *p < 0.05. ***p < 0.001. See also Figure S6.

demonstrate the potential of germline heteroplasmy shift to prevent the transgenerational transmission of mitochondrial genomes. In addition, injection of mRNA encoding mitochondria-targeted NZB mito-TALEN into oocytes led to a significant reduction of NZB mtDNA levels. Finally, fusion of human patient cells carrying mtDNA mutations to mouse oocytes followed by injection of mito-TALENs against these mutations demonstrated a specific reduction in the levels of mutated mtDNA.

The use of restriction nucleases for the induction of heteroplasmy shift has been previously demonstrated in the NZB/BALB mouse as well as in patient somatic cells by us and other groups (Alexeyev et al., 2008; Bacman et al., 2010; 2012). However, the application of restriction enzymes to target clinically relevant mutations is limited to only m8993T>G, which is responsible for some cases of NARP and MILS, a mutation that generates a unique restriction site that can be targeted using the restriction endonuclease XmaI (Alexeyev et al., 2008). The use of other approaches using different types of nucleases including TALENs might allow for the custom-designed targeting of a wider range of human mitochondrial mutations responsible for mito-

chondrial diseases. Along this line, several reports have recently demonstrated the use of mitochondria-targeted TALENs and zinc finger nucleases (ZFNs) for the specific elimination of mutated mitochondrial genomes in somatic cells (Bacman et al., 2013; Gammage et al., 2014; Minczuk et al., 2006; 2008). When compared to mitochondria-targeted restriction endonucleases, the use of mito-TALENs for preventing transmission of mitochondrial diseases in the germline may be less robust. However, we speculate that their therapeutic use will achieve specific reduction of mutated mitochondrial genomes below the threshold levels (60%–95%) required for biochemical and clinical defects to manifest (Russell and Turnbull, 2014). In addition, we anticipate that the future development and application of more specific and efficient gene editing technologies will allow for a greater reduction of mutated mtDNA levels in the germline.

Transmission of mitochondrial diseases by female carriers directly correlates with the levels of mutated mtDNA present in oocytes. In many cases, asymptomatic female carriers with intermediate levels of mutant load may produce oocytes with different ranges of mutated mtDNA (Chinnery et al., 2000; Cree et al., 2009). Due to the lack of mtDNA replication in oocytes and pre-implantation embryos, targeting of mutated mtDNA in oocytes with high mutant loads using the approach presented here may lead to a dramatic reduction in mtDNA copy number. In mice, embryos with mtDNA levels below a specific threshold develop normally during the pre-implantation stages but subsequently fail to

implant in the uterus or undergo development arrest (Wai et al., 2010). Consequently, oocytes containing high levels of mutated mtDNA that are subjected to heteroplasmy shift may result in embryos with low mtDNA copy number that may fail to implant in the uterine wall. In this case, though heteroplasmy shift may not result in a viable embryo, it would attain the goal of hampering the development and implantation of embryos with high mutant loads, thereby preventing the transmission of mitochondrial diseases to the next generation. In this scenario, PGD could be used as a complementary approach to select embryos with mtDNA copy numbers sufficient for implantation.

Due to the non-Mendelian segregation of mtDNA, current therapeutic approaches, including genetic counseling and PGD, can only partially reduce, but not eliminate, the risk of transmission of mitochondrial diseases (Brown et al., 2006). The recent development of mitochondrial replacement techniques based on spindle, pronuclear, or polar body transfer into healthy enucleated donor oocytes or embryos, soon to be allowed in the UK and currently under review by US regulatory agencies, represent a valid and powerful alternative to current approaches (Craven et al., 2010; Paull et al., 2013; Tachibana et al., 2013; Wang et al., 2014). Mitochondrial replacement techniques involve a series of complex technical manipulations of nuclear genome between patient and donor oocytes that will result in the generation of embryos carrying genetic material from three different origins. For these reasons, mitochondrial replacement techniques have raised biological, medical, and ethical concerns (Hayden, 2013; Reinhardt et al., 2013). Despite their great potential, more studies are still required to show that these techniques are safe in human oocytes. The approach presented here relies on a single injection of mRNA into patient oocytes, which is technically simpler and less traumatic to the oocyte compared to mitochondrial replacement techniques (Craven et al., 2010; Paull et al., 2013; Tachibana et al., 2013; Wang et al., 2014). Importantly, it does not require healthy donor oocytes, thus avoiding ethical issues related to the presence of donor mtDNA.

Induction of mtDNA heteroplasmy shift using restriction endonucleases or TALENs has the potential to eliminate mutated mitochondrial genomes in the germline, and consequently, prevent the transgenerational transmission of mitochondrial diseases. In addition, since mtDNA mutations in the germline have been recently linked to aging (Ross et al., 2013), this strategy could also be applied to prevent the transmission of mtDNA variants with potential roles in aggravating aspects of human aging and age-associated diseases.

EXPERIMENTAL PROCEDURES

Plasmids

A synthetic gene coding for the ApaI restriction endonuclease with a C-terminal HA (Hemagglutinin antigen) tag was purchased from Integrated DNA Technologies (Coralville) with codon usage optimized for mammalian translation. For the generation of the mito-ApaI construct, ApaI was subcloned into the pVAX plasmid containing the mitochondria localization signal derived from ATP5B, a unique Flag immunotag in the N terminus, 5' and 3' UTR from ATP5B to localize the mRNA to ribosomes associated with mitochondria, an independent fluorescent marker to select for expression (enhance GFP [EGFP]) and a recoded picornaviral 2A-like sequence (T2A') between the

mito-ApaI and the fluorescent marker. Subsequently, the fragment described was subcloned into the pcDNA3 plasmid containing a T7 promoter for in vitro transcription. For the generation of the mito-GFP construct, EGFP was subcloned into the previously described pVAX construct lacking the independent fluorescent marker and the recoded picornaviral 2A-like sequence (T2A') but containing a T7 promoter. For the generation of ApaI construct, ApaI RE was subcloned into the previously described pVAX plasmid lacking the N terminus mitochondria localization signal derived from ATP5B and the 5' and 3' UTRs from ATP5B with a T7 promoter. Cloning was done using the In-Fusion HD cloning kit (Clontech Laboratories).

Construction of Mito-TALENs

TALEN target sites for NZB and NARP m.9176T>C were identified using the TAL effector-Nucleotide Targeter (TALE-NT) software (Christian et al., 2010). To increase TALEN specificity, TALEN with targeting sequences of various lengths ranging from 7.5 to 13.5 base pairs were designed. TALENs were constructed into the TALEN cloning vector of the TALE Toolbox kit from Addgene (cat#1000000019) (Sanjana et al., 2012), and the TALENs recognizing the target sites were constructed using the Golden Gate Assembly method. Mito-TALEN, were constructed by addition of mitochondria localization signals derived from ATP5B or SOD2 mitochondria localization signal, inclusion of a unique immuno-tag in the N terminus of the mature protein (hemagglutinin [HA] or Flag), inclusion of the 5' and 3' UTRs from ATP5B or SOD2, inclusion of an independent fluorescent marker to select for expression (EGFP in one monomer and mCherry in the other) and inclusion of a recoded picornaviral 2A-like sequence (T2A') between the mito-TALEN and the fluorescent marker.

Animals

All animal procedures were performed according to NIH guidelines and approved by the Committee on Animal Care at Salk Institute. NZB/BALB heteroplasmic founder females were originally generated (Jenuth et al., 1996). NZB/BALB colony was maintained by breeding the females with BALB/cByJ males. Tail tip genotyping was routinely performed in order to exclude females carrying low levels of one of the two mtDNA haplotypes. BALB/c, BALB/cByJ and NZB mice were obtained from Jackson laboratory.

Cells, Transfection, and Sorting

Simian virus 40 (SV40) immortalized NZB/BALB fibroblasts containing NZB and BALB mtDNA were derived from tail tip of NZB/BALB mice. Human patient cells harboring the NARP m.9176T>C mutation were obtained by skin biopsy after signed informed consent of the donor and with the approval of the Institutional Review Board of the Hospital Clinic, Spain. Cells were immortalized using SV40 and cultured at 37 °C in DMEM (Invitrogen) containing GlutaMAX, non-essential amino acids and 10% fetal bovine serum (FBS). 143B osteosarcoma cybrid cells harboring the LHOND m.14459G>A mutation were obtained and cultured as previously described (Bacman et al., 2013). Cells were transfected with Lipofectamine 2000 (Invitrogen) according to the manufacturer's instructions. After 72 hr, cells were sorted using a BD Influx (Becton, Dickinson and Company) by gating on single-cell fluorescence using a 488-nm laser with a 505LP, 530/40 filter set for EGFP and a 561-nm laser with a 600LP, 610/20 filter set for mCherry. Total DNA was extracted from sorted cells using the DNeasy Blood and Tissue Kit (QIAGEN) following the protocol suggested by the manufacturer.

Single Strand Annealing Reporter Assay

Please refer to Extended Experimental Procedures.

Production of mRNA

In vitro transcription of mRNA was performed using mMACHINE T7 ULTRA kit (Life Technologies) according to the manufacturer's instructions using linearized and gel purified (QIAGEN) plasmid template. The mRNA was purified using MEGAclear kit (Life Technologies) and quantified using NanoDrop 8000 (Thermo Scientific).

Oocyte Collection and mRNA Injection

Female mice were superovulated with pregnant mares serum gonadotropin (PMSG) and human chorionic gonadotropin (hCG). MII oocytes were

collected 14 hr after hCG injection in M2 medium (Millipore) and freed of cumulus cells using hyaluronidase. For collection of 1-cell embryos, superovulated female mice were mated to BALB/c males and fertilized embryos were collected 18–20 hr after hCG injection from oviduct. mRNA (50–250 ng/ μ l) was injected into the cytoplasm of MII oocytes and fertilized embryos in M2 medium using Eppendorf micromanipulator. The injected MII oocytes were in vitro cultured in KSOM (Millipore) for 48 hr before analysis. The injected embryos were cultured in KSOM at 37°C under 5% CO₂ in air until blastocyst stage. Subsequently, blastocysts were collected for analysis or transferred to BALB/c pseudopregnant females. Live pups were obtained by natural delivery.

Cell Fusion

Cell fusion was achieved by using inactivated Sendai virus (GenomeOne, Cosmo Bio). Sendai virus stock solutions were prepared according to the manufacturer instructions and further diluted 1:20 in cell fusion buffer. The 143B osteosarcoma cybrid cells harboring LHON m.14459G>A mutation and patient cells harboring NARP m9176T>C mutation were used for fusion with mature MII oocytes. Cells were cultured for 48 hr in DMEM no glucose medium supplemented with galactose before using for cell fusion to increase mtDNA content. On the day of fusion, cells were trypsinized and re-suspended in M2 medium. For each MII oocyte, five cells briefly placed in Sendai virus were injected under the zona pellucida. After 3 hr successfully fused oocytes were selected for mito-TALEN mRNA injection. Lastly, surviving oocytes were cultured in KSOM for 48 hr before analysis.

Immunofluorescence

Cells were seeded on coverslips before transfection. Forty-eight hours after transfection cells were incubated in the presence of 350 nM Mitotracker (Invitrogen) for 30 min. Subsequently, cells were fixed and permeabilized with 4% PFA and 0.1% Triton X-100, respectively. After fixation, cells were blocked for 1 hr at room temperature with 1% BSA/PBS. Next, cells were incubated with an anti-Flag M2 primary antibody (Sigma) or anti-HA antibody (Millipore) overnight at 4°C. The next day, cells were washed three times with PBS and incubated for 1 hr at room temperature with Alexa Fluor 488-conjugated donkey antibodies to goat IgG (Molecular Probes) or Alexa Fluor 647-conjugated donkey antibodies to mouse IgG and 10 min with Hoechst 33342 (0.5 μ g ml⁻¹ in PBS) (Invitrogen). Finally, cells were washed three times with PBS and mounted using Fluoromount-G (Southernbiotech). Confocal image acquisition was performed using a Zeiss LSM 780 laser-scanning microscope (Carl Zeiss Jena).

“Last-Cycle Hot” PCR and RFLP

Total DNA from cells, tail biopsies, and oocytes/embryos were used to determine mtDNA heteroplasmy by “Last-cycle hot” PCR using the mtDNA 5' Fluorescein amidite (FAM) labeled primers as listed in Table S2. NZB/BALB PCR products were digested with ApaI or HindIII, which digests BALB mtDNA at positions 5461 (ApaI targeting site) and 9136 respectively. NARP PCR products were digested with BsrI which digest mutated NARP mtDNA at position 9176. The levels of LHON m.14459G>A were determined as previously reported (Bacman et al., 2013). Digested PCR products were subjected to electrophoresis in a 12% polyacrylamide gel. The fluorescein signal was quantified using a Typhoon 8600 system (Molecular Dynamics) and gels were quantified using ImageQuant 5.2 (Molecular Dynamics).

Quantification of mtDNA Copy Number

Absolute mtDNA copy numbers were quantified by real-time PCR using iQSyber Green on Bio-Rad iCycler (Bio-Rad). Individual oocytes and embryos were transferred into lysis buffer (200 mM KOH) and incubated for 10 min at 65°C. The reaction was neutralized by addition of 200 mM HCl. Absolute mtDNA copy number per 1 μ l of lysate was calculated using a standard curve derived from the Q-PCR amplification of a fragment of mtDNA genome. First, a standard curve was generated by a 10-fold serial dilution of a PCR product obtained using Standard curve primers for the different regions of mtDNA analyzed. Subsequently, to quantify the absolute levels of mtDNA, quantitative real-time PCR was performed using qPCR primers listed in Table S2.

Blood and Plasma Parameters

Blood collection was performed by sub-mandibular bleeding. Whole EDTA blood samples were analyzed in duplicates for Complete Blood Count (CBC) on a Hemavet 950FS Multi Species Hematology System (Drew Scientific). Plasma glucose concentration was determined using the Glucose (GO) Assay Kit (Sigma) according to the manufacturer's instructions. Plasma lactate concentration was determined using the Lactate Assay Kit (Sigma) according to the manufacturer's instructions. Please refer to Extended Experimental Procedures.

Behavioral Analysis

Behavioral testing was carried out at the Salk Institute for Biological Studies Behavioral Testing Core. Basic sensorimotor function was assessed in the Open Field Test, Rotarod, Grip Strength, and Neurological Screen. Please refer to Extended Experimental Procedures.

Array Comparative Genomic Hybridization

aCGH was performed following Agilent Oligonucleotide Array-Based CGH for Genomic DNA Analysis (Agilent Technologies, Santa Clara, CA). Please refer to Extended Experimental Procedures.

Exome Capture and High-Throughput Sequencing

Exome capture was using the SeqCap EZ Mouse Exome Design probe pool (54 Mb, NimbleGen) according to the manufacturer's protocol. Please refer to Extended Experimental Procedures.

Statistical Evaluation

Statistical analyses were performed by using standard unpaired Student's *t* test with Welch's correction using Prism 6 software (GraphPad). All data are presented as mean \pm SEM and represent a minimum of two independent experiments. Statistical significance is displayed as **p* < 0.05, ***p* < 0.01, ****p* < 0.001, and *****p* < 0.0001.

ACCESSION NUMBERS

The GEO database accession number for the aCGH data sets reported in this paper is GSE67371. The GEO accession number for the exome sequencing data sets reported in this paper is SRP056327.

SUPPLEMENTAL INFORMATION

Supplemental Information includes Extended Experimental Procedures, six figures, and two tables and can be found with this article online at <http://dx.doi.org/10.1016/j.cell.2015.03.051>.

AUTHORS CONTRIBUTIONS

P.R., A.O., C.T.M., and J.C.I.B. designed all experiments. P.R., A.O., I.S.-M., and J.C.I.B. prepared the figures and wrote the manuscript. P.R., A.O., K.S., S.R.B., Y.T., J.W., D.L., X.X., N.M., and C.R.E., performed and analyzed all in vitro experiments. P.R., A.O., J.L., A.S., and D.O. performed and analyzed all in vivo experiments. S.R.B., S.L.W., G.H.L., D.M., S.C., M.d.M.O'., H.Z., and C.T.M. provided reagents. F.C., J.C., and J.M.C. contributed to the design of the project.

ACKNOWLEDGMENTS

We thank M. Schwarz for administrative support. We thank S. Heinz and M.M. Ku from H.A. and Mary K. Chapman Charitable Foundations Genomic Sequencing Core at the Salk Institute for help with sequencing analysis. We thank M. Chang from the Integrative Genomics and Bioinformatics Core at the Salk Institute for sequencing data analysis. We thank C.B. Farrokhi from the Behavioral Testing Core at the Salk Institute for help with behavioral studies. We thank Eric Shoubridge from McGill University, Montreal, Canada for sharing with us the NZB/BALB/c heteroplasmic mice. We thank Julio Montoya Villarroya from the University of Zaragoza, Zaragoza, Spain, and M^o Ángeles Ruiz Gómez from the Hospital de Son Espases, Palma de Mallorca,

Spain. Financial support: M.M. Ku and S. Heinz are supported by the Leona M. and Harry B. Helmsley Charitable Trust. A.O. was partially supported by an NIH Ruth L. Kirschstein National Research Service Award Individual Postdoctoral Fellowship. G.-H.L. was supported by National Basic Research Program of China (973 Program, 2015CB964800; 2014CB964600), the Strategic Priority Research Program of the Chinese Academy of Sciences (XDA01020312), National Natural Science Foundation of China (NSFC: 81271266; 31222039; 31201111; 81371342). C.T.M. was supported by NIH grants 5R01EY010804, 1R01AG036871, the JDM Fund, the Muscular Dystrophy Association and the United Mitochondrial Disease Foundation. S.L.W. is supported by Florida Department of Health Grant 3KN09. Work in the laboratory of J.C.I.B. was supported by the G. Harold and Leila Y. Mathers Charitable Foundation and the Leona M. and Harry B. Helmsley Charitable Trust (2012-PG-MED002).

Received: February 2, 2015

Revised: March 5, 2015

Accepted: March 25, 2015

Published: April 23, 2015

REFERENCES

- Alexeyev, M.F., Venediktova, N., Pastukh, V., Shokolenko, I., Bonilla, G., and Wilson, G.L. (2008). Selective elimination of mutant mitochondrial genomes as therapeutic strategy for the treatment of NARP and MILS syndromes. *Gene Ther.* *15*, 516–523.
- Alexeyev, M., Shokolenko, I., Wilson, G., and LeDoux, S. (2013). The maintenance of mitochondrial DNA integrity—critical analysis and update. *Cold Spring Harb. Perspect. Biol.* *5*, a012641–a012641.
- Anderson, S., Bankier, A.T., Barrell, B.G., de Bruijn, M.H., Coulson, A.R., Drouin, J., Eperon, I.C., Nierlich, D.P., Roe, B.A., Sanger, F., et al. (1981). Sequence and organization of the human mitochondrial genome. *Nature* *290*, 457–465.
- Bacman, S.R., Williams, S.L., Garcia, S., and Moraes, C.T. (2010). Organ-specific shifts in mtDNA heteroplasmy following systemic delivery of a mitochondria-targeted restriction endonuclease. *Gene Ther.* *17*, 713–720.
- Bacman, S.R., Williams, S.L., Duan, D., and Moraes, C.T. (2012). Manipulation of mtDNA heteroplasmy in all striated muscles of newborn mice by AAV9-mediated delivery of a mitochondria-targeted restriction endonuclease. *Gene Ther.* *19*, 1101–1106.
- Bacman, S.R., Williams, S.L., Pinto, M., Peralta, S., and Moraes, C.T. (2013). Specific elimination of mutant mitochondrial genomes in patient-derived cells by mitoTALENs. *Nat. Med.* *19*, 1111–1113.
- Brown, D.T., Herbert, M., Lamb, V.K., Chinnery, P.F., Taylor, R.W., Lightowlers, R.N., Craven, L., Cree, L., Gardner, J.L., and Turnbull, D.M. (2006). Transmission of mitochondrial DNA disorders: possibilities for the future. *Lancet* *368*, 87–89.
- Chinnery, P.F., Thorburn, D.R., Samuels, D.C., White, S.L., Dahl, H.M., Turnbull, D.M., Lightowlers, R.N., and Howell, N. (2000). The inheritance of mitochondrial DNA heteroplasmy: random drift, selection or both? *Trends Genet.* *16*, 500–505.
- Christian, M., Cermak, T., Doyle, E.L., Schmidt, C., Zhang, F., Hummel, A., Bogdanove, A.J., and Voytas, D.F. (2010). Targeting DNA double-strand breaks with TAL effector nucleases. *Genetics* *186*, 757–761.
- Craven, L., Tuppen, H.A., Greggains, G.D., Harbottle, S.J., Murphy, J.L., Cree, L.M., Murdoch, A.P., Chinnery, P.F., Taylor, R.W., Lightowlers, R.N., et al. (2010). Pronuclear transfer in human embryos to prevent transmission of mitochondrial DNA disease. *Nature* *465*, 82–85.
- Cree, L.M., Samuels, D.C., and Chinnery, P.F. (2009). The inheritance of pathogenic mitochondrial DNA mutations. *Biochim. Biophys. Acta* *1792*, 1097–1102.
- Dyall, S.D., Brown, M.T., and Johnson, P.J. (2004). Ancient invasions: from endosymbionts to organelles. *Science* *304*, 253–257.
- Gammage, P.A., Rorbach, J., Vincent, A.I., Rebar, E.J., and Minczuk, M. (2014). Mitochondrially targeted ZFNs for selective degradation of pathogenic mitochondrial genomes bearing large-scale deletions or point mutations. *EMBO Mol. Med.* *6*, 458–466.
- Haas, R.H., Parikh, S., Falk, M.J., Saneto, R.P., Wolf, N.I., Darin, N., and Cohen, B.H. (2007). Mitochondrial disease: a practical approach for primary care physicians. *Pediatrics* *120*, 1326–1333.
- Hayden, E.C. (2013). Regulators weigh benefits of ‘three-parent’ fertilization. *Nature* *502*, 284–285.
- Jenuth, J.P., Peterson, A.C., Fu, K., and Shoubridge, E.A. (1996). Random genetic drift in the female germline explains the rapid segregation of mammalian mitochondrial DNA. *Nat. Genet.* *14*, 146–151.
- Jun, A.S., Brown, M.D., and Wallace, D.C. (1994). A mitochondrial DNA mutation at nucleotide pair 14459 of the NADH dehydrogenase subunit 6 gene associated with maternally inherited Leber hereditary optic neuropathy and dystonia. *Proc. Natl. Acad. Sci. USA* *91*, 6206–6210.
- Marc, P., Margeot, A., Devaux, F., Blugeon, C., Corral-Debrinski, M., and Jacq, C. (2002). Genome-wide analysis of mRNAs targeted to yeast mitochondria. *EMBO Rep.* *3*, 159–164.
- Minczuk, M., Papworth, M.A., Kolasinska, P., Murphy, M.P., and Klug, A. (2006). Sequence-specific modification of mitochondrial DNA using a chimeric zinc finger methylase. *Proc. Natl. Acad. Sci. USA* *103*, 19689–19694.
- Minczuk, M., Papworth, M.A., Miller, J.C., Murphy, M.P., and Klug, A. (2008). Development of a single-chain, quasi-dimeric zinc-finger nuclease for the selective degradation of mutated human mitochondrial DNA. *Nucleic Acids Res.* *36*, 3926–3938.
- Paull, D., Emmanuele, V., Weiss, K.A., Treff, N., Stewart, L., Hua, H., Zimmer, M., Kahler, D.J., Golland, R.S., Noggle, S.A., et al. (2013). Nuclear genome transfer in human oocytes eliminates mitochondrial DNA variants. *Nature* *493*, 632–637.
- Reinhardt, K., Dowling, D.K., and Morrow, E.H. (2013). Medicine. Mitochondrial replacement, evolution, and the clinic. *Science* *341*, 1345–1346.
- Rogers, D.C., Fisher, E.M., Brown, S.D., Peters, J., Hunter, A.J., and Martin, J.E. (1997). Behavioral and functional analysis of mouse phenotype: SHIRPA, a proposed protocol for comprehensive phenotype assessment. *Mamm. Genome* *8*, 711–713.
- Ross, J.M., Stewart, J.B., Hagström, E., Brené, S., Mourier, A., Coppotelli, G., Freyer, C., Lagouge, M., Hoffer, B.J., Olson, L., and Larsson, N.G. (2013). Germline mitochondrial DNA mutations aggravate ageing and can impair brain development. *Nature* *501*, 412–415.
- Russell, O., and Turnbull, D. (2014). Mitochondrial DNA disease—molecular insights and potential routes to a cure. *Exp. Cell Res.* *325*, 38–43.
- Sanjana, N.E., Cong, L., Zhou, Y., Cunniff, M.M., Feng, G., and Zhang, F. (2012). A transcription activator-like effector toolbox for genome engineering. *Nat. Protoc.* *7*, 171–192.
- Shoubridge, E.A., and Wai, T. (2007). Mitochondrial DNA and the mammalian oocyte. *Curr. Top. Dev. Biol.* *77*, 87–111.
- Tachibana, M., Amato, P., Sparman, M., Woodward, J., Sanchis, D.M., Ma, H., Gutierrez, N.M., Tippner-Hedges, R., Kang, E., Lee, H.-S., et al. (2013). Towards germline gene therapy of inherited mitochondrial diseases. *Nature* *493*, 627–631.
- Taylor, R.W., and Turnbull, D.M. (2005). Mitochondrial DNA mutations in human disease. *Nat. Rev. Genet.* *6*, 389–402.
- Vogel, G. (2014). Assisted reproduction. FDA considers trials of ‘three-parent embryos’. *Science* *343*, 827–828.
- Wai, T., Ao, A., Zhang, X., Cyr, D., Dufort, D., and Shoubridge, E.A. (2010). The role of mitochondrial DNA copy number in mammalian fertility. *Biol. Reprod.* *83*, 52–62.
- Wallace, D.C., and Chalkia, D. (2013). Mitochondrial DNA genetics and the heteroplasmy conundrum in evolution and disease. *Cold Spring Harb. Perspect. Biol.* *5*, a021220.
- Wang, T., Sha, H., Ji, D., Zhang, H.L., Chen, D., Cao, Y., and Zhu, J. (2014). Polar body genome transfer for preventing the transmission of inherited mitochondrial diseases. *Cell* *157*, 1591–1604.

Inspire your peers with Cell Reports



Breaking new ground? From molecular genetics to developmental neurobiology, *Cell Reports* publishes thought-provoking, cutting edge research spanning the spectrum of life sciences.

Cell Reports is an open access journal that offers the quality, rigor, and visibility you've come to expect from Cell Press.

Do you have a new biological insight? Submit your paper to *Cell Reports*.

For more information visit www.cell.com/cell-reports

An open access journal with impact.
From Cell Press.

**Cell
Reports**

Recycling plastic is fantastic!

Rainin TerraRack
reduces tip rack waste.

Request your free
sample today!

► mt.com/rainin-tr



RAININ

Because the future is in your hands™

We make really good antibodies.
Not really good ads.

For really good antibodies, visit bethyl.com/trialsize

